Numerical Simulation of Turbulent Mixing Caused by Internal Wave Reflection from Sloping Boundaries

by

Donald N. Slinn

A dissertation submitted in partial fulfillment
of the requirements for the degree of

Doctor of Philosophy

University of Washington

1995

Approved by_____
(Chairperson of Supervisory Committee)

Program Authorized
to Offer Degree_____

Date_____

In presenting this dissertation in partial fulfillment of the requirements for the Doctoral degree at the University of Washington, I agree that the Library shall make its copies freely available for inspection. I further agree that extensive copying of this dissertation is allowable only for scholarly purposes, consistent with "fair use" as prescribed in the U.S. Copyright Law. Requests for copying or reproduction of this dissertation may be referred to University Microfilms, 1490 Eisenhower Place, P.O. Box 975, Ann Arbor, MI 48106, to whom the author has granted "the right to reproduce and sell (a) copies of the manuscript in microform and/or (b) printed copies of the manuscript made from microform."

Signature_____

Date_____

University of Washington

Abstract

Numerical Simulation of Turbulent Mixing Caused by Internal Wave Reflection from Sloping Boundaries

by Donald N. Slinn

Chairperson of Supervisory Committee: *Professor James J. Riley*

Department of Mechanical Engineering

When an internal gravity wave reflects from a sloping boundary, its energy density and amplitude may increase significantly, especially if the angle of propagation of the wave matches the bottom slope. The reflection can result in wave breakdown into a turbulent boundary layer. The process is thought to make a large contribution to diapycnal mixing in the ocean.

Internal wave reflection from sloping boundaries is examined using a high-resolution, three-dimensional numerical model using state-of-the-art numerics developed for this study. Of particular interest is a new method for generating a monochromatic oncoming train of internal gravity waves of specified wavelength and frequency.

Results indicate that the type of turbulent layer that develops is a function of the slope of the bottom, the angle of wave propagation, as well as the Reynolds and Richardson number of the waves. For steep slopes the flow develops into a quasi-steady turbulent bore that moves through the boundary layer at the phase speed of the incident waves. For shallow slopes the boundary layer exhibits intermittent turbulence, where approximately every 1.3 wave periods the boundary layer mixes energetically and then restratifies until the next mixing cycle.

A new exact solution to the Navier-Stokes equations is used to examine features of mixing for a viscously decaying plane internal gravity wave. Simulations demonstrate that the net effects of turbulent mixing are not confined to the boundary layer but are communicated to the interior stratified fluid by the motions induced by the incident

waves, resulting in progressive weakening of the background density gradient and the production of mean currents.

Transition to turbulence is determined to be a function of Richardson number and the bottom slope and occurs for Reynolds numbers of approximately 500 for steep bottom slopes and 1500 for shallow slopes. The boundary layer thickness depends almost linearly on the Reynolds number or wave amplitude for low Richardson numbers, with a maximum depth of approximately one half of the vertical wavelength.

TABLE OF CONTENTS

LIST OF FIGURES

LIST OF TABLES

ACKNOWLEDGMENTS

The author would like to express sincere appreciation to Prof. James Riley for encouragement, direction, patience, and support in researching this work. In addition, thanks to Dr. George Slinn, my father, for guiding me into his field of study and for preparing me to be successful. And most of all, thanks are due to my wife, Tara, who has worked together with me towards common goals. Support for this work was received from the Office of Naval Research and the NSF National Center for Supercomputer Applications.

Chapter 1

INTRODUCTION

Fluid flows are strongly influenced by their boundaries. This is true for both small-scale flows of engineering interest and large-scale geophysical flows. In this study we examine certain, strong fluid-boundary interactions that occur in stratified fluids. The specific problem chosen for study is relevant to the fundamental problem of transition of laminar flows to turbulence. The flow is investigated using computational fluid dynamics.

Although the problem is one of basic research interest, the study is also motivated by practical applications: improved understanding of vertical mixing in the ocean is important in physical, chemical, and biological oceanography. Large-scale dynamic models of the ocean require accurate parameterizations for turbulent mixing to make realistic predictions for the transport of heat, salt, and chemical species. Vertical mixing within the ocean's ecosystem supplies necessary ingredients, e.g., when heavy, nutrient rich bottom water is lifted to the surface to support plant and animal life.

Within the ocean, vertical mixing is inhibited by its stable stratification. Munk (1966) has show that a basin-averaged vertical eddy diffusivity of roughly $\kappa_v = 10^{-4}$ m^2/s must exist to balance the effects of upwelling and downward turbulent diffusion. Field studies, however, have failed to observe such large vertical diffusivities in the ocean interior: measured values for vertical diffusivity in the open ocean are roughly $\kappa_v = 1.2 \times 10^{-5}$ m^2/s (Ledwell et al., 1993). The conclusion from the experiments is that 80-90% of the vertical mixing is not taking place in the ocean interior.

Instead, the mixing is expected to occur at boundaries (near continental slopes, islands, seamounts, and other topographic features). The idealized picture is one of active mixing in the benthic boundary layers with mixed fluid communicated to the

interior along constant density surfaces. The exchange of mixed boundary fluid with interior stratified fluid provides a mechanism to weaken the interior density gradient and continuously supply fresh stratified fluid to be mixed in the boundary layer. The overall process can work efficiently since horizontal advection is not inhibited by the surrounding stratification. Gargett (1984) has reviewed estimates of horizontal eddy diffusivities and found them to be in the range of $10^2 \mathrm{m}^2/\mathrm{s} < \kappa_H < 10^3 \mathrm{m}^2/\mathrm{s}$, roughly seven orders of magnitude larger than vertical diffusivities for large- and meso-scale motions. Armi (1978) suggested that the energy source for the turbulent boundary layer could come from meso-scale currents and eddies, but this suggestion was disputed by Garrett (1979) on the grounds that the currents contain insufficient energy or shear.

Recent field experiments (Eriksen, 1985, 1995) have suggested that the oceanic internal wave field can provide sufficient energy to activate strong mixing near sloping boundaries and account for a significant portion of the overall oceanic vertical mixing. One mechanism by which this may occur is the breaking of internal gravity waves as they reflect off the continental shelf or other sloping boundaries near islands or seamounts.

This thesis presents the results of numerical experiments simulating the reflection of internal waves from bottom terrain of various slopes. The numerical experiments complement previous field and laboratory studies with the ability to address the energetics and turbulence dynamics in detail. Additional strengths of the numerical approach include facilitating both flow visualization and also parametric studies of influences from key physical and nondimensional quantities. The numerical approach permits investigation of important aspects of internal wave reflection that are not yet possible in laboratory experiments. For example, it offers the ability to simulate critical angle reflection for shallow slopes down to about 3 degrees, which are typical of oceanic conditions (Thorpe, 1992).

1.1 Problem Description

Many dynamical properties of internal gravity waves are well understood and accurately described by linear theory. When an internal wave of frequency ω propagating in a uniformly stratified environment reflects from a larger-scale sloping boundary, its angle of propagation with respect to the horizontal, θ, is preserved (Phillips, 1977). This angle between the group velocity vector (or the angle of wave propagation) and the horizontal depends upon the wave frequency, ω, and the background density stratification according to the dispersion relation $\omega = N \sin\theta$, where N is the buoyancy frequency defined by $N^2 = (-g/\rho_o)(\partial\rho/\partial z)$. This reflection from a sloping boundary can lead to an increase in the energy density of the reflected wave, as the energy in the oncoming wave is concentrated into a more narrow ray tube upon reflection, and possibly to wave breaking and turbulence, especially if the propagation angle is close to the angle of slope of the boundary.

Figure 1.1 shows the wave reflection process using a ray-tube diagram from linear theory and illustrates the basic problem geometry. In Figure 1.1 α is the angle that the sloping boundary makes with the horizontal, g is the direction of gravity, the x' direction is alongslope, and the z' direction is perpendicular to the sloping boundary. (Note that Appendix C contains a complete list of symbols used). The narrowing of the ray-tube in Figure 1.1 indicates compression of the energy density in the reflected wave. The associated increase in wave amplitude is suggested by the larger amplitude sine wave associated with the reflected ray-tube.

The situation probably most effective for boundary mixing arises when an oncoming wave reflects from a bottom slope that nearly matches the angle of wave propagation. In this case a small amplitude oncoming wave may be reflected with large amplitude and exhibit nonlinear behavior. This nonlinearity can cause the wave to become turbulent near the boundary and enhance mixing of the boundary layer fluid. The angle of wave propagation such that the wave reflects at the same angle as the bottom slope is called the critical angle, e.g., for $\alpha = \theta$. In this case linear wave theory predicts a reflected wave of infinite amplitude and infinitesimal wave-

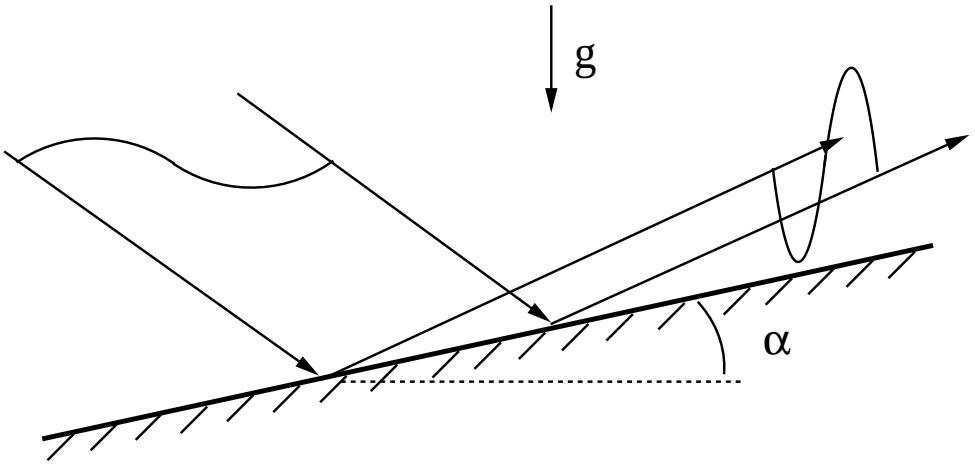

Figure 1.1: Ray tube reflection diagram for internal gravity waves reflecting from a sloping boundary using linear theory analysis.

length and the trapping of oncoming wave energy in the boundary region. In such a case linear theory is inadequate to predict the flow behavior, as nonlinearities and turbulence must come into play.

The flux of reflected energy from the slope is adjusted in two ways. The wave energy is transferred to shorter wavelength (higher wavenumber) and the group velocity also decreases. Figure 1.2 shows the magnitude of the group velocity of a reflected wave normalized by the magnitude of the oncoming wave for wave reflection from a 20^o bottom slope. Here, positive values indicate the reflected wave continues to move downward, that is, in the same direction as the oncoming wave, and negative values mean that the reflected wave is propagating upward, e.g., in the opposite direction of the oncoming wave. The horizontal axis is the angle between the horizontal direction and the angle of propagation of the group velocity. Near the critical angle (20^o) the flux of energy away from the wall approaches zero. The ratio of energy density of the reflected and incident waves is given by

$$E_r/E_i = (m_r/m_i)^2 \,, \tag{1.1}$$

where m_r and m_i are the vertical wavenumbers of the reflected and incident waves.

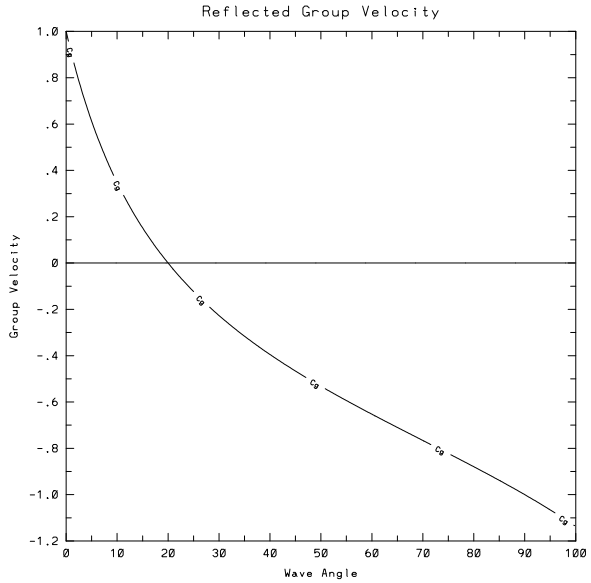

Figure 1.2: Group velocity of a reflected wave near the critical angle.

The energy density increases by the square of the wavenumber because it must adjust for decreases in both the ray tube width and the group velocity.

This chapter will discuss results of work by previous researchers related to this problem, outline the emphasis of this thesis study, and introduce the methods of analysis to be used in the investigation.

1.2 Historical Perspective

Internal gravity waves and turbulence in a stratified fluid have been the subject of detailed study. Turner's (1973) book, *Buoyancy effects in fluids,* provides an introduction to the subject, covering both engineering and ocean-atmosphere applications. Recent reviews of internal waves research in oceanography have been written by Garrett and Munk (1979), Olbers (1983), and Müller et al. (1986). Several important aspects of the boundary reflection problem have been addressed in the scientific literature. Understanding has been gained by studies using a variety of approaches, including field measurements in the ocean, laboratory experiments with stratified

fluids, and mathematical analysis using linear theory.

1.2.1 Boundary Mixing in a Stratified Fluid

Vertical Mixing

Recent reviews of turbulent mixing in a stratified fluid have been written by Gregg (1987), Hopfinger (1987), and Thorpe (1987). Key concepts related to the present investigation are discussed briefly below.

Thorpe (1982) has studied the layered structure produced in the laboratory by turbulence generated by a rapidly oscillating vertical grid in a uniformly stratified fluid. He has identified stratified intrusion layers, which bridge the turbulent and laminar zones of the flow. He demonstrated that the horizontal length scales of the intrusions scale with the intensity of the turbulence. He has also found that the vertical stirring used to force the turbulence does not alter the mean background density gradient in the turbulent zone. This, however, is not the case in experiments with horizontal or inclined forcing. Figure 1.3 shows how intrusion layers achieve horizontal mixing by exchanging intermediate-density mixed fluid with interior stratified fluid.

In a related experiment Ivey and Corcos (1982) used an oscillating grid to simulate boundary mixing in a rectangular tank. The turbulence was generated by a oscillating grid near a side wall in stratified fluid. The laboratory measurements indicated that the turbulence was confined to a thin boundary region. Eventually a well mixed region of constant density was produced near the boundary and drove intrusions into the laminar interior fluid.

Ivey (1987b) has extended his results to include the effects of rotation, by carrying out an axisymmetric version of his earlier (1982) experiments. He found that rotation did not play a significant role in the vertical mixing process. The effects of rotation were limited to changing the time scales associated with horizontal density gradients.

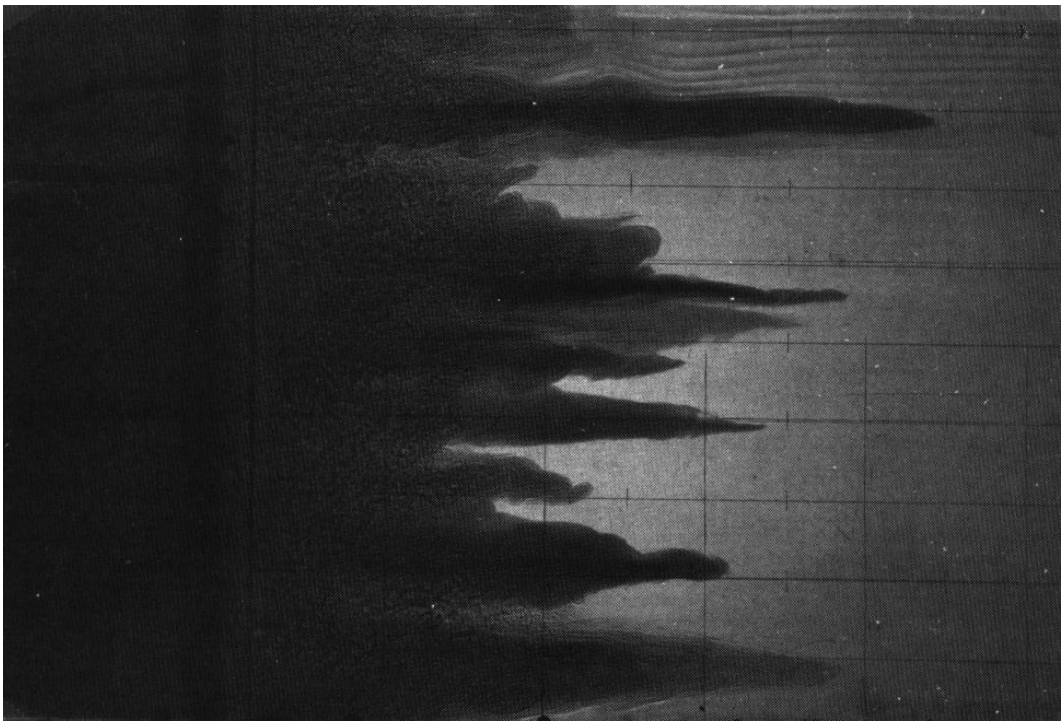

Figure 1.3: Intrusions of intermediate-density fluid from the boundary mixed layer work their way into the interior stratified fluid and are visualized by dye injected into the boundary layer. Taken from Hopfinger (1987).

Boundary Mixing

Munk (1966) suggests boundary mixing as a likely source of vertical mixing in the ocean. A strong localized source of vertical mixing is required to reconcile field measurements of diffusivities with basin averages quantities required to maintain the observed vertical profiles of salt and chemical species. Canonical estimates of vertical diffusivities are approximately $\kappa_v = 10^{-4}\mathrm{m}^2/\mathrm{s}$. Munk concludes that laminar processes contribute less than 1 % to the total mixing. He proposes that strong mixing occurs in the oceanic boundary layer, of order 50–500 meters thick, due to current shear and internal wave breaking near topographic features. The localized mixing could then be enhanced by the mixed fluid being carried to the interior along constant density surfaces. He expresses doubt that any substantial progress can be made beyond presenting recipes fitting experimental data until the processes of turbulent advection and mixing are understood.

Garrett (1991a) points out that many features of the oceanic internal wave field are inconsistent with a diapycnal diffusivity of more than $10^{-5}\mathrm{m}^2/\mathrm{s}$ in the interior thermocline. Recent field experiments by Ledwell et al. (1993) confirm these predictions. Thus, it is likely that a major portion of vertical mixing must be associated with events in either the surface or bottom boundary layers in order to obtain the canonical basin averaged value of $10^{-4}\mathrm{m}^2/\mathrm{s}$. Mixing in the surface layer however is inhibited from exchanging fluid with the interior ocean by the presence of a strongly stratified pycnocline just below the surface mixed layer. The emphasis, therefore, must be on the benthic (bottom) boundary layer that, because of sloping boundaries, can exchange mixed fluid horizontally with the interior stratified ocean at all ocean depths. Garrett emphasizes the need for additional observational work to address mixing in the bottom boundary layer by internal wave breaking near a slope. He theorizes that if the mixing due to internal wave reflection is restricted to a relatively thin mixed layer, δ_{mixed}, and the exchange of boundary fluid with the interior stratified fluid occurs on a slow time scale driven by buoyancy forces, then boundary mixing makes little contribution to the basin averaged quantity. If, however, the mixing extends beyond δ_{mixed}, and there is a strong exchange of mixed and stratified fluid,

then buoyancy forces can be effective at restratifying the mixed fluid and provide a continuous source for diapycnal mixing. Garrett agrees with Gregg's (1987) suggestion that vertical mixing in the thermocline may be a relatively unimportant process compared to mixing and fluid exchange with the boundary regions. In addition, he points out that the boundary mixing process may set up a "slippery boundary layer" (MacCready et al., 1992) for low frequency flows and may be important in establishing the optimum velocity boundary conditions for ocean modeling. Analysis by Hirst (1991) has shown that a significant portion of oceanic internal wave energy penetrates deeply into the ocean and is likely to reflect from the bottom topography.

Buoyancy Induced Boundary Layers

Boundary mixing in a stratified fluid is complicated by other physical phenomena that occur in the vicinity of boundaries. For example, boundary layers may be caused by mean currents in the interior flow or induced by buoyancy forces near the boundary, and these may complicate interactions and their interpretations.

Phillips (1970) studies boundary currents induced by diffusion near a sloping bottom in a stably stratified fluid subject to a no-flux boundary condition on the density field. The no-flux condition is analogous to an adiabatic boundary in a temperature-stratified fluid or a no-source or sink condition in a salt-stratified fluid. Phillips finds a steady-state, laminar solution in which diffusion is balanced by upslope convection. Figure 1.4 shows the total density contours in the near-wall region for the steady flow and Figure 1.5 illustrates the velocity and density perturbation contours.

The steady solution in terms of nondimensional variables used below (see Section 2.2) is

$$\rho(z) = \frac{-e^{-\gamma z}\,\cos\gamma z}{\gamma}\,, \tag{1.2}$$

$$u(z) = \frac{2\gamma\, e^{-\gamma z}\,\sin\gamma z}{\sin\alpha\; Pr\; Re}\,, \tag{1.3}$$

$$w(z) = v(z) = 0 \tag{1.4}$$

where $\gamma = \left(\dfrac{Ri\; Pr\; Re^2\;\sin^2\alpha}{4}\right)^{1/4}$. Phillips also demonstrates the steady solution in laboratory experiments using salt-stratified water and predicted that, for some ranges

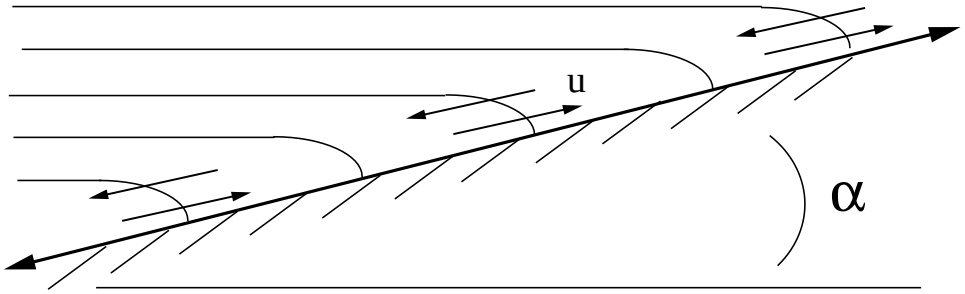

Figure 1.4: Isopycnals near a sloping boundary with an adiabatic boundary condition showing secondary currents generated for a constant interior stratification.

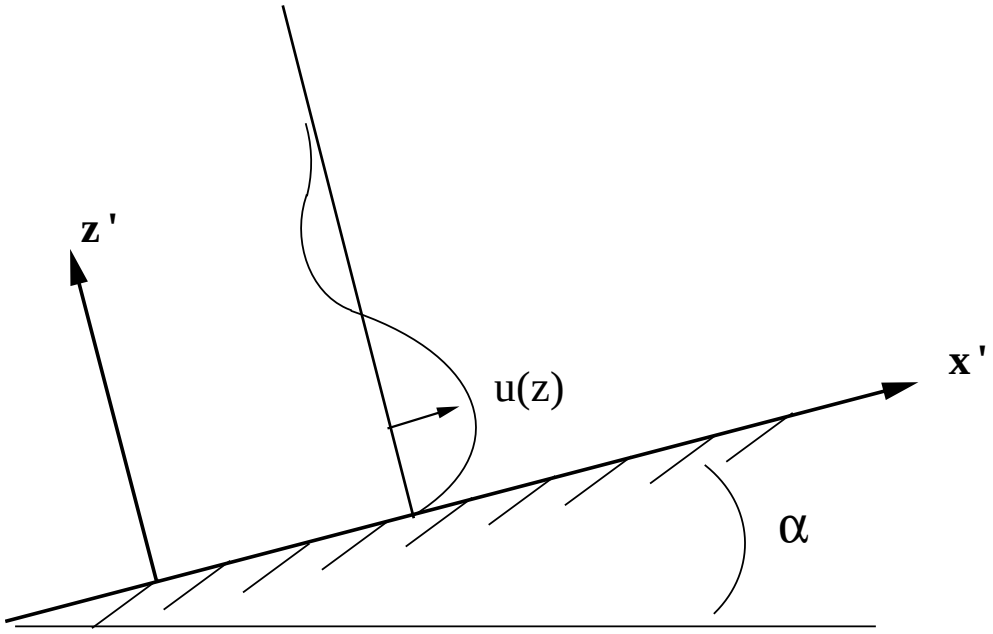

Figure 1.5: Alongslope velocity profiles to maintain steady-state buoyancy boundary currents.

of slope, length scales, and diffusivities, the motion could spontaneously become turbulent.

Wunsch (1970) also investigates the boundary layer caused by buoyancy forces with an adiabatic boundary condition applied to a sloping ocean floor. He independently derives the same result as Phillips (1970) and includes the effects of rotation. He estimates that the thickness of the buoyancy layer is $\delta \approx (\nu\kappa_v)^{1/4}/N^{1/2}$, where ν and κ_v are to be interpreted as eddy diffusivities, and N is the buoyancy frequency. He considers all estimates to be unreliable to some extent, but typical ocean parameters might yield estimates for δ anywhere between 20 cm and 20 meters.

Garrett (1990) again draws attention to the role of vertical mixing at sloping boundaries by studying the role of secondary circulations. He extends Phillips (1970) result by including the effects of rotation, free- or no-slip boundary conditions, and depth-dependent eddy diffusivities. He raises the question of whether the secondary circulation is able to restratify mixed water in the boundary region, which could increase the effectiveness of boundary mixing. He suggests that a fundamental question yet to be answered is whether turbulence persists to the same degree above a sloping bottom as above a flat bottom, or whether it is suppressed by restratification. In addition, he estimates that near-boundary mixing caused by internal wave breakdown is effective because the stratification is continuously restored by the secondary circulation.

1.2.2 Internal Wave Reflection from Sloping Boundaries

Field Studies

Considerable work has been done in the laboratory and by field measurement to determine the importance of internal wave breakdown over sloping boundaries. Observations of the oceanic internal wave field near sloping bottom topography by Eriksen (1982) draw attention to the probable role of wave breakdown and mixing in the bottom boundary layer. Measurements taken near three sites indicate that the nearly universal oceanic internal wave field, the Garrett-Munk (GM) spectrum, is strongly modified within 100 m of the bottom over sloping terrain. Eriksen demon-

strates that the observations of spectral enhancement are centered about the critical frequency associated with the bottom slope and occur over the breadth of frequency range expected from linear theory. However, the observed amplitudes of the reflected waves were much smaller than linear theory predicts. He attributed the differences to frictional dissipation near the boundary and to highly nonlinear interactions. Eriksen finds evidence of wave breaking caused by shear instability near the bottom and concludes that the sloping terrain is a likely sink for internal wave energy, and contributes significantly to vertical mixing in the ocean. In an earlier paper, Eriksen (1978) attempts to determine whether the dominant instability of breaking gravity waves is caused by shear (Kelvin-Helmholtz), convective, or static buoyancy induced instabilities. It is still an open question as to how the waves transition to turbulence.

In a follow up study, Eriksen (1995) measures frequent density overturns of stratified fluid in the boundary layer region over the flank of a seamount with a slope of about 24 degrees. The density overturns indicate that turbulent mixing is occurring in the bottom boundary layer. The current and temperature spectra differ from background Garrett-Munk spectra in a narrow frequency band associated with internal wave reflection at the frequency corresponding to the bottom slope, indicating that critical angle wave reflection is a dominant process. Eriksen finds that the local vertical eddy diffusivity is in the range of $1.6 - 6.4 \times 10^{-4}$ m^2/s, approximately two orders of magnitude higher than found in the open ocean. He also suggests that if only 1–5% of the energy in the oceanic internal wave field went into mixing boundary fluid by this process, it would provide sufficient energy to account for all of the mixing required in the ocean to maintain the steady vertical profiles in Munk's (1966) analysis.

Figure 1.6 shows internal wave spectra from Eriksen's seamount observations at several different heights from the bottom of the ocean. At 20 meters from the bottom there is a strong signal at a frequency of 0.5 cph, the critical frequency associated with the local bottom slope. The enhancement of energy in this frequency band is indicative of strong amplification of the reflected waves near the critical frequency. As the distance from the bottom increases the spectra relax towards the background

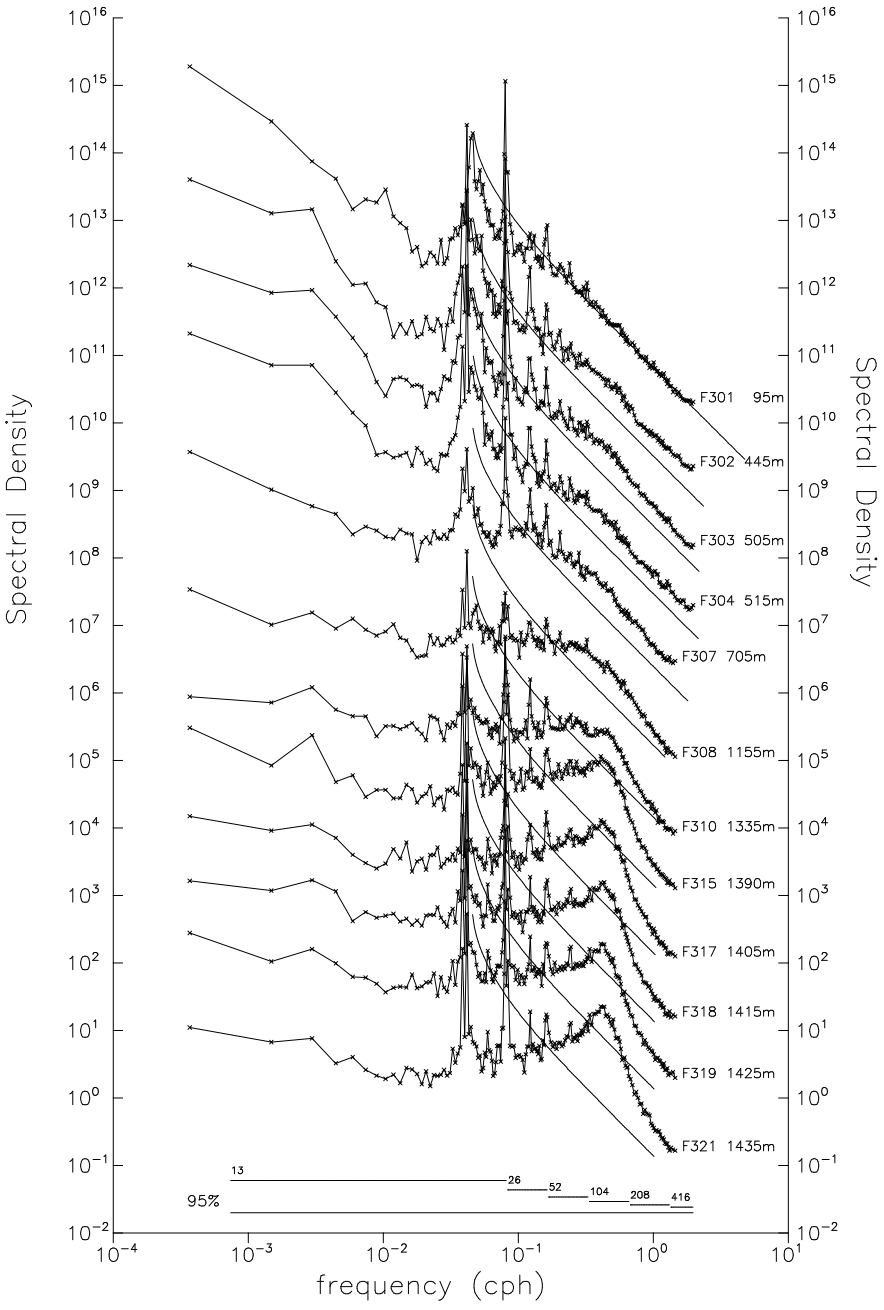

Figure 1.6: Energy-frequency spectra of the internal wave field from Eriksen (1994) showing the strong amplification of energy near the critical frequency near the bottom of the water column located over a 24^o slope of a underwater seamount.

Garrett-Munk spectrum. The evidence suggests that nonlinear fluid interactions, including turbulent mixing, have absorbed the energy from what linear theory would predict to be in the large amplitude reflected waves in the bottom in boundary region.

Laboratory Experiments

The first experimental study of internal waves over a sloping boundary is by Cacchione and Wunsch (1974). They limit their laboratory experiments to the case of small amplitude waves propagating in the plane of the slope in order to test some of the simpler ideas from linear theory. They consider separately the cases where the angle of wave propagation was less than (supercritical), equal to (critical), or greater than (subcritical) the angle of slope. The terms subcritical and supercritical have reference to the frequency of the internal wave compared to a critical frequency wave that propagates at the same slope as the bottom topography. When the frequency is subcritical the angle of propagation is shallower than the bottom slope and the wave will reflect downward. A supercritical frequency wave travels at a steeper angle than the bottom slope and reflects upslope as shown in Figure 1.1.

The geometry of the wave tank in their experiments makes a large distinction between the behavior of the subcritical and supercritical cases. In the supercritical cases the waves reflect upslope and energy accumulates at the top of the slope where it intersects the free surface, creating a local region of strong dissipation and turbulence in the corner of the tank. In the subcritical case the wave energy reflects downslope and, upon reaching the bottom of the tank, reflects away from the slope into the interior fluid. In this case there is no region of strong dissipation and wave breakdown is less dramatic. For the parameters in their experiments, the buoyancy boundary layer established by diffusion is estimated to be an order of magnitude smaller than the turbulent layer thickness established by the reflecting waves and is ignored in the interpretation of the results.

Cacchione and Wunsch find that the wave amplification is in good agreement with linear theory for cases sufficiently far away from the critical angle. Near the critical angle they find that the reflected wave amplitudes are much less than those predicted

by linear theory because of strong viscous dissipation in the boundary layer. The largest wave amplification measured in any of the experiments is a reflected wave of three times the amplitude of the incident wave. Near the critical angle they observe a distinctive turbulent bore surging upslope, which eventually collapses after losing its energy, leaving behind regions of still fluid. They compare this phenomenon to the familiar breaking of surface waves on a beach, which after breaking wash back into the interior fluid. They find that wave breakdown is more violent for the subcritical cases, where the entire boundary region exhibits instability and wave breakdown. Observations indicate that the wave instability takes a long time to develop: it takes approximately 20 wave periods after the first waves reach the wall before the flow begins to exhibit turbulent behavior. As the wave breakdown continues, intrusions of well mixed fluid are convected into the interior fluid along constant density surfaces. They conclude that the singularity of infinite amplitude reflected waves predicted by linear theory is removed by diffusive and nonlinear (turbulent) mixing process.

Cacchione and Wunsch point out that the flow near the wall for the case of reflection from slopes not close to the critical angle is similar to Stokes oscillating flow over a flat plate. The Stokes oscillating boundary layer is a stable flow, but certain differences exist for the wave reflection problem. Here the flow is stratified and the boundary is not perpendicular to the gravity vector. For reflection from a near critical sloping bottom the flow is not similar to Stokes flow and a strong instability is observed.

Cacchione and Southard (1974) and Southard and Cacchione (1972) investigate the effect that the shoaling gravity waves have on the ocean environment, particularly looking for bottom sediment movement caused by the strong currents induced by the gravity waves in their laboratory model. Since the fluid velocities are strongly amplified in the boundary layer region, strong wall shear stresses may develop that are capable of suspending significant amounts of particles. They find that strong sediment suspension occurs during the upslope phase of the wave breakdown, followed by mixing and a net downslope sediment deposit. In a later analysis Cacchione and Drake (1986) propose this mechanism to account for observations of strong plumes

of particles observed over the California continental slope at a water depth of about 300 meters.

Ivey and Nokes (1989) study the problem of vertical mixing due to internal wave breaking on a sloping bottom boundary using laboratory experiments similar to those of Cacchione and Wunsch, but restricting their study to the critical angle case. They force internal waves in a salt stratified tank with a paddle oscillating at the critical frequency corresponding to the bottom slope. They observe the formation of a turbulent boundary layer characterized by an advancing turbulent bore rushing upslope during each wave cycle as the internal wave breaks down. They find that, when the wave amplitude decreased, the wave still surges upslope but does not break into turbulence. Still smaller incident amplitude waves do not exhibit any turbulent-like behavior at all. They characterize the experiments by a dissipation Reynolds number, defined as $Re_d = \omega A_w^2/\nu$, where ω is the wave frequency, A_w is the initial wave amplitude, and ν is the kinematic viscosity. They find that, below a critical value of Re_d in the range 15–20, the flow in the boundary layer does not transition to turbulence. They find that the boundary layer thickness is a function of the incident wave amplitude, approximately given by $\delta = 5A_w$. They also observe the boundary layer exchange fluid with the quiescent interior region. A quasi-steady circulation is set up, which works to maintain the stratification in the boundary layer. The circulation is not characterized by intrusions, as observed by Thorpe (1982), but by a basin scale circulation, with fluid entering the boundary layer at the top and bottom boundaries and slowly being ejected throughout the middle of the tank along isopycnals by horizontal mixing.

Figure 1.7 shows results from Ivey and Nokes' experiment indicating the turbulence which develops in the boundary layer during wave breakdown. They find that there is no preferential mixing near the top or bottom of the tank but rather a steady weakening of the mean density gradient throughout the water column due to horizontal mixing. They also measure the mixing efficiency (the ratio of the increase in potential energy to the input energy of the wave) of the wave breakdown process. They find that the mixing efficiency grows linearly with wave amplitude up to the

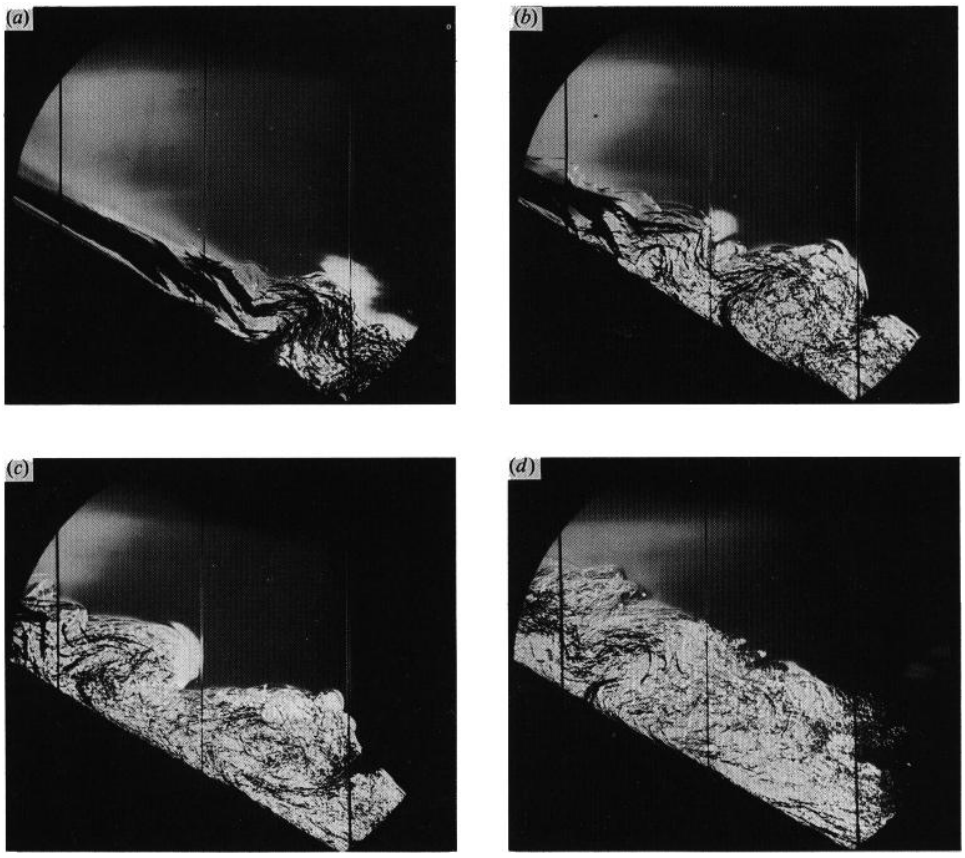

Figure 1.7: From Ivey and Nokes (1989). This Schlieren image shows the turbulent boundary layer which develops when a internal wave reflects off of a 30^o critical angle bottom slope.

point of an incident wave with amplitude about one tenth of the amplitude of an overturning wave, A_o. Above this wave amplitude the efficiencies appear to approach an upper bound of about 0.185. They observe that, below a certain wave amplitude of about 0.01 A_o, there is no measurable mixing due to internal wave breaking. They characterize the level at which transition to a mixing flow is achieved as one that has an average dissipation rate $\epsilon \geq 10\nu N^2$. Finally, they also determine that the mixing efficiency is a function of the overall Richardson number.

The most recent laboratory study of the problem was done by Taylor (1993) using the experimental setup of Ivey and Nokes. The difference between Taylor's and Ivey and Nokes' experiment is that Taylor reduces the bottom slope from 30^o to 20^o. In his experiment Taylor sees an intermittent turbulent boundary layer develop rather than a quasi-steady turbulent bore. The key difference between his work and Ivey and Nokes' experiment is that the wave period is significantly longer than the buoyancy period (and the inverse of the turbulence decay time scale). The turbulence is generated and decays each wave cycle so that there is more time for the flow to restratify and relaminarize between each wave period. Taylor's experimental results are especially useful for comparing with numerical results from the present study and therefore will be described in more detail in a later section.

Linear Theory

Gordon (1980) makes estimates of the boundary layer thickness scales for waves reflecting from critical slopes. He restricts his analysis to near inertial waves for which the bottom slope is less than 10^{-3}. He finds that the resulting boundary layer for critical angle reflection is quite thin, scaling as $\nu_\tau^{1/3}$ (where ν_τ is the turbulent eddy viscosity). This result may be compared to boundary layers for reflecting waves away from the critical angle, which scale as $\nu_\tau^{1/2}$.

Eriksen (1985) uses linear theory to study the probable effects of reflection from sloping terrain on the canonical Garrett-Munk internal wave spectrum. The major goal of the study is to determine how bottom reflection modifies the shape of the internal wave spectrum. He estimates how the internal wave field redistributes its

energy back to the canonical spectrum in the bottom region by nonlinear processes after reflection. Observations of oceanic internal wave spectra support the assumption that the reflected wave field adjusts back to the mean oceanic state within a few hundred meters of the ocean bottom. He finds that the reflected spectrum has less energy at low-wavenumbers and more at high-wavenumbers for nearly all frequencies, especially near the critical frequency corresponding to the bottom slope. His estimates of the wave adjustment process suggest that bottom reflection contributes strongly to diapycnal mixing. The results indicate that the reflected waves need a mixing efficiency of only 0.08 to provide the canonical value of a basin averaged vertical diffusivity of $10^{-4}\mathrm{m}^2/\mathrm{s}$. Eriksen also discusses an inherent difference in character of reflected waves that reflect from the wall in the downslope (subcritical case) rather than the upslope (supercritical case) direction.

Gilbert and Garrett (1989) have extended linear analysis to consider situations with concave and convex bottom topography. They find that energy dissipation rates over locally convex topography should be enhanced. Eriksen (1994) points out that ray traces of internal waves for variable stratifications typical of the deep ocean render most topography effectively convex. Together these arguments strengthen the assertion that bottom reflection is a key process for diapycnal mixing.

1.3 Goals of this Study

As illustrated in the previous section, earlier researchers suggest that bottom reflection represents a significant sink for internal wave energy in the ocean and the laboratory. This reflection therefore contributes significantly to vertical mixing in the ocean, associated with frequent breakdown of internal waves near sloping boundaries. In this study we approach the problem from a new direction, namely numerical simulation.

We utilize results from linear theory and numerical simulations of the Navier-Stokes equations to complement previous methods of investigation; thereby, we can examine influences of key physical parameters in the gravity wave reflection problem. As a complement to laboratory experiments numerical simulations possess several

advantages: making available detailed information on the flow field and energetics, allowing simple adjustment of flow parameters, and facilitating measurement and visualization techniques. Several different high speed computers are used for the simulation of the flow, including Cray-YMP and Cray-2 super-computers, a Stardent mini-super-computer, and Hewlett-Packard 700 series workstations.

Several aspects of the internal wave reflection problem are addressed in this study. Of fundamental interest is the transition of the incident waves into turbulence, in particular, the types of instabilities present and how the waves break. More information is sought both about the physical mechanisms and about the relevant time scales for the turbulent boundary layer. One of the major advantages of this investigation over previous use of linear inviscid theory is the ability to include nonlinear and diffusive effects into the model. The behavior of reflected waves when the angle of incidence approaches the critical angle is not well understood, linear theory is not valid in this range, and visualizations from laboratory studies are limited in their abilities to present a clear picture of the transition process. The sensitivity to the key physical parameters (including wave amplitude, wave propagation angle, bottom slope, Richardson number, Reynolds number, Prandtl number, and the presence of a buoyancy induced boundary layer) will be examined.

The overall mixing efficiency of the wave-reflection process is of fundamental interest, and we will seek to measure it in the simulations. We will quantify and identify the dependencies for which bottom reflection is a sink of internal wave energy. In addition, we will address the issue of how the mixed fluid in the turbulent boundary layer exchanges fluid with the interior region, and determine the influence of the physical boundary conditions at the wall. Other areas of interest include making estimates of the boundary layer thickness and determining what parameters are important in determining the length scales. We will also investigate the amplitude of waves that are required to cause significant mixing and the differences between subcritical and supercritical reflection.

Another key aim of this study is to develop a state-of-the-art numerical model that may be used to simulate other problems related to stratified turbulence in a

boundary layer. The investigation of optimum numerical tools for use in this model has already contributed to a paper (Durran et al., 1993) on more accurate wave-permeable numerical boundary conditions.

The possibilities for treatment of the problem are quite broad and efforts were taken to limit the scope of the study. Several interesting related issues must be deferred to future work. For example, the three-dimensional problem allows for waves to approach the boundary out of the plane of the slope, which might enhance the turbulent breakdown of the wave. Alternatively, the three-dimensional direct numerical simulations provide a possible means of testing mixing models for turbulent dissipation. Consideration of these aspects of the problem was placed beyond the scope of this thesis.

There are limitations on the ability of numerical simulations to address the full complexity of the oceanic flow of interest. One limitation is that accurate simulation of fluid flow is restricted to moderately low Reynolds and Prandtl numbers, to permit adequate resolution of small scales of the flow without the introduction of ad hoc subgrid-scale modeling. The approach taken here is to define a model problem that is closely related to the ocean physics problem and that can be treated accurately within the capabilities of our computational facilities.

The basic mathematical model and the model problem to be studied are described in Chapter 2 and the numerical methods developed for the simulations are described in detail in Chapter 3. In Chapter 4 the introductory results, model validation, and a detailed study of a critical angle wave reflection simulation are presented. Chapter 5 continues with detailed results for several critical angle simulations with bottom slopes ranging from 3^o to 30^o. Chapter 6 completes the discussion of the results from the numerical experiments, emphasizing important physical aspects of the problem and Chapter 7 contains the conclusions and discusses possible future work on this problem.

Chapter 2

INCOMPRESSIBLE STRATIFIED FLOW MODEL

2.1 Basic Equations

Consider incompressible flow in a rotating reference frame. Within the Boussinesq approximation, the governing equations of continuity, momentum, and energy (density) become, respectively:

$$\tilde{\nabla} \cdot \tilde{\mathbf{u}} = 0 \ , \tag{2.1}$$

$$\frac{\partial \tilde{\mathbf{u}}}{\partial \tilde{t}} + \tilde{\mathbf{u}} \cdot \tilde{\nabla} \tilde{\mathbf{u}} + 2\boldsymbol{\Omega} \times \tilde{\mathbf{u}} = -\frac{\tilde{\nabla} \tilde{p}}{\rho_o} - \imath_3 \frac{g}{\rho_o} \tilde{\rho} + \nu \tilde{\nabla}^2 \tilde{\mathbf{u}} \ , \tag{2.2}$$

$$\frac{\partial \tilde{\rho}}{\partial \tilde{t}} + \tilde{\mathbf{u}} \cdot \tilde{\nabla} \tilde{\rho} + \tilde{u}_3 \frac{d\overline{\rho}}{d\tilde{x}_3} = \kappa \tilde{\nabla}^2 \tilde{\rho} \ . \tag{2.3}$$

Equations (2.1) - (2.3) are five equations for the five unknowns $\tilde{\mathbf{u}} = (\tilde{u}, \tilde{v}, \tilde{w})$, $\tilde{p}$, and $\tilde{\rho}$, where the ($\tilde{}$) represents a dimensional quantity; therefore, (2.1) - (2.3) with appropriate initial and boundary conditions completely define the flow system. Here $\tilde{\mathbf{u}}$ is the fluid velocity, $\boldsymbol{\Omega}$ is the rotation vector of the reference frame attached to the Earth (Gill, 1982), g is the gravitational acceleration, $\tilde{p}$ is the perturbation pressure field, $\tilde{\rho}$ is the fluctuating density field, ρ_o is the constant background density, and $\frac{d\overline{\rho}}{d\tilde{x}_3}$ is the background density stratification, which will be negative in all cases considered in this work (i.e., density increasing with depth in the ocean or decreasing with height in the atmosphere.) The parameters ν and κ are coefficients of diffusion of momentum and density.

Density fluctuations and stratification are considered small compared to ρ_o in the Boussinesq approximation. The total density and pressure fields may be written

$$\tilde{\rho}_t = \rho_o + \frac{d\overline{\rho}}{d\tilde{x}_3} \ \tilde{x}_3 + \tilde{\rho} \ , \tag{2.4}$$

$$\tilde{p}_t = p_o + \tilde{p} \ . \tag{2.5}$$

Here, p_o is a reference state in hydrostatic balance with the background density field in the Boussinesq approximation, e.g.,

$$\frac{dp_o}{d\tilde{x}_3} = -\rho_o \, g \, \tilde{x}_3 \, . \tag{2.6}$$

In the Boussinesq approximation $|-\rho_o \, g \, \tilde{x}_3| \gg \left|\frac{d\overline{\rho}}{d\tilde{x}_3} \, \tilde{x}_3 \, g \, \tilde{x}_3\right|$ so that the hydrostatic balance is only between pressure and the background density field. The hydrostatic balance has already been removed from (2.2), which is written in terms of the pressure and density fluctuations.

2.2 Nondimensionalization

The governing equations may be nondimensionalized as follows:

$$\mathbf{u} = \frac{\tilde{\mathbf{u}}}{U} \, , \tag{2.7a}$$

$$\mathbf{x} = \frac{\tilde{\mathbf{x}}}{L} \, , \tag{2.7b}$$

$$t = \frac{\tilde{t}}{L/U} \, , \tag{2.7c}$$

$$p = \frac{\tilde{p}}{\rho_o U^2} \, , \tag{2.7d}$$

$$\rho = \frac{\tilde{\rho}}{L\left|\frac{d\overline{\rho}}{d\tilde{x}_3}\right|} \, . \tag{2.7e}$$

Here U is the characteristic velocity of the gravity wave, L is a characteristic (vertical) length scale, pressure is nondimensionalized with the dynamic pressure, and density is nondimensionalized using the background density gradient. With (2.7), and neglecting Coriolis effects, the momentum equation, (2.2), becomes:

$$\frac{\partial \mathbf{u}}{\partial t} + \mathbf{u} \cdot \nabla \mathbf{u} = -\nabla p - \imath_3 Ri \, \rho + \frac{1}{Re} \nabla^2 \mathbf{u} \, , \tag{2.8}$$

since

$$\frac{g}{\rho_o}\tilde{\rho} = \frac{g}{\rho_o} L \left|\frac{d\overline{\rho}}{d\tilde{x}_3}\right| \rho = \frac{U^2}{L} \frac{L^2(\frac{-g}{\rho_o}\frac{d\overline{\rho}}{d\tilde{x}_3})}{U^2} \rho =$$

$$\frac{U^2}{L}\left(\frac{LN}{U}\right)^2\rho = \frac{U^2}{L}\left(\frac{2\pi}{F}\right)^2\rho = \frac{U^2}{L}Ri\,\rho\ , \tag{2.9}$$

in which the buoyancy (or Brunt-V*äisälä*) frequency, N, is defined by

$$N^2 = \left(\frac{-g}{\rho_o}\frac{d\overline{\rho}}{d\tilde{x}_3}\right)\ . \tag{2.10}$$

The nondimensional parameters, the Froude, Richardson, Reynolds, and Prandtl numbers are defined as:

$$Fr = \frac{2\pi U}{NL}\ , \tag{2.11}$$

$$Ri = \left(\frac{2\pi}{F}\right)^2 = \left(\frac{NL}{U}\right)^2\ , \tag{2.12}$$

$$Re = \frac{UL}{\nu}\ , \tag{2.13}$$

$$Pr = \frac{\nu}{\kappa}\ . \tag{2.14}$$

Using (2.7) in (2.1) gives:

$$\nabla\cdot\mathbf{u} = \mathbf{0}\ . \tag{2.15}$$

The density equation, (2.3), becomes:

$$\frac{\partial\rho}{\partial t} + \mathbf{u}\cdot\nabla\rho - u_3 = \frac{1}{Pr\,Re}\nabla^2\rho\ , \tag{2.16}$$

since

$$\tilde{u}_3\frac{d\overline{\rho}}{d\tilde{x}_3} = U\frac{d\overline{\rho}}{d\tilde{x}_3}u_3 = -U\left|\frac{d\overline{\rho}}{d\tilde{x}_3}\right|u_3\ . \tag{2.17}$$

2.3 Two-Dimensional Flow

Two-dimensional flow is presented first to simplify the discussion of the fluid physics and the governing equations. Consider a vertical (x-z) plane, with the x-direction horizontal and the z-direction vertical. The equations simplify to

$$\frac{\partial u}{\partial x} + \frac{\partial w}{\partial z} = 0\ , \tag{2.18}$$

$$\frac{\partial u}{\partial t} + u\frac{\partial u}{\partial x} + w\frac{\partial u}{\partial z} = -\frac{\partial p}{\partial x} + \frac{1}{Re}\left(\frac{\partial^2 u}{\partial x^2} + \frac{\partial^2 u}{\partial z^2}\right)\ , \tag{2.19}$$

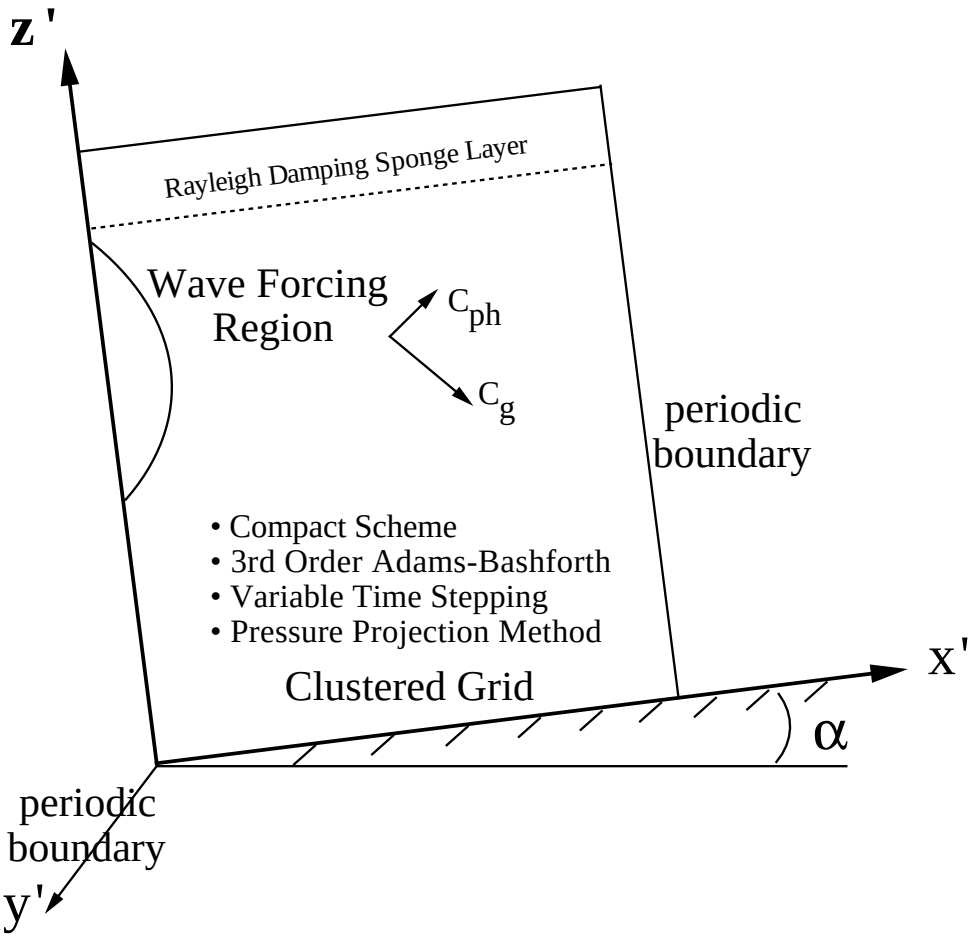

Figure 2.1: The computational domain and some of the key numerical methods in the model are suggested.

$$\frac{\partial w}{\partial t} + u\frac{\partial w}{\partial x} + w\frac{\partial w}{\partial z} + Ri\,\rho = -\frac{\partial p}{\partial z} + \frac{1}{Re}\left(\frac{\partial^2 w}{\partial x^2} + \frac{\partial^2 w}{\partial z^2}\right) , \tag{2.20}$$

$$\frac{\partial \rho}{\partial t} + u\frac{\partial \rho}{\partial x} + w\frac{\partial \rho}{\partial z} - w = \frac{1}{Pr\,Re}\left(\frac{\partial^2 \rho}{\partial x^2} + \frac{\partial^2 \rho}{\partial z^2}\right) . \tag{2.21}$$

Equations (2.18) - (2.21), together with appropriate boundary and initial conditions, form the system to be solved numerically. Figure 2.1 shows the computational domain, geometry, and numerical methods used in the problem. In the text to follow in Chapter 3, details of the numerical solution techniques will be described.

2.4 Pressure Treatment

2.4.1 Poisson's Equation

Experience with numerical simulation has shown the advisability of solving explicitly for the pressure field, to allow it to adjust instantaneously to the velocity field in such a manner as to ensure incompressible flow. This approximation of infinitely fast pressure waves is warranted for low Mach number (incompressible) flows, since pressure waves propagate much faster (acoustic speeds) than other adjustments (gravity waves, turbulence) in the flow. The governing equation for the pressure is a Poisson equation.

Poisson's equation for pressure may be derived by differentiating the x-momentum equation with respect to x, and the z-momentum equation with respect to z, adding the results, and using the continuity equation to simplify. An intermediate step of this procedure is

$$\begin{aligned} &\frac{\partial}{\partial t}\left(\frac{\partial u}{\partial x}+\frac{\partial w}{\partial z}\right)+u\frac{\partial}{\partial x}\left(\frac{\partial u}{\partial x}+\frac{\partial w}{\partial z}\right)+w\frac{\partial}{\partial z}\left(\frac{\partial u}{\partial x}+\frac{\partial w}{\partial z}\right) \\ &+2\frac{\partial w}{\partial x}\frac{\partial u}{\partial z}+\left(\frac{\partial u}{\partial x}\right)^2+\left(\frac{\partial w}{\partial z}\right)^2+Ri\,\frac{\partial \rho}{\partial z}=-\left(\frac{\partial^2 p}{\partial x^2}+\frac{\partial^2 p}{\partial z^2}\right) \\ &\qquad+\frac{1}{Re}\left[\frac{\partial^2}{\partial x^2}\left(\frac{\partial u}{\partial x}+\frac{\partial w}{\partial z}\right)+\frac{\partial^2}{\partial z^2}\left(\frac{\partial u}{\partial x}+\frac{\partial w}{\partial z}\right)\right]\ . \end{aligned} \tag{2.22}$$

For an incompressible flow field at every time level, the final expression would simplify to

$$\nabla^2 p=-Ri\,\frac{\partial \rho}{\partial z}+2\left(\frac{\partial u}{\partial x}\frac{\partial w}{\partial z}-\frac{\partial w}{\partial x}\frac{\partial u}{\partial z}\right)\ . \tag{2.23}$$

However, when the governing equations are discretized for numerical solution, numerical errors from truncation and roundoff are large enough so that the representation of the flow field may not be considered exactly non-divergent, and some form of equation (2.22) must be discretized rather than (2.23).

2.4.2 Pressure Boundary Conditions

Bottom Boundary

The boundary condition for pressure at the bottom wall is derived by evaluating the momentum equations arbitrarily close to the boundary. Experience has shown (Gresho and Sani, 1987, Kim and Moin, 1985) that it is advantageous to use the normal momentum equation to derive the pressure boundary condition rather than the tangential momentum equation when a choice is available.

At the bottom wall the momentum equations with the no-slip condition yield

$$\frac{\partial p}{\partial x} = \frac{1}{Re}\,\frac{\partial}{\partial z}\left(\frac{\partial u}{\partial z}\right), \quad \text{or} \tag{2.24}$$

$$\frac{\partial p}{\partial z} = -Ri\,\rho + \frac{1}{Re}\frac{\partial^2 w}{\partial z^2}\ . \tag{2.25}$$

The free-slip condition, $\left.\dfrac{\partial u}{\partial z}\right|_w = 0$, leads to

$$\frac{\partial p}{\partial z} = -Ri\,\rho\ , \tag{2.26}$$

since assuming continuity holds at the wall

$$\frac{\partial}{\partial z}\left(\frac{\partial u}{\partial x} + \frac{\partial w}{\partial z}\right) = \frac{\partial}{\partial x}\left.\frac{\partial u}{\partial z}\right|_w + \frac{\partial^2 w}{\partial z^2} = 0\ . \tag{2.27}$$

Lateral Boundaries

At the lateral boundaries the periodic boundary condition is easily implemented in the solution of Poisson's equation.

$$p(0, z, t) = p(L_x, z, t) \tag{2.28}$$

Top Boundary

The discussion of the boundary condition at the upper open boundary is deferred to section 3.3.1 on numerical boundary conditions. It is implemented using Rayleigh damping in the top region of the domain.

2.5 Initial Conditions

The problem of interest is to simulate the reflection of internal waves from the ocean floor. This simulation is accomplished either by solving an initial value problem in which the flow is initialized to represent a downward propagating wave packet or by creating a continuous wave source in the domain (following section).

The initial value problem in which the flow field is set to represent a wave packet propagating downward at angle θ with respect to the horizontal, with group velocity $\vec{C}_g$ and wavenumber $\vec{k} = (k, m)$, is presented here. A similar method was utilized by Winters (1989). The analytic expression, or polarization condition, for a wave packet of this type is given below. It is determined by seeking a sinusoidal solution to the linearized non-diffusive governing equations. (Winters' equations (3.3.1) - (3.3.4) *corrected*.)

$$u(x,z,0) = -\frac{Am}{k}\, F(z)\cos(kx+mz) - \frac{A}{k}\, F'(z)\sin(kx+mz)\ , \tag{2.29}$$

$$w(x,z,0) = A\, F(z)\cos(kx+mz)\ , \tag{2.30}$$

$$\rho(x,z,0) = -\frac{A}{\omega}\, F(z)\sin(kx+mz)\ , \tag{2.31}$$

$$\omega^2 = \frac{Ri\, k^2}{k^2+m^2}\ \ ,\ \ \omega = \frac{\pm\sqrt{Ri}\, k}{(k^2+m^2)^{1/2}}\ \ , \tag{2.32}$$

$$F(z) = \exp\left[-b(z-\frac{L_z}{2})^2\right]\ ,\ \ 0 \le z \le L_z\ , \tag{2.33}$$

$$F'(z) = -2b(z-\frac{L_z}{2})\ \exp\left[-b(z-\frac{L_z}{2})^2\right]\ ,\ \ 0 \le z \le L_z\ . \tag{2.34}$$

The function $F(z)$ is used to localize the wave packet in the domain. It is important that the characteristic wavelength λ_P of the wave packet be much longer than the vertical wavelength $\lambda_z = 2\pi/m$ of the gravity waves. A ratio of 10:1 is sufficient to minimize dispersive effects in the wave packet. The initial wave will propagate with group velocity downward and to the right for positive values of k and m. The term $F'(z)$ in the equation for u ensures non-divergence of the wave packet.

The phase and group velocities are given by

$$\vec{C}_{ph} = \frac{\omega}{\left|\vec{k}\right|}\frac{(k\hat{i}+m\hat{k})}{\left|\vec{k}\right|} = \frac{\omega}{(k^2+m^2)}(k\hat{i}+m\hat{k}) = \frac{\sqrt{Ri}\, k}{(k^2+m^2)^{3/2}}\left(k\,\hat{i}+m\,\hat{k}\right)\ , \tag{2.35}$$

$$\vec{C}_g = C_{gx}\hat{i} + C_{gz}\hat{k} = \frac{\partial\omega}{\partial k}\hat{i} + \frac{\partial\omega}{\partial m}\hat{k} = \frac{\sqrt{Ri}\, m}{(k^2+m^2)^{3/2}}\left(m\,\hat{i} - k\,\hat{k}\right) \ . \tag{2.36}$$

Note that the phase and group velocities are perpendicular, and their magnitudes are related by $\left|\vec{C}_g\right| = \dfrac{m}{k}\left|\vec{C}_{ph}\right|$.

The buoyancy period is

$$T_B = \frac{2\pi}{\sqrt{Ri}} \ . \tag{2.37}$$

The period of a wave, T_w, with wavenumber $\vec{k}$ and propagating downward at angle $\theta = \tan^{-1}\left(\frac{k}{m}\right)$ from the horizontal is

$$T_w = \frac{2\pi}{\sqrt{Ri}\,\sin\theta} \ . \tag{2.38}$$

Figure 2.2 presents constant density contours of a large amplitude initial wave packet with peak amplitude $\dfrac{3A_o}{4}$, 3/4 the amplitude of an overturning wave. The direction of propagation of the phase and group velocities are indicated on the figure. Note that even though the waves in this packet are of large amplitude (nonlinear) compared to an overturning wave, they do not appear to be near the point of incipient breaking. In the studies to be presented below, large waves of approximately this amplitude are frequently employed.

2.6 Mechanical Wave Forcing

The second method to generate incoming waves is to force them continuously from inside the computational domain during the simulation. This is accomplished by adding forcing terms to the right hand sides of the governing equations. A simplified variation of this method was introduced by Fovell et al. (1992). In our model the forcing is generalized to include forcing of the density field in a manner that generates a single monochromatic wave train with specified frequency and wavenumber vector incident upon the sloping terrain. This method offers several advantages over the wave packet approach, including allowing a longer time for the waves to break down and closer comparison with laboratory experiments. Additional flexibility with the wave source may be gained by using a time dependent forcing amplitude.

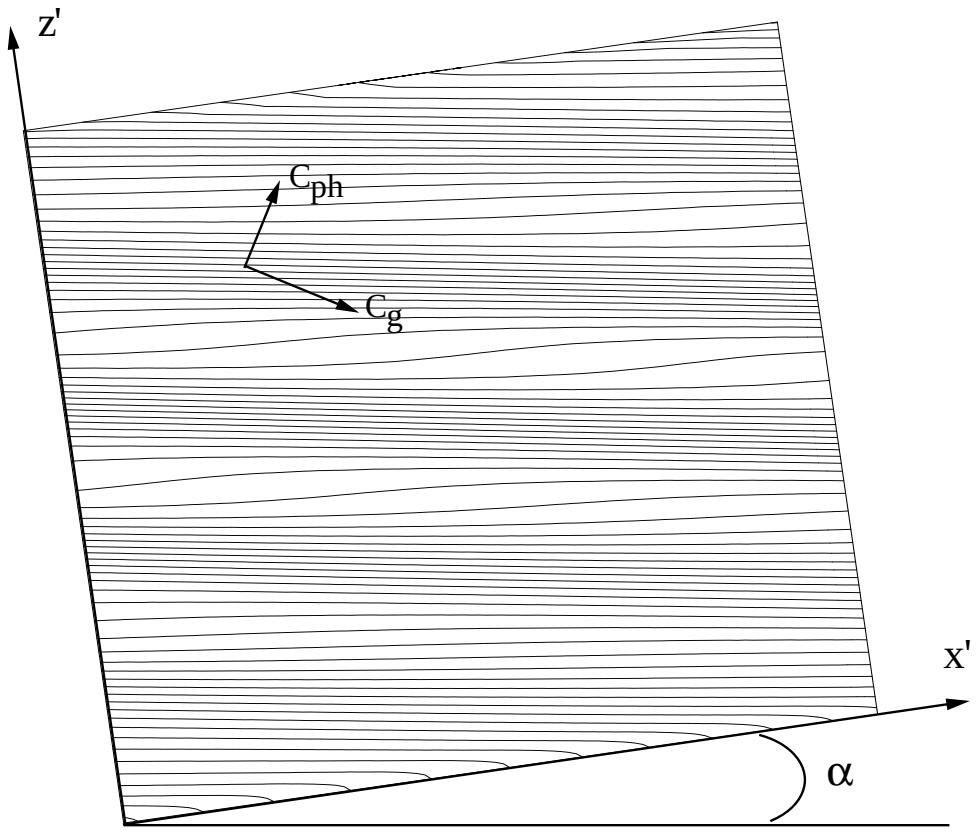

Figure 2.2: For the initial value problem, density contours are shown of the initial wave packet with amplitude $0.75A_o$, 3/4 the amplitude of an overturning wave.

2.6.1 Method

The forcing of the velocity field is written in terms of a stream function, which is convenient because it guarantees a non-divergent disturbance.

$$\frac{\partial u}{\partial t} + u\frac{\partial u}{\partial x} + w\frac{\partial u}{\partial z} = -\frac{\partial p}{\partial x} + \frac{1}{Re}\left(\frac{\partial^2 u}{\partial x^2} + \frac{\partial^2 u}{\partial z^2}\right) - \frac{\partial \Psi}{\partial z} \ , \tag{2.39}$$

$$\frac{\partial w}{\partial t} + u\frac{\partial w}{\partial x} + w\frac{\partial w}{\partial z} + Ri\ \rho = -\frac{\partial p}{\partial z} + \frac{1}{Re}\left(\frac{\partial^2 w}{\partial x^2} + \frac{\partial^2 w}{\partial z^2}\right) + \frac{\partial \Psi}{\partial x} \ . \tag{2.40}$$

$$\frac{\partial \rho}{\partial t} + u\frac{\partial \rho}{\partial x} + w\frac{\partial \rho}{\partial z} - w = \frac{1}{Pr\ Re}\left(\frac{\partial^2 \rho}{\partial x^2} + \frac{\partial^2 \rho}{\partial z^2}\right) + F_\rho \ . \tag{2.41}$$

The forcing functions are specified using the same basic relations as used for the wave packet, e.g.,

$$\frac{\partial \Psi}{\partial z} = \frac{A(t)\, m}{k}\, F(z) \cos(kx + mz - \omega t) + \frac{A(t)}{k}\, F'(z) \sin(kx + mz - \omega t) \ , \tag{2.42}$$

$$\frac{\partial \Psi}{\partial x} = A(t)\ F(z) \cos(kx + mz - \omega t) \ , \tag{2.43}$$

$$F_\rho = -\frac{A(t)}{\omega}\ F(z) \sin(kx + mz - \omega t) \ , \tag{2.44}$$

where the localization functions $F(z)$ and $F'(z)$ are of the form given above in Section 2.5, but more localized and centered at $2L_z/3$ rather than in the center of the domain. The amplitude, $A(t)$, may be varied in time or (more commonly) held constant. Experience indicates that the characteristic length of $F(z)$ may be equal to the vertical wavelength of the desired monochromatic wave train to yield satisfactory results. The forcing stream function Ψ may be written as

$$\Psi = \frac{A(t)\ F(z)}{k} \sin\left(kx + mz - \omega t\right) . \tag{2.45}$$

The flow is started from rest, and after a short startup period a quasi-steady flow develops in which a steady beam of sinusoidal waves propagates toward the bottom boundary with phase and group velocities appropriate to gravity waves with wavenumber ratio k/m. Figure 2.3 shows isopycnals of the waves emerging from the region of wave forcing and approaching the sloping bottom boundary.

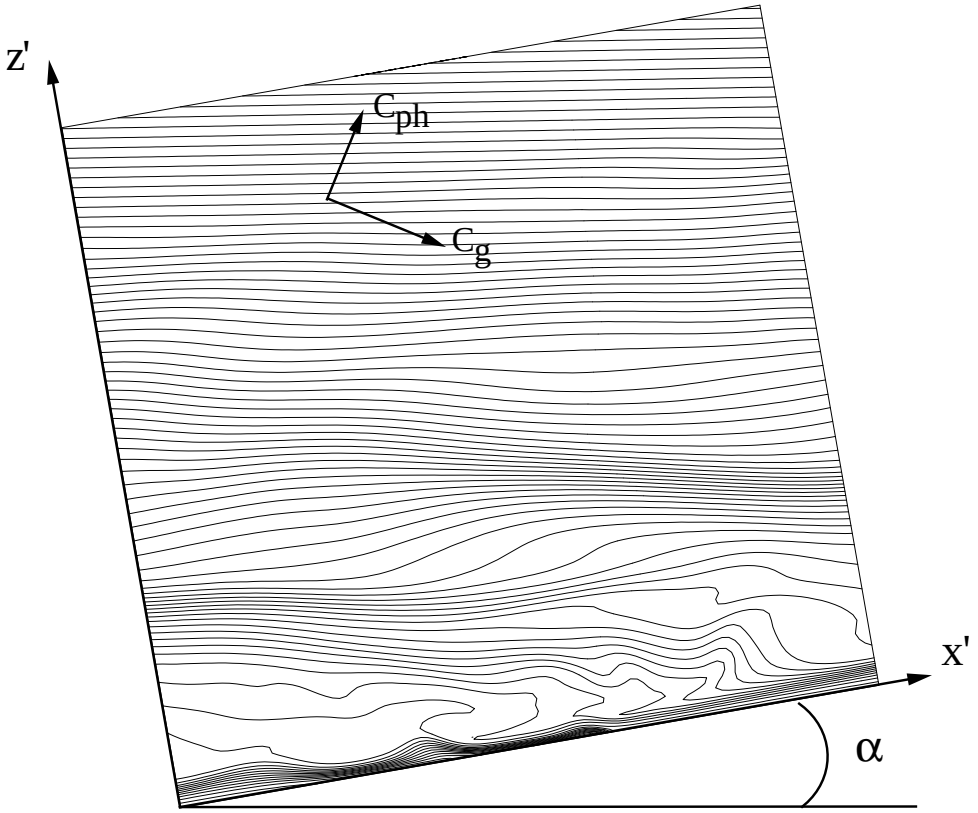

Figure 2.3: Steady wave forcing method showing constant density surfaces of an internal wave propagating downward toward the bottom boundary from the forcing region.

2.6.2 Analytic Solution

An analytic solution can be obtained for the flow that propagates from the forcing region. The solution may be obtained by writing the linearized equations of motion with forcing added and looking for solutions whose time dependence is wavelike. The solution extends naturally to three-dimensions.

The solution begins with the two-dimensional linearized system:

$$\frac{\partial u}{\partial t} = -\frac{\partial p}{\partial x} - \frac{\partial \Psi}{\partial z} \ , \tag{2.46}$$

$$\frac{\partial w}{\partial t} = -Ri\ \rho - \frac{\partial p}{\partial z} + \frac{\partial \Psi}{\partial x} \ . \tag{2.47}$$

$$\frac{\partial \rho}{\partial t} = w + F_\rho \ . \tag{2.48}$$

Pressure may be eliminated from the system using a stream function, defining $u = \frac{\partial \psi}{\partial z}$, and $w = -\frac{\partial \psi}{\partial x}$. Taking the curl of the linearized momentum equations and adding them yields:

$$\frac{\partial}{\partial t}\nabla^2\psi - Ri\frac{\partial \rho}{\partial x} = -\nabla^2\Psi \ . \tag{2.49}$$

Density may be eliminated from (2.49) by taking the partial derivative with respect to x of the density equation (2.48) and the partial derivative of (2.49) with respect to time and combining the results, which gives:

$$\frac{\partial^2}{\partial t^2}\nabla^2\psi + Ri\frac{\partial^2 \psi}{\partial x^2} = -\frac{\partial}{\partial t}\nabla^2\Psi + Ri\frac{\partial F_\rho}{\partial x} \ . \tag{2.50}$$

Here Ψ and F_ρ are specified by (2.44) and (2.45) above with $A(t) = A$, a constant, so that the right hand side of (2.50) is:

$$-\frac{A\omega}{k}\left[2(k^2+m^2)F(z) - F''(z)\cos\phi + 2mF'(z)\sin\phi\right] \ , \tag{2.51}$$

where $\phi = (kx + mz - \omega t)$.

A solution to the system may be found of the form:

$$\psi = A_f(z)\cos\phi + B_f(z)\sin\phi \ , \tag{2.52}$$

for which the entire time dependence of the solution is contained in the wave forms of $\sin\phi$ and $\cos\phi$. Substituting ψ into (2.50) and equating the sine and cosine parts leads to the following third order equations for $A_f(z)$ and $B_f(z)$:

$$B_f'''(z) + 4m^2 B_f'(z) = \frac{4Am}{\omega k}(k^2 + m^2)F(z) = C_1 F(z) \tag{2.53}$$

$$A_f'''(z) + 4m^2 A_f'(z) = -\frac{A}{\omega k}F'''(z) + \frac{2A(k^2 - m^2)}{\omega k}F'(z) = C_2 F'''(z) + C_3 F'(z)\ . \tag{2.54}$$

For certain specified forms of $F(z)$ on the interval $0 < z < \pi$, such as $F(z) = \sin^2(z)$, analytic expressions for $A_f(z)$ and $B_f(z)$ can be found. For the form of $F(z)$ used above, however, a numerical solution of the third order ordinary differential equations (2.53) and (2.54) is obtained by inverting a pentadiagonal matrix representing a finite difference discretization for the derivatives of $A_f(z)$ and $B_f(z)$. The relative magnitudes of C_1, C_2, and C_3 to $4m^2$ are the important parameters that determine the shape of the solutions for $A_f(z)$ and $B_f(z)$.

The numerical solution is approximated at the interior nodes, with fourth and second order accurate stencils for the derivatives, e.g.,

$$\frac{dB_f}{dz} = \frac{-B_{i+2} + 8B_{i+1} - 8B_{i-1} + B_{i-2}}{12\Delta z}\ , \tag{2.55}$$

$$\frac{d^3 B_f}{dz^3} = \frac{B_{i+2} - 2B_{i+1} + 2B_{i-1} - B_{i-2}}{2\Delta z^3}\ . \tag{2.56}$$

Three boundary conditions on $B_f(z)$ are used: as $z \to \infty$, $B_f = 0$ and $\dfrac{dB_f}{dz} = 0$ are both valid, and as $z \to -\infty$, $\dfrac{dB_f}{dz} = 0$ is used. The same boundary conditions are used for $A_f(z)$.

An alternate solution method has also been used, yielding equivalent results by solving Equation (2.53) for $B'(z)$ using the method of variation of parameters, and numerically integrating both the right hand side of the equation and B' to find B.

Figure 2.4 shows solutions for $A_f(z)$ and $B_f(z)$ for the shape function of the forcing region, $F(z)$, indicated. Here m (the vertical wavenumber) is chosen so that $\lambda_z = 2\pi/m$ is smaller ($\lambda_z \approx L_F/1.6$) than the characteristic length scale of $F(z)$, defined by L_F, which is the width of $F(z)$ at $F(z) = 1/10F_{max}$. The solutions indicate

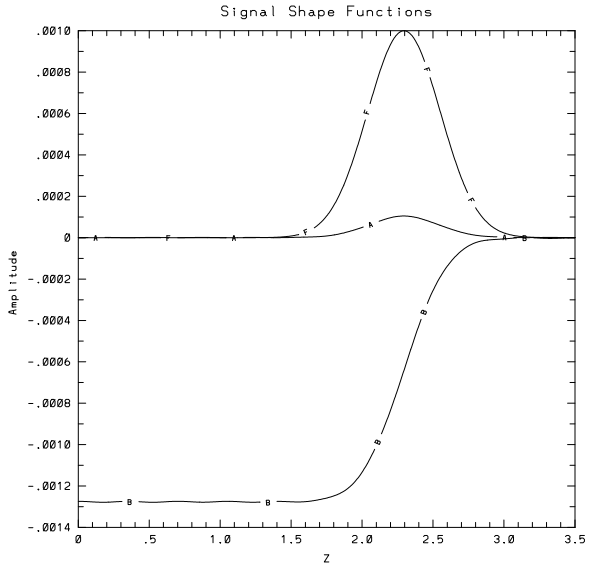

Figure 2.4: Signal shape function for $A_f(z)$ and $B_f(z)$ for a broad forcing region of shape $F(z)$ and wavelength $\lambda_z = 0.7$.

that the signal coming out of the forcing region is steady and smooth and confined within the carrier wave envelope shown. The envelopes' smoothness is a function of the ratio of $\frac{2\pi}{m}/L_F$. When this ratio is greater than one, such that the forcing region is wider than a vertical wavelength of the forced wave, then the signal that emerges has the desirable features of being uniform in shape and time. When the forcing region is narrower than a wavelength of the emitted signal, then the output is modulated by a irregular, non-constant envelope. In Figure 2.4 the emitted signal propagates from right to left (downward). $A_f(z)$ represents the shape of the internal wave train emerging from the forcing region having the sine ϕ dependence. $A_f(z)$ represents a local disturbance with cosine ϕ dependence within the forcing region, which satisfies the nondivergence criteria required by incompressible flow. $B_f(z)$ vanishes outside of the forcing region due to the symmetry of $F(z)$ when the forcing region is sufficiently broad.

Figures 2.5 and 2.6 show solutions for relatively broad and narrow forcing regions

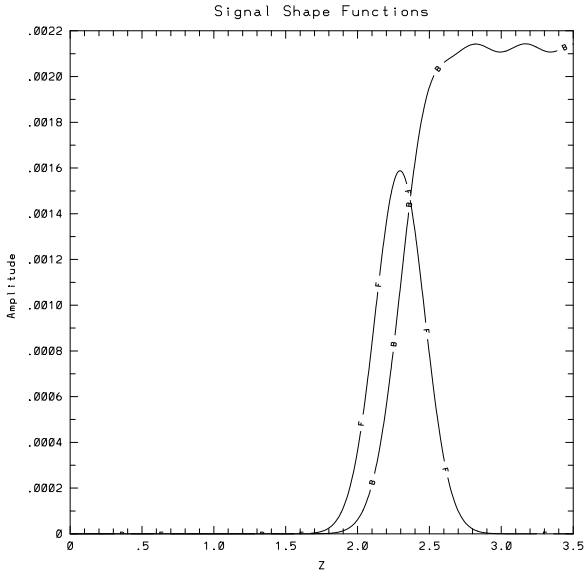

Figure 2.5: A marginally broad forcing region, approximately the same width as the vertical wavelength of the emitted wave ($F_l = 1.05\lambda_z$) has fairly smooth properties for the shape function $B_f(z)$ Also shown is the forcing region, $F(z)$, with the height normalized to be of the same scale as B_f.

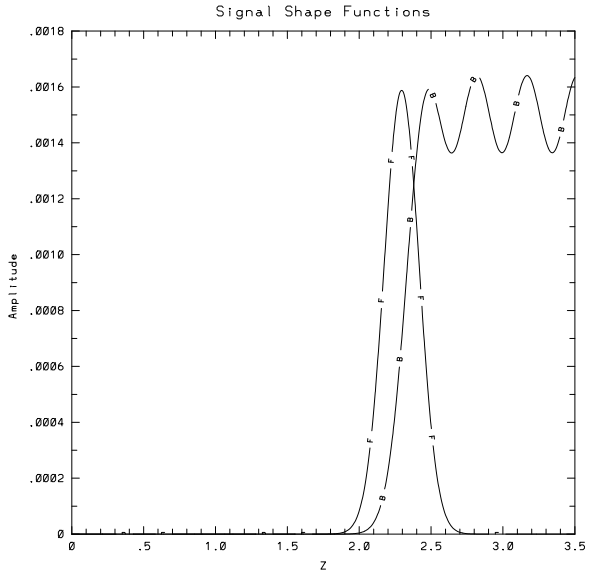

Figure 2.6: A narrow forcing region, smaller in width than the vertical wavelength of the emitted sine wave ($F_l = 0.73\lambda_z$) leads to oscillations in the shape function $B_f(z)$ Also shown is the forcing region, $F(z)$, with the height normalized to be of the same scale as B_f.

defined by ratios of $\frac{2\pi}{m}/L_F$ of 1.05 and 0.73. The envelope and signal wavelength are shown here in comparison with the forcing region width. Figure 2.5 shows a satisfactorily smooth signal coming from a broad forcing region and Figure 2.6 shows the modulated signal and envelope coming from a narrower forcing region. In Figures 2.5 and 2.6 the emitted wave propagates upwards (left to right). These analytic results have been tested by numerical simulations which verify the influence and importance of the width of the wave forcing region compared to the vertical wavelength. The main result is that for satisfactory resolution such that an unmodulated wave is produced the forcing region should be wider than a vertical wavelength of the emitted wave.

2.7 Velocity and Density Boundary Conditions

With the non-dimensionalization specified above, the boundary conditions for velocity and density are given below.

2.7.1 Lateral Boundaries

A periodic domain in x is chosen to simplify numerical boundary conditions at the lateral boundaries. The periodic problem also allows waves propagating at small angles to the horizontal to be tracked in the computational domains for longer times, allowing more interaction between incident and reflected waves. The lateral boundary conditions are:

$$u(0,z,t) = u(L_x,z,t)\ , \quad w(0,z,t) = w(L_x,z,t)\ , \quad \rho(0,z,t) = \rho(L_x,z,t)\ . \tag{2.57}$$

2.7.2 Bottom Boundary

No Slip Condition

No slip (and no penetration) boundary conditions are specified at the bottom boundary ($z = 0$) with

$$u(x,0,t) = 0, \quad w(x,0,t) = 0\ . \tag{2.58}$$

Free Slip Condition

Free-slip (and no penetration) boundary conditions may be specified at the bottom boundary with

$$\frac{\partial u(x,0,t)}{\partial z'} = 0, \quad w(x,0,t) = 0\ , \tag{2.59}$$

where the z'-direction is perpendicular to the boundary (rotation of the coordinate frame is presented below in Section 3.4.1). Note, however, that the numerical solution of the free-slip boundary condition may not satisfy the continuity equation exactly and, therefore, may introduce divergence into the flow at the wall, since

$$\frac{\partial}{\partial x}\left(\frac{\partial u}{\partial z}\right)\bigg|_w = \frac{\partial}{\partial z}\left(\frac{\partial u}{\partial x}\right)\bigg|_w = 0 \neq \frac{\partial}{\partial z}\left(-\frac{\partial w}{\partial z}\right)\bigg|_w\ . \tag{2.60}$$

Appropriate modification of the free-slip condition to maintain approximate nondivergence is discussed below in Section 3.3.2, dealing with numerical boundary conditions.

2.7.3 Density Boundary Conditions

The bottom boundary condition for density is a no-flux condition. In a temperature stratified fluid this would be equivalent to an adiabatic boundary condition. In a salt stratified fluid the no-flux boundary condition means that there are no sources or sinks of salt at the wall, but that the salt in the interior flow is conserved.

Adiabatic Wall

A no-flux (adiabatic) wall may be simulated with the condition

$$q = -\frac{\partial \rho_t(x,0,t)}{\partial z'} = 0 \ , \tag{2.61}$$

where $\rho_t = \rho_o + \dfrac{\partial \overline{\rho}}{\partial z} + \rho$ is the total density field, or equivalently, by setting the derivative of the perturbation density equal to a constant at the wall

$$\frac{\partial \rho(x,0,t)}{\partial z'} = -\cos\alpha \frac{\partial \overline{\rho}}{\partial z} = C \ , \tag{2.62}$$

where α is the angle of the bottom slope.

Phillips (1970) and Wunsch (1970) have shown that an adiabatic wall gives rise to a steady circulation in a density stratified fluid. Their results for the induced boundary currents and density profiles are given above in Section 1.2.1. In the simulations conducted in this study the steady profiles develop on time scales fast compared with wave propagation time scales. Consequently, the flow is initialized to include the fully developed steady profiles, as given by equations (1.2) - (1.4) above and repeated here

$$\rho(z) = \frac{-e^{-\gamma z}\ \cos\gamma z}{\gamma} \ , \tag{2.63}$$

$$u(z) = \frac{2\gamma\ e^{-\gamma z}\ \sin\gamma z}{\sin\alpha\ Pr\ Re} \ , \tag{2.64}$$

$$w(z) = v(z) = 0 \ , \tag{2.65}$$

where $\gamma = \left(\frac{Ri\ Pr\ Re^2\ \sin^2\alpha}{4}\right)^{1/4}$.

We have derived similar steady state profiles for an adiabatic, free-slip wall with velocity and density profiles:

$$\rho(z) = \frac{e^{-\gamma z}}{2\gamma}(\sin\gamma z - \cos\gamma z)\ , \tag{2.66}$$

$$u(z) = \frac{\gamma\ e^{-\gamma z}}{\sin\alpha\ Pr\ Re}(\sin\gamma z + \cos\gamma z)\ . \tag{2.67}$$

2.8 Summary

For the two-dimensional model, the system to be solved numerically comprises equations (2.18) - (2.21) and (2.23), together with an appropriate set of boundary conditions from (2.24) - (2.28), (2.57) - (2.62), upper boundary conditions to be presented later, and initial conditions from (2.29) - (2.34) and (2.63) - (2.67) or a mechanical wave source given by (2.39) - (2.45).

Chapter 3

NUMERICAL METHODS FOR INCOMPRESSIBLE FLOW

3.1 Spatial Treatment

Two numerical codes have been developed in this study: a two-dimensional (2-D) flow model and a three-dimensional (3-D) model. A variety of numerical schemes are used in the codes. Details of the numerical methods are discussed below, primarily in the context of the two-dimensional model. Except where noted, the three-dimensional model uses the same algorithms. The standard resolution for the two-dimensional model is 201 x 401 grid points; the three-dimensional model uses grid resolutions of up to 129 x 129 x 130 grid points. The three-dimensional high resolution calculations were conducted on the Cray-2 and Cray-YMP computers at the National Center for Supercomputing Applications located at the University of Illinois, Urbana-Champaign. The fourth-order compact method is used to calculate derivatives in the horizontal (x) and vertical (z) directions. Modifications for the different geometries, including the use of a variable grid, are discussed below.

3.1.1 Compact Scheme

Velocity derivatives are calculated using Hermitian compact, or Padé series techniques, following the work of Hirsh (1975), Adam (1977), and Lele (1992). These methods offer improved resolution over traditional finite-difference schemes, and spectral-like behavior in their ability to represent a wide range of wavenumbers accurately. In addition, the compact scheme may be used in other applications, such as accurate interpolation, spectral-like filtering, or with non-uniform meshes (Lele, 1992).

Standard finite difference techniques are based upon truncated Taylor-series representations, e.g., $T_N(x) = \sum_{n=0}^{N_m} a_n x^n$. The basic idea of the Padé series technique is

to use a rational function approximation to gain better accuracy with fewer terms of the series (e.g., Bender and Orszag, 1978). The Padé approximant is written

$$P_M^N(x) = \frac{\sum_{n=0}^{N_m} A_n x^n}{\sum_{m=0}^{M} B_m x^m} \ . \tag{3.1}$$

A comparison between standard finite difference formulas and those resulting from the Padé series expansions is illustrative. To achieve fourth-order accuracy in estimating a first derivative with Taylor series basis functions, five terms of the series must be kept. In the Padé approximant the same order of accuracy may be achieved by keeping three terms of the series in the numerator and two in the denominator. The Taylor series method results in the difference formula

$$\frac{\partial u}{\partial x}_i = \frac{-u_{i+2} + 8u_{i+1} - 8u_{i-1} + u_{i-2}}{12h} - \frac{h^4 \frac{\partial^5 u}{\partial x^5}_i}{30} \ . \tag{3.2}$$

For the Padé representation the result is a tridiagonal system of the form

$$\frac{1}{3}u_{x(i+1)} + \frac{4}{3}u_{xi} + \frac{1}{3}u_{x(i-1)} = \frac{1}{h}(u_{i+1} - u_{i-1}) \ , \tag{3.3}$$

where h is the distance between grid points, and the velocity derivatives are written $\frac{\partial u}{\partial x}\Big|_i = u_{xi}$. The scheme is called "compact" because it involves relations between grid points on a smaller stencil than the standard difference formula. The major advantage of the compact scheme is its increased accuracy for high wavenumber disturbances, which will be discussed in some detail below. An additional advantage is that the truncation error for the compact scheme is $-\frac{h^4 \frac{\partial^5 u}{\partial x^5}_i}{180}$, six times smaller than the truncation error of the standard scheme.

Formal fourth-order accuracy is maintained throughout the numerical model. Second-derivatives are calculated using the compact representation

$$\frac{1}{12}u_{xx(i+1)} + \frac{5}{6}u_{xxi} + \frac{1}{12}u_{xx(i-1)} = \frac{1}{h^2}(u_{i+1} - 2u_i + u_{i-1}) \ , \tag{3.4}$$

where $\frac{\partial^2 u}{\partial x^2}\Big|_i = u_{xxi}$. The boundary nodes for first and second-derivatives require special treatment and will be discussed below.

For finite-difference representations of first and second derivatives, Lele (1992) discusses the appropriate measure of accuracy or *resolving efficiency* of different

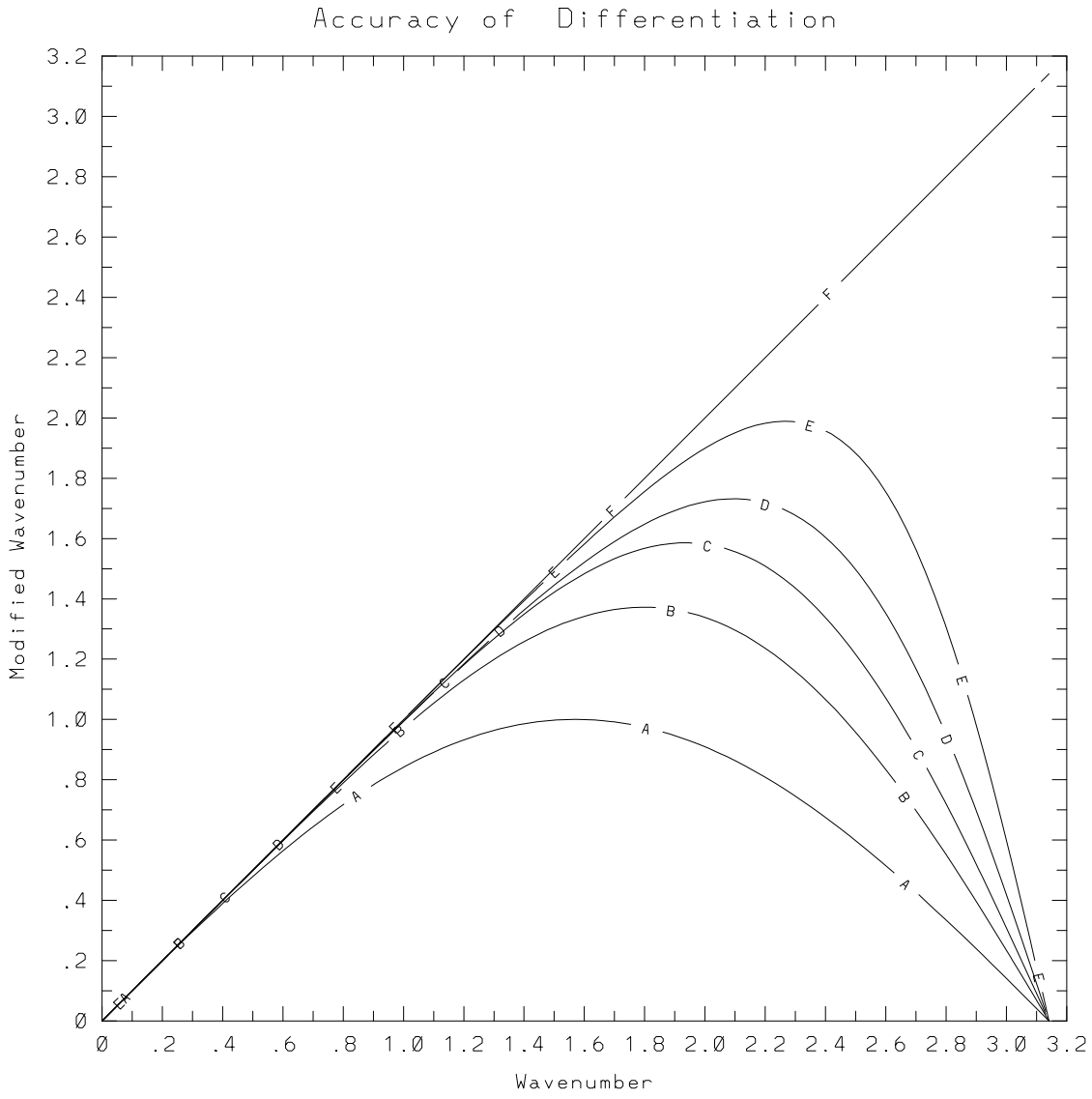

Figure 3.1: Modified wavenumbers vs. wavenumber for first derivatives, for (A) second-order central differences, (B) fourth-order central differences, (C) sixth-order central differences, (D) Padé scheme, fourth-order, (E) sixth-order tridiagonal compact scheme, (F) exact differentiation.

compact-scheme implementations. This measure, called the modified wavenumber, represents the accuracy of the difference formula as a function of wavenumber. Figure 3.1 shows the modified wavenumbers for several discretization formulae, illustrating the superiority of the compact scheme over standard explicit schemes in resolving first derivatives of high-wave number (small-scale) features. Exact differentiation is represented by line (F) in Figure 3.1. The other lines illustrate how close the difference schemes come to exact differentiation over a range of wavenumbers. A wavenumber of π is the highest wavenumber that can be represented on the numerical mesh, corresponding to the 2 Δx wave. Figure 3.2 shows the phase speed errors in differentiation for several explicit schemes compared to the Padé approximation.

Figure 3.3 illustrates the differencing errors for the second derivatives for the numerically resolvable wavenumbers, $|k\Delta x| < \pi$, on the finite differencing grid. Compared to explicit finite difference schemes the compact scheme offers better resolution of derivatives together with smaller phase speed errors. The modified wavenumbers of the Padé scheme, for the first and second derivatives, are

$$w'_m(k\Delta x) = \frac{a\sin k\Delta x + (b/2)\sin 2k\Delta x + (c/3)\sin 3k\Delta x}{1 + 2\alpha\cos k\Delta x + 2\beta\cos 2k\Delta x} = \frac{3\sin(k\Delta x)}{2+\cos(k\Delta x)} \ , \text{ and}$$

$$w''_m(k\Delta x) = \frac{2a(1-\cos k\Delta x) + (b/2)(1-\cos 2k\Delta x) + (2c/9)(1-\cos 3k\Delta x)}{1 + 2\alpha\cos k\Delta x + 2\beta\cos 2k\Delta x} = \frac{12(1-\cos(k\Delta x))}{5+\cos(k\Delta x)} \ , \quad (3.5)$$

where the coefficients α, β, a, b, and c are from the respective generalized first and second compact derivative formulae

$$\beta u'_{i-2} + \alpha u'_{i-1} + u'_i + \alpha u'_{i+1} + \beta u'_{i-2} =$$
$$\tfrac{a}{2h}(u_{i+1} - u_{i-1}) + \tfrac{b}{4h}(u_{i+2} - u_{i-2}) - \tfrac{c}{6h}(u_{i+3} - u_{i-3}) \ , \text{ and}$$

$$\beta u''_{i-2} + \alpha u''_{i-1} + u''_i + \alpha u''_{i+1} + \beta u''_{i-2} =$$
$$\tfrac{a}{h^2}(u_{i+1} - 2u_i + u_{i-1}) + \tfrac{b}{4h^2}(u_{i+2} - 2u_i + u_{i-2}) - \tfrac{c}{9h^2}(u_{i+3} - 2u_i + u_{i-3}) \ . \quad (3.6)$$

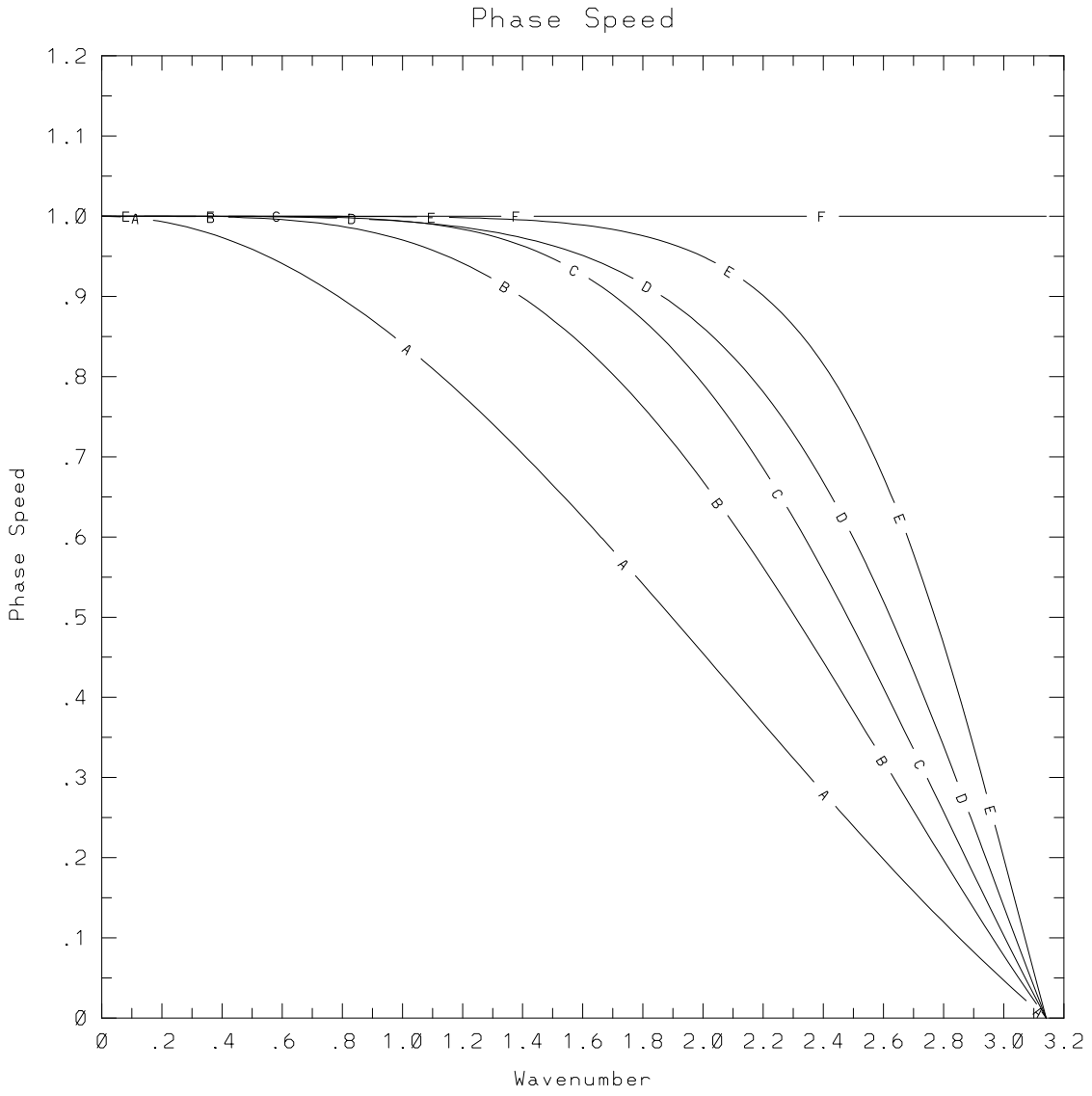

Figure 3.2: Phase speed vs. wavenumber for first derivatives showing the improved performance of the compact scheme over traditional finite difference methods, for (A) second-order central differences, (B) fourth-order central differences, (C) sixth-order central differences, (D) Padé scheme, fourth-order, (E) sixth-order tridiagonal compact scheme, (F) exact differentiation.

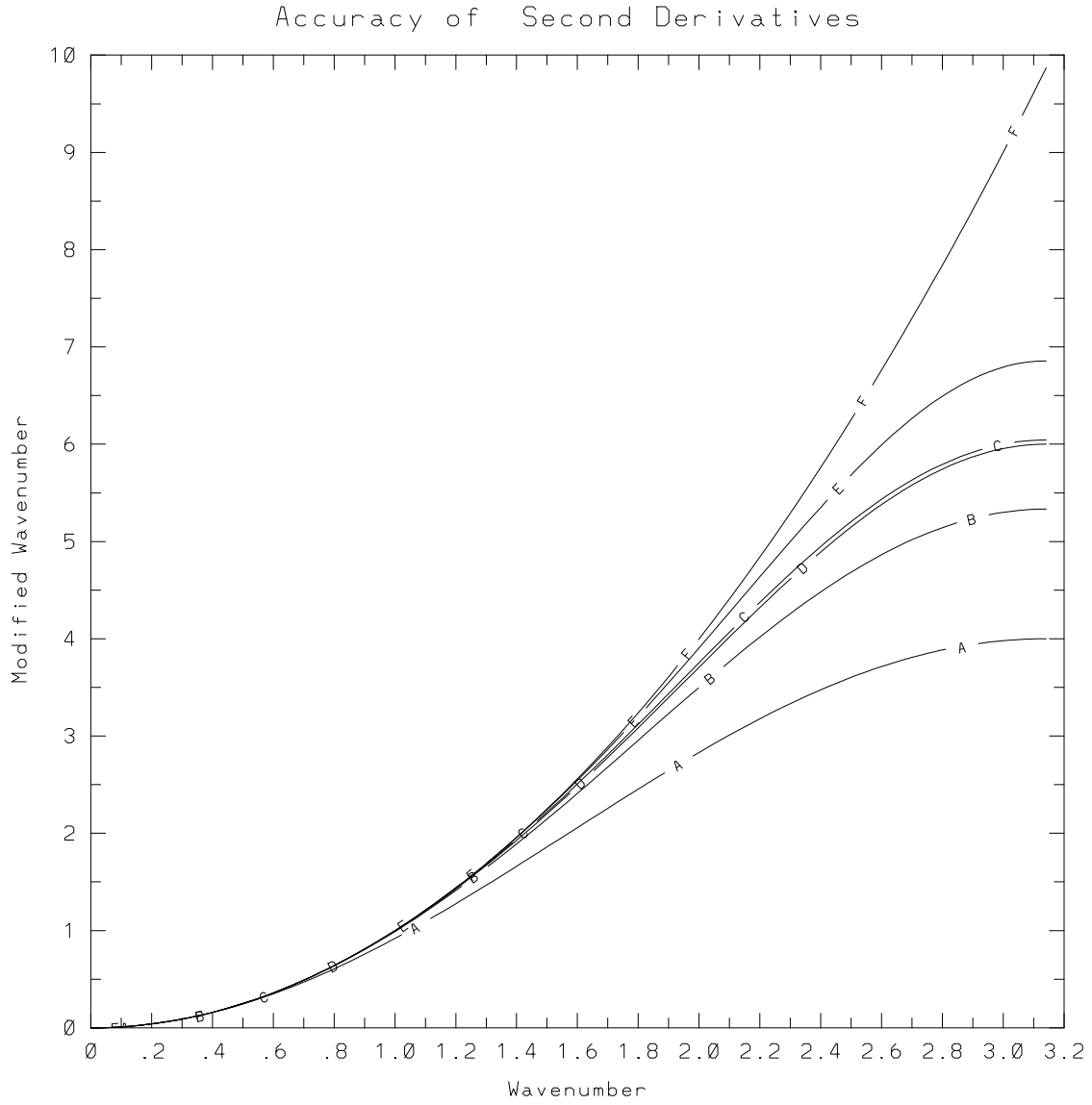

Figure 3.3: Modified wavenumbers vs. wavenumber for second derivatives, for (A) second-order central differences, (B) fourth-order central differences, (C) sixth-order central differences, (D) Padé scheme, fourth-order, (E) sixth-order tridiagonal compact scheme, (F) exact differentiation.

A linear von Neumann stability analysis for Burgers' equation,

$$\frac{\partial u}{\partial t} + u\frac{\partial u}{\partial x} = \nu\frac{\partial^2 u}{\partial x^2} \ , \tag{3.7}$$

(a simple one-dimensional analog to the momentum equations) may be performed to illustrate the limits on the maximum time step for the compact scheme compared with more traditional finite differencing techniques. With leap-frog time differencing for the advection term and a $2\Delta t$ forward Euler step for the diffusion term, the stability limits on the Courant number, C_{fl}, and the diffusion stability parameter, β, for the fourth-order compact scheme are

$$C_{fl} = \frac{u\Delta t}{\Delta x} \leq 0.577 \ \ , \ \ \beta = \frac{\nu\Delta t}{\Delta x^2} \leq \frac{1}{6} \ . \tag{3.8}$$

These results appear restrictive compared with the usual limits for second order spatial differencing with leap-frog time stepping for Burgers' equation, e.g., $C_{fl} \leq 1$, $\beta \leq \frac{1}{4}$. Hirsch (1975) points out that for the same accuracy, however, the fourth-order scheme can use significantly larger values of Δx, and therefore, even with the more stringent restrictions on C_{fl}, the compact scheme allows larger values of Δt. Table 3.1 extends Hirsch's comparison of maximum stable values for the Courant number to include additional spatial difference schemes, compared for Burgers' equation using leap-frog time stepping. The pertinent stability limitations for the numerical methods used in this problem are discussed below in the section on time differencing.

3.1.2 Boundary Conditions for the Compact Scheme

First Derivative - Dirichlet Conditions

It is well known that boundary schemes may be one order less accurate than an interior domain scheme without degrading the overall accuracy of the interior difference scheme (e.g., Kreiss, 1972). Third-order accurate boundary schemes for Dirichlet boundary conditions (u is specified at the boundary) are given by Adam (1977):

$$2u_{x1} + 4u_{x2} = \frac{1}{h}(-5u_1 + 4u_2 + u_3) \ , \tag{3.9}$$

$$4u_{x2} + 2u_{x3} = \frac{1}{h}(-u_1 - 4u_2 + 5u_3) \ , \tag{3.10}$$

Table 3.1: Stability Criteria for Burgers' Equation.

Difference Method	Maximum C_{fl}	Maximum β
Second Order Explicit	1.0	0.250
Fourth-Order Explicit	.728	0.187
Fourth-Order Compact	.577	0.167
Sixth-Order Explicit	.630	0.165
Tenth-Order Compact	.430	0.127
Spectral Method	.318	0.101

$$2u_{x(m-2)} + 4u_{x(m-1)} = \frac{1}{h}(-5u_{m-2} + 4u_{m-1} + u_m) \ , \tag{3.11}$$

$$4u_{x(m-1)} + 2u_{xm} = \frac{1}{h}(-u_{m-2} - 4u_{m-1} + 5u_m) \ , \tag{3.12}$$

where $i = m$ represents the last (maximum) grid point. The resulting tridiagonal matrix is computationally inexpensive to solve.

$$\begin{bmatrix} 2 & 4 & & & & & & 0 \\ & 4 & 2 & & & & & \\ & \frac{1}{3} & \frac{4}{3} & \frac{1}{3} & & & & \\ & & \ddots & \ddots & \ddots & & & \\ & & & \frac{1}{3} & \frac{4}{3} & \frac{1}{3} & & \\ & & & & \ddots & \ddots & \ddots & \\ & & & & & \frac{1}{3} & \frac{4}{3} & \frac{1}{3} \\ & & & & & & 2 & 4 \\ 0 & & & & & & 4 & 2 \end{bmatrix} \begin{bmatrix} u_{x1} \\ u_{x2} \\ u_{x3} \\ \vdots \\ u_{xi} \\ \vdots \\ u_{x(m-2)} \\ u_{x(m-1)} \\ u_{xm} \end{bmatrix} =$$

$$\begin{bmatrix} \frac{1}{h}(-5u_1 + 4u_2 + u_3) \\ \frac{1}{h}(-u_1 - 4u_2 + 5u_3) \\ \frac{1}{h}(u_4 - u_2) \\ \vdots \\ \frac{1}{h}(u_{i+1} - u_{i-1}) \\ \vdots \\ \frac{1}{h}(u_{m-1} - u_{m-3}) \\ \frac{1}{h}(-5u_{m-2} + 4u_{m-1} + u_m) \\ \frac{1}{h}(-u_{m-2} - 4u_{m-1} + 5u_m) \end{bmatrix} . \tag{3.13}$$

First Derivative - von Neumann Conditions

When von Neumann boundary conditions are specified, which means the normal derivative $\dfrac{\partial u}{\partial n}$ is given on the boundary, the tridiagonal matrix is simplified, with all off diagonal elements equated to zero at the boundary by setting $u_{x1} = \dfrac{\partial u}{\partial z}$.

Second Derivative - Dirichlet Conditions

Lele (1992) gives an appropriate boundary condition compatible with the compact scheme for the second derivative of a function f when the value of the function is specified at the boundary. He specifies a formally 3rd-order accurate boundary scheme (Lele, equation (4.3.1)) by the relation

$$f_1'' + 11f_2'' = \frac{1}{h^2}\left[13f_1 - 27f_2 + 15f_3 - f_4\right] . \tag{3.14}$$

The truncation error is $\frac{1}{12}h^3 f^{(5)}$, which is ten times smaller than the truncation error of a standard explicit third order boundary scheme. The resulting tridiagonal system is

$$\begin{bmatrix} 1 & 11 & & & & & 0 \\ \frac{1}{12} & \frac{5}{6} & \frac{1}{12} & & & & \\ & \ddots & \ddots & \ddots & & & \\ & & \frac{1}{12} & \frac{5}{6} & \frac{1}{12} & & \\ & & & \ddots & \ddots & \ddots & \\ & & & & \frac{1}{12} & \frac{5}{6} & \frac{1}{12} \\ 0 & & & & & 11 & 1 \end{bmatrix} \begin{bmatrix} u_{xx1} \\ u_{xx2} \\ \vdots \\ u_{xxi} \\ \vdots \\ u_{xx(m-1)} \\ u_{xxm} \end{bmatrix} =$$

$$\begin{bmatrix} \frac{1}{h^2}(-u_4 + 15u_3 - 27u_2 + 13u_1) \\ \frac{1}{h^2}(u_3 - 2u_2 + u_1) \\ \vdots \\ \frac{1}{h^2}(u_{i+1} - 2u_i + u_{i-1}) \\ \vdots \\ \frac{1}{h^2}(u_m - 2u_{m-1} + u_{m-2}) \\ \frac{1}{h^2}(13u_m - 27u_{m-1} + 15u_{m-2} - u_{m-3}) \end{bmatrix} . \tag{3.15}$$

Second Derivative - von Neumann Conditions

When the von Neumann boundary condition is specified, a different formulation is required. There are two possible approaches. The first method is simply to take the first derivative of f', which has been previously determined as given above. In this approach the boundary scheme for the second derivative becomes the Dirichlet condition for f'. Therefore, the solution of equation (3.14), with u_x replaced by u_{xx} and u replaced by u_x, would be sufficient.

The second (and more direct) method of calculating the second derivative is to use the appropriate boundary condition that will preserve the tridiagonal nature of the solution matrix, given f'_1 and the function values f_2, f_3, and f_4. Limited testing indicates that calculating f'' directly is more accurate than calculating $(f')'$. This is especially true near the boundaries where the two-step approach leads to a wider

influence of the third-order accurate boundary scheme.

The derivation of the von Neumann boundary condition for second derivatives is given in Appendix A. The third-order accurate boundary condition is

$$29f_1'' + 85f_2'' = -\frac{78}{h}f_1' + \frac{1}{h^2}\left[-81f_2 + 84f_3 - 3f_4\right] \ . \tag{3.16}$$

Periodic Boundary Conditions

The case of periodic boundary conditions are the simplest to implement numerically. The formulation maintains fourth-order spatial accuracy throughout. The resulting tri-diagonal matrix is not simply banded, but includes two extra off-diagonal coefficients, one each in the upper-right and lower-left corners of the left-hand-side coeffient array. These additional coefficients do not present additional difficulties to inverting the matrix. Standard modifications for the Thomas (1949) tri-diagonal inversion algorithm are commonly available for the periodic case.

3.1.3 Spatial Filtering

Introduction

Spatial filtering is included as a feature of the model for two potential uses. First, the filter acts to partially de-alias the calculation, i.e., remove spurious accumulations of energy from the smallest scales of motion (Canuto *et al.*, 1988, p. 118). When the filter is limited to this use the calculations are direct numerical simulations (DNS) of the flows. The second use of the filter, employed occasionally here, is as a simple subgrid-scale model. When used as a subgrid-scale model the filter is similar in principle to using a variable viscosity, or hyperviscosity, that increases dissipation at smaller scales (higher wavenumbers). Hyperviscosity techniques are frequently used in simulations of geophysical flows (e.g., Winters, 1989; Lesieur, 1987). When the filter is used in this fashion the calculations are large-eddy simulations (LES).

In the gravity-wave reflection flow being studied, the main interactions that occur are at large scales and can be well resolved. Both DNS and LES are used to investigate the flows over a large range of Reynolds numbers. For the higher Reynolds number

cases, using the large-eddy simulations, attention is focused on the large scales of motions and the manner in which energy is transferred to the intermediate-scale motions; phenomena at the smaller, dissipative scales are modeled. For these cases the model damps out interactions that occur on scales too small to be resolved on the numerical mesh. This is accomplished by adding to the real viscous dissipation in the system a scale-dependent filter. Two types of filtering techniques, the explicit and compact methods, are described below.

Explicit Filter Method

To enhance the performance of the finite difference method, a small amount of fourth-order spatial smoothing may be added to the right-hand sides of (2.19) - (2.21) to decrease aliasing errors without decreasing the formal accuracy of the scheme. Aliasing errors appear in finite-difference schemes mainly as the buildup of spurious amplitudes at the wavelengths corresponding to the smaller resolvable grid scales. In nonlinear equations, aliasing errors are related to the cascade of energy towards unresolvable scales, finer than the computational mesh. A one-dimensional fourth-order accurate filter is of the form

$$\breve{u}_i = u_i - \gamma_4(u_{i+2} - 4u_{i+1} + 6u_i - 4u_{i-1} + u_{i-2}) \ , \tag{3.17}$$

where $\breve{u}_i$ represents a filtered value of u_i, and γ_4 represents the strength of the filter. In this model a two-dimensional fourth-order accurate filter of the form

$$\begin{aligned} \breve{u}_{i,k} \ &= \ u_{i,k} - \ \gamma_4 \left(u_{i,k+2} - 4u_{i,k+1} + 6u_{i,k} - 4u_{i,k-1} + u_{i,k-2}\right. \\ &\quad \left. + u_{i+2,k} - 4u_{i+1,k} + 6u_{i,k} - 4u_{i-1,k} + u_{i-2,k}\right) \end{aligned} \tag{3.18}$$

can be used to selectively filter out the buildup of energy at the most poorly resolved scales. The filter may be applied after the velocity field has been time stepped or included in the time-stepping scheme as an extra term on the right hand side of (2.19).

If the filter is incorporated into the time-stepping scheme, it is necessary to evaluate the filter at the $n-1$ time level because of stability considerations which arise

when using the leap-frog time differencing scheme discussed below. The maximum stable value of γ_4 is 1/16. For the boundary nodes, e.g., $k = 1, 2, 3, n-2, n-1, n$, no filter, a lower-order filter, or a one-sided filter can be used.

The filter in (3.20) is a second-order finite difference representation that models the term

$$\gamma_4 \, (\Delta x)^4 \, \frac{\partial^4 u}{\partial x^4} \ ,$$

which has a dissipative effect on u and smoothes the solution. The leading order truncation-error term resulting from taking derivatives with the compact scheme is of the form

$$O(\Delta x)^4 \, \frac{\partial^5 u}{\partial x^5} \ ,$$

which has dispersive effects on the solution. This fourth-order filter preserves the global fourth-order truncation error of the compact scheme. Leading order error terms that contain odd-order derivatives are dispersive in nature; even-order derivatives have a dissipative effect.

To understand why filtering may alternatively be thought of simply as a desirable modification of the truncation error, consider that the filtered x-momentum equation when spatially discretized is of the form

$$\begin{aligned} \frac{\partial u}{\partial t} = & -u\frac{\partial u}{\partial x} - w\frac{\partial u}{\partial z} - \frac{\partial p}{\partial x} + \frac{1}{Re}\left(\frac{\partial^2 u}{\partial x^2} + \frac{\partial^2 u}{\partial z^2}\right) \\ & + u\frac{(\Delta x)^4}{30}\,\frac{\partial^5 u}{\partial x^5} + w\frac{(\Delta z)^4}{30}\,\frac{\partial^5 u}{\partial z^5} + \frac{(\Delta x)^4}{30}\,\frac{\partial^5 p}{\partial x^5} \\ & - \frac{(\Delta x)^4}{Re\,240}\,\frac{\partial^6 u}{\partial x^6} - \frac{(\Delta z)^4}{Re\,240}\,\frac{\partial^6 u}{\partial z^6} \\ & - \gamma_4 \, (\Delta x)^4 \, \frac{\partial^4 u}{\partial x^4} - \gamma_4 \, (\Delta z)^4 \, \frac{\partial^4 u}{\partial z^4} \ . \end{aligned} \tag{3.19}$$

Here the top line of (3.19) is the differential equation to be approximated by fourth-order differences. The second and third lines represent the leading order truncation error terms from approximating each term of the equation. (The time derivative discretization is not represented here but, with the third-order Adams Bashforth time stepping scheme discussed below, also gives rise to a truncation error term of order $(\Delta t)^3$.) Finally, note that the last two terms on the fourth line of (3.19)

represent artificial diffusion, added to the system to help maintain a smooth solution, and these do not degrade the overall fourth-order accuracy of the difference equation. It is more common, however, to consider the addition of spatial filtering to the true viscous diffusion terms to be like a hyperviscosity, which is scale dependent, more strongly damping the small scale fluctuations.

Compact Filter Method

It is advantageous to use the properties of the compact scheme to improve accuracy and scale selectivity of the spatial filter. Lele (1992) presents families of fourth- and sixth-order filters. He demonstrates compact filtering to be superior to normal explicit filtering for damping the shortest waves. In many formulations, as illustrated by the figures below, fourth-order compact filters can be superior to sixth-order explicit filters.

In the internal wave model a fourth-order compact filter is used. The scheme requires solution of another tridiagonal matrix. Lele's Equation (C.2.1),

$$\begin{aligned} \beta_1 \breve{u}_{i-2} + \alpha_1 \breve{u}_{i-1} + \breve{u}_i + \alpha_1 \breve{u}_{i+1} + \beta_1 \breve{u}_{i-2} = \\ a_1 u_i + \tfrac{b_1}{2}(u_{i+1} + u_{i-1}) + \tfrac{c_1}{2}(u_{i+2} + u_{i-2}) - \tfrac{d_1}{2}(u_{i+3} + u_{i-3}) \ , \end{aligned} \tag{3.20}$$

represents the filtering process.

The filter is represented by the transfer function, $T_c(\omega_c)$, satisfying $\breve{u}_j = T_c(\omega_c)\, u_j$. It is derived by assuming Fourier component wave solutions

$$u_j = \hat{u}\, e^{i\omega_c j} \ , \quad \omega_c = k\Delta x \tag{3.21}$$

in (3.20). The transfer function for (3.20) is

$$T_c(\omega_c) = \frac{a_1 + b_1 \cos(\omega_c) + c_1 \cos(2\omega_c) + d_1 \cos(3\omega_c)}{1 + 2\alpha_1 \cos(\omega_c) + 2\beta_1 \cos(2\omega_c)} \ . \tag{3.22}$$

Several explicit and compact filters for various coefficients are compared in Figures 3.4 and 3.5.

A family of fourth-order tridiagonal schemes is found when the constraints $T_c(\pi) = 0$, and $\dfrac{dT_c}{d\omega_c}(\pi) = 0$ are imposed together with $\beta_1 = 0$. The coefficients for fourth-order

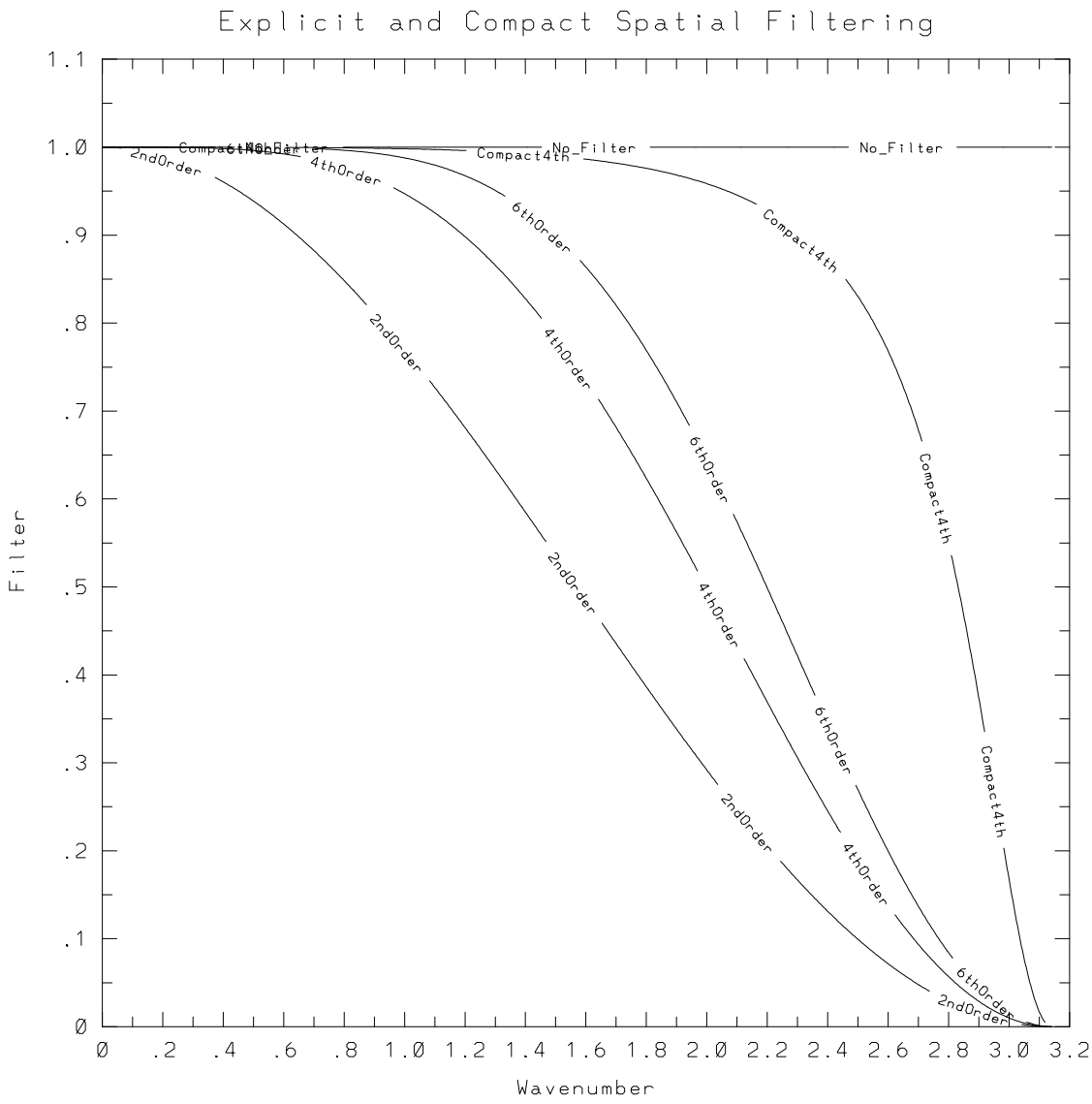

Figure 3.4: Compact and explicit filter functions for second-order explicit filter, fourth-order explicit filter, sixth-order explicit filter, tridiagonal four-order compact filter, and no-filter.

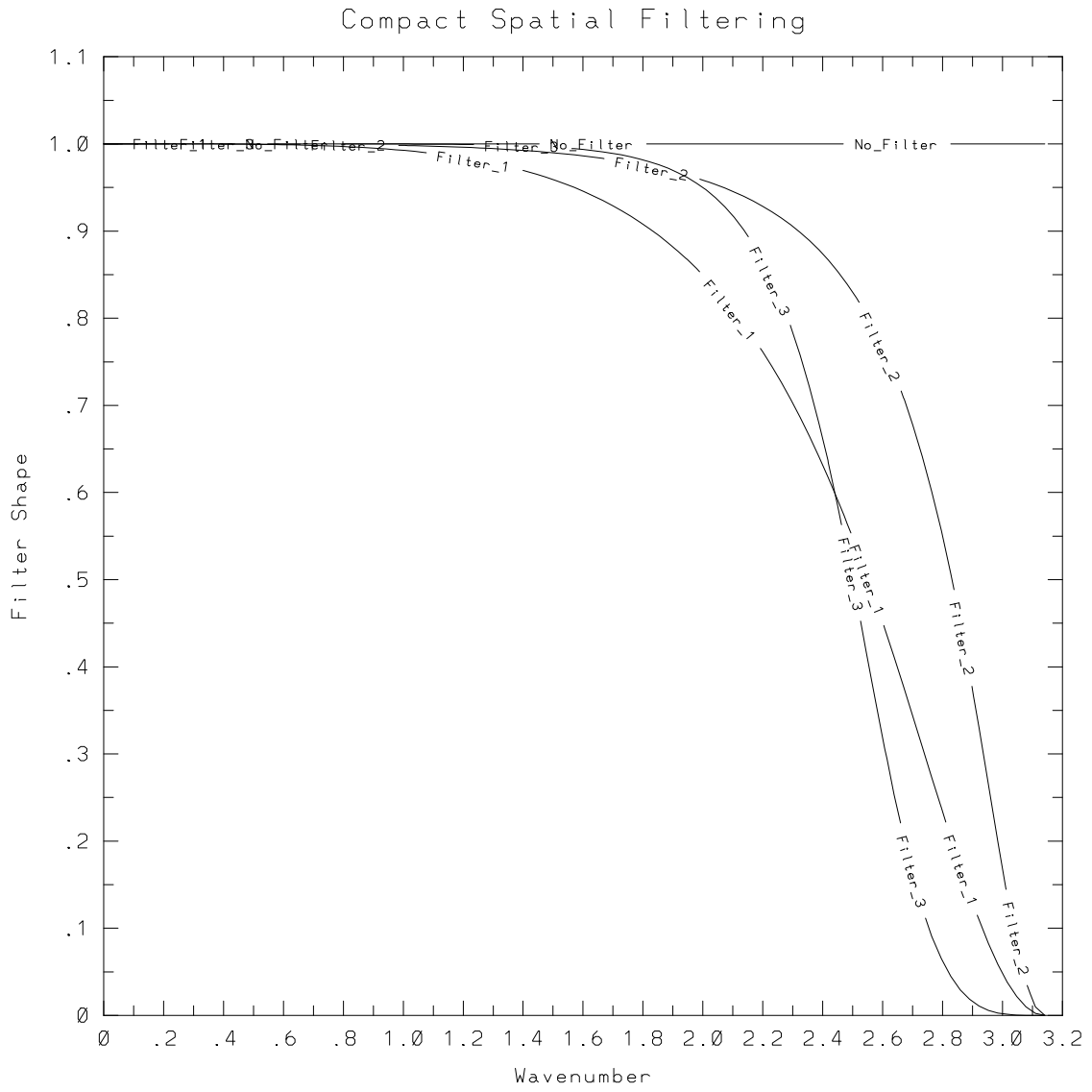

Figure 3.5: Comparison of three compact filters obtained by varying the coefficients α_1 and β_1. Filters 1 and 2 are described in the text; see text next page. Filter 3 is a pentadiagonal filter with coefficients $\alpha_1 = 0.6522474$, $\beta_1 = 0.1702929$.

accuracy are

$$a_1 = \frac{1}{8}(5 + 6\alpha_1 + 16d_1),\ b_1 = \frac{1}{2}(1 + 2\alpha_1 - 2d_1),\ c_1 = \frac{-1}{8}(1 - 2\alpha_1 + 16d_1)\ . \quad (3.23)$$

Similarly, a family of sixth-order tridiagonal filters has coefficients

$$a_1 = \frac{1}{16}(11 + 10\alpha_1)\ ,\ \ b_1 = \frac{1}{32}(15 + 34\alpha_1)\ ,$$
$$c_1 = \frac{1}{16}(-3 + 6\alpha_1)\ ,\ \ d_1 = \frac{1}{32}(1 - 2\alpha_1)\ . \quad (3.24)$$

From inspection of various filters satisfying (3.23), two have been chosen that confine most of their effects below the $4\Delta x$ wave. The first is represented by Filter 1 in Figure 3.5 and has coefficients

$$\alpha_1 = 0.4,\ a_1 = 0.925,\ b_1 = 0.9,\ c_1 = -0.025,\ d_1 = 0\ . \quad (3.25)$$

Therefore, the first selected one-dimensional filter is

$$0.4\check{u}_{i-1} + \check{u}_i + 0.4\check{u}_{i+1} =$$
$$0.925u_i + 0.45(u_{i+1} + u_{i-1}) - 0.0125(u_{i+2} + u_{i-2})\ , \quad (3.26)$$

or equivalently,

$$0.4\check{u}_{i-1} + \check{u}_i + 0.4\check{u}_{i+1} = 0.4u_{i-1} + u_i + 0.4u_{i+1}$$
$$-\tfrac{1}{80}\left(u_{i+2} - 4u_{i+1} + 6u_i - 4u_{i-1} + u_{i-2}\right)\ . \quad (3.27)$$

The second filter is confined even more strongly to high wave numbers and is represented by Filter 2 in Figure 3.5. It has coefficients

$$\alpha_1 = 0.475,\ a_1 = 0.98125,\ b_1 = 0.975,\ c_1 = -0.00625,\ d_1 = 0\ . \quad (3.28)$$

Therefore, the second filter is

$$0.475\check{u}_{i-1} + \check{u}_i + 0.475\check{u}_{i+1} = 0.475u_{i-1} + u_i + 0.475u_{i+1}$$
$$-\tfrac{1}{320}\left(u_{i+2} - 4u_{i+1} + 6u_i - 4u_{i-1} + u_{i-2}\right)\ . \quad (3.29)$$

The two-dimensional version of (3.27) or (3.29) is realized by performing two passes of the one-dimensional filter orthogonally. Note that there are alternative

fourth-order schemes utilizing a seven point stencil on the right hand side of (3.20). The additional free parameter, d_1, can be used to specify other properties that may be desirable for filtering, with the condition $\frac{d^2T_c}{d\omega_c^2}(\pi) = 0$, which Lele suggests can be a desirable condition.

Explicit fourth-order formulations are necessary for the boundary nodes of the filter. Formulations that exactly filter the $\omega_c = \pi$ waves are

$$\check{u}_1 = \frac{15}{16}u_1 + \frac{1}{16}(4u_2 - 6u_3 + 4u_4 - u_5) \ , \tag{3.30}$$

$$\check{u}_2 = \frac{3}{4}u_2 + \frac{1}{16}(u_1 + 6u_3 - 4u_4 + u_5) \ . \tag{3.31}$$

3.1.4 Solution of Poisson's Equation

A variety of schemes are available to solve for the pressure. The relative advantages and disadvantages of the various schemes change depending on whether a two- or three-dimensional problem is considered and the order of accuracy desired. Two sophisticated Poisson solution packages have been obtained from the National Center for Atmospheric Research (NCAR), and one entitled SEPX4 is implemented in the two dimensional model. SEPX4 solves separable elliptic equations of the form

$$A_l(x)\frac{\partial^2 p}{\partial x^2} + B_l(x)\frac{\partial p}{\partial x} + C_l(x)\, p + \frac{\partial^2 p}{\partial z^2} = R(x,z) \ , \tag{3.32}$$

a simplified form of which is Poisson's equation. Using the method of deferred corrections, SEPX4 accepts periodic, Dirichlet, or von Neumann boundary conditions at either second- or fourth-order spatial accuracy. The three-dimensional pressure solver and the method of deferred corrections will be discussed below in Sections 3.6.5 and 3.6.6.

3.1.5 Pressure Gradient Terms

After the Poisson solver yields the pressure at every grid point, it is necessary to form the pressure derivatives, $\frac{\partial p}{\partial x}$ and $\frac{\partial p}{\partial z}$. This is accomplished using the compact scheme discussed above.

3.2 Time Differencing

3.2.1 The Projection Method

A major focus of the time-differencing scheme is to ensure that the flow satisfies the continuity equation. A third-order time accurate implementation of the projection method is utilized. The first-order accurate projection method was proposed independently by Chorin (1968) and Temam (1969) and extended to explicit time schemes by Fortin et al. (1971). The projection method and a family of related time discretization schemes are discussed in detail by Fletcher (1991), and appropriate boundary conditions are derived by Kim and Moin (1985). Additional valuable discussion of the projection method appears in Gresho (1990), and recent applications are presented by Karniadakis, Israeli, and Orszag (1991), Bell, Colella, and Glaz (1989), and Rai and Moin (1991).

The projection method solves the momentum equations in two fractional steps. The first step forms an auxiliary flow field, $\mathbf{u}^*$, at the new time level by integration of the nonlinear, buoyancy, and dissipation terms. The second step then corrects the auxiliary flow field by applying the pressure gradient to guarantee incompressible flow.

An implementation of the first step of the projection method is illustrated here using second-order Adams-Bashforth time stepping:

$$\frac{\mathbf{u}^* - \mathbf{u}^n}{\Delta t} = \frac{3}{2}\left(-\mathbf{u}\cdot\nabla\mathbf{u} - \imath_3 Ri\,\rho + \frac{1}{Re}\nabla^2\mathbf{u}\right)^n - \frac{1}{2}\left(-\mathbf{u}\cdot\nabla\mathbf{u} - \imath_3 Ri\,\rho + \frac{1}{Re}\nabla^2\mathbf{u}\right)^{n-1} . \tag{3.33}$$

It is followed by the projection step, in which $\mathbf{u}^*$ is projected onto its non-divergent subspace, $\mathbf{u}^{n+1}$, according to the relations

$$\frac{\mathbf{u}^{n+1} - \mathbf{u}^*}{\Delta t} + \nabla\overline{p}^{n+1} = 0 , \tag{3.34}$$

$$\nabla\cdot\mathbf{u}^{n+1} = 0 . \tag{3.35}$$

The appropriate pressure field for the projection step is formed by taking the divergence of (3.34) with the condition (3.35) and solving the resulting Poisson equa-

tion,

$$\nabla^2 \overline{p}^{n+1} = \frac{\nabla \cdot \mathbf{u}^*}{\Delta t} \ . \tag{3.36}$$

Boundary conditions for Poisson's equation of the Neumann type are obtained by using the component of (3.34) normal to the boundary, e.g. at $z = 0$,

$$\left.\frac{\partial \overline{p}}{\partial \mathbf{N}}\right|_B^{n+1} = -\frac{\left(\mathbf{u}_B^{n+1} - \mathbf{u}_B^*\right) \cdot \mathbf{N}}{\Delta t} = \left.\frac{\partial p}{\partial z}\right|_B^{n+1} = -\frac{w_B^{n+1} - w_B^*}{\Delta t} \ . \tag{3.37}$$

The boundary values $\mathbf{u}_B^{n+1} \cdot \mathbf{N}$ are updated according to known boundary conditions, such as those appropriate for no-slip, free-slip, or periodic boundaries. The key to making (3.37) a stable boundary condition is correctly evaluating $\mathbf{u}_B^* \cdot \mathbf{N}$. Following Kim and Moin, (3.33) is solved at the boundaries using one-sided derivatives as if no true boundary condition were known. Thus, the auxiliary velocity field, $\mathbf{u}_B^*$, influences the determination of the pressure field at the boundary, which in turn influences the determination of the boundary velocity, $\mathbf{u}_B^{n+1}$, at the new time level. The projection step is completed by updating the boundary velocities to their prescribed values at each new time level to eliminate the buildup of roundoff and truncation errors.

In their discussion of the projection method, Peyret and Taylor (1983) erroneously state that, since the auxiliary velocity field appears both in the boundary condition for pressure (3.37) and Poisson's equation (3.36), it cancels identically, and therefore, a homogeneous boundary condition for pressure is sufficient. Chorin (1984) points out that their scheme is unstable and inconsistent. This inconsistency is demonstrated by Kim and Moin. Gresho (1990) claims, however, that he has experienced no inconsistency using the homogeneous boundary condition, and discusses the two options in detail, giving preference to use of the simpler homogeneous boundary condition.

In the present work, the pressure field was found to be unstable when the homogenous boundary condition was applied and that the instability became significant at long integration times. The numerical instability appears depend on the type of physical velocity boundary conditions chosen. For a no-slip condition at the wall the instability was evident but very weak, and the time integration of the flow could be completed without significant loss of accuracy using the approximate homogeneous

pressure boundary condition. For a free-slip boundary condition, however, the instability was too large to proceed with the approximate boundary condition. The probable cause is the relative magnitude of w_B^* for the two cases, because it is nearly zero for the no-slip wall but becomes much larger in the free-slip case. It may be that the disagreement in the literature as to the nature and effect of the instability arises from experiments conducted using differing physical boundary conditions. Fletcher (1991) adds that, for the closely related MAC method, the permissible use of $\left.\dfrac{\partial \overline{p}}{\partial \mathbf{N}}\right|_B = 0$ is specific to a particular second-order staggered grid spatial discretization, suggesting that other choices of numerical methods besides boundary conditions may also influence the strength and nature of the instability.

The projection method uses the fact that the pressure is a Lagrange multiplier and the pressure gradient acts only to maintain nondivergence in an incompressible flow. This fact may be illustrated by considering aspects of the momentum and continuity equations in wave number space. In the standard manner, the continuity equation is written in wave number space as

$$\mathbf{k} \cdot \hat{\mathbf{u}} = 0 \,, \tag{3.38}$$

signifying that the wave number amplitude $\hat{\mathbf{u}}$ is perpendicular to the wave number vector $\mathbf{k}$.

The pressure gradient is written $\mathbf{k}\hat{p}$ in wave number space and acts in the direction of $\mathbf{k}$. Therefore, when the nonlinear, buoyancy, or diffusion terms act in a direction in wave number space to force the flow out of the plane of incompressibility, the pressure gradient provides the restoring force to maintain incompressibility.

The scheme is called the projection method because it forms $\mathbf{u}^{n+1}$ by taking the projection of the velocity vector, $\mathbf{u}^*$, onto the incompressibility plane in wave number space. With this understanding of the limited influence of the pressure gradient, it is evident that pressure may be treated separately in the time scheme without degrading the formal order of accuracy.

Karniadakis et al. (1991) demonstrate that the temporal treatment of the projection step is exact and that the accuracy of the overall method is determined only

by the accuracy used for other terms in governing equations. They formalize the demonstration by writing the definition (following their nomenclature)

$$\nabla \overline{p}^{n+1} = \frac{1}{\Delta t} \int_{t_n}^{t_{n+1}} \nabla p \, dt \; . \tag{3.39}$$

Thus, the projection method is compatible with the explicit Adams-Bashforth scheme, except that the average pressure field, $\overline{p}^{n+1}$, is used to guarantee incompressible flow at the $n+1$ time level rather than the pressure field p^n from time level n.

From this view, advantages of the projection method become evident. The average pressure field $\overline{p}^{n+1}$ properly compensates for the truncation errors of the time and spatial discretization schemes that occur during the time integration, and thus the projection method is not susceptible to the accumulation of errors from the right hand side of Poisson's equation in the same way as an explicit pressure treatment (see, e.g., Equation (2.22)). A slightly divergent flow field arising from roundoff and truncation errors associated with the discretization of $\dfrac{\partial u}{\partial x} + \dfrac{\partial w}{\partial z}$ in Poisson's equation does not become more divergent. Furthermore, it is evident that the right hand side of (3.36) is much easier to evaluate than a discretized form of Poisson's equation for pressure given above as either (2.22) or (2.23). Finally, (3.39) demonstrates that the method does not degrade the second-order accuracy of the time integration scheme. Alternate second- and third-order formulations of the projection method with implicit treatment of the diffusion terms are employed by Kim and Moin (1985), Karniadakis et al. (1991), and Bell et al. (1989).

3.2.2 Third-order Adams-Bashforth Scheme

The projection method is implemented together with the third-order Adams-Bashforth (AB3) scheme. Advantages of the AB3 scheme, compared with several other time differencing methods, are discussed in Durran (1991). The AB3 method is given by

$$u^{n+1} = u^n + \Delta t \left(\frac{23}{12} \mathcal{F}^n - \frac{16}{12} \mathcal{F}^{n-1} + \frac{5}{12} \mathcal{F}^{n-2} \right) \; , \tag{3.40}$$

where $\mathcal{F}^n$ represents the flux of u evaluated at time level n.

The main advantage of the AB3 scheme over more commonly used explicit second-order schemes, such as the leap-frog (L-F) method or the second-order Adams-Bashforth (AB2) scheme, is that it is stable. The leap-frog (L-F) scheme is subject to a temporal oscillation of period $2\Delta t$. The second-order Adams-Bashforth (AB2) scheme has a weak unstable growth of order $(\Delta t)^3$ (Canuto *et al.*, 1988, p. 102).

The amplitude error for AB3 time differencing is $1 - \dfrac{3(\omega_c \Delta t)^4}{8}$, and it has a leading phase error of $1 + \dfrac{289(\omega_c \Delta t)^4}{720}$. These errors may be compared to the amplitude and phase errors of the L-F and AB2 schemes. The L-F scheme has no amplitude error but has a leading phase error of $1 + \dfrac{(\omega_c \Delta t)^2}{6}$ and is subject to the familiar time-splitting instability. The AB2 scheme has an amplitude error of $1 + \dfrac{(\omega_c \Delta t)^4}{4}$ (unstable) and a leading phase error $1 + \dfrac{5(\omega_c \Delta t)^2}{12}$.

Startup of the simulation is done by using a forward Euler (AB1) time step for the first step and a AB2 time step for the second time step.

3.2.3 Variable Time Step Scheme

Greater efficiency is introduced in the model by using a variable time-stepping scheme that allows the time step to change based upon local and temporal stability criteria. (When a spatially variable grid is used the local stability is proportional to the grid spacing, see Sections 3.2.5 and 3.4.4.) Gear and Watanabe (1974) demonstrate that the variable time-stepping (multistep) methods have the same stability properties as the constant step Adams-Bashforth schemes if the time step is changed in a relatively smooth fashion. Third-order accurate time stepping is maintained by integrating according to the relations

$$u_{n+1} = u_n + A_t \Delta t_1 u'_n + B_t(\Delta t_1 + \Delta t_2) u'_{n-1} + C_t(\Delta t_1 + \Delta t_2 + \Delta t_3) u'_{n-2} \,, \qquad (3.41)$$

where Δt_1 is the time step between time level $n+1$ and n, Δt_2 is the time step between time level n and $n-1$, Δt_3 is the time step between time level $n-1$ and $n-2$, and

$$A_t = 1 + \frac{\Delta t_1(2\Delta t_1 + 6\Delta t_2 + 3\Delta t_3)}{6\Delta t_2(\Delta t_2 + \Delta t_3)} \,, \qquad (3.42)$$

$$B_t = \frac{-\Delta t_1^2(2\Delta t_1 + 3\Delta t_2 + 3\Delta t_3)}{6\Delta t_2 \Delta t_3(\Delta t_1 + \Delta t_2)} \ , \tag{3.43}$$

$$C_t = \frac{\Delta t_1^2(2\Delta t_1 + 3\Delta t_2)}{6\Delta t_3(\Delta t_1 + \Delta t_2 + \Delta t_3)(\Delta t_2 + \Delta t_3)} \ . \tag{3.44}$$

Figure 3.6 shows the actual time step used throughout a three-dimensional simulation. In the beginning of the simulation a constant time step fixed by the diffusion stability limit is used (see Section 3.2.5 for definitions of the advection and diffusion stability criteria). After approximately time 30, the advection stability limit is more restrictive, and the time step is adjusted so that the most severe Courant number criteria is held at a stable value of 99% of the maximum allowable value. This condition is typically encountered at the very fine mesh nearest to the wall during the wave amplification process. By using the variable time step approach an efficiency of more than 50 % is saved. The calculation shown here (Case 19 from Table 4.1) took 12,000 time integration steps to complete, but if a constant time step had been used that was small enough to maintain numerical stability throughout the simulation, the calculation would have taken over 25,000 time steps. Additional difficulty is avoided with the variable time step method, because a priori (before the simulation) the size of a sufficiently small (constant) time step is unknown. In contrast, in the variable time step approach, the flow field itself sets the most economical stable time step.

3.2.4 Treatment of the Diffusion Term

The diffusion term is treated explicitly with AB3 time stepping in this model. Other researchers have developed models that treat the diffusion term implicitly; e.g., Karniadakis et al. (1991) uses third-order Adams-Moulton time differencing. Implicit treatment of the diffusion term allows larger stable time steps. However, experience has shown that, for typical cases of the problem being studied here, the non-linear advection term has more restrictive stability criteria than the explicit treatment of the diffusion term (see the following section). Thus, there is no clear advantage to using the more complicated implicit diffusion treatment.

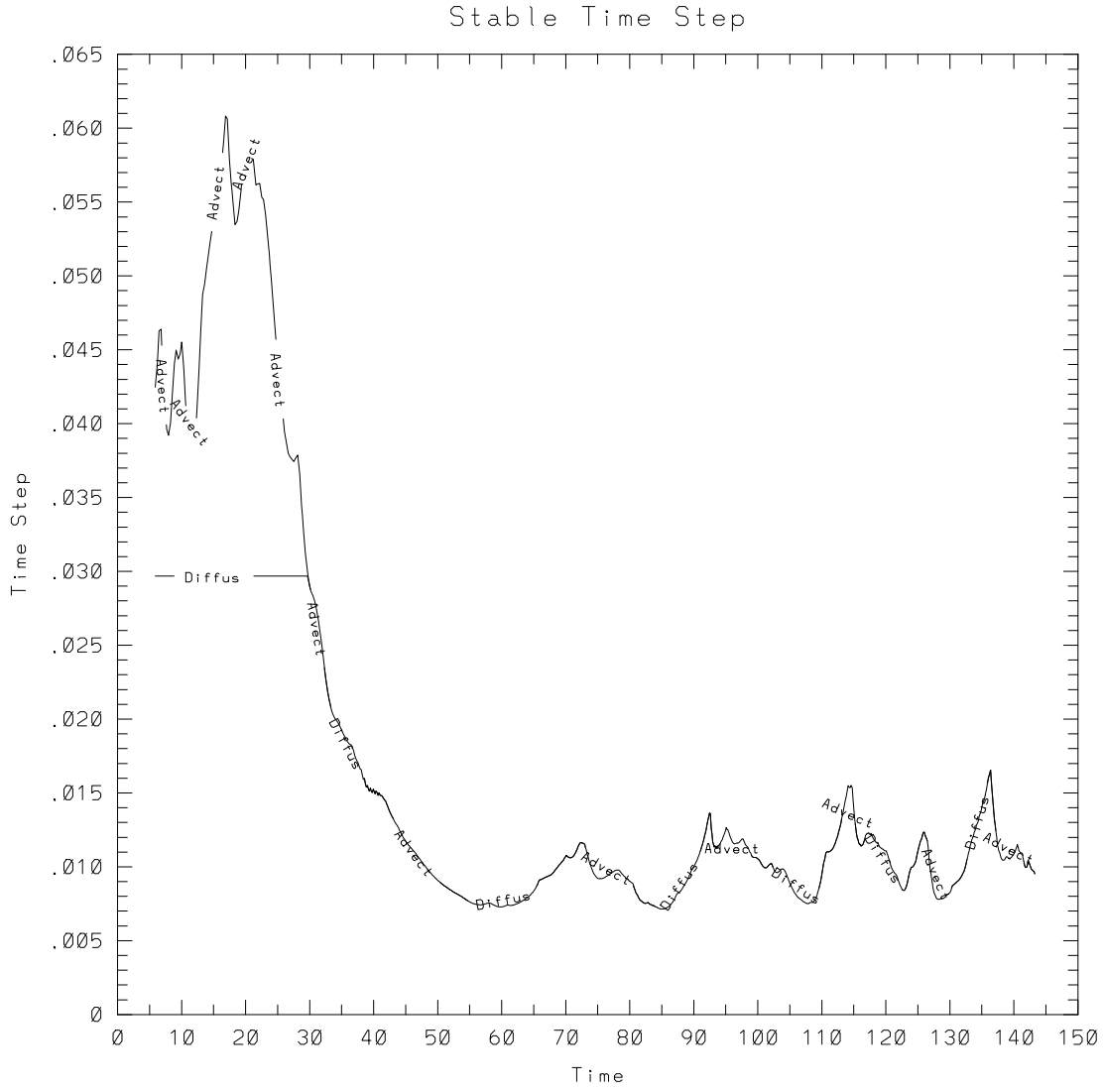

Figure 3.6: The time step used in the numerical simulations is allowed to adjust during the simulation to achieve the largest stable time step during the transient process. The diffusion stability limit (marked by "Diffus") is constant throughout the computation with a maximum stable time step of approximately 0.0295. For the first 30 time units this is the time step used. The line marked "Advect" is the stable value derived from the advection-buoyancy analysis below by Equation (3.53). The advection stability limit becomes smaller than the diffusion limit after time 30 and varies throughout the calculation. The "Diffus" line follows the actual time step used in the simulation after time 30.

3.2.5 Numerical Stability Criteria

Advection, Buoyancy, and Pressure Terms

The stability limits of the combined time and space differencing schemes may be analyzed by performing a von Neumann stability analysis on the linearized system of governing equations. Following the approach of Durran (1992, pg. 152) limits on the maximum stable time steps for the numerical simulation are obtained. The equations are linearized about a mean velocity $\bar{U}(x)$.

$$\frac{\partial u}{\partial t} + \bar{U}\frac{\partial u}{\partial x} + \frac{\partial p}{\partial x} = 0 \,, \tag{3.45}$$

$$\frac{\partial w}{\partial t} + \bar{U}\frac{\partial w}{\partial x} + Ri\,\rho + \frac{\partial p}{\partial z} = 0 \,, \tag{3.46}$$

$$\frac{\partial \rho}{\partial t} + \bar{U}\frac{\partial \rho}{\partial x} - w = 0 \,, \tag{3.47}$$

$$\frac{\partial u}{\partial x} + \frac{\partial w}{\partial z} = 0 \,. \tag{3.48}$$

With Fourier component wave solutions for u, w, p, and ρ, of the form $u^n_{j,m} = \hat{u}e^{i(kj\Delta x + lm\Delta z - \omega_c n\Delta t)}$ and with leap-frog time stepping to illustrate the analysis, Equations (3.45) - (3.48) may be written in wave number space as

$$\begin{bmatrix} -\sin\omega_c\Delta t + C_{fl}D_x & 0 & 0 & \frac{\Delta t}{\Delta x}D_x \\ 0 & -\sin\omega_c\Delta t + C_{fl}D_x & -i\,Ri\,\Delta t & \frac{\Delta t}{\Delta z}D_z \\ 0 & i\,\Delta t & -\sin\omega_c\Delta t + C_{fl}D_x & 0 \\ \frac{D_x}{\Delta x} & \frac{D_z}{\Delta z} & 0 & 0 \end{bmatrix} \begin{bmatrix} \hat{u} \\ \hat{w} \\ \hat{\rho} \\ \hat{p} \end{bmatrix} = \begin{bmatrix} 0 \\ 0 \\ 0 \\ 0 \end{bmatrix}, \tag{3.49}$$

where $C_{fl} = \dfrac{\bar{U}\Delta t}{\Delta x}$, $D_x = \dfrac{\Delta t}{\Delta x}\dfrac{3\sin(k\Delta x)}{2+\cos(k\Delta x)}$, and $D_z = \dfrac{\Delta t}{\Delta z}\dfrac{3\sin(l\Delta z)}{2+\cos(l\Delta z)}$.

For non-trivial solutions the determinant of the coefficient matrix must be zero, which leads to the condition

$$(-\sin\omega_c\Delta t + C_{fl}D_x)^2 = \frac{Ri\Delta t^2 D_x^2}{\frac{\Delta x^2}{\Delta z^2}\left(\frac{D_z}{\Delta z}\right)^2 + \left(\frac{D_x}{\Delta x}\right)^2} \ . \tag{3.50}$$

The right hand side has a maximum at $Ri\,\Delta t^2$, for all $0 \le k\Delta x \le \pi$ and $0 \le l\Delta z \le \pi$, and so the stability criteria becomes

$$|-\sin\omega_c\Delta t| \ge \left|C_{fl}D_x + \sqrt{Ri}\Delta t\right| \ . \tag{3.51}$$

The maximum value of D_x is $\sqrt{3}$ at $k\Delta x = \frac{2\pi}{3}$; thus, for leap-frog time stepping, for $\omega_c\Delta t$ to be real valued, the stability criteria reduces to

$$\sqrt{3}\,C_{fl} + \sqrt{Ri}\Delta t \le 1\,. \tag{3.52}$$

Adams-Bashforth third-order time stepping has a stronger stability restriction than the leap-frog scheme (see Durran, 1991). In this case it is required that

$$\sqrt{3}\,C_{fl} + \sqrt{Ri}\Delta t \le 0.724\,. \tag{3.53}$$

For this model $\Delta z < \Delta x$, which requires modification of the forgoing analysis using the alternate definition of

$$C_{fl} = \frac{\overline{U}_{max}\,\Delta t}{\Delta z}\ , \tag{3.54}$$

where the largest value of $\frac{\overline{U}_{max}}{\Delta z}$ is sought in the domain on the variable grid to be discussed below (Section 3.4.4) and $\overline{U}_{max} = \sqrt{u^2+v^2+w^2}_{max}$ is defined so that $\frac{\overline{U}_{max}}{\Delta z}$ represents the most stringent stability restriction in the domain.

Diffusion Terms

The diffusion terms require additional stability criteria for the governing equations and may be analyzed separately because of the linearity of the terms. Again for wave solutions, and with the discrete wave number representation for the second derivative from the compact scheme, (3.6), then the AB3 method yields the restriction

$$\beta = \frac{\Delta t}{Re\Delta z^2} \le \frac{0.545}{6}\ . \tag{3.55}$$

This result is less restrictive than the time-lagged explicit treatment necessary for the leap-frog scheme, which yields $\beta \leq \frac{0.5}{6}$. The stability analysis for the density equation is equivalent, except that it requires a modified definition of $\beta_\rho = \frac{\Delta t}{Re\ Pr\ \Delta z^2}$.

3.3 Numerical Boundary Conditions

3.3.1 Rayleigh Damping Sponge Layer

A wave-absorbing sponge layer is frequently used as an open boundary condition. In this model a sponge layer is used in the upper region of the finite computational domain. This layer is typically located far below the free surface of the fluid, and its purpose is simply to mimic the presence of the fluid above the computational domain. Rayleigh damping is an efficient wave-absorbing sponge layer, and is competitive with the best radiation boundary schemes for certain parameter ranges. The accuracy, however, is highly dependent upon the number of points used in the sponge layer. Durran et al. (1992) compare the wave absorbing layer to other wave permeable outflow boundary conditions. Typically, in the present model, ten percent of the total grid points ($\sim 13 - 40$) are used to form the sponge layer. The damping coefficients are suggested by Klemp and Lilly (1978) and are graphed in Figure 3.7. The method is given by Davies (1983) and Durran et al (1992).

Rayleigh damping is of the form

$$\bar{\mu}_i^{n+1} = \mu_i^{n+1} - \sigma_i \left(\mu_i^{n+1} - \mu_{io} \right) \ , \tag{3.56}$$

where $\bar{\mu}$ is the damped value of an arbitrary function (such as $\mathbf{u}$ or ρ), μ is the predamped value, μ_{io} is the relaxed value of the function in the sponge region (usually zero), and σ_i is the damping coefficient given for the present case by the Gaussian shape

$$\sigma_z = e^{\frac{-z^2}{2}} \ \ , \ \ 0 \leq z \leq 3.5 \ \ . \tag{3.57}$$

The two major disadvantages with the sponge layer are that it becomes computationally expensive in two- or three-dimensional problems, and it has the property that longer waves are absorbed less efficiently than short waves.

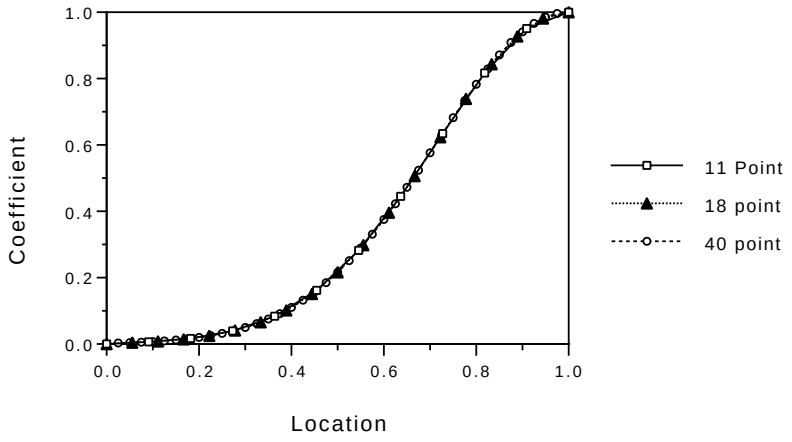

Figure 3.7: Rayleigh damping coefficients for sponge layers of Gaussian shape. The location is normalized by the thickness of the sponge layer.

Additional complexity arises in the implementation of the sponge layer because it does not damp the flow in a nondivergent manner. The divergence is evident since the coefficients σ_i are only functions of z. This problem is solved by implementing the Rayleigh damping step before the projection step. In this manner the total damping procedure is

$$\bar{u}_i^{n+1} = u_i^* - \sigma_i \left(u_i^* - u_{io}\right) - \Delta t \frac{\partial p^{n+1}}{\partial x} \,, \tag{3.58}$$

where the value of the pressure gradient is determined by the projection method.

3.3.2 Free-Slip Boundary Conditions

The free-slip boundary conditions require numerical implementation of at least third-order accuracy to maintain global fourth-order accuracy in the model. A second-order implementation of the condition $\left.\dfrac{\partial u}{\partial z}\right|_b = 0$ is simple and intuitive, i.e., $u_b^{n+1} = u_{b+1}^{n+1}$. The third- and fourth-order free-slip conditions are found by matching Taylor series coefficients to the desired order of accuracy. On a uniform mesh they are, respectively,

$$u_1 = \frac{4}{3}u_2 - \frac{1}{3}u_3 \,, \tag{3.59}$$

$$u_1 = \frac{18}{11}u_2 - \frac{9}{11}u_3 + \frac{2}{11}u_4 \,. \tag{3.60}$$

On a mesh with a clustered grid the third-order accurate free-slip boundary condition is

$$u_1 = \frac{(\Delta z_1 + \Delta z_2)^2}{(\Delta z_1 + \Delta z_2)^2 - \Delta z_1^2}\, u_2 + \frac{\Delta z_1^2}{\Delta z_1^2 - (\Delta z_1 + \Delta z_2)^2}\, u_3 \;, \tag{3.61}$$

where Δz_1 is the distance between the locations of u_1 and u_2, and Δz_2 is the distance between the locations of u_2 and u_3.

The specification of the free-slip condition is implemented before the projection step so that any divergence associated with the boundary condition is corrected during the projection step.

Density Boundary Condition

Another Neumann boundary condition arises in the implementation of the zero flux boundary condition for density. A shear stress, partial-slip velocity boundary condition would have the same form. The density boundary condition, $\left.\frac{\partial \rho}{\partial z}\right|_b = -\frac{\partial \overline{\rho}}{\partial z}$, with fourth-order accuracy on the uniform mesh is

$$\rho_1 = \frac{-6}{11}\Delta z \left(-\frac{\partial \overline{\rho}}{\partial z}\right) + \frac{18}{11}\rho_2 - \frac{9}{11}\rho_3 + \frac{2}{11}\rho_4 \;. \tag{3.62}$$

The formula for third-order accuracy on a variable grid is

$$\rho_1 = \frac{-\Delta z_1 \Delta z_2 (\Delta z_1 + \Delta z_2)}{(\Delta z_1 + \Delta z_2)^2 - \Delta z_1^2} \left.\frac{\partial \rho}{\partial z}\right|_1 + \frac{(\Delta z_1 + \Delta z_2)^2}{(\Delta z_1 + \Delta z_2)^2 - \Delta z_1^2}\, \rho_2 + \frac{\Delta z_1^2}{\Delta z_1^2 - (\Delta z_1 + \Delta z_2)^2}\, \rho_3 \;. \tag{3.63}$$

3.4 Problem Geometry

3.4.1 Rotation of Coordinate System

To accommodate a sloping ocean floor, it is advantageous to rotate the coordinate system so that the x' axis is directed along the floor and z' is perpendicular to x'. This complicates some other aspects of the problem. For example, the x' momentum equation has a component of the gravity force, and the density equation has the velocity component u' (in addition to w') multiplying the mean density gradient. The background density and pressure fields are not periodic at the lateral boundaries. Since

they have been subtracted from the governing equations, however, if the remaining perturbation density and pressure fields are initially periodic in the x' direction, they will remain so.

The governing equations, (2.18) - (2.21), are presented below for a coordinate system rotated through angle α; the ($'$)'s, have been dropped from the equations for convenience. Dropping the ($'$)'s will be the standard convention throughout the remainder of the thesis. Hereafter, the (x, y, z) coordinate system refers to the (x', y, z') coordinate system and the primes are only included in the text when it is especially important to emphasize that the rotated coordinate system is implied. The bottom slope is a key parameter throughout the present work and will be specified in each circumstance. Even the flat bottom case will be referred to by (x, y, z) coordinates without special notation except for detailing that $\alpha = 0$. The governing equations are

$$\frac{\partial u}{\partial x} + \frac{\partial w}{\partial z} = 0 \,, \tag{3.64}$$

$$\frac{\partial u}{\partial t} + u\frac{\partial u}{\partial x} + w\frac{\partial u}{\partial z} + Ri\ \rho\ \sin\alpha = -\frac{\partial p}{\partial x} + \frac{1}{Re}\left(\frac{\partial^2 u}{\partial x^2} + \frac{\partial^2 u}{\partial z^2}\right) \,, \tag{3.65}$$

$$\frac{\partial w}{\partial t} + u\frac{\partial w}{\partial x} + w\frac{\partial w}{\partial z} + Ri\ \rho\ \cos\alpha = -\frac{\partial p}{\partial z} + \frac{1}{Re}\left(\frac{\partial^2 w}{\partial x^2} + \frac{\partial^2 w}{\partial z^2}\right) \,, \tag{3.66}$$

$$\frac{\partial \rho}{\partial t} + u\frac{\partial \rho}{\partial x} + w\frac{\partial \rho}{\partial z} - w\ \cos\alpha - u\ \sin\alpha = \frac{1}{Pr\ Re}\left(\frac{\partial^2 \rho}{\partial x^2} + \frac{\partial^2 \rho}{\partial z^2}\right) \,. \tag{3.67}$$

The Poisson equation for pressure (3.36) used in the projection method as discussed in Section 3.2.1 is unchanged by the rotation.

$$\nabla^2 \overline{p}^{n+1} = \frac{1}{\Delta t}\left(\frac{\partial u^*}{\partial x} + \frac{\partial w^*}{\partial z}\right) \,. \tag{3.68}$$

3.4.2 Flow Initialization

Gravity waves may be initialized by specifying the wave as a perturbed density field, together with the instantaneous velocities associated with the wave. The initialization method of Section 2.5 is presented here for the rotated reference frame. The polarization conditions for a wave packet localized in z' (the primes have been dropped for

convenience throughout) are given by:

$$u(x,z,0) = -\frac{Am}{k}\,F(z)\cos(kx+mz) - \frac{A}{k}\,F'(z)\sin(kx+mz)\ , \tag{3.69}$$

$$w(x,z,0) = AF(z)\cos(kx+mz)\ , \tag{3.70}$$

$$\rho(x,z,0) = \frac{-A\cos\alpha}{\omega}\,F(z)\sin(kx+mz) + \frac{A\,m\sin\alpha}{\omega\,k}\,F(z)\sin(kx+mz) - \frac{A\sin\alpha}{\omega\,k}\,F'(z)\cos(kx+mz)\ , \tag{3.71}$$

$$\omega^2 = \frac{Ri\ (k\cos\alpha - m\sin\alpha)^2}{k^2+m^2}\ , \tag{3.72}$$

$$F(z) = \exp[-b(z-\frac{L_z}{2})^2],\ \ 0 \le z \le L_z\ , \tag{3.73}$$

$$F'(z) = -2b(z-\frac{L_z}{2})\ \exp\left[-b(z-\frac{L_z}{2})^2\right]\ ,\ \ 0 \le z \le L_z\ . \tag{3.74}$$

The phase and group velocities in the rotated coordinate system are given by

$$\vec{C}_{ph} = \frac{\sqrt{Ri}\ (k\cos\alpha - m\sin\alpha)}{(k^2+m^2)^{3/2}}\ \left(k\,\hat{i} + m\,\hat{k}\right)\ , \tag{3.75}$$

$$\vec{C}_{g} = \frac{\sqrt{Ri}\ (m\cos\alpha + k\sin\alpha)}{(k^2+m^2)^{3/2}}\ \left(m\,\hat{i} - k\,\hat{k}\right)\ . \tag{3.76}$$

A wave with group velocity propagating downward and to the right at angle θ to the horizontal has wave numbers defined by $\theta = \tan^{-1}\left(\frac{k}{m}\right) - \alpha$. Table 3.2 presents the angle of propagation for several combinations of wave numbers.

The function $F(z)$ is used to localize the wave packet in the computational domain. Typical parameters used in the model initialization are:

$$A = \frac{w}{U} = 0.015\ ,$$

$$b = \frac{30}{L_z^2}\ ,$$

$$k = \frac{2\pi}{\lambda_x/L_x} = \frac{2\pi}{3}\ ,$$

$$m = \frac{2\pi}{\lambda_z/L_z} = 2\pi\ .$$

Table 3.2: Propagation Angle and Wave Aspect Ratio.

θ	k	m	λ_x	λ_z
45.0^o	$\frac{2\pi}{1}$	$\frac{2\pi}{1}$	1	1
26.5^o	$\frac{2\pi}{2}$	$\frac{2\pi}{1}$	2	1
18.4^o	$\frac{2\pi}{3}$	$\frac{2\pi}{1}$	3	1
14.0^o	$\frac{2\pi}{4}$	$\frac{2\pi}{1}$	4	1
11.3^o	$\frac{2\pi}{5}$	$\frac{2\pi}{1}$	5	1
8.1^o	$\frac{2\pi}{7}$	$\frac{2\pi}{1}$	7	1
5.7^o	$\frac{2\pi}{10}$	$\frac{2\pi}{1}$	10	1
2.9^o	$\frac{2\pi}{20}$	$\frac{2\pi}{1}$	20	1

3.4.3 Mechanical Wave Forcing

In the rotated coordinate system the wave forcing of Section 2.6 takes the form

$$\frac{\partial \Psi}{\partial z} = \frac{Am}{k}\, F(z) \cos(kx + mz - \omega t) + \frac{A}{k}\, F'(z) \sin(kx + mz - \omega t)\ , \tag{3.77}$$

$$\frac{\partial \Psi}{\partial x} = A\, F(z) \cos(kx + mz - \omega t)\ , \tag{3.78}$$

$$F_\rho = \frac{-A\cos\alpha}{\omega}\, F(z) \sin(kx + mz - \omega t) + \frac{A\, m \sin\alpha}{\omega\, k}\, F(z) \sin\left(kx + mz - \omega t\right) - \frac{A \sin\alpha}{\omega\, k}\, F'(z) \cos\left(kx + mz - \omega t\right)\ . \tag{3.79}$$

The forcing scheme adds energy to the flow at each time step. The total work input is the sum of the kinetic and potential energies added to the internal wave train. The work input to the kinetic W_{KE} and potential W_{PE} energies may be calculated by the volume integrals:

$$W_{KE} = \int\int (u\frac{\partial \Psi}{\partial x} + w\frac{\partial \Psi}{\partial z})\, dx\, dz\ , \tag{3.80}$$

$$W_{PE} = \int\int\ Ri\ \rho\ F_\rho\, dx\, dz\ . \tag{3.81}$$

3.4.4 Variable Grid Spacing

A variable-mesh grid is used to cluster computational nodes near the physical boundary at the ocean floor. A simple algebraic grid transformation from physical space (x, z) to the rectangular computational space (x, ζ) as shown in Figure 3.8 is described here. The chosen transformation is only a function of the z (that is z') coordinate and is given by

$$z = a_\zeta \zeta + b_\zeta \zeta^2 \ , \ \ 0 \leq \zeta \leq 1 \ . \tag{3.82}$$

The inverse transform, $\zeta = G(z)$, is

$$\zeta = \frac{-a_\zeta}{2b_\zeta} + \sqrt{\left(\frac{a_\zeta}{2b_\zeta}\right)^2 + \frac{z}{b_\zeta}} \ . \tag{3.83}$$

The coefficients a_ζ and b_ζ are chosen so that the grid spacing closest to the wall, Δz_{min}, is about ten times smaller than the grid spacing near the top of the domain. For a two-dimensional realization with 400 grid points in the vertical, a typical choice employed is $a_\zeta = 2$ and $b_\zeta = 5$.

The z-derivatives in the governing equations may be expanded by the chain rule, e.g.,

$$\frac{\partial u}{\partial z} = \frac{\partial u}{\partial \zeta}\frac{\partial \zeta}{\partial z} \ , \tag{3.84}$$

where

$$\frac{\partial \zeta}{\partial z} = \frac{1}{2b_\zeta \sqrt{(\frac{a_\zeta}{2b_\zeta})^2 + \frac{z}{b_\zeta}}} = G_1(z) = \Gamma_1(\zeta) = \frac{1}{a_\zeta + 2b_\zeta \zeta} \ , \tag{3.85}$$

which yields

$$\frac{\partial u}{\partial z} = \Gamma_1(\zeta)\, \frac{\partial u}{\partial \zeta} \ . \tag{3.86}$$

By repeating this procedure $\dfrac{\partial^2 u}{\partial z^2}$ is obtained:

$$\frac{\partial^2 u}{\partial z^2} = \frac{\partial^2 u}{\partial \zeta^2}\left(\frac{\partial \zeta}{\partial z}\right)^2 + \frac{\partial u}{\partial \zeta}\frac{\partial^2 \zeta}{\partial z^2} \ . \tag{3.87}$$

With the definition

$$G_2(z) = \frac{\partial^2 \zeta}{\partial z^2} = \frac{-1}{4b_\zeta^2 \left((\frac{a_\zeta}{2b_\zeta})^2 + \frac{z}{b_\zeta}\right)^{\frac{3}{2}}} = \Gamma_2(\zeta) = \frac{-1}{4b_\zeta^2 \left[\zeta + \frac{a_\zeta}{2b_\zeta}\right]^3} \ , \tag{3.88}$$

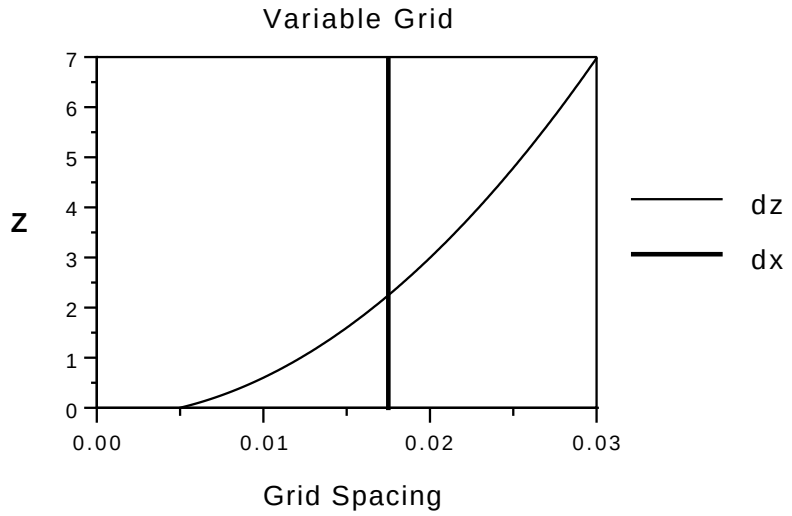

Figure 3.8: The variable-mesh grid in the z direction is presented by showing the grid spacing Δz vs. z. Also shown is the constant value of Δx, the grid spacing used in the x direction.

equation (3.87) may be written

$$\frac{\partial^2 u}{\partial z^2} = \Gamma_1^2(\zeta)\frac{\partial^2 u}{\partial \zeta^2} + \Gamma_2(\zeta)\frac{\partial u}{\partial \zeta} \ . \tag{3.89}$$

In addition, the fourth-order spatial filter requires the use of the term

$$\begin{aligned}\frac{\partial^4 u}{\partial z^4} &= \Gamma_1^4(\zeta)\frac{\partial^4 u}{\partial \zeta^4} + 6\Gamma_1^2(\zeta)\,\Gamma_2(\zeta)\frac{\partial^3 u}{\partial \zeta^3} \\ &+ \left[4\Gamma_1(\zeta)\Gamma_3(\zeta) + 3\Gamma_2^2(\zeta)\right]\frac{\partial^2 u}{\partial \zeta^2} + \Gamma_4(\zeta)\frac{\partial u}{\partial \zeta} \ ,\end{aligned} \tag{3.90}$$

where $\Gamma_3(\zeta)$ and $\Gamma_4(\zeta)$ are defined by

$$\Gamma_3(\zeta) = \frac{3}{8b_\zeta^3\left(\zeta + \frac{a_\zeta}{2b_\zeta}\right)^5} \ , \tag{3.91}$$

$$\Gamma_4(\zeta) = \frac{-3}{8b_\zeta^4\left(\zeta + \frac{a_\zeta}{2b_\zeta}\right)^7} \ . \tag{3.92}$$

See Appendix B for details concerning the fourth-order compact filter on the variable-mesh grid.

A major motivation for choosing an algebraic grid transformation of this type is that the inverse transform may be determined exactly. To maintain fourth-order spatial accuracy in the model, the transformed derivatives such as $\frac{\partial \zeta}{\partial z}$ must be known to at least fourth-order accuracy. By choosing the algebraic transform given above, the derivatives for the transformation are known exactly, and the spatial accuracy is not compromised. Further discussion of these concerns and various approaches to resolving them may be found in Rai and Moin (1991). Alternative transforms are available that allow for higher-order clustering near the boundary. One such choice would be $z = a_\zeta \zeta^2 + b_\zeta \zeta^4$. Alternative, commonly used hyperbolic grid transforms are give in Anderson et al. (1984).

Applying these relations to the governing equations (2.18) - (2.21) and the pressure projection equation (3.36) leads to the modified set

$$\frac{\partial u}{\partial x} + \Gamma_1(\zeta)\, \frac{\partial w}{\partial \zeta} = 0 \,, \tag{3.93}$$

$$\frac{\partial u}{\partial t} + u\frac{\partial u}{\partial x} + \Gamma_1(\zeta)\, w\frac{\partial u}{\partial \zeta} = -\frac{\partial p}{\partial x} + \frac{1}{Re}\left(\frac{\partial^2 u}{\partial x^2} + \Gamma_1^2(\zeta)\frac{\partial^2 u}{\partial \zeta^2} + \Gamma_2(\zeta)\frac{\partial u}{\partial \zeta}\right) \,, \tag{3.94}$$

$$\frac{\partial w}{\partial t} + u\frac{\partial w}{\partial x} + \Gamma_1(\zeta)\, w\frac{\partial w}{\partial \zeta} + Ri\,\rho = -\Gamma_1(\zeta)\frac{\partial p}{\partial \zeta} + \frac{1}{Re}\left(\frac{\partial^2 w}{\partial x^2} + \Gamma_1^2(\zeta)\frac{\partial^2 w}{\partial \zeta^2} + \Gamma_2(\zeta)\frac{\partial w}{\partial \zeta}\right) \,, \tag{3.95}$$

$$\frac{\partial \rho}{\partial t} + u\frac{\partial \rho}{\partial x} + \Gamma_1(\zeta)\, w\frac{\partial \rho}{\partial \zeta} - w = \frac{1}{Pr\ Re}\left(\frac{\partial^2 \rho}{\partial x^2} + \Gamma_1^2(\zeta)\frac{\partial^2 \rho}{\partial \zeta^2} + \Gamma_2(\zeta)\frac{\partial \rho}{\partial \zeta}\right) \,, \tag{3.96}$$

$$\frac{\partial^2 p^{n+1}}{\partial x^2} + \Gamma_1^2(\zeta)\frac{\partial^2 p^{n+1}}{\partial \zeta^2} + \Gamma_2(\zeta)\frac{\partial p^{n+1}}{\partial \zeta} = \frac{1}{2\Delta t}\left(\frac{\partial u^*}{\partial x} + \Gamma_1(\zeta)\,\frac{\partial w^*}{\partial \zeta}\right) \,. \tag{3.97}$$

Note that the pressure equation may still be solved with the NCAR package SEPX4. As shown in (3.32) SEPX4 permits variable coefficients in the x direction. Equation (3.97) satisfies this criteria if the x and ζ coordinates are switched in the package.

Two implications of using the variable grid deserve brief comment. For many numerical schemes there is appropriate concern about their order of accuracy, whether it be second-order, fourth-order or spectral accuracy. The present model consistently maintains fourth-order spatial accuracy, meaning that the leading order error terms are $O(\Delta z)^4$. It should be realized, however, that when the grid spacing Δz changes by an order of magnitude across the domain, the absolute errors involved also may vary across the domain, in this example by relative magnitudes of up to 10^4. Consequently, grid clustering is an even stronger tool for achieving desired numerical resolution than using higher-order schemes. Standard finite-difference schemes use second-order accuracy, and some even use first-order spatial accuracy locally, (e.g., the Total Variation Diminishing (TVD) scheme). This accuracy can be satisfactory if a high enough concentration of grid points is used. In the case of limited resources and marginally sufficient resolution, however, higher order schemes such as the compact scheme are very useful.

Our second comment related to variable grids addresses modeling turbulence in regions of high aspect ratios. The present model the ratio of $\Delta x : \Delta z$ is approximately 5:1 at the wall. Other models use ratios of up to 100:1. A complication that may arise if the flow is turbulent in these regions is that gradients in z, adequately resolved in the high resolution direction, may be rotated (as by an eddy) into the low resolution direction and hence be unresolved. The use of high aspect ratio grids is justified when applied in regions of non-isotropic flows, such as in the viscous layer near a wall where high shears occur predominately in one direction.

3.5 Flow Measurement

3.5.1 Statistics

Statistical quantities of interest are calculated during the simulation. Below are listed the equations for calculating the volume integrated kinetic energy (KE_t), potential energy (PE_t), total energy (TE_t), dissipation of kinetic energy (D_{ke}), dissipation of potential energy (D_{pe}), mean square vorticity (MSV_t), buoyancy flux (BF_t), and

mixing efficiency (ME_t), respectively.

$$KE_t = \frac{1}{2}\int\int\ u^2 + w^2\ dx\ dz = \frac{1}{2}\sum_{i=1}^{nx-1}\sum_{k=1}^{nz-ns}\left[u^2(i,k) + w^2(i,k)\right]\ \Delta x\ \frac{\Delta\zeta}{\Gamma_1(k)}\ , \quad (3.98)$$

$$PE_t = \frac{Ri}{2}\int\int\ \rho^2\ dx\ dz = \frac{Ri}{2}\sum_{i=1}^{nx-1}\sum_{k=1}^{nz-ns}\rho^2(i,k)\ \Delta x\ \frac{\Delta\zeta}{\Gamma_1(k)}\ , \quad (3.99)$$

$$TE_t = KE_t + PE_t\ , \quad (3.100)$$

$$D_{ke} = \int\int\ \frac{u}{Re}\left(\frac{\partial^2 u}{\partial x^2} + \frac{\partial^2 u}{\partial z^2}\right) + \frac{w}{Re}\left(\frac{\partial^2 w}{\partial x^2} + \frac{\partial^2 w}{\partial z^2}\right)\ dx\ dz\ , \quad (3.101)$$

$$\chi = \int\int\ \frac{Ri\ \rho}{Pr\ Re}\left(\frac{\partial^2 \rho}{\partial x^2} + \frac{\partial^2 \rho}{\partial z^2}\right)\ dx\ dz\ , \quad (3.102)$$

$$MSV_t = \int\int\ \left(\frac{\partial u}{\partial z} - \frac{\partial w}{\partial x}\right)^2\ dx\ dz\ , \quad (3.103)$$

$$BF_t = \int\int\ \rho\ w\ dx\ dz = \sum_{i=1}^{nx-1}\sum_{k=1}^{nz-ns}\left(\rho(i,k)\ w(i,k)\right)\ \Delta x\ \frac{\Delta\zeta}{\Gamma_1(k)}\ , \quad (3.104)$$

$$ME_t = \frac{\int_{t_i}^{t_f}\ \chi\ dt}{TE_i - TE_f}\ dx\ dz\ . \quad (3.105)$$

3.5.2 Flow Visualization

The complete velocity and density fields are stored throughout the simulation to enable visualizations of the flow field at times of interest. Flow visualizations are achieved with standard postprocessing graphics packages (NCAR Graphics and Tecplot). Additional visualizations are made of the vorticity and stream-function fields. The stream function Ψ_v is defined according to the relations

$$u = \frac{\partial \Psi_v}{\partial z}\ ,\quad w = -\frac{\partial \Psi_v}{\partial x}\ , \quad (3.106)$$

such that Ψ_v may be determined by solving the Poisson equation

$$\nabla^2 \Psi_v = \frac{\partial u}{\partial z} - \frac{\partial w}{\partial x}\ , \quad (3.107)$$

with appropriate boundary conditions.

In addition, frequent measurements are made of the velocity and density fields at a vertical line in the center of the periodic domain. These measurements give a dynamic picture of the developing flow and simulate the data which would be collected in the ocean by a vertical line of stationary probes in an internal wave field.

3.5.3 Particle Traces

A key issue related to the wave breakdown process is whether the turbulent boundary layer exchanges fluid with the interior domain or whether it predominantly continues to mix the same fluid (Garrett, 1991a). Two additional features were added to the model experiments to study this issue. The first feature is the ability to track fluid particles released at various heights. Particle trajectories are examined to determine if a statistically significant number of these particles escape from the boundary mixed layer or if particles initially outside the boundary layer are entrained into it.

A set of 2000 Lagrangian particles are released in the flow in a rectangular lattice, after the flow has begun to develop. The equations describing their trajectories are time stepped using an Euler scheme with variable time steps. The fluid velocities $\vec{u}_p(x, y, z, t)$, at the particle locations, $\vec{X}_p(x, y, z, t)$, are calculated using tri-linear interpolation, and then the particle locations are updated with the equation

$$\vec{X}_p^{n+1} = \vec{X}_p^n + \Delta t \, \vec{u}_p^n \, . \tag{3.108}$$

The particles are tracked for a number of wave periods and their locations are written out every ten time steps. Particles released in a region of linear wave dynamics return to their initial locations after one wave period. Deviations from this simple pattern are a measure of the nonlinearity, turbulence, and mean flows induced by the wave breakdown process. It is straightforward to modify the particle trajectory equation to include other effects on the particles (e.g., buoyancy, drag), thereby describing motion of particles whose trajectories differ from the local fluid motion (e.g., Squires and Eaton, 1990).

3.5.4 Dye Injection

A passive scalar field is added in some of the simulations in order to observe net mass transport from one region to another. For the three-dimensional model a transport equation for the scalar quantity S_D is added to the system of momentum and density

transport equations, e.g.,

$$\frac{\partial S_D}{\partial t} + u\frac{\partial S_D}{\partial x} + v\frac{\partial S_D}{\partial y} + w\frac{\partial S_D}{\partial z} = \frac{1}{Sc\,Re}\left(\frac{\partial^2 S_D}{\partial x^2} + \frac{\partial^2 S_D}{\partial y^2} + \frac{\partial^2 S_D}{\partial z^2}\right) . \qquad (3.109)$$

The new parameter in this equation is the Schmidt number, $Sc = \dfrac{\nu}{\kappa_s}$, the ratio of diffusivities for momentum and for the scalar. To maintain adequate resolution of scalar gradients, a Schmidt number of 0.5 is used in the experiments.

The scalar field acts as a "dye", allowing observations of the transport of dyed fluid from the boundary layer region into the interior stratified domain. The dye is released after the flow has developed for a few wave periods and reached a quasi-steady state of mixing. Initially the dye is released within the turbulent boundary layer. The location of the dye is monitored as the flow develops for a time of about five wave periods.

3.5.5 Energetics

To understand the physical processes in the flow, its energetics are fundamental. The kinetic energy equation is a useful tool in examining flow development. Below, the volume integrated kinetic energy equation is presented for the problem geometry, including periodic boundaries in the x'-direction, the ocean floor, and a sponge layer at the top boundary.

Kinetic Energy Equation

$$\frac{\partial\, KE_t}{\partial t} = \int\int \left[-Ri\, w\, \rho + \frac{u}{Re}\left(\frac{\partial^2 u}{\partial x^2} + \frac{\partial^2 u}{\partial z^2}\right) + \frac{w}{Re}\left(\frac{\partial^2 w}{\partial x^2} + \frac{\partial^2 w}{\partial z^2}\right) + u\frac{\partial p}{\partial x} + w\frac{\partial p}{\partial z} + Sp_{ke} + D_{f_{ke}} + W_{KE}\right] dx\, dz \ , \qquad (3.110)$$

where Sp_{ke} represents the kinetic energy lost in the sponge layer, $D_{f_{ke}}$ is the dissipation of kinetic energy by the filter, and W_{KE} is the work input of kinetic energy from the wave forcing mechanism. An alternate final form of the integrated kinetic energy equation can be obtained from intermediate forms (not presented here) through use of the divergence theorem at the upper boundary. In that situation the sponge loss

term can be eliminated and replaced with terms representing the flux of pressure and kinetic energy across the open boundary at the top surface.

$$\frac{\partial\, KE_t}{\partial t} = \int\int \left[-Ri\, w\, \rho + \frac{u}{Re}\left(\frac{\partial^2 u}{\partial x^2} + \frac{\partial^2 u}{\partial z^2}\right) + \frac{w}{Re}\left(\frac{\partial^2 w}{\partial x^2} + \frac{\partial^2 w}{\partial z^2}\right) + D_{f_{ke}} + W_{KE} \right] dx\, dz + \int_0^{x_l} (w \cdot KE)|_{z=top}\, dx + \int_0^{x_l} (w \cdot p)|_{z=top}\, dx \quad . \quad (3.111)$$

The potential energy equation is derived by multiplying the density equation by $\rho\, Ri$ and integrating over the computational domain.

Potential Energy Equation

$$\frac{\partial\, PE_t}{\partial t} = \int\int \left[Ri\, w\, \rho + \frac{Ri\, \rho}{Pr\, Re}\left(\frac{\partial^2 \rho}{\partial x^2} + \frac{\partial^2 \rho}{\partial z^2}\right) + D_{f_{pe}} + W_{PE} \right] dx\, dz + \int_0^{x_l} (w \cdot PE)|_{z=top}\, dx \quad , \quad (3.112)$$

where $D_{f_{pe}}$ is the dissipation of potential energy by the filter, and W_{PE} is the work input of potential energy from the wave forcing mechanism. When added these equations form the total energy equation.

Total Energy Equation

$$\frac{\partial\, TE_t}{\partial t} = \int\int \left[\frac{u}{Re}\left(\frac{\partial^2 u}{\partial x^2} + \frac{\partial^2 u}{\partial z^2}\right) + \frac{w}{Re}\left(\frac{\partial^2 w}{\partial x^2} + \frac{\partial^2 w}{\partial z^2}\right) + u\frac{\partial p}{\partial x} + w\frac{\partial p}{\partial z} + D_{f_{ke}} + \frac{Ri\, \rho}{Pr\, Re}\left(\frac{\partial^2 \rho}{\partial x^2} + \frac{\partial^2 \rho}{\partial z^2}\right) + D_{f_{pe}} + W_{TE} \right] dx\, dz + \int_0^{x_l} \left[(w \cdot KE)|_{z=top} + (w \cdot p)|_{z=top} + (w \cdot PE)|_{z=top} \right] dx \quad . \quad (3.113)$$

3.5.6 Energy and Dissipation Spectra

The energy and dissipation spectra provide tools for examining nonlinearities and small-scale behavior of the flow. The spectra are straightforward to compute in planes parallel to the slope, because the flow field is known on a uniform (and periodic) grid. The vertical energy spectrum is determined by interpolating the velocity and density fields from the clustered grid onto a higher density uniform grid, e.g., from

400 grid points in the vertical to 1024 for the two-dimensional model or from 130 to 512 grid points in the three-dimensional model. Then the velocity fields are Fourier decomposed using a fast Fourier transform (FFT) package.

Assuming Fourier component wave solutions for the primitive variables u, w, and ρ of the form $u(x) = \hat{u}e^{i(kx)}$, and that the flow is periodic with period $2P_x$, then the fields can be expanded in Fourier series, e.g.,

$$u(x) = \sum_k \hat{u}(k)e^{ikx} \ , \tag{3.114}$$

$$\hat{u}(k) = \frac{1}{2P_x}\int_{-P_x}^{P_x} u(x)e^{-ikx}dx \ . \tag{3.115}$$

The Fourier series given by equation (3.114) is truncated, which also produces a discrete summation in place of (3.115). In one dimension the transforms are

$$u(x_j) = \sum_{k=-N_m/2}^{N_m/2-1} \hat{u}(k)e^{ikx_j} \ , \qquad j = 0, 1, ..., N_m - 1 \ , \tag{3.116}$$

where $k = \frac{2\pi}{2P_x}n$, with $n = 0, \pm 1, ... \pm (\frac{N_m}{2} - 1)$, so that the cutoff wavenumber is $K = \frac{2\pi}{2P_x}\frac{N_m}{2} = \frac{\pi N_m}{2P_x}$. The inverse is

$$\hat{u}(k) = \frac{1}{N_m}\sum_{j=0}^{N_m-1} u(x_j)e^{-ikx_j} \ , \qquad -N_m/2 \le k \le N_m/2 - 1 \ , \tag{3.117}$$

where $x_j = \dfrac{2P_x\, j}{N_m}$ (Canuto *et al.*, 1988, p. 38).

Equations (3.116) and (3.117) are implemented using a fast Fourier transform (FFT) package. The exponential transform of a set of real data is used from the package CFFT99, written by Clive Temperton (Temperton, 1983), which allows grid densities using any multiples of 2, 3, and 5 (e.g., ... 8, 9, 10, 12, 15, 16, 18, 20, 24, 25, 30, ...).

In the vertical direction only the half-domain nearest the wall is decomposed, because most of the dynamics of interest occur there. Periodicity in the vertical direction is imposed by adding a mirror image of the flow field to the bottom half domain before decomposition, e.g.,

$$u(x, \frac{L_z}{2} + z) = u(x, \frac{L_z}{2} - z) \ , \quad \text{for } 0 \le z \le \frac{L_z}{2} \ . \tag{3.118}$$

The final energy spectrum is formed from the Fourier wave amplitudes of the velocity fields by multiplying by their complex conjugates, dividing the result by two, and integrating these values over the domain.

The dissipation spectra are formed as in the three-dimensional case by defining the viscous dissipation function at every grid point. For a three-dimensional Newtonian, incompressible, viscous fluid the dissipation function, Φ, is given by:

$$\Phi = \frac{1}{Re}\left[2\left(\frac{\partial u}{\partial x}\right)^2 + 2\left(\frac{\partial v}{\partial y}\right)^2 + 2\left(\frac{\partial w}{\partial z}\right)^2 + \left(\frac{\partial v}{\partial x} + \frac{\partial u}{\partial y}\right)^2 + \left(\frac{\partial w}{\partial y} + \frac{\partial v}{\partial z}\right)^2 + \left(\frac{\partial u}{\partial z} + \frac{\partial w}{\partial x}\right)^2\right] . \tag{3.119}$$

The associated density (or potential energy) dissipation function, and spectra are formed in like manner as

$$\Phi_\rho = \frac{1}{Pr\ Re}\left[\left(\frac{\partial \rho}{\partial x}\right)^2 + \left(\frac{\partial \rho}{\partial y}\right)^2 + \left(\frac{\partial \rho}{\partial z}\right)^2\right] . \tag{3.120}$$

After the fields are formed they are interpolated onto a uniform mesh and Fourier decomposed. The amplitude of the complex Fourier wave components are integrated over the domain and plotted as the dissipation spectrum.

3.6 Three-Dimensional Model Extensions

In the three-dimensional model the x'-direction is upslope, y is alongslope, and z' is perpendicular to the slope. The x' and z' axes are rotated from the horizontal and vertical about the y axis by the angle α.

3.6.1 Governing Equations

The Navier-Stokes equations within the Boussinesq approximation for three-dimensional flow in the rotated coordinate system are (where the $(\ )'$ notation has been suppressed)

$$\frac{\partial u}{\partial x} + \frac{\partial v}{\partial y} + \frac{\partial w}{\partial z} = 0 , \tag{3.121}$$

$$\frac{\partial u}{\partial t} + u\frac{\partial u}{\partial x} + v\frac{\partial u}{\partial y} + w\frac{\partial u}{\partial z} + Ri\,\rho \sin\alpha = -\frac{\partial p}{\partial x} + \frac{1}{Re}\left(\frac{\partial^2 u}{\partial x^2} + \frac{\partial^2 u}{\partial y^2} + \frac{\partial^2 u}{\partial z^2}\right) , \tag{3.122}$$

$$\frac{\partial v}{\partial t} + u\frac{\partial v}{\partial x} + v\frac{\partial v}{\partial y} + w\frac{\partial v}{\partial z} = -\frac{\partial p}{\partial y} + \frac{1}{Re}\left(\frac{\partial^2 v}{\partial x^2} + \frac{\partial^2 v}{\partial y^2} + \frac{\partial^2 v}{\partial z^2}\right) , \tag{3.123}$$

$$\frac{\partial w}{\partial t} + u\frac{\partial w}{\partial x} + v\frac{\partial w}{\partial y} + w\frac{\partial w}{\partial z} + Ri\,\rho\cos\alpha = -\frac{\partial p}{\partial z} + \frac{1}{Re}\left(\frac{\partial^2 w}{\partial x^2} + \frac{\partial^2 w}{\partial y^2} + \frac{\partial^2 w}{\partial z^2}\right) , \tag{3.124}$$

$$\frac{\partial \rho}{\partial t} + u\frac{\partial \rho}{\partial x} + v\frac{\partial \rho}{\partial y} + w\frac{\partial \rho}{\partial z} - w\cos\alpha - u\sin\alpha = \frac{1}{Pr\ Re}\left(\frac{\partial^2 \rho}{\partial x^2} + \frac{\partial^2 \rho}{\partial y^2} + \frac{\partial^2 \rho}{\partial z^2}\right) . \tag{3.125}$$

The numerical methods used for three-dimensional flow are straightforward extensions of those discussed above for two-dimensional flow except where noted below. The flow is taken to be periodic in the y-direction, and discretized on a uniform grid.

The initial conditions for the three-dimensional model consist of three distinct parts: the wave packet or forced waves, boundary currents, and a background flow consisting of white noise or low level turbulence.

3.6.2 Wave Packet

The three-dimensional initialization method of sections 2.5 and 3.4.2 is presented here in the rotated reference frame. The polarization conditions for a wave packet localized in z' (the primes have been dropped for convenience throughout) are given by:

$$u(x,y,z,0) = -\frac{Amk}{k^2+l^2}\,F(z)\cos(kx+ly+mz) - \frac{Ak}{k^2+l^2}\,F'(z)\sin(kx+ly+mz) , \tag{3.126}$$

$$v(x,y,z,0) = -\frac{Aml}{k^2+l^2}\,F(z)\cos(kx+ly+mz) - \frac{Al}{k^2+l^2}\,F'(z)\sin(kx+ly+mz) , \tag{3.127}$$

$$w(x,y,z,0) = AF(z)\cos(kx+ly+mz) , \tag{3.128}$$

$$\rho(x,y,z,0) = \frac{-A\cos\alpha\,F(z)}{\omega}\,\sin(kx+ly+mz) + \frac{Amk\sin\alpha\,F(z)}{\omega\,(k^2+l^2)}\,\sin(kx+ly+mz) - \frac{Ak\sin\alpha\,F'(z)}{\omega\,(k^2+l^2)}\,\cos(kx+ly+mz) , \tag{3.129}$$

with $F(z)$ and $F'(z)$ defined as in the two-dimensional problem.

The dispersion relation for three-dimensional flow is given by

$$\omega^2 = \frac{Ri\ [(k\cos\alpha - m\sin\alpha)^2 + l^2]}{k^2 + l^2 + m^2}\ . \tag{3.130}$$

The phase and group velocities in the rotated coordinate system are given by

$$\vec{C}_{ph} = \frac{\sqrt{Ri}\ [(k\cos\alpha - m\sin\alpha)^2 + l^2]^{1/2}}{(k^2 + l^2 + m^2)^{3/2}}\ \left(k\,\hat{i} + l\,\hat{j} + m\,\hat{k}\right)\ , \tag{3.131}$$

$$\vec{C}_g = \frac{\partial\omega}{\partial k}\hat{i} + \frac{\partial\omega}{\partial l}\hat{j} + \frac{\partial\omega}{\partial m}\hat{k}\ , \tag{3.132}$$

where the partial derivatives of ω are

$$\frac{\partial\omega}{\partial k} = \frac{\sqrt{Ri}\,[(k^2 + l^2 + m^2)(k\cos\alpha - m\sin\alpha)\cos\alpha - k((k\cos\alpha - m\sin\alpha)^2 + l^2)]}{(k^2 + l^2 + m^2)^{3/2}((k\cos\alpha - m\sin\alpha)^2 + l^2)^{1/2}}\ , \tag{3.133}$$

$$\frac{\partial\omega}{\partial l} = \frac{\sqrt{Ri}\ l\,[k^2 + m^2 - (k\cos\alpha - m\sin\alpha)^2]}{(k^2 + l^2 + m^2)^{3/2}((k\cos\alpha - m\sin\alpha)^2 + l^2)^{1/2}}\ , \tag{3.134}$$

$$\frac{\partial\omega}{\partial m} = \frac{\sqrt{Ri}\,[(k^2 + l^2 + m^2)(k\cos\alpha - m\sin\alpha)(-\sin\alpha) - m((k\cos\alpha - m\sin\alpha)^2 + l^2)]}{(k^2 + l^2 + m^2)^{3/2}((k\cos\alpha - m\sin\alpha)^2 + l^2)^{1/2}}\ . \tag{3.135}$$

In the flat-bottom case, i.e., when $\alpha = 0$, these expressions reduce to the simpler forms

$$\frac{\partial\omega}{\partial k} = \frac{\sqrt{Ri}\,k\,m^2}{(k^2 + l^2 + m^2)^{3/2}(k^2 + l^2)^{1/2}}\ , \tag{3.136}$$

$$\frac{\partial\omega}{\partial l} = \frac{\sqrt{Ri}\,l\,m^2}{(k^2 + l^2 + m^2)^{3/2}(k^2 + l^2)^{1/2}}\ , \tag{3.137}$$

$$\frac{\partial\omega}{\partial m} = \frac{-\sqrt{Ri}\,m\,(k^2 + l^2)}{(k^2 + l^2 + m^2)^{3/2}(k^2 + l^2)^{1/2}}\ . \tag{3.138}$$

In the flat bottom case positive values for k, l, and m yield a wave packet that propagates in the positive x and y and negative z directions. This is not generally the case for arbitrary angle α. For instance, when $k\cos\alpha - m\sin\alpha < 0$, positive wave numbers can lead to a wave packet propagating in the negative x direction. A wave with group velocity propagating downward and in the positive x' and y' directions at angle θ to the horizontal has wave numbers defined from $\theta = \tan^{-1}\left(\frac{(k'^2 + l'^2)^{1/2}}{m'}\right) - \alpha$.

3.6.3 Mechanical Wave Forcing

The wave forcing method may be extended to the three-dimensional system by including forcing $\left(+\frac{\partial \Psi}{\partial y}\right)$ to the y-momentum equation and by generalizing the wave number $\mathbf{k} = (k, l, m)$ to allow waves propagating out of the plane of the sloping boundary. (Note from the sign convention from Equations (2.39) - (2.41) that the forcing term in the x'-momentum equation, $(-\frac{\partial \Psi}{\partial z})$, has opposite sign from the other forcing terms.) The generalized forcing functions are given in the rotated coordinate system by

$$\frac{\partial \Psi}{\partial z} = \frac{Amk}{k^2+l^2}\, F(z)\cos(kx+ly+mz-\omega t) + \frac{Ak}{k^2+l^2}\, F'(z)\sin(kx+ly+mz-\omega t)\ , \tag{3.139}$$

$$\frac{\partial \Psi}{\partial y} = -\frac{Aml}{k^2+l^2}\, F(z)\cos(kx+ly+mz-\omega t) - \frac{Al}{k^2+l^2}\, F'(z)\sin(kx+ly+mz-\omega t)\ , \tag{3.140}$$

$$\frac{\partial \Psi}{\partial x} = AF(z)\cos(kx+ly+mz-\omega t)\ , \tag{3.141}$$

$$F_\rho = \frac{-A\cos\alpha\, F(z)}{\omega}\, \sin(kx+ly+mz-\omega t) + \frac{Amk\sin\alpha\, F(z)}{\omega\,(k^2+l^2)} \times$$
$$\sin(kx+ly+mz-\omega t) - \frac{Ak\sin\alpha\, F'(z)}{\omega\,(k^2+l^2)}\, \cos(kx+ly+mz-\omega t)\ . \tag{3.142}$$

The forcing is similar in form to the stream function defined in two-dimensions. The forcing function, $\dfrac{\partial \Psi}{\partial y}$, is added to the v-velocity equation and is zero if the wavenumber l is zero. The analytical solution describing the waves that come out of the forcing region (developed in Section 2.6) is also appropriate for the three-dimensional case.

3.6.4 White Noise and Turbulence

When the wave packet is initialized with $l = 0$ the problem is two-dimensional, in that the oncoming wave approaches the wall in the plane of the slope. In this case additional flow features are required to break the symmetry of the problem and allow the reflected waves to break down three-dimensionally. In order to accomplish this a small amount of white noise is added to the background flow. Experience has shown that a background noise level that contains roughly one percent of the local energy

density of the oncoming wave train is sufficient to allow the wave instabilities to develop quickly and allow the waves to break down into turbulence.

This white noise is generated by taking the incompressible projection of a pseudo-random velocity field localized near the wall. The density field is also initialized with random fluctuations added to the background profile. These perturbation velocity and density fields are then filtered to remove energy at high wave numbers, and then set in motion to develop for about one buoyancy period. This allows the noise field to begin to develop into low level turbulence containing some coherence. After a short developmental period the wave packet is superimposed on the background noise field, and the wave packet begins to propagate towards the wall.

3.6.5 Pressure Solution

Several methods have been examined to solve for the pressure field in an efficient and accurate manner. The first attempt used iterative solution techniques from the NCAR software package MUDPACK, using relaxation and multigrid techniques to achieve fourth-order accuracy for general three-dimensional elliptic equations having variable coefficients. The software package MUD34 (MUltigriD, 3-D, 4th-order) allows solution of the general non-separable equation

$$A_{xx}(x,y,z)\frac{\partial^2 p}{\partial x^2} + A_x(x,y,z)\frac{\partial p}{\partial x} + B_{yy}(x,y,z)\frac{\partial^2 p}{\partial y^2} + B_y(x,y,z)\frac{\partial p}{\partial y}$$
$$+C_{zz}(x,y,z)\frac{\partial^2 p}{\partial z^2} + C_z(x,y,z)\frac{\partial p}{\partial z} + C_m(x,y,z)\, p = R(x,y,z)\ . \qquad (3.143)$$

Although MUDPACK is a versatile elliptic solver, it requires significant computational CPU time and memory resources. The iterative solution technique requires setting a predesignated tolerance limit for satisfactory convergence. The solution of (3.143) with MUDPACK requires work space equivalent to ten field arrays, and computational expense greater than half of the total computations per time step. Unfortunately, even with these relatively high costs, the method does not produce a sufficiently accurate pressure field to maintain an incompressible flow field.

Consequently, two new solution methods were developed that replace the iterative techniques with direct matrix inversion. The new methods are more accurate,

eliminate the uncertainty of iterating subject to a convergence criteria, and require less memory and CPU time. They are, however, limited to situations in which the problem has one or more directions of periodicity and of uniform discretization. In the first method, chosen for its ease of implementation and extension from the two-dimensional system, the governing Poisson equation,

$$\frac{\partial^2 p}{\partial x^2} + \frac{\partial^2 p}{\partial y^2} + \Gamma_1^2(\zeta)\frac{\partial^2 p}{\partial \zeta^2} + \Gamma_2(\zeta)\frac{\partial p}{\partial \zeta} = \frac{\nabla \cdot \vec{u}}{\Delta t} = R(x, y, \zeta) \ , \tag{3.144}$$

is Fourier transformed in the y-direction to form a set of separable equations for the pressure coefficients $\hat{p}$

$$\frac{\partial^2 \hat{p}}{\partial x^2} - l^2 \hat{p} + \Gamma_1^2(\zeta)\frac{\partial^2 \hat{p}}{\partial \zeta^2} + \Gamma_2(\zeta)\frac{\partial \hat{p}}{\partial \zeta} = \hat{R}(x, l, \zeta) \ . \tag{3.145}$$

The modified Poisson equation is then solved for each wave number l using the two-dimensional solver SEPX4, described above, after which the solution for $\hat{p}$ is transformed back into physical space to obtain the pressure field. The implementation of this method also requires transforming the pressure boundary conditions. Experience has shown that this method is sufficiently accurate to maintain a nondivergent flow field (to about five significant figures when integrated over the volume). The disadvantage of the method is that the SEPX4 package is not vectorized and therefore slows down the overall solution when done on a vector processing computer such as the Cray-YMP.

An alternative method has been developed that extends the Fourier transform in two dimensions and can be vectorized for faster solution. An overall speed up of the pressure solution by an order of magnitude was achieved by implementing this method, which increased the overall computational speed by almost a factor of two. The method requires transforming the Poisson equation in both the x and y directions before solving for the pressure coefficients. The pressure solution has spectral accuracy in the horizontal directions and achieves fourth-order accuracy in the vertical direction by using five and four point stencils, respectively, to estimate $\frac{\partial^2 p}{\partial \zeta^2}$ and $\frac{\partial p}{\partial \zeta}$. The method requires subsequent inversion of a pentadiagonal matrix of

the form

$$\left(\frac{-\Gamma_1^2(i)}{12\Delta\zeta^2}+\frac{\Gamma_2(i)}{12\Delta\zeta}\right)\hat{\hat{p}}_{-2}+\left(\frac{4\Gamma_1^2(i)}{3\Delta\zeta^2}-\frac{2\Gamma_2(i)}{3\Delta\zeta}\right)\hat{\hat{p}}_{i-1}+\left(\frac{-5\Gamma_1^2(i)}{2\Delta\zeta^2}-k^2-l^2\right)\hat{\hat{p}}_i$$
$$+\left(\frac{4\Gamma_1^2(i)}{3\Delta\zeta^2}+\frac{2\Gamma_2(i)}{3\Delta\zeta}\right)\hat{\hat{p}}_{i+1}+\left(\frac{-\Gamma_1^2(i)}{12\Delta\zeta^2}-\frac{\Gamma_2(i)}{12\Delta\zeta}\right)\hat{\hat{p}}_{i+2}=\hat{\hat{R}}(k,l,i)\quad , \tag{3.146}$$

with special consideration required for the first two boundary nodes.

3.6.6 Method of Deferred Corrections

Higher-order accuracy (e.g., sixth-order) may be achieved in the vertical direction using the method of deferred corrections (Bickley, 1948; Motz, 1946). Increased accuracy is gained at the expense of an additional inversion of a pentadiagonal matrix. The method is outlined below for a second-order, one-dimensional elliptic equation on a uniform grid; extensions to the current model is straightforward.

The method of deferred corrections is used in the current two-dimensional model to upgrade a second-order pressure field solution obtained by tridiagonal matrix inversion to fourth-order accuracy. The method is not used in the three-dimensional model because the desired fourth-order accuracy is already achieved using a pentadiagonal solver. The method is useful, however, and would be employed if sixth-order accuracy of the three-dimensional model were desired. The following steps illustrate the procedure to upgrade a fourth-order pressure field estimate to sixth-order. Analogous steps are used in the two-dimensional model to go from second- to fourth-order.

Beginning with the difference approximation

$$\left.\frac{\partial^2 p}{\partial z^2}\right|_i=\frac{-p_{i+2}+16p_{i+1}-30p_i+16p_{i-1}-p_{i-2}}{12\Delta z^2}+\frac{1}{90}\left.\frac{\partial^6 p}{\partial z^6}\right|_i\Delta z^4+O(\Delta z^6)\ , \tag{3.147}$$

the elliptic equation

$$\left.\frac{\partial^2 p}{\partial z^2}\right|_i=R(z) \tag{3.148}$$

is inverted to obtain a fourth-order estimate for $p_4(z)$ (i.e., $p(z)+O(\Delta z^4)$) using the pentadiagonal stencil (3.147). Then, with this approximate solution for $p(z)$, the

sixth derivative, $\left.\frac{\partial^6 p}{\partial z^6}\right|_i$, is formed with finite differences, e.g.,

$$\left.\frac{\partial^6 p}{\partial z^6}\right|_i = \frac{p_{i+3} - 6p_{i+2} + 15p_{i+1} - 20p_i + 15p_{i-1} - 6p_{i-2} + p_{i-3}}{12\Delta z^6} + O(\Delta z^2) \ , \quad (3.149)$$

(or, alternatively, with compact derivatives). The third step is to include this estimate for $\left.\frac{\partial^6 p}{\partial z^6}\right|_i$ on the right hand side of equation (3.148), e.g.,

$$R_6(z) = R(z) - \frac{1}{90} \left.\frac{\partial^6 p}{\partial z^6}\right|_i \Delta z^4 \ , \quad (3.150)$$

so that the leading-order truncation error term in (3.147) is compensated for, and eliminated from, the approximation to $\left.\frac{\partial^2 p}{\partial z^2}\right|_i$. Inversion of the modified elliptic (Poisson) equation (3.148) using the pentadiagonal system now yields a sixth-order accurate pressure field. If desired, the procedure can be repeated to eliminate also the sixth-order truncation errors to achieve an eighth-order accurate representation of the pressure field.

A variation of the scheme, also requiring two matrix inversions, is available. In this approach, after obtaining the fourth-order pressure field, $p_4(z)$, and estimating $\left.\frac{\partial^6 p}{\partial z^6}\right|_i$, define a field, $q(z)$, satisfying

$$\left.\frac{\partial^2 q}{\partial z^2}\right|_i = -\frac{1}{90} \left.\frac{\partial^6 p}{\partial z^6}\right|_i \Delta z^4 \ , \quad (3.151)$$

and invert $q(z)$ by the usual method. The final pressure is then $p_6(z) = p_4(z) + q(z)$, and is equivalent to the pressure field from the first approach within roundoff errors.

3.7 Code Optimization

To minimize in-core computer memory usage, as few data fields as feasible are stored at each time level. The approach used is to save the fluxes for the right hand side of the governing equations after every time step. The three-dimensional model, using third-order Adams-Bashforth time stepping, requires saving 12 flux fields (3 for each

equation), 5 primitive variable fields, and 6 work arrays usually containing derivative fields to form the fluxes.

Particular attention has been paid during code development to allow the code to take advantage of increased performance speed achieved through vectorization and parallelization. The usual approach is to calculate for one plane at a time and to vectorize across the plane (i.e., while calculating values of $\frac{\partial u}{\partial x}$, the code is vectorized to calculate 128 derivatives for an entire y plane simultaneously). This approach is ideally designed for gains by parallelization of the code when ported to a parallel computer. Limited testing on a 6 processor Silicon Graphics Server show that the code runs approximately 3.9 times faster when run concurrently on 5 processors than when run on a single processor.

3.8 Physical Parameters

3.8.1 Reynolds Number

Following conventions, we define four different Reynolds numbers in the model. The first is the dissipation Reynolds number,

$$Re_d = \frac{\epsilon}{\nu N^2} \sim \frac{u^3}{\nu\, L\, N^2} = \left(\frac{u\, L}{\nu}\right)\left(\frac{u}{NL}\right)^2 \sim Re\, Fr^2 \,, \tag{3.152}$$

which relates the dissipation rate of kinetic energy, ϵ, to the viscosity and buoyancy frequency. The second is the boundary layer Reynolds number,

$$Re_\delta = \frac{U_\infty \delta}{\nu} \,, \tag{3.153}$$

where U_∞ is the maximum velocity within the boundary layer, and δ is the boundary layer thickness. The third is the wave Reynolds number

$$Re_w = \frac{C_{ph}\lambda_z}{\nu} \sim \frac{\lambda N \lambda}{\nu} = \left(\frac{u\lambda}{\nu}\right)\left(\frac{N\lambda}{u}\right) \sim Re\, \frac{1}{Fr} \,, \tag{3.154}$$

which relates the wave phase speed, C_{ph}, and vertical wavelength, λ_z, to the viscosity. The last is called simply the Reynolds number of the flow and is

$$Re = \frac{U_w \lambda}{\nu} \,, \tag{3.155}$$

where U_w is the maximum current speed in the oncoming wave train, and $\lambda = \frac{2\pi}{|\vec{k}|}$ is its wavelength.

From the simulations, typical values for these Reynolds numbers are as follows:

$$5 \leq Re_d \leq 200 \ , \tag{3.156}$$

$$10 \leq Re_\delta \leq 200 \ , \tag{3.157}$$

$$5,000 \leq Re_w \leq 40,000 \ , \tag{3.158}$$

$$300 \leq Re \leq 4000 \ . \tag{3.159}$$

It is important to note that the simulations are conducted at moderately low Reynolds numbers, far below values typical for oceanic conditions. The simulations are similar to Reynolds numbers achieved in related laboratory experiments. Typical oceanic internal waves may have Reynolds numbers of 10^8 based upon a length scale of 100 m, current speed of 10 cm/s, and kinematic viscosity of 10^{-7} m^2/s.

The present experiments are not designed to include the full complexity of oceanic conditions but rather to study the fundamental physics of the internal wave reflection problem. The goal is to seek qualitative and semi-quantitative information about physical processes that are not well understood. Important questions regarding the dependence on Reynolds number, and effects of other oceanic flow features, are not accessible within the present approach. However, since internal wave reflection is not microscale driven, small-scale turbulence and viscosity do not dominate or invalidate the useful information derived from the results. Here, the role of turbulence and small scale features is primarily to dissipate internal wave energy. The present model, with its inherent limitations, serves as a useful starting point for numerical studies of internal wave reflection that may be enhanced in subsequent work.

3.8.2 Other Model Parameters

Several additional dimensional and dimensionless parameters are used in the simulations, and some typical values are listed here. The slope of the bottom topography

is in the range

$$0^o \leq \alpha \leq 30^o \; . \tag{3.160}$$

Most of the values for velocity and length scales used here, characteristic of short period oceanic internal waves, are taken from Roberts (1975). The speeds of currents associated with internal waves are in the range

$$10^{-3} \leq U \leq 10^{-1} \; \mathrm{m/s} \, . \tag{3.161}$$

Physical constants for gravity and background density are

$$g = 9.8 \; \mathrm{m/s} \; , \quad \rho_o = 1000 \; \mathrm{kg/m^3} \; . \tag{3.162}$$

Ivey and Nokes (1989) and Garrett (1991b) review past work on vertical eddy diffusivities, and give values typically in the range

$$10^{-6} \leq \nu_\tau \leq 1.5 \times 10^{-4} \; \mathrm{m^2/s} \; . \tag{3.163}$$

In turbulent simulations it is often necessary to have the diffusivity of density greater than the diffusivity of momentum to adequately resolve strong density gradients throughout the time integration. It is generally agreed that Prandtl number relating the turbulent eddy viscosity coefficients for density and momentum should be of order 1. So we choose

$$0.6 \leq Pr_\tau \leq 1. \tag{3.164}$$

The background density gradient is estimated based upon temperature and salinity effects in the sea water (Pond, 1983):

$$\frac{d\bar{\rho}}{dz} = \frac{\partial \bar{\rho}}{\partial T} \frac{\partial T}{\partial z} + \frac{\partial \bar{\rho}}{\partial S} \frac{\partial S}{\partial z} \; , \tag{3.165}$$

$$10^{-3} \leq -\frac{d\bar{\rho}}{dz} \leq 10^{-2} \; \mathrm{kg/m^4} \; . \tag{3.166}$$

This range for the density gradient is used to choose a constant value for the buoyancy frequency

$$3 \times 10^{-3} \leq N \leq 10^{-1} \; \mathrm{s^{-1}} \; . \tag{3.167}$$

Garrett (1990) uses the value of $N = 10^{-3}$ in his estimates for basin averaged boundary mixing.

The length scales are selected to fix a Reynolds number for which the calculations can be adequately resolved. Vertical wavelengths of the internal waves in the model are typically in the range

$$10 \leq \lambda_z \leq 50 \text{ m} , \tag{3.168}$$

where similarly, λ_z is chosen largely based upon the need to resolve each vertical wavelength with about twenty grid points.

The horizontal wavelength, λ_x, is chosen according to the relation $\dfrac{k}{m} = \tan\theta$, for a wave with group velocity propagating at angle θ to the horizontal. For the problem to be periodic in x' the width of the domain L_x is set to an integral number of wavelengths (typically, $n = 1$ or $n = 2$) appropriate to $L_x = n\,\lambda_x$. Typically, small values of θ are of interest, $3 \leq \theta \leq 30^o$.

Within the numerical model the wave Reynolds number is used. The characteristic vertical length scale chosen for the nondimensionalization is $L = \lambda_z$, which together with N and ν leads to nondimensional parameters in the range

$$10^{-1} \leq Ri_{\lambda_z} \leq 2.5 \times 10^5 , \tag{3.169}$$

$$20 \leq Re_w \leq 5 \times 10^4 . \tag{3.170}$$

The wave phase and group velocities are related by

$$\left|\vec{C}_g\right| = \frac{\lambda_x}{\lambda_z} \left|\vec{C}_{ph}\right| , \tag{3.171}$$

and are in the range

$$0.1 \leq C_{ph} \leq 1 \text{ m/s} , \quad 0.2 \leq C_g \leq 500 \text{ m/s} . \tag{3.172}$$

The ranges of the dimensional and nondimensional parameters in the ocean related to internal waves are very broad. A set of physical parameters, chosen in the mid-range of velocity and stratification appropriate for this study, leads to the consistent set of nondimensional parameters

$$Re_w = \frac{(10^{-1}\text{m/s})\ (10\text{m})}{10^{-4}\text{m}^2/\text{s}} = 10,000 , \tag{3.173}$$

$$Ri_{\lambda_z} = \left[\frac{(10^{-2}\mathrm{s}^{-1})\ (10\mathrm{m})}{10^{-1}\mathrm{m/s}} \right]^2 = 1\ , \tag{3.174}$$

$$Pr_\tau = 1. \tag{3.175}$$

This set of nondimensional parameters has been used in well-resolved, direct numerical simulations of the gravity wave reflection problem. They are presented here to provide a reference point for understanding the relationship between the parameters in the model problem and the quantities of the related oceanographic problem. It is possible to reinterpret the same dimensionless parameters in terms of shorter length and time scales with a smaller viscosity.

3.9 Summary

The numerical models developed herein provide state-of-the-art computational techniques for simulating incompressible, stratified flows. These models include several new features, such as the wave forcing mechanism and the combination of variable time-stepping with the third-order Adams-Bashforth projection method. The models are designed for accuracy and, when used at low Reynolds number, represent a direct numerical simulation (DNS) of a turbulent boundary layer. At higher Reynolds number the model may be considered a large eddy simulation (LES) of the flow, with a simple hyperviscosity filter used to dissipate energy from the subgrid scales of motion. The majority of the simulations conducted for this study are direct numerical simulations. In the following chapter results of both DNS and LES simulations are presented. The gravity wave reflection problem for which the code was designed illustrates the capabilities of the numerical model and permits insightful analyses of the physics of the flow.

Chapter 4

INTRODUCTORY RESULTS

4.1 Overview of Experiments

This chapter contains results from the computational fluid dynamics experiments. Before discussing results for the dynamics of the flows, an overview of the experiments and a presentation of the methods of model validation are given. The internal wave reflection results are divided into five main sections: 1) critical angle reflection from a 9^o slope (Chapter 4), 2) critical angle reflection from other slopes (Chapter 5), 3) boundary layer and background flow features (Chapter 5), 4) energetics and mixing efficiencies (Chapter 5), and 5) specialized experiments used to investigate additional physical issues (Chapter 6). Over forty different high resolution three-dimensional simulations were conducted to investigate the internal wave reflection problem. Additional two-dimensional simulations and linear analyses were used for comparison, to help understand the influence of nonlinearity and three-dimensional interactions.

4.1.1 Critical Angle Experiments

Table 4.1 lists identifying details for some of the three-dimensional critical angle experiments along with some of the parameters for each case. These experiments used the wave forcing technique described in Section 3.6.3. The list is not a complete set of the critical angle experiments carried out for the study but includes the simulations selected for discussion below. These runs used oncoming waves of moderate amplitudes and were designed to observe the nonlinear interactions that occur in the bottom boundary layer.

The critical angle simulations were done for bottom slopes between 3.4^o and 30^o, with special focus on the 9.2^o and 20^o cases. The Reynolds (Re) and Richardson (Ri) numbers indicated in Table 4.1 are based upon the current speed and wavelength

Table 4.1: Critical Angle Simulations

Case	α	Re	Ri	ω	Classification
1	3.4	620	131	0.06	laminar
2	3.4	830	72	0.06	laminar
3	3.4	2100	44	0.06	turbulent
4	3.4	2600	29	0.06	turbulent
5	5.0	1860	59	0.09	transition
6	5.0	2400	36	0.09	turbulent
7	5.0	3300	33	0.09	turbulent
8	7.7	750	126	0.13	laminar
9	7.7	1500	126	0.13	turbulent
10	7.7	3000	126	0.13	turbulent
11	9.2	850	61	0.16	laminar
12	9.2	1200	53	0.16	transition
13	9.2	2000	43	0.16	turbulent
14	9.2	2800	40	0.16	turbulent
15	9.2	3600	46	0.16	turbulent
16	20.0	540	125	0.34	laminar
17	20.0	800	120	0.34	transition
18	20.0	850	430	0.34	transition
19	20.0	1100	110	0.34	turbulent
20	20.0	1200	235	0.34	turbulent
21	20.0	1800	92	0.34	turbulent
22	20.0	1800	92	0.34	2 x y_l
23	20.0	1800	92	0.34	2 x x_l
24	20.0	2400	53	0.34	turbulent
25	30.0	450	490	0.50	laminar
26	30.0	800	625	0.50	turbulent
27	30.0	800	156	0.50	turbulent
28	30.0	1700	138	0.50	turbulent

as discussed in Section 3.8. The wave frequency ω is normalized by the buoyancy frequency N. One of the quantities of interest in these experiments is the transition point from laminar flow to wave breakdown into turbulence. The information in the "Classification" column of Table 4.1 is related to this point; further discussion will be presented later, including the dependence of the transition point on slope, Reynolds, and Richardson numbers. These results are obtained employing the no-slip boundary condition together with the no-flux density boundary condition.

4.1.2 Non-Critical Angle Series

Table 4.2 identifies a series of simulations conducted away from the critical angle. In this set of experiments the wave frequency was held constant at $\omega = 0.16$, the critical frequency associated with a bottom slope of 9.2^o. The bottom slope was changed in each of these trials to investigate flow behavior when linear theory predicts reflected wave amplification of varying degrees.

The effect of the sloping bottom is to increase the energy density of the reflected wave. Using linear theory, Phillips (1977) predicts, for the ratio of the reflected to incident wave amplitude and energy density, respectively:

$$\frac{A_r}{A_i} = \frac{\cos\left(\alpha - \pi + \theta_{Cg_i}\right)}{\cos\left(\alpha + \pi - \theta_{Cg_i}\right)}\,, \tag{4.1}$$

$$\frac{E_r}{E_i} = \left[\frac{\cos\left(\alpha - \pi + \theta_{Cg_i}\right)}{\cos\left(\alpha + \pi - \theta_{Cg_i}\right)}\right]^2 = \left(\frac{A_r}{A_i}\right)^2\,, \tag{4.2}$$

where $\theta_{Cg_i} = \tan^{-1}(k'/m') - \alpha$ is the angle of the group velocity of the incident wave measured from the horizontal plane. The ratio of wave amplitudes predicted by linear, inviscid theory, A_r/A_i, is listed in Table 4.2 together with the Reynolds number, Richardson number, and bottom slope for the runs.

Note that Cases 34 to 38 are the same as Cases 11 to 15; because they belong to both series of runs, they appear twice in the tables.

Table 4.2: Off Critical Angle Simulations

Case	α	Re	Ri	(A_r/A_i)	Classification
29	0.0	620	235	1.0	laminar
30	0.0	1250	59	1.0	laminar
31	5.0	1100	170	3.3	laminar
32	5.0	1900	94	3.3	transition
33	8.0	1500	37	13.9	turbulent
34	9.2	850	61	∞	laminar
35	9.2	1200	53	∞	transition
36	9.2	2000	40	∞	turbulent
37	9.2	2800	40	∞	turbulent
38	9.2	3600	46	∞	turbulent
39	10.5	950	84	15.1	transition
40	10.5	2470	77	15.1	turbulent
41	10.5	3690	35	15.1	turbulent
42	13.5	970	74	5.2	laminar
43	13.5	2120	62	5.2	turbulent

4.1.3 Additional Numerical Experiments

Additional three-dimensional experiments not listed in Tables 4.1 and 4.2 will also be discussed below. These runs differ from those listed in these tables because of different boundary and initial conditions. For example, one of the other sets of simulations used free-slip boundary conditions. Another set of simulations used the wave packet initialization scheme rather than the wave forcing method. A third set of experiments was conducted with small amplitude (linear) oncoming waves.

4.2 Code Validation and Elementary Flow Studies

A variety of methods were used to validate the code. This section discusses eight different validation techniques used to gain confidence in the accuracy of the numerical experiments. These fall into four main categories: 1) comparison with analytical solutions, 2) internal consistency checks, such as conservation of mass, momentum, and energy, 3) comparison with experiments, and 4) meeting established resolution criteria.

4.2.1 Analytic and Linear Methods

Phillips' Steady-State Solution

The flow field explained by Phillips (1970) and presented in Section 2.7.3 provides an analytic solution available for testing the accuracy of the code. This test was used with both the two and three-dimensional models in two ways. The first test was simply to initialize the model with the Phillips' boundary layer velocity and density profiles. This test was done to see if the flows remained steady for a variety of boundary layer Reynolds, Richardson, and Prandtl numbers, as well as for different bottom slopes. The codes passed these simple tests which were also valuable for determining how many grid points are required near the wall to adequately resolve the buoyancy driven flows as a function of Reynolds number.

Transient Test Using Philips' Solution

The second validation technique involving the Phillips' solution was a transient test. The model was initialized with no flow and a linear density gradient extending to the wall. At time zero the flow was allowed to start from rest by applying the zero-flux boundary condition on the density field. This forced the flow towards the steady state solution. The energetics of the transient test are illustrated in Figure 4.1. The transient tests indicated that it took about two buoyancy periods for the boundary layer profiles to overshoot the energy in the steady solutions. The kinetic energy in the transient case reached about 1.5 times the kinetic energy of the steady flow before rebounding toward the steady solution. The transient solution exhibited damped oscillations about the steady solution with a period of about five buoyancy periods. After approximately twenty buoyancy periods the variations in the transient solution had decayed and the flow nearly achieved the steady state predictions. The magnitude of the oscillations, at the last times in this experiment, were less than 5 percent of the energy in the steady solution. For comparison, the wave period of a critical frequency wave for the bottom slope, 9.2^o, is approximately 6 buoyancy periods. The response time scale of the buoyancy boundary layer is shorter than the convective or wave propagation time scales associated with the overall wave reflection process. For example, in simulations discussed below a typical wave packet takes 15 to 20 buoyancy periods to complete reflection compared to an adjustment period of about 2 to 5 buoyancy periods in the transient buoyancy driven boundary layer. These results are typical of tests at different slopes, between 5^o and 30^o; however, very shallow slopes have slower response times, and Phillips's analytic solution is not valid for the flat bottom case.

Figure 4.2 shows energy density profiles for one of these transient test cases after 2 and 9 buoyancy periods after startup, together with the steady state profile (S). For this case with a viscosity of 10^{-4}, a characteristic Phillips's boundary layer thickness of 1.13 meters (defined as the height at which the flow changes direction), and an induced maximum velocity of 0.1134 cm/s, which are parameters typical of the simulations of internal wave reflection, the boundary layer Reynolds number, Re_δ, is 13, the

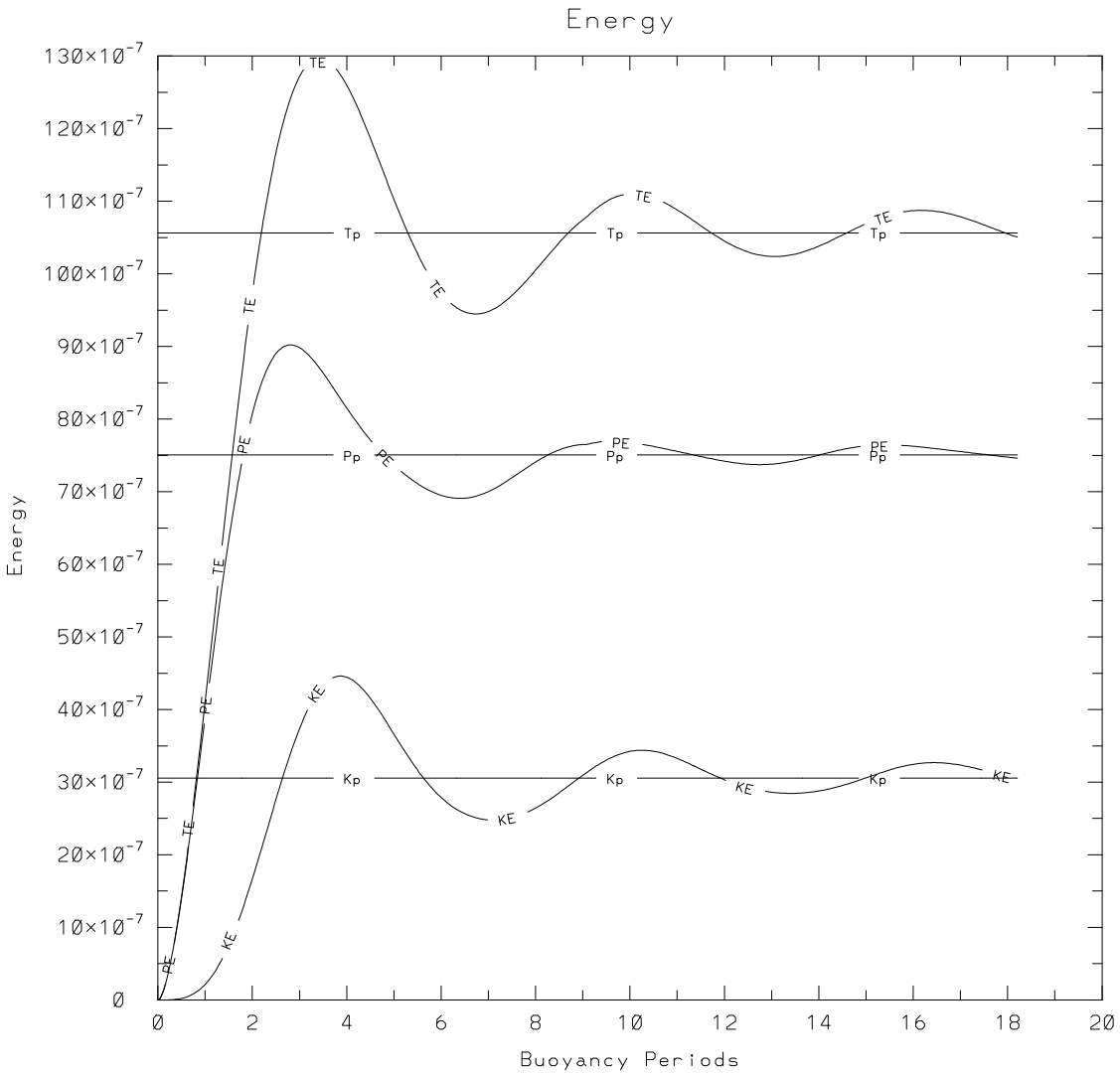

Figure 4.1: Kinetic, potential and total energy integrated over the control volume for the transient Phillips' test. The steady state values for energy are plotted for comparison.

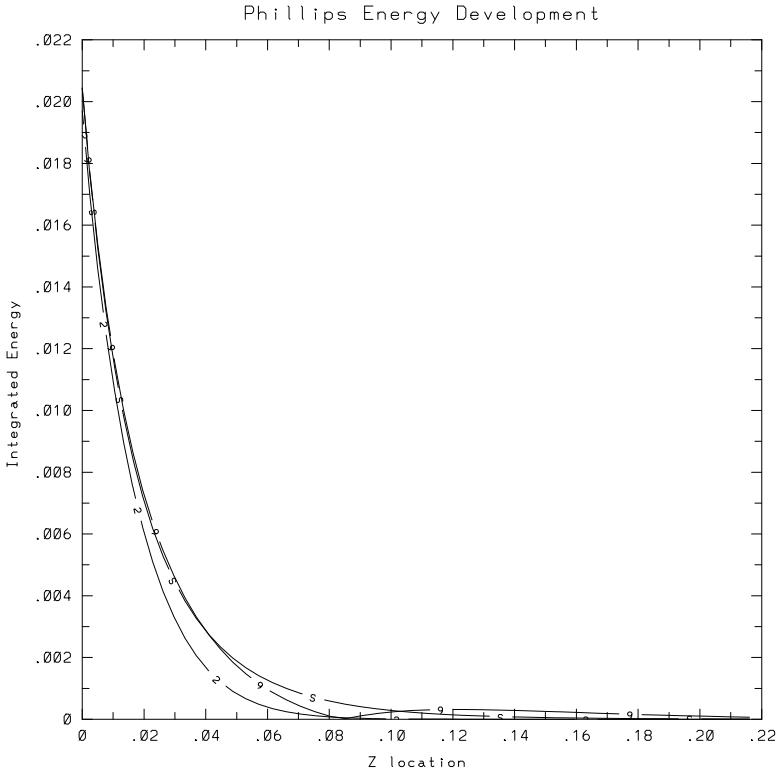

Figure 4.2: Energy density profiles for the transient startup to the Phillips' boundary layer solution after 2 and 9 buoyancy periods compared to the (S) steady state profile.

Prandtl number, Pr, is 1, and the bottom slope is 9.2^o. These tests showed the relative strengths and the response time scales for the buoyancy driven boundary currents compared to the main flows to be studied, those induced by wave reflection. The buoyancy boundary currents set up to satisfy the no-flux (adiabatic) boundary condition are relatively weak and quick to adjust. An interesting feature of this flow is that the buoyancy boundary layer draws available potential energy from the background density profile and converts it to kinetic and potential energy.

In the numerical model the flux of available potential energy across the boundary is included in the dissipation term. The potential energy dissipation rate is calculated by integrating $\frac{Ri}{Pr\,Re}\rho\nabla^2\rho$, which includes both the dissipation and diffusion of potential energy. The net integrated diffusion is zero in the interior of the domain, but diffusive

flux can be a source or sink across a physical boundary. Several numerical simulations were conducted where the two quantities were calculated separately. Typically, in the gravity wave reflection simulations, the diffusion of energy across the boundary was less than 1% of the dissipation. Since it is much more efficient to calculate the two quantities together, it is the procedure that is generally followed. Only in this present case, where the flow is driven by the flux of potential energy at the boundary, is the discrepancy noteworthy.

As the steady state flow is achieved there is a balance between a flux of background potential energy to available potential energy at the boundary, balanced by dissipation of kinetic energy with a steady buoyancy flux of potential to kinetic energy. Figure 4.3 shows the energy balance terms for the kinetic and potential energy equations.

The buoyancy boundary layer is restricted to a thin region near the wall, and the energy is much less than that contained in the finite amplitude gravity waves used in the numerical simulations. For example, the energy density in the steady Phillips profile over a 9.2^o slope is approximately 0.5% of the energy density of a typical oncoming wave train described below (e.g., Case 15, Table 4.1) for a wave of critical frequency and large enough amplitude to become turbulent.

Experiments by MacCready and Rhines (1991, 1992) suggest that, for a similar Ekman boundary layer which develops over a sloping bottom in a rotating reference frame, the no-flux boundary condition creates a slippery bottom boundary layer. Wave interaction with this slippery boundary layer could allow internal waves to reflect from the bottom terrain with less dissipation than if no local flow were present. They anticipate that this is a significant aspect of the boundary mixing problem.

Flat Bottom Wave Reflection

Code validation was also investigated by studying some of the simplest wave reflection problems, for which linear theory and intuition give a good picture of the flow behavior. One such case is the reflection of a train of internal waves of small amplitude from a flat bottom. Here the oncoming wave is expected to reflect from the bottom without changing wavelength or amplitude (in the absence of significant

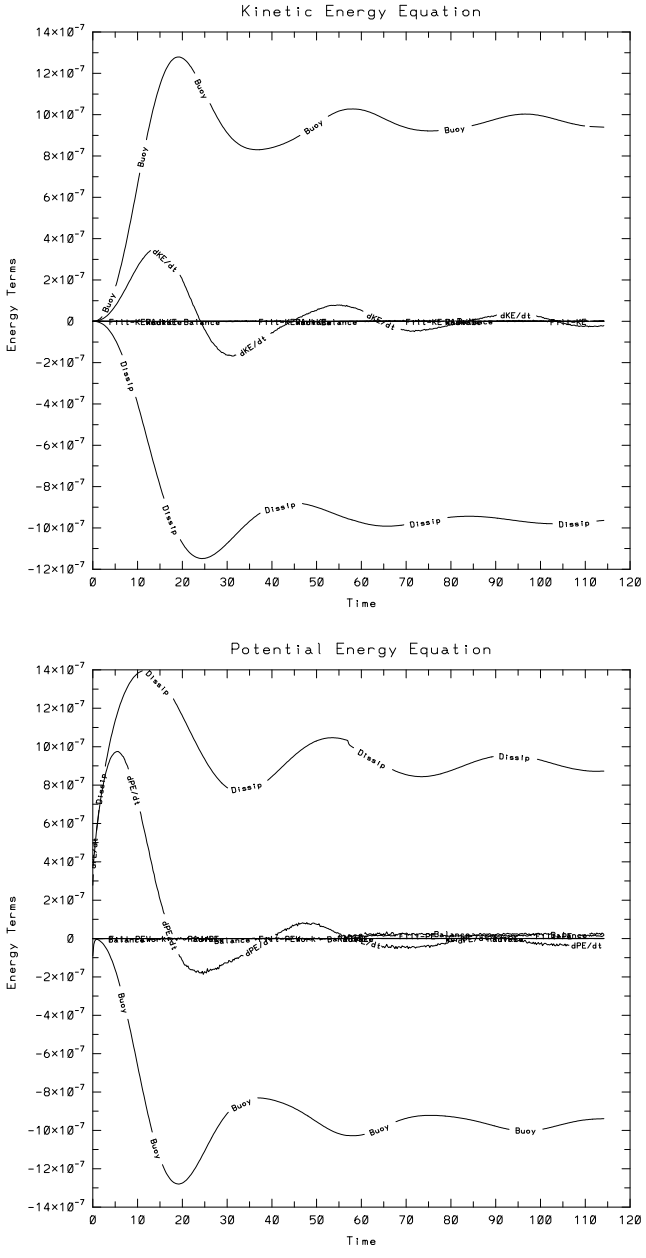

Figure 4.3: Energy balances for transient Phillips problem. Kinetic energy dissipation is balanced by a positive buoyancy flux.

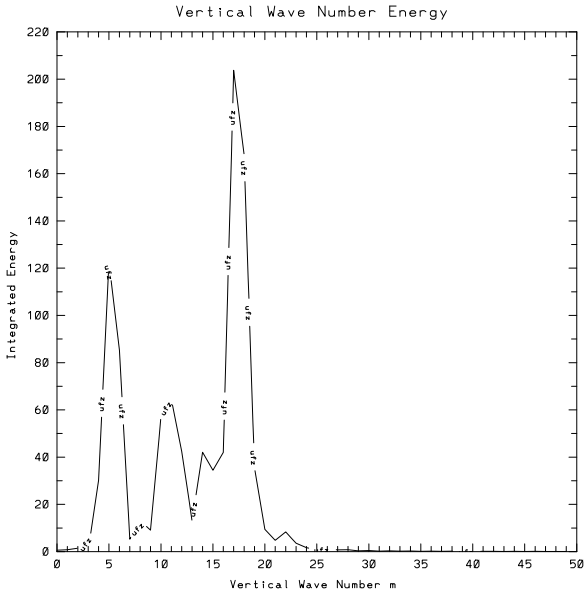

Figure 4.4: Kinetic energy spectra in the vertical direction for a linear amplitude wave train reflecting from a sloping boundary.

dissipation). In addition the interactions between the oncoming and outgoing wave trains are expected to be minimal, so that they simply add constructively while passing through one another and can set up a standing wave pattern away from the wall. This case was approximated using a free-slip wall at high Reynolds number to minimize dissipation. The test was successfully completed. A steady flow was achieved as the oncoming wave train reflected from the bottom boundary, without changing wavenumber or frequency, and passed through the incident wave train without event, ultimately progressing into the upper sponge layer where the wave energy was absorbed. The absorption layer effectively absorbed the outgoing energy without significant reflection.

Linear Wave Reflection

A fourth test, allowing direct comparison with linear theory, examined vertical spectra of small amplitude waves reflecting from sloping boundaries. Provided the waves

are somewhat removed from the critical angle, linear theory predicts the vertical wavenumbers of the reflected waves. Analysis of the energy spectra of the computed flow shows the transfer of energy to the predicted higher wavenumber. In this way it is straightforward to identify the energy associated with the oncoming and the reflected wave trains.

It is necessary to use the linear theory predictions in the rotated coordinate system to obtain the wavenumbers of the reflected waves. In the unrotated (x, z) coordinate system, $\frac{k_r}{m_r} = \frac{k_i}{m_i}$ and

$$\frac{m_r}{m_i} = \frac{A_r}{A_i} = A_f \ , \tag{4.3}$$

where A_f is the amplification factor as given by Equation (4.1). In the rotated coordinate system, however, $\lambda_{x'i} = \lambda_{x'r}$, or equivalently $k'_r = k'_i$, and thus all change in wavelength is observed in the z' direction. The ratio $\frac{m'_r}{m'_i}$ may be determined by considering the relationships:

$$k = k' \cos\alpha - m' \sin\alpha \ , \tag{4.4}$$

$$m = k' \sin\alpha + m' \cos\alpha \ , \tag{4.5}$$

$$k' = k \cos\alpha + m \sin\alpha \ , \tag{4.6}$$

$$m' = -k \sin\alpha + m \cos\alpha \ . \tag{4.7}$$

Algebraic manipulation between the reference frames leads to the results

$$\frac{m_r}{m_i} = \frac{k'_r \sin\alpha + m'_r \cos\alpha}{k'_i \sin\alpha + m'_i \cos\alpha} = A_f \ , \tag{4.8}$$

$$\frac{m'_r}{m'_i} = A_f \left[\frac{k'_i \sin\alpha + m'_i \cos\alpha}{\cos\alpha} \right] - \frac{k'_i \sin\alpha}{\cos\alpha} \ , \tag{4.9}$$

$$\frac{k'_r}{k'_i} = 1 \ . \tag{4.10}$$

Figure 4.4 shows the vertical kinetic energy spectra for a small amplitude wave train, with amplitude approximately $A_1 = A_o/30$ and frequency 0.16, which has reflected from a bottom slope of 5^o. This case was run at a wave Reynolds number of 5×10^5, with a free-slip bottom boundary condition, and (at the time shown)

has reached a quasi-steady state. Here the oncoming wave train has a wavenumber m_i' of 5, and linear theory predicts amplification factor $A_f = 3.3$ with a reflected wavenumber m_r' (in the z'-direction) of 17.1 for the inviscid case. Note that the reflected peak contains more energy than the oncoming wave train consistent with the linear relationships, even though some dissipation has occurred in the model. The results are thus in good agreement with predictions.

The intermediate peak at a wavenumber of approximately 11.5 appears to be related to resonant triad interactions. Resonant theory (e.g., Riley et. al., 1991) implies that wave energy may be transferred to waves with wavenumbers and frequencies satisfying or near resonant conditions. In the rotated coordinate system, the resonant conditions are $\omega_f = \omega_r \pm \omega_i$ and $m_f = m_r \pm m_i$ (since $k_r' = k_i'$), where the subscript m_f indicates the forced wave. The wave number vector summation permits resonantly forced waves at $m = 12$. The frequency condition at $m = 12$ is close to the resonant condition. Repeating the experiment with a smaller wave amplitude ($A_2 = 0.75A_1$) decreases the amplitude of the intermediate peak by approximately 50%, consistent with a resonantly forced response. An additional circumstance related to the width of the peaks is that the oncoming wave is not uniform across the entire domain, but generated in the wave forcing region. The shape of the wave forcing region may also contribute to the small, intermediate, and high wave number peaks. The boundary layer flow, of Phillips's (free-slip) type, also has a characteristic thickness and makes small contributions (less than one on this scale) to wave numbers below approximately 25. Additional flow features, such as the sponge layer thickness, also make small contributions to the spectra in the z'-direction.

4.2.2 Internal Consistency Checks

Global Divergence

To predict flows accurately the numerical model must satisfy the governing physical laws. The code was checked to ensure that it conserves mass, momentum, and energy. These checks of internal consistency are an important part of developing confidence in the model predictions. The conservation of mass for an incompressible

flow is represented by the continuity equation $\nabla \cdot \mathbf{u} = \mathbf{0}$. The model was designed using the pressure projection method (detailed above in section 3.2.1) to guarantee nondivergence. Two measures of the divergence of the flow are monitored during the simulations: local and global divergence.

The global divergence criterion in the three-dimensional model compares the volume integrals of $\int \left(\frac{\partial u}{\partial x} + \frac{\partial v}{\partial y}\right)^2 dV$ and $-\int \left(\frac{\partial w}{\partial z}\right)^2 dV$. For all of the simulation results presented in this thesis the error in the global divergence is negligible. Typically the ratio of $\int \left(\frac{\partial u}{\partial x} + \frac{\partial v}{\partial y}\right)^2 + \left(\frac{\partial w}{\partial z}\right)^2 dV / \int \left(\frac{\partial w}{\partial z}\right)^2 dV$ is approximately 1/10,000. This measure of accuracy is maintained throughout the simulations, so that the overall consistency is very good. This global divergence criterion is a useful measure of the resolution in the simulations. At the beginning of the simulations when the flow is laminar and the waves are approaching the wall, the flow is incompressible to one part in one hundred thousand, approximately the same magnitude as roundoff errors in single precision calculations. As the flow begins to transition to turbulence and the resolution limits are approached, divergence grows to approximately one part in ten thousand.

In one test case that was inadequately resolved (which did not use the subgrid-scale model) the global divergence grew to about one part in one hundred before the model failed completely. In that case (results not presented here) the fourth-order pressure solver was unable to maintain pace with the rapidly changing pressure gradients, and the simulation "crashed" (giving meaninglessly large pressure and velocity fields). Although the experiment failed it was useful in determining the limits of stability of the model and revealing the potential for and signature of catastrophic failure.

Local Divergence

The local divergence criteria is a normalized measure that gives the magnitude and location of the largest divergence in the model. The maximum of the local divergence is normalized by the mean shear at each level z, e.g., $\overline{\frac{\partial u}{\partial x}}(z) = \frac{1}{L_x}\left(\int \left(\frac{\partial u}{\partial x}\right)^2 dx\right)^{1/2}(z)$,

and in the two-dimensional model is calculated by

$$\frac{\frac{\partial u}{\partial x} + \frac{\partial w}{\partial z}}{\frac{1}{L_x}\left(\int \left(\frac{\partial u}{\partial x}\right)^2 dx\right)^{1/2}} \,. \tag{4.11}$$

For a large number of simulations the largest local divergence consistently occurred near the wall. Usually this occurred at the third or fourth grid point from the wall, in the region where Δx is three to ten times larger than Δz (associated with the variable grid). A typical maximum local divergence is about one to two percent. The facts that the divergence is small and is located in a region where it might be expected (because special treatment is used to resolve strong gradients in the z' direction) build confidence in the accuracy of the model results.

Energy Conservation

Every simulation provides information about the balance of energy for the flow. All of the terms of the kinetic, potential, and total energy equations are calculated at each tenth time step during the simulations. The terms are summed and graphed to ensure that energy is conserved. The energy balance requirement is a more severe test of the accuracy of the model than either conservation of mass or momentum, because the energy terms are calculated using higher-order spatial derivatives. Figure 4.5 shows the kinetic, potential and total energy balances for Case 21 from Table 4.1, a 20^o critical-angle simulation. It is typical of the degree of energy conservation observed in the three-dimensional simulations. The largest terms in the energy equation are the input of work and the dissipation of energy. For the kinetic and potential energy equations, the buoyancy flux (or transfer of energy between kinetic and potential) is also quite large and oscillates throughout the simulation. The sum of all of the energy terms except for the work input, shown by the curve marked "Balance", should be equal to the "Work" input curve. Figure 4.5 shows that all of the energy is accounted for in the model and the overall energy conservation is very good.

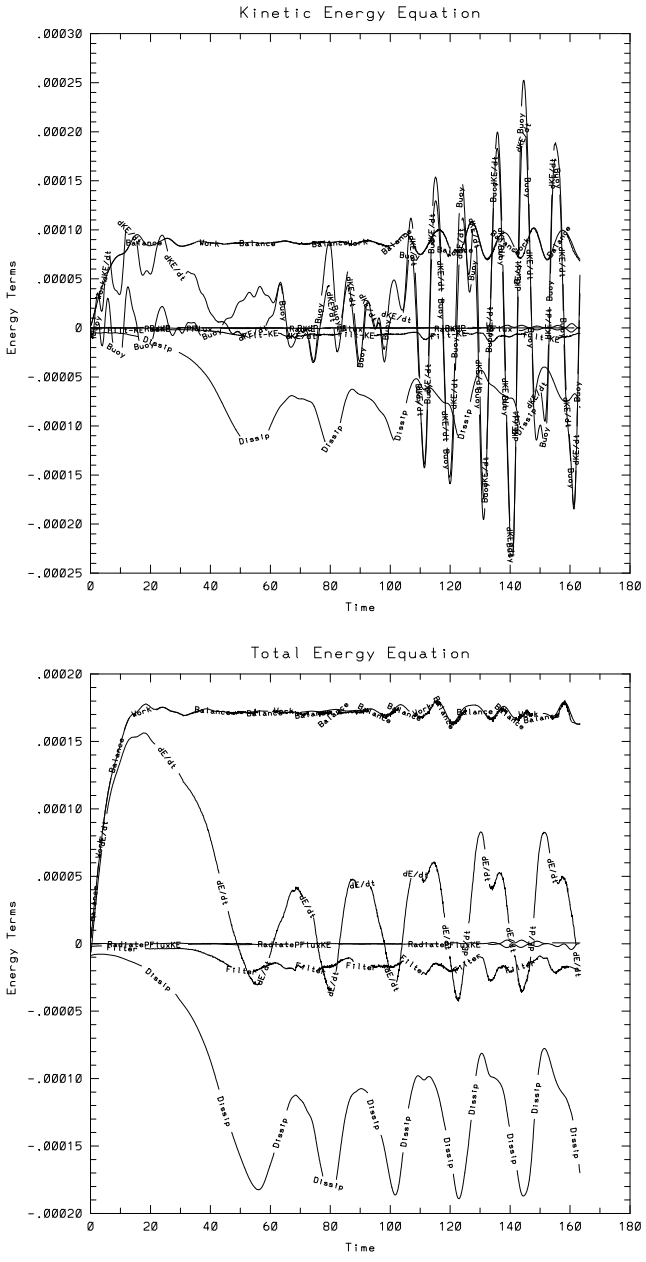

Figure 4.5: Kinetic and total energy balances for a turbulent wave breakdown case, showing the degree of energy conservation in the model.

Two- vs. Three-Dimensional Tests

The last type of internal consistency check is comparison between the two- and three-dimensional models. Some of the three-dimensional calculations were repeated in two-dimensions to provide a comparison, to study the three-dimensional characteristics of the flow, and to check relationships between accuracy and resolution. The two-dimensional simulations were typically very well-resolved at grid resolutions of 201 x 400. The coarsest grid used for low resolution three-dimensional simulations (appropriate for some low Reynolds number flows) was 65 x 33 x 130. Comparison of energetics and flow fields between the two-dimensional and three-dimensional flows helped to ensure that the three-dimensional model was working properly.

4.2.3 Comparison with Experiment

Perhaps the strongest code validation method comes from direct comparison with laboratory experiments of similar flows. Taylor (1993) has studied critical angle reflection over a 20^o bottom slope. There were some features of his laboratory setup that are not exactly duplicated by the numerical model. One difference is the method of wave generation. The model uses an oncoming wave train, whereas (because of the tank geometry) the laboratory experiments used a mode-one internal wave that has vertical wavelength equal to the depth of the fluid. The experiments were also conducted at somewhat higher Reynolds and Richardson numbers than attainable with direct numerical simulations, although both were well within the range for turbulent wave breakdown to occur.

Figure 4.6 shows the velocity fields in the boundary layer at one time during a wave period as measured by Taylor. He used particle image velocimetry to determine the two-dimensional flow field. This involved adding neutrally buoyant particles to the flow, and tracing their displacement by shining a sheet of light through the boundary layer and filming the location of individual particles. Figure 4.7 shows the corresponding flow fields from a similar simulation with the same bottom slope. The similarity in the near wall region (bottom 1/2 of Figure 4.7 covers approximately the same vertical dimension as the full height of Figure 4.6) between the flow fields

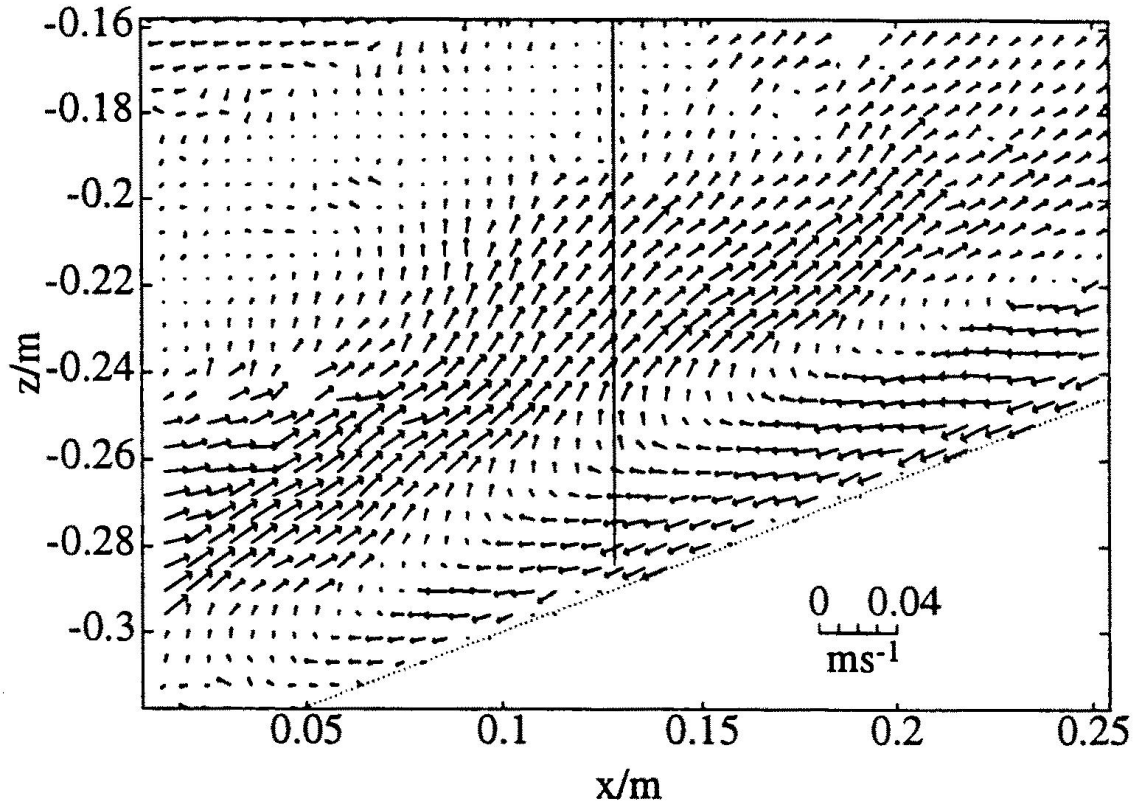

Figure 4.6: Measured velocity field in laboratory critical angle wave reflection over a slope. From Taylor (1993).

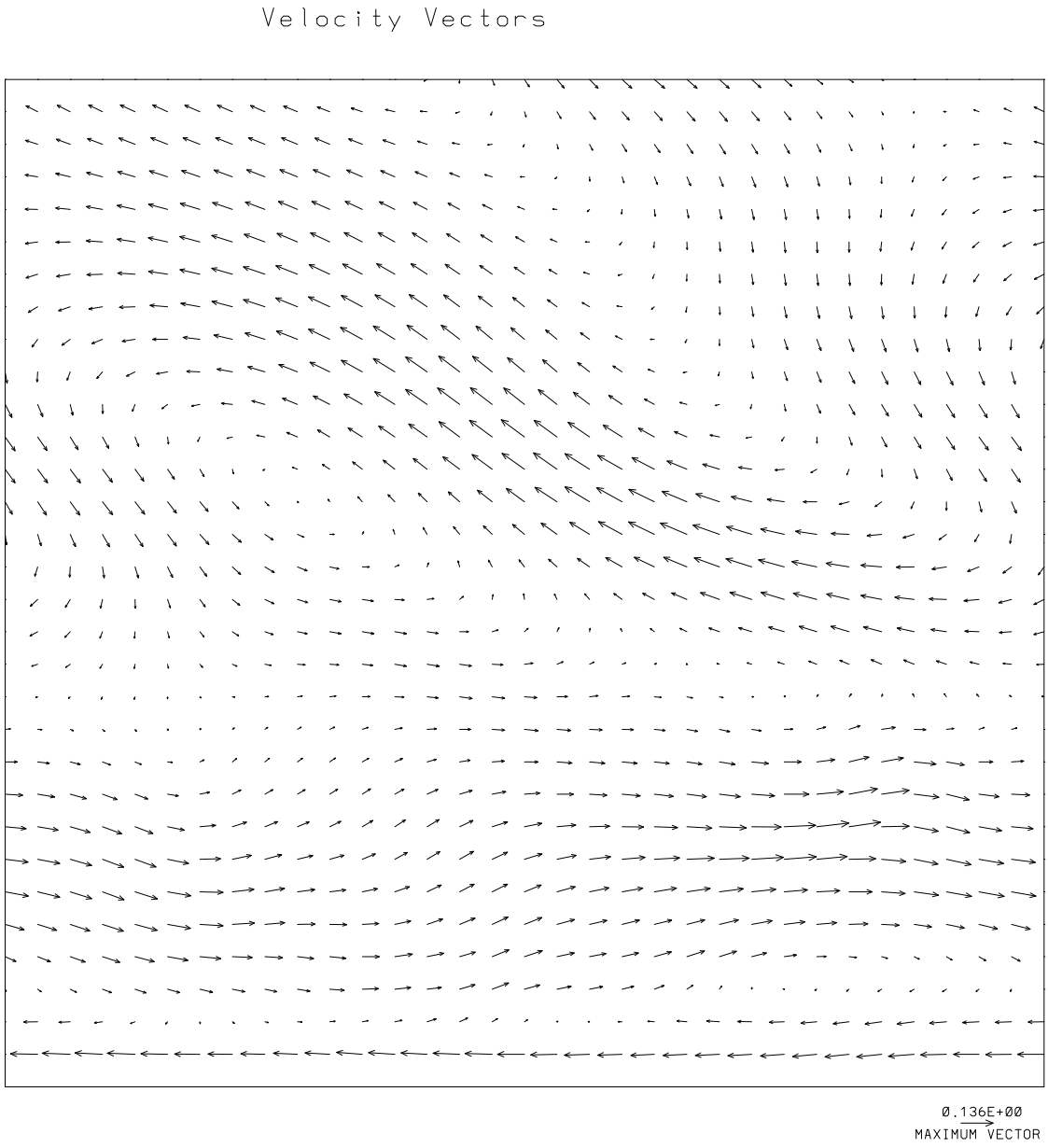

Figure 4.7: Calculated velocity field for the same bottom slope and wave period from the numerical simulations.

is strong. The two flows go through the same periodic behavior, with qualitatively similar flow features developing at each stage of the cycle. Additional comparisons between these cases will be made below. Close agreement exists between the laboratory and numerical experiments in the cases where similar experiments are available. This builds confidence for additional numerical results for which no laboratory experiments have been conducted. The numerical experiments have the advantage of being able to study cases not accessible to laboratory experiments. For example, small bottom slopes (which are common in oceanic applications) are very difficult to simulate in the laboratory.

4.2.4 Resolution and Repetition

The final code validation method to be discussed is a check of numerical accuracy. When a direct numerical simulation is resolved satisfactorily, it gives the correct solution; e.g., increasing the resolution significantly and repeating the simulation does not alter the results materially. A standard method to determine if a simulation is resolved satisfactorily is to examine the energy spectra. A well-resolved spectra will contain significantly less energy at higher wave numbers (small scales) than at the low wave numbers (large, energy-containing scales). A rule-of-thumb for the DNS of turbulence is that the energy level at the largest scales should be approximately three orders of magnitude higher than that at the smallest scales of motion.

Figure 4.8 shows the horizontal energy spectra averaged on four different x - y planes at various z' heights from the three-dimensional simulation listed in Table 4.1 as Case 28. Each of the spectra are taken in the turbulent boundary layer region, at $t = 79.5$ at distances from the wall of $z = 0.019$, 0.052, 0.095, and 0.15, respectively. The spectra are for a turbulent wave breakdown case at the critical angle with a bottom slope of 30^o, and are calculated from the flow field, five wave periods after startup. At this stage the flow has reached a quasi-steady turbulent state. Further details of this case will be presented in Chapter 5 below.

The horizontal spectrum gives a good measure of the resolution of the simulation, without adding the complication of interpreting the spectrum on the variable grid.

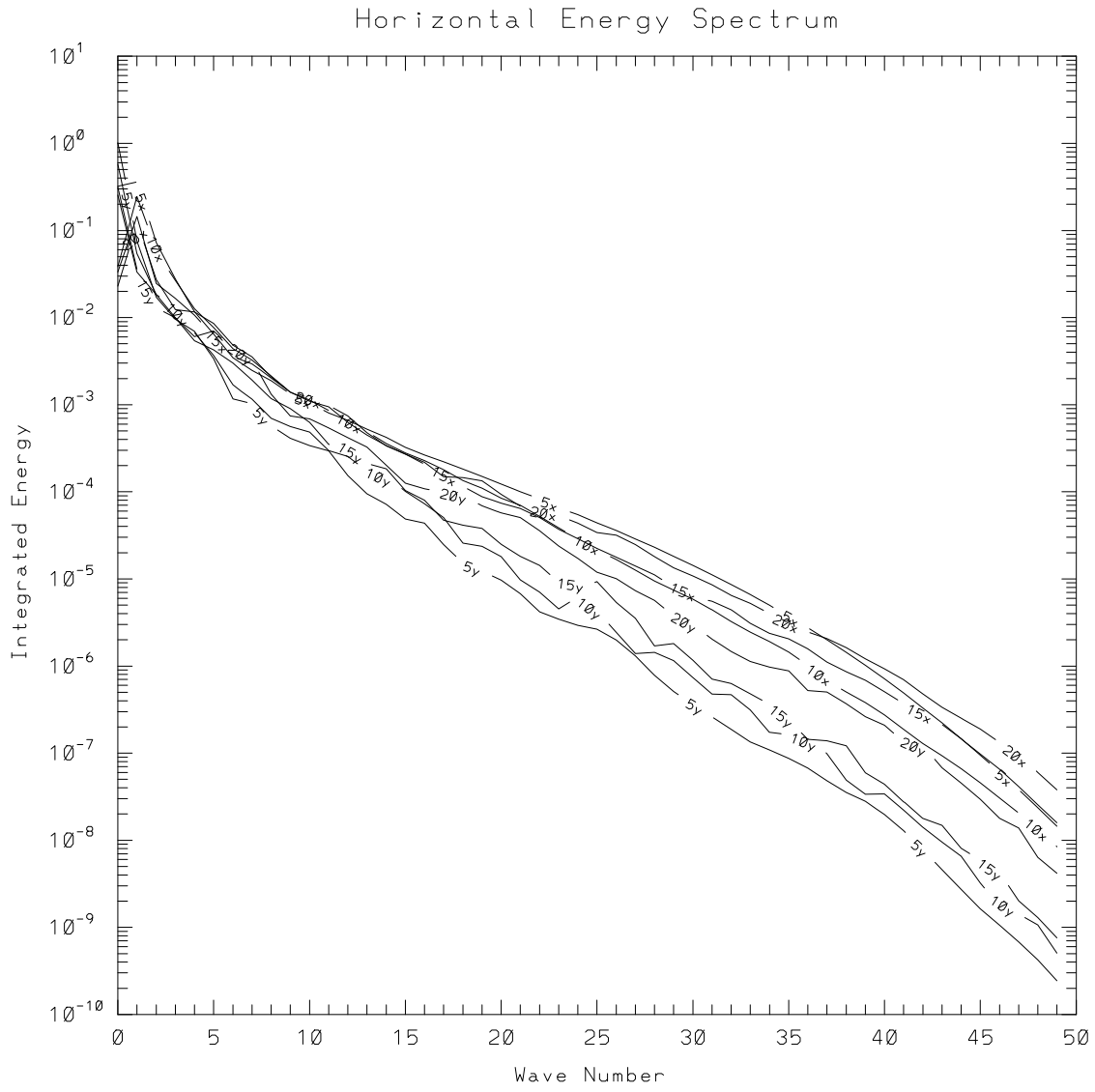

Figure 4.8: Horizontal energy spectrum from a three-dimensional calculation. There are 8 curves in the figure, four energy spectra decomposed in the x direction, labeled as 5x, 10x, 15x, and 20x, and four energy spectra decomposed in the y direction, labeled 5y, 10y, 15y, and 20y. They are at heights $z = 0.019$, 0.052, 0.095, and 0.15 respectively.

The flow was computed on a 128 x 128 x 130 grid; therefore, the highest horizontal wave number on the mesh is 64. The highest wavenumber plotted is 50 because above that value the energy spectra fall off rapidly, by approximately another five orders of magnitude. The region of wavenumber space above $k = 50$ is strongly influenced by the removal of energy by the compact filtering. The aspect ratio $\Delta x/\Delta y = 1.1$ is very close to one; therefore, here the x and y spectra are considered together. Figure 4.8 indicates that the flow was well-resolved at this point, and additional analysis indicates good resolution throughout the simulation, and shows the strong rolloff of energy at higher wavenumbers.

The final point to be made here, with regard to model validation, is that over two hundred simulations were conducted in this study. By doing numerous experiments, the model capabilities and limitations became familiar and reasonably well understood. The overall consistency of the validation tests (with linear theory, comparison with laboratory data, conservation properties, and internal numerical tests), together with the physical coherence of the results, to be discussed in detail in the remainder of Chapters 4, 5, and 6, allow confidence that the model accurately represents the fundamental physics of the flows.

4.3 Running the Experiments

This section presents a brief description of how the numerical experiments are monitored and adjusted throughout the computations. After choosing the parameters for each three-dimensional simulation the flow is initialized with white noise in the lower half of the domain as described in section 3.6.4. On a low resolution grid of 65 x 33 x 130 (x, y, z) grid points the noise is then allowed to adjust for 1-2 buoyancy periods into low-level, stratified turbulence exhibiting coherent structures. At this point the wave forcing mechanism is turned on in the top half of the domain and the waves begin to propagate downward towards the wall in a linear fashion. During this transient stage of the calculation no additional resolution is required to resolve the developing flow field.

Typically after 4-5 buoyancy periods the leading edge of the wave train reaches

the bottom slope. By this time the energy in the noise near the boundary has typically died away by roughly an order of magnitude from its initial level to a weak background perturbation field. At this time the energy density level in the noise field is approximately one to five percent the energy density of the oncoming wave. After 2-3 more buoyancy periods, the flow starts to exhibit nonlinear behavior as the wave reflection process begins to strengthen. A typical flow feature observed during this stage is a strong density gradient developing in the boundary layer region. At this stage of flow development the simulation is moved onto a higher resolution numerical grid. The process of regridding is done by using Fourier interpolation, for example, onto a 129 x 33 x 130 grid point mesh.

During the next wave period it usually becomes apparent if the flow will develop into turbulence or remain laminar. The turbulent cases often required further regridding onto more refined grids to resolve the three-dimensional structures that developed in the boundary layer. This is also done by Fourier interpolation in the y-direction, onto grids of either 129 x 65 x 130, or when warranted 129 x 129 x 130, depending upon the physical dimensions of the problem and resolution criteria. The grid clustering in the z-direction is not changed during the simulations, but rather is set at the beginning, based upon experience, to a degree that will adequately resolve the boundary layer.

After regridding to the highest resolution for the simulation the flow is run out for 10 to 30 more buoyancy periods. This typically allows a quasi-steady flow pattern of wave reflection and breakdown to develop and be recorded. The resolution requirements are determined by a number of factors. These include analysis of the energy spectrum as discussed above, comparisons of the energy removed at well resolved scales and by the scale-dependent filter, and determination of whether a direct numerical or large eddy simulation is being conducted. Some of the numerical simulations may be considered a hybrid between direct numerical and large eddy simulations. This may be the most appropriate description for cases in which approximately 90% of the energy is dissipated at well-resolved scales by the true molecular effects (e.g., through the kinetic energy dissipation rate) and approximately 10% of the energy was

dissipated by the hyperviscosity filter at the smallest scales on the numerical mesh. In these cases, it is expected that the small degree of subgrid-scale dissipation does not significantly affect the development of the flow at the large, energy-containing scales of motion.

4.3.1 Computational Issues

The simulations are run in segments for a predetermined number of time steps, usually approximately 5,000, with the flow fields saved at every 1,000th time step. At the end of each segment the simulation is evaluated to see if it requires a higher resolution grid. Typically, the simulations are run for 20,000 time steps, with exceptional cases run for up to 30,000 time steps. The simulations are ended when it is determined that the flow has achieved a steady state for a required number of wave periods. In some of the simulations the forcing is turned off, or varied in time, to imitate the approach of a long wave packet rather than a steady oncoming wave train. Statistical information and samples from the flow are written to disk every ten time steps. In addition, sparse data sets (every 8th grid point for the lower half of the domain) of the velocity and density fields are saved at every 250th time step in order to retain information on the temporal development of the flow.

The three-dimensional simulations are computationally expensive and time consuming. The high resolution runs at 129 x 129 x 130 grid points take approximately 24 hours of CPU time on the Cray-YMP to complete 4,500 time steps. The code is written in portable FORTRAN 77 and the simulations have been conducted without modification on four platforms. A grant of 190 hours of computer time, on the Cray 2 and Cray-YMP computers, was awarded for this study at the National Center for Supercomputing Applications at the University of Illinois, Urbana-Champagne. Additional simulations were conducted on a Stardent mini-supercomputer and Hewlett-Packard workstations at the University of Washington. A simulation at a resolution of 129 x 33 x 130 requires approximately 55 megabytes of memory using single precision on the HP workstations. It takes about one minute of CPU time per time step on a HP-9000 series 715 workstation, 1.2 minutes of CPU time per step on the

Stardent mini-supercomputer, 10 seconds of CPU time per time step on the Cray-2, and 6 seconds of CPU time per time step on the Cray-YMP. Frequently, to make the best use of computer resources, the low resolution portions of the simulation were conducted on the local computers and then restarted on the Cray computers after regridding for the turbulent portions of the simulation.

4.4 Primary Critical Angle Case

Throughout the remainder of this chapter, concepts about wave reflection and boundary layer development are examined by studying a case in detail. This case is a critical angle simulation for a 9.2^o sloping bottom, corresponding to Case 15 in Table 4.1. It is representative of cases where transition to turbulence occurs during wave breakdown, and is especially representative of experiments over shallow bottom slopes. Experiments with bottom slopes between 3^o and 15^o respond similarly and may be characterized as shallow, based upon the results of this study. Following this examination of Case 15, details will be presented in Chapter 5 of additional critical angle experiments, with bottom slopes of 30^o, 20^o, 5^o, and 3.4^o.

Figure 4.9 shows intermediate time isopycnals taken from a numerical experiment in which an internal wave train propagates toward the bottom boundary in the plane of the slope. It is a two-dimensional (x', z') cross section of a three-dimensional simulation. These constant density surfaces show that the oncoming wave train is of moderate amplitude and that a region of strong density gradient has developed near the bottom boundary. In this case the fundamental frequency of the oncoming wave ($\omega = 0.161$) is chosen so that, upon the wave's reflection, the angle of the group velocity vector to the horizontal matches the bottom slope, i.e., the wave is at the critical angle.

The Reynolds number, Re, for Case 15, based upon the maximum wave current speed, U, and wavelength, λ, is 3500. Case 15 was run for 25,500 time steps, to a time of $t = 191$, using the regridding approach discussed above. For the geometry of Figures 4.9 - 4.43, $\lambda_x = 3\lambda_z$, where λ_x and λ_z refer to the wavelengths in the x' and z' directions. The aspect ratios, x':y:z', are shown to scale throughout the figures.

The wavelength in the direction of the wavenumber vector is $\lambda = 0.95\lambda_z$, according to the relation $1/\lambda^2 = 1/\lambda_x^2 + 1/\lambda_z^2$.

The model is taken to be periodic in the y direction with the width of the domain, y_l, set comparable to λ_x and λ_z; in this case $y_l = 1.7\lambda_z$. The model is made periodic in the x' (upslope) direction by subtracting off the background (linear) density stratification from the governing equations and formulating conservation equations for perturbation density and pressure fields about the mean state. It is possible to reformulate the problem in this manner, within the Boussinesq approximation, for constant N, since the background density stratification is in hydrostatic balance with the pressure field (see Section 2.1).

4.4.1 Flow Development

Figure 4.10 shows a time sequence of constant density surfaces, depicting the flow throughout one and one-half wave periods of its development. Each figure focuses on the near wall region. The dimensions of each frame are one wavelength, $\lambda_z = 2\pi/m'$, in the z' direction by one wavelength, $\lambda_x = 2\pi/k'$, in x' direction. Here time is nondimensionalized by the buoyancy frequency, N, the wave period is 39.2, and the buoyancy period is 2π. Contours are shown at intervals of 0.05, where the background density gradient $\dfrac{\partial\overline{\rho}}{\partial z} = 1$.

At time $t = 70$, the wave train has reached the wall, and a strong gradient in density has formed. This feature, called a thermal front by Thorpe (1992), moves upslope at the x' component of the phase speed of the oncoming wave. As time progresses, wave overturning develops in the lee of the thermal front, and at time $t = 88$, statically unstable fluid is apparent near the center of the domain. Another significant feature is also apparent at times of 88, 94, and 102. Near the wall, a region of strong density gradient has developed in the z'-direction across the entire breadth of the domain. As time continues, the overturned regions break down into small-scale turbulence and dissipate the wave energy in a three-dimensional fashion. Also, the strong density gradient in the z'-direction is relieved so that, by $t = 109$, it is no longer a dominant feature of the flow. By time $t = 133$ the flow has relaminarized

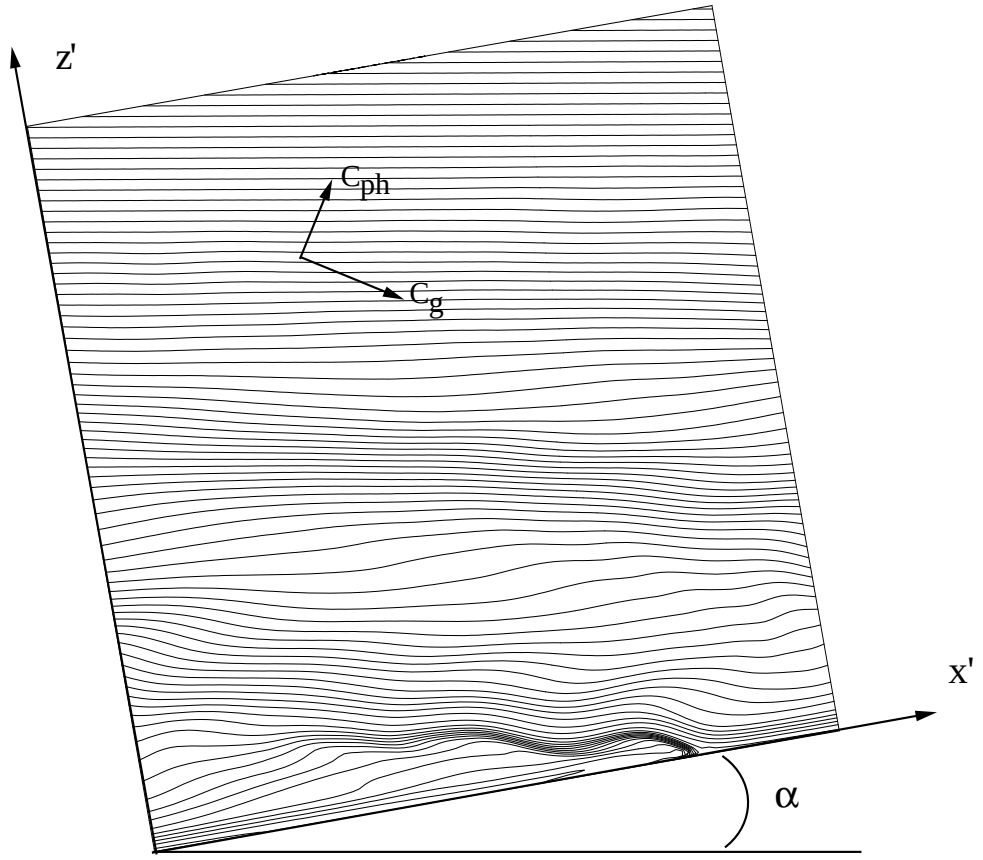

Figure 4.9: Density contours for an oncoming wave train generated in a forcing region above the bottom boundary propagate downward with phase and group velocities as indicated.

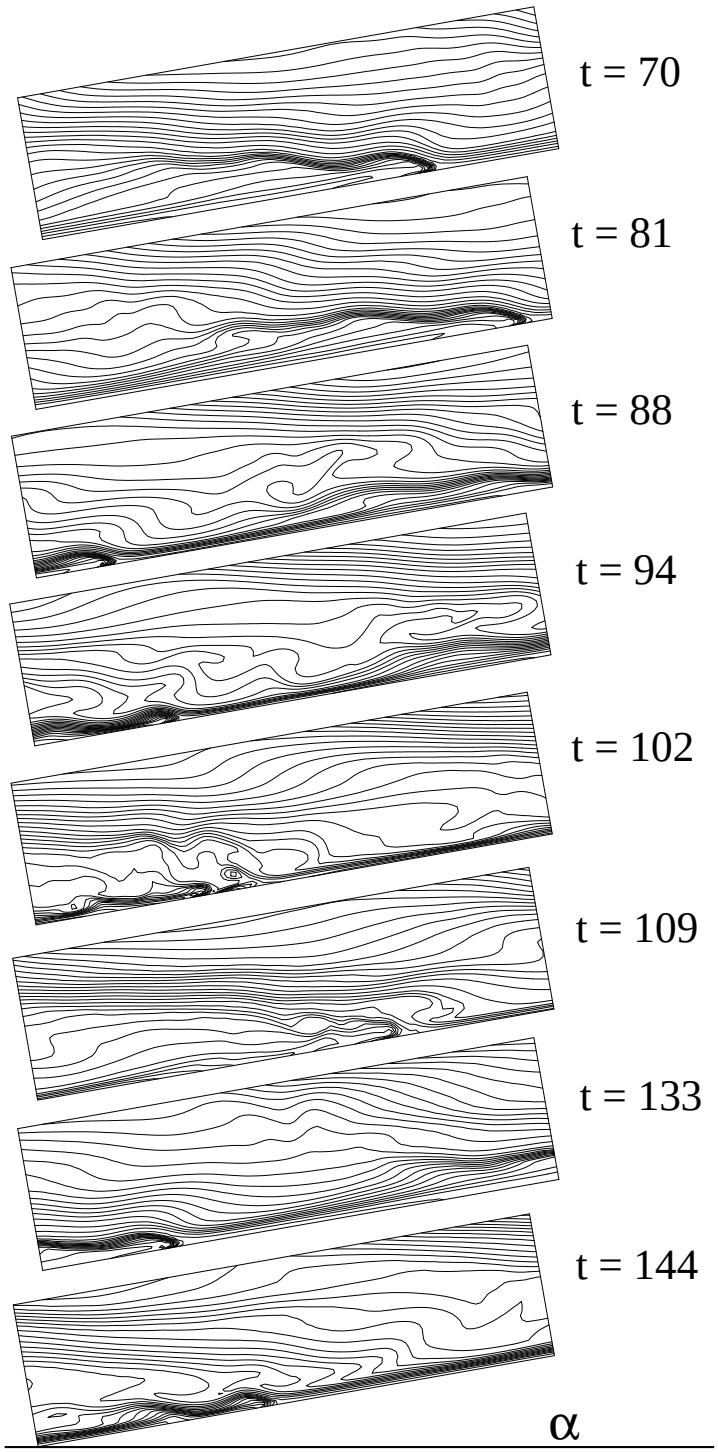

Figure 4.10: Time sequence of flow in the near wall region for Case 15.

and the boundary layer has almost entirely restratified. At the last time pictured, $t = 144$, the flow is once again statically unstable throughout the boundary layer and is similar to the flow at $t = 94$. The periodic nature of the flow development will be examined in more detail below (see Section 4.4.3).

It should be noted that the actual simulation was conducted on a higher density mesh than appears in these contour plots. The isopycnal graphs were made from sparse data sets that are saved frequently throughout the simulations. The figures are take from two simulations conducted on grids refined up to 129 x 33 x 130 and 129 x 65 x 130 points, but the figures are made from data sets with corresponding resolutions of 65 x 17 x 35 and 65 x 33 x 35 grid points covering the bottom half domain.

The flow development in the boundary region is also illustrated in Figures 4.11 and 4.12. Here the two-dimensional velocity vectors (from the u and w components) are shown in the same x-z plane as in Figure 4.10. Again the two-dimensional cross section is taken from the center plane of the three-dimensional domain. The velocity vectors are presented on a 65 x 19 uniform grid, which was interpolated from a 129 x 65 variable grid (x-z) used for the computation in this region of the flow. The length of the vectors in each of the four frames of Figure 4.11 and 4.12 are scaled slightly differently to enhance visibility in each frame. The longest vector in each region is scaled to reach from its point of origin to the neighboring grid point. The maximum local two-dimensional velocities in each frame are noted below each frame as: Figure 4.11(a) 0.292, (b) 0.309, (c) 0.249, (d) 0.189, Figure 4.12(a) 0.194, (b) 0.216, (c) 0.314, (d) 0.253, where (a) refers to the top frame of the figure and (d) is at the bottom.

In several of the frames of Figures 4.11 and 4.12, e.g., $t = 70$, 88, 94, 102, and 109, the strong shear of the oncoming internal wave is evident. In the other frames, the internal wave field appears diminished compared with the stronger currents in the near wall region. The role of the oncoming internal wave field in boundary mixing will be examined below in Section 4.7.2. At times 70 and 81 the dominant flow feature evident from the velocity field is the upwelling of fluid associated with the location of the thermal front. The upwelling fluid is drawn into the phase of the internal

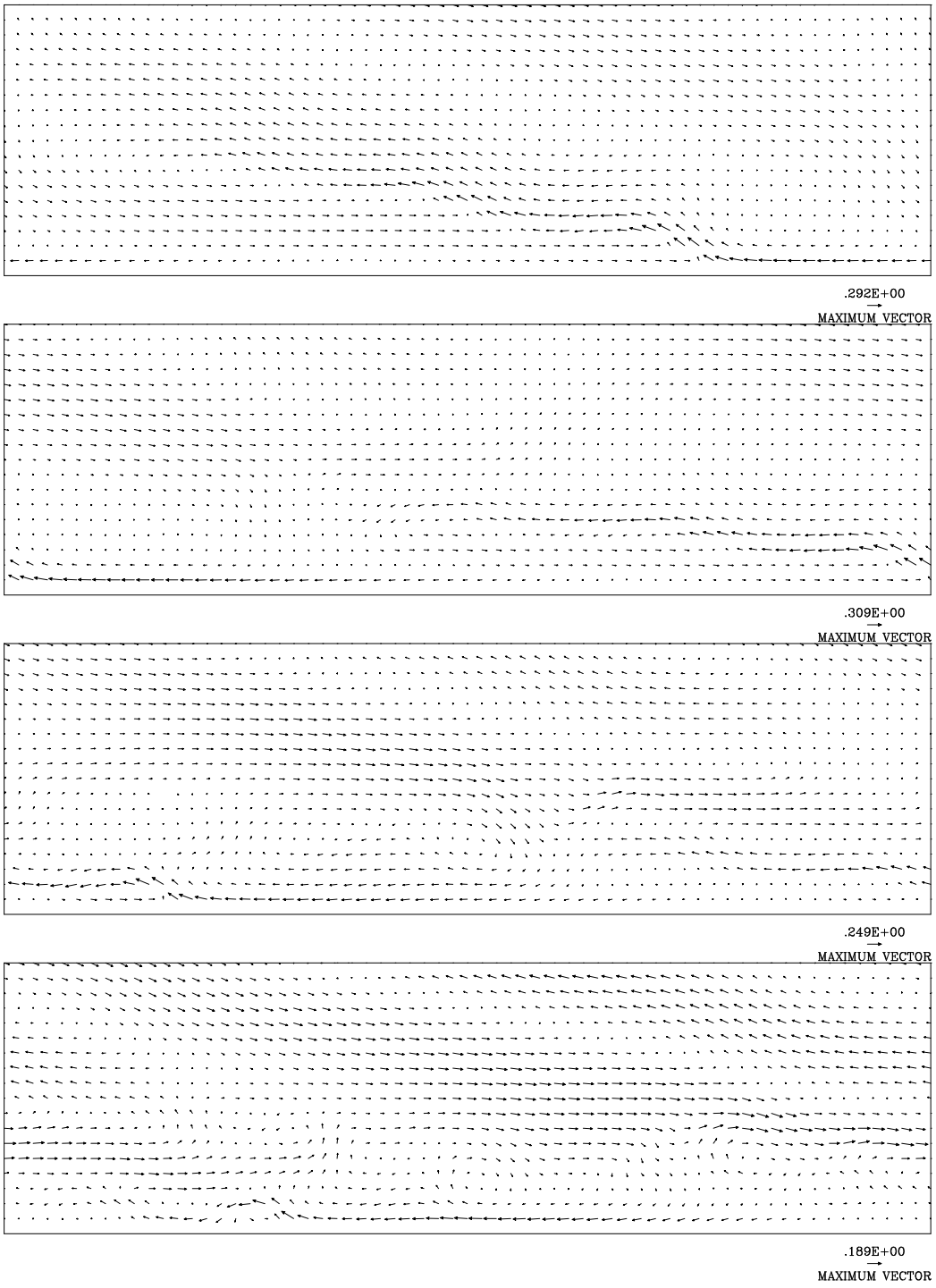

Figure 4.11: Part 1 of velocity vectors in the boundary region for the same time sequence of flow development as Figure 4.10, at $t = 70$ (top), 81, 88, and 94 (bottom).

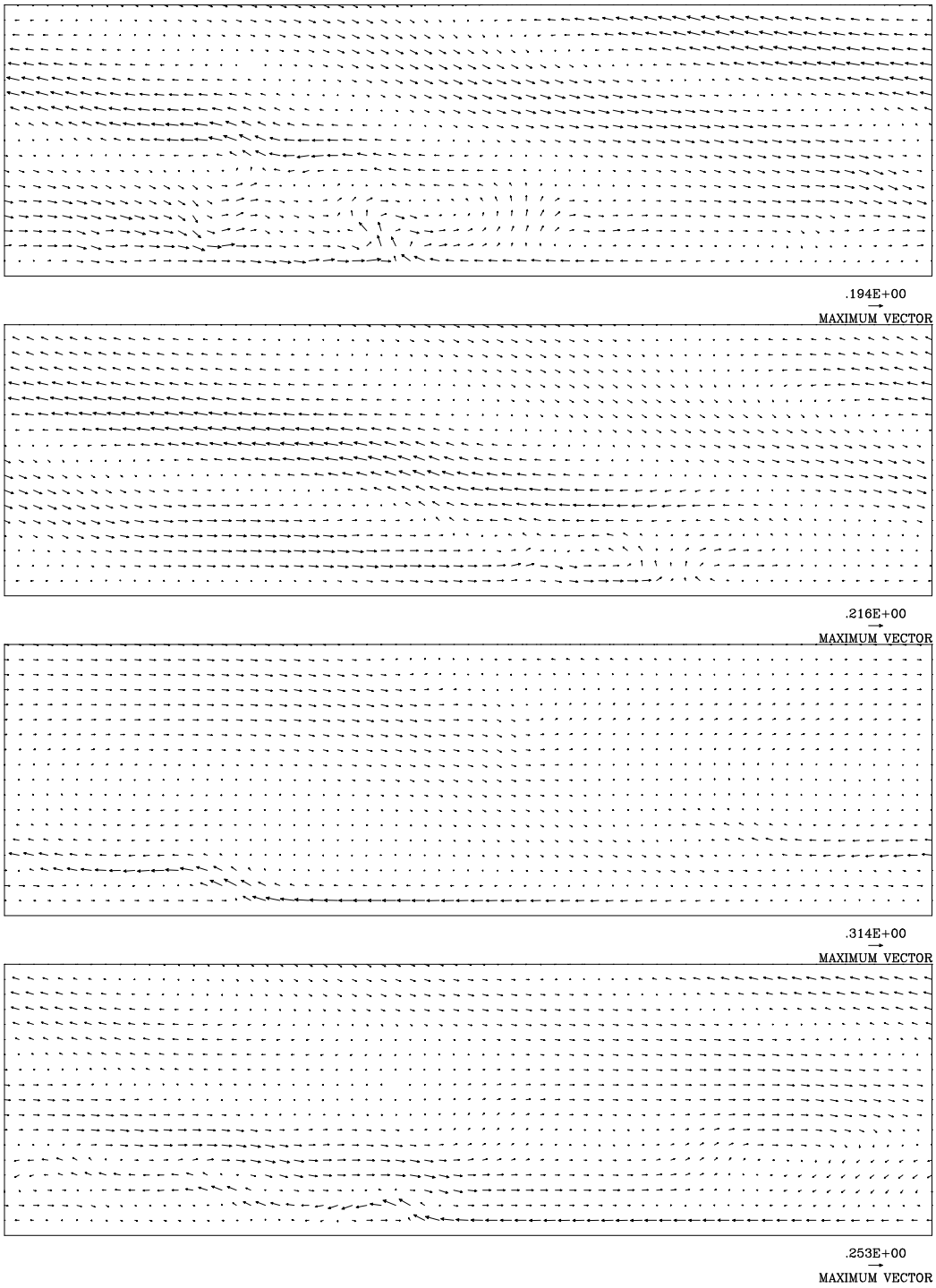

Figure 4.12: Part 2: Velocity vectors in boundary region for the same sequence of flow development as Figure 4.10, $t = 102$ (top), 109, 133, and 144 (bottom).

wave with upward directed currents. At t=70, the flow field appears predominantly laminar and wavelike. As time progress, for example, at t=88, 94, and 102, regions of vertically recirculating fluid appear throughout the boundary region. Additional analysis indicates that the eddies are three-dimensional in character and correlated with the location of overturned isopycnals (e.g., Figure 4.10 above or Figure 4.19, below). The eddies actively participate in strong local vertical mixing. The quasi-periodic nature of the problem is again suggested by comparing the similarity of certain pairs of velocity fields (e.g., $t = 109$ with $t = 70$ and $t = 133$ with $t = 88$); these pairs of fields are 39, 45, and 42 time units apart. The visual evidence here supports more compelling evidence from the energy and dissipation budgets (Section 4.4.3) that the mixing in the boundary layer has a periodicity of approximately 45. The nonlinearities of turbulence, and other flow dynamics discussed below, may account for a departure of this time scale from the wave period of 39.2.

An important feature of the flow, which shows up for almost all of the critically sloping cases, is apparent in the bottom frame of Figure 4.11 ($t = 94$). Associated with the strong density gradient in the z'-direction (Figure 4.10), a region of downslope flow occurs very near the wall across most of the breadth of the domain. The flow is similar to the backwash produced on a beach after a wave has broken on shore and is a type of restratification driven by buoyancy forces. During this phase, the backwash creates what may be termed a slippery boundary layer, which may facilitate the breakdown of the oncoming waves further away from the wall. When an oncoming wave interacts with a boundary that includes a slippery boundary layer, the influence of the no-slip boundary condition is decreased and the wave does not lose a significant portion of its energy to viscous dissipation in the laminar sub-layer. Thus, the wave retains additional wave kinetic energy to enhance the strength of mixing in the turbulent boundary layer. For critical frequency waves, whether a slippery boundary layer is present or not, nearly all the wave energy is dissipated, but when a slippery boundary layer exists, mixing is enhanced. MacCready and Rhines (1991) have discussed slippery boundary layers and their importance to changing the bottom friction experienced by large scale flows.

Loss of wave energy by viscous dissipation near the wall is a significant sink of energy in these experiments. A numerical experiments will be described below that eliminated this loss of energy by implementing a free-slip wall (Section 6.4). Then, the boundary layer may be even more "slippery", and the waves exhibit stronger turbulence. In the no-slip case, the waves break into turbulence during the phase when a secondary flow has been established, which effectively decreases the wall friction experienced by the oncoming wave (above the viscous sublayer in the turbulent boundary layer).

4.4.2 Three-Dimensionality

The previous figures have indicated the structure of the flow in only one vertical plane. This section examines the three-dimensional nature of the flow during wave breakdown into turbulence. Some features important to the description of turbulence include irregularity and randomness. Also, turbulent flows possesses a wide range of scales of motion, and are unstable and strongly nonlinear. They are characterized by large amounts of vorticity, are highly dissipative, and have high rates of transport of mass, momentum, and scalar properties such as heat or salt. Finally, an essential component of a turbulent flow is that it is three-dimensional. This section presents evidence that the wave breakdown process is three-dimensional, supporting the conclusion that the two-dimensional oncoming waves transition to turbulence.

Figure 4.13 shows vectors of the u'-v velocity components in an x'-y plane parallel to the sloping bottom plane at a distance from the wall of $z' = 0.126\lambda_z$. The vectors appear to indicate a divergent flow because they show only the components of velocity in the x' - y plane and do not include the w' component. The velocity field is taken at $t = 94$, and the dimensions of the domain in the x' and y directions are $3\lambda_z$ and $1.7\lambda_z$, respectively. Several distinct horizontal structures are apparent in the flow, including jets and fronts associated with the unstable density profiles. The observed variability in the y direction is an indication of the importance of using a three-dimensional model to capture the physics of the wave breakdown process.

Figure 4.14 indicates another aspect of the three-dimensionality of the flow. Here,

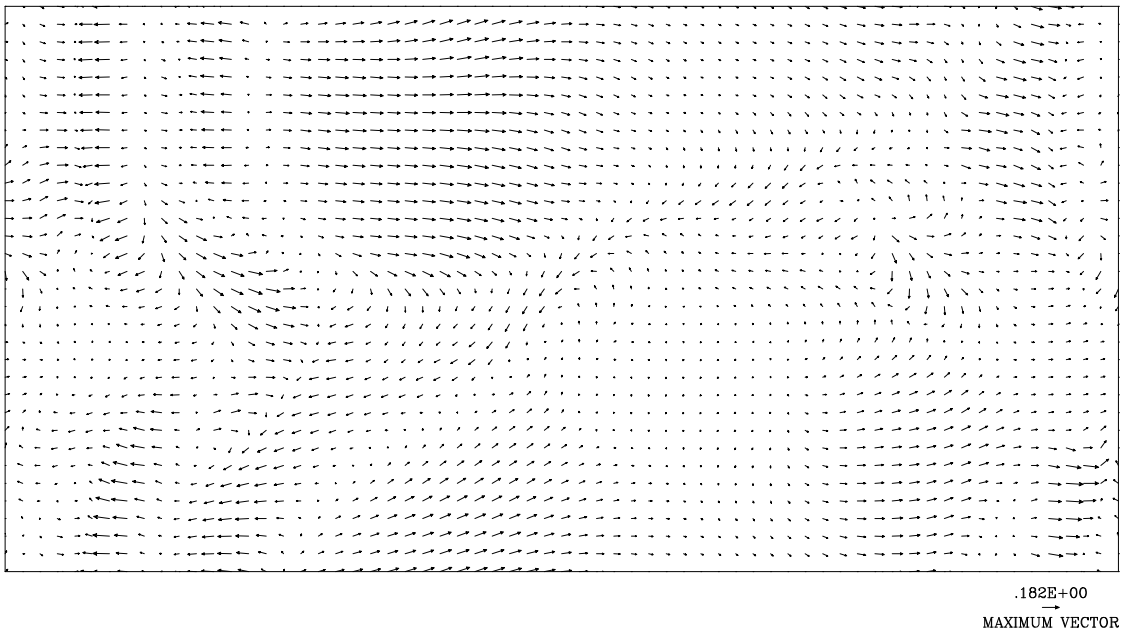

Figure 4.13: Velocity vectors illustrating the velocity components in a plane located parallel to the bottom slope at $t = 94$ at a height $z' = 0.126\lambda_z$. Some of the 3-D structure of the wave breakdown is evident from the vector field.

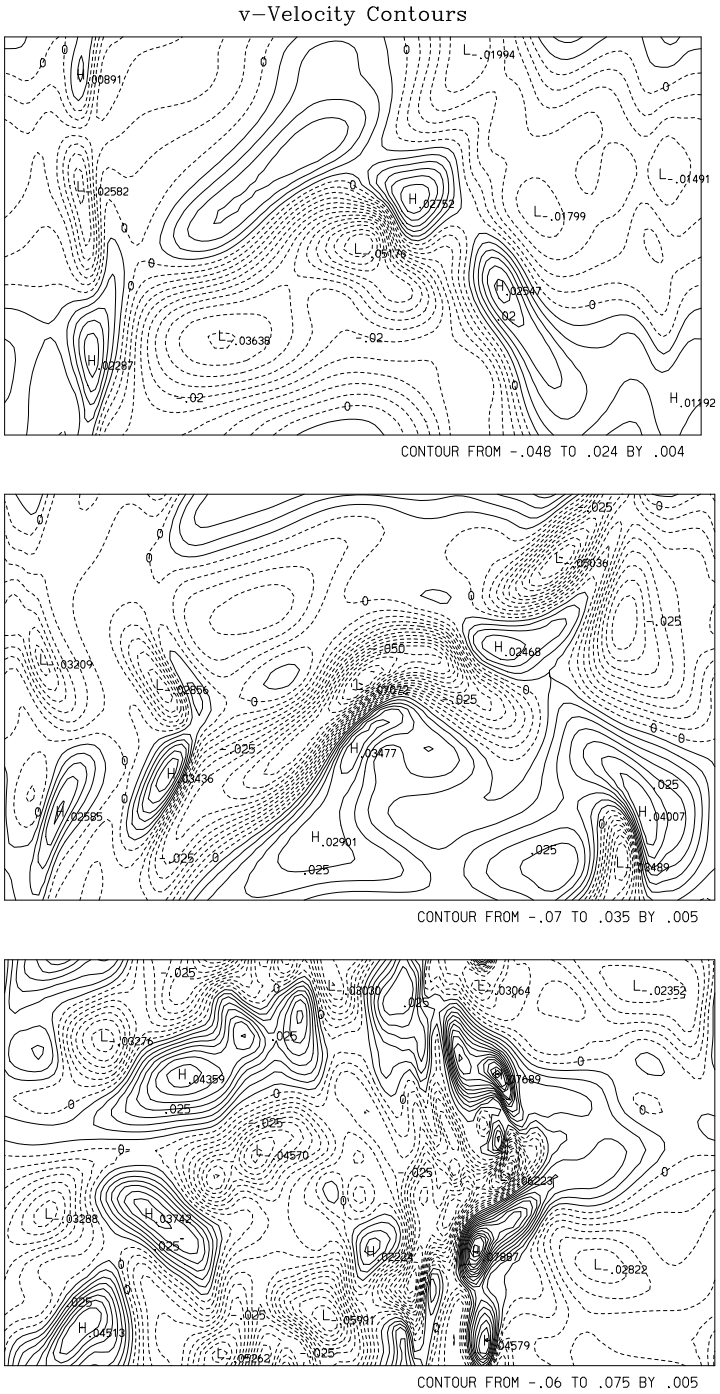

Figure 4.14: v - velocity contours in a plane parallel to the bottom plane at $z = 0.08$, within the turbulent boundary layer, at $t = 88$ (top), 94, 109 (bottom).

a series of velocity contours of the v component of velocity are shown in the same x-y plane located at $z = 0.08$ (the 15th grid point plane from the wall), within the lower part of the turbulent boundary layer. The frames in Figure 4.14 are at $t = 88$ (top), 94, and 102 (bottom).

The v component of the velocity is not contained by the oncoming wave. If the regions of high intensity of the v component are compared with the density fields of Figure 4.10, then the strongest three-dimensionalities are seen to occur at (and move with) the location of the thermal front. An explanation of this behavior is given below in Section 4.7 on vorticity dynamics.

At $t = 71$ (not pictured) the energy in the v component is primarily associated with the low level background noise used to initialize the flow. At later times, the largest amounts of the v component have apparently been generated by wave breakdown. The strongest regions of turbulent generation move upslope with the thermal front and the overturned regions, leaving decaying turbulence in their wake.

Indications of the relative strength of the three-dimensional aspects of the flow are given in Figures 4.15 and 4.16. Figure 4.15 shows the volume integrals of the square of the shears involving the w velocity component, e.g., $\left(\frac{\partial w}{\partial x}\right)^2$, $\left(\frac{\partial w}{\partial y}\right)^2$, and $\left(\frac{\partial w}{\partial z}\right)^2$. These integrals cover the entire computational domain and thus include the energy of the oncoming wave. In calculating the volume integrals the contribution of each finite volume is weighted according to the local grid spacing of the variable grid and normalized by the total number of grid points, giving an average energy or shear level rather than the total sums. The oncoming wave contains shear components $\frac{\partial w}{\partial x}$ and $\frac{\partial w}{\partial z}$, but does not include shear in the y direction. Hence, the growth of the $\frac{\partial w}{\partial y}$ component is indicative of three-dimensionality and wave breakdown into turbulence.

At early times, $t < 60$, the variability in the y-direction decreases, indicating the viscous decay of the initial white noise. During the early period, the wave train approaches the wall and grows in amplitude in the wave forcing region, as indicated by the values of $\left(\frac{\partial w}{\partial x}\right)^2$ and $\left(\frac{\partial w}{\partial z}\right)^2$. When wave reflection begins in earnest around

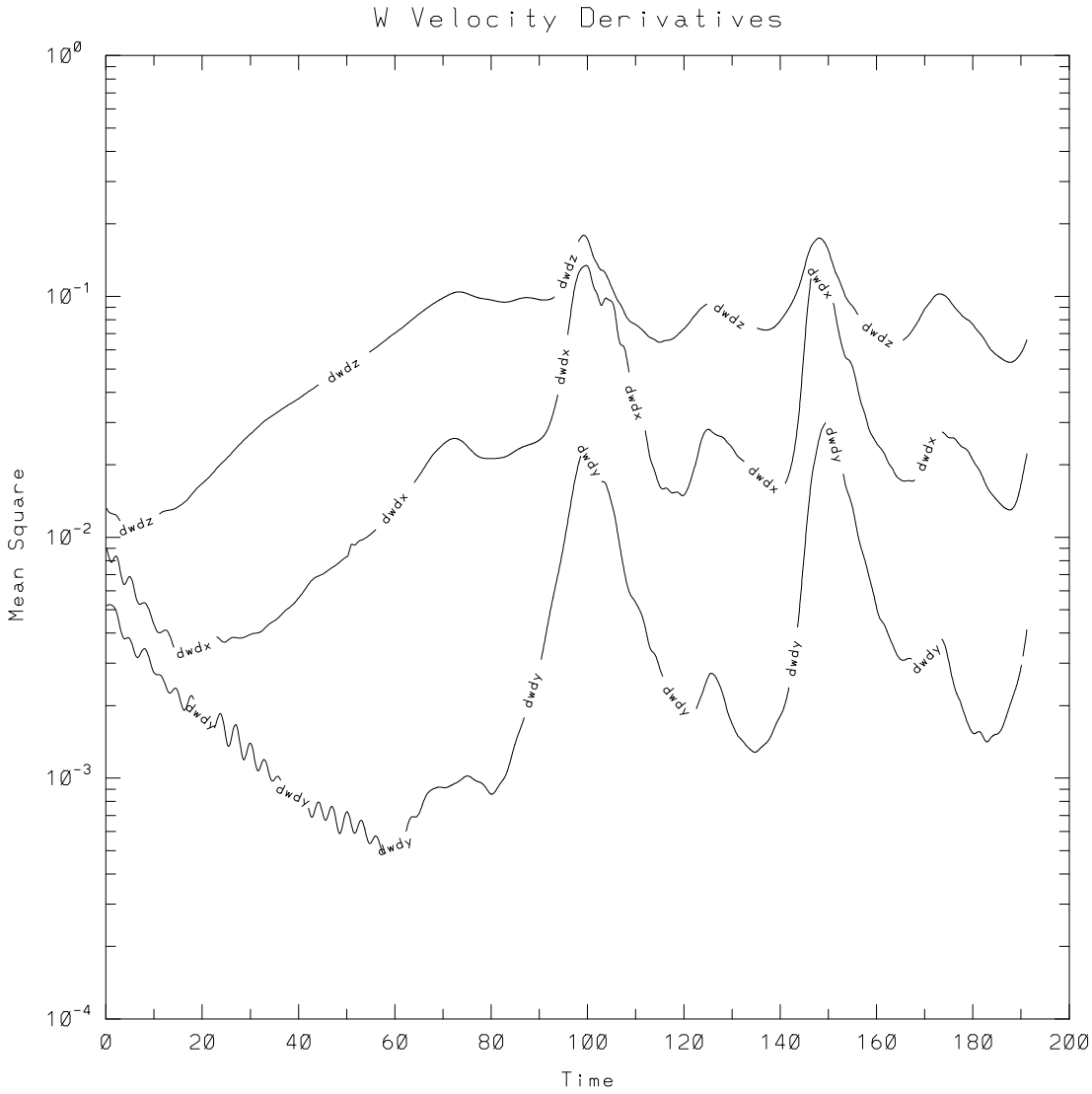

Figure 4.15: Volume integrals of mean square quantities of shear involving the w component of velocity, $\left(\frac{\partial w}{\partial x}\right)^2$, $\left(\frac{\partial w}{\partial y}\right)^2$, and $\left(\frac{\partial w}{\partial z}\right)^2$

$t = 70$, the three-dimensionality of the flow grows rapidly and $\left(\frac{\partial w}{\partial y}\right)^2$ increases by factor of approximately 40, from about 5×10^{-4} to 2×10^{-2}. During the period of strong mixing, from about $t = 90$ to $t = 110$, the shear in both the x and y directions is strongly enhanced. After the mixing cycle is completed, the shear decreases rapidly and, within about two buoyancy periods ($2T_b = 12.6$), has dropped by over an order of magnitude. During this period of relaminarization, the flow is also being restratified (i.e., the mixed fluid settles back to a staticallly stable profile through a combination of diffusion and buoyancy forces.)

The next mixing cycle occurs near $t = 150$ and is of approximately the same strength as the previous event. Again the three-dimensionality of the flow, as measured by the strength of the shear in the y-direction, increases by over an order of magnitude. Based upon other experiments, which indicate that the flow would continue to repeat the periodic mixing behavior, the simulation was stopped at $t = 191$. Figures 4.15 and 4.16 show that at $t = 191$ a third mixing cycle is just beginning. This should be remembered below when examining Figures 4.30 - 4.32, which suggest the mixing may have already reached the peak by $t = 188$. Note also that secondary peaks occur at approximately $t = 120$ and $t = 170$. While the secondary peaks are apparent, in many of the simulations, their cause is not understood. A similar situation that is more clearly interpretable is described below in Section 6.1.

Figure 4.16 shows the volume integrals of the three components of kinetic energy per unit mass, $u^2/2$, $v^2/2$, and $w^2/2$. The volume integrals are summed over the entire computational domain, including the wave forcing region and hence include energy from the oncoming wave. The most evident features are the growth of energy in the v-velocity field during wave breakdown and its subsequent decay during relaminarization. The magnitude of the oscillation of kinetic energy in the v velocity field is approximately an order of magnitude. The magnitudes of energy in u^2 and w^2 are considerably larger than v^2, and their variation during wave breakdown is less pronounced. Since the oncoming wave does not contain any v^2 component of kinetic energy, this component is a good measure of the increase of three-dimensionality in

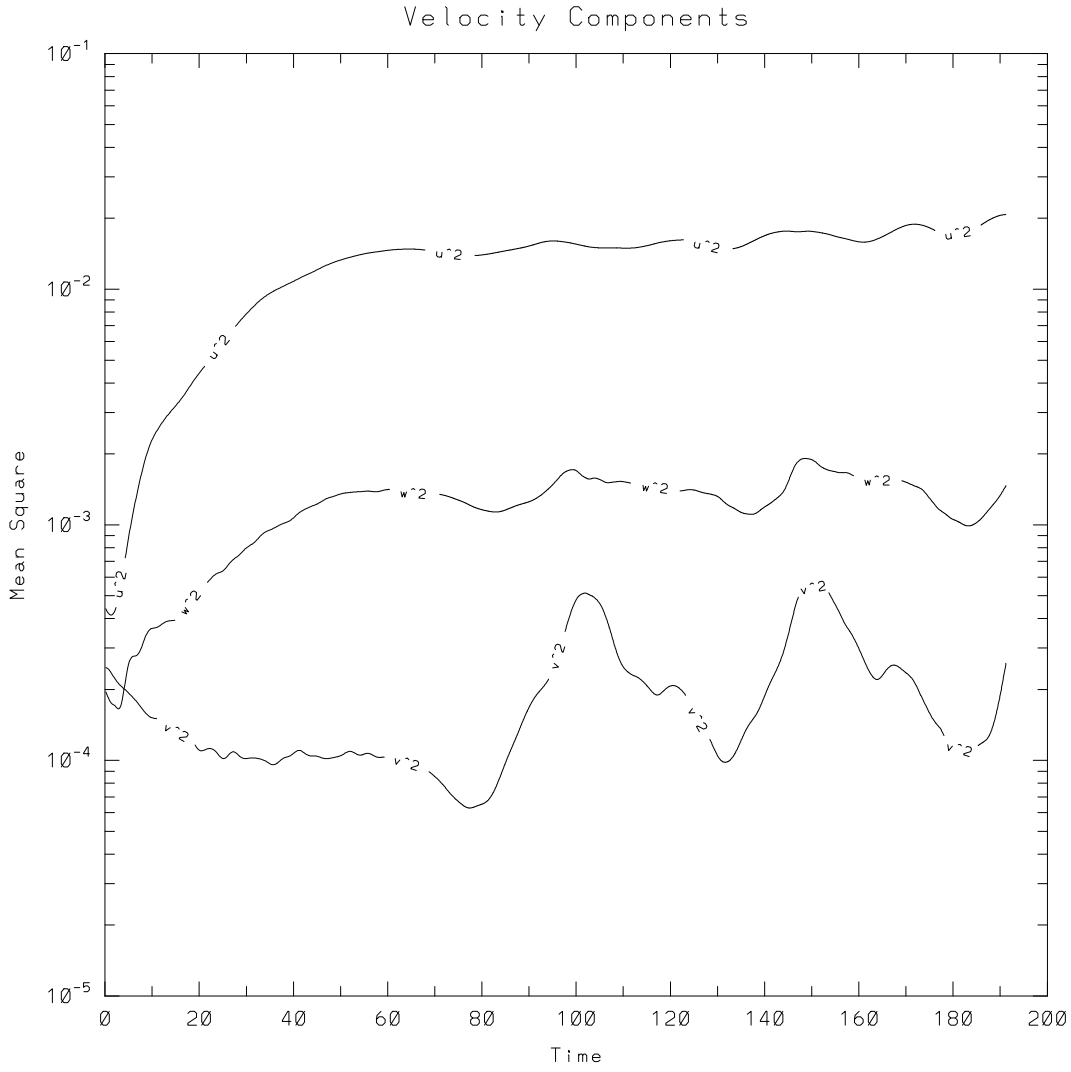

Figure 4.16: Volume integrals per unit mass of the individual components of the kinetic energy, u^2, v^2, and w^2.

the boundary region.

Figures 4.13 - 4.16 indicate in various ways that wave breakdown for this case is highly three-dimensional. In the sections to follow, other important aspects of the turbulence will be presented, including instabilities, intermittency, vorticity dynamics, and dissipation rates.

4.4.3 Intermittency

Analysis indicates that the flow is quasi-periodic, going through a cycle of strong mixing and small-scale dissipation, followed by a quieter period of relaminarization and weaker dissipation. As indicated above in reference to Figures 4.10 - 4.12, the flow at time $t = 133$ is similar in character to the flow at about $t = 81$; also, the flows at $t = 144$ and $t = 94$ are similar, suggesting that the flow is undergoing another mixing cycle. Additional simulations, with shorter wave periods, have been run out for 10-20 wave cycles, strengthening the conclusion that the flows are quasi-steady. It should be noted, however, that the flow is not completely quasi-steady, in that a mean flow may be created and the background density stratification is gradually weakened throughout the process.

Figure 4.17 shows the volume integrals of the kinetic energy dissipation rate, and the potential energy dissipation rate (Equations 3.119 and 3.120), and the total dissipation rate (sum of kinetic and potential) as a function of time for Case 15. The dissipation rates are small at first and grow steadily until the first mixing cycle gets under way; a maximum is reached at around $t = 98$. A second peak in dissipation occurs at approximately $t = 147$. The period for this to occur is 49, approximately 25% longer than the wave period for this flow of 39.2.

Other simulations conducted for approximately five mixing cycles also have wave and mixing periods with approximately the same duration. The mixing periods for critical angle simulations are 10 to 30% longer than the wave periods, but never shorter. Nonlinearities in the flow may account for some of the variations between the duration of each cycle.

While evidence exists that the forcing of the mixing cycle is related to the wave

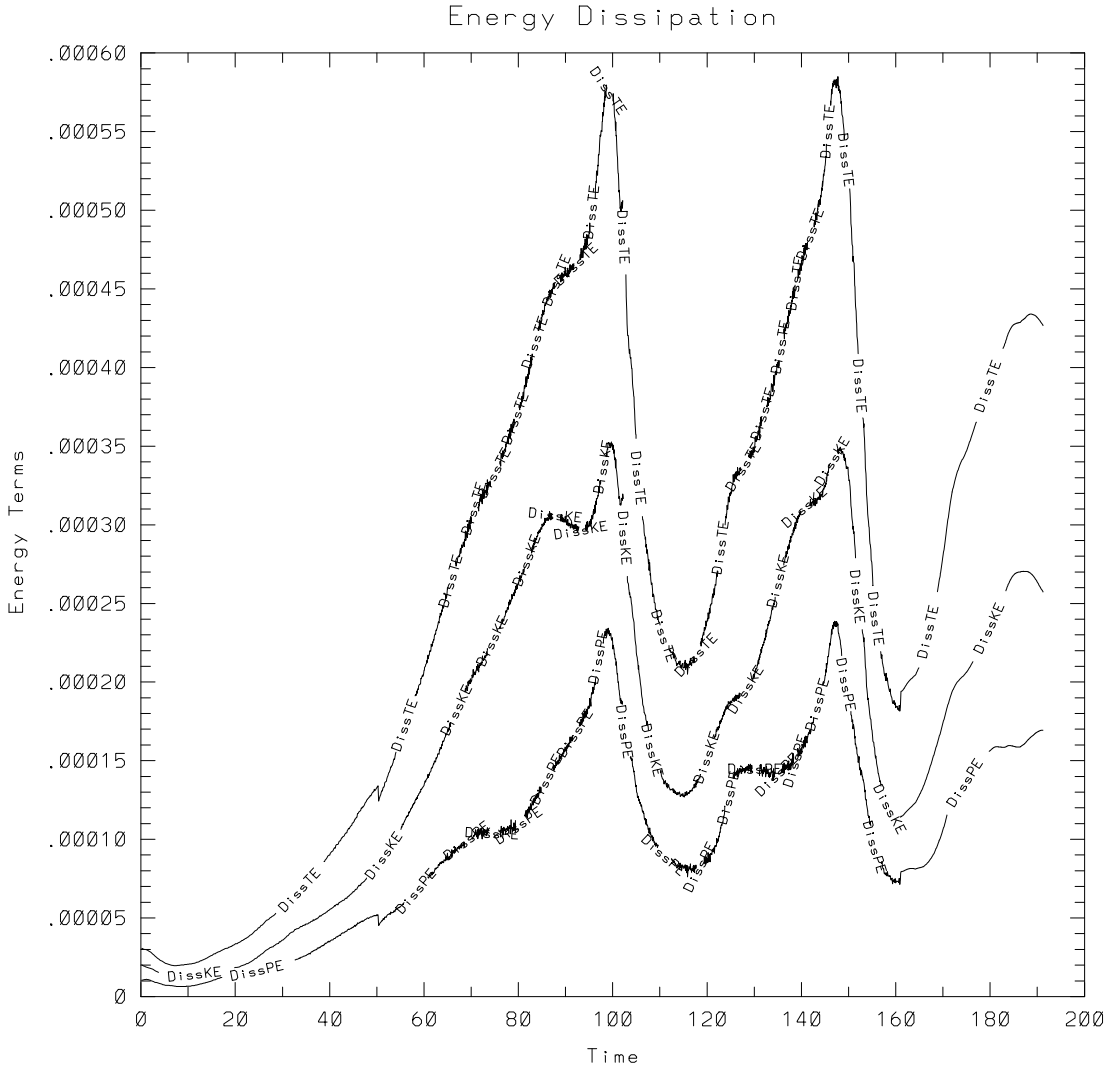

Figure 4.17: Volume integrated dissipation rates of kinetic, potential, and total energy throughout two mixing cycles for the 9.2^o slope critical angle reflection case.

period (Section 6.1), it is not unexpected that the turbulence in the system responds somewhat differently for each cycle. The dissipation rate falls off rapidly after achieving its peak; from peak to trough takes approximately two buoyancy periods (from $t = 100$ to $t = 115$). This is consistent with other observations of the collapse time for episodic events of stratified turbulence (e.g., Hopfinger, 1987; Stillinger et al., 1983). During the period of weakest dissipation, the flow restratifies and relaminarizes, i.e., the three-dimensionality of the flow decreases rapidly. The buildup to the second dissipation maximum takes longer (from $t = 115$ to $t = 145$) than the rate at which the turbulence collapses. During the buildup phase, the wave instabilities (static and dynamic) grow and develop before energy is strongly dissipated through turbulence.

Two small irregularities visible on the graph should be mentioned briefly. The first is that the dissipation rates plotted in Figure 4.17 are the sum of the two types of dissipation in the model, the resolved part and the energy removed by the filter. The resolved part makes up about 80-90% of the total and is a smooth curve. The removal of energy by the filter appears somewhat noisy, making the full curve somewhat jagged. This is due to roundoff errors experienced in single precision (32-bit) mode for the calculations. The calculation to determine the energy removed by the filter involves integrating the total energy immediately before and after the filtering process, and then dividing the difference by the time step. It is a classic case of generating observable roundoff errors by taking the difference of two large numbers which are nearly equal (to 4-5 significant figures) and dividing by a small number. The noise was removed later in the calculation ($t > 160$) by doing the procedure in double precision (64-bit mode). Other calculations, conducted on the Cray-YMP, did not experience this noise, because those calculations are carried out in 64-bit mode. The second point is that at $t = 50$, the flow was changed from a 64 x 33 x 130 grid to a 129 x 33 x 130 grid, which explains the small decrease in dissipation at that time. At this time, the amount of energy removed by the filter decreased on the more refined grid, while the resolved dissipation remained fairly constant.

Figure 4.18 is similar to Figure 4.17, but is taken from Case 21, which was extended for 5-6 mixing cycles. The figure shows dissipation rates from a critical angle case

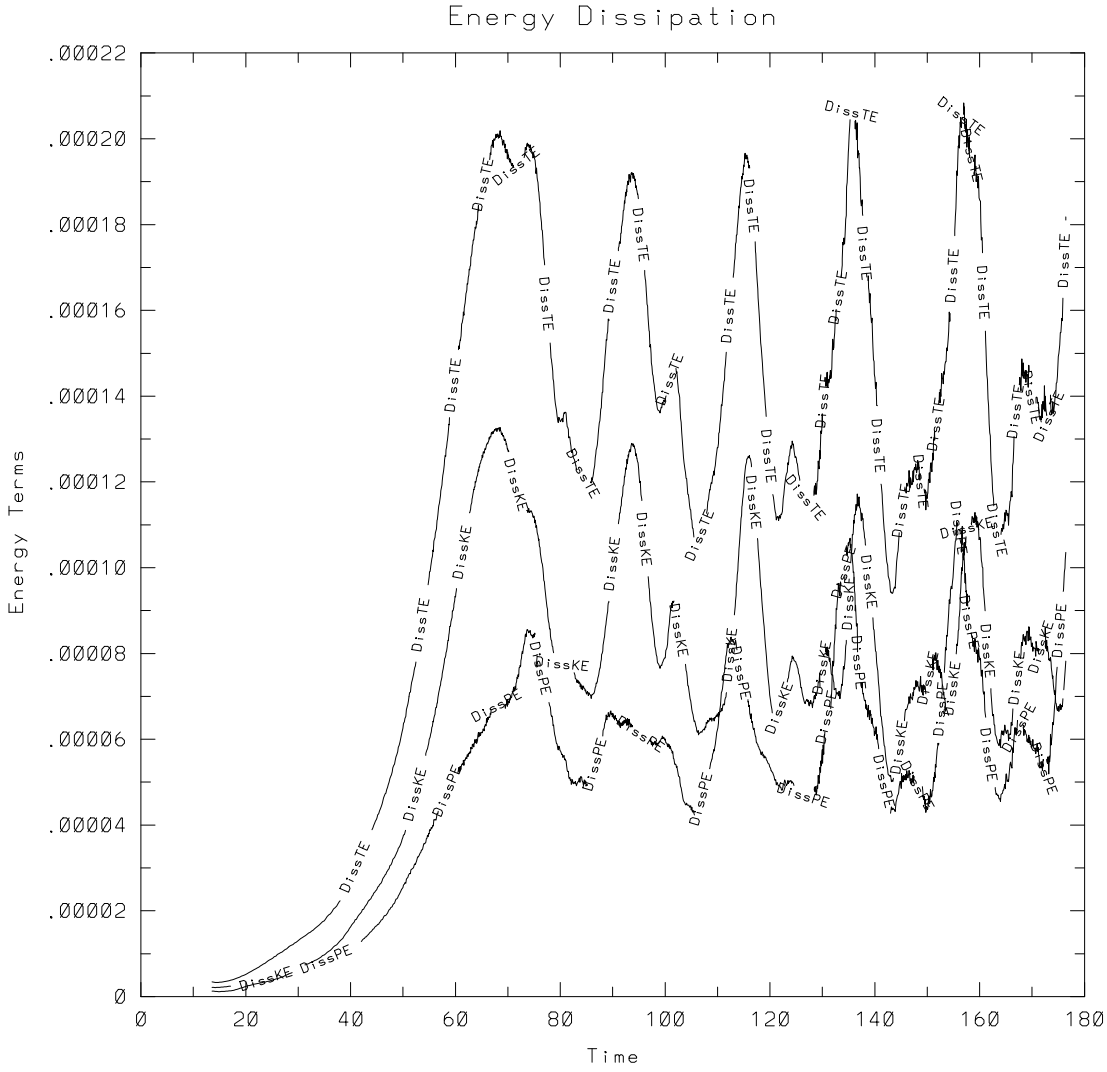

Figure 4.18: Volume integrated dissipation rates of kinetic, potential, and total energy through six mixing cycles for a critical angle reflection case with bottom slope of 20^o.

with a bottom slope of 20^o and wave period of 18.4. The first 5 peaks in dissipation rates appear approximately at times 70, 92, 115, 135, and 155, or approximately 20 to 22 time units apart. As for Case 15, the interval between mixing cycles is close to (but somewhat longer than) the wave period.

A possible contributing factor to the mixing period being longer than the wave period is that, through each mixing cycle, the background density gradient in the boundary layer region is weakened, which modifies the local buoyancy frequency N. When an internal wave reaches a change in propagation medium the wave frequency is preserved and the angle of wave propagation adjust. Thus, as N decreases $\cos\theta$ increases and θ decreases, and the angle of wave propagation becomes closer to horizontal (a subcritical situation). Additional experiments have shown that oncoming waves with frequencies close to (but not equal to) the critical frequency still break down into turbulence in nearly the same fashion as the critical angle cases. An issue to be presented in more detail below (Section 6.6) is that the mixing period of oncoming waves adjusts away from the wave period when the wave frequency differs from the critical frequency. The primary result is that subcritical waves have elongated mixing cycles and supercritical waves have shorter mixing cycles than the critical situation. This result is consistent with the argument presented here that, as the density gradient weakens, the mixing period could lengthen. This effect may be fairly small, however, because changes to the background density profile occur on a fairly long time scale compared to the wave period.

A more likely mechanism suggested by the observations is that, even if the forcing of the system is regular (e.g., at the period of the oncoming wave), the system may respond sluggishly, as nonlinearities take time to develop and unstable modes grow at finite rates. An important factor in this hypothesis is that the flow may need to restratify before it can support the next cycle of wave breakdown. The full wave breakdown cycle may be divided into six distinctive phases: (1) initial buildup of density gradients, (2) wave amplification and overturning, (3) growth of instabilities and onset of turbulence, (4) strong mixing, (5) decay of turbulence, and (6) restratification. The time scales of wave amplification and boundary layer density gradients

can be tied to the periodicity of the oncoming wave, but other time scales (such as the growth rate of the instabilities, the decay time of the turbulence, and the time to restratify the boundary layer) may depend on other factors. For example, if the time for growth of the turbulence is too long, the flow could remain laminar. On the other hand, if the turbulence lasts too long, the fluid may become so well mixed near the boundary that it may not support oncoming internal gravity waves. As the turbulence decays, buoyancy forces act to restratify the boundary layer. Not until the boundary layer is reorganized can the next cycle of wave overturning and breakdown proceed. If wave amplification associated with critical angle reflection must wait for favorable conditions to reappear in the boundary layer, it is not surprising that the wave period and mixing period differ.

If this observation (that the mixing and wave periods differ) is valid, then the previous observation (Section 4.4.1) that the wave breakdown has a preferential phase associated with the strong downslope boundary layer current would be inconclusive. If the process is limited by the completion of each of the six stages, then over a number of mixing cycles, the turbulent dissipation phase could occur at any phase of the waves. To determine which explanation is most accurate for this flow, and to examine wave/mixing phase correlations, would require extending a simulation for a shallow slope case (such as Case 15) for 10 to 20 mixing cycles. Unfortunately, such a long integration in time is presently too expensive computationally. Other questions of equal interest (see Chapter 7) are less computationally intensive to investigate and have higher priority for future study.

4.5 Instabilities

4.5.1 Static

Two types of flow instabilities, static and dynamic, are expected to contribute to turbulent wave breakdown. Static instabilities are addressed in this section; dynamic instabilities in the next section.

Static instabilities are driven by the instantaneous density field, when heavier

fluid is located above lighter fluid. Thereby, for a motionless flow, gravitational forces would act to change the density structure to a stable configuration, causing irreversible mixing in the process. Immediately prior to the growth of strong three-dimensionality there are widespread overturns in the density field. These statically unstable regions occur across the breadth of the boundary layer and appear to be caused by a strong upslope flow at a distance of approximately $\lambda_z/4$ from the wall that is induced by the amplified wave when it reaches the proximity of the bottom boundary. A significant contribution of overturned fluid also appears to arise from the convergence zone near the boundary at the location of the thermal front that causes flow away from the wall. The upwelled fluid may then spread horizontally as it approaches regions of lighter surrounding fluid.

Figure 4.19 shows the density field in the boundary layer region at $t = 88$ (top), 91, 94, and 102 (bottom). The two-dimensional cross sections of the flow are taken in the same vertical plane as in Figure 4.10. Overlaid on top of the isopycnals are shaded regions, indicating the regions in which the flow is statically unstable. The unstable regions stretch across the breadth of the domain and are centered at a height of approximately $\lambda_z/4$ away from the wall. They appear predominantly in this structure from about $t = 90$ to $t = 100$, for a time of approximately 1/4 of a wave period. Note that the turbulence and wave overturning occur above the thermal front, and in regions of steep density gradient near the wall (viscous sublayer) that experience strong shear and viscous dissipation caused by the proximity of the no-slip boundary.

Statistical analysis of the overturned regions of fluid indicates that the static instabilities all occur below a height of $\lambda/3$ from the wall, and are present somewhere in the boundary layer region about 50 percent of the time. This result is typical of critical angle cases for many different slopes when Reynolds numbers are sufficiently high for transition to turbulence.

In Figure 4.20 are presented results of a time integration of the frequency of statically unstable regions as a function of distance from the bottom slope. Here an array of points on a line perpendicular to the boundary is examined for local

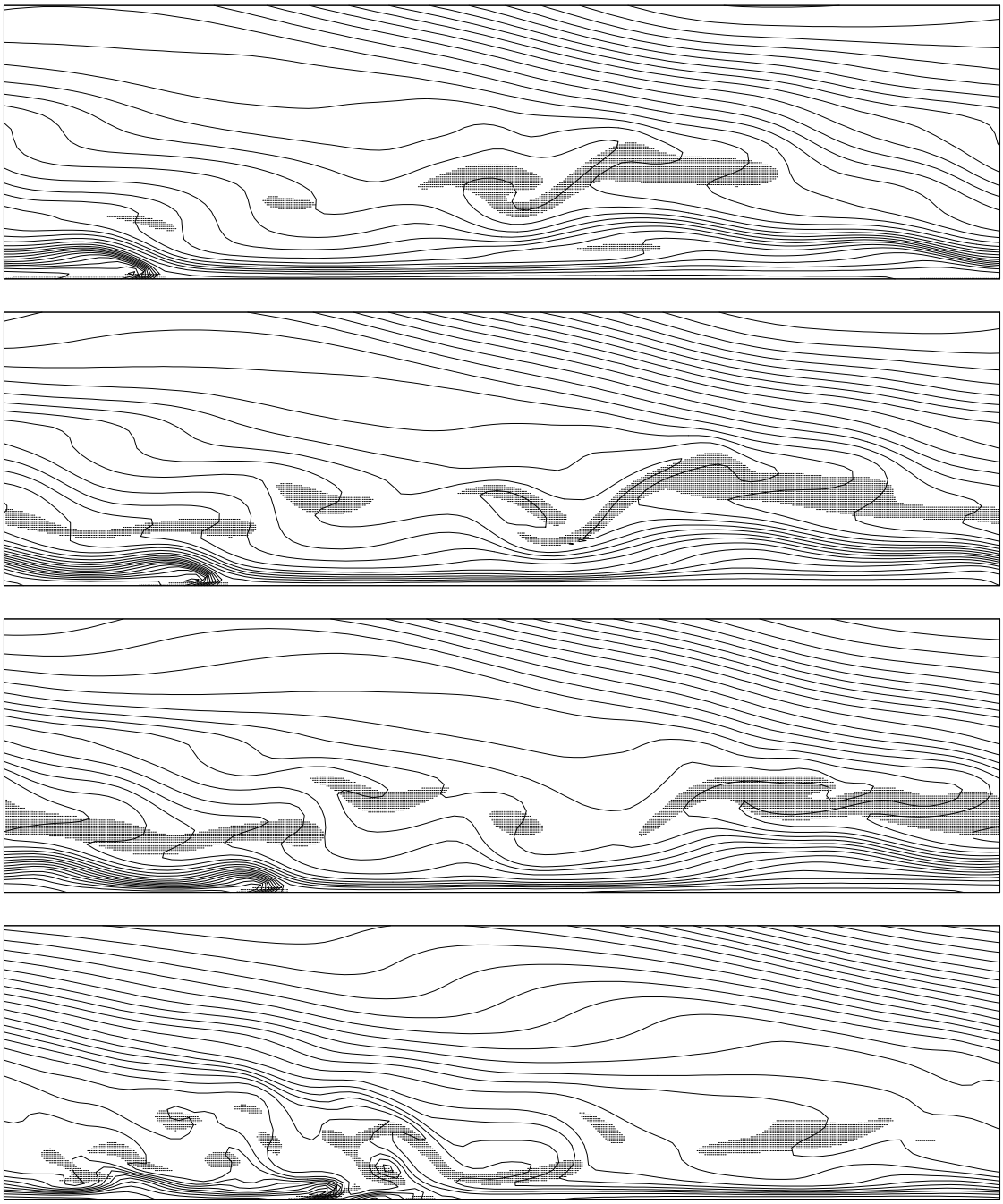

Figure 4.19: Density fields with statically unstable overturned regions at at $t = 88$ (top), 91, 94, and 102 (bottom) shown shaded .

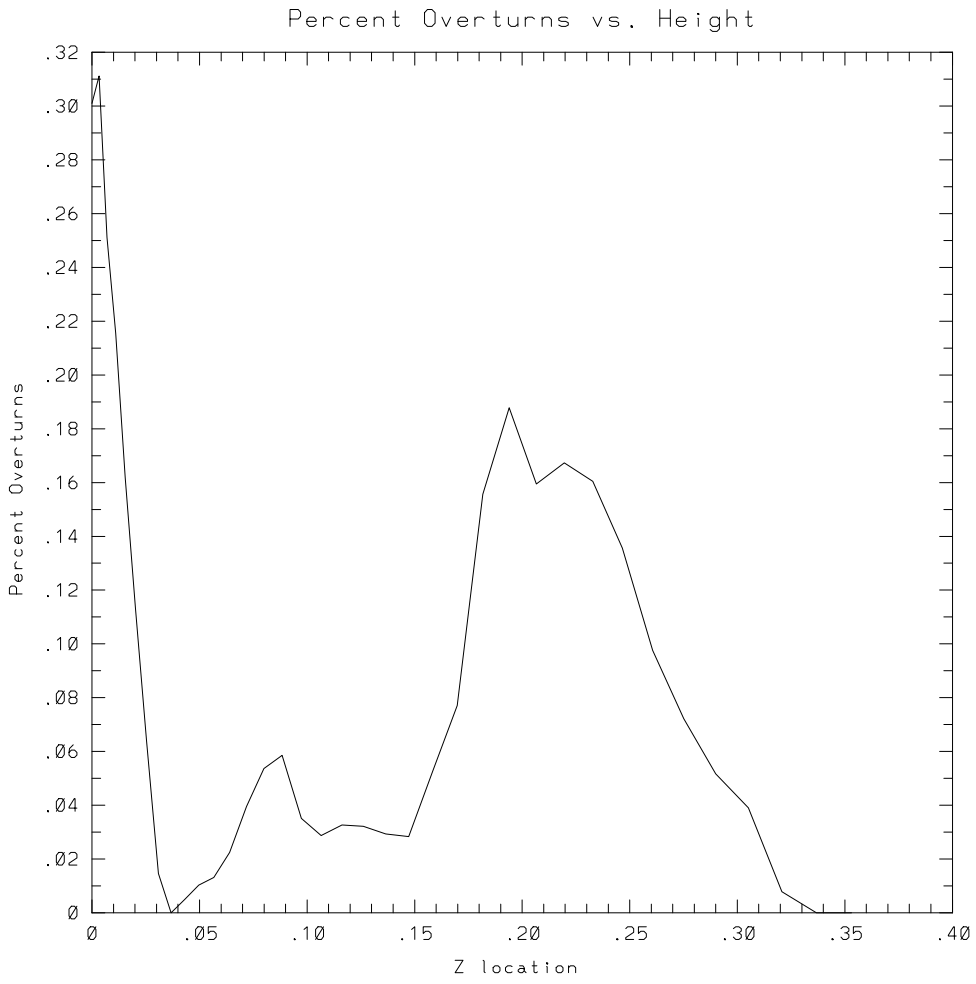

Figure 4.20: Time averaged statistics taken along a vertically oriented line indicating the frequency and height of static instabilities.

overturns throughout two wave periods. The results show the percentage of time in which a static instability was observed at each height. The horizontal axis of Figure 4.20 represents the height z', and as in other figures is normalized by the vertical wavelength. Notice that there are two prominent peaks in the figure, which will be examined immediately below.

The dominant peak in Figure 4.20 is located very near the wall. It is indicative of a very thin viscous sublayer in which the density stability structure is sensitive to small scale perturbations. This is related to the thickness of the boundary layer (e.g., as shown in Phillips' solution) which is driven by the buoyancy imbalance due to the no-flux boundary condition for the density field. Whereas the steady Phillips' profile has isopycnals perpendicular to the slope at the boundary so that small fluctuations about the steady profile may appear as local instabilities. In addition, throughout the wave period the near-wall region experiences both upslope and downslope flows. When the flow is upslope, heavier fluid from downslope can be carried far enough upslope to be statically unstable. This does not necessarily lead to turbulence, however, because motions are inhibited by viscosity (with the presence of the wall with its no-slip, no-penetration boundary condition). Rather, laminar near-wall currents can be established, such as the backwash observed along the slope. This layer of frequent static instabilities near the wall is restricted to a region of thickness 0.04 and occurs approximately 20 to 30% of the time.

The second major peak in Figure 4.20 is farther from the wall, centered at a height of approximately 0.20. This peak reflects static instabilities related to turbulent wave breakdown. These instabilities have a maximum frequency of occurrence of approximately 20% of the time. These results are consistent with the approximate duration of the aspect of the mixing cycle consisting of initial wave overturning, prior to the period of strongest turbulence.

4.5.2 Dynamic

Dynamic and static instabilities are intrinsically related in a stratified flow. When dynamic instabilities develop, leading to turbulence, they invariably develop regions of

overturned fluid. Conversely, when (linear) wave amplification processes cause overturned regions, static instabilities break down dynamically into a variety of unstable modes (Lombard, 1994). Hence, it is difficult to separate the influence of dynamic and static instabilities. The value of the local Richardson number is a commonly used criterion to identify stratified regions that may be dominated by dynamic instabilities. The local Richardson number can be used to distinguish flow regimes that may experience either shear or convective instabilities.

Shear instability is usually cited (e.g., Eriksen, 1978; Garrett and Munk, 1979) as the most likely means by which oceanic internal waves break down and generate fine scale mixing. Garrett and Munk suggest that random superposition of different internal wave modes occasionally leads to regions with local Richardson number below 0.25, the value necessary for Kelvin-Helmholtz billows to develop in a steady parallel shear flow. In addition, other instabilities have been studied, such as Holmboe instabilities (Holmboe, 1962), which can occur at higher Richardson numbers than required for Kelvin-Helmholtz billows. Field measurements by Eriksen show that Richardson numbers in the range of 0.25 to 1.0 are frequently present in the ocean.

Considerable attention in the literature has been focused on the critical Richardson number of 0.25, a value derived from the analysis of stratified, steady, parallel shear flows. Differences exist, however, between instabilities in internal waves and in a shear layer oriented perpendicular to gravity. These differences make the critical value of 0.25 probably inappropriate when applied to flows produced by internal waves. Orlanski (1972) and Delisi and Orlanski (1975) show that internal waves are unstable for Richardson numbers less than about 2. Significantly, Drazin (1977) and Meid (1976) show that even very small amplitude internal gravity waves (with corresponding large Richardson number) are unstable to small disturbances (through resonant triad interactions). Lombard and Riley (1995) extend this analysis to finite amplitude gravity waves and show that the primary instabilities are three-dimensional and grow rapidly. For example, they show that a gravity wave with minimum local Richardson number of 7.2 (corresponding to initial wave amplitude one half that of an overturning wave) and with Reynolds number 300 becomes unstable and breaks

down into turbulence within about 4 wave periods.

The local Richardson number, $Ri_L = N_L^2/(\frac{\partial u}{\partial z})^2$, is the ratio of the square of two important frequencies: the local buoyancy frequency, $N_L = \sqrt{\frac{-g}{\rho_o}\frac{\partial \rho}{\partial z}}$, and the vertical shear $\left(\frac{\partial u}{\partial z}\right)$. If the nondimensionalization of Section 2.2 is used, the local Richardson number can be related to the global Richardson number, Ri, by

$$\frac{Ri_L}{Ri} = -\frac{\partial \rho}{\partial z}/(\frac{\partial u}{\partial z})^2 \ . \tag{4.12}$$

Note that for calculating Ri_L, the z-derivatives refer to the direction parallel to gravity. As suggested in the previous paragraph, there are no clearly established criteria for defining a critical Richardson number appropriate for internal waves. Nonetheless, because Ri_L relates two significant time scales, then for values of $Ri_L < 1$, the buoyancy time scale (stabilizing effect) is smaller than the shear time scale (destabilizing effect). Consequently, to identify dynamically unstable regions, it appears appropriate to examine regions where local Richardson numbers are below 1.

Alternate definitions for a local Richardson number may be appropriate. For example, the shear in the direction of the wavenumber vector could be used instead of the vertical shear because it is more significant (and larger) in an internal wave. Another choice might be to include the influence of $\frac{\partial v}{\partial z}$. But because the analysis herein is used to develop only qualitative and semi-quantitative pictures of the relative importance of shear and convective instabilities, use of Equation 4.12 will be adequate.

Figure 4.21 shows the velocity field in the same plane as shown in Figure 4.19 and indicates that strong shears exist in the boundary region. The two-dimensional cross section and two-dimensional velocity projections shown in Figure 4.21 are taken from the three-dimensional critical angle simulation. Additional analysis (i.e., simultaneous plots of Ri_L, $\left(\frac{\partial u}{\partial z}\right)^2$, and $\left(\frac{\partial \rho}{\partial z}\right)^2$) suggests that, during wave breakdown, regions with high shear values are more strongly correlated with regions of low Ri_L (less than 1) than are regions with low values of density gradient.

Figure 4.22 illustrates contours of the shear squared, $\left(\frac{\partial u}{\partial z}\right)^2$, the quantity that makes up the denominator of the local Richardson number. Contour levels for integers

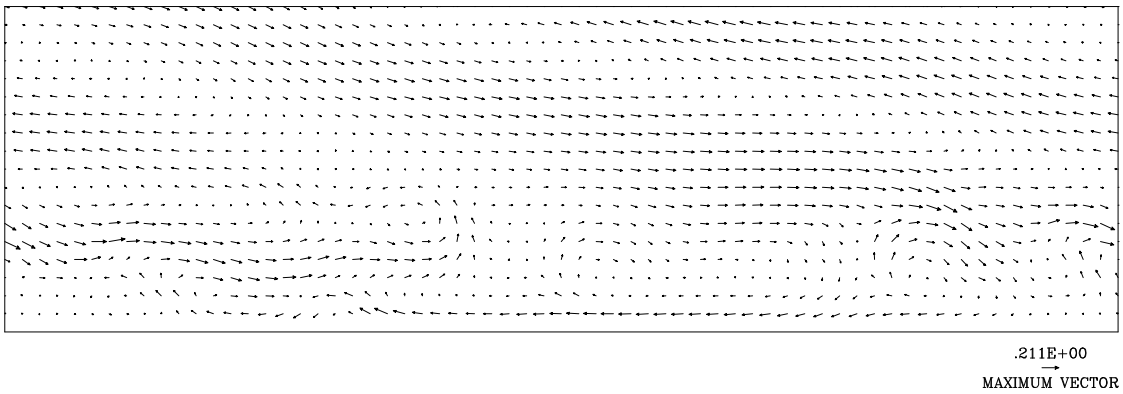

Figure 4.21: Velocity components in the center vertical x'-z' plane at t=96. Eddies in the boundary layer indicate diapycnal mixing.

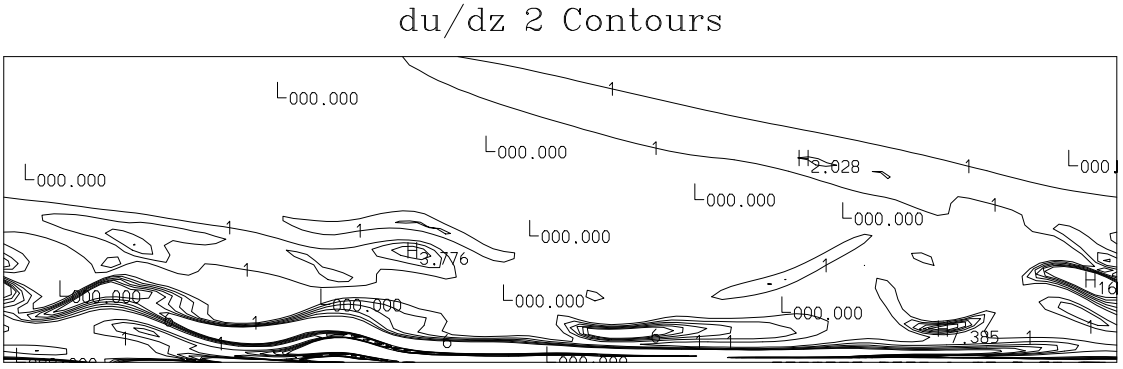

Figure 4.22: Contour values of 1, 2, 3, 4, 5, and 6 for the vertical shear component $\left(\frac{\partial u}{\partial z}\right)^2$ at t=96.

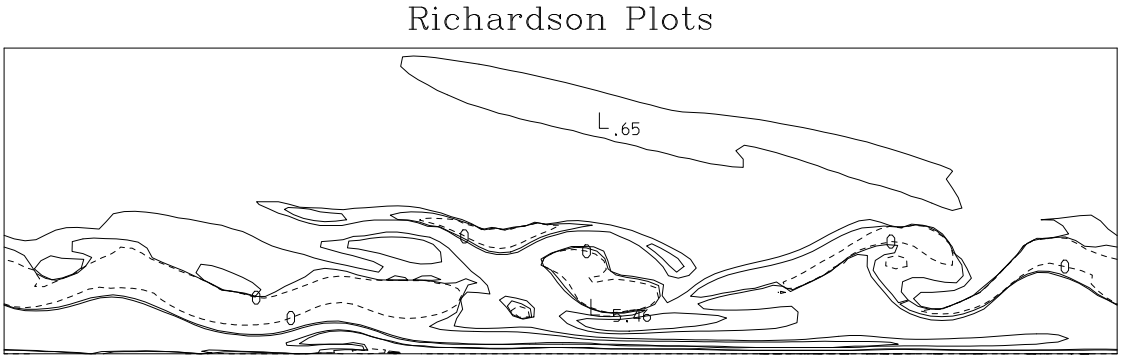

Figure 4.23: Contours of the local Richardson number at t=96, as the wave instabilities develop, indicating regions of the flow that may be dynamically unstable. Contours of $Ri_L = 0$ (dashed), 0.5 (solid), and 1 (outer solid lines), are shown.

1 through 6 indicate regions with high shear. In this and the two following figures, L indicates values of local lows, and H indicates values of local highs.

Figure 4.22 might usefully be compared visually with Figure 4.23, which shows contours of the local Richardson number in the same plane as in Figures 4.21 and 4.22 at $t = 96$. Local Richardson number contours of 0, 0.5, and 1.0 are shown in Figure 4.23. Negative values of Ri_L (encircled by contour values of zero) correspond to the statically unstable regions. As can be seen from these figures, significantly larger proportions of the boundary layer region have $Ri_L < 1$ than are statically unstable ($Ri_L < 0$). Details of these proportions are given below. Figure 4.23 suggests a strong correlation between dynamic and static instabilities as measured by the Richardson number criteria. For the most part, the statically unstable regions are surrounded by regions with small positive values of local Richardson numbers.

The three-dimensionality of regions of dynamic instability is indicated by contours of Ri_L in a plane parallel to the wall within the turbulent boundary layer. Figure 4.24 is taken at a height $z = 0.275$ (the 32nd grid point) from the wall at $t = 96$. Here the horizontal axis is the x'-axis and the vertical axis is the y-axis. Contours of Ri_L with values of 0.0 (short dashes), 0.5 (long and short dashes), and 1.0 (solid curves) are drawn. Labels for some of the local high and low values (automatically selected by graphics package) are included in the figure. The total range of Ri_L on

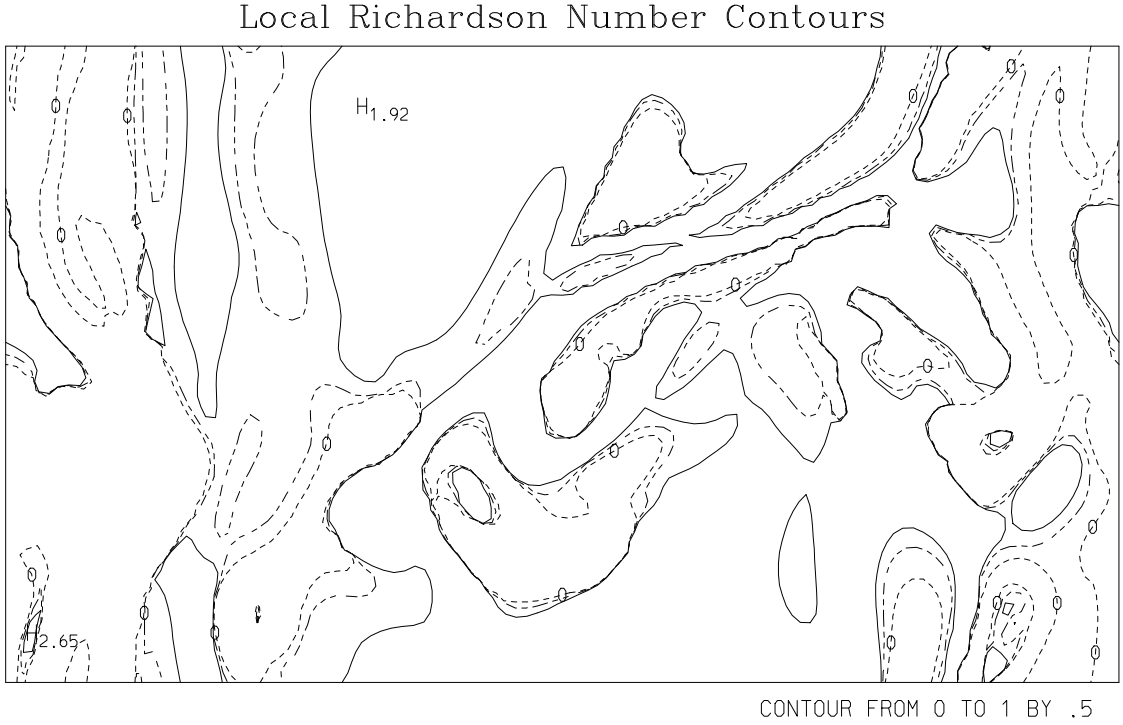

Figure 4.24: Contours of the local Richardson number in a plane parallel to the wall located in the turbulent boundary layer. The figure indicates some of the three-dimensional structure of the flow during this period and represents the plane at $z = 0.275$ for $t = 96$. The contours are for $Ri_L = 0$ (short dash), 0.5 (long and short dashes), and 1 (solid lines).

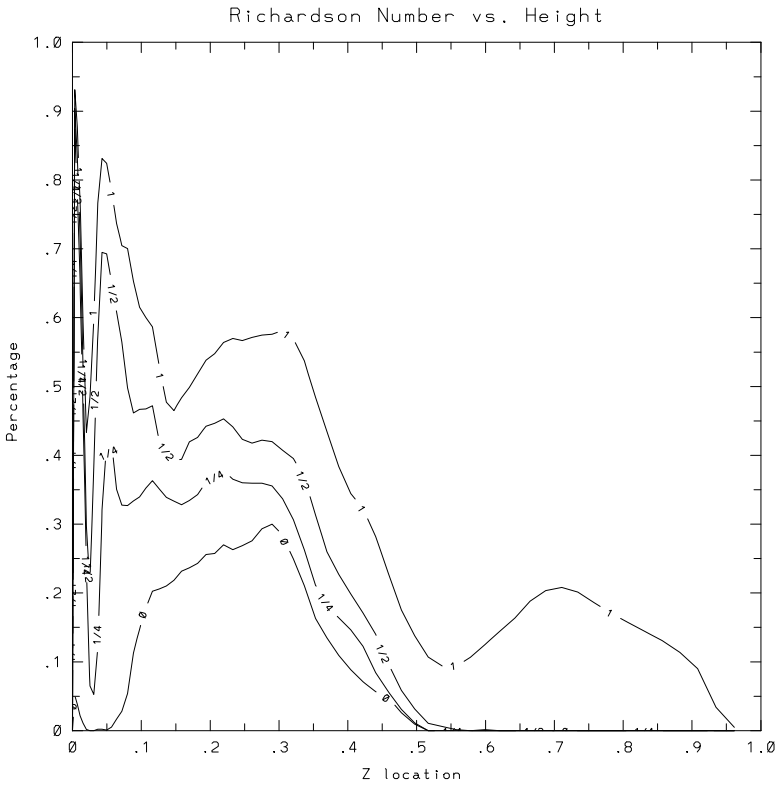

Figure 4.25: Percentage of volume with local Richardson numbers less than 0, 1/4, 1/2, and 1 as a function of height from the bottom wall at $t = 96$.

this plane is between -4.8 and 10.0 (values over 10.0 were set to 10.0 for plotting purposes). Figure 4.23 corresponds to the center vertical plane of Figure 4.24. Figure 4.24 shows that many of the overturned and dynamically unstable regions are small scale and would be missed by two-dimensional simulations.

The distribution of regions of low Richardson number may by quantified for this flow as a function of space and time. Figure 4.25 indicates the average spatial distribution in the offwall direction of regions where the Richardson number is below 0.0, 0.25, 0.5, and 1.0 for the flow at $t = 96$. In this figure the abscissa indicates the distance from the wall and the ordinate indicates the percentage area at that height with Ri_L below the specified value. For example, at a height of $0.3(\lambda_z)$ from

the wall, approximately 30% of the flow has a negative Richardson number, 35% has $Ri_L < 1/4$, 40% has $Ri_L < 1/2$, and 55% has $Ri_L < 1$.

The region near the wall with $z' < 0.04$ has very high percentages of low Richardson number. As for static instabilities, there are two important causes (which are different from the causes in the regions of turbulent wave breakdown farther from the wall). Near the wall, the no-slip wall boundary condition causes very high shear. In addition, the no-flux boundary condition ensures that isopycnals are perpendicular to the bottom slope in this region. Together these factors produce a thin region with very low Ri_L. This region is evident even without turbulent wave breakdown and therefore may be considered separately.

The dominant regions of low Ri_L associated with wave breakdown are located from $0.1 < z' < 0.45$. The regions from $0.5 < z' < 1.0$ in which $Ri_L < 1$ appear to be the farthest distance from the boundary at which Ri_L of the oncoming wave train is significantly amplified by the boundary and its turbulent zone. Volume integrals of Ri_L (covering $z' < \lambda_z$ at $t = 96$) show that approximately 8% of the volume has $Ri_L < 0$, 13% has $Ri_L < 1/4$, 18% has $Ri_L < 1/2$, and 32% has $Ri_L < 1$.

Figure 4.26 presents volume integrals (integrated over the bottom vertical wavelength) of regions with low Richardson numbers as a function of time. As the flow develops, the familiar periodic behavior of strong mixing and dissipation, followed by a more stable situation, is evident. There is also suggestion over the first two mixing cycles that there are peaks in the volume percentage of the Richardson numbers of 1, 0.5, and 0.25, somewhat before the peaks in volume percentage of the Richardson numbers less than 0.0 (associated with static instabilities). For example, there appear to be local maxima of $Ri_L < 1$ and $1/4$ at $t = 140$ followed by a peak in $Ri_L < 0$ at $t = 150$.

The analysis of local Richardson numbers associated with the flow during periods of wave breakdown suggests that the wave field becomes dynamically unstable before significant regions of static instabilities develop. This is indicated by the increased values of Ri_L in the region $0.5 < z < 1.0$ as the wave approaches the boundary before static instabilities are observed. While this conclusion may be too simplified

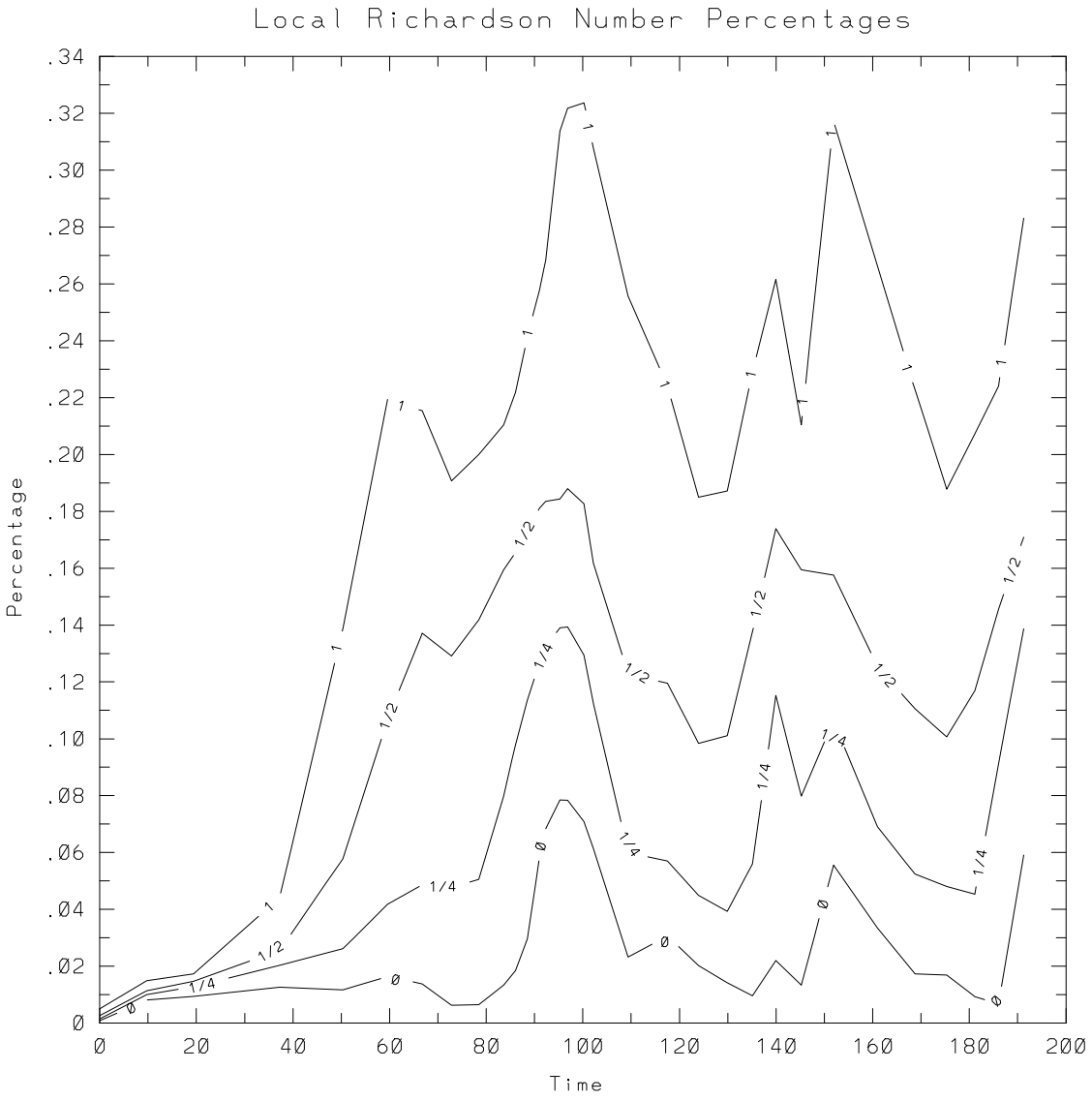

Figure 4.26: Percentage of volume of bottom vertical wavelength with local Richardson numbers less than 0, 1/4, 1/2, and 1 as a function of time.

to include the full complexities of the instability process, larger regions with low Ri_L clearly develop before overturning occurs and frequently develop all the way to overturning. There is a complicated interaction between shear and convective instabilities. Dynamic (shear) instabilities occur most frequently during the turbulent wave breakdown process and can lead to statically unstable situations. As these develop, the static instabilities contribute to local regions of strong convection as local sources of available potential energy are released and heavier fluid is restored to its stable location in a stable density profile.

4.6 Energetics

While the flow exhibits characteristics of periodicity, certain aspects also appear to achieve quasi-steady-state behavior. Figure 4.27 shows that the volume integrals of kinetic, potential, and total energies over the whole computational domain (excluding the sponge layer region) begin to level off after the flow starts up from rest. Potential energy is defined as $Ri\,\rho'^2/2$ (e.g., Equation 3.112), where ρ' is the variation from a linear background profile (Winters, 1989). Advantages of this definition include that it is simpler to implement and is theoretically justifiable for constant N and that the oncoming gravity waves have equipartition of energy (i.e., equal kinetic and potential energy). The expression for the buoyancy flux, $Ri\,\rho' w$ (with opposite sign), appears in the kinetic and potential energy equations, representing the exchange between potential and kinetic energy due to buoyancy. Also shown in Figure 4.27 is the time integrated buoyancy flux; its negative value indicates a net transfer of potential to kinetic energy during mixing. After about $t = 60$ the energy input from the wave forcing mechanism nearly equals the dissipation of energy when averaged over a wave period.

Two types of situations have been observed in the simulations. In the first, the total energy in the system levels off after a few wave cycles, and the system reaches quasi-equilibrium as the energy oscillates about a mean value. A second observed situation is that wave breakdown establishes a mean flow and/or alters the background density profile in the boundary layer. The alteration of the background density profile

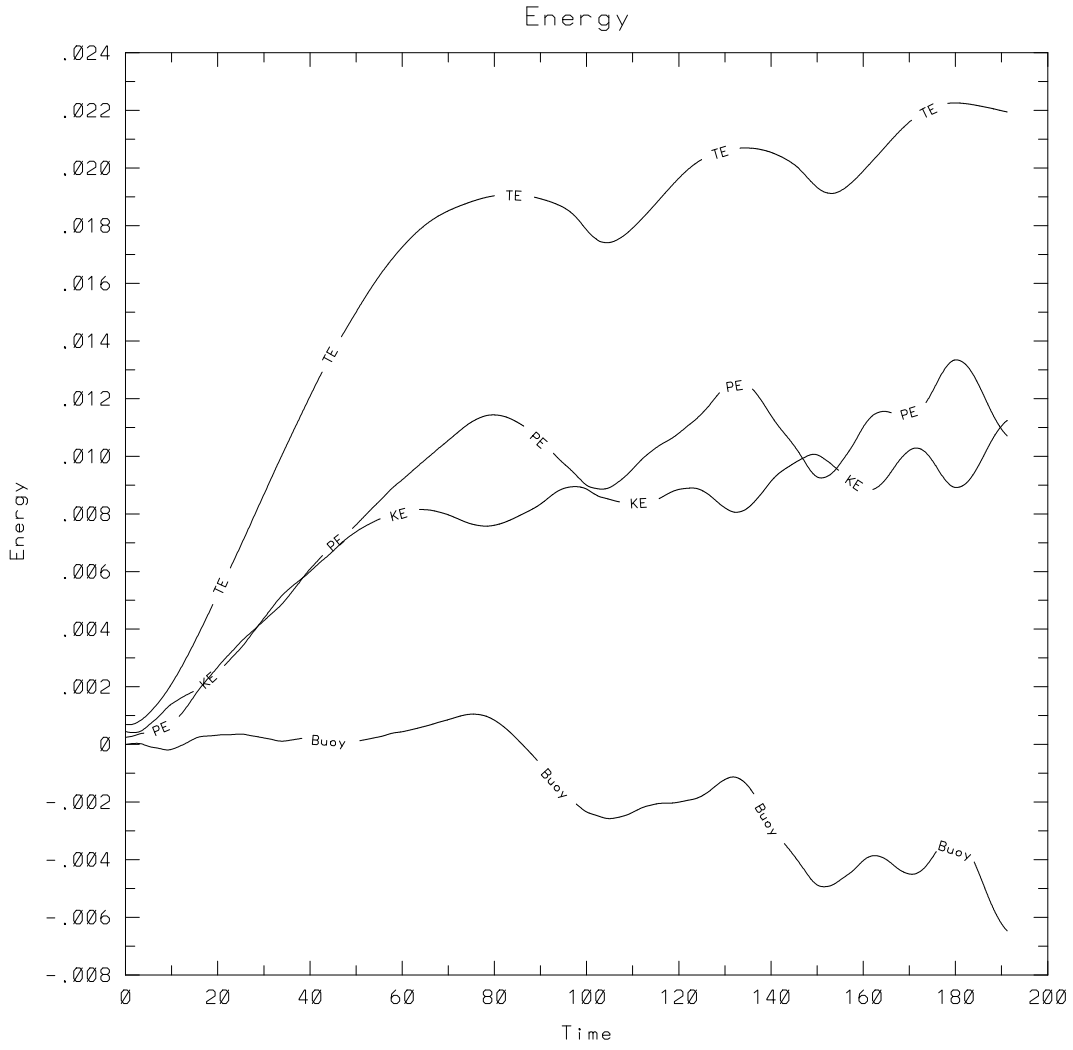

Figure 4.27: Volume integrals of kinetic, potential, and total energy and the time integrated buoyancy flux for the 9.2^o critical angle case, shown over three mixing periods.

appears in the energy integral as an accumulation of potential energy, because any deviation from a linear profile is considered potential energy by definition (even if it is unavailable to do work). An adjustment to the mean flow in the boundary layer will appear as an accumulation of kinetic energy. Either of these flow modifications can lead to a steady increase in the total energy in the system.

Figure 4.27 shows for the present case that the flow has greater potential energy than kinetic energy during each mixing phase. This is consistent with Figure 4.17 which showed a higher dissipation rate of kinetic energy than of potential energy. A significant cause of this difference is the different boundary conditions on each field at the wall. The no-slip boundary condition creates a strong sink of kinetic energy which is not duplicated by the no-flux (adiabatic) boundary condition on the density field. As the kinetic energy is annihilated by turbulence and wall interaction, buoyancy effects transfer excess potential energy to kinetic energy. The buoyancy flux will be considered in more detail below in the context of examining terms in the energy equations.

It is convenient at this point to illustrate the two dominant behaviors of the energy in the system. Figures 4.28 and 4.29 are taken from critical angle simulations for 30^o and 20^o (Cases 28 and 23) which will be discussed in more detail in Chapter 5. All three cases are taken from simulations in which the wave broke down into turbulence in the boundary layer. Figure 4.28 shows the energy integrals for the 30^o slope case (which has a wave period of 12.6) calculated for about 15 mixing cycles after a quasi-steady state has been achieved. In this case, the energy levels in the system achieve quasi-steady values after the startup period ($t < 30$) as the wave train approaches the wall. Again the net buoyancy flux is from potential to kinetic energy, but the magnitude of the oscillations between potential and kinetic energy are relatively small.

Figure 4.29 illustrates the second dominant behavior, for the case with a 20^o bottom slope (wave period of 18.4). This simulation is for 5-6 mixing periods and shows a steady accumulation of energy. Here, the energy accumulates both as a mean flow and an adjustment to the background density profile. Later, wave and mean flow

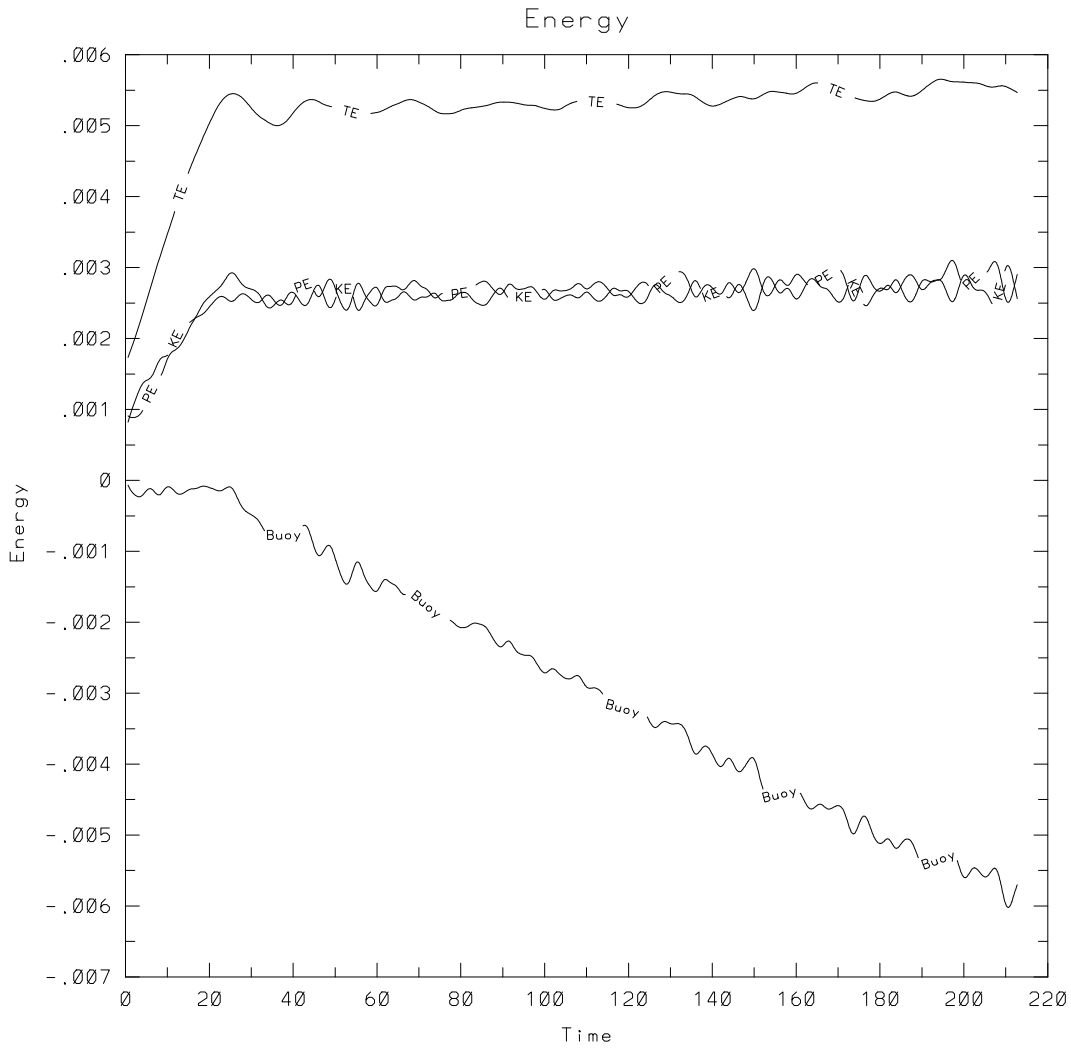

Figure 4.28: The volume integrals of kinetic, potential, total energy and time integrated buoyancy flux for a critical angle case with bottom slope of 30^o and a wave period of 12.6, indicating that the energy levels achieve a quasi-steady state after the wave train has reached the wall.

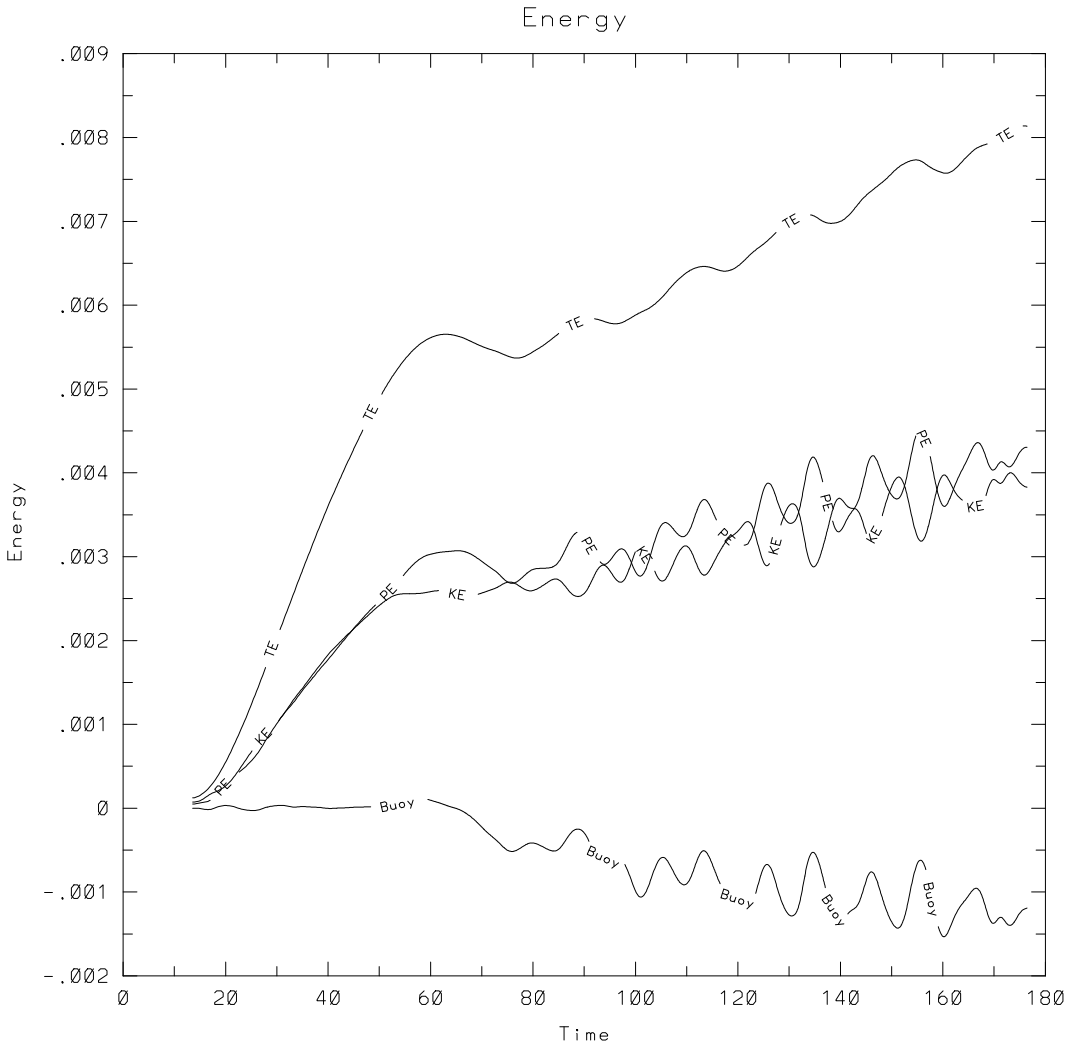

Figure 4.29: The volume integrals of kinetic, potential, total energy and time integrated buoyancy flux for a critical angle case with bottom slope of 20^o and a wave period of 18.4, indicating that the energy levels slowly increase with each mixing period after the wave train has reached the wall.

interactions will be shown to be effective for drawing the mixed fluid in the boundary layer into the interior stratified regions.

Figure 4.30 returns to the 9.2^o bottom slope case and shows the volume integrals of the various terms of the kinetic energy equation (Equation 3.111) as a function of time. Case 15 was conducted twice at two different resolutions: on the Cray YMP on a 129 x 65 x 130 grid and on the local Stardent and HP workstations on a 129 x 33 x 130 grid. The higher resolution simulation was only extended through the first mixing cycle, until $t = 108$, because of high computational expense and limited computational resources. The lower resolution case was continued until a time of $t = 191$. Detailed comparisons between the two cases will not be presented; at corresponding times the two simulations were not significantly different. The results presented above have been intermixed without distinction (with preference given to the higher resolution simulation when they overlap at earlier times). The only discernible differences were small changes in the values of derivatives in the y-direction, the intensity of the v component of velocity, and slightly more filtering occurring in the lower resolution case (details will be presented below).

The dominant terms in Figure 4.30 represent the work input by the wave forcing mechanism, the rate of dissipation of kinetic energy (ϵ), the loss of energy by filtering, the buoyancy flux, and the time rate of change of kinetic energy. Additional terms represent the flux of energy out of the top of the control volume (from the bottom boundary to the bottom of the sponge layer) into the sponge layer by advection and pressure flux. The final term plotted is the energy balance curve, the sum of all the other terms except the work input. This term is designed to check the degree of energy conservation in the system; when the balance and work input curves are equal, kinetic energy is conserved.

The balance curve is somewhat noisy for the same reasons as discussed above in Section 4.4.3 (e.g., the calculation of $\frac{\partial KE}{\partial t}$ and of the kinetic energy lost by filtering were done in single precision for most of the calculation.) The time derivative, for example, was calculated by taking the difference in the kinetic energy between two adjacent time steps and dividing by the time step. After $t = 160$ the simulation used

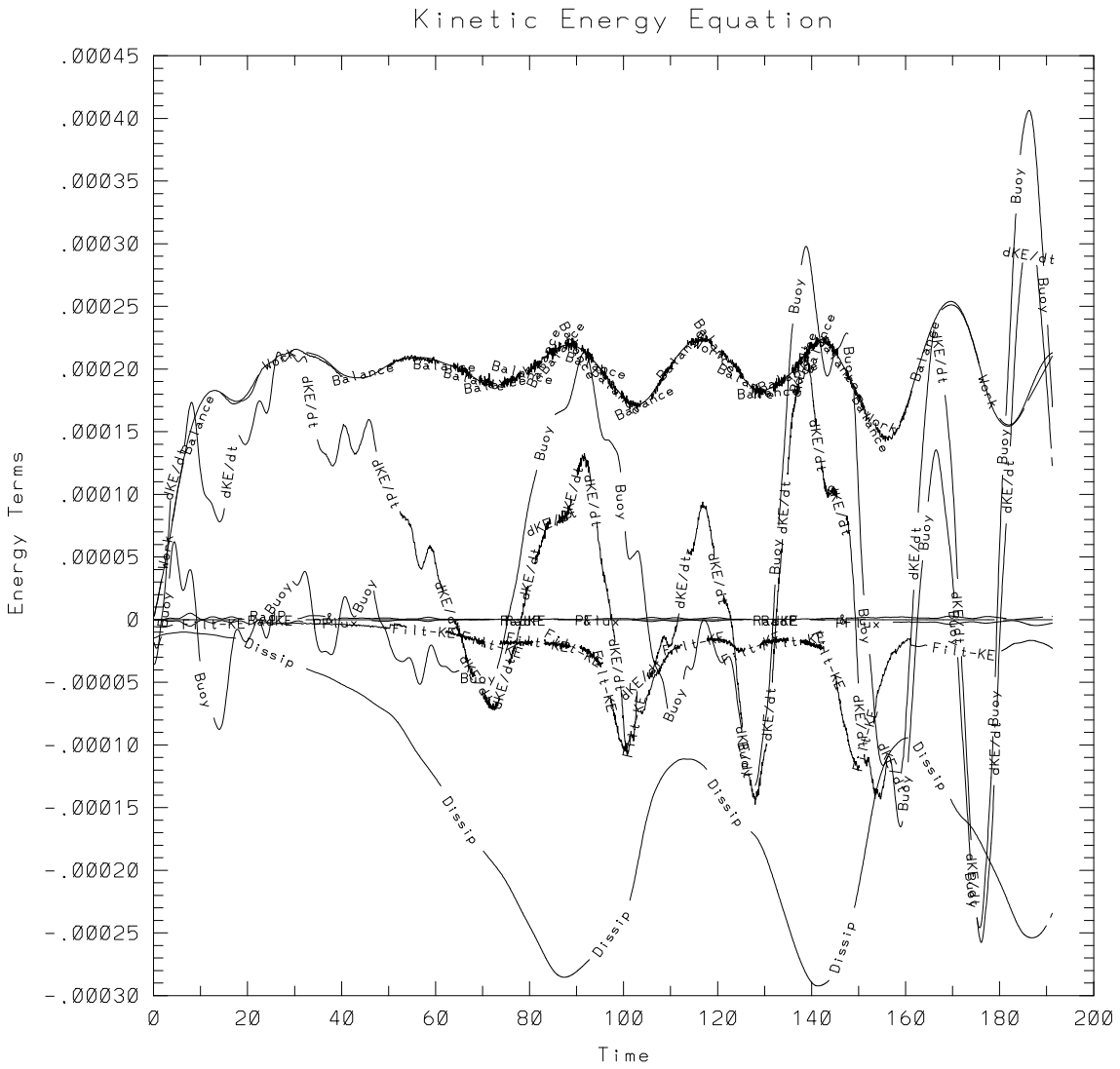

Figure 4.30: Volume integrals of terms in the kinetic energy equation, Equation (3.111): work input, $\frac{\partial KE}{\partial t}$, dissipation, filter dissipation, buoyancy flux, radiation loss, and balance.

double precision, and the noise was eliminated. Yet, even including the noise, the balance of energy is very good; typically the errors are less than 1%. This small error may be attributed to different integration techniques. A simple method of integration was used for the energy rate terms, based upon summation of the grid values for the velocities, weighted by the local volume of the variable grid. It was found later that the use of a more sophisticated numerical integration method, such as the trapezoidal rule, could alter some of the integrals by up to 2%. The general conclusion is that the energy balance is very good, and the individual terms are representative of the energetics in the fluid.

The buoyancy flux in Figure 4.30 is plotted so that it represents a gain in kinetic energy when it is positive. The work input achieves a fairly steady value of about 0.002. (The energy terms have been normalized by the total number of grid points and represent an average per unit volume.) The oscillation of the work input is attributable to at least two factors. First, a fairly narrow forcing region compared to the wavelength of the oncoming wave (approximately 1.5:1) was used for this case (see Section 2.6.2). Second, as time progresses, reflected waves propagate upwards from the turbulence in the boundary layer and enter into the wave generation region, affecting the strength of the work input (though this does not change the amplitude of the downward directed wave train).

The dissipation rate in Figure 4.30 appears as a negative quantity, meaning a loss of kinetic energy, and has been discussed in Section 4.4.3. Here the loss of kinetic energy by the compact filter has been separated from the resolved dissipation. Comparison of these magnitudes shows that most of the dissipation has been resolved. The maximum energy removal by filtering occurs at approximately $t = 100$ and $t = 150$, when the turbulence has cascaded down to smaller unresolved scales. Time integration of the losses of energy shows that overall 86% of the total energy dissipation has been achieved by the resolved dissipation and 14% of the total energy dissipation has been accomplished by the filter. These percentages are slightly adjusted by the higher resolution calculation to 89% and 11%, respectively.

Figures 4.31 and 4.32 show similar behaviors for the terms in the equations for

the potential and total energies. In these figures the resolved dissipation accounts respectively for 80% of the potential and 84% of the total energy on the 129 x 33 x 130 grid, and 82% of the potential and 87% of the total energies for the 129 x 65 x 130 grid. Further analysis, not pictured here, shows that the filter makes its dominant contribution in the same region as the strongly three-dimensional portion of the flow, within the turbulent boundary layer at a distance from the wall of approximately $0.15 < z < 0.4$. In addition, the filter was found to remove energy primarily in the x and y directions, suggesting that if additional computational resources could be employed, it would be desirable first to increase the resolution in those directions. This conclusion is consistent with the fact that, in the boundary layer region, the variable grid has $\Delta z \approx 1/3\Delta x \approx 1/6\Delta y$.

Figure 4.30 shows that the rate of change of kinetic energy follows the buoyancy flux more closely than any other term. Over each mixing period the net input of work is roughly equal to the total dissipation. But the change of kinetic energy fluctuates rapidly from positive to negative approximately twice per wave period.

Figure 4.31 shows terms of the potential energy equation (Equation 3.112). It is very similar in character to terms in the kinetic energy equation. Note, however, that the dissipation rate of potential energy is only 1/2 the dissipation rate of kinetic energy. Here the buoyancy flux is plotted with opposite sign compared to its plot for the kinetic energy equation, so that a positive buoyancy flux in Figure 4.31 means a net gain of potential energy. Again the balance of potential energy is reasonably good; the numerical noise vanishes after $t = 160$ when the difference is calculated using double precision sums and differences. The main point related to the buoyancy flux in these two figures will be addressed in conjunction with Figure 4.33 below.

Figure 4.32 shows the terms from Equation 3.113 for the total energy, the sum of kinetic and potential energies. Here, much of the complication of the preceding figures is eliminated because the buoyancy flux drops out of the total energy equation and the balance between work input and dissipation is more readily apparent. The rate of change of total energy oscillates between positive and negative values between periods of strong mixing and dissipation and periods of restratification and relaminarization.

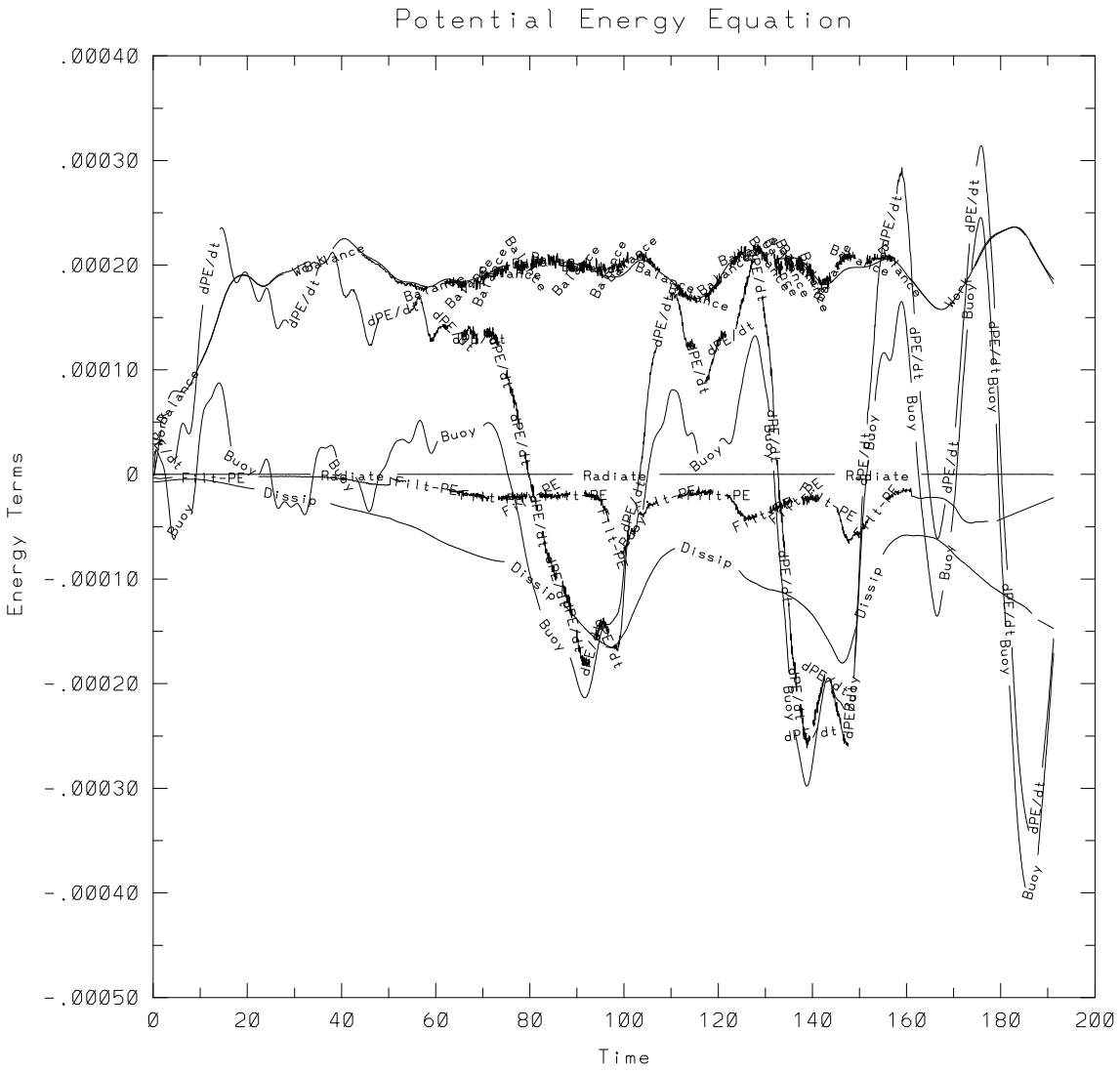

Figure 4.31: Volume integrals of the various terms of the potential energy equation, Equation (3.112): work input, $\frac{\partial PE}{\partial t}$, dissipation, filter dissipation, buoyancy flux, radiation loss, and balance.

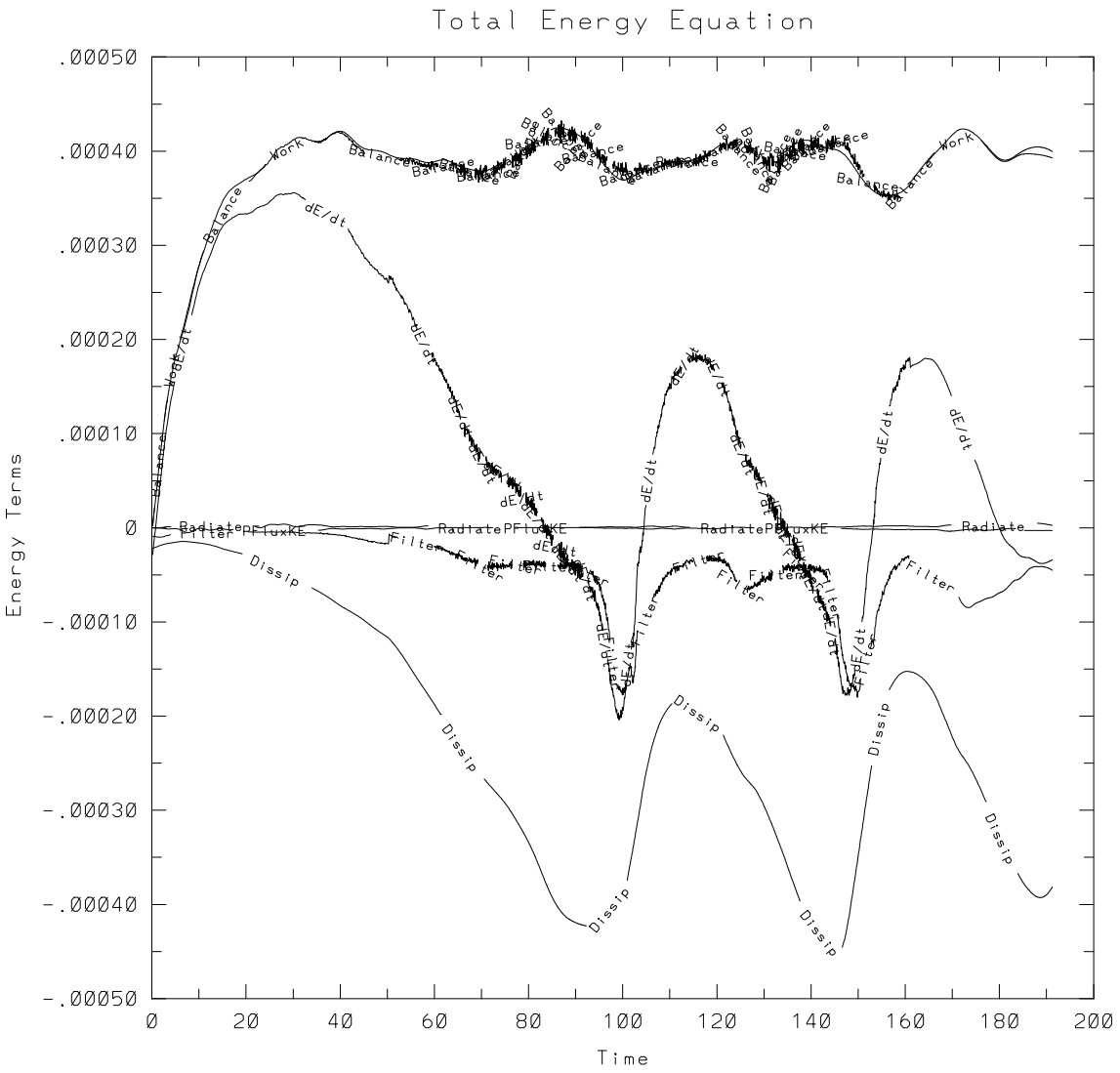

Figure 4.32: Volume integrals of the various terms of the total energy equation, Equation (3.113): work input, $\frac{\partial TE}{\partial t}$, dissipation, filter dissipation, radiation loss, and balance.

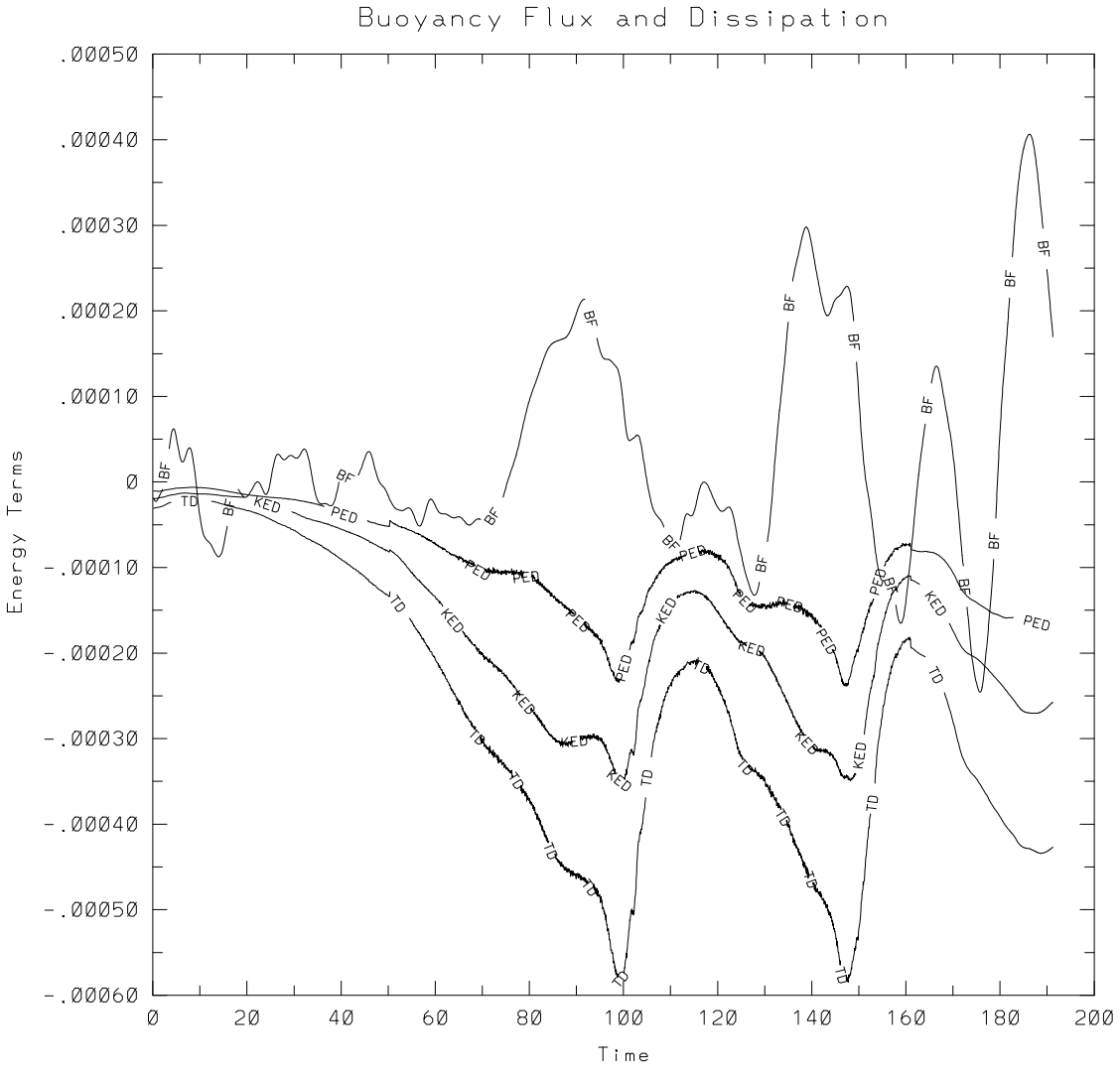

Figure 4.33: Buoyancy flux and dissipation rate terms from the energy equations, showing the strong transfer of potential to kinetic energy during periods of strong wave breakdown and turbulent dissipation.

Figure 4.33 shows the strong correlation that exists between the phase of the buoyancy flux and the periodicity of the mixing cycles. Four curves are plotted in Figure 4.33: the buoyancy flux (plotted in the sense that a positive value means a net gain of kinetic energy), the total potential energy dissipation rate (χ) (which includes both resolved and filter dissipation), the total kinetic energy dissipation rate (ϵ), and the total energy dissipation rate. There is a strong transfer of potential to kinetic energy at the same times that the dissipation is strongest. It should be recalled that the oncoming gravity waves contain equal amounts of kinetic and potential energy. Therefore, when the waves break down in the turbulent boundary layer, and kinetic energy is dissipated more strongly than potential energy, the waves try to adjust and maintain their structure by transferring potential to kinetic energy. There is a significant sink of kinetic energy caused by the no-slip boundary condition, as energy is lost in the strong shear layer causing ϵ to be greater than χ. The rapid drop in buoyancy flux, to negative values, occurs at the same time as the mixing and dissipation decrease, near times 105 and 150.

Figure 4.34 shows horizontally integrated total energy (kinetic and potential) as a function of height. The energy profiles are shown at six different times, $t = 60$, 73, 86, 94, 109, and 117 (curves labeled 1 through 6), following the flow through the first mixing cycle. The top panel shows the energy as a function of distance from the wall ($0 \leq z' \leq 3.5$) and the bottom panel shows the same data plotted against the grid level, ($1 \leq k \leq 130$). The bottom panel is easier to read because most of the energy is concentrated in a region near the bottom wall. This is caused by strong wave amplification that occurs when the wave reflects from the critically sloping bottom topography. In effect all of the oncoming energy is trapped near the bottom slope, as suggested by the linear ray theory, until it builds up to sufficient intensity to transition into turbulence and dissipate.

The following examination of Figure 4.34 will focus on the lower panel. The wave forcing region for this simulation extends approximately from grid points 75 to 110 ($1.3 \leq z \leq 2.7$), and the Rayleigh damping sponge layer covers points 118 to 130. At the earliest time pictured, $t = 60$ (curve 1), wave amplification near the wall is the

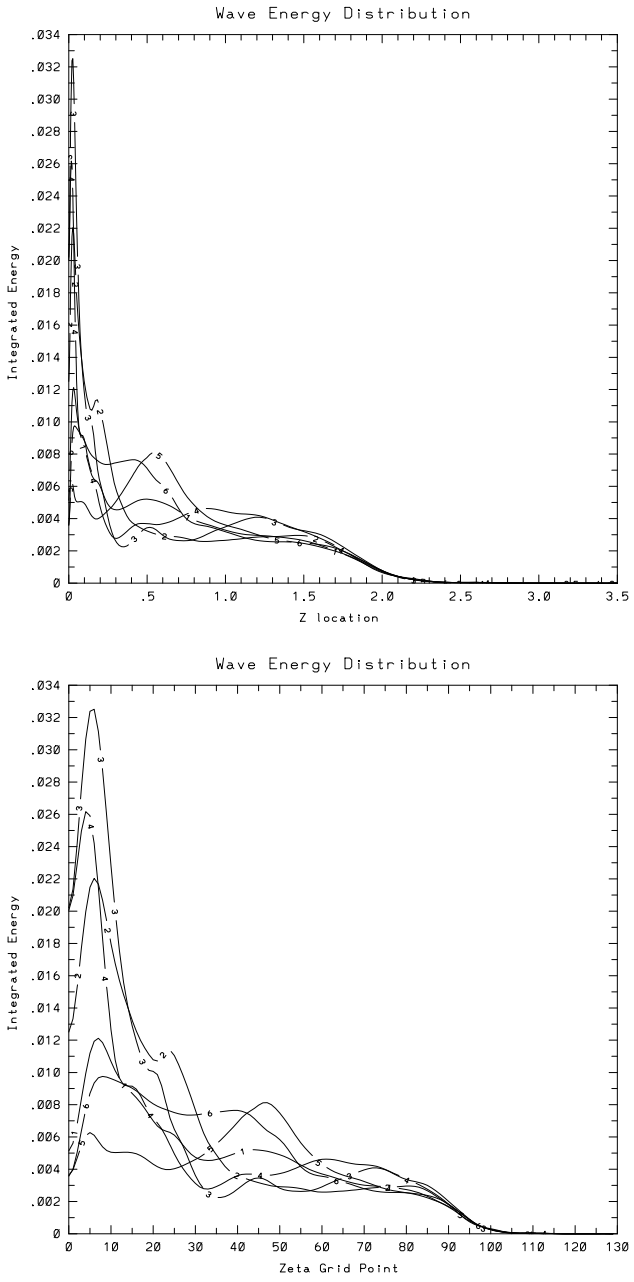

Figure 4.34: Horizontally (x'-y plane) integrated energy as a function of distance from the bottom slope, z' (top), and of the grid index from the bottom wall ζ (bottom). The integrals include the total of both potential and kinetic energy and are shown at six time levels $t = 60$, 73, 86, 94, 109, and 117 (curves labeled 1 through 6). The forcing region extends from approximately $z = 1.4$ to $z = 2.6$.

dominant feature evident. The amplification grows dramatically stronger in curve 2, reaches a peak with curve 3, and begins to fall off in curve 4. For curve 5 ($t = 102$) the energy near the wall is less than any other time. However, curve 5 also shows a significant peak of energy reflected from the wall (centered at about grid point 50) from the turbulent region and meandering upwards towards the wave forcing zone.

It may be noted that the oscillations in work input seen in Figure 4.30 begin at about this time ($t \approx 100$) and may be attributed to the superposition of incoming and outgoing energy, modulating the local velocity field in the forcing region and hence the work input, which is the product of the local velocity and forcing terms. At $t = 109$ (curve 6) the outgoing energy has dissipated somewhat and energy amplification in the near wall zone has begun again, starting the next cycle. The next mixing cycle proceeds in a similar fashion, with a peak in energy in the boundary layer of approximately the same magnitude and duration. The wave amplification zone, for which the observed energy density increases to greater than twice the energy density of the oncoming wave during some period of the mixing cycle, covers approximately the bottom 55 vertical grid points, corresponding to a thickness of $z = 0.75$, or 3/4 of a vertical wavelength.

4.7 Vorticity Dynamics

An important characteristic of a turbulent flow is that it contains large amounts of vorticity. The Helmholtz vorticity equation describes the evolution of vorticity,

$$\frac{\partial \vec{\omega}}{\partial t} + \mathbf{u} \cdot \nabla \vec{\omega} = \vec{\omega} \cdot \nabla \mathbf{u} + \frac{\nabla \rho \times \nabla p}{\rho^2} + \nu \nabla^2 \vec{\omega} \, , \tag{4.13}$$

in which the terms on the left hand side represent the time rate of change of vorticity and the transport of vorticity by convection, together forming the material derivative. The first term on the right hand side represents the change in the vorticity due to turning and stretching of vortex lines. The second term represents the generation of vorticity by baroclinic torque, which occurs when constant density surfaces are inclined to constant pressure surfaces. In the Boussinesq approximation the background pressure gradient, the hydrostatic part, is much larger than perturbation

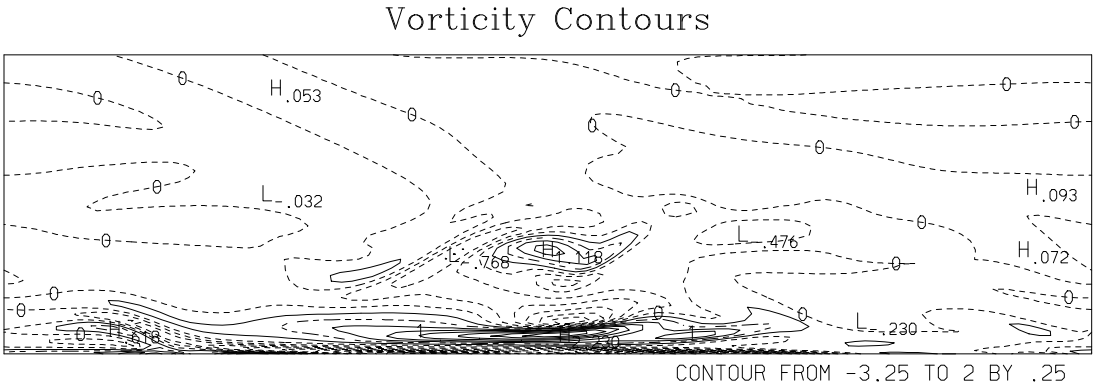

Figure 4.35: The vorticity component ω_x in the plane of the slope at $t = 88$.

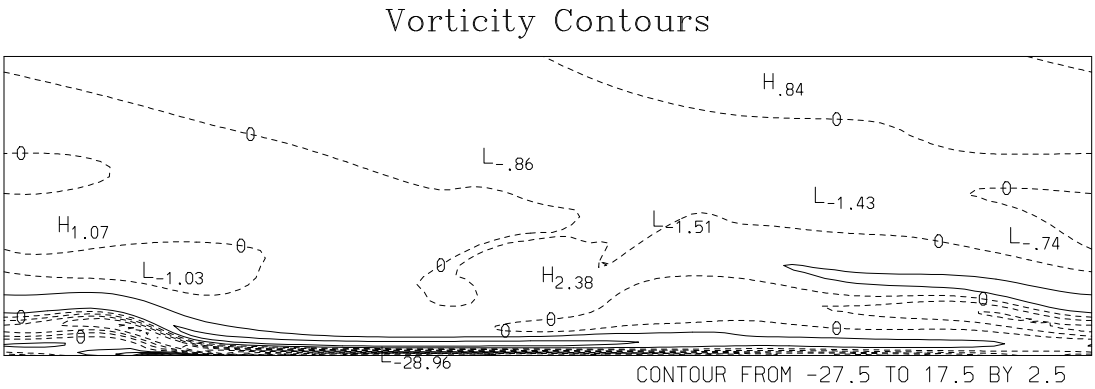

Figure 4.36: The vorticity component ω_y in the plane of the slope at $t = 88$.

pressures caused by local fluid accelerations. Therefore, the pressure gradient is directed vertically and baroclinic generation of vorticity occurs when density surfaces are displaced from their resting (horizontal) state. The last term in the Helmholtz equation represents the diffusion of vorticity, which may have a strong source at a boundary.

Figures 4.35, 4.36, and 4.37, show, respectively, the three components of vorticity, ω_x, ω_y, and ω_z, in the center plane of the computational domain at $t = 88$. Here, ω_x and ω_z refer to vorticity perpendicular to and in the direction of gravity. The only component of vorticity contained by the oncoming wave is ω_y. It is clear from examining the contour levels in Figure 4.36 that the ω_y component is much stronger than either ω_x or ω_z. There is a thin layer of large vorticity very near the bottom wall

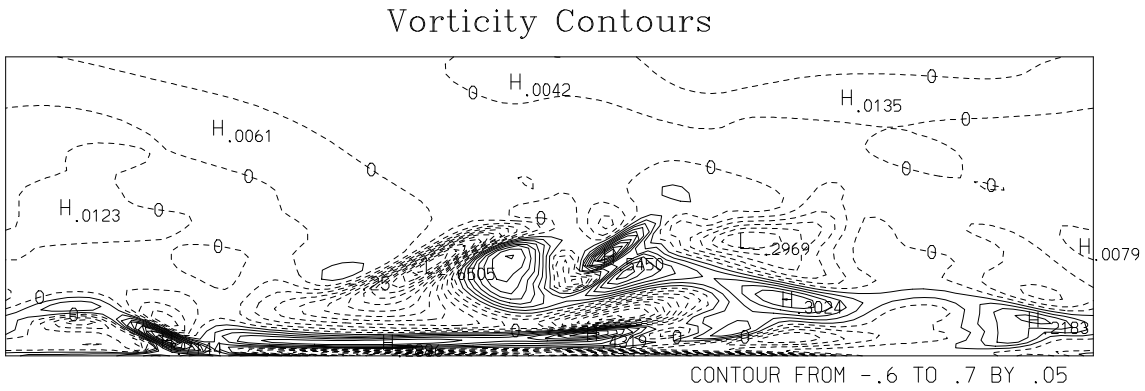

Figure 4.37: The vertical vorticity component ω_z in the plane of the slope at $t = 88$.

associated with the no-slip boundary condition. At the wall there is a strong flux of vorticity into the flow. It is evident, however, by the proximity of zero contours of ω_y very near the wall that this source of vorticity does not diffuse far into the domain, or alternatively, that the periodic production of positive and negative vorticity at the wall limits the effective depth of the diffusion. For linear wave reflection, near the wall the flow becomes a Stokes flow (Cacchione and Wunsch, 1974) in which the boundary layer oscillates back and forth, upslope and downslope. For the linear case there is no net production of ω_y throughout the wave period, i.e., there is equal production of positive and negative vorticity. The restriction of the strongest vorticity to the viscous sublayer indicates that molecular diffusion is inefficient at transporting the vorticity throughout the turbulent boundary layer. The upwelling region associated with the convergence zone at the location of the thermal front appears to contain the strongest transport of boundary vorticity into the interior of the flow. Figures 4.35 and 4.37 show that there is considerable vorticity of lower amplitude located at heights up to $z \approx 0.5$ (the vertical dimension of the figures is $z = 1.0$). It is also apparent that ω_x is somewhat stronger than ω_z.

Figure 4.38 shows a top view of the three vorticity components in a plane parallel to the wall located within the viscous sublayer at a height of $z = 0.0154$ (the fifth grid point from the wall). Here the sublayer depth is defined by the average distance from the wall at which the flow contains a kinetic energy density of 0.9 the kinetic

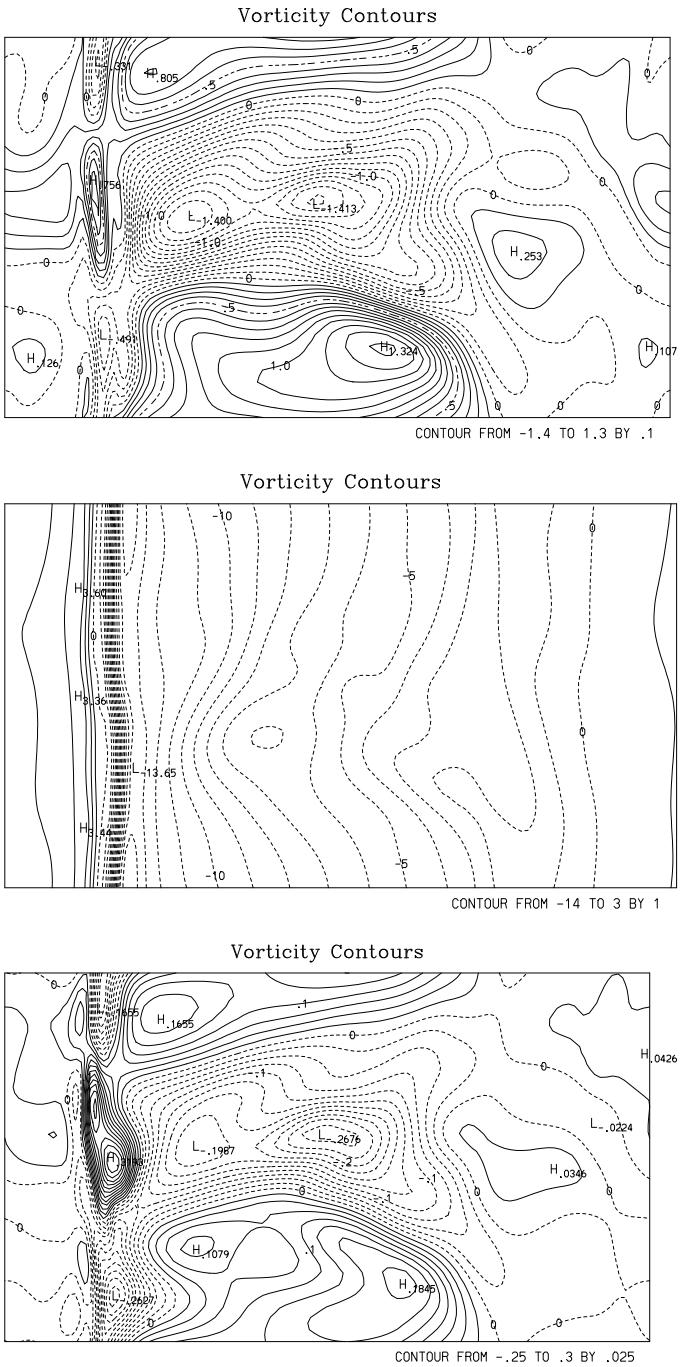

Figure 4.38: Vorticity components ω_x (top), ω_y, and ω_z (bottom) in a plane parallel to the slope located very close to the wall at a height $z = 0.0154$ (the fifth grid point from the wall) at $t = 88$.

energy density in the turbulent boundary layer. In this figure the strongest vorticity is located near the left hand side of the domain at the location of the thermal front (see Figure 4.19). Note that the y-vorticity, Figure 4.38 (middle), is predominantly two-dimensional, caused by the strong shear of the (two-dimensional) oncoming wave in contact with the wall. Also correlated with the location of the thermal front are the strongest regions of ω_x and ω_z. These appear much more three-dimensional in nature, though approximately an order of magnitude smaller than ω_z. If the (large) two-dimensional part of ω_y were subtracted, it might also appear as strongly three-dimensional at approximately the levels of intensity of ω_x and ω_z. As time progresses, the strongest regions of vorticity and vorticity production move upslope together with the thermal front.

Figure 4.39 also shows the three components of vorticity at $t = 88$ in a plane parallel to the slope located at $z = 0.32$, which is in the turbulent boundary layer well above the viscous sublayer. Here the vorticity magnitudes are comparable, indicating both that the sublayer vorticity has not extended this far from the wall and that turbulent mechanisms are dominant. The vorticity is strongest here in the center portion of the domain, where the flow is statically unstable (see Figure 4.19). Further analysis indicates that in this region both baroclinic generation and turning and stretching make large contributions to the vorticity. The center panel, showing ω_y, still appears somewhat more two-dimensional than either ω_x or ω_z. This results from the superposition of the vorticity of the oncoming wave with the vortex structure of the wave breakdown regions.

The vertical vorticity, ω_z, in these figures is not associated with the two-dimensional incident wave and indicates that there is strong production of ω_z in the region of overturning. In the wake of the overturning region, similar to the turbulent bore observed in the laboratory by Ivey and Nokes (1989), the vorticity indicates that the flow is forming into a variety of organized structures. In strongly stratified turbulence, ω_z is may be larger than ω_x because, for ω_z to exist, work against gravity is unnecessary. The fact that ω_x is roughly the same as ω_z suggests that, once the wave starts breaking, the flow becomes strongly three-dimensional, and stratification plays less

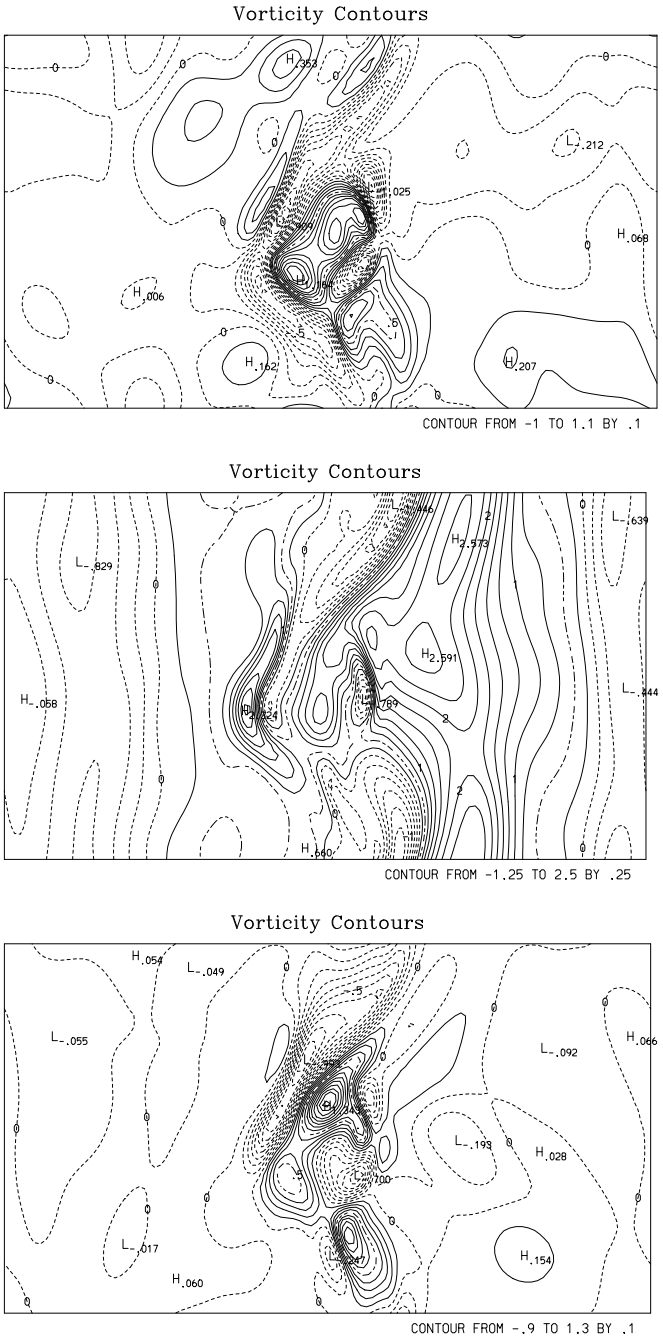

Figure 4.39: Vorticity components ω_x (top), ω_y, and ω_z (bottom) in a plane parallel to the slope located very close to the wall at a height $z = 0.32$ (the 35th grid point from the wall) at $t = 88$.

of a role in the structure that develops.

Figure 4.40 shows the integrated root mean square (rms) vorticity magnitudes of ω_x, ω_y, ω_z, and $|\vec{\omega}| = \sqrt{\omega_x^2 + \omega_y^2 + \omega_z^2}$ as a function of height at two time levels, $t = 88$ and $t = 109$. The height is plotted in the stretched ζ coordinate system to make the vertical dependence easier to see. As in the previous figures, ω_y is the dominant component. The strongest vorticity is located close to the wall and exists at enhanced levels out to approximately grid point 60 ($z = 0.83$). Above this level, $z > 0.8$, all of the vorticity is from the oncoming wave. Outside of the viscous layer, the peak rms vorticity levels are approximately five times larger than observed in the oncoming wave train. This enhancement is caused both by the increase in energy density from wave reflection and by production of vorticity from turbulent effects. It is noteworthy that the magnitudes of ω_x and ω_z in the turbulent zone are approximately the same size as the magnitude of ω_y in the oncoming wave before it reaches the turbulent zone.

Figure 4.41 reproduces the information from Figure 4.40, but shows only the smaller ω_x and ω_z components. These curves indicate that the transfer and production of ω_x and ω_z are strongest in the regions where ω_y is largest, suggesting that there is a turning of vorticity from ω_y into the other components. Also evident is that the average values of ω_x are larger than ω_z throughout the flow. It is significant that the bottom slope interferes with the development of large scale horizontal structures containing significant amounts of ω_z. This is especially true in regions close to the wall where the difference is most apparent.

Figure 4.42 shows the x and y components of the baroclinic torque terms from the vorticity equation plotted at $t = 94$ (again refer to Figure 4.19). There is no production of ω_z by this mechanism, because in this direction the density and pressure gradients are parallel. The contributions are essentially equivalent to plotting contours of $\dfrac{\partial \rho}{\partial y}$ (the contribution to the $\dfrac{\partial \omega_x}{\partial t}$ equation), and $\dfrac{\partial \rho}{\partial x}$ (the contribution to the $\dfrac{\partial \omega_x}{\partial t}$ equation). The strongest regions of baroclinic generation are associated with the thermal front, which moves upslope as time progresses. Other regions located farther from the wall are also active in creating vorticity through this mechanism. Overall,

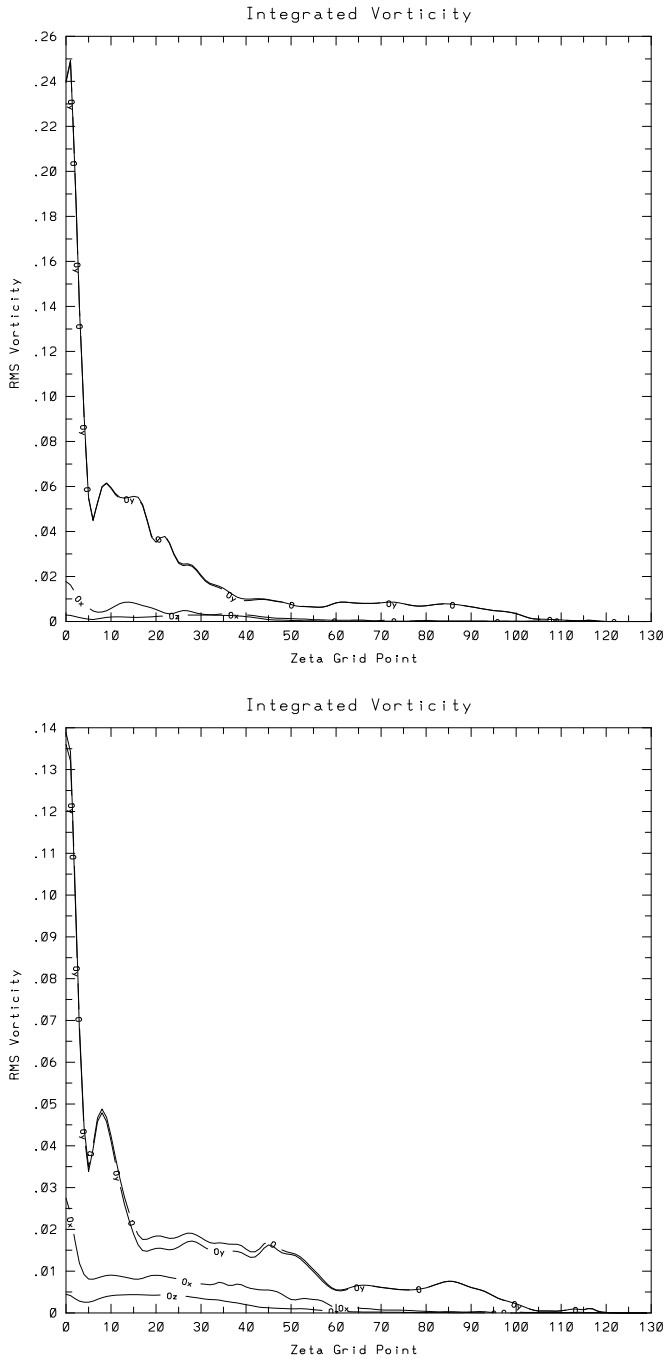

Figure 4.40: Vorticity as a function of height (by grid points) at $t = 88$ (top), and $t = 109$ (bottom). Curves indicate the total root mean square vorticity (O), the rms value of ω_x (Ox), ω_y (Oy), and ω_z (Oz).

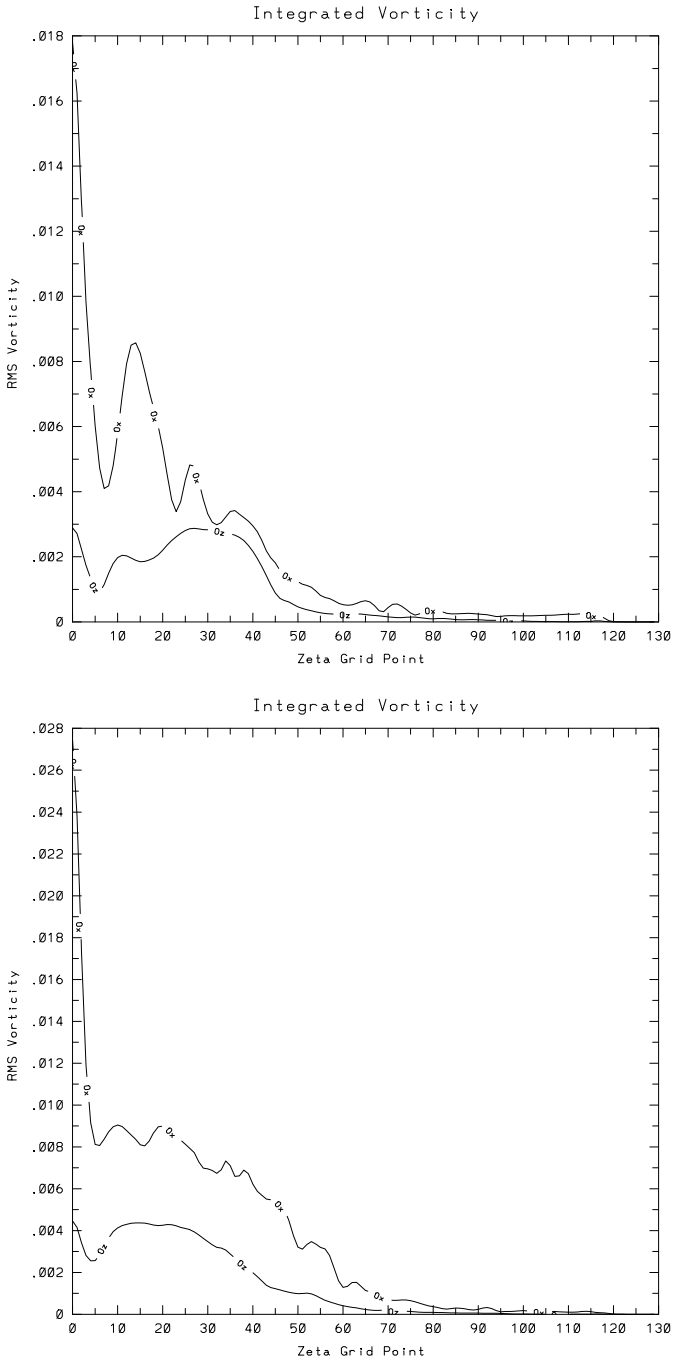

Figure 4.41: Vorticity for ω_x and ω_z is shown as a function of height (by grid points) at $t = 88$ (top), and $t = 109$ (bottom). Curves indicate the rms value of ω_x (Ox) and ω_z (Oz).

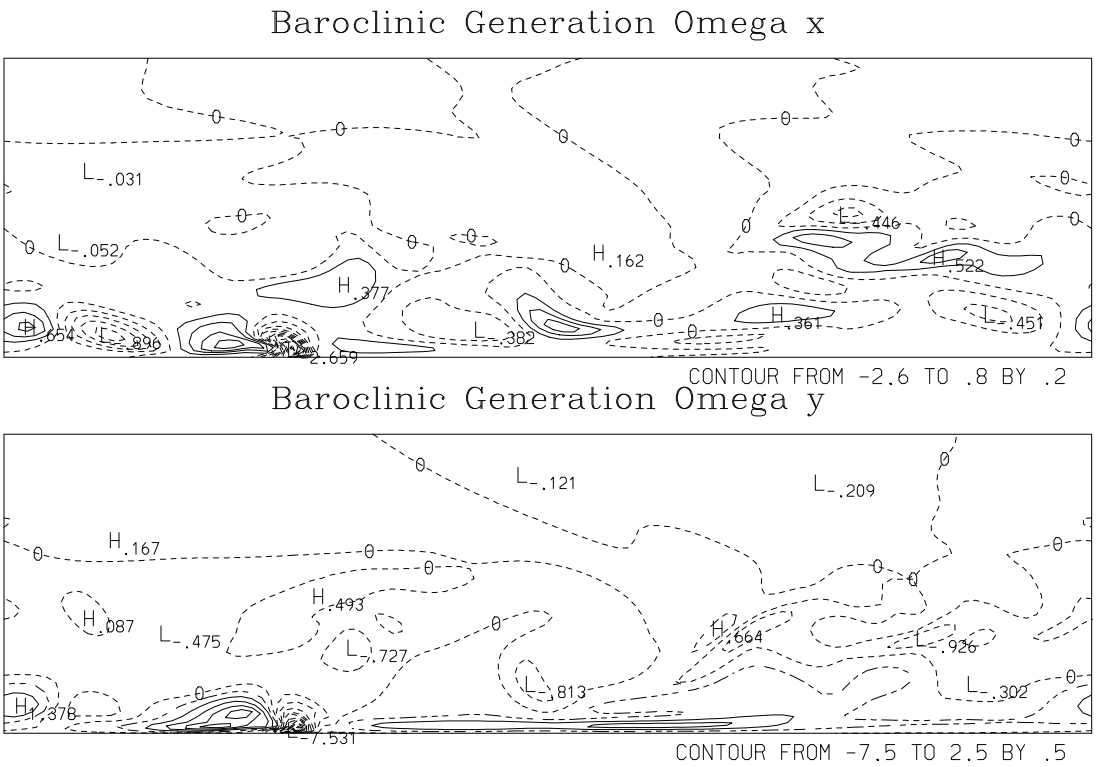

Figure 4.42: The two components, contributing to the change of ω_x and ω_y respectively, of baroclinic generation of vorticity in the plane of the slope at $t = 94$.

the baroclinic generation of ω_y is significantly stronger than the baroclinic generation of ω_x.

Finally, Figure 4.43 indicates the strength of the turning and stretching terms for the three components of the Helmholtz equation at $t = 94$; e.g., for the ω_x component the terms are $\omega_x \frac{\partial u}{\partial x} + \omega_y \frac{\partial u}{\partial y} + \omega_z \frac{\partial u}{\partial z}$. Here, as with baroclinic generation, the production of vorticity is strongest in the viscous sublayer, where there is stronger vorticity to be manipulated. There are also significant increases in vorticity within the turbulent boundary layer away from the wall and within the turbulent region. Generally speaking the increase of vorticity from turning and stretching is comparable in magnitude to the production by baroclinic torque, though each production term is a function of space and time.

4.8 Summary of Primary Case

Case 15 has provided an example of the flow that develops when an oncoming internal wave reflects from a critical bottom slope. This case is representative of critical angle reflection for shallow slopes. Other cases from this class, particularly the 3^o and 5^o slopes, will be presented in less detail in the following chapter.

There are several main observations for Case 15. The oncoming wave transitions to turbulence in a boundary layer of approximate thickness $\lambda/3$ as it reflects from the bottom wall. The turbulence is cyclical in nature, going through a mixing phase approximately once in 1.2 wave periods. A quasi-steady state develops in which the oncoming wave energy accumulates and then is dissipated near the wall while adjusting the background density profile and creating a mean flow. The results from the kinetic energy balance indicate that there is a strong positive buoyancy flux of energy from the available wave potential energy into kinetic energy. Between mixing cycles, the boundary layer relaminarizes and restratifies and sets up a flow field whose most defining feature is a thermal front, which moves upslope at the x-component of the phase speed of the oncoming wave. In the following chapter additional features of this flow will be discussed and compared with other critical angle simulations.

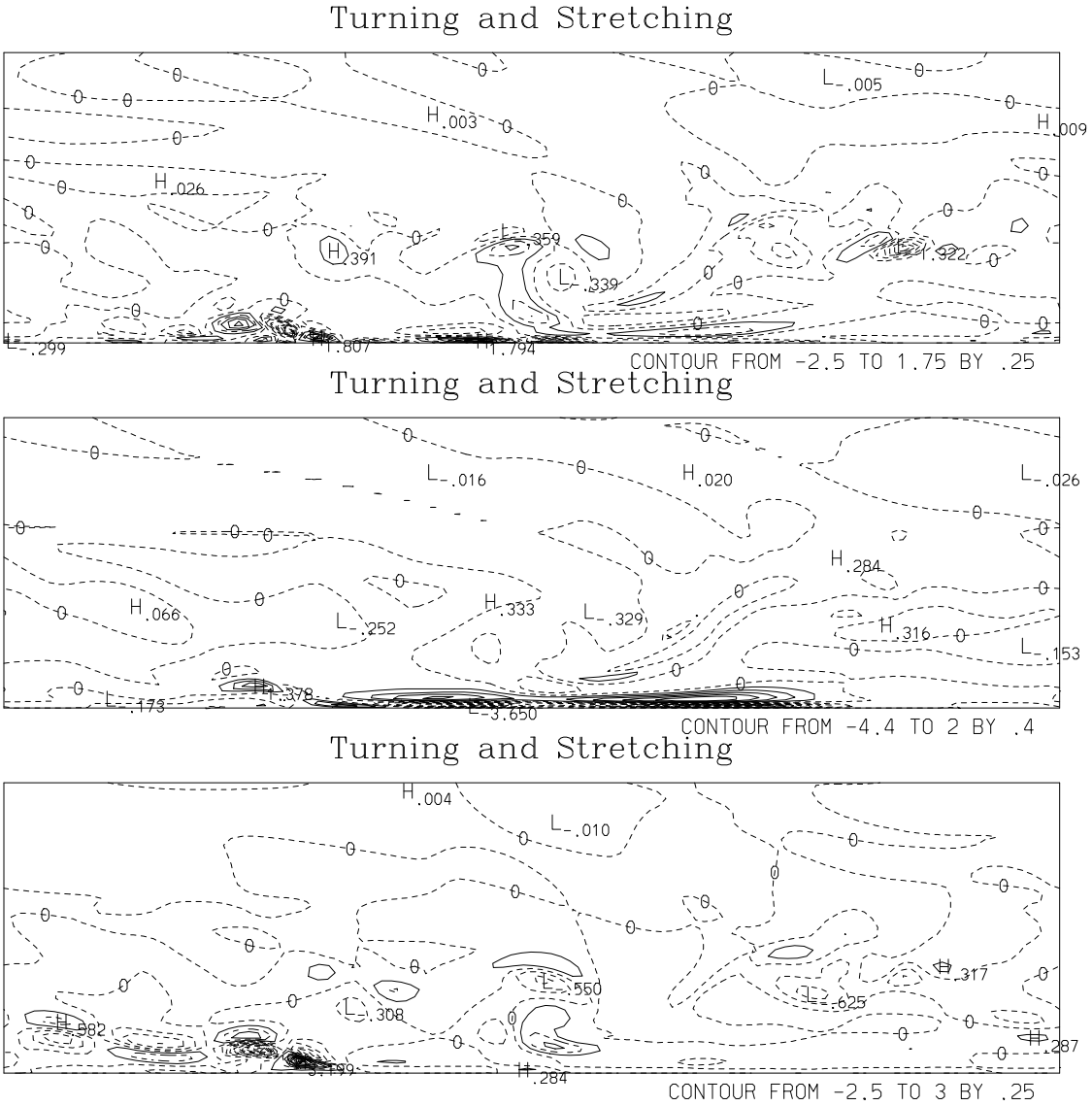

Figure 4.43: The three components, x (top), y, and z (bottom), contributing to the change of ω_x, ω_y, and ω_z respectively, caused by turning and stretching of vortex lines due to turbulence in the plane of the slope at $t = 94$.

Chapter 5

RESULTS – TURBULENT MIXING

The previous chapter presented detailed results for a single computational experiment, Case 15. This chapter presents additional results of the computational fluid dynamics experiments from Cases 1 - 28, listed in Table 4.1. All of the simulations discussed here were conducted for critical angle conditions, with bottom slopes between 3^o and 30^o. The first section examines cases at different Reynolds and Richardson numbers for the 9.2^o slope. These results are followed by cases at steeper slopes of 30^o and 20^o. The third section presents simulations for the shallowest slopes simulated, 5^o and 3.4^o. These results are followed by discussions of important general flow features such as transition to turbulence, boundary layer thickness, changes in the background density profiles, and mixing efficiencies.

5.1 Additional 9^o Critical Angle Cases

Five different simulations were conducted at the critical frequency over a bottom slope of 9.2^o. The primary emphasis for the additional simulations was to study transition to turbulence. Case 15, presented in Chapter 4, was conducted at a Reynolds number of 3600 (based upon the wavelength, the oncoming wave current speed, and the kinematic viscosity). Additional simulations were conducted at Reynolds numbers of 2800, 2000, 1200, and 850. Figure 5.1 compares the volume integrals of the mean square shear components $\left(\frac{\partial w}{\partial y}\right)^2$ and $\left(\frac{\partial v}{\partial z}\right)^2$ for these five simulations. These integrals indicate when the wave breakdown becomes three-dimensional. Other measures, such as local dissipation rates, and the intensities of the volume integrals of v^2, are consistent with the indications of the development of three-dimensionality, and hence turbulence, from the mean square shear rates.

The lower Reynolds number simulations used a different geometry than for Case

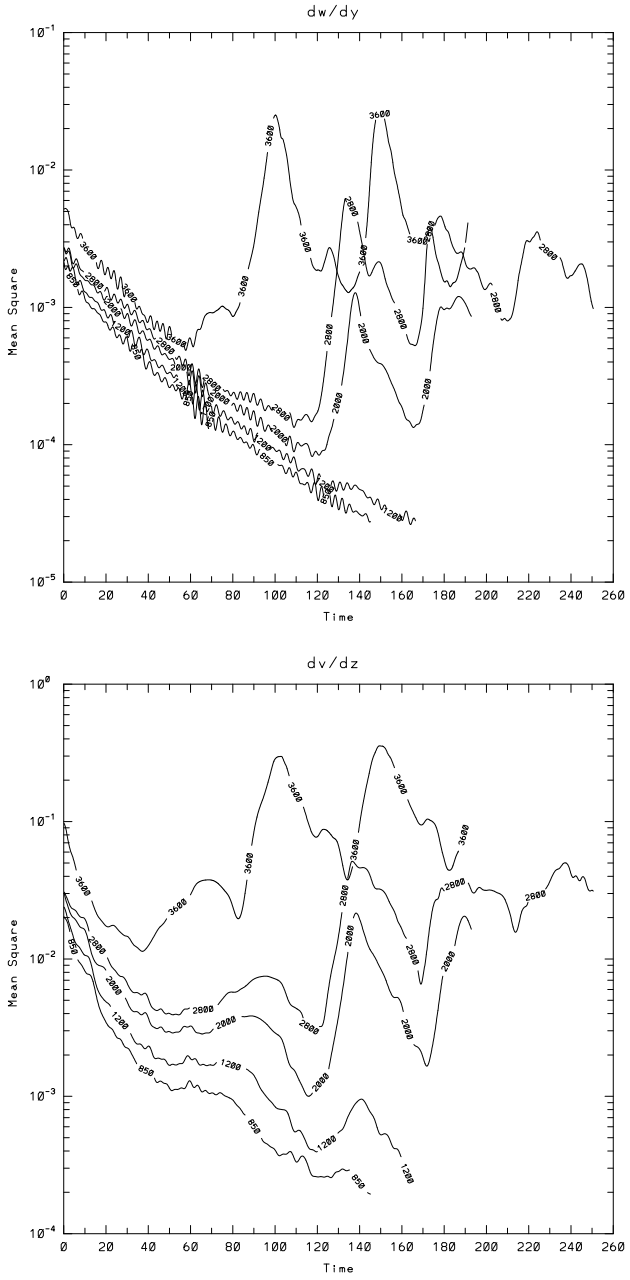

Figure 5.1: Transition to a three-dimensional (turbulent) flow occurs at a Reynolds number of about 1200 for the 9.2^o bottom slope. Here the mean square shear quantities $\left(\frac{\partial w}{\partial y}\right)^2$, top figure, and $\left(\frac{\partial v}{\partial z}\right)^2$, bottom figure, are plotted for five simulations conducted at different Reynolds numbers, 850, 1200, 2000, 2800, and 3600.

15. The first difference is that the forcing region is located farther from the bottom slope. The wave train begins to develop three-dimensionally at a later time because it takes the wave longer to reach the bottom boundary. The second difference is that the ratio of the width of the wave forcing region to the vertical wavelength (L_F/λ_z) was adjusted for Cases 11 - 14 to produce a steadier wave train. The final difference is that the length scales were decreased for the lower Reynolds number simulations, which only has the effect of lowering the Reynolds number and is equivalent to increasing the viscosity. Cases 11 - 14 have vertical and horizontal wavelengths $\lambda_z = 0.7$ and $\lambda_x = 2.1$, while Case 15 had $\lambda_z = 1.17$ and $\lambda_x = 3.5$. The normalized wave amplitudes A/λ_x or A/A_o (and hence the Richardson numbers) are approximately the same for each case.

Cases 13 and 14, with $Re = 2000$ and 2800, respectively, behaved very similar to Case 15, presented in the previous Chapter. A degree of Reynolds number independence is achieved for the simulations with Reynolds number above 2000. The waves transition and break down in very similar fashions, differing primarily in the intensity and duration of small scale motions.

Cases 11-14 (lower Reynolds numbers) differed only in the viscosity of the fluid, which was increased until the three-dimensionality of the wave breakdown was suppressed. Note from the plot of $\left(\frac{\partial w}{\partial y}\right)^2$ for $Re = 1200$ and $Re = 850$ in Figure 5.1 that the quantity continues to decay at $t = 120$. The three-dimensionality of the case at $Re = 1200$ is weak and not readily apparent in $\left(\frac{\partial w}{\partial y}\right)^2$. The flow is very near transition to turbulence and evidence of the three-dimensional development of the wave is only apparent in the $\left(\frac{\partial v}{\partial z}\right)^2$ shear. Case 12 is described as a transition case in Table 4.1, while Case 11 ($Re = 850$) is categorized as laminar.

For the higher Reynolds number simulations the periodic nature of the intensity of the turbulence is apparent. Two aspects of the periodicity of the wave breakdown are explored here and below (see Section 6.1). One aspect relates wave breakdown to the wave period and seeks to identify favorable conditions during the wave cycle for turbulence to develop. The second aspect examines the dependence of the turbulence

on the energy flux of the oncoming wave. The energy density in the boundary layer varies significantly with Richardson number and Reynolds number, causing wave breakdown and mixing to develop differently.

Figure 5.1 shows that wave breakdown occurs at similar times for the cases with $Re = 2800$ and 2000. Peaks in the shear rates occur at $t = 140$ and 185. The wave amplitudes (and Richardson numbers) and energy fluxes for both cases are comparable, differing only in the viscous losses as the wave approaches the boundary. There is a slight time lag in the maxima for the lower Reynolds number case, but the mixing period for each case is approximately 45, compared to the wave period of 39.4. Even the transitional case ($Re = 1200$) starts to develop three-dimensionality at approximately the same time. The higher Reynolds number case, $Re = 3600$, has a mixing period of approximately 48. Though this case has somewhat higher Reynolds number, the Richardson numbers and energy density of the oncoming waves are similar (see Table 4.1 and Figure 5.27). Again, as discussed above in Section 4.4.3 (Intermittency), it would be desirable to continue the simulations for additional wave periods to observe whether the mixing periods remain constant. Extending a set of critical angle simulations to a greater number of mixing cycles was accomplished for higher frequency waves and is discussed below in Sections 5.3 and 6.1.

Figure 5.2 shows the maximum velocities from the simulations as a function of time for the same five cases. At a time of 40 - 60 the maximum velocity represents the maximum current speed of the oncoming wave train as it approaches the boundary. For the four lower Reynolds number cases the wave forcing region produces identical wave trains. The waves in the simulations with higher viscosities, however, are damped more while approaching the wall, resulting in slightly lower observed wave velocities (hence decreasing the flow Reynolds numbers as well).

The main point from Figure 5.2 is that the reflected waves produce much higher velocity currents in the boundary layer than occur in the oncoming wave train. The peak velocities in the boundary layer are approximately 2.3 times as large as the oncoming wave velocities for the two highest Reynolds number cases. The case with $Re = 3600$ has a higher peak velocity partly because the oncoming wave has a higher

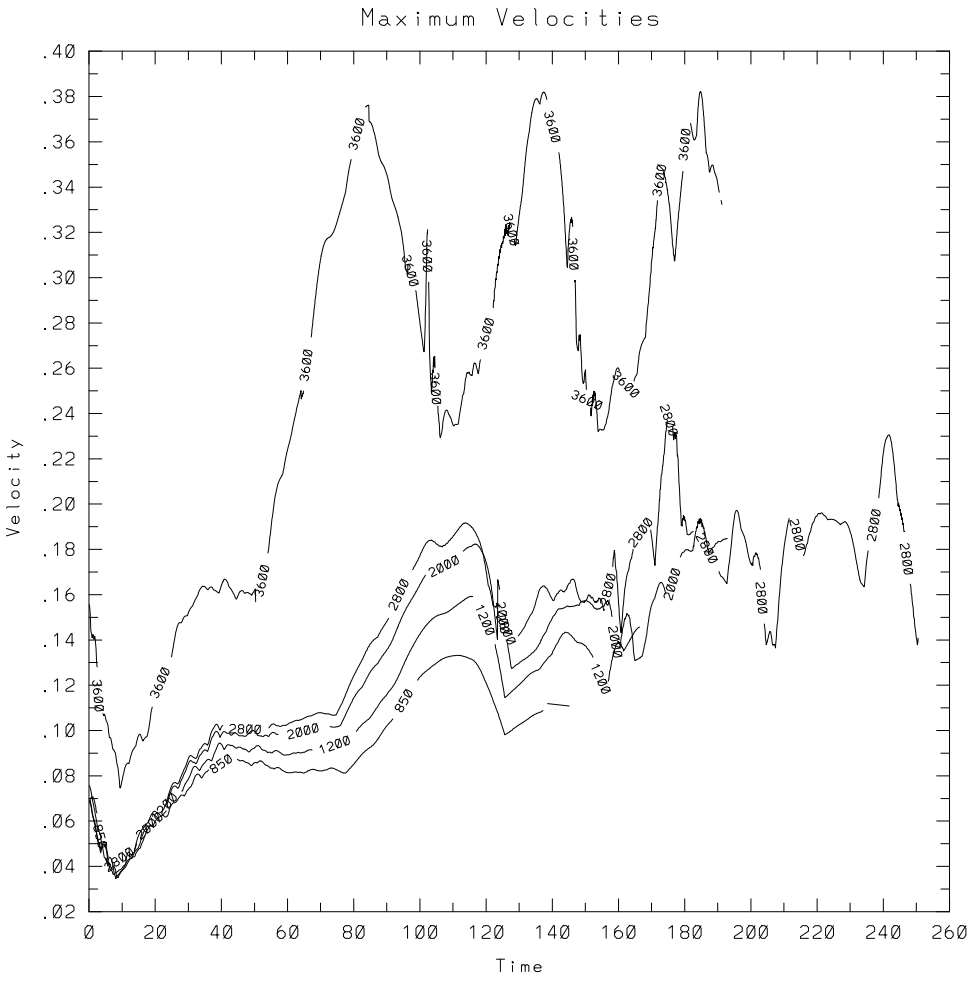

Figure 5.2: The maximum fluid velocity for the 9.2^o critical angle, bottom slope cases is plotted as a function of time. The Reynolds numbers for these simulations are 850, 1200, 2000, 2800, and 3600.

velocity. The important point is that the ratio of the maximum velocity to the oncoming wave velocity is similar for the turbulent simulations. These results are consistent with lab measurement by Ivey and Nokes (1989) who observed maximum velocities of reflected waves of approximately 2 - 3 times the velocities of oncoming waves. They determined that the peak velocity in the boundary layer, U_p, was a linear function of the oncoming wave amplitude A (Ivey and Nokes, Figure 5b):

$$U_p = 1.82\omega A + 0.61 \; . \tag{5.1}$$

This consistency should not be overemphasized, however, in view of differences in the wave amplitudes (Richardson numbers), wave generation mechanisms, and experimental geometries. Nonetheless, it is noteworthy that the maximum velocities occur approximately half a wave period before the peaks in dissipation (e.g., Figure 4.17).

A focus of the numerical experiments, discussed in more detail below, has been to determine the transition Reynolds numbers of the flow. The Reynolds number ($Re = \frac{U\lambda}{\nu}$) can be adjusted by changing the length scales, the velocity of the oncoming waves, or the viscosity. In order to resolve the small scales of motion in these experiments, especially within the viscous boundary layer, the simulations have been conducted at moderate and low Reynolds number. The most successful way to observe turbulent breakdown is to have fairly large amplitude waves ($A > A_o/2$) approach the boundary. This approach differs somewhat from the laboratory experiments of Ivey and Nokes (1989) and Taylor (1993), who used relatively small amplitude mode-one waves ($A < A_o/5$). The global Richardson numbers, $Ri = (N\lambda/U)^2$, have been relatively low (30 to 300) for most of the turbulent simulations, compared to those used in laboratory experiments ($Ri \sim 10,000$). The Reynolds numbers of the numerical experiments (300 to 4,000), however, are comparable to the laboratory values (2,000 to 8,000), but they are achieved using larger amplitude waves in a more viscous fluid.

Figure 5.3 shows a short sequence of constant density surfaces for the simulation at the Reynolds number of 2000; the dimensions of the figure are 1.4 λ_z in the vertical (z') and one horizontal wavelength ($\lambda_x = 3\lambda_z$) in the horizontal (x') direction. The frames should be inclined 9^o counter-clock-wise to be in their natural reference frame.

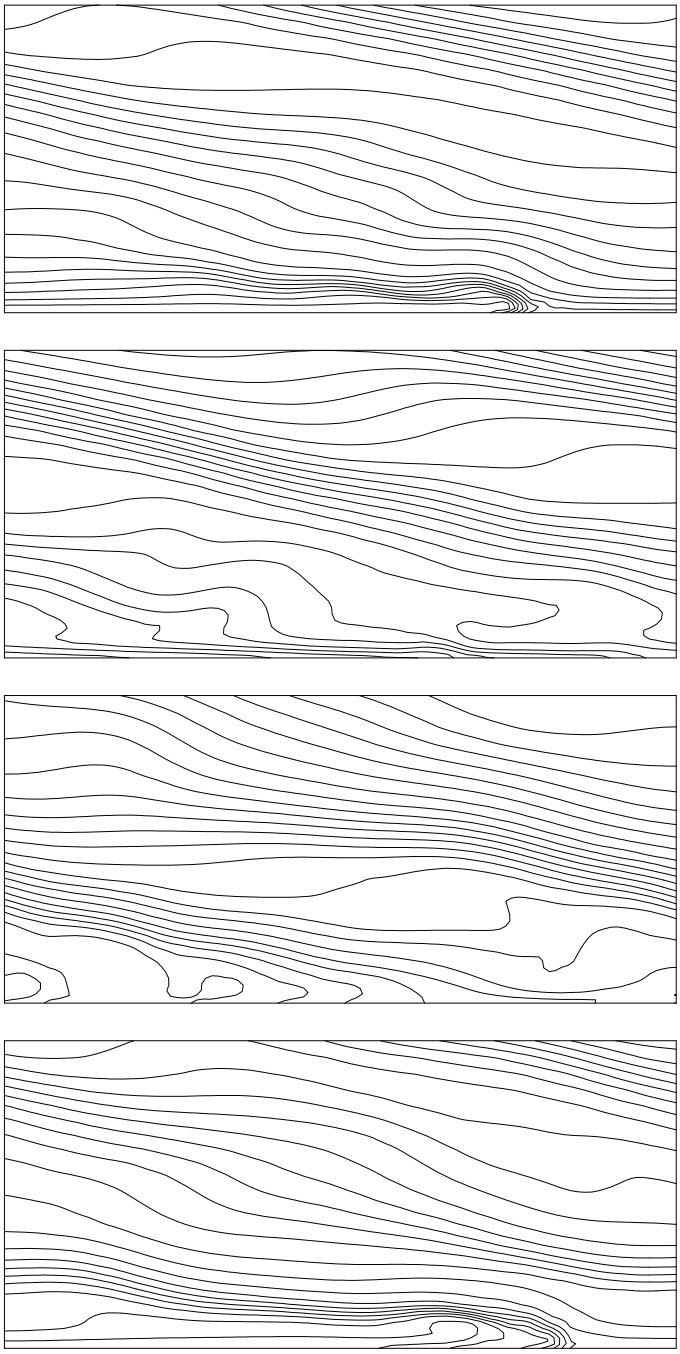

Figure 5.3: Isopycnals and statically unstable regions for Case 13 with a 9.2^o bottom slope at $t = 113.8$ (top), 127.7, 142.6, and 157.7 (bottom).

The wave period is 39.2 and the top and bottom frames, which illustrate very similar flows, are 43.9 time units apart (approximately one wave period). The sequence is very similar to that of Case 15 presented in Chapter 4 (Figure 4.10), and shows the wave overturning in the boundary layer preceding the generation of strong turbulence in the boundary layer. While the flow does not develop into structures as small as for the higher Reynolds number case, the overall fluid dynamics are essentially the same as for Case 15.

5.2 Steep Slope

This section presents results of critical-angle reflection experiments conducted over a 30^o bottom slope. The most significant difference between this case and those previously examined is that now the nondimensional wave period, $T_w = 12.6$, is much shorter for fixed N. The frequency of the oncoming wave, $\omega = 0.5$, is much closer to the buoyancy frequency, $N = 1$, bringing the time scales for turbulent decay and wave forcing much closer together. Observations of the density field that develops in the boundary layer for Case 28, with $Re = 1600$, are presented throughout two wave periods in Figure 5.4 at $t = 135.5$, 139.4, 143.5, and 148, and continued in Figure 5.5 at $t = 151.9$, 156.3, 160.6, and 165. A depth of only the lower 1.1 vertical (z') wavelengths of the computational domain (the full domain is 4 vertical wavelengths high) is included in the figure, thus emphasizing the near-wall region. Two wavelengths are included in the x'-direction. Although the calculation was conducted for one horizontal wavelength, two wavelengths in x' are shown in the figures to enhance visualization.

The sequence of the flow development is markedly different for the shallow slope simulations. Here the flow appears to be quasi-steady, with a locally turbulent region of statically unstable fluid moving upslope together with the thermal front. This result supports the observations of Ivey and Nokes (1989), who conducted a related experiment in the laboratory over a 30^o slope. They describe a turbulent bore that passed through the boundary layer each wave period. The numerical experiments are consistent with this description. For example, note that at $t = 143$ there is a distinct

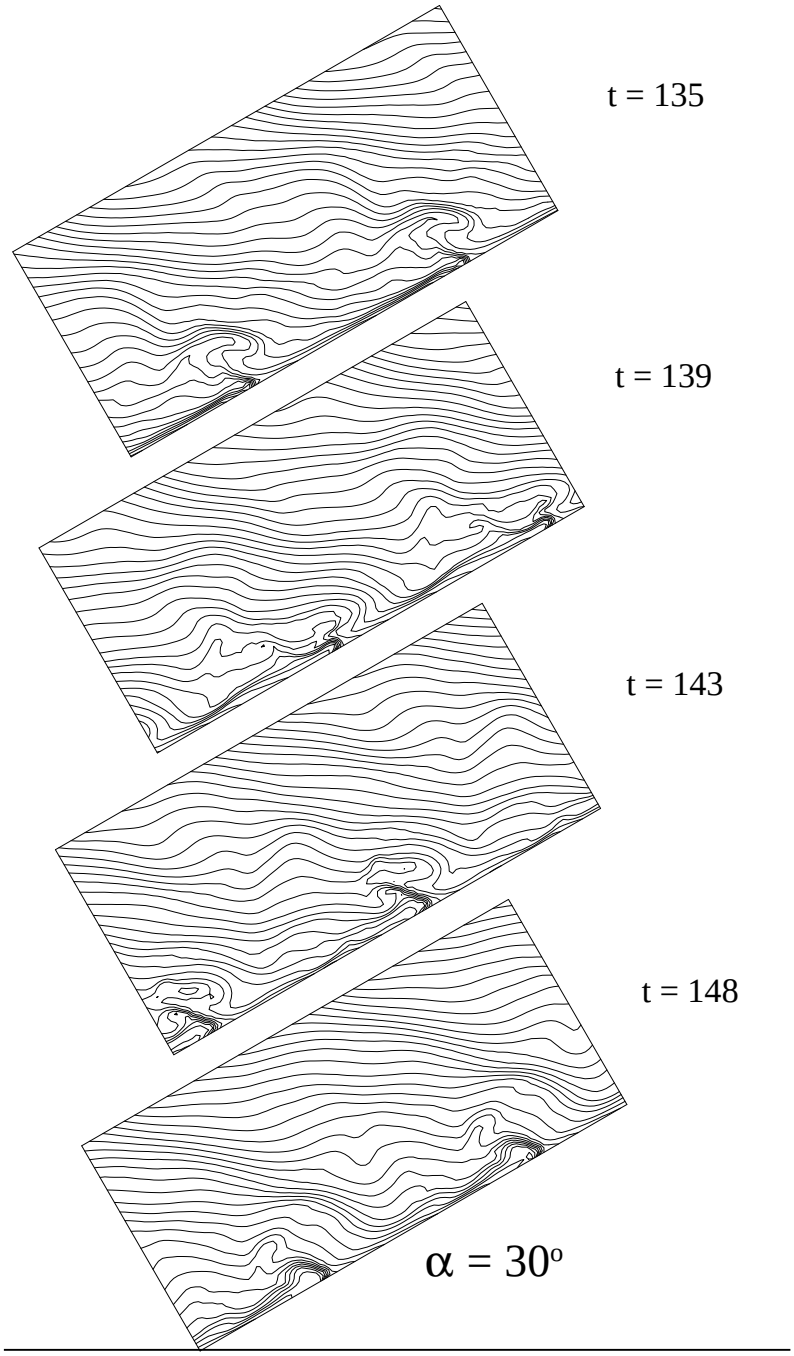

Figure 5.4: Isopycnals and statically unstable regions for Case 28 for a 30^o bottom slope at $t = 135.5$, 139.4, 143.5, and 148.

stratified region between the two bores. As with the previous cases, the thermal front moves upslope at the x' component of the phase velocity. Note that the frames at $t = 152$ and $t = 165$ are approximately one wave period apart and the location of the turbulent region is essentially the same.

The flow forms a pattern of quasi-steady, localized mixing. Interestingly, this type of mixing is just as efficient at dissipating the energy of the oncoming gravity wave as the temporally periodic mixing observed for the shallow slopes. Instead of the mixing occurring during only a portion of the cycle and over the entire breadth of the boundary layer, however, the mixing occurs throughout the cycle and across only a portion of the domain [see Figures 5.11, 5.12 (bottom) 5.28, 5.29 and 5.30]. Another difference between the two cases is that for the steeper slope, more energy is radiated away from the wall in the form of small scale gravity waves than for the shallow bottom slope (see Figure 5.51). The outgoing radiation is indicated by the strength of the energy flux across the upper open boundary (e.g., Figure 5.11) and the temporal variability in the signal of the oncoming gravity wave caused by reflected waves (e.g., Figure 5.7). The sequence shown in Figure 5.4 is continued in Figure 5.5 through a second wave period to illustrate the long term quasi-steady nature of the flow.

These figures may be compared with Figure 1.7 in Chapter 1 taken from Ivey and Nokes. The Schlieren images of the turbulent bore from their work appear to contain more complicated structure than are suggested by Figures 5.4 and 5.5; this difference, however, this may be an artifact of the measurements. The Schlieren images integrate all density fluctuations across the full width of the boundary layer (in the y-direction), whereas Figures 5.4 and 5.5 represent instantaneous fluctuations on a single y-plane. Additional figures below (e.g., Figures 5.28 - 5.30) show the three dimensional structure of the flow and suggest that, if the density fluctuations across the width of the boundary layer were shown in a single image, the results would be similarly complex.

Figure 5.6 pictures velocity vectors in the same planes as the density fields in Figure 5.4 above. Figure 5.6 shows the same fairly steady flow development as for

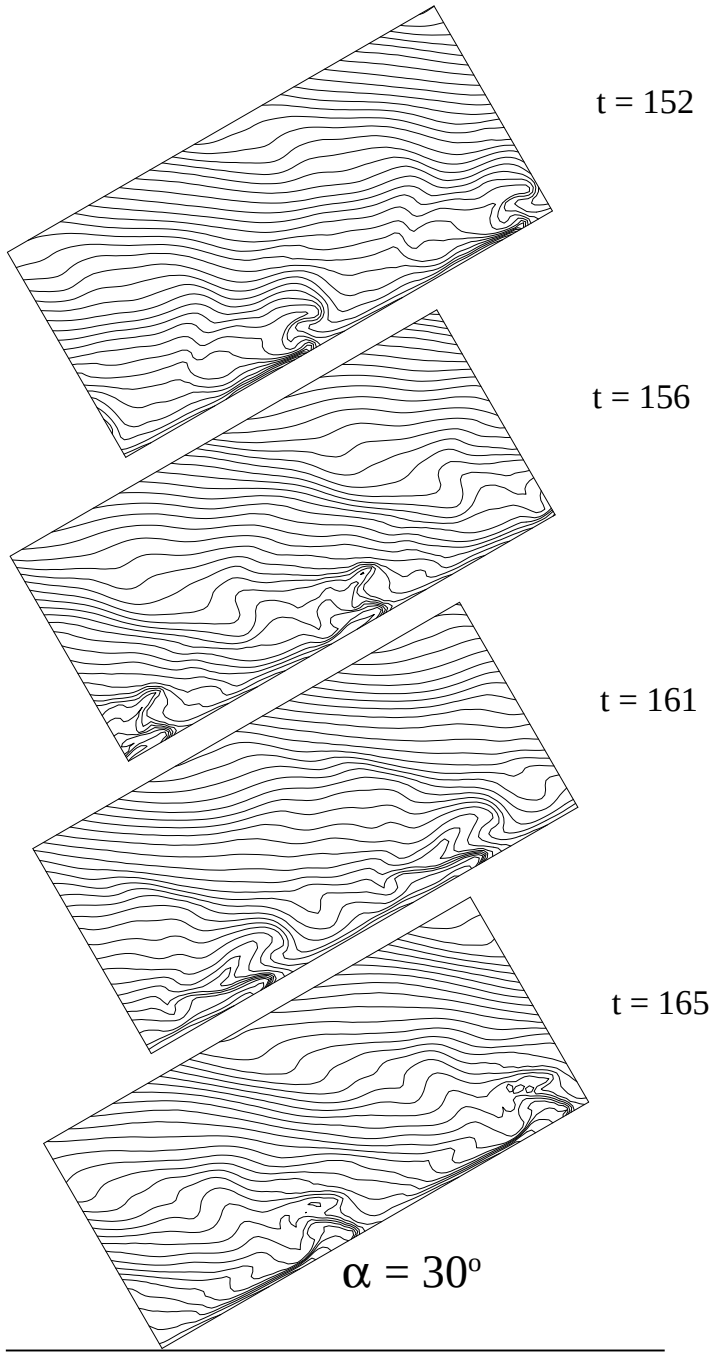

Figure 5.5: Isopycnals sequence for Case 28 for a 30^o bottom slope at $t = 151.9$, 156.3, 160.6, and 165, for Case 28.

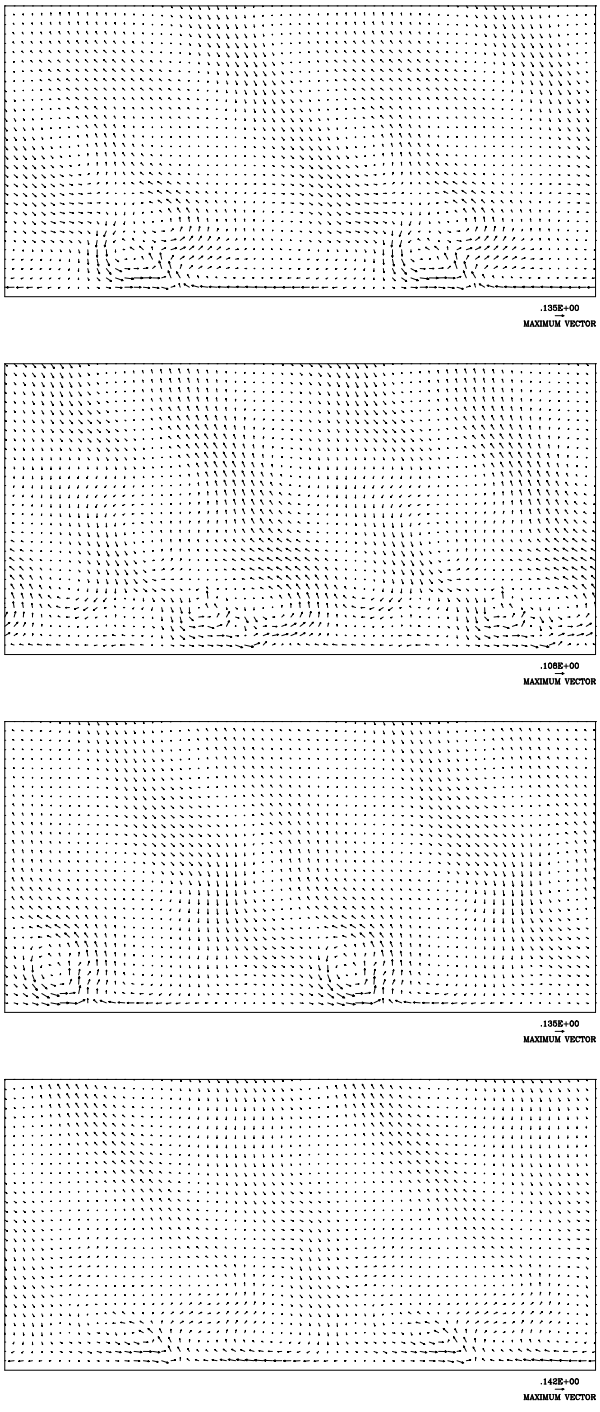

Figure 5.6: Velocity vectors for Case 28 for a 30^o bottom slope at the same times as Figure 5.4: $t = 135.5$, 139.4, 143.5, and 148.

the density fields. (The velocity vector figures should be rotated 30^o counter-clockwise to be in the same reference frame as the density contours, but they are larger and more visible when plotted as shown.) Strong currents converge in the region of the turbulent bore and create a strong region of local mixing and dissipation in the boundary layer. (Again this point is clarified by Figures 5.28 - 5.30.) The nonlinearities (roughly gauged by deviations from the currents of the linear oncoming wave field), as observed from the velocity field, appear to extend into the domain about twice as high as suggested by the depth of the overturned isopycnals in the turbulent bore. The shear of the oncoming wave is evident in the upper portions of the domain and merges into the bore region as an integral part of the dynamics occurring there. The bore might be termed the "turn around" zone for the internal wave, where the downward moving fluid and upward moving fluid change direction as the plane wave is interrupted by the wall. In the boundary layer there are regions of both convergence and divergence as the wave sets up a characteristic reflection pattern. It is noteworthy that the location of upwards flow ahead of the bore is out of phase with the upward motion in the oncoming wave.

5.2.1 Measurements at a Fixed Location

Figures 5.7 through 5.9 represent the flow in a different fashion. Here data are presented at a fixed x'-location along the z'-direction (ordinate) as a function of time (abscissa) for Case 28. The vertical dimension spans the distance from the bottom boundary to one wavelength (λ_z') away from the wall. The horizontal dimension covers from $t = 32$ to $t = 147$ for a total of 115 time units, equivalent to 9.1 wave periods. The data are similar to time series information collected in an open ocean experiment with a vertical array of velocity, temperature, and salinity probes.

Figure 5.7 shows constant contours of the density field as a function of time and the z' coordinate. In the upper regions of the figure the strongest part of the signal represents the oncoming gravity waves. The variability in the sinusoidal motion here is caused by smaller-scale motions reflected from the turbulent boundary layer, which has an approximate thickness of $\lambda_z/3$. In this presentation of the data, the amplitude

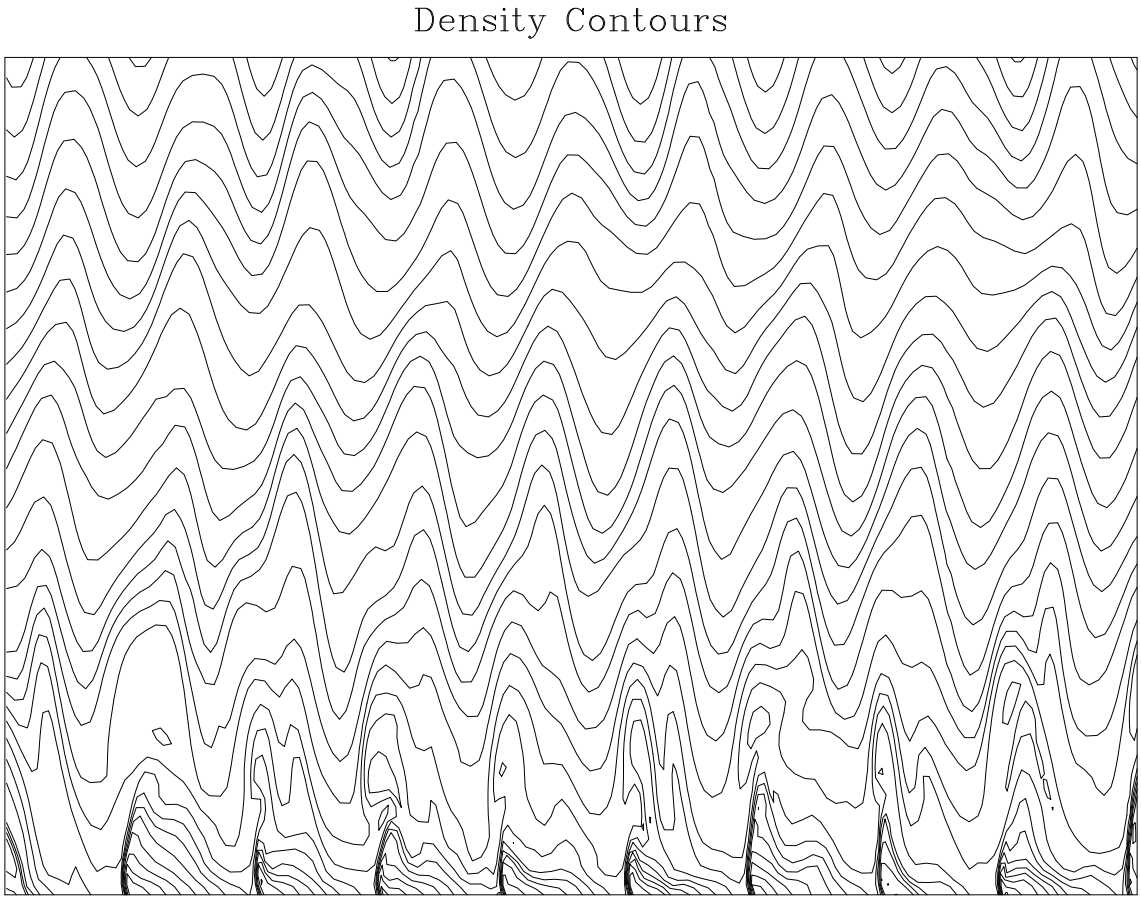

Figure 5.7: Density field measurements taken along a line perpendicular to the slope from $t = 32$ to $t = 147$ throughout 9 wave periods for Case 28.

of the oncoming waves appears quite large; however, this is an artifact of the scale chosen for the horizontal axis. The most significant feature of the flow evident in Figure 5.7 is the periodically strong density gradient near the bottom boundary. This density gradient is the signature of the turbulent bore and associated thermal front, passing through the location of the density probe each wave period. There are nine appearances of the thermal front, corresponding to the 9.1 wave periods during this portion of the experiment.

Above the location of the strong gradient are frequent regions of statically unstable density structures. The closed contours of the isopycnals indicate the passing of the flow within the bore. Details of the frequency and location of the overturned regions will be described below in the context of the boundary layer thickness.

Figure 5.8 shows the u'-component of the velocity field corresponding to the density field shown in Figure 5.7. Solid contours represent upslope flow; the dashed lines represent downslope flow. The strong convergence and divergence associated with the passing of the bore is evident in this figure. The steep density gradient of Figure 5.7 is located where there is a sudden transition from upslope to downslope flow, and hence strong convergence and localized upwelling. The upwelling fluid appears to be instrumental in establishing the overturned fluid in the turbulent boundary layer because, after flowing over the thermal front, it continues upward and is turned upslope. This process aids in bringing heavier fluid, located near the boundary (from both in front of and behind the thermal front), away from the wall into an unstable configuration. Figure 5.8 shows that, during the passing of the turbulent bore, the regions of overturned fluid, located between $0.1 < z < 0.3$, experience predominantly upslope flow. The variability in the velocity field indicates the departure of the flow in the boundary region from the regular nature of linear wave dynamics. Further away from the wall the signal of the oncoming waves is present, but significantly smaller than the magnitude of the velocities occurring in the boundary layer.

Figure 5.9 shows the v-velocity component at the same location as the previous figures. Here the main feature is the depth at which significant three-dimensionality exist. The v-velocity is produced during wave-breakdown and is strongest in the wave

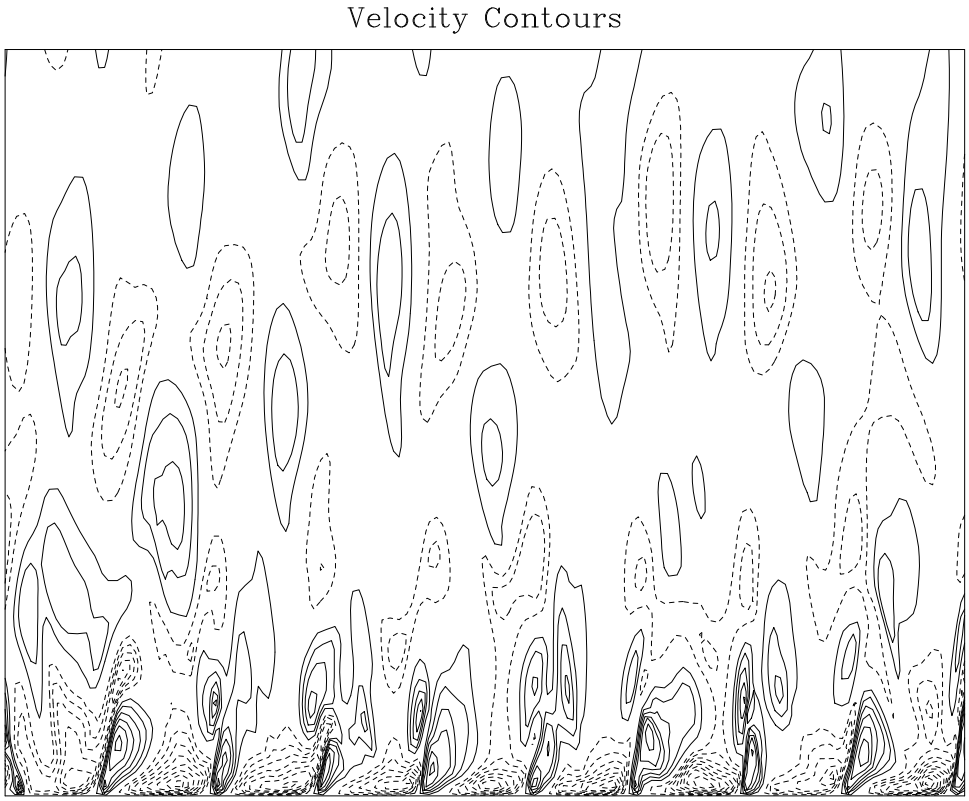

Figure 5.8: For Case 28, the u-velocity at the same location as in Figure 5.7 as a function of time with solid lines, upslope; dashed lines, downslope.

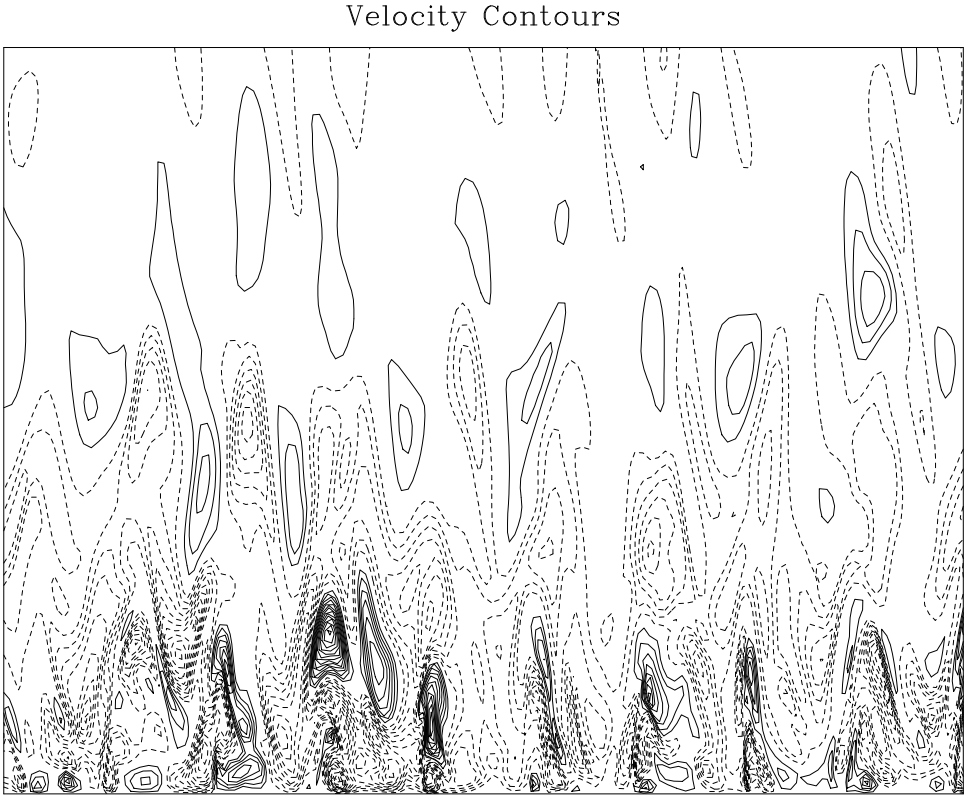

Figure 5.9: For Case 28, the v-velocity at the same location as in Figure 5.7 as a function of time with solid lines, out of the plane; dashed lines, into the plane.

overturning region. As observed above, there is a definite periodicity in the intensity of the v-velocity associated with the passing of the thermal front. While the strongest three-dimensionality occurs within a height of approximately $\lambda_z/4$, significant interactions extend to approximately $0.7\lambda_z$.

5.2.2 Energetics

For the simulation with the 30^o bottom slope, the energetics of the flow develop significantly differently from those for the shallower slopes. Just as the character of the flow changed from periodic mixing across the entire boundary layer to localized constant mixing, the energetics show significant departure from the behavior of cases described previously. Figure 5.10 shows the terms of the volume integrals of the terms of the kinetic energy equation (3.111) from startup to $t = 170$. Figure 5.11 below shows the total energy terms out to $t = 215$, the full duration of this simulation. The scales of the abscissa (time axis) differ between Figures 5.10 (Kinetic Energy) and 5.11 (Total Energy) in order to emphasize different points. Presenting the kinetic (or potential) energy terms out to $t = 215$ would make Figure 5.10 more cluttered and difficult to interpret because of the rapid oscillations in the buoyancy flux and time rate of change of kinetic energy. After approximately $t = 50$ the energetics of the flow develop in a quasi-steady manner.

A dominant feature of the terms of the kinetic energy equation in Figure 5.10 is the rapid oscillation of the buoyancy flux. Associated with this is the time rate of change of kinetic energy, which follows the buoyancy flux closely. The key difference between this flow and those previously discussed is the significantly shorter wave period. The wave period is 4π and the buoyancy period is 2π. The oscillations in the buoyancy flux occur at approximately the buoyancy period. For example, there are 24 maxima and minima in the buoyancy flux between $t = 55$ to $t = 215$, or approximately two per buoyancy period.

While not all maxima have the same magnitude, the consistent pattern suggests that oscillations at the buoyancy frequency are a dominant feature of the energetics of the flow. Simulations for shallower bottom slopes, discussed below, indicate that the

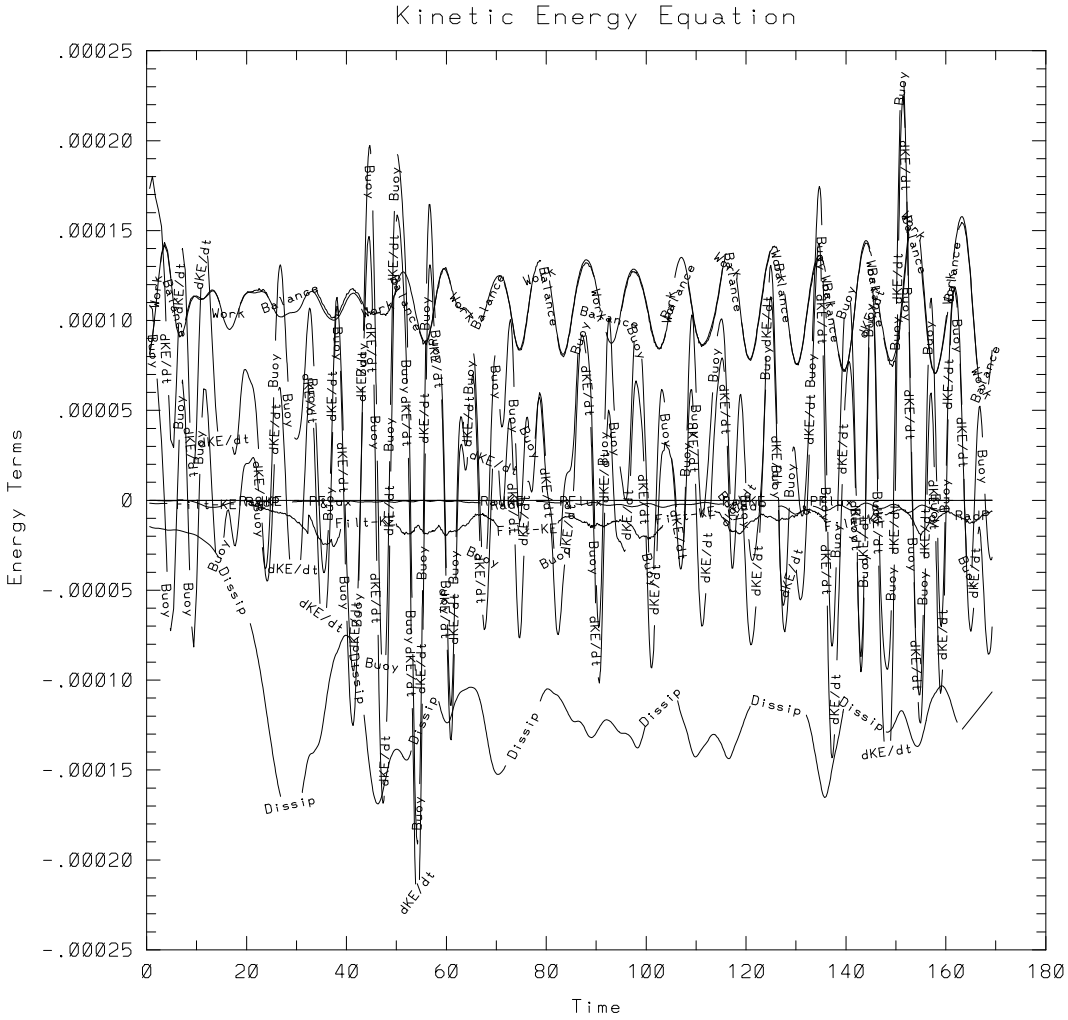

Figure 5.10: Evolution of terms in the kinetic energy equation are plotted for Case 28. See text for details.

buoyancy flux oscillates at twice per wave period, independent of the ratio of the wave and buoyancy period. The time scale for viscous decay at this Reynolds number (e.g., for a turbulent patch to dissipate approximately half its energy) is approximately 10-15 time units, similar to the result for the shallow slope case. For the 30^o slope the turbulence generated during one wave period ($T_w = 12.6$) has not decayed before the next period of turbulence begins. Consequently, the flow remains strongly three-dimensional continuously, with mild fluctuations, in a quasi-steady manner. For the 9^o slope the time scales for wave forcing ($T_w \approx 40$) and turbulence decay ($T_d \approx 10$) are widely separated. The flow has time to restratify and relaminarize in the boundary layer between each mixing cycle.

While the mixing cycles are qualitatively different between the 30^o and 9^o slope cases, they are not the only differences. In addition, the turbulence in the steep slope case is primarily localized about the position of the thermal front, which is in the form of a turbulent bore. For the shallow slope case, the turbulence extends across the breadth of the horizontal wave length in the boundary layer.

The difference appears to be related to the geometry of the problems, particularly the aspect ratio of the horizontal and vertical wavelengths of the oncoming wave, and to the steepness of the bottom slope. Turbulent patches develop initially above the location of the thermal front and have a characteristic thickness of approximately $\lambda_z/3$. After the turbulence is formed it then appears to favor horizontal spreading.

For the shallow slopes, horizontal spreading can more easily reach across the breadth of the boundary layer because the bottom slope has a relative small rise, and the turbulence is less inhibited by having to overcome larger stratification. An additional contribution to horizontal spreading comes from the thermal front moving upslope approximately one-quarter of a wavelength during wave breakdown. During this period the thermal front leaves turbulence in its wake at different mean depths.

Conversely, the steep slope effectively partitions the boundary layer into regions above and below the turbulent bore and helps to confine the turbulence to a localized region. The fluid in the boundary layer above (ahead) and below (behind) the bore are more insulated from the turbulence by the stratification. An additional influence

appears to be the ratio of the waves vertical and horizontal wavelengths of the wave. Wave overturning and breakdown develop within the general framework of the wave's vertical and horizontal dimensions. For waves propagating at shallow angles this leads to more horizontally oriented development while the steep slope is comparatively more vertically oriented.

A consequence for the energetics of the quasi-steady wave breakdown for the steep slope case is that the dissipation rate is nearly constant throughout the simulation after a short startup period. This differs qualitatively from the shallow slope case. The explanation again appears to be that the turbulence created in the boundary layer has insufficient time to decay before the next turbulent event begins. Note finally from Figure 5.10 that the dissipation rate is much larger than the energy loss by filtering; that is, the simulation is well resolved on the 129 x 129 x 130 point grid.

A second feature apparent from Figure 5.10 is that oscillations in the magnitude of the work input grow in time. This is caused by the radiation of small scale disturbances from the boundary layer upward into the wave forcing region. As discussed above, though the work input is changed by this reflection, the amplitude of the oncoming waves remains steady.

The terms of the potential energy equation present a description similar to the kinetic energy equation and are not presented here.

Figure 5.11 shows the terms in the total energy equation for Case 28. The dominant terms are the work input and loss of energy by turbulent dissipation. The net result is a near constant balance between the major terms in the total energy equation. After approximately $t = 140$ there is a non-zero amount of energy in the "radiation" term, representing the flux of energy out of the top of the computational domain into the sponge layer. The overall balance of energy contains some errors (up to 5%) at early times ($t < 60$), when the calculation was started out on a low resolution grid, but the balance is very good at later times, when the calculation was continued on a higher resolution grid. Because of the quasi-steady nature of the flow development, it is improbable that the imbalance of energy at early times has an influence on the accuracy of the simulation at later time.

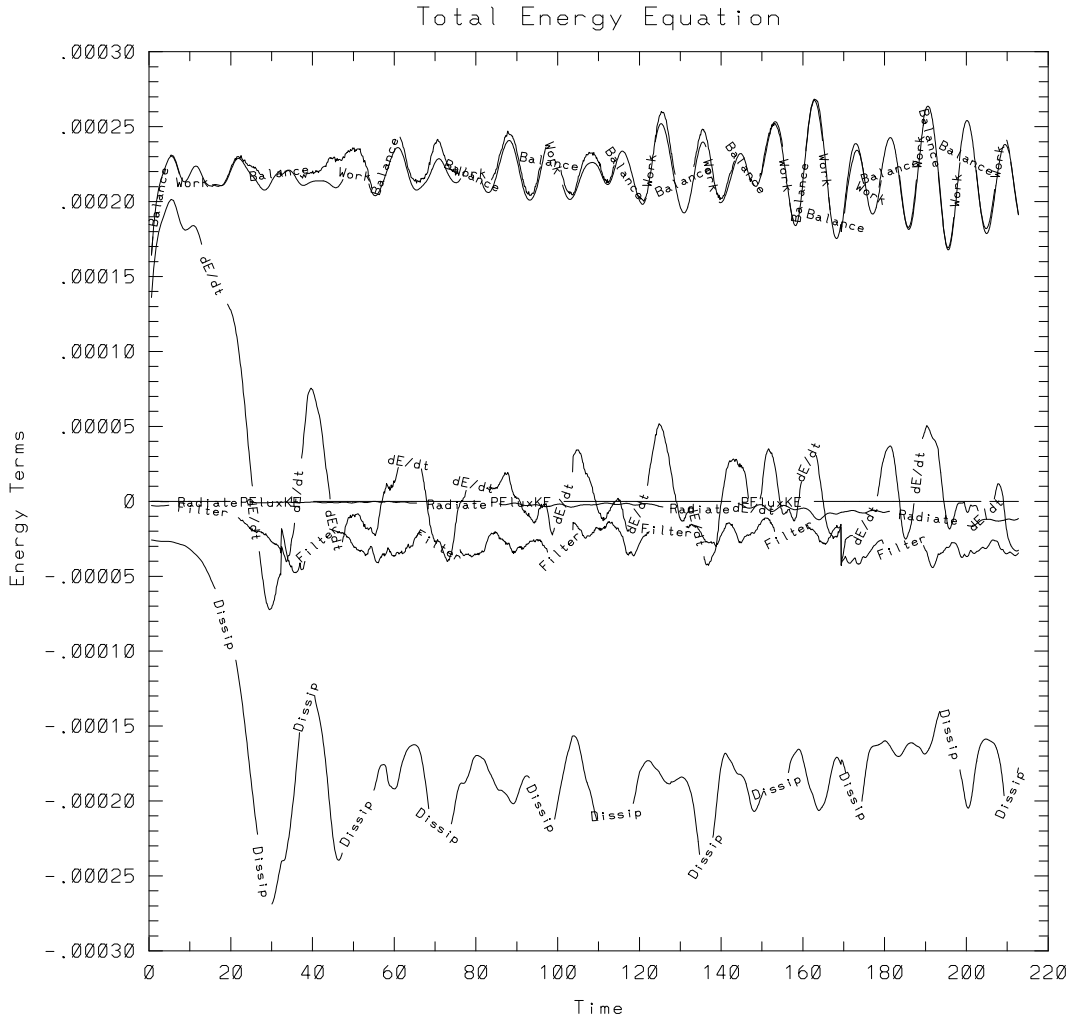

Figure 5.11: Evolution of terms in the total energy equation plotted for Case 28.

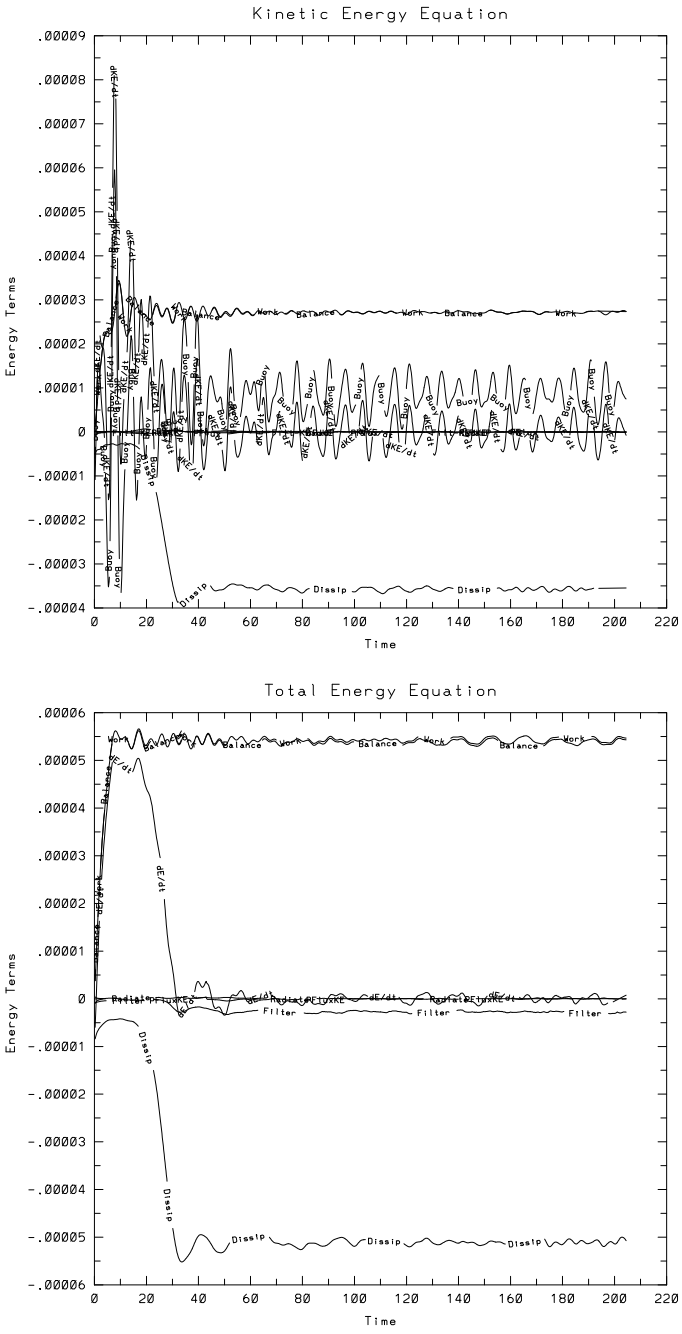

Figure 5.12: The terms of the kinetic (top) and total energy equations are plotted for Case 26.

Figure 5.12 shows the kinetic and total energy equations for Case 26, a simulation with $Re = 800$ and $Ri = 625$ over a 30^o slope. The amplitude of the oncoming wave for Case 26 is one half the wave amplitude in Case 28, while the other parameters (viscosity, stratification, wavelengths) were held constant. Therefore the Reynolds number is approximately one-half and the Richardson number four times the values of Case 28. This flow exhibited moderately weak three-dimensionality in a turbulent bore similar to that shown in Case 28 above. Here the steadiness of the wave forcing and the dissipation rates are remarkable. The buoyancy flux oscillates at approximately the buoyancy frequency as before, but now exhibits much weaker oscillations compared to the higher Reynolds number simulation. Interestingly in this case, after approximately $t = 30$ the buoyancy flux is always positive, illustrating the previous point (see Section 4.6) that there is a net flux of potential energy into kinetic energy, compensating for the strong sink of kinetic energy by viscous dissipation near the wall.

Though the flow develops in a somewhat random fashion within the region of the turbulent bore, the overall energetics of the flow exhibit many steady properties, after the short startup period when $t < 30$. In this case, turbulence in the boundary layer fails to cause strong radiation of wave energy from the wall, or to cause the work input to oscillate significantly.

Figure 5.13 compares dissipation rates for two critical angle simulations over 9^o and 30^o bottom slopes (Cases 15 and 28 from Table 4.1). Case 15 was conducted at $Re = 3600$ compared to $Re = 1700$ for Case 28. The different mean values for the dissipation rates depend on the scaling, since the plots are dimensional. They show that there is a higher average dissipation rate for Case 15, which is related to the greater energy content of the oncoming waves. The important point from the figure is the contrast between the cyclical nature of the dissipation rate for the shallow slope case (9.2^o), and the much more constant rate of dissipation for the steep case (30^o). The difference is not attributable to the difference in Reynolds number. Additional simulations conducted over 9^o bottom slopes (e.g., Cases 12-14) at Reynolds numbers between 1200 and 2800 exhibited the same periodic wave breakdown and dissipation,

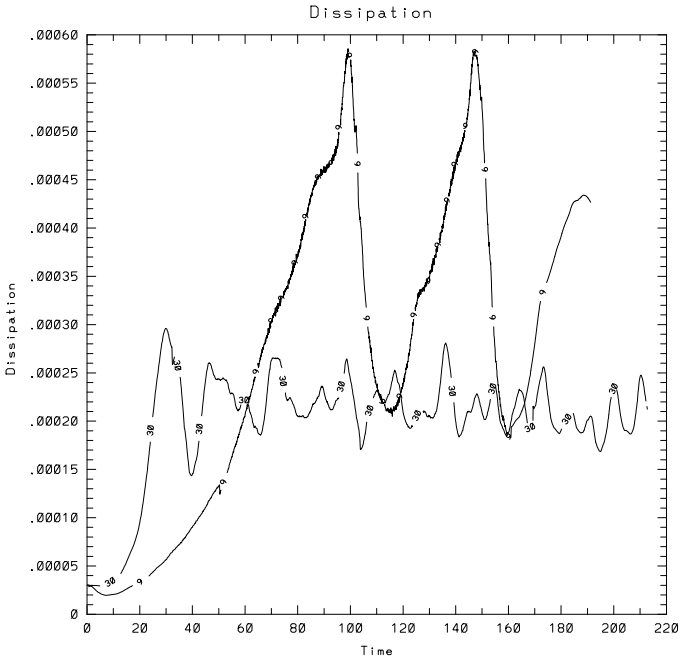

Figure 5.13: Evolution of dissipation rates for 9^o and 30^o slopes.

while additional turbulent simulations over the 30^o slope exhibited steady dissipation rates (e.g., Figure 5.12).

It is of interest that the observed behavior of breaking internal waves has significant similarities with breaking surface waves on a beach. Eriksen (1995) and Thorpe (1987b) have used the analogy between the turbulent boundary layer that develops from internal wave breakdown over sloping topography to the surf zone at a beach. Sorenson (1993) has summarized turbulent wave breakdown of surface gravity waves, occurring in the near shore surf zone, into four types or classes. He describes these as spilling, plunging, collapsing, and surging. The two most commonly observed types are spilling and plunging. Spilling breakers create turbulence over large regions and are more common for smaller bottom slopes (and smaller amplitude waves). Plunging breakers, the type that curls forward and plunges all at once, create more localized turbulence (similar to a turbulent bore) and are more frequent for steeper bottom slopes (and larger amplitude waves). While the mechanisms differ between breaking

surface and internal gravity waves, the type of wave breakdown is a strong function of the bottom slope (and amplitude).

5.3 Intermediate Slopes

A series of nine three-dimensional simulations, Cases 16 - 24, was conducted for critical angle reflection over a bottom slope of 20^o. These intermediate slope simulations exhibited characteristics of both steep (30^o) and shallow (9^o) slope wave breakdown. The wave period for these simulations is 18.4, approximately three times the buoyancy period of 2π. The 20^o slope cases compare more closely with the shallow than the steeper slope simulations in that the mixing is cyclical and related to the wave period; they also exhibit, however, behavior more characteristic of the steeper slope cases, such as strong radiation of internal gravity waves from the turbulence and the rapid exchange of boundary layer fluid into the interior. A description of the flow development and energetics are given for Cases 19 and 21 in this section. Additional discussion and comparison of the full set of the nine critical angle simulations over a 20^o bottom slope appear below in Sections 5.6 - 5.10 and 6.1 - 6.4.

Figures 5.14 and 5.15 shows isopycnals of the flow development for Case 21, with $Re = 1800$ and $Ri = 92$. The flow fields illustrated by these figures are nearly identical to the flow fields from Case 19, with $Re = 1100$ and $Ri = 110$. The two cases simulated oncoming gravity waves of the same amplitude and length scales, differing only in the viscosity of the fluid. The Richardson numbers vary slightly because the more viscous flow damps the velocity of the oncoming waves. The large-scale features of the flows develop in similar fashions.

The four frames of Figure 5.14 (in order: upper left, upper right, lower left, lower right) are at $t = 78.8$, 80.6, 82.6, and 85.1. The frames of Figure 5.15 (in the same order) are at $t = 88.1$, 91.1, 93.9, and 96.4. Together, the figures depict the flow through approximately one wave period. The figures are shown to scale and the dimensions are 1.1 λ_z in the vertical and $\lambda_x = 1.2\lambda_z$ horizontally. As in other examples, to enhance the comparisons the figures are presented without rotating them counter-clockwise; the figures should be rotated 20^o to align the bottom slope in its

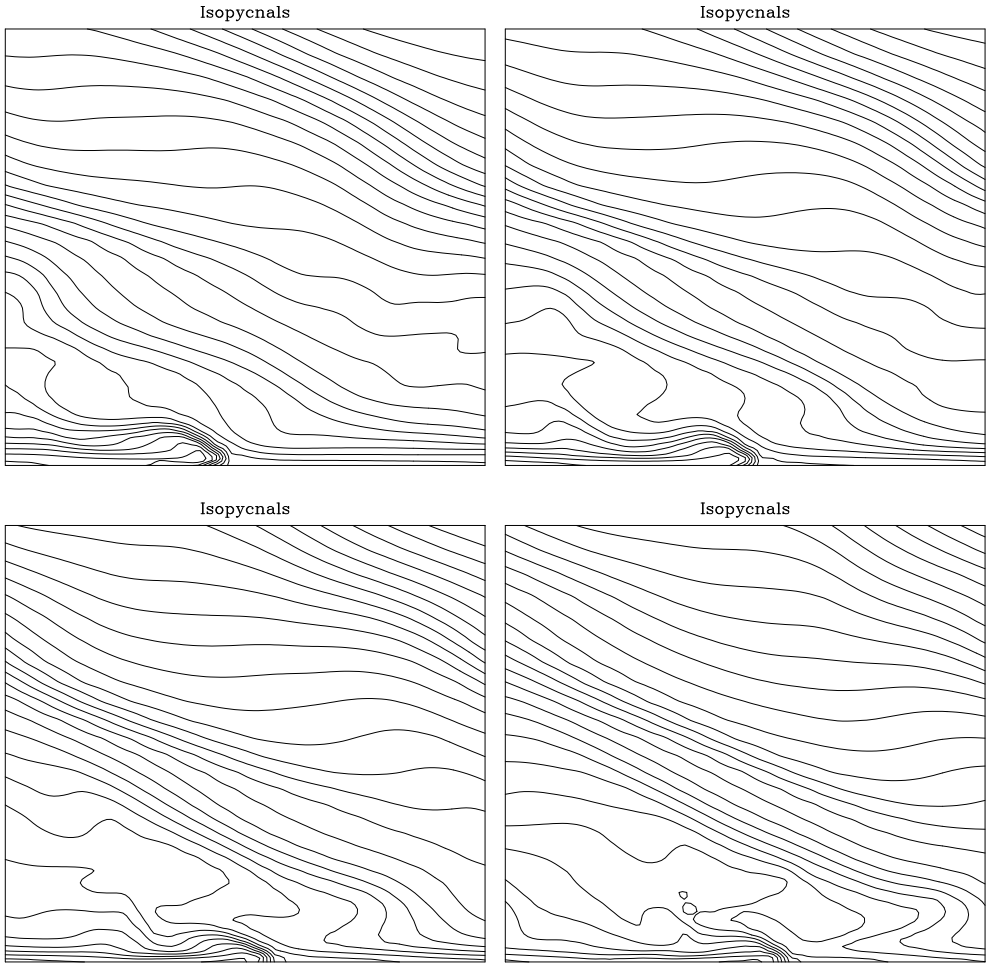

Figure 5.14: For a bottom slope of 20^o (Case 21), isopycnals of the flow in the near wall region at $t = 78.8$, 80.6, 82.6, and 85.1. (In order: upper left, upper right, lower left, lower right.)

natural reference frame. The first frame of Figure 5.14 shows the thermal front in the near wall region. This feature moves upslope as time progresses and develops large scale statically unstable density inversions above and in the lee of the front. The oncoming gravity waves can be seen in the upper portion of the figures.

As time progresses, the instability breaks down and the wave energy is dissipated by small scale mixing, which reaches a peak at approximately $t = 88$ (Figure 5.15, Frame 1.) Between $t = 88$ and 96 the boundary layer restratifies and relaminarizes, decreasing the three-dimensionality of the flow as measured by indicators such as the volume integrals of v^2, and $\frac{\partial w}{\partial y}$, which reached a maximum at about $t = 84$. By the last frame of Figure 5.15, the flow has returned to a situation very similar to the initial frame. Additional analysis, given below, shows that the pattern repeats itself during the next wave period with only minor variation. The variability may be attributed to the complexity of the nonlinear interactions of the turbulence during the subsequent (and previous) mixing cycles.

Generally, the flow development and vorticity dynamics follow the flow description of the 9^o slope simulations described in Chapter 4. Elements of the present flow are shown in detail to permit comparison with the laboratory results of Taylor (1993). Taylor studied a similar flow involving critical reflection over a 20^o bottom slope. A primary difference between his study and this one is that Taylor's wave field was generated in a fashion to produce a horizontally-propagating mode one internal wave (one vertical mode filling the depth of the fluid), rather than an oncoming wave train propagating at an angle to the horizontal. Depending on the frequency of the waves the laboratory experiments produce a situation in which the horizontal wavelength of the internal wave can be long compared to the length of the bottom slope. Related to this there are significant top and bottom effects. Energy is strongly dissipated in the top corner of the tank, and large scale recirculation is established between boundary mixed fluid and interior fluid on the scale of the tank depth. This situation differs from idealized oceanic conditions for continental shelves and slopes, for which the bottom slopes are long compared to the wavelength of the internal waves, but may be similar to conditions from seamounts and ridges or to tidally generated waves (Thorpe

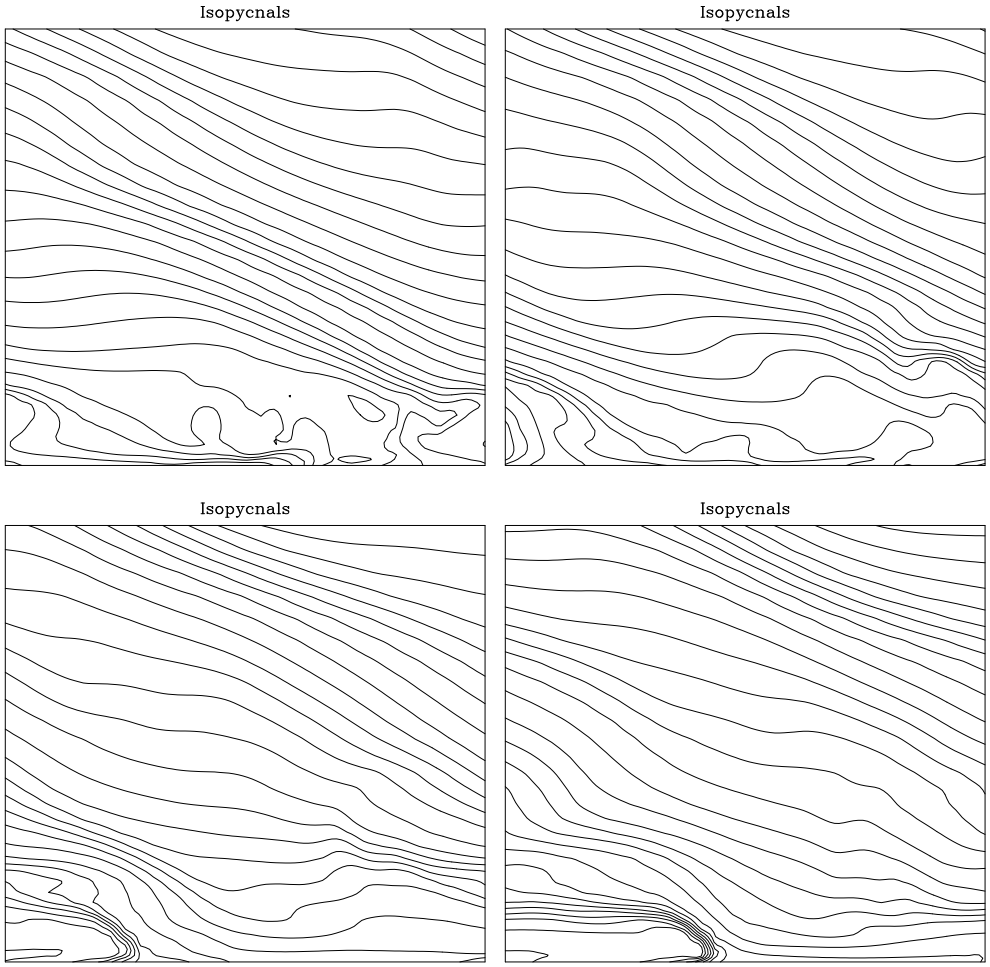

Figure 5.15: The sequence in Figure 5.14 is continued in the same order through one wave period at times $t = 88.1$, 91.1, 93.9, and 96.4, for a bottom slope of 20^o (Case 21).

1987a). The numerical experiments, using periodic alongslope boundary conditions, model the situation of a bottom topography long compared to the wavelength. The differences between oncoming waves in the laboratory and numerical experiments suggest that the laboratory methods might be a better model for internal tides while the numerical model might be better for open ocean internal waves.

Despite the significant differences in method, many of the flow features that develop are similar. Figure 4.6 showed typical results taken from Taylor's study, during a phase of upslope flow. A result of the type of wave used for the wave tank experiments is that the mixing results are phase locked with the wave period. This restriction is overcome in the numerical simulations, where the dynamics are free to develop at rates different from the wave period.

In the simulations, the boundary layer experiences a spatially periodic oncoming wave, including regions of both upslope and downslope flows occurring all of the time. Figures 5.16 and 5.17 show two-dimensional velocity vectors for Case 21, at the same times as Figures 5.14 and 5.15. As before the calculations were carried out on a higher resolution (3-D) mesh, but are presented on a coarse, uniform mesh to enhance the visibility of the larger scale features. The magnitude of the velocity vectors in each frame are scaled so that the maximum vector reaches across one grid spacing. The maximum velocities for the frames are 0.162, 0.166, 0.131, and 0.115, in the following order: upper left, upper right, lower left, lower right.

The location of the thermal front is indicated in the first three frames of Figure 5.16 by the upwelling seen in the velocity field near the wall. Above the thermal front, there is an upslope flow across a considerable portion of the horizontal (x') domain. The upslope phase of the flow, especially evident at $t = 80.6$ and 82.6, extends from the downward flow of the oncoming gravity wave and spreads out in the horizontal (x') direction. As the jet of fluid moves upslope parallel to the boundary it carries denser fluid, creating a locally statically unstable arrangement. This mechanism leads to overturning and breakdown in the boundary layer. In addition, there is a strong region of shear between upwelling fluid from the thermal front and the upslope jet. The turbulent phase of the wave cycle is apparent during the next two frames (Frame

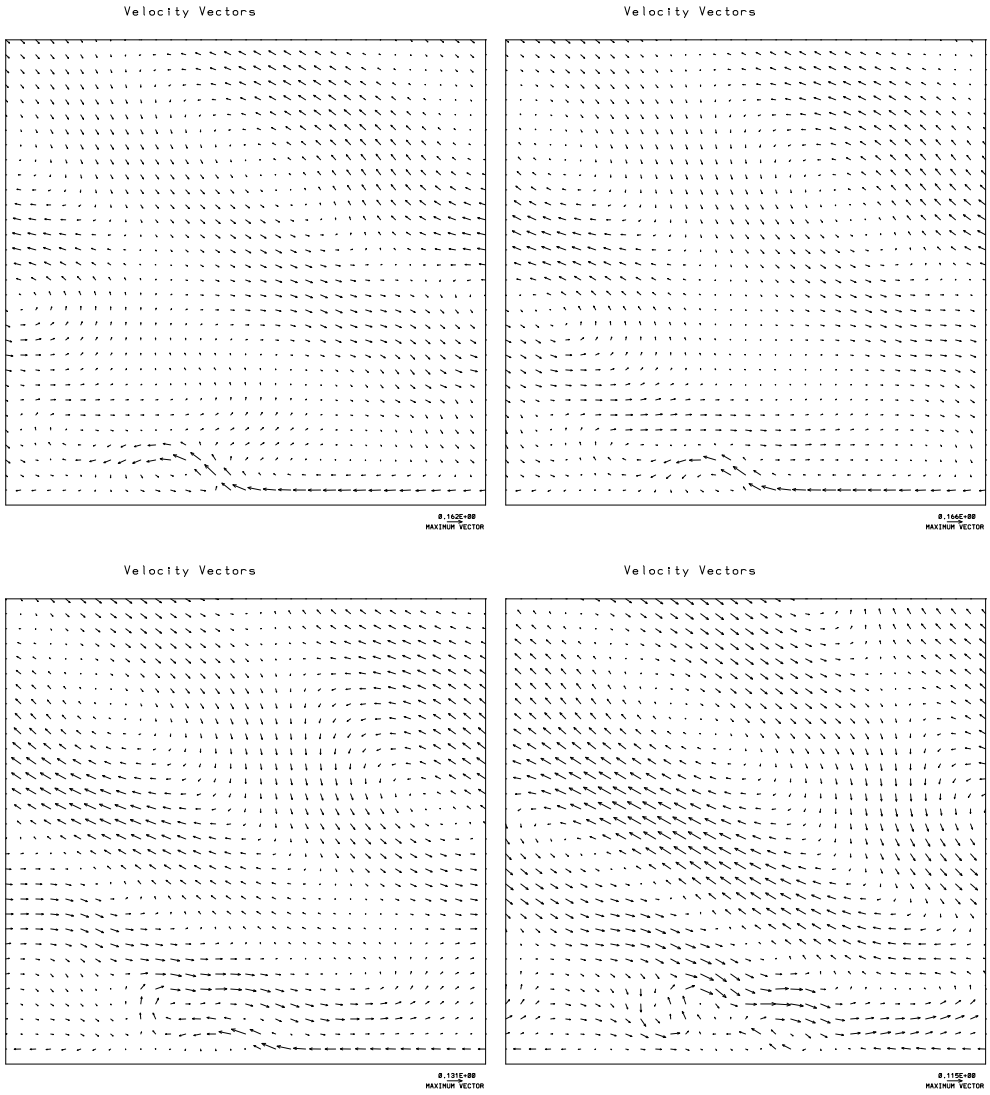

Figure 5.16: Velocity vectors corresponding to the same sequence as Figure 5.14 are shown throughout one wave period at t = 78.8, 80.6, 82.6, and 85.1, for a bottom slope of 20^o (Case 21).

4 of Figure 5.16 and Frame 1 of Figure 5.17). Throughout the wave cycle, advection from the oncoming wave shear plays an important role in the development of the boundary layer. During mixing, the phase of the wave with downward flow injects ambient stratified fluid into the base of the boundary layer, while the phase of the wave with upward flow extracts fluid from the top of the turbulent boundary layer.

During the period of boundary layer relaminarization and restratification, the flow near the boundary is predominantly downslope. For example, Frame 3 of Figure 5.17 shows a strongly downslope flow in the boundary layer region located at approximately the distance from the wall where earlier the upslope flow had set up static instabilities (e.g., Frame 3 of Figure 5.17). Notice also the visible perturbations to the signal of the oncoming wave that indicate large-scale vertical circulations extending a considerable distance from the wall, to at least a height of $0.8\lambda_z$.

While the oscillation of upslope and downslope flow are consistent with the observations of Taylor, they arise from different mechanisms. The numerically simulated flows are not uniformly upslope or downslope across the full breadth of the boundary layer in the region $0.1 < z < 0.3$. It is clear, however, that localized regions leading to the development of turbulence and wave breakdown are set up by similar patterns to those observed in the laboratory. The formation of locally unstable regions appear to be related to a complicated nonlinear interaction between the phase of the oncoming wave and buildup of energy (radiated waves) in the boundary layer region. The simulations indicate that turbulence is correlated with the development of locally statically unstable regions.

A description of the energetics of Case 19, with $Re = 1100$ and $Ri = 110$, are summarized here. These are followed by a discussion of the total energy equation for Case 21. Note also that Figure 4.5 presented plots of the kinetic and total energy equation balances for another 20^o slope simulation, Case 24, which differed from Case 21 only in that the x dimension was twice as large, and two horizontal wavelengths of the oncoming wave were generated in the wave forcing region. The results of Cases 21 and 24 are very similar and are discussed again in Section 6.1.

Figure 5.18 (top) shows the volume integrals from the kinetic energy equation for

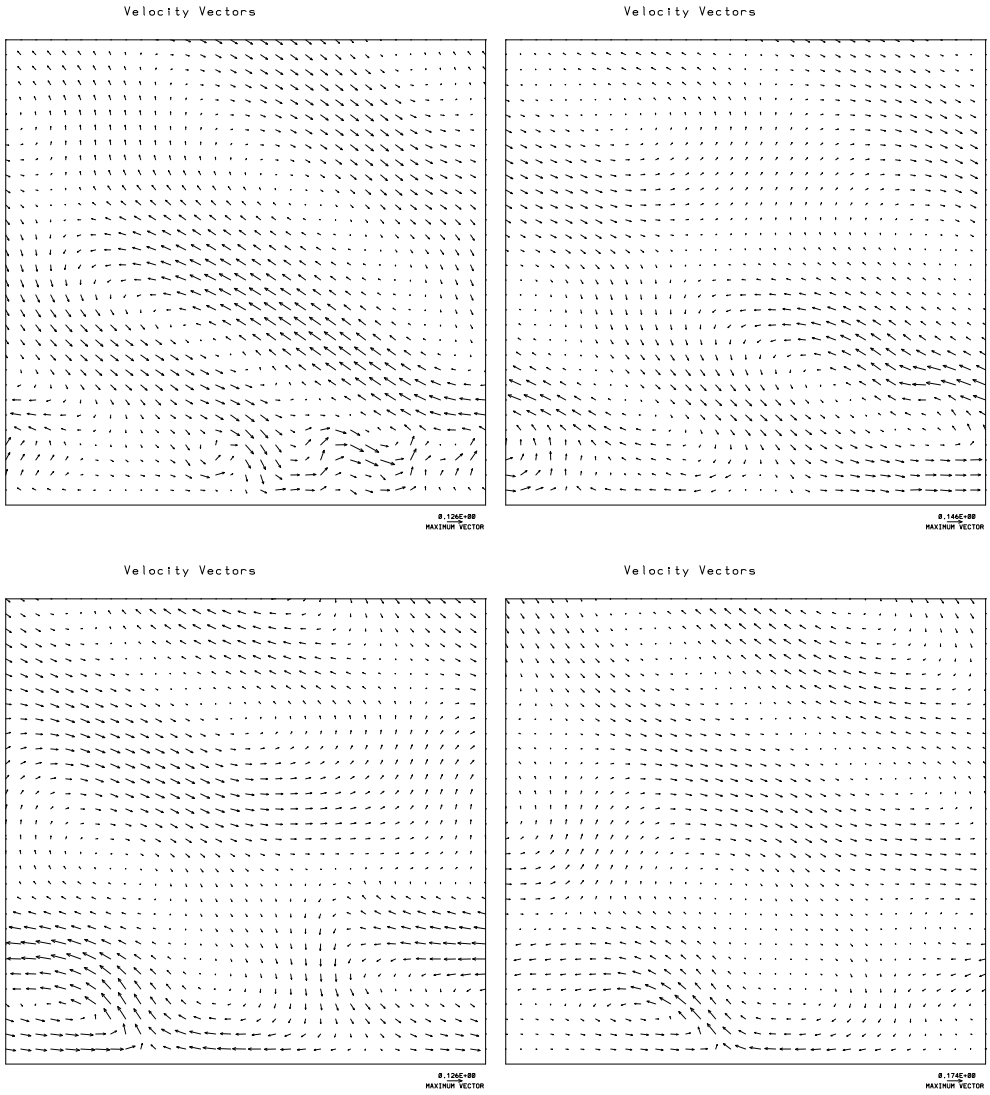

Figure 5.17: Velocity vectors corresponding to the same sequence as Figure 5.15 are shown throughout one wave period at times t = 88.1, 91.1, 93.9, and 96.4, for a bottom slope of 20^o (Case 21).

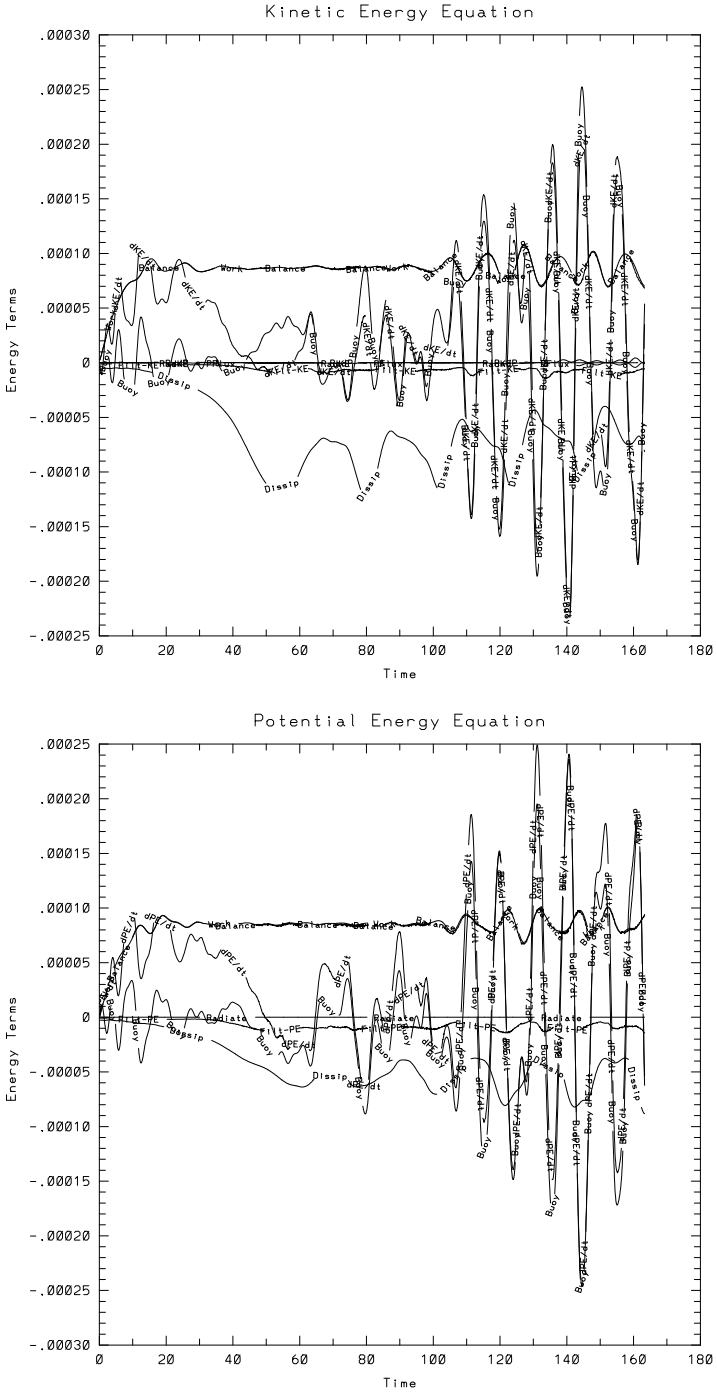

Figure 5.18: The terms of the kinetic (top) and potential (bottom) energy equations plotted for Case 19.

Case 19. The balance of kinetic energy indicates a high degree of energy conservation in the simulation. The first mixing cycle has a peak at $t = 56$. Subsequent maxima, confirmed by additional measures, occur at $t = 80$, 102, 122, and 144, indicating mixing intervals of 24, 22, 20, and 22. These may be compared to the wave period of 18.4.

The dominant balance in the kinetic energy equation is between the energy input and the oscillatory dissipation rate. After approximately $t = 100$, however, the integrated buoyancy flux becomes large, indicating the strength of the vertical transport occurring both in the boundary layer and in the interior fluid. The period for the buoyancy flux oscillations is 10, or approximately twice per mixing cycle. It will be seen below that the buoyancy flux oscillates approximately two to three times per mixing cycle for simulations with cycles lasting as long as $T_M = 150$. The buoyancy flux oscillations appear to be correlated with the wave dynamics rather than the buoyancy period, which is 2π.

The weak oscillation in the work input term after $t = 110$ indicates that by this time radiated waves from the turbulent boundary layer have reached upwards into the wave forcing region. Note, also, that the dissipation rate of kinetic energy by the filter is approximately an order of magnitude smaller than the kinetic energy dissipation rate.

The potential energy equation balance, presented for Case 19 in the bottom panel of Figure 5.18, is quite similar to the kinetic energy balance. The major difference is that the potential energy dissipation rate (χ) is approximately 1/2 the kinetic energy dissipation rate (ϵ). In addition, the ratio of χ to the energy removal by the filter (χ_f) is somewhat higher. The filter losses of kinetic (ϵ_f) and potential energy are approximately equal, but since $\chi \approx \frac{\epsilon}{2}$, $\frac{\chi_f}{\chi} > \frac{\epsilon_f}{\epsilon}$.

The two largest terms in the potential energy equation are the transfer of energy between kinetic energy and potential energy by the buoyancy flux and the time rate of change of potential energy in the system ($\frac{\partial PE}{\partial t}$). The buoyancy flux can be as much as 2.5 times larger than other significant terms, e.g., work input and dissipation rate. While this seems to suggest a buoyancy driven flow, it is the interaction of the internal

wave field with the boundary that creates strong upslope and downslope flows, which in turn make the dominant contribution to the buoyancy flux.

Figure 5.19 shows the volume integrals of the terms of the total energy equation for Cases 19 (top) and 21 (bottom). The total energy equation is the sum of the kinetic and potential energy equations; the buoyancy flux cancels from the sum. A comparison between the figures indicates that the results are very similar (the time axis is shorter for Case 21). The two cases are compared in more detail below, in Section 6.1. The dominant balance in the total energy equation is the nearly steady positive work input balanced by the oscillatory dissipation rate. For both cases there is a net gain of energy with time (see Figure 4.29) as indicated by the time rate of change of energy remaining predominantly positive. This buildup of energy is discussed below in Section 5.8. The two simulations were conducted at low resolution, 65 x 33 x 130. An increase of energy removal by the filter for the higher Reynolds number case (bottom) is evident, but the overall balance of energy is considered satisfactory. The quasi-periodic nature of the mixing cycle is evident in both of these turbulent simulations.

The intermediate slope case (20^o) belongs to the class of flows with the 9^o slope, in which the flow has time to restratify and relaminarize between mixing events. The 20^o slope case is particularly useful for the numerical investigation because its higher frequency waves allow simulations to be carried out for a larger number of mixing cycles to determine the flow development as it achieves a quasi-steady state.

The key distinguishing feature of steep and shallow flows appears to be the ratio of the wave period to the buoyancy period. For ratios greater than about 3:1, the flows develop a thermal front and periodic mixing; for ratios less than 2:1, a turbulent bore develops, which mixes the fluid in a localized region of the boundary layer. While the turbulent bore may be described as a turbulent thermal front, the thermal front (in the shallow slope cases) would not be described as a turbulent bore because it is not locally turbulent. Other significant factors, such as wave amplitude and Reynolds number, do not change the flow classification.

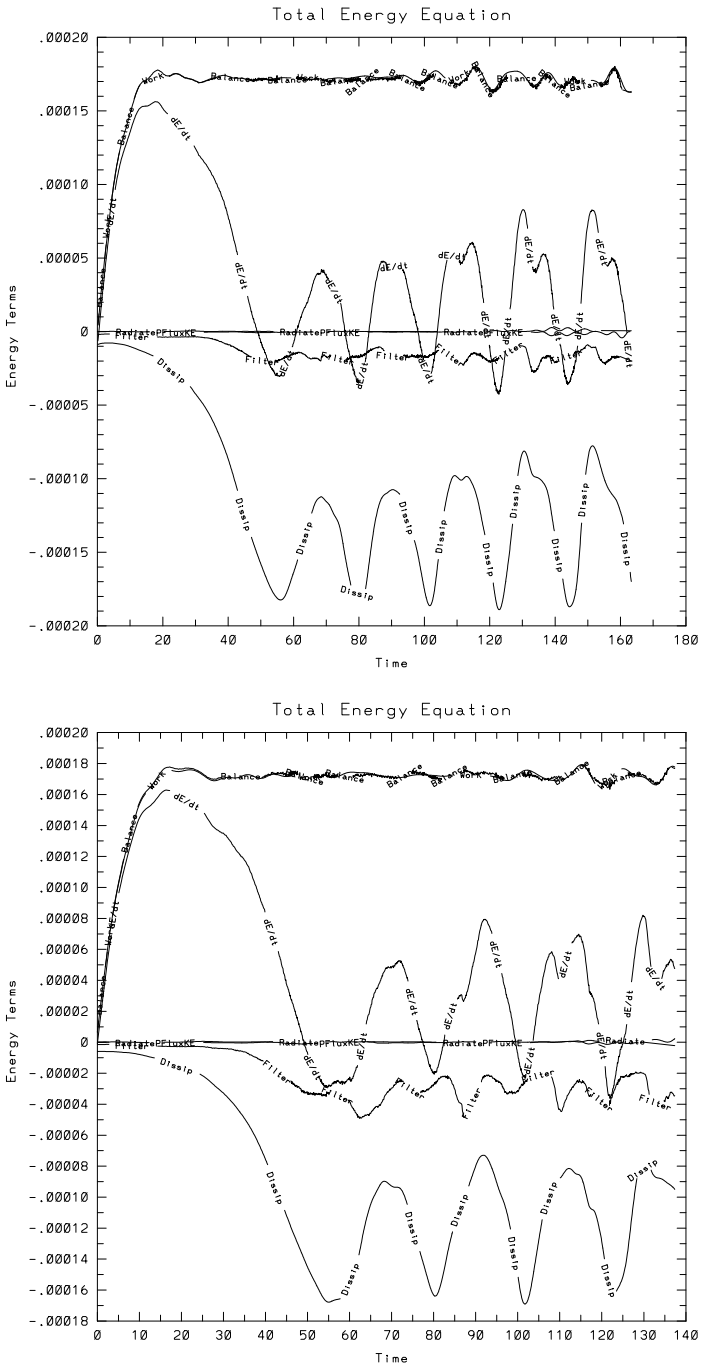

Figure 5.19: The terms of the total energy equation for Case 19 (top) and Case 21 (bottom).

5.4 Shallow Slopes

In this section results from critical angle simulations for the shallowest bottom slopes are presented. Cases 1-7 from Table 4.1 were conducted over slopes of 3.4^o and 5.0^o at Reynolds numbers between 600 and 3300. Simulations were conducted in the laminar, transitional, and turbulent regimes. The focus in this section is on reporting details of the flow development for turbulent wave breakdown. The first set of results are for Case 7, with a 5^o bottom slope, Reynolds number of 3300, and Richardson number of 33.

The wave period for critical frequency waves over a 5^o bottom slope is 71.8. Figure 5.20 shows isopycnals of the flow in the near wall region at $t = 205$, 217, 226, 237, and 255 for Case 7. The dimensions of the figure are $0.96\lambda_z$ in the z'-direction and $\lambda_x = 5.66\lambda_z$ in the x'-direction. The dimension of the simulation in the y-direction was $4.3\lambda_z$. As with previous figures, to be viewed in their natural reference frame the panels should be rotated counter-clockwise 5^o. Figure 5.20 follows the flow through the initial development of static instabilities, wave breakdown and small scale mixing, similar to the flow sequence for the 9.2^o bottom slope of Figure 4.10. Isopycnals for the 3.4^o slope case are not presented because they are very similar to Figure 5.20. The oncoming waves for Case 7 have large amplitude, approximately $0.7A_o$, and especially in Frames 2 - 4, can be seen as they approach the region of the turbulent boundary layer. The turbulent boundary layer has approximate depth of $\lambda_z/2$.

Because the oncoming waves propagate at a shallow angle to the horizontal (e.g., 5^o), a significantly long time is required for the wave train to approach the bottom boundary from the wave forcing region, located at a height of $1.5\lambda_z$ to $3\lambda_z$. In addition, because of the long wave period, the results cover only two mixing cycles, even though the simulation was continued until $t = 310$.

Figure 5.21 shows the various terms in the kinetic and total energy equations (volume integrals) for Case 7. The first peak in the combined (total) dissipation rates occurs at approximately $t = 210$, followed by a second peak at $t = 300$. Again, the interval appears to be approximately 25% longer than the wave period.

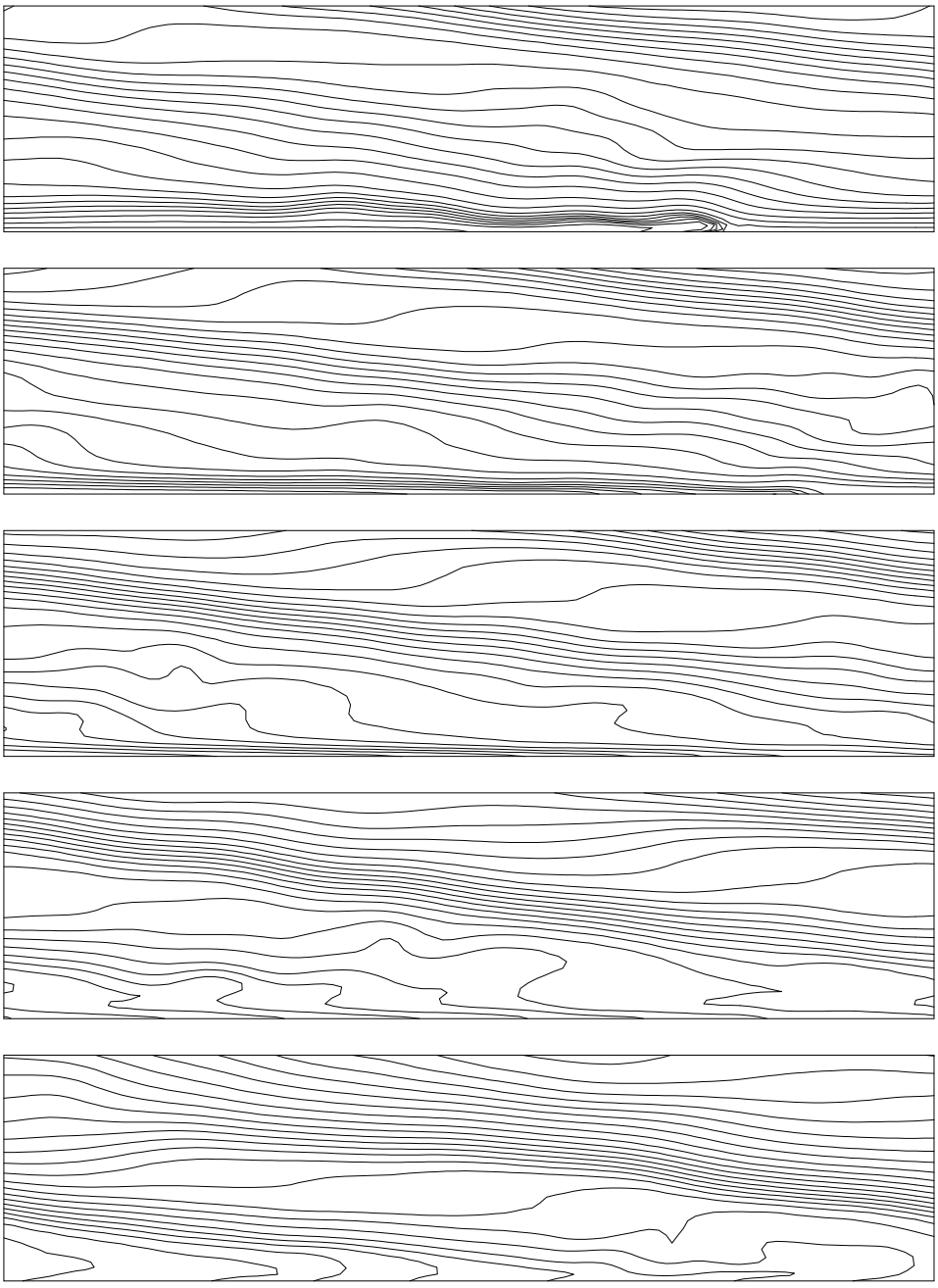

Figure 5.20: Isopycnals of the flow in the near wall region at $t = 205$, 217, 226, 237, and 255, for a bottom slope of 5^o (Case 7).

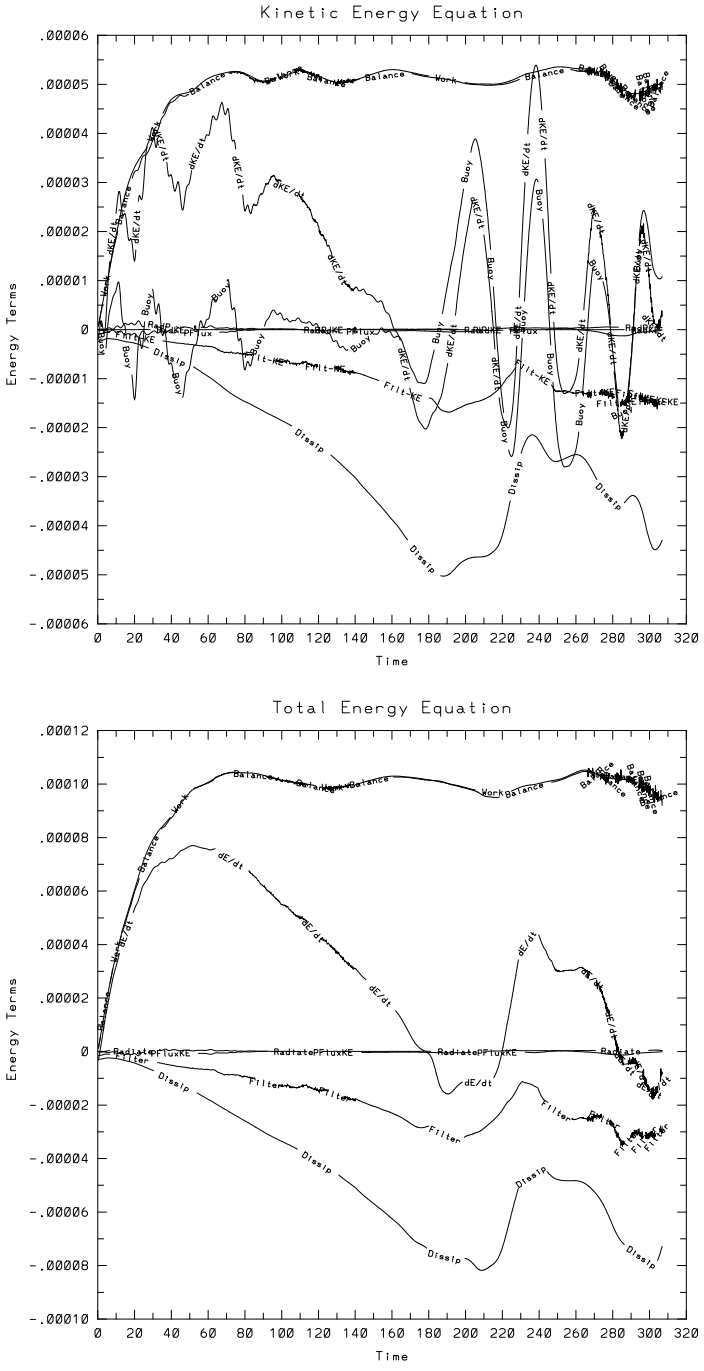

Figure 5.21: The terms of the kinetic and total energy equations for Case 7.

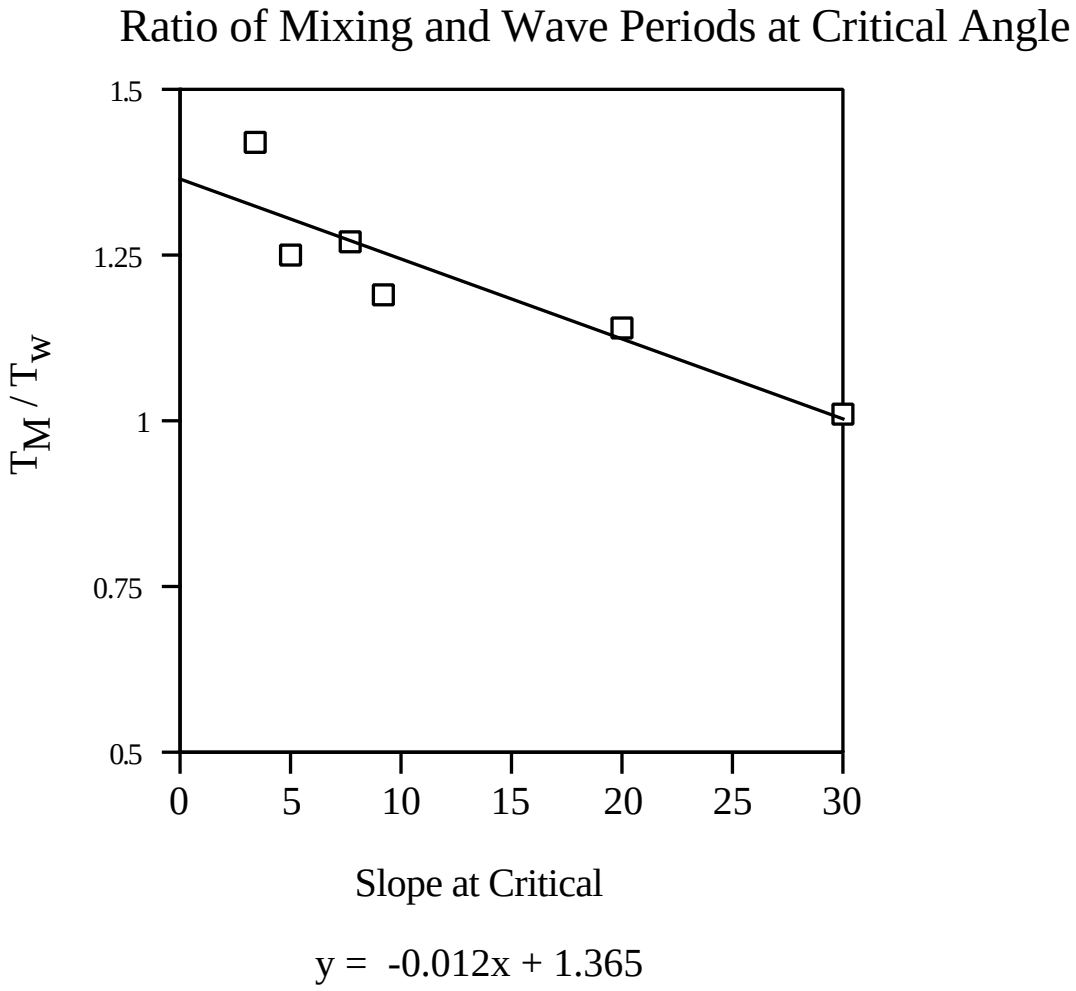

Figure 5.22: The ratio of the mixing period to the wave period for critical angle simulations between 3^o and 30^o.

Figure 5.22 shows the ratio of the mixing period to the wave period for critical angle simulations between 3^o and 30^o. Some approximations are involved in estimating the data. For example, for the 30^o slope, the estimate was made by examining the peaks in the total dissipation rate from Figure 5.13. There are approximately 15 maximum during the interval $20 < t < 210$, yielding a mixing period of 12.6 which is equal to the wave period. The data show that there are higher ratios of T_M/T_w for smaller slopes. The maximum value observed in the simulations is $T_M/T_w = 1.42$ for the 3.4 degree slope.

After the mixing has begun the buoyancy flux oscillates approximately twice per wave period, similar to the behavior for the 20^o slope described previously. The ratio of the loss of energy by the filter to the dissipation rate is larger than for most of the previous simulations. The simulation was carried out at moderate resolution, 129 x 33 x 130, considering the high Reynolds number, in order to reduce the CPU time required to carry out the simulation to such a late time (18,500 time steps). Even though the filter removed significant amounts of energy at the smallest scales on the numerical grid, the larger scale motions associated with the initiation of overturning and breakdown are represented accurately in the simulation.

Figures 5.23 - 5.25 present results from Case 3, a critical angle simulation over a 3.4^o bottom slope with $Re = 2100$ and $Ri = 44$. The wave period for this case is 105.3 and the simulation was carried out to a time of approximately 450. The leading edge of the large amplitude wave train reaches the bottom boundary at approximately $t = 150$, and there are approximately two mixing periods observed in the remainder of the simulation.

Figure 5.23 shows the various terms in the kinetic energy balance for the simulation. The peaks in the dissipation rate occur at approximately $t = 270$ and 420. This is in agreement with additional measures of the mixing period, e.g., from Figures 5.24 and 5.25, which indicate that the mixing cycle is approximately 150. The integrated buoyancy flux for the flow has a period of approximately 55.

Figure 5.24 presents the mean square derivatives $\left(\frac{\partial v}{\partial x}\right)^2$, $\left(\frac{\partial v}{\partial y}\right)^2$, and $\left(\frac{\partial v}{\partial z}\right)^2$ for Case 3 as a function of time. The v-velocity derivatives indicate the three-

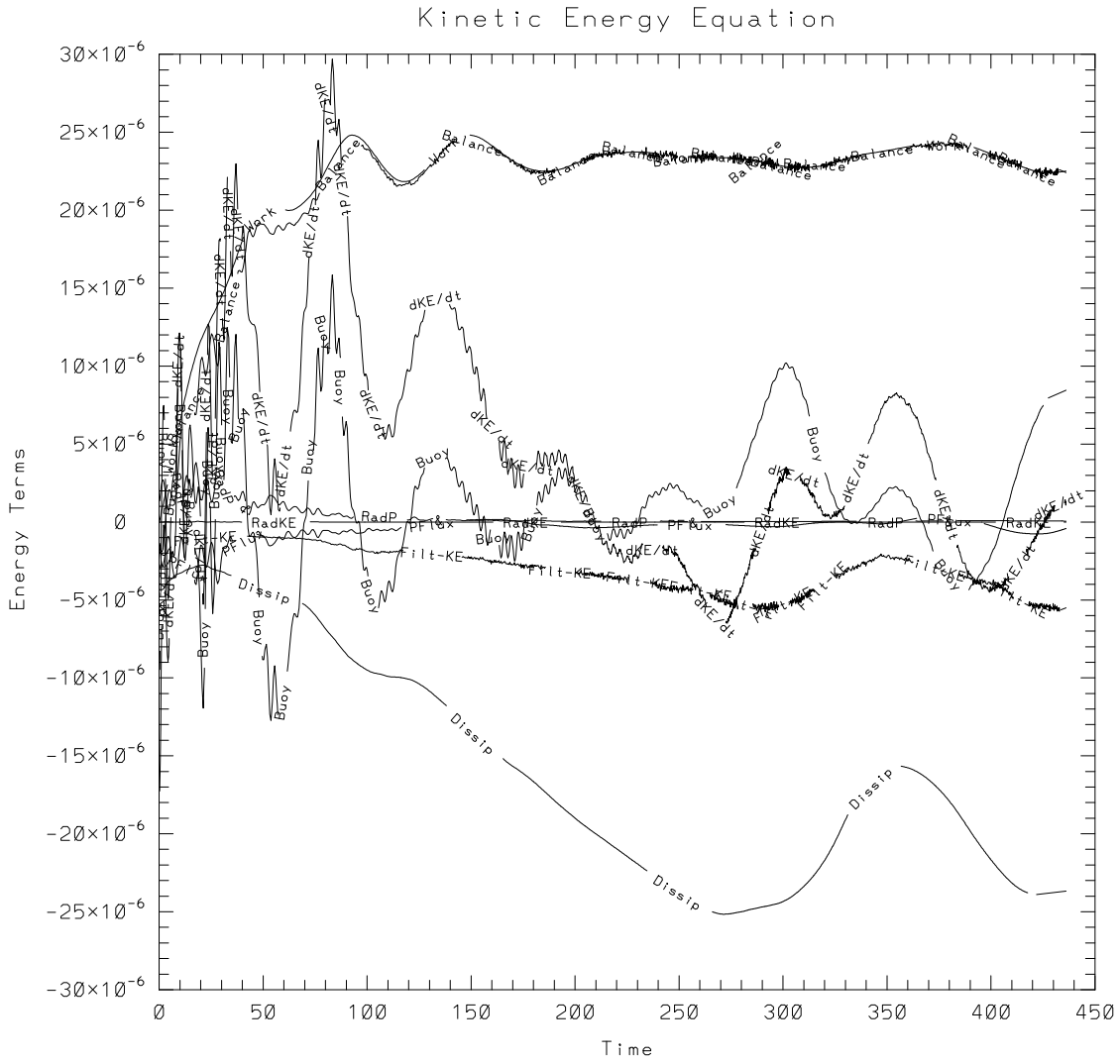

Figure 5.23: The terms of the kinetic energy equation for Case 3.

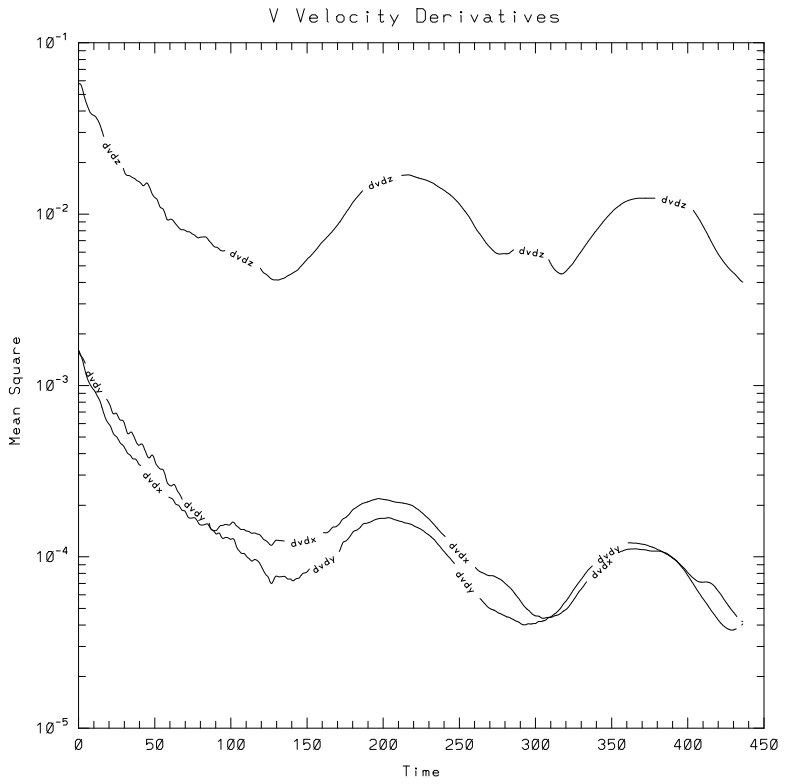

Figure 5.24: For Case 3, time evolution of the three components of the mean square shears, $\left(\frac{\partial v}{\partial x}\right)^2$, $\left(\frac{\partial v}{\partial y}\right)^2$, and $\left(\frac{\partial v}{\partial z}\right)^2$.

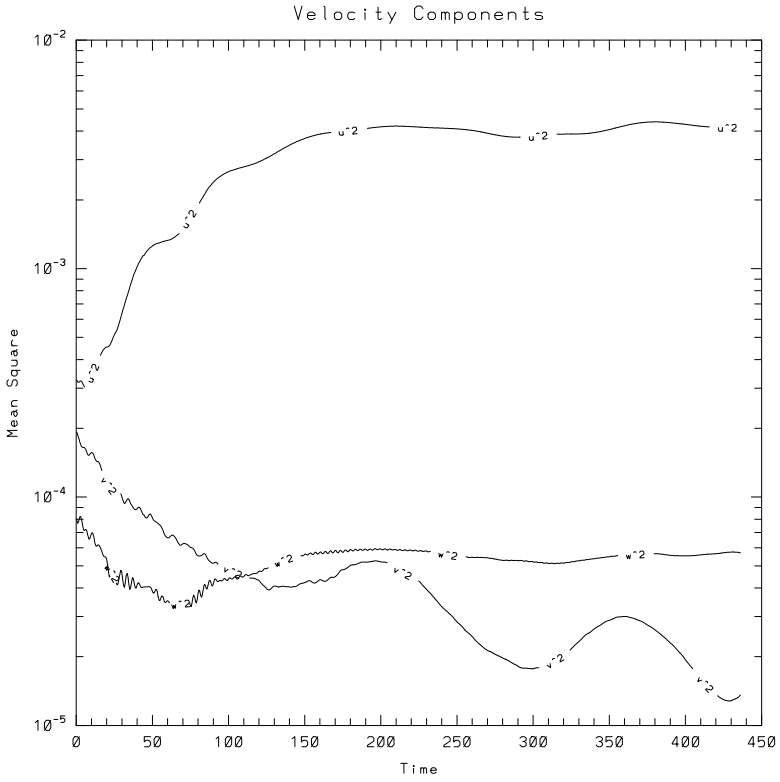

Figure 5.25: For Case 3, evolution of the three components of kinetic energy, u^2, v^2, and w^2.

dimensionality of the flow that develops during the turbulent phase of the wave breakdown cycle. The shear in the z-direction is stronger than in the x'- and y-directions because of the proximity of the bottom boundary.

Figure 5.25 also indicates the three-dimensionality of the flow in Case 3. It shows the volume integrals over the full domain of the three components of kinetic energy, u^2, v^2, and w^2, as functions of time, and compares their relative strengths. The oncoming wave, propagating at a shallow angle and aligned in the plane of the slope, contains predominantly u-velocity (note that u^2 is approximately two orders of magnitude larger than w^2). The strength of the turbulence has not yet achieved a stable value after the first two mixing cycles, but appears to be continuing to decay in the mean between periods of turbulence. As time continues it is expected that the simulation

would achieve a quasi-steady cycle similar to the other shallow slope simulations.

5.5 Summary of Critical Angle Basic Cases

The preceding sections presented results from critical angle simulations for bottom slopes ranging between 3^o and 30^o. Typically, one or two of the simulations at each slope has been presented. Sections to follow in this chapter emphasize comparisons between the additional critical angle simulations, as well as on their dependencies on Reynolds and Richardson numbers.

The main conclusion from the simulations discussed above is that there is a marked difference between the flow behavior and the nature of the turbulence that develops over shallow in contrast to steep slopes. Previous laboratory studies (Ivey and Nokes, 1989; Taylor, 1993) have focused on internal wave reflection over the steeper slopes, 30^o and 20^o, primarily due to difficulties in designing wave tanks with sufficiently large aspect ratios to examine low frequency waves. An advantage of the numerical approach is that it is possible to perform experiments over the shallow bottom slopes that are more typical of oceanic conditions.

The simulations have demonstrated that oncoming waves at the critical frequency break down in a turbulent boundary layer when they reflect from the bottom topography. For the steep slope case (30^o) the flow may be characterized as consisting of a turbulent bore, which moves upslope at the phase speed of the oncoming wave. The turbulent bore might also be characterized as a turbulent version of a thermal front. It produces continuous, localized mixing that restratifies behind the bore. For the shallower slopes (3^o to 20^o) the flow creates a periodically turbulent boundary layer. In this case a thermal front develops that moves upslope similar to the turbulent bore. The thermal front differs from the turbulent bore in that it appears periodically, especially during phases of initial wave overturning and the onset of breakdown, and reorganizes itself during the phase of relaminarization. The thermal front is not characterized by steady localized mixing. For the shallow slopes there is a cycle of strong mixing across the boundary, followed by a period of relaminarization and restratification of the boundary. The complete cycle is approximately 10-40%

longer than the wave period for a broad range of conditions. The dynamics of the wave breakdown appear to be associated with local upslope/downslope flow induced by the oncoming wave. Further details of the processes and general flow features are discussed below.

5.6 Transition

Increased understanding of transition to turbulence of the oncoming gravity waves has been an aim of the numerical experiments. Sets of experiments have been conducted at bottom slopes between 3^o and 30^o to examine necessary conditions for transition. Table 4.1 on Page 97 presented the flow classification used together with the slopes, frequencies, Reynolds and Richardson numbers for 28 critical angle simulations. The classification (turbulent, transition, or laminar) was determined primarily by examining the growth of volume integrals of components requiring three-dimensionality, such as v^2 and $\left(\frac{\partial w}{\partial y}\right)^2$. Simulations with strong positive response during periods of wave breakdown were classified turbulent; weak responses, transitional; and continuous decay of the three-dimensional components, laminar. Figure 5.1 provides an example of the classification. The simulations at $Re = 3600$, 2800, and 2000 were classified as turbulent; at $Re = 1200$, transitional; and at $Re = 850$, laminar.

The results from Table 4.1 are presented in Figures 5.26 and 5.27. Figure 5.26 locates flow classification with Reynolds number and slope; six laminar simulations are plotted with squares, and four transitional simulations are plotted with diamonds. The remaining 18 turbulent simulations are plotted with circles; however, two of the circles are hidden. The trend is for transition and turbulence to begin at lower Reynolds number for increasing slope. For the 3^o and 5^o bottom slopes, transition occurs near $Re = 1800$, whereas for the 30^o bottom slope, transition occurs at approximately $Re = 500$. The intermediate slopes follow this trend, with transition occurring near $Re = 1200$ for the 9.2^o slope;

Figure 5.27 suggests another aspect of transition. Here the simulations are located by their Richardson number and bottom slope. There are two frames in Figure 5.27,

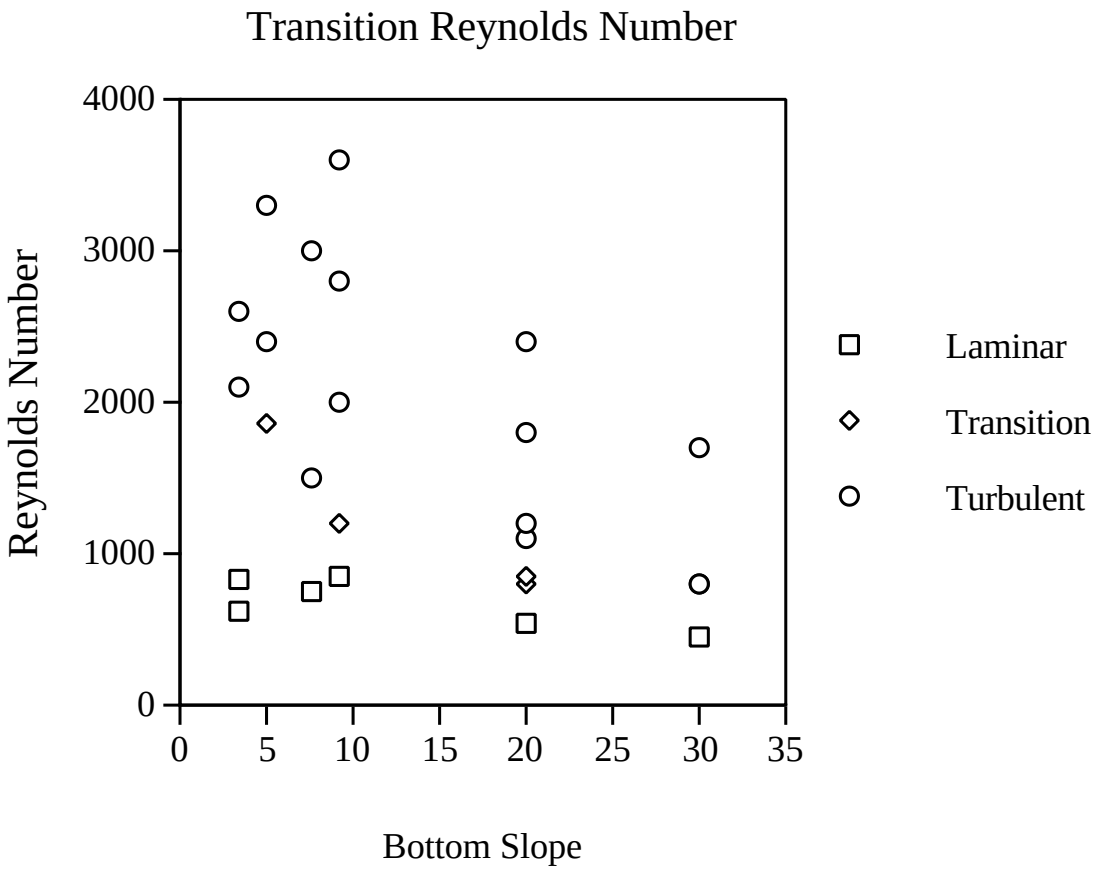

Figure 5.26: Simulations located on ranges of Reynolds number and slope. Turbulent simulations are located with circles; laminar simulations with squares; and approximate transitional simulations with diamonds.

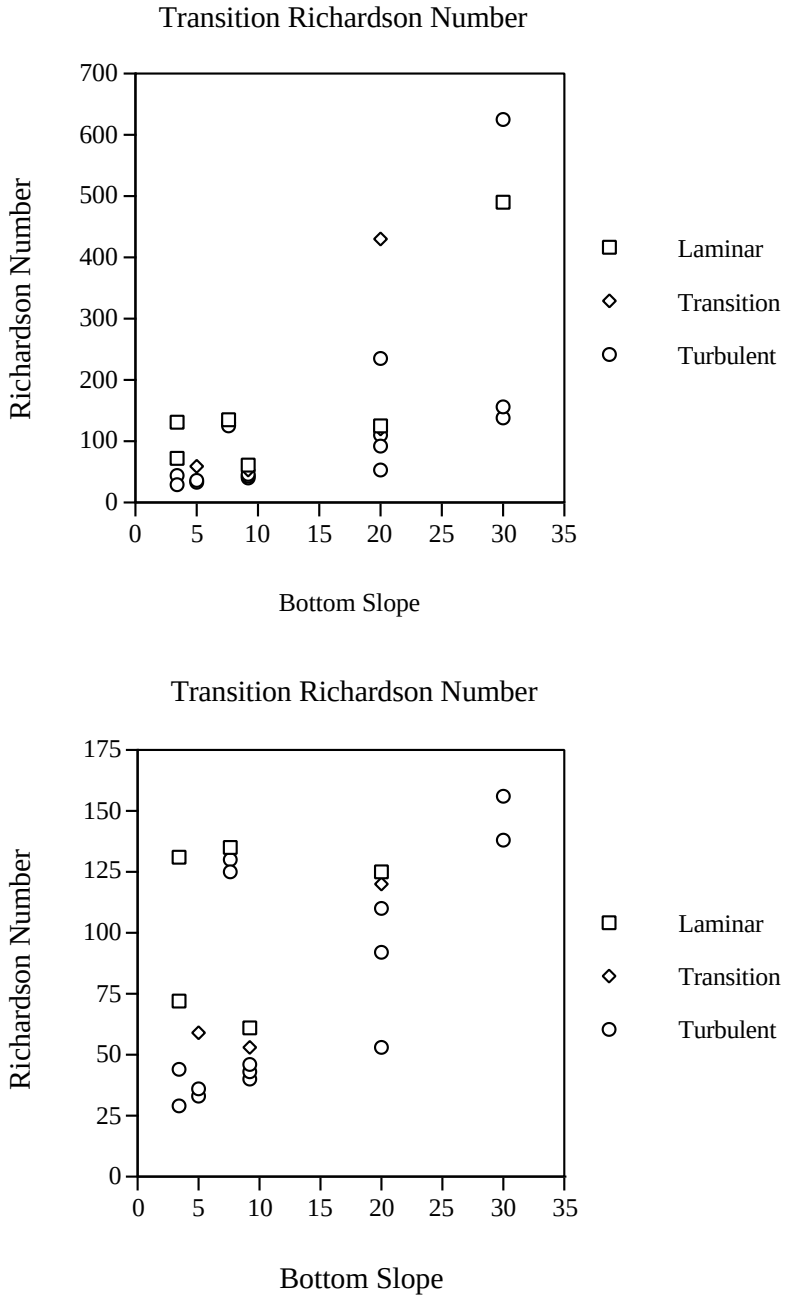

Figure 5.27: Simulations located on ranges of Richardson number and slope. Turbulent simulations are plotted with circles; laminar simulations with squares, and approximate transitional simulations with diamonds. Notice the different scales for the ordinates of the two frames.

differing only in the scale of the ordinate. The top frame includes all simulations, while the bottom frame focuses on the cases conducted at Richardson numbers below 175. The Richardson number dependence of transition appears to be more complicated than the Reynolds number dependence, although both parameters need to be considered for a more complete understanding.

The influence of higher Richardson number (smaller amplitude waves) is typically to stabilize the flow. For the cases with bottom slope less than 20^o, this generalization holds. It should be remembered, however, that for some simulations (7^o, 9^o) the Richardson number varies slightly as a result of lower Reynolds number conditions. (The more viscous fluid slightly decreases wave amplitudes as they approach the boundary.) For the cases in which different amplitude waves are generated (3^o, 5^o, 20^o and 30^o), the results still follow the expected behavior. There are exceptions, however; for example, at 20^o and 30^o some higher Richardson number (more stable) simulations become turbulent while other lower Richardson number simulations remain laminar. These exceptions occur, of course, for simulations at higher Reynolds number.

Ivey and Nokes (1989) emphasize another aspect of transition. They suggest that an important parameter to describe transition is the dissipation Reynolds number, $Re_d = \epsilon/\nu N^2$. The idea has arisen from experiments with very different mixing mechanisms, i.e., grid generated turbulence (Stillinger, Helland and Van Atta, 1983; Rohr and Van Atta, 1987; and Itsweire, Helland, and Van Atta, 1986), that there may be a universal transition point for stratified turbulence, i.e., when $Re_d > 10$.

Figures 5.28 - 5.30 plot gray scale contours of Re_d at two different times for Case 28 with a 30^o bottom slope. Figure 5.28 shows Re_d in two planes at $t = 78.5$. The top frame is a side view (x - z plane) located at $y = 0.25$, and the bottom frame is a top view (x - y plane) located at $z = 0.15$. The darkest contours have values of Re_d exceeding 50, while the lightest regions have contours less than 1. The main point of the figure is that nearly all of the dissipation occurs in the turbulent boundary layer, in a very inhomogeneous fashion. The streaks nearest the wall, seen in the top frame of Figure 5.28, have $Re_d > 700$, while the core of the turbulent bore has regions with $Re_d \approx 100$. The bottom frame of Figure 5.28, illustrating a top view of a plane

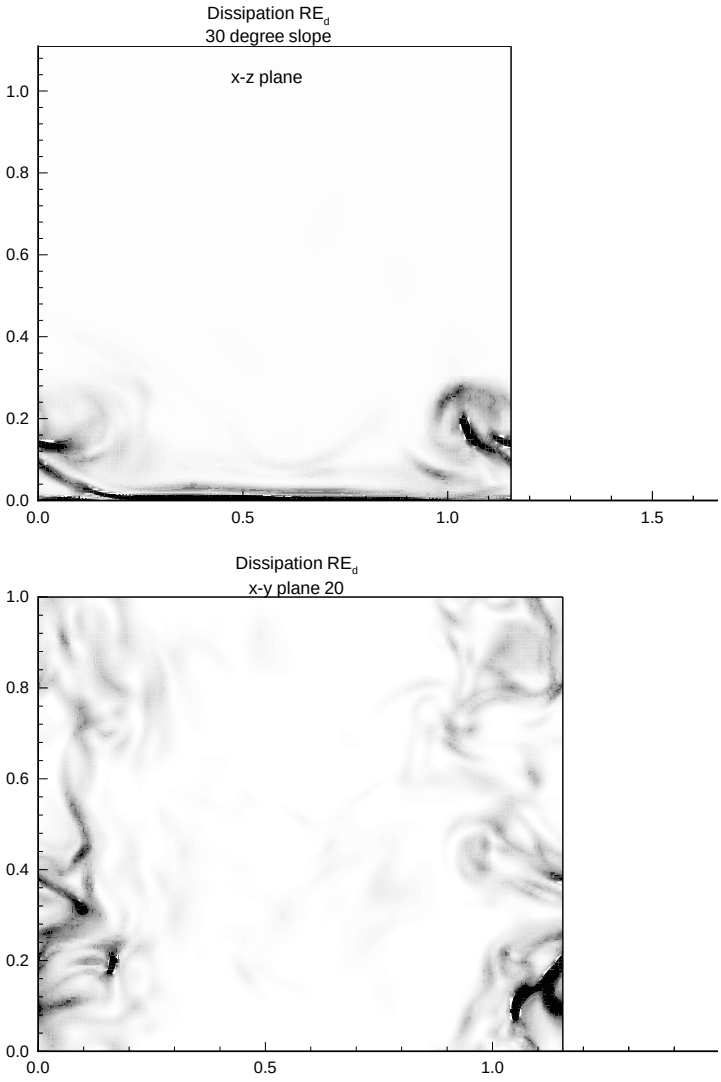

Figure 5.28: The kinetic energy dissipation rate normalized by the viscosity and buoyancy frequency squared, $Re_d = \epsilon/\nu N^2$, shown in two planes for 30^o slope (Case 28) and $t = 78.5$. The top frame is a side view (x - z plane) located at $y = 0.25$, and the bottom frame is a top view (x - y plane) located at $z = 0.15$.

parallel to the boundary, shows the three-dimensional structure of the turbulence. The values of Re_d in this plane range from 0 to 97. While the average values of the dissipation rate are somewhat uniform in the y-direction, the contours of dissipation rate are comprised of strong streaks indicative of local variability.

Figure 5.29 shows another view of Re_d at $t = 78.5$ (top) and the average dissipation rate as a function of height (bottom). The top frame is an end view (y-z plane) located at $x = 1.1$ cutting through the region of strongest vorticity and dissipation. Here, the dissipation appears to be strongly restricted to the boundary layer. The spatial inhomogenity of the flow for the 30^o case (the flow resembles a turbulent bore) makes it difficult to determine an appropriate average dissipation rate for estimating a total Re_d for the flow. If ϵ is averaged just in the core of the turbulent bore, then $Re_d \approx 30$, exceeding the predicted transition value. If, however, ϵ is spatially averaged across the boundary layer, to a height of $z = \lambda_z/3$ (including both the viscous sublayer and large regions of low dissipation), then $Re_d \approx 7$. Including the laminar region above the turbulence further decreases the average Re_d to 2.5 by a height of $z = \lambda_z$.

The bottom frame of Figure 5.29 shows the horizontally averaged value of Re_d as a function of height at $t = 83.8$. These horizontal averages are over both regions of strong dissipation rates (within the turbulent bore) as well as larger regions of low dissipation rates (in the stratified regions between bores). Generally the averages misrepresent the state of the flow, and suggest a flow with insufficient energy to be turbulent.

Figure 5.30 shows contours of the dissipation Reynolds number for the same flow at a later time, $t = 83.8$. The region of strong turbulence has moved to a different location, but the flow is qualitatively similar. Similar plots from laminar simulations indicate that maximum local values of $10 < Re_d < 20$ are commonly observed in limited regions of the boundary layer for flows that develop and waves that break down in a two-dimensional fashion.

Additional figures, not pictured here, of potential energy dissipation rates were analyzed from other simulations. Potential energy dissipation rate contours are very similar in structure to the kinetic energy dissipation rate contours shown, except for

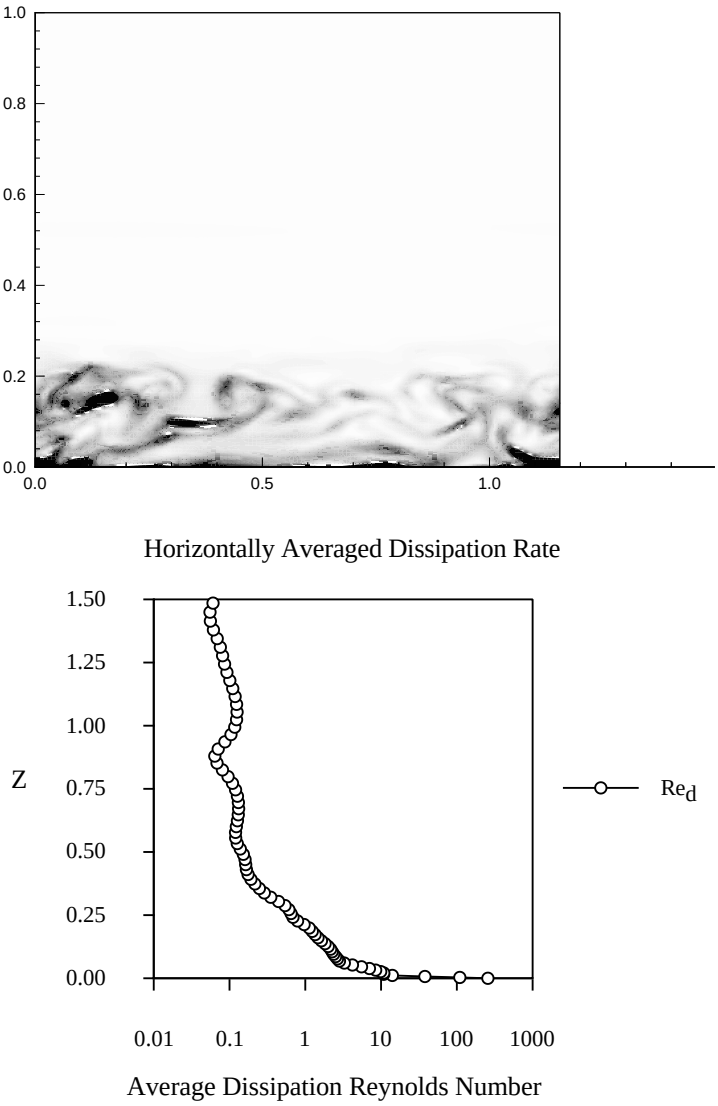

Figure 5.29: The dissipation Reynolds number, Re_d for 30^o slope (Case 28) and $t = 78.5$ (top). The top frame shows an end view (y - z plane) located at $x = 1.1$. Also plotted is the horizontally averaged kinetic energy dissipation rate as a function of height from the boundary at $t = 83.8$.

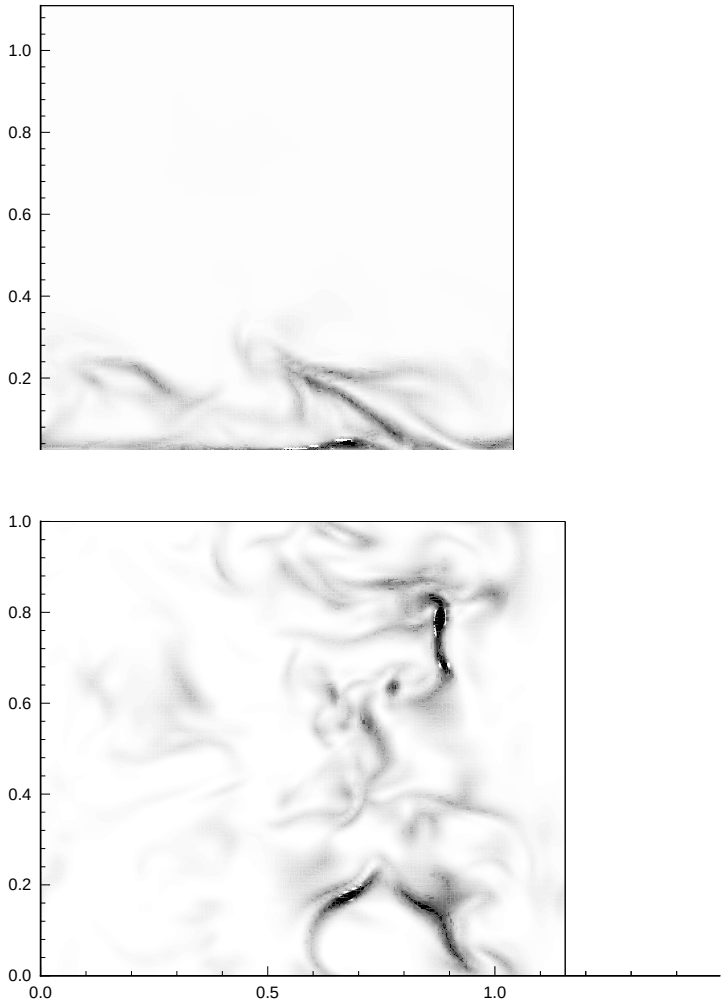

Figure 5.30: The dissipation Reynolds number, Re_d, in two planes for 30^o slope (Case 28) and $t = 83.8$. The top frame is a side view (x - z plane) located at $y = 0.25$, and the bottom frame is a top view (x - y plane) located at $z = 0.15$.

the absence of enhanced dissipation rate in the viscous sublayer. Shallower slopes increase difficulties in determining appropriate average dissipation rates because of flow intermittencies. Approximately 1/3 of the wave period involves active turbulent mixing. Consequently, the transition rule suggested by Ivey and Nokes, for homogeneous turbulence, must be modified to include temporal and spatial dependencies in order to be extended to the intermittent and spatially inhomogeneous turbulent boundary layers that develop from internal wave reflection. Development of the appropriate criteria were placed beyond the scope of this study.

5.7 Boundary Layer Thickness

Determination of a practical measure for the (turbulent) boundary layer thickness, δ, is considerably more complicated for the internal wave reflection problem than for simpler types of boundary layer flows. For example, a standard measure of δ for flow over a flat plate is the height to where the boundary layer velocity is $0.99U_\infty$, where U_∞ is the free stream velocity. But the wave driven flows in this study are different, since, velocities in the boundary layer are typically 2 - 3 times *higher* than the "free stream" velocities (where free stream velocities refer to mean current speeds of the oncoming wave field). In addition, the transition zone (e.g., $\frac{\lambda_z}{3} < z < \frac{2\lambda_z}{3}$) between the boundary layer and the oncoming wave field is temporally and spatially variable. Further complexity is added when radiated gravity waves from the turbulence propagate upwards, passing through and interacting with downward propagating waves. These, and other factors, complicate defining a measure of the boundary layer depth. One of the advantages in attempting the analysis, however, is that the oncoming waves are two-dimensional (e.g., uniform in the y-direction and containing no v-velocity). Consequently, the variability in the y-direction distinguishes incident waves from responses produced in the boundary layer.

A variety of methods have been used to determine the boundary layer thickness for the simulations described herein. Figure 5.31 shows the root mean square (rms) v-velocity component as a function of height for Case 15, for flow over a 9^o bottom slope. The horizontally (parallel to boundary) averaged (rms) velocities are calculated

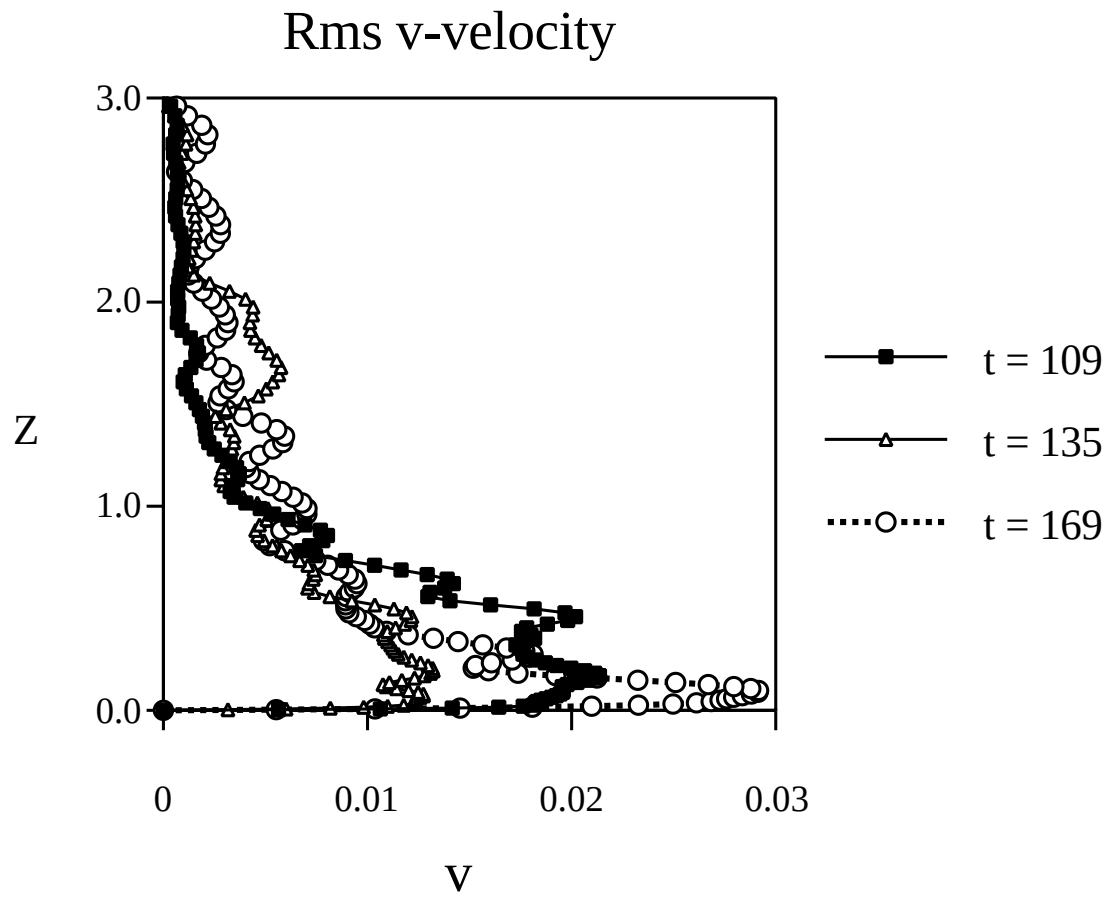

Figure 5.31: The horizontally integrated rms v-velocity component as a function of height at $t = 109$, 135, and 169 for a 9^o bottom slope (Case 15).

from

$$\overline{v}_{rms}(z) = \sqrt{\frac{1}{N_x N_y} \sum_{i=1}^{N_x} \sum_{j=1}^{N_y} v_{i,j}^2(z)} \; . \tag{5.2}$$

The scale of the vertical axis covers the bottom three vertical wavelengths of the simulation (the total height was $3.5\lambda_z$). The rms v-velocity provides an estimate of the strength of the three-dimensionality in the flow and is shown in Figure 5.31 at $t = 109$, 135, and 169, after the flow has achieved a quasi-steady state. Times 109 and 169 are during periods of active wave breakdown, while at $t = 135$, during a period of restratification, the flow contains minimal three-dimensionality. The main point of the figure is that the three-dimensionality and turbulence occur in the near wall region within a "boundary layer" of approximate thickness $\delta \approx \lambda_z/2$. The v-velocity located above δ (e.g., at $z = 1.8$ for $t = 135$) is associated with gravity waves radiated from the turbulent region. The strongest generation of v-velocity, associated with turbulence and wave breakdown, is in the region with $z < 0.3\lambda_z$.

Another measure for the boundary layer thickness is suggested in Figure 5.32 taken from Case 21, for the 20^o slope. Two different measures of three-dimensionality are shown in Figure 5.32. The top frame shows the rms value of the shear rate, $\dfrac{\partial u}{\partial y}$, and the bottom frame shows the rms of the v-velocity. The shear rate is presented at four time levels, $t = 48$, 83, 136, and 167. At $t = 48$ the first cycle of wave mixing is just beginning, which gives an indication of the amount of y-variability remaining from the initial background white noise. In the top frame the vertical axis includes only the bottom vertical wavelength λ_z, while the bottom frame extends to $2\lambda_z$. For $t > 83$ the flow has experienced a number of stages of the mixing cycle, and the curves for the shear rate for $t = 83$, 136, and 167 indicate that mixing is strongest in the region $z < 0.3$. The v-velocity suggests a more gradual transition between turbulent and wave zones, with a characteristic depth $z \approx 0.4$. Both frames of Figure 5.32 indicate the viscous sublayer ($z < 0.07$), which is not measured directly from the figures but by examining the numerical values of the shear, rms of the v-velocity, and the grid locations. The sublayer depth is approximately defined to be equal to the height at which the rms of the v-velocity reaches 95% of its peak value in the boundary

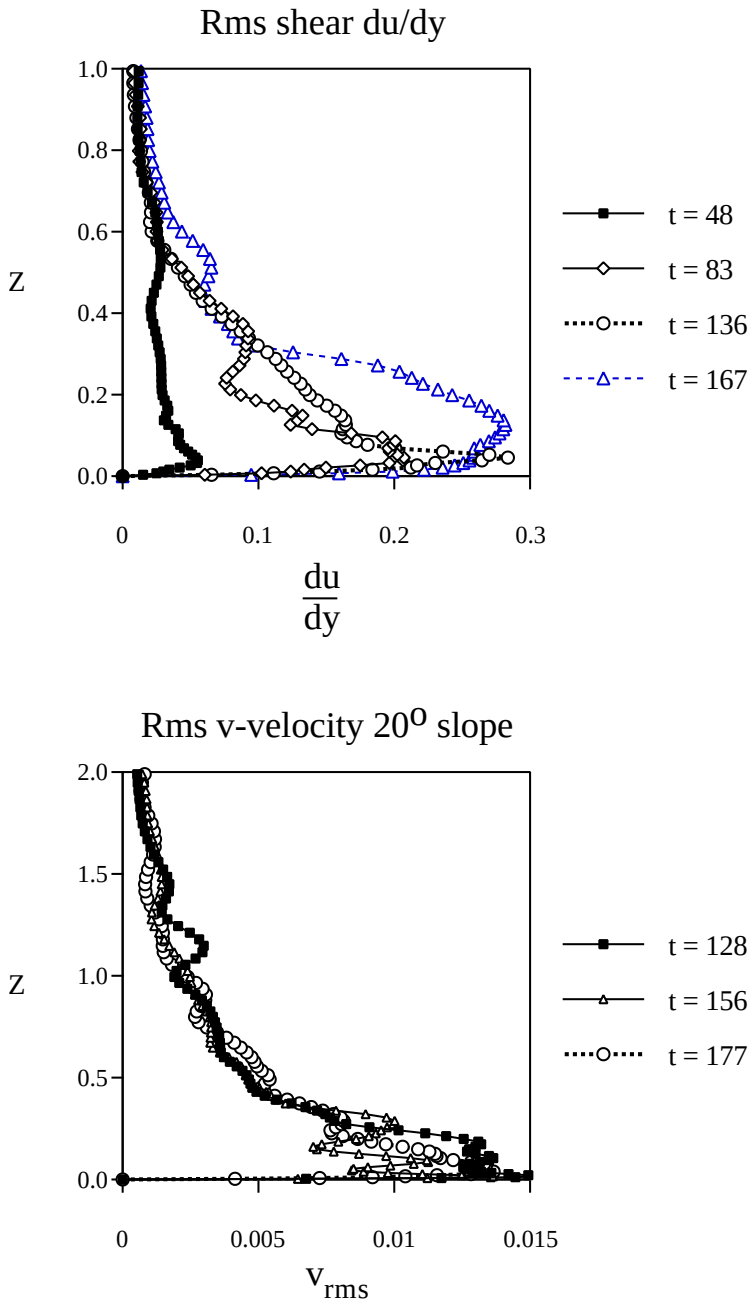

Figure 5.32: The horizontally integrated rms intensity of $\overline{\frac{\partial u}{\partial y}}$ at $t = 48$, 83, 136, and 167 (top frame) and the rms v-velocity component at $t = 128$, 156, and 177 (bottom frame) near the sloping 20^o plane boundary for Case 21.

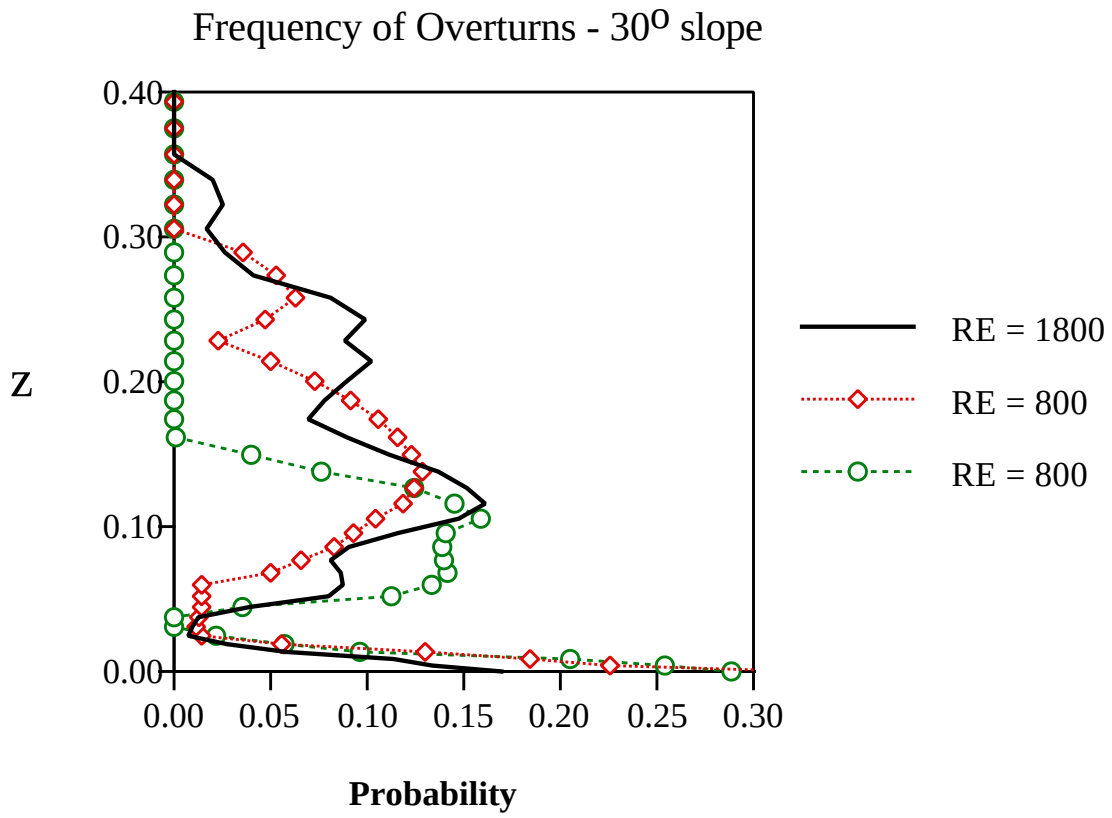

Figure 5.33: The statistical frequency of statically unstable fluid as a function of height for Case 28, Re = 1800, solid line; Case 27, Re = 800, diamonds; and Case 26, Re = 800, circles.

layer (averaged at several different times). The symbols on the figures are plotted at locations of the grid points in the z-direction and therefore indicate, to some degree, the resolution of the boundary gradients arising from the no-slip boundary condition.

Figure 5.33 suggests still another measure of the boundary layer thickness, and yields δ-values generally in good agreement with the measures already indicated. This method is the same as shown in Figure 4.20 and indicates the frequency of static instabilities as a function of distance from the wall. The results are presented for three 30^o slope simulations: Case 26 with $Re = 800$ and $Ri = 625$ (circles),

Case 27 with $Re = 800$ and $Ri = 156$ (diamonds), and Case 28 with $Re = 1700$ and $Ri = 138$ (solid line). The results are determined by integrating time series of the density profiles at a fixed location. The results indicate that the boundary layer thickness is approximately $\lambda_z/3$ for the two lower Richardson number cases, and $\lambda_z/6$ for higher Richardson number case. The lower Richardson number cases used approximately the same wave amplitude, $A \approx A_o/2$, and the difference in Reynolds number was achieved by changing the viscosity of the fluid. The higher Richardson number case used a smaller wave amplitude and achieved $Re = 800$ by using a less viscous fluid.

These results indicate that the boundary layer thickness is more sensitive to the Richardson number than to the Reynolds number for these fairly low Richardson number experiments. Ivey and Nokes (1989) examined a much higher range of Richardson number (of the order of 10,000 to 100,000) and showed that, in that Richardson number range, the boundary layer thickness is nearly a linear function of the Reynolds number. They showed that for small amplitude waves, the boundary layer thickness is proportional to the wave amplitude according to the relation $\delta \approx 5A$. Direct numerical simulations of turbulent wave breakdown could not be conducted over a wide enough range of Richardson number to confirm the laboratory result conclusively, but do show over a limited range that δ does appear to scale linearly with the wave amplitude (see Section 6.1). In the numerical simulations, wave breakdown occurs in a two-dimensional (laminar) fashion for Richardson numbers above approximately 1000, for Reynolds numbers that can be satisfactorily resolved. Future work utilizing large-eddy simulations, for higher Reynolds numbers, should prove useful for examining the dynamics of smaller amplitude waves.

Figure 5.34 also reveals the boundary layer for Case 28. Here, the rms v-velocity component is presented at $t = 118$, 144, and 161. These results suggest agreement with those from the frequency of static instabilities, i.e., $\delta \approx \lambda_z/3$. As already mentioned, the v-velocity above $z = 1$ is attributed to the radiation of gravity waves from regions of turbulence.

Indications are that smaller amplitude waves generate thinner boundary layers,

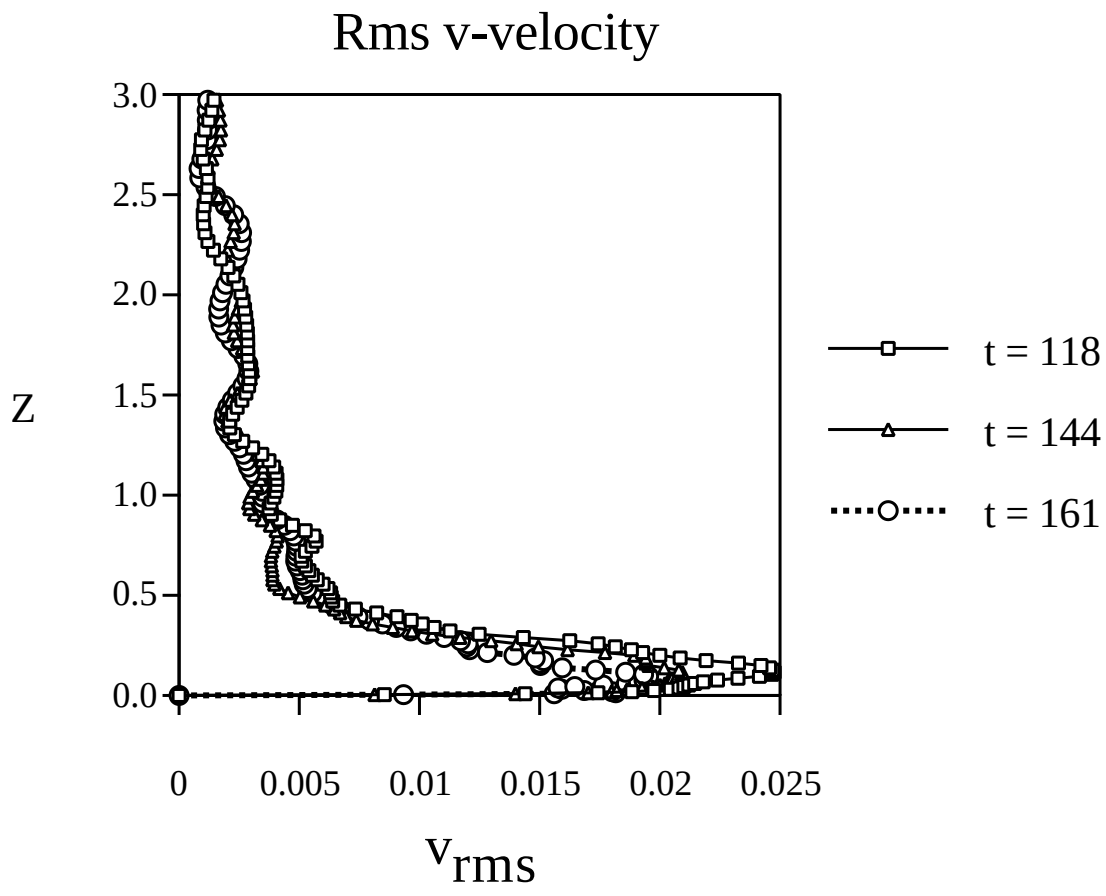

Figure 5.34: The rms v-velocity as a function of height for Case 28 (30^o slope) at $t = 118$, 144, and 161.

but the exact relationship has not been determined by the numerical experiments (see Section 6.1 for further details). Turbulent boundary layers that develop in the numerical simulations, for large amplitude oncoming gravity waves, have approximate thickness $\delta \approx \lambda_z/2$. This may provide an upper bound for the depth of the boundary layer in oceanic flows generated by wave reflection, given the large amplitude of the waves and the insensitivity of the result to Reynolds number.

5.8 Changes to Background Field

An issue of considerable interest, to both the dynamics of the model problem and its oceanic implications, is the long term response of the background flow which is modified by internal wave breakdown and mixing in the boundary layer. Two significant results that may appear in both the boundary layer and the interior fluid are changes to the background density profiles and creation of mean currents. Each of these flow adjustments are indicators that net mixing effects are communicated to the interior stratified fluid. In this section changes to the mean background fields will be examined. The presentation begins with changes to the density fields that appear as an increase in potential energy (defined in this model as $PE = \frac{1}{2} Ri\, \rho'^2$).

Indications of net changes to the background velocity and density profiles were suggested in Figures 4.27 (9^o slope) and 4.29 (20^o slope) by the volume integrals of the kinetic, potential, and total energy. The kinetic, potential, and total energies in the system continued to grow in time, indicating increased currents (kinetic energy) and changes to the background density stratification (appearing as increased potential energy). The same evidence was conspicuously absent from Figure 4.28 (30^o slope), as the energy in the system achieved a stable value, holding constant for 10-15 mixing cycles. The difference is that for the steeper slope a significantly higher percentage of the oncoming wave energy is dissipated to heat, and less is radiated away from the boundary layer (see Section 5.9.2).

Figure 5.35 shows profiles of the horizontally (parallel to wall) averaged density profiles, $\overline{\rho_t}$ for Case 15 (9^o slope) at $t = 59$, 169 and 191. The horizontal averages (i.e., mean not rms values) eliminate from the profiles the presence of the oncoming waves,

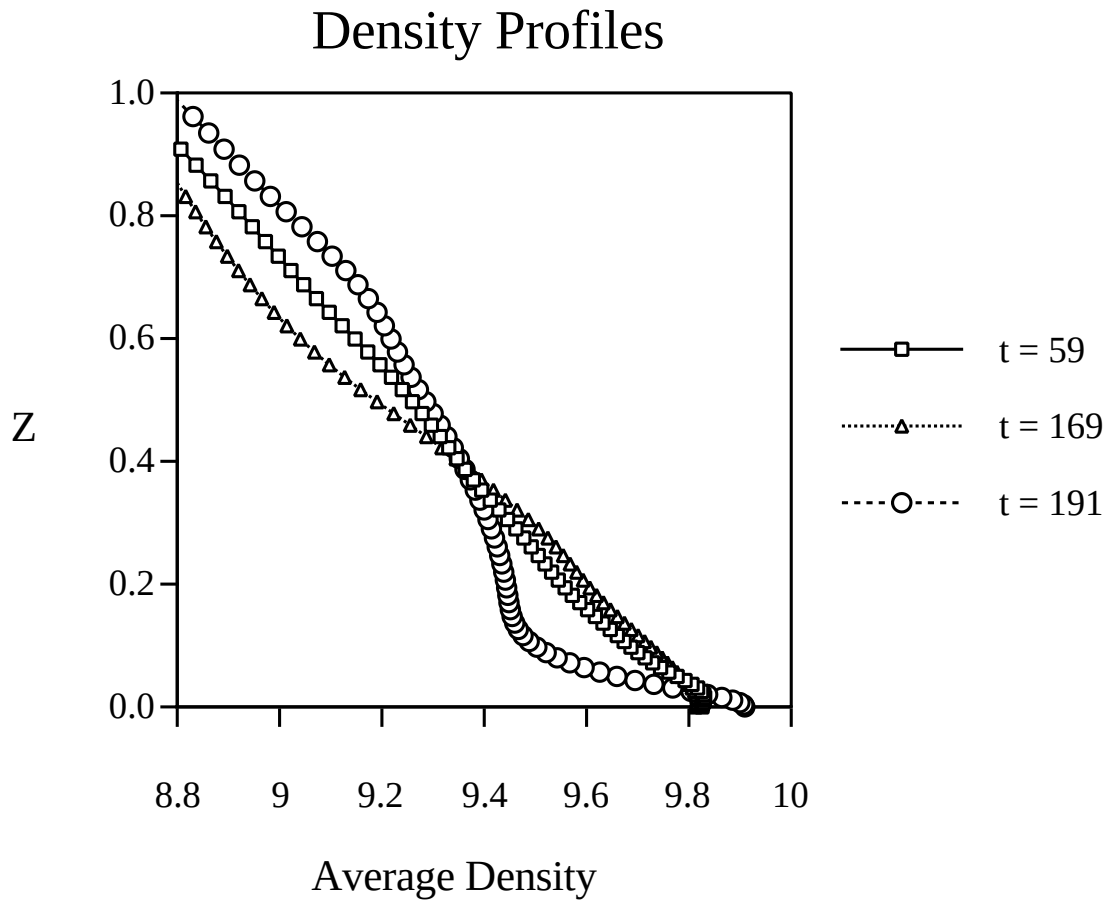

Figure 5.35: Horizontally averaged density profiles for the 9^o bottom slope (Case 15) at $t = 59$, 169, and 191.

because their average is zero over a wavelength. An arbitrary reference value for the constant background density, $\rho_o = 10$, has to be added in Figure 5.35 to form the total density field before averaging the values, because it is eliminated from the governing equations in the Boussinesq approximation, which assumes that $\rho_o >> \rho' + z\frac{\partial\overline{\rho}}{\partial z}$. Recall that the total density is the sum of the constant background value, ρ_o, a part due to the constant density gradient, $\left(\frac{\partial\overline{\rho}}{\partial z}\right) z$, and the density fluctuations, ρ', e.g., $\rho_t = \rho_o + z\frac{\partial\overline{\rho}}{\partial z} + \rho'$

The first profile ($t = 59$, squares) is taken before the first mixing cycle begins and shows the approximately linear profile from the initial conditions. Two later profiles are presented after approximately two and three mixing cycles, and show that adjustments to the initial profile have reached a height of at least λ_z. While the variability in the near wall region ($z < 0.4$) may be attributed to the temporal phase of the upslope/downslope flow and the stage of mixing, the change in the density profile above $z = 0.5$ represents transport of the mixed fluid into the stably-stratified interior. The temporal oscillation may be caused by low frequency waves that also appear in the mean u'-velocity fields.

At $t = 169$ the boundary layer is in a period of relaminarization and restratification, and the profile in the boundary layer is similar to the initial conditions. At $t = 191$ the flow is beginning another cycle of mixing, and the density gradient between $0.1 < z < 0.5$ has been substantially weakened. While a general trend has not yet been established it is apparent that the density profile adjusts. At different times the mean density profile is either stronger or weaker, depending on the height, compared with the initial linear profile. At the times shown in these figures the density profiles vary approximately $\pm 10\%$ from the initial profile. As the profiles change, the local buoyancy frequency, N, will also change, resulting in a progressive mismatch between the angle of propagation of the oncoming waves $\theta(\omega, N)$ and the bottom slope.

Figure 5.36 shows similar development of the mean density profile for Case 21 with a 20^o bottom slope. The profile at $t = 34$ provides a reference (before the first period of mixing has occurred) for the later profiles at $t = 128$ (after four mixing periods)

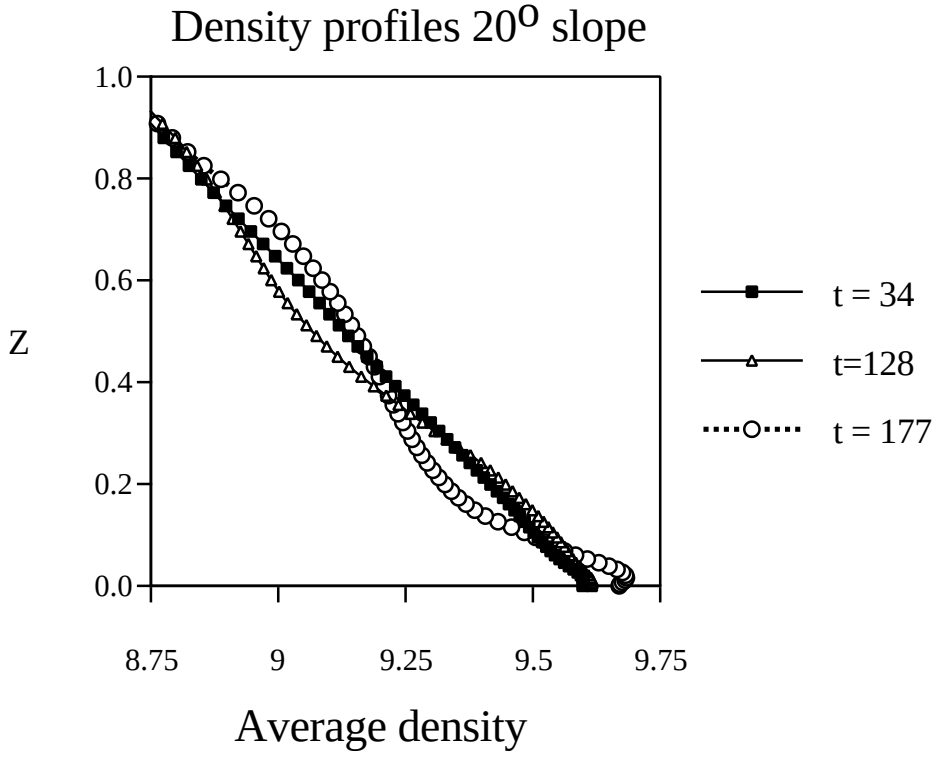

Figure 5.36: Horizontally averaged density profiles as a function of height for the 20^o bottom slope (Case 21) at $t = 34$, 128, and 177.

and at $t = 177$ (after six). Again there are significant adjustments to the background density profiles to a height of $z \approx \lambda_z \approx 3\delta$. Profiles for additional simulations with 20^o slopes confirm the behavior. The simulations with 9^o and 20^o slopes indicate that wave generated turbulence is not just mixing the same fluid with each subsequent cycle but that, as the boundary layer is restratified, the interior density gradient is continuously adjusted.

Oceanic conditions imply that a vast reservoir of stratified fluid exists in proximity to the sloping boundaries, providing a sufficient source to restratify the boundary layers between mixing events for extended periods of time. Further experiments regarding communication of boundary layer fluid with the interior stratification are presented below in Section 6.2.

Interestingly, Figure 5.37 does not show the same degree of adjustment to the interior density stratification for a 30^o slope (Case 28). Average density profiles are compared at $t = 15$ (before mixing), $t = 144$, (10 wave periods after mixing begins) and $t = 161$ (two wave periods later). The results are representative of still later times ($t \approx 210$) and of other lower Reynolds number simulations for the same bottom slope. The adjustments to the mean density profiles appear to be confined largely to the boundary layer thickness $\delta \approx \lambda_z/3$. It appears that the reason the steeper slope experiments are less effective at communicating mixing into the interior than the shallower slopes is that there is a more complete annihilation of the wave energy in the turbulent bore that occurs in the steep slope experiments. Observations reported above (Sections 5.2 and 5.2.1) suggest, however, that there is significant radiation of small-scale wave energy from the steep slopes. It appears that this radiated wave energy is ultimately dissipated and while the radiated waves can carry significant energy away from the region of localized mixing, they do so in a manner capable of passing through the stratification without causing turbulent mixing.

The next set of figures, Figure 5.38 - 5.46, shows average and instantaneous velocity profiles for Cases 15, 21, and 28, which are the three primary critical-angle simulations over 9^o, 20^o, and 30^o slopes. Figures showing mean and/or rms velocity profiles are used to address the development of mean currents and background flows

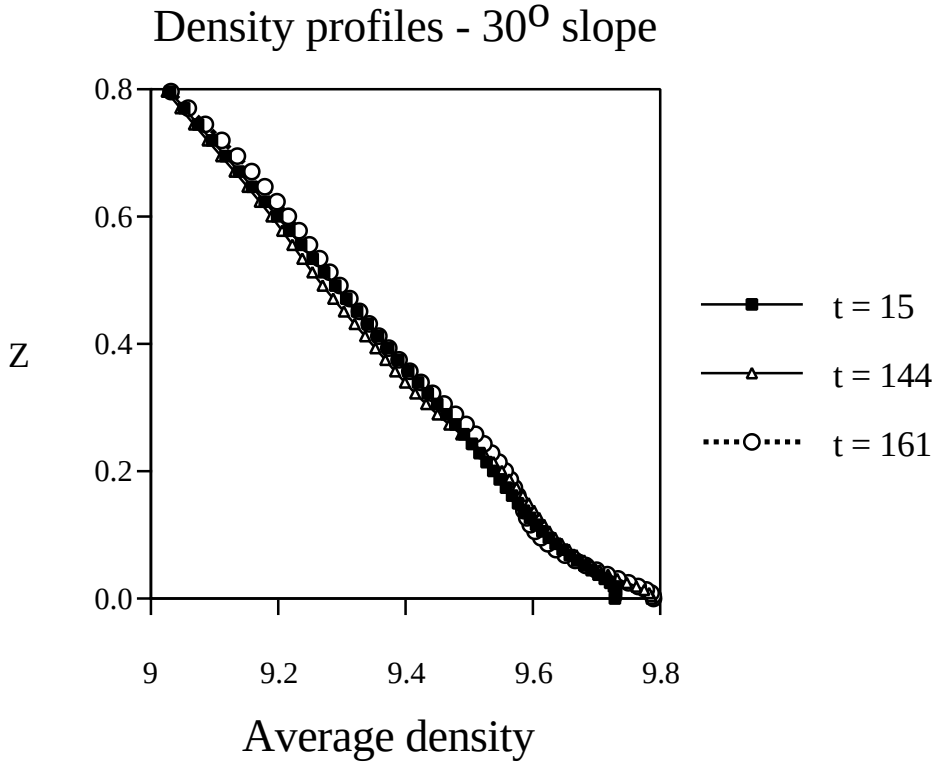

Figure 5.37: Horizontally averaged density profiles as a function of height for a 30^o bottom slope of (Case 28) at $t = 15$, 144, and 161.

that contain significant kinetic energy and participate in communication between boundary and interior fluids. Figures showing instantaneous velocity profiles will be used to address the strength of local flow features and serve as a basis for comparison with cases of weaker induced mean velocities.

Figure 5.38 shows instantaneous u-velocity profiles at $t = 59$, 84, and 109 for Case 15. The top frame extends to a height of $3\lambda_z$ and the bottom frame emphasizes the near boundary region, $z < 0.5$. The primary signal in the region $0.5 < z < 2.5$ is from the oncoming wave. The wave forcing region approximately spans the region: $1.0 < z < 2.5$. The profiles represent the u'-velocity component at $x = \lambda_x/4$ and $y = y_l/2$. In the near wall region, strong velocity gradients are apparent.

Figure 5.39 shows similar profiles at later times, $t = 135$, 169, and 191. Strong upslope/downslope flows are observed near the wall, and typically the downslope maxima are greater than the upslope maxima. Figure 5.38 and 5.39 are presented for comparisons with the corresponding mean flows in the following figures.

Figure 5.40 shows the mean u-velocity profiles for Case 15 at the same times as in Figures 5.38 and 5.39. As with the density profiles, the horizontal mean eliminates the wave from the result, because of the periodicity of the wave in the x'-direction. Note that the mean velocities are on scales approximately 1/2 the magnitude of the instantaneous velocities. At $t = 59$, before the first mixing event, the mean velocity above a height of 0.5 is fairly weak, arising from the background noise. As time progresses, the strength and depth of penetration of the mean velocities increase. The mean currents contain significant amounts of kinetic energy and account for the steady growth of kinetic energy observed in Figure 4.27. The oscillation away from the wall of the direction of the currents (e.g., between times 169 and 191) suggests that the currents are not steady mean flows, but rather low frequency waves, implying buoyant interactions with the mean density fields, which were also observed to oscillate on similar time scales (e.g., Figures 5.35 and 5.36).

Figure 5.41 shows the rms w-velocity profiles for Case 15 at the same times as the bottom frame in Figure 5.40. The mean transport in the z' direction is always zero because of non-divergence and the bottom boundary. The rms w-velocity component

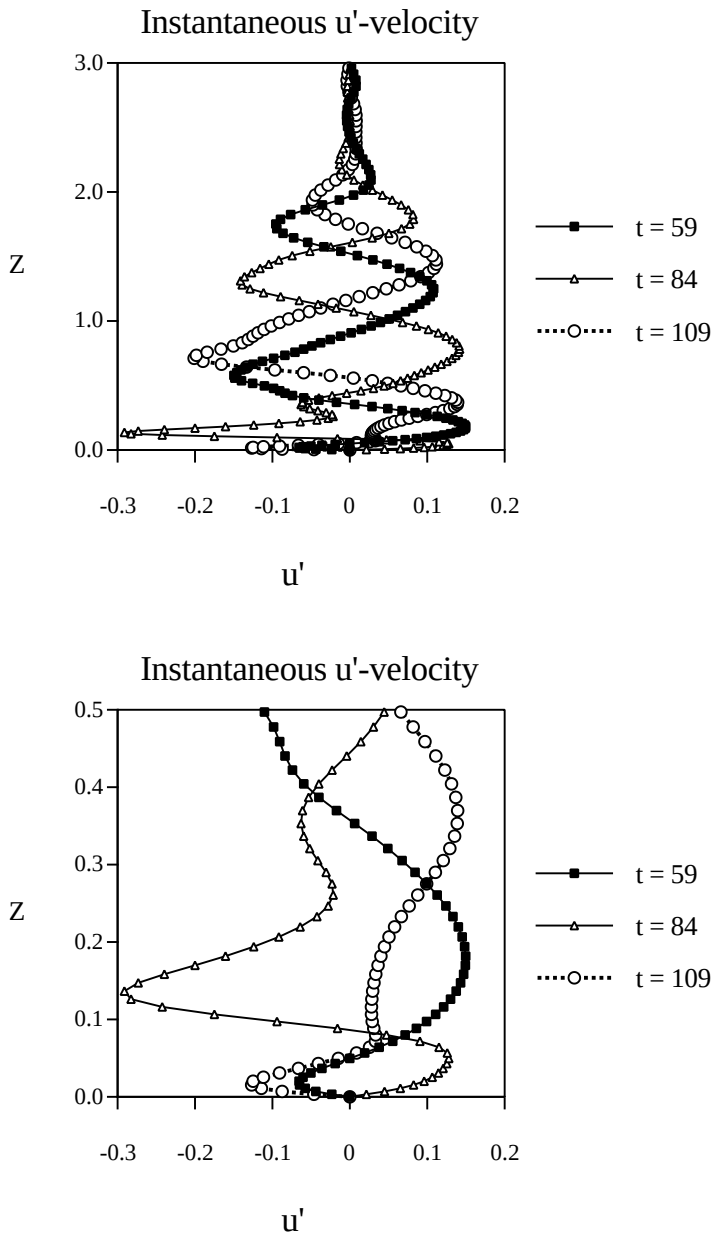

Figure 5.38: Instantaneous u-velocity profiles for Case 15 (9^o slope) at t = 59, 84, and 109. The bottom frame is a close up of the near wall region and indicates the model's resolution of the velocity gradients in the boundary layer.

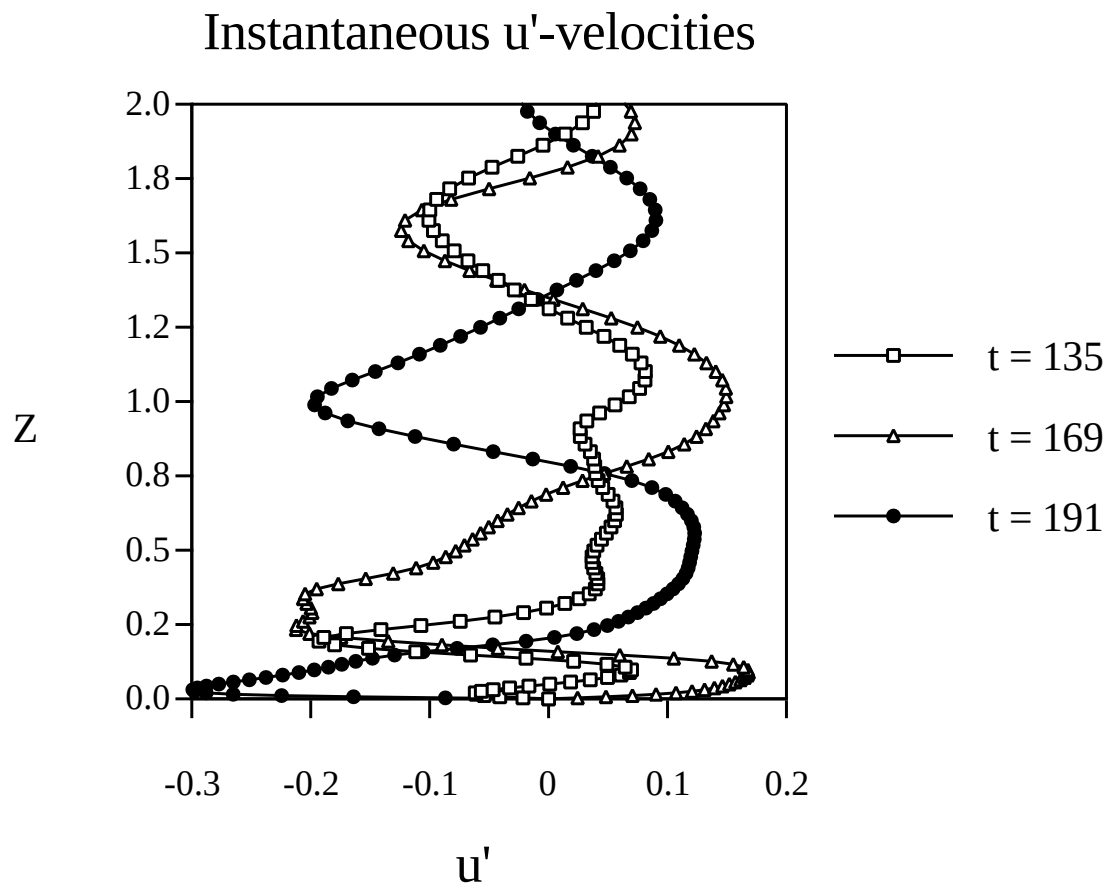

Figure 5.39: Instantaneous u'-velocity profiles for Case 15 (9^o slope) at times $t = 135$, 169, and 191.

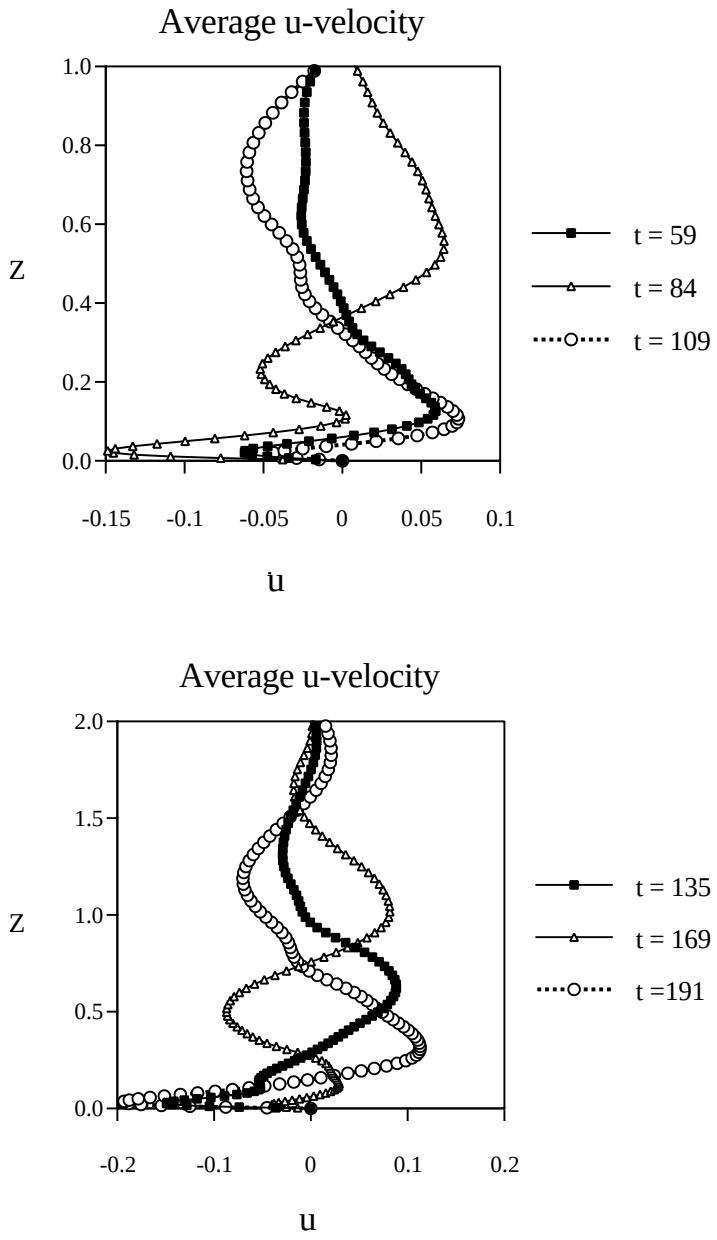

Figure 5.40: Mean u-velocity profiles for Case 15 (9^o slope) at $t = 59$, 84, 109, 135, 169 and 191, the same as in Figures 5.38 and 5.39.

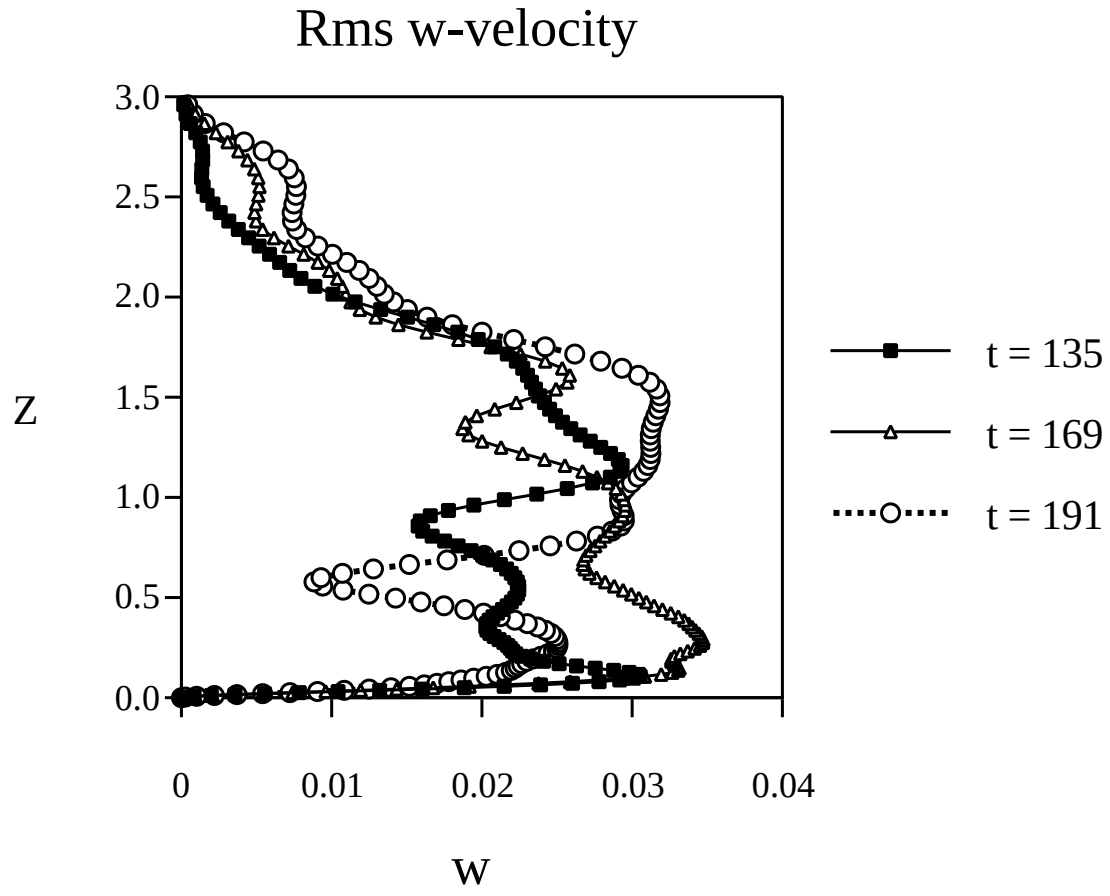

Figure 5.41: Rms w-velocity profiles for Case 15 (9^o slope) at $t = 135$, 169, and 191.

is nonzero, however, and gives an indication of the intensity of the activity across each plane. While the average of the three samples is representative of the dynamics of the oncoming wave, the fluctuations about the average indicate the intensity of local upwelling/downwelling features. It is apparent that there are significantly active local features up to a height of approximately $2\lambda_z$. The wave forcing region extends between approximately $1.5 < z < 2.8$ and Rayleigh damping occurs between $2.9 < z < 3.5$, which explains why the w component of velocity does not extend above $z = 3.0$.

Figure 5.42 presents instantaneous u-velocity profiles for Case 21 with a 20^o slope at $t = 34$, 128, and 177. It is useful for comparison with the magnitude of the mean velocity profiles in 5.43. The profiles are taken at $x = \lambda_x/4$ and $y = y_l/2$. At the three times shown the flow is downslope near the boundary. For this case Rayleigh damping occurs between $3.3 < z < 4.0$ and the wave forcing region extends between approximately $1.7 < z < 2.9$.

Figure 5.43 shows the corresponding mean u-velocity profiles for the 20^o slope. At $t = 34$, before the first mixing cycle, the mean velocity is negligible, but at later times there are appreciable currents at heights up to $z = 1.5$. In this case, as before, the mean currents are approximately 1/2 the strength of the local velocities.

Figure 5.44 shows the rms w-velocity profiles for the same 20^o slope simulation. The curve at $t = 34$ is representative of the signature of the oncoming wave. The fluctuations about this reference level at later times give another measure of local vertical transports. The full z domain for this simulation is $z = 4.0$. At the last time shown, $t = 177$, activity associated with upward propagating waves is observed at a height of 3.0 and above. Consistent with this observation, the energetics of the flow show wave energy radiating out of the domain into the upper sponge layer at this time.

Finally, Figures 5.45 and 5.46 show the mean u-velocity and rms w-velocity for the 30^o bottom slope of Case 28 at $t = 15$, 144, and 161. The observed instantaneous velocities were as high as 0.15, with off-wall maxima near $z = 0.06$, similar to the previous cases. The ratio of the mean velocities to the instantaneous velocities are smaller for the 30^o bottom slope than for the 9^o and 20^o simulations. This is consistent

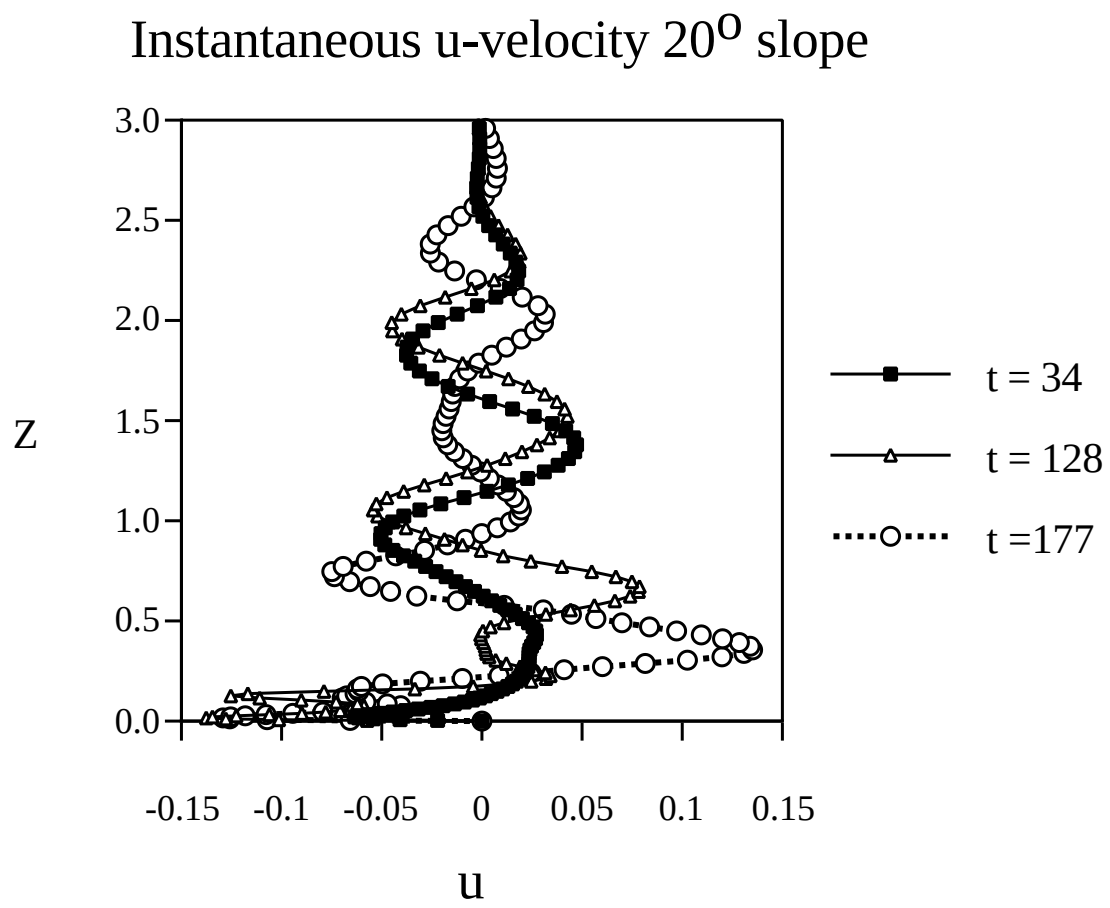

Figure 5.42: Instantaneous u-velocity profiles for Case 21 (20^o slope) at $t = 34$, 128, and 177.

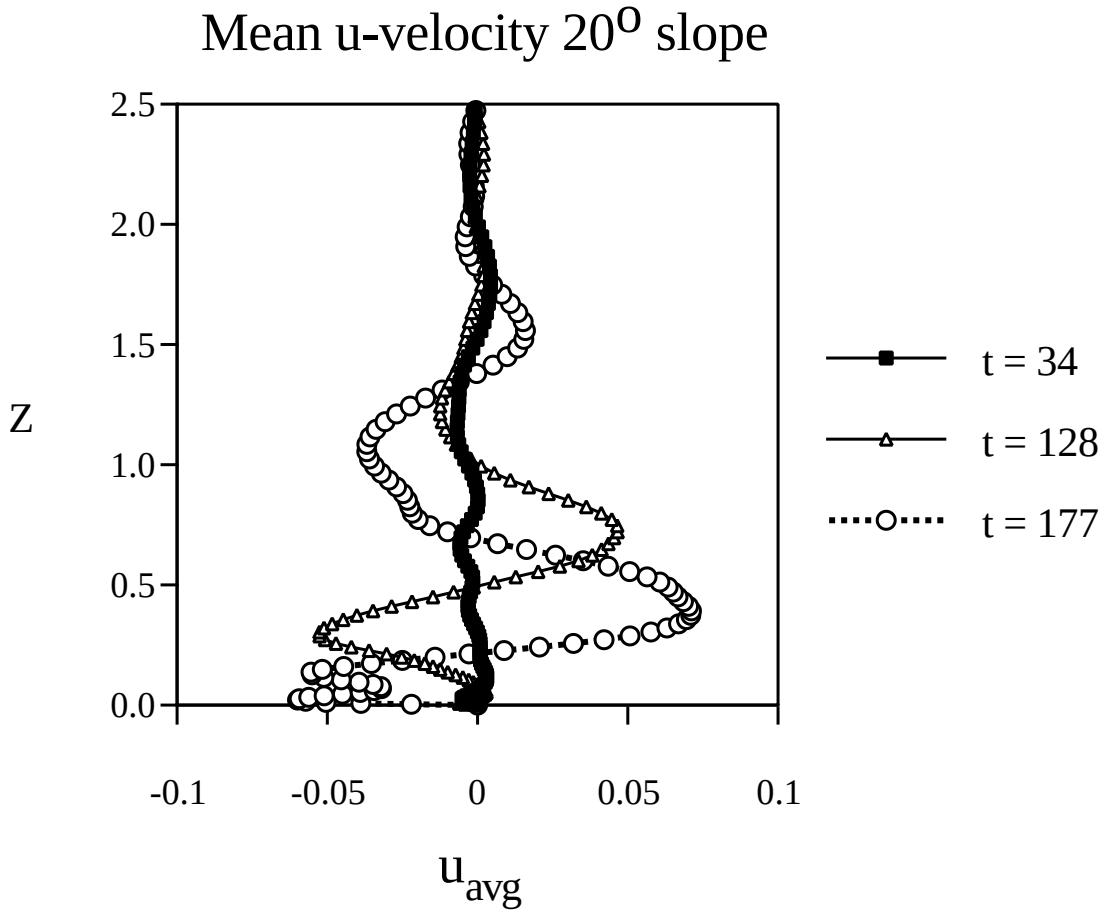

Figure 5.43: The mean u-velocity profiles for Case 21 (20^o slope) at $t = 34$, 128, and 177.

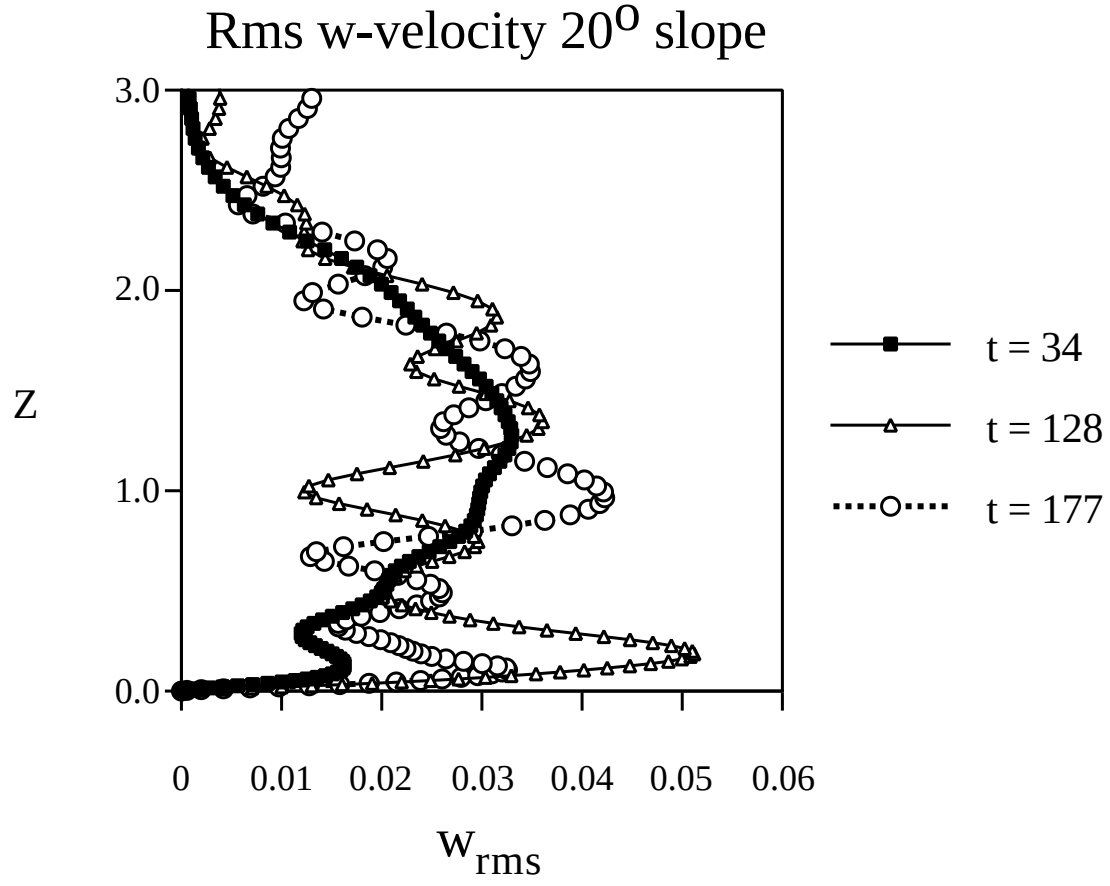

Figure 5.44: Rms w-velocity profiles at the same times as in Figures 5.42 and 5.43 for Case 21.

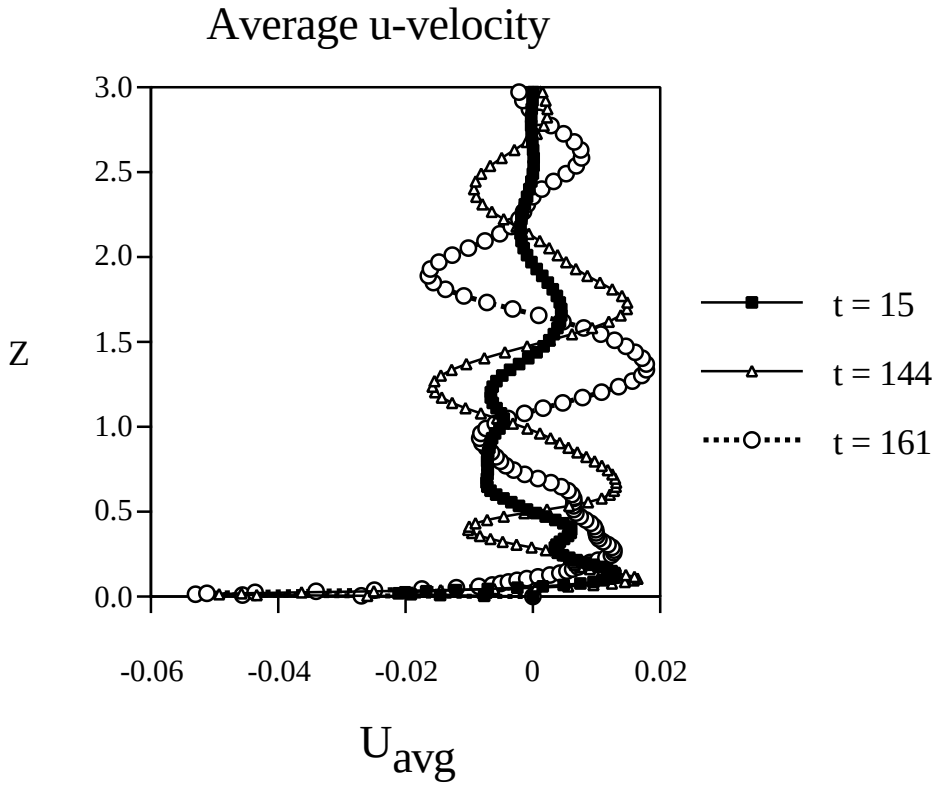

Figure 5.45: Mean u-velocity profiles for Case 28 (30^o slope) at $t = 15$, 144, and 161.

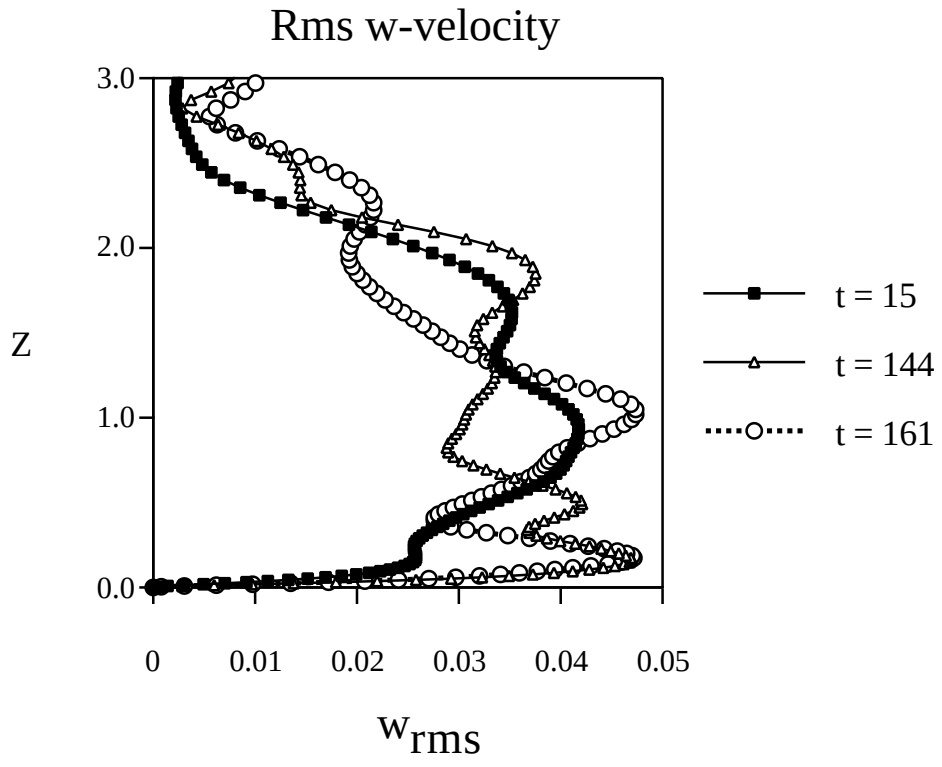

Figure 5.46: Rms w-velocity profiles are shown for Case 28 at $t = 15$, 144, and 161.

with a lack of buildup of kinetic energy described earlier (Section 4.6) and similar to the results from the density field (Figure 5.37). The steep slope case does not experience the buildup of either potential or kinetic energy away from the wall as large as occurred for the shallow slope cases.

Similar behavior is observed from the rms w-velocity profiles. Though significant radiation of energy from the boundary occurs, the fluctuations do not appear so pronounced as for the shallow slopes. The fluctuations may represent transmissive internal waves radiating from the turbulent bore rather than vertically recirculating fluid associated with mixing.

In summary, this section has shown that the buildup of kinetic and potential energy observed in Figures 4.27 and 4.29 for the shallow slope simulations consists

of mean changes to the background density and velocity profiles that extend above the boundary layer into the interior stratified fluid (see also Section 6.2). In contrast, Figure 4.28 showed that the steep slope experiments did not experience a buildup of kinetic and potential energy. The velocity and density profiles shown in this section corroborated this finding and indicated that the relative changes to the background fields were much smaller than for the shallow slope cases. For the shallow slope experiments, the mean currents were shown to extend to a height of approximately $2\lambda_z$ and it was suggested that there is an wavelike interaction with the mean density fields.

5.9 Mixing Efficiencies

In this section's analysis of the simulations, emphasis is placed on energetics of the flows. A quantity of particular interest is the mixing efficiency, which in general is related to the portion of wave energy that goes to irreversible mixing of the density field. In this section, first, different definitions of mixing efficiency are considered, then, the numerical simulations are analyzed, and finally, some new, exact solutions to the Navier Stokes equations are presented which give insight into mixing.

5.9.1 Definitions

A variety of definitions for the mixing efficiency have been constructed, often based on data most readily measured in a given experiment. For example, Ivey and Nokes (1989) have defined two parameters, the overall mixing efficiency, $\eta_o = P/W$, and the actual mixing efficiency,

$$\eta_1 = \frac{P}{W - D} \, , \tag{5.3}$$

where P is the gain in potential energy per wave period, W is the work input to generate the internal wave field, and D is an estimate of viscous dissipation experienced by the waves as they propagate towards the sloping boundary (with the dissipation arising from both internal dissipation and energy losses in the sidewall boundary layers).

Alternatively, oceanic field observations have frequently been interpreted using the mixing efficiency $\eta_2 = \chi/\epsilon$ (e.g., Oakey, 1982), a definition motivated by data from velocity, temperature, and salinity measurements. If a quasi-steady state exists in the field, then the definition $\eta_3 = \dfrac{\chi}{\chi + \epsilon}$ would be more in accord with the laboratory-based definition.

Previous numerical experiments have used still other definitions for the mixing efficiency. Winters et al. (1995), for example, have used (among other definitions) $\eta_4 = \int_{t=0}^{t_f} B_f \, dt / TE_i$ to determine the net buoyancy flux normalized by the total initial energy, and hence, the energy irreversibly lost to mixing. The numerical studies by Winters et al. of free shear flows differ significantly from the present boundary layer study in that their studies yield a net positive buoyancy flux, that is, a net transfer of kinetic to potential energy. In the present study the strong dissipation rate of kinetic energy in the boundary layer, and the initial equipartition of kinetic and potential energy in the gravity waves, makes the definition based upon the net buoyancy flux yield inappropriate (negative) mixing efficiencies.

Figure 5.47 shows the horizontally integrated buoyancy flux as a function of height for Case 21, with a bottom slope of 20^o and $Re = 1800$, at $t = 48$, 83, 137, and 167. As described in relation to Figures 4.27 - 4.29, the net time-integrated buoyancy flux is negative, while the temporal dependence is characterized by rapid positive to negative oscillations. Figure 5.47 indicates the importance of the near boundary region in the total integral of the buoyancy flux. The strongest fluxes occur near the boundary and are predominantly negative.

In the present numerical experiments, therefore, the mixing efficiency is represented as the ratio of the potential energy dissipated to the work input to generate the oncoming waves,

$$\eta = \frac{-\int_{t_i}^{t_f} \chi \, dt}{\int_{t_i}^{t_f} W \, dt} \; . \tag{5.4}$$

This method is more approximate than the rigorous treatment proposed by Winters *et al.* (1995) but remains sufficient for the purposes of this investigation. The values of χ and W are integrated over the full domain from the time when the oncoming wave train has reached the boundary, t_i, until the end of the simulation, t_f. Two

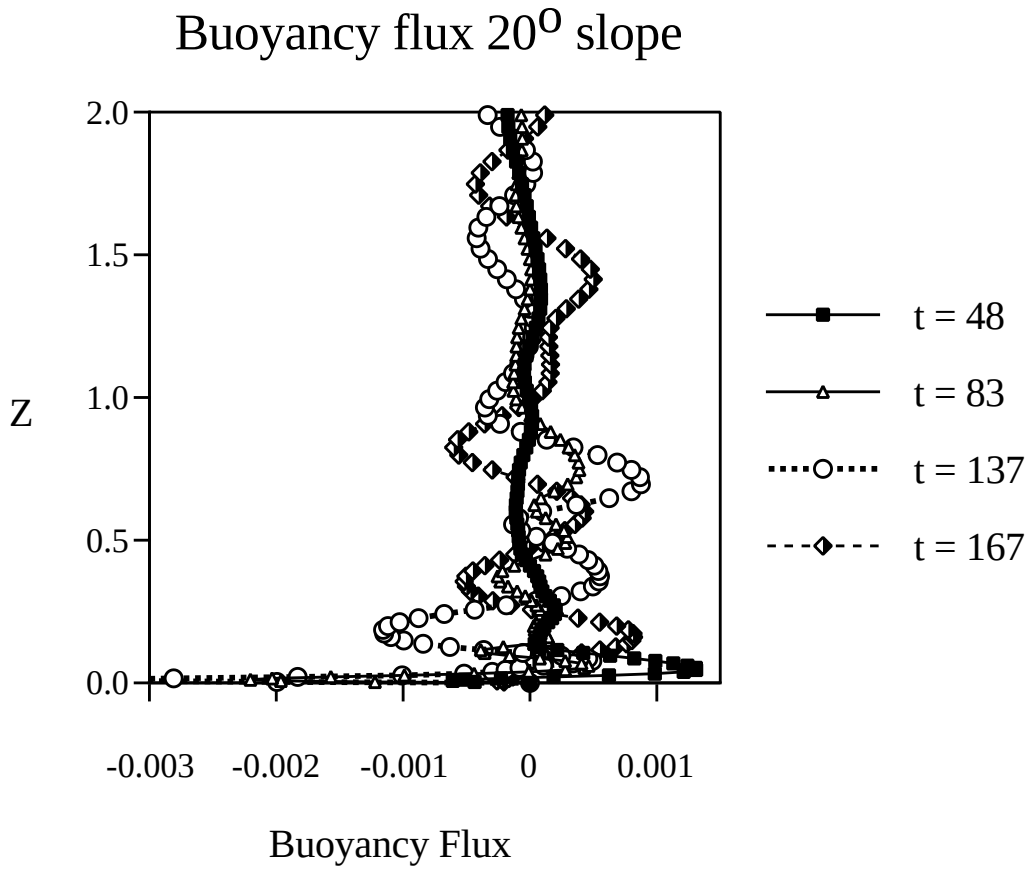

Figure 5.47: The horizontally averaged buoyancy flux for Case 21 (20^o slope) at $t = 48$, 83, 137, and 167. The time averaged buoyancy flux has a net negative value, dominated by a strong flux of potential to kinetic energy in the near-wall region.

examples of the integration technique and the resulting mixing efficiency are presented in Figures 5.48 and 5.49.

5.9.2 Simulation Results

Figure 5.48 presents the calculation of the mixing efficiency for Case 26 with $\alpha = 30^o$ and $Re = 800$. The values for the integrals of the work input (Work) and the potential energy dissipation rate (PED) (right axis) are shown together with their ratio (Mixing) (left axis). The ratio of the integrals of $-\chi$ and W quickly achieves a stable value of approximately 0.31 after the wave train reaches the boundary at $t_i \approx 30$. This first example arrives at the determination of a steady mixing efficiency (0.31) very quickly, because the case represents a quasi-steady flow with nearly constant rates of χ and ϵ. Ivey and Nokes found mixing efficiencies [using the definition in Equation (5.3)] of approximately 0.21 for experiments with significantly higher Richardson and Prandtl numbers.

Figure 5.49 presents the determination of the mixing efficiency for Case 15, with a 9^o bottom slope and periodic mixing cycles. Here the oncoming waves reach the wall near $t_i = 60$ and begin the first of three mixing cycles. For this case, χ oscillates throughout the mixing cycle (e.g., Figure 4.17), while the work input remains almost constant. The resulting determination of η therefore oscillates about a mean value over each mixing cycle, but should dampen in time as the respective integrals become larger. For this simulation, the approximate mean value during $100 < t < 191$ is $\eta = 0.32$. In the experiments of Ivey and Nokes, the work input and gain in background potential energy were averaged over a wave period in determining the mixing efficiency. For the wave trains in the present simulations, however, the mixing cycles are longer than the wave periods, and it is therefore more appropriate to integrate over the duration of the simulation after a quasi-steady state develops. As can be seen in Figure 5.49, however, this introduces a certain degree of subjectivity to the problem in determining the average value of η. For each of the simulations, the best approximation for t_i was chosen based upon energetics and flow visualizations, and the sensitivity of the result on η was examined to arrive at a best estimate for

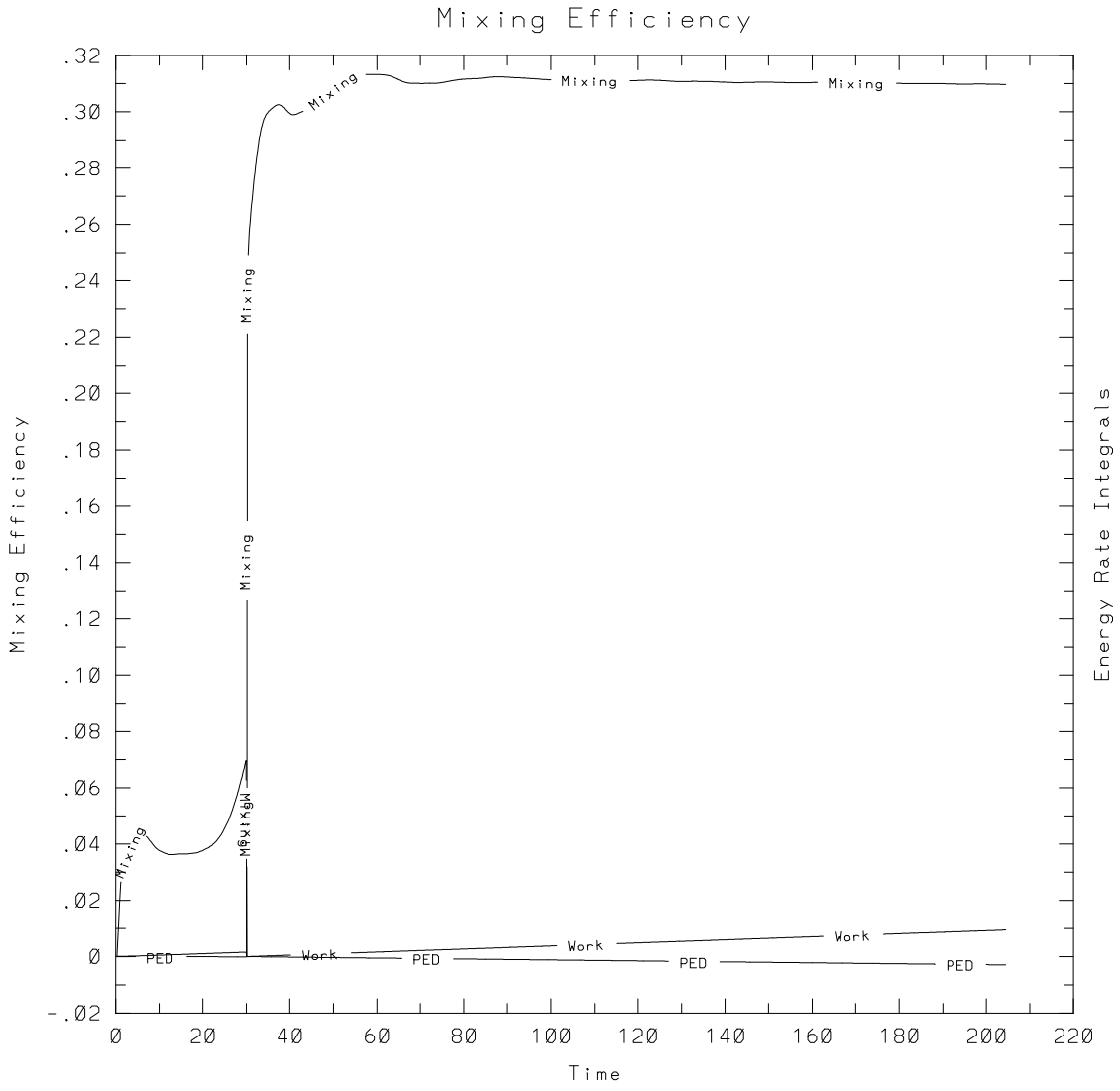

Figure 5.48: The mixing efficiency as a function of time for Case 26 (30^o slope). This mixing efficiency is determined by integrating the potential energy dissipation rate and normalizing it by the time integrated work input to the oncoming waves. For this case the mixing efficiency reaches a stable value of 0.31 after the wave train reaches the boundary at approximately $t = 30$.

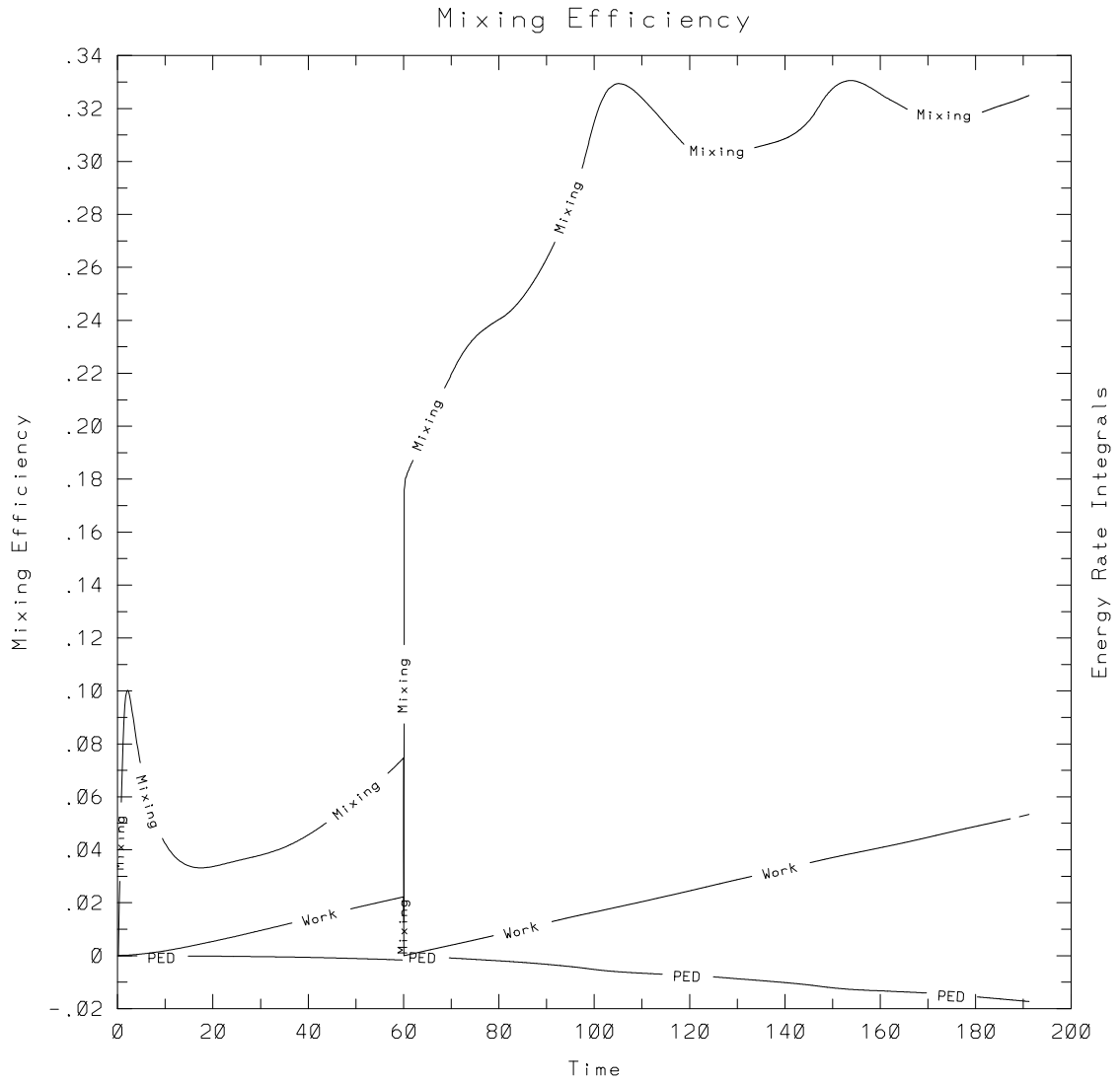

Figure 5.49: The mixing efficiency for Case 15 (9^o slope) as a function of time. The calculation is begun at $t = 60$, after the wave train reaches the wall and achieves a fairly steady value of 0.32 after two mixing cycles.

the mixing efficiency.

Table 5.1 presents the mixing efficiencies, heat loss coefficients, and radiation coefficients for the simulations of Table 4.1 covering a number of different critical slopes and Reynolds numbers. The heat gain coefficient is defined similar to the mixing efficiency as the ratio of the integrals of the kinetic energy dissipation rate to the work input

$$H = \frac{-\int_{t_i}^{t_f} \epsilon \, dt}{\int_{t_i}^{t_f} W \, dt} \; . \tag{5.5}$$

The radiation coefficient, R, is the remainder of energy not dissipated as either heat or mixing, i.e., $R = 1 - \eta - H$. For the critical angle simulations, carried out for a wide range of bottom slopes and Reynolds numbers, the mixing efficiencies are near 35%. A typical energy budget for the oncoming waves is that approximately 35% of the wave energy goes into mixing the stratified fluid, approximately 55% is dissipated as heat, and (thus it may be inferred that) approximately 10% of the incident energy is reradiated away from the turbulent boundary layer by smaller scale gravity waves.

For the critical angle simulations the mixing efficiencies vary between 0.32 and 0.39. The error bars on the data are between ± 0.01 and ± 0.02 based upon the subjectivity introduced by choosing t_i and t_f for the integrations of χ and W. There is no obvious dependency of the mixing efficiency on either Reynolds number or bottom slope. The main generalization that can be made is that, for a given bottom slope, the lower Reynolds number simulations radiate less energy away from the boundary layer. While one might assume that higher Reynolds number flows should generally be more efficient at mixing, the analysis in the next section suggests that low Reynolds number internal waves have mixing efficiencies of 0.5 (for a Prandtl number of 1.). Thus, the separation of viscous from turbulent dissipation rates may be ineffective in the simulations. Mixing efficiencies for off-critical frequency waves will be described in the following chapter.

Figure 5.50 plots the values of mixing efficiency (circles) and heat loss coefficient (diamonds) for the simulations listed in Table 5.1. The solid lines are least-square linear fits to the data. The equations of the lines are given below the figure but should not be considered to be definitive. The lines are given for visualization purposes only.

Table 5.1: Energy Budgets at Critical Angle

Case	Slope	Reynolds No.	Mixing	Heat	Radiate
1	3.4	620	0.33	0.62	0.05
2	3.4	830	0.35	0.55	0.10
3	3.4	2100	0.39	0.54	0.07
4	3.4	2600	0.39	0.48	0.13
5	5.0	1860	0.38	0.60	0.02
6	5.0	2400	0.39	0.52	0.09
7	5.0	3300	0.37	0.50	0.13
8	7.7	750	0.37	0.61	0.02
9	7.7	1500	0.33	0.55	0.12
10	7.7	3000	0.35	0.57	0.08
11	9.2	850	0.36	0.58	0.06
12	9.2	1200	0.38	0.50	0.12
13	9.2	2000	0.36	0.45	0.19
14	9.2	2800	0.37	0.48	0.15
15	9.2	3600	0.32	0.56	0.12
16	20.0	540	0.37	0.60	0.03
17	20.0	800	0.36	0.57	0.07
18	20.0	850	0.36	0.62	0.02
19	20.0	1100	0.35	0.54	0.11
20	20.0	1200	0.36	0.61	0.03
21	20.0	1800	0.34	0.53	0.13
22	20.0	1800	0.34	0.54	0.12
23	20.0	1800	0.35	0.53	0.12
24	20.0	2400	0.35	0.50	0.15
25	30.0	450	0.34	0.66	0.00
26	30.0	800	0.32	0.66	0.02
27	30.0	800	0.37	0.58	0.05
28	30.0	1700	0.37	0.61	0.02

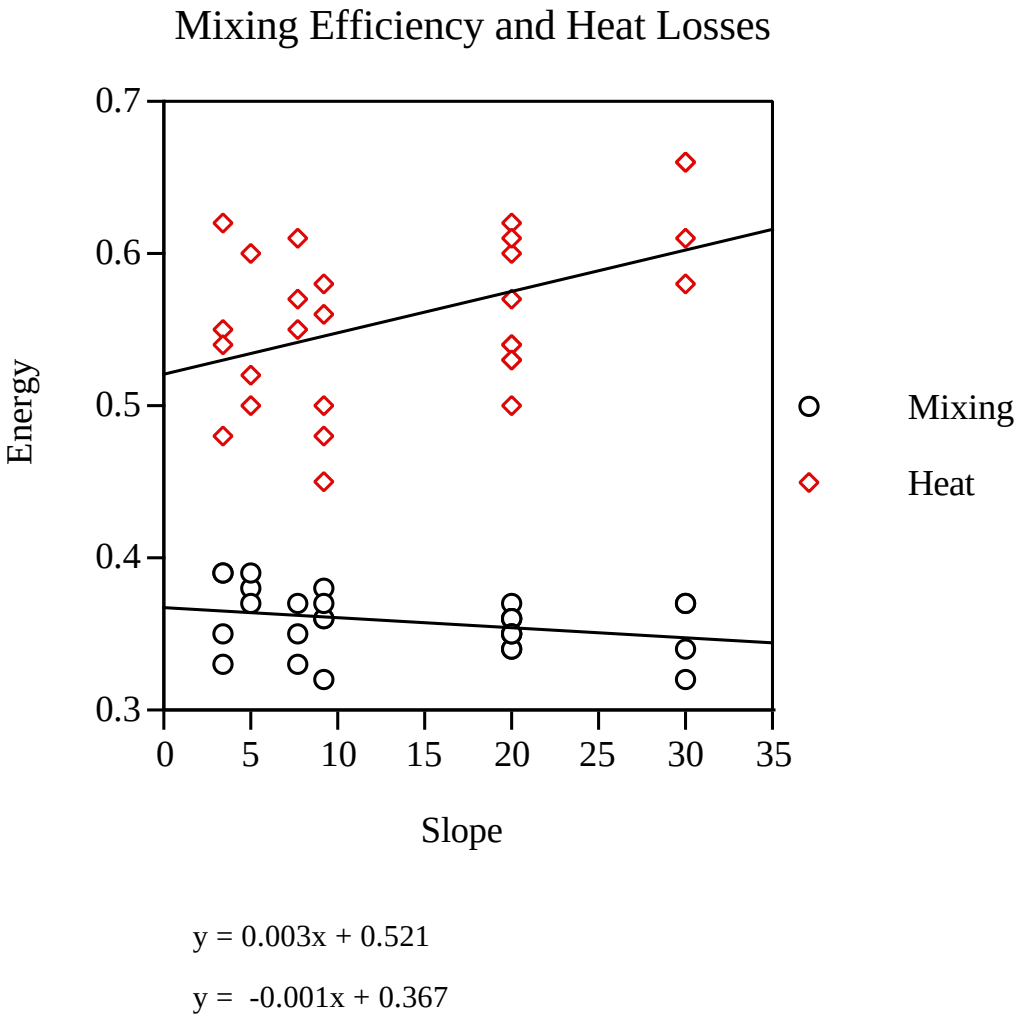

Figure 5.50: The mixing efficiencies and heat loss coefficients are locate for the critical angle simulations as a function of their bottom slopes.

The averages are made across different numbers of simulations at different Reynolds numbers and therefore may not be accurate representations of the dependencies in the data. There appear to be weak general trends, however, indicating lower "average" mixing efficiencies and somewhat higher heat losses for the steeper slope simulations.

Figure 5.51 shows the radiation coefficients for the simulations listed in Table 5.1. Again a least squares linear fit to the data is included for emphasis of the downward trend towards less radiation of energy for the steeper slope cases. The trend should not be overemphasized, however, as the "averaging" may be inappropriate for the wide range of Reynolds numbers and different types of flow development that occur (e.g., laminar, turbulent, steady, intermittent). The spread in the data is considerably larger than the variation in the overall trends and should therefore be considered inconclusive. In certain respects it is more informative to examine the data in Table 5.1 for trends than to rely on Figures 5.50 and 5.51, which do not include Reynolds numbers or other simulation parameters.

5.9.3 Internal Wave Dissipation

To further the understanding of mixing efficiencies in these numerical simulations it is important to learn as much as possible from any exact solutions for an internal gravity wave propagating in a viscous fluid. While the following derivations appear to be straightforward, they do not appear to have been previously published.

Beginning with the three-dimensional Navier Stokes equations within the Boussinesq approximation, as given in Equations (3.121) - (3.125) with $\alpha = 0$, we seek a plane-wave solution with $v = 0$ of the form:

$$\begin{pmatrix} u \\ w \\ \rho \\ p \end{pmatrix} (x, z, t) = \begin{pmatrix} \hat{u} \\ \hat{w} \\ \hat{\rho} \\ \hat{p} \end{pmatrix} e^{i(kx+mz-\omega t)} , \tag{5.6}$$

where ω is complex. This plane-wave form of the solution allows the problem to be examined in two dimensions by aligning the x axis in the direction of the wave

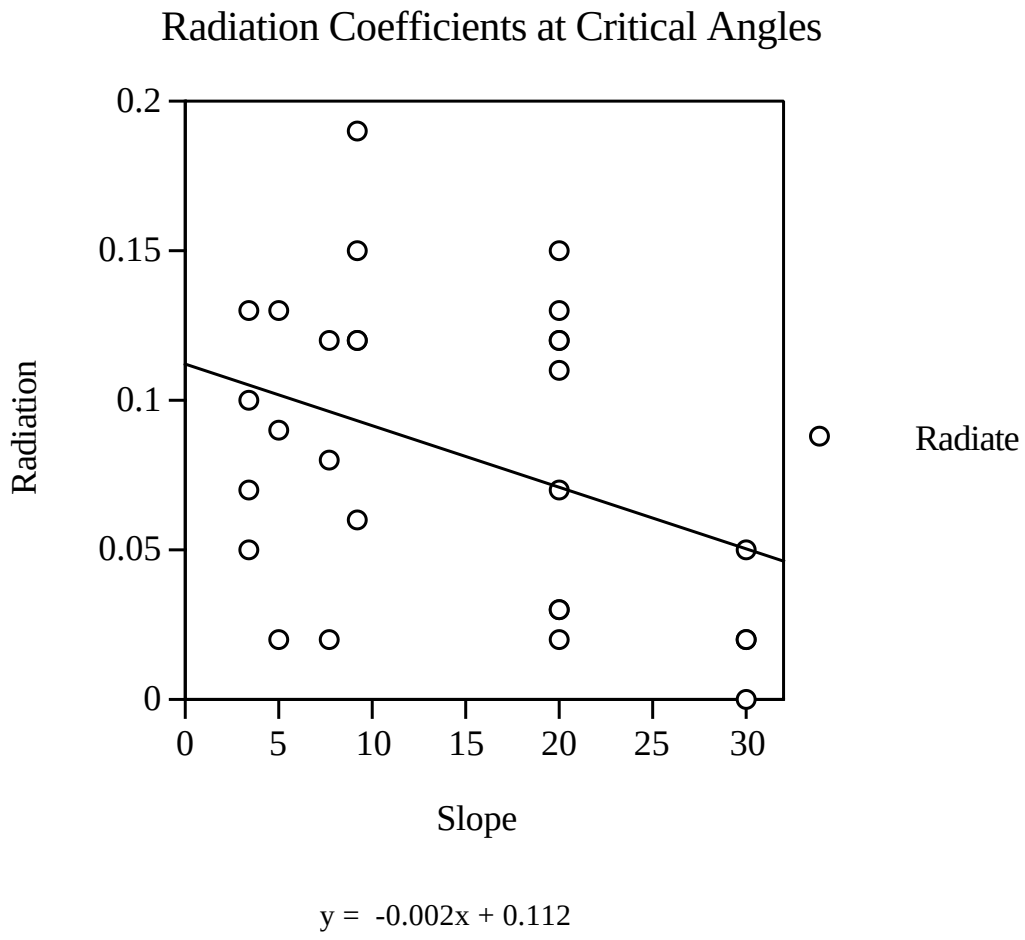

Figure 5.51: The critical angle simulations are located as a function of their radiation coefficients and slopes.

propagation. The nonlinear terms are all identically zero for plane waves, because, for example (and with $\frac{\partial u}{\partial x} = -\frac{\partial w}{\partial z}$ from continuity):

$$-u\frac{\partial w}{\partial z} + w\frac{\partial u}{\partial z} = (-\hat{u}im\hat{w} + \hat{w}im\hat{u})e^{2i(kx+mz-\omega t)} = 0 \; . \tag{5.7}$$

With Equation 5.6 the dispersion relation becomes

$$\omega = i\omega_I + \omega_R \; , \tag{5.8}$$

where

$$\omega_I = \frac{-1}{2}\left[\frac{k^2+m^2}{Re\,Pr} + \frac{k^2+m^2}{Re}\right] \; , \tag{5.9}$$

and

$$\omega_R = \left[\frac{Ri\,k^2}{k^2+m^2} - \frac{1}{4}\left(\frac{k^2+m^2}{Re\,Pr} - \frac{k^2+m^2}{Re}\right)^2\right]^{1/2} \; . \tag{5.10}$$

For $Re \to \infty$, the dispersion relation simplifies to the inviscid, nondiffusive dispersion relation (Equation 2.32). For $Pr = 1$, the dispersion relation simplifies to

$$\omega = -i\,\frac{k^2+m^2}{Re} + \frac{\sqrt{Ri}\,k}{(k^2+m^2)^2} \; , \tag{5.11}$$

and for $Pr \to \infty$, it becomes

$$\omega = \frac{-i}{2}\frac{k^2+m^2}{Re} + \left[\frac{Ri\,k^2}{k^2+m^2} - \frac{1}{4}\left(\frac{k^2+m^2}{Re}\right)^2\right]^{1/2} \; . \tag{5.12}$$

Consequently, the time-dependent flow field for a viscously-decaying, nonlinear internal gravity wave is described by

$$w(x,z,t) = Ae^{\omega_I\, t}\, \cos\phi \; , \tag{5.13}$$

$$u(x,z,t) = \frac{-Am}{k}\, e^{\omega_I\, t}\, \cos\phi \; , \tag{5.14}$$

$$\rho(x,z,t) = \frac{A}{2}\left(\frac{k^2+m^2}{Re\,Pr} - \frac{k^2+m^2}{Re}\right)\frac{k^2+m^2}{Ri\,k^2}\, e^{\omega_I t}\cos\phi$$
$$-A\left(\frac{k^2+m^2}{Ri\,k^2}\right)\left[\frac{Ri\,k^2}{k^2+m^2} - \frac{1}{4}\left(\frac{k^2+m^2}{Re\,Pr} - \frac{k^2+m^2}{Re}\right)^2\right]^{1/2} e^{\omega_I t}\sin\phi \; , \tag{5.15}$$

where $\phi = (kx + mz - \omega_R t)$ and ω_I and ω_R are defined by Equations (5.9) and (5.10). The results are valid for any wave amplitude, A, as no assumptions were made in the derivation restricting the result to linear or small amplitude waves.

While these results are interesting in themselves, they are used here to investigate the energetics of a decaying wave. The kinetic energy, $KE = \frac{1}{2}(u^2 + w^2)$, potential energy, $PE = \frac{1}{2} Ri\, \rho^2$, and the buoyancy flux, $B_f = Ri\, \rho\, w$, may be integrated in space, over horizontal and vertical wavelengths, to determine their overall temporal dependence. The results are

$$\overline{KE}(t) = \frac{A^2\pi}{2}\, e^{2\omega_I t} \left(\frac{k^2 + m^2}{k^2} \right) , \tag{5.16}$$

$$\overline{PE}(t) = \frac{A^2\pi}{2}\, e^{2\omega_I t} \left(\frac{k^2 + m^2}{k^2} \right) , \tag{5.17}$$

$$\overline{B_f}(t) = \frac{A^2\pi}{2}\, e^{2\omega_I t} \left(\frac{k^2 + m^2}{k^2} \right) \left(\frac{k^2 + m^2}{Re\, Pr} - \frac{k^2 + m^2}{Re} \right) , \tag{5.18}$$

where $\overline{(\ )}$ denotes a spatially integrated value.

Note that the solutions show equipartion between kinetic and potential energy. The most significant use of these solutions for the current purposes is to examine χ and ϵ and their ratio, particularly as functions of the Prandtl number. From (5.13) to (5.15)

$$\epsilon = \frac{1}{Re} \left[2 \left(\frac{\partial u}{\partial x} \right)^2 + 2 \left(\frac{\partial w}{\partial z} \right)^2 + \left(\frac{\partial u}{\partial z} + \frac{\partial w}{\partial x} \right)^2 \right] , \text{ and} \tag{5.19}$$

$$\chi = \frac{Ri}{Re\, Pr} \left[\left(\frac{\partial \rho}{\partial x} \right)^2 + \left(\frac{\partial \rho}{\partial z} \right)^2 \right] . \tag{5.20}$$

Spatially integrating over wavelengths then gives

$$\overline{\epsilon}(t) = \frac{A^2\pi}{Re}\, e^{2\omega_I t} \left(\frac{k^2 + m^2}{k} \right)^2 , \text{ and} \tag{5.21}$$

$$\overline{\chi}(t) = \frac{A^2\pi}{Re\, Pr}\, e^{2\omega_I t} \left(\frac{k^2 + m^2}{k} \right)^2 . \tag{5.22}$$

The result shows that the ratio $\dfrac{\overline{\epsilon}}{\overline{\chi}} = Pr$ is a simple function of the Prandtl number. Note, in particular, that for comparison with the numerical simulations conducted in this study, for $Pr = 1$, then $\overline{\chi} = \overline{\epsilon}$.

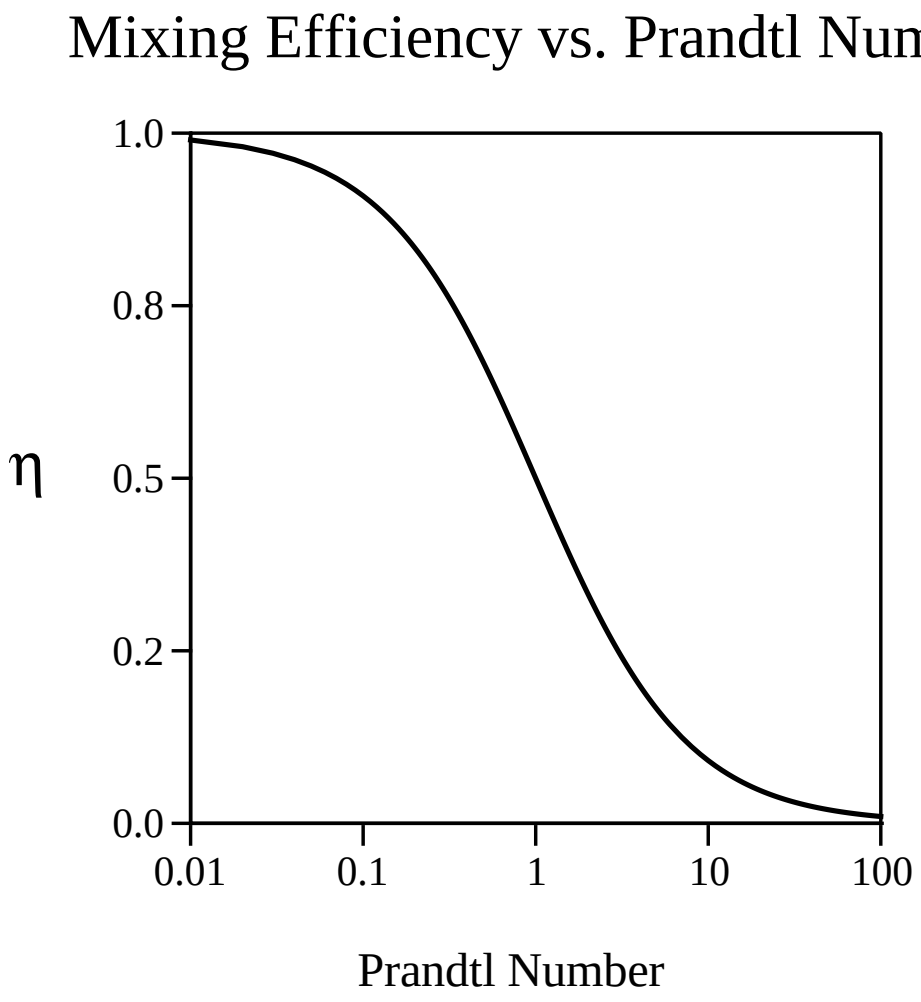

Figure 5.52: The mixing efficiency, defined here as $\overline{\chi}/(\overline{\chi}+\overline{\epsilon})$, is presented as a function of Prandtl number.

These exact results can be translated into a mixing efficiency, here defined as $\eta = \dfrac{\overline{\chi}}{\overline{\chi} + \overline{\epsilon}} = \dfrac{1}{1 + Pr}$, which is graphed in Figure 5.52. Thus for $Pr = 1$, the mixing efficiency is 0.5. This is the primary result of this section. Physically the result means that a viscously decaying internal gravity wave with $Pr = 1$ dissipates kinetic and potential energy at the same rate.

The exact solution is valid for plane waves at all Reynolds numbers. The rate of viscous decay of energy in a plane gravity wave decreases rapidly with increasing Reynolds number [see Equations (5.9) and (5.16)], while the same quantity in a turbulent flow is approximately independent of Reynolds number. It is therefore desired to compare the dissipation rates caused by viscous decay of internal waves in the simulations to dissipation rates caused by turbulence. At high Reynolds number, the dissipation due to turbulence may be much larger than viscous dissipation for internal waves; but for low and moderate Reynolds number flows, such as those conducted in the simulations, the viscous (laminar) dissipation of energy of the internal waves may be comparable to dissipation caused by turbulence.

Field and laboratory measurements have frequently measured mixing efficiencies of approximately 0.2 for stratified turbulence. The results of the numerical simulations are approximately 0.35, or about 75% higher than other results. In addition to the differences in Richardson numbers (wave amplitudes) described in Section 5.1, lower Reynolds numbers than in the field and lower Prandtl numbers than in the laboratory may contribute significantly to differences in mixing efficiencies. Oceanic field measurements cover a range of scales that may be characterized by very large Reynolds numbers, so that nearly all significant mixing occurs through turbulence. While laboratory experiments use Reynolds numbers similar to those in the numerical experiments, the Prandtl number of salt water (700) is significantly higher than used in the numerical simulations. (In addition, the Richardson numbers differ significantly.) To preserve adequate numerical resolution of the small density structures that develop, Prandtl numbers of $O(1)$ must be used. A complication that arises from this constraint is that the dissipation rates of kinetic and potential energy are approximately equal for the internal wave, and influence the resulting determination

of η by driving it towards 0.5.

Rehmann and Koseff (1994) have described Prandtl number dependence on mixing efficiency for decaying grid-generated turbulence. For the Reynolds numbers in their laboratory experiments they find that Prandtl number effects are small, but their analysis shows that for higher Richardson numbers Prandtl number effects may become important for smaller dissipation Reynolds numbers. Rehmann and Koseff also use a different definition for mixing efficiency (similar to Equation 5.3) than used in the numerical experiments. Under their definition a decaying internal gravity wave would not make any contribution to the mixing efficiency even if half of the wave energy was dissipated by χ. The difference in definitions makes it difficult to compare the results of the exact solution presented in this section to Rehmann and Koseff's analysis.

Turbulent dissipation rates of both kinetic and potential energy are expected to be higher than laminar values. It is possible that the turbulent mixing efficiencies could be similar or even higher for turbulent simulations. In the numerical simulations we observe values near 0.35 instead of 0.5. The reason is partially related to the influence of the no-slip boundary condition at the wall. In the viscous sublayer, strong dissipation of kinetic energy occurs; this has no counterpart in dissipation of potential energy because of the no-flux boundary condition on the density field. In these simulations, additional analysis (not pictured) focusing only on the turbulent boundary layer ($0.1 < z < 0.4$) indicates that dissipation rates of χ and ϵ are approximately equal. Thus, it might be expected that low Reynolds number simulations conducted for a free-shear flow, remote from the presence of a boundary, should have mixing efficiencies near 0.5 (for $Pr = 1$). The use of large eddy simulations, modeling the dissipation of small scale density structures, may provide a future means of investigating flows with larger Prandtl and Reynolds numbers.

When $Pr > 1$, the internal wave loses more kinetic than potential energy to viscous dissipation. For the wave to retain its wave structure (including equipartition of energy), there is a compensating buoyancy flux from potential to kinetic energy. Figure 5.53 compares results for $\overline{\chi}$, $\overline{\epsilon}$, and $\overline{B}_f$ as a function of Prandtl number.

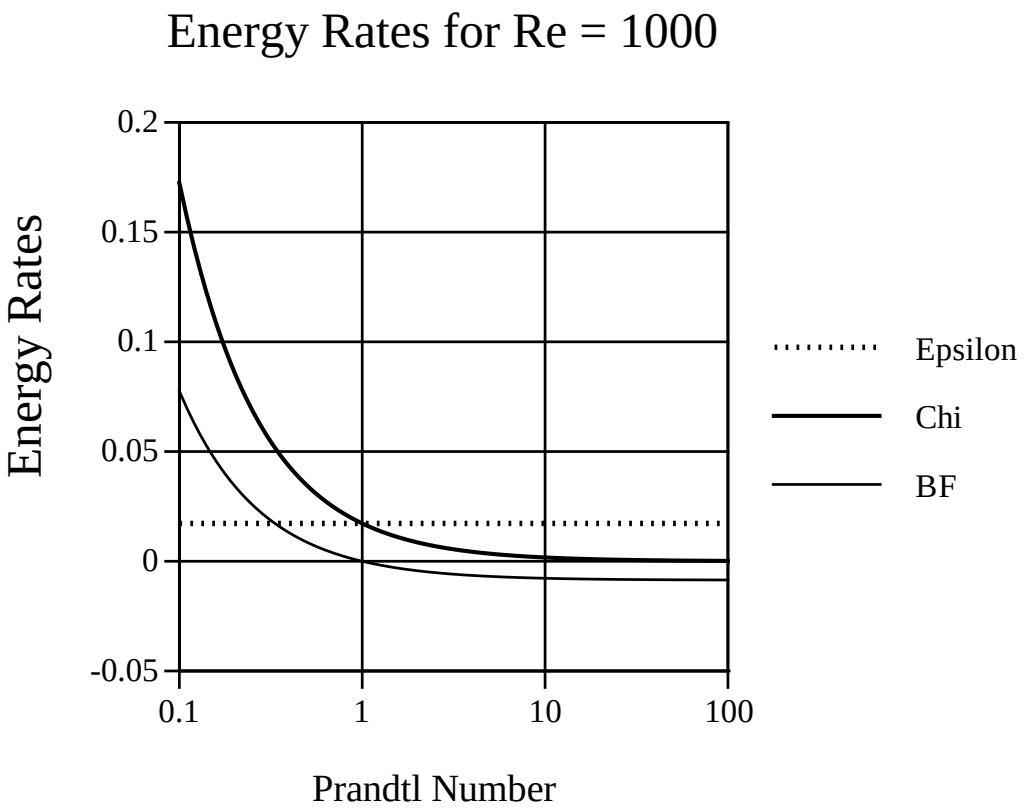

Figure 5.53: The average buoyancy flux ($\overline{B_f}$), $\overline{\epsilon}$, and $\overline{\chi}$ as a function of Prandtl number for $Re = 1000$.

Parameters for this plot are: $k = 2\pi/1.5$, $m = 2\pi/0.7$, $Ri_{\lambda_z} = 1$, $A = 0.1$, and $Re = 1000$. For Prandtl numbers below one, $\overline{\chi}$ is greater than $\bar{\epsilon}$, so that the wave loses more potential than kinetic energy. In this range, therefore, the buoyancy flux is positive, transferring excess kinetic to potential energy. For $Pr > 1$, the opposite is true: as more kinetic energy is dissipated, the deficit is resupplied by a negative buoyancy flux, transferring potential to kinetic energy. Note that the magnitude of the buoyancy flux is exactly $(\overline{\chi} - \bar{\epsilon})/2$.

Finally, this section on mixing efficiencies is concluded by comparing these theoretical results with numerical results obtained for homogenous stratified turbulence for Prandtl numbers between 0.5 and 5. These numerical results support the suggested importance of Prandtl number effects on turbulent mixing dynamics. It should be noted, however, that for turbulent dynamics, at high Reynolds number, ϵ and χ are thought to be controlled by the rate of transfer of energy to small scales. A linear theory would not predict this dependency and may only be useful at lower Reynolds numbers.

The particular series of direct numerical simulations of interest was conducted using a spectral turbulence model used by Riley et al. (1991) for homogeneous turbulence in a triply periodic domain. The flow was initialized for this comparison with random velocity and density fluctuations (with specified energy content in all wavenumbers) at initial turbulent Reynolds numbers of 100 and 200 (based upon rms velocity and domain length scales). The simulations were conducted on a 64^3 grid with a Froude number of 4, at Reynolds numbers sufficiently low to insure that the density structure would be adequately resolved at Prandtl numbers up to five. The simulations were continued until over 90% of the energy in the system was dissipated and then analyzed to determine the proportions dissipated by χ and ϵ, and to examine the net integrated buoyancy flux.

The results of these low Reynolds number simulations, presented in Figure 5.54, are similar to those in Figure 5.53, obtained theoretically. Similar to the case for internal waves, as the Prandtl number increases, ϵ increases, χ decreases, and the buoyancy flux becomes more positive. This trend in the buoyancy flux shows that

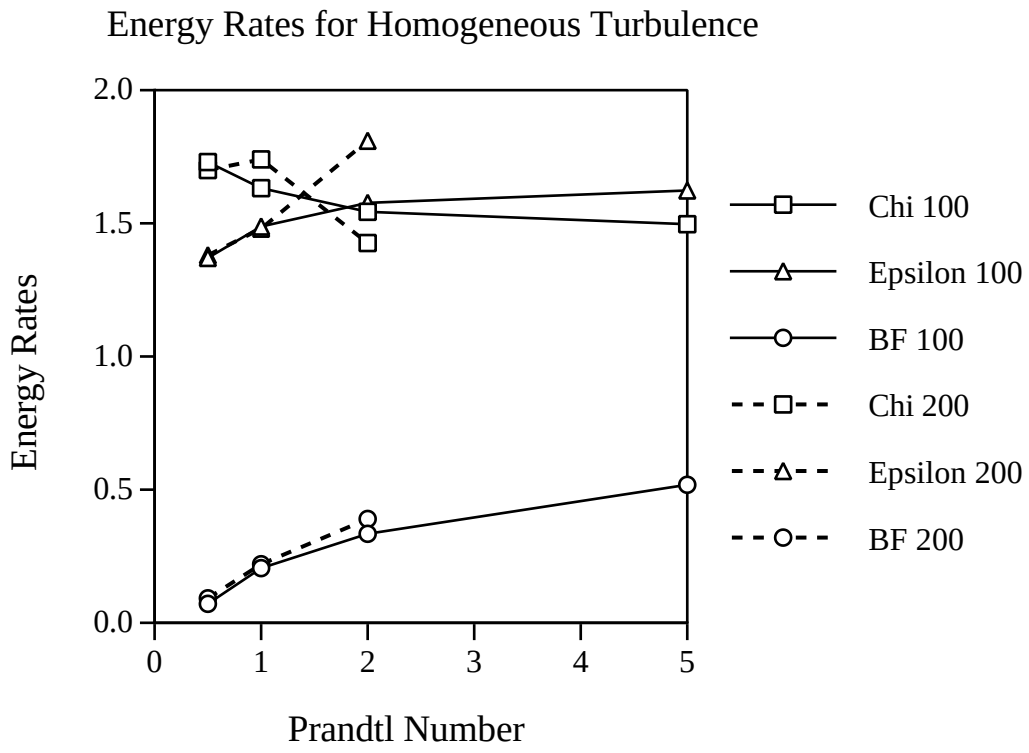

Figure 5.54: Dissipation rates and buoyancy flux as a function of Prandtl number calculated in simulations of homogeneous turbulence. The integrated values of χ, ϵ, and buoyancy flux are presented for Prandtl numbers between 0.5 and 5, for Reynolds number of 100 and 200.

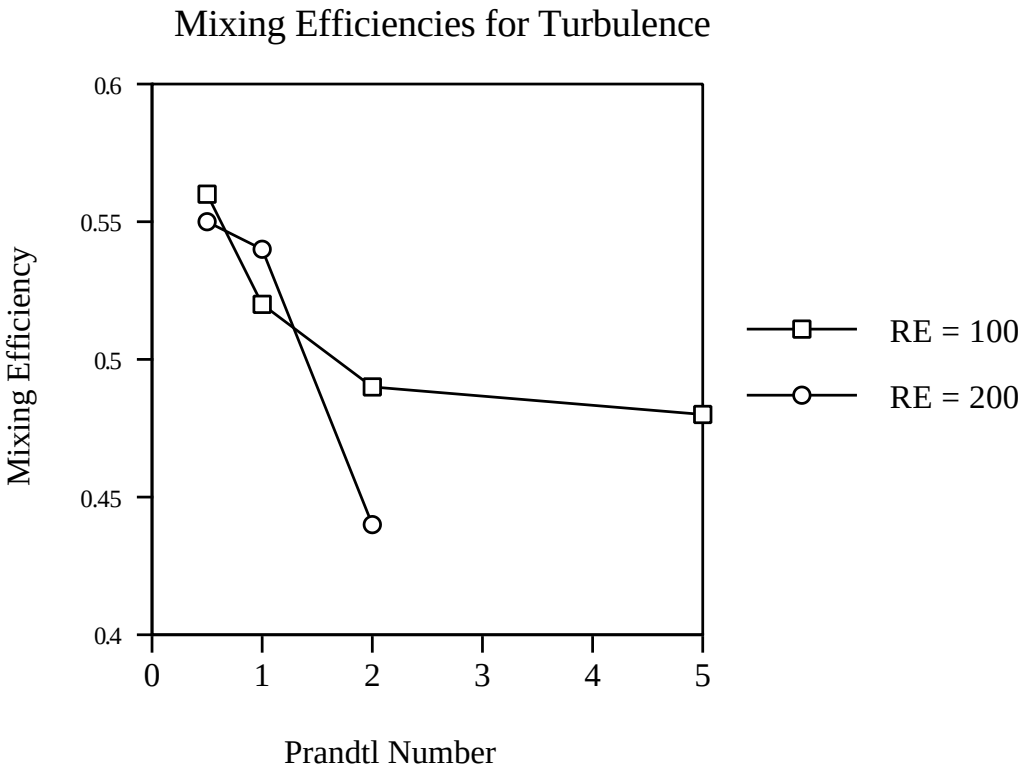

Figure 5.55: Mixing efficiencies for homogeneous turbulence as functions of the Prandtl number for simulations. The mixing efficiency, $\eta = \chi/(\chi + \epsilon)$ is presented for Prandtl numbers of 0.5, 1, 2, and 5, for Reynolds number of 100 and 200.

there is an increase in the rate of transfer of potential to kinetic energy as the kinetic energy is more strongly dissipated.

Similarly, Figure 5.55 presents the mixing efficiencies for the simulations. Though the mixing efficiencies fall into a relatively narrow range between 0.44 to 0.56, they show Prandtl number dependence. The conclusion is that the Prandtl and Reynolds numbers are significant in determining mixing efficiencies in low to moderate Reynolds number simulations. Direct numerical simulations are useful for understanding key physical processes in fluid flows, and for determining qualitative and semi-quantitative estimates of flow behavior as well as trends for different parameter values. They will

not, however, produce the same values for mixing efficiencies as measured in related laboratory and field experiments until appropriate Prandtl and Reynolds numbers can be used in the numerical simulations, i.e., until more computational speed and memory become available.

5.10 Summary

This Chapter has presented results for turbulent mixing caused by critical angle reflection for a number of different bottom slopes and wave parameters. Transition to turbulence has been determined to be a function of bottom slope, Reynolds number, and Richardson number. An average value for the Reynolds number at transition is approximately $Re = 1000$ based upon the wavelength and maximum wave current speed.

It was determined that the steepness of the bottom slope significantly influences type of turbulent boundary layer that develops. Steep slopes develop quasi-steady, localized turbulent bores, and gentle slopes develop intermittent, periodic turbulence across the breadth of the boundary layer.

The mixing period was found to be up to 50% longer than the wave period and to increase in proportion to the wave period as the slope decreased. The turbulence in the boundary layer radiates energy upwards across the path of the oncoming internal waves. It was observed that changes to the background density profile and the generation of mean currents occur in regions significantly farther from the wall than the depth of the turbulent boundary layer, and that the mixed fluid is advected into the interior stratified fluid on relatively short time scales.

Critical angle reflection is an effective means of dissipating the oncoming wave energy, and, for a broad range of simulations, over 90% of the wave energy is dissipated in the boundary layer into heat and mixing of the background density profile. The energetics of the flow showed that there is a net negative buoyancy flux for most of the simulations, transferring some wave potential energy into kinetic energy to be dissipated as heat, especially in the viscously dominated region near the wall.

A prominent feature of the energetics is a strongly oscillating buoyancy flux,

indicative of strong upslope/downslope flow that occurs twice per wave period. It appears that the upslope flow, generated by a phase of the oncoming wave interacting with the presence of the boundary, is responsible for setting up wave overturning in the boundary layer that leads to subsequent wave breakdown into turbulence.

The results are in qualitative agreement with related laboratory studies and show similar development of features such as boundary layer current velocities, flow dynamics, and transition Reynolds numbers. Boundary layer profiles for these simulations have shown that δ, the boundary layer thickness, has a maximum value of approximately $\lambda_z/3$ for large amplitude oncoming waves. The boundary layer thickness was shown to be nearly a linear function of wave amplitude (as also determined in the laboratory for low Richardson number) for the 20^o slope, but insufficient simulations were performed to permit determining the dependence of δ as a function of slope, Richardson and Reynolds number.

Finally, mixing efficiencies for the simulations have been examined and it has been argued that the higher values obtained here than for laboratory and field measurements can be attributed to differences in Prandtl, Reynolds, and Richardson numbers. The exact plane-wave solution developed in Section 5.9.3 was shown to contain many features of the mixing discovered by numerical studies.

To conclude this thesis, Chapter 6 continues the presentation of results, focusing on specialized experiments designed to investigate individual aspects of the flow behavior, such as the exchange of boundary layer fluid with the interior stratified regions and shear stresses on the boundary.

Chapter 6

SPECIAL FLOW STUDIES

This chapter completes the presentation of results from the computational fluid dynamics experiments. Additional specialized studies are summarized that investigate important flow features and parameters. There are eight topics covered in Chapter 6: (1) effects of varying wave amplitude, (2) exchange of fluid between the boundary layer and the interior stratified region, (3) transport of fluid particles, (4) flow development for a free-slip wall, (5) wall shear stresses, (6) off critical angle simulations, (7) comparison of simulations to linear theory, and (8) two-dimensional simulation results.

6.1 Wave Amplitude and Mixing

Effects of variations in wave amplitude have been mentioned above briefly in relation to boundary layer thickness, Richardson number, current velocities in the boundary layer, and the duration of the mixing cycle. A set of computational experiments was conducted for the 20^o slope (Cases 18, 20 - 24, and an additional simulation not listed in Table 4.1) to isolate the effects of adjusting the wave amplitude. The wave amplitudes (A/A_o) for the simulations are 0.15, 0.3, 0.45, 0.6, and 0.8, where A_o is the amplitude of a wave that has $\dfrac{\partial \rho}{\partial z} = 0$ at its steepest point, and z is directed opposite the gravity vector. Three realizations (Cases 21, 22, and 23) were conducted with $A/A_o = 0.6$ using different domain sizes. An additional laminar simulation (not listed in Table 4.1), with $A/A_o = 0.15$, $Re = 425$, and $Ri = 1700$, is included in the wave amplitude comparison but is not presented elsewhere in the thesis, because a higher Reynolds number laminar simulation (Case 16 with $Re = 540$, $Ri = 125$) already established the transition point for a slope of 20^o.

6.1.1 Mixing Period

A primary interest is to examine if the mixing period is more strongly linked to the wave period, or if variation in wave amplitude (and hence, the energy flux of the oncoming wave) more strongly influences the duration of the mixing cycle. Amplitudes of the oncoming waves varied by a factor of 5.3, from smallest ($A/A_o = 0.15$) to largest ($A/A_o = 0.8$), with corresponding variation in energy densities of a factor of 28. All other parameters were held fixed in the comparisons except for variations between three cases conducted at $A/A_o = 0.6$ discussed below. Wave amplitude is an important parameter, influencing both Reynolds number ($Re \propto A$) and Richardson number ($Ri \propto \frac{1}{A^2}$). The Reynolds and Richardson numbers for these cases are listed in Table 4.1.

Figure 6.1 compares isopycnals of the flows that develop for wave amplitudes (A/A_o) of 0.3, 0.45, 0.6, and 0.8 at approximately $t = 85$ (in order: upper left, upper right, lower left, lower right). The location of the thermal front in Panel 3 appears ahead of the location in the other panels at $t = 85$ because the oncoming wave has a different phase lag than for the other simulations. The apparent boundary layer thickness, as visualized in Figure 6.1, demonstrates a significant difference in the flow response. For the smallest amplitude wave, there is a small region of overturned fluid just above the thermal front. The depths of the regions of static instability increase with wave amplitude. The simulations suggest that the manner in which the boundary layer dissipates different amounts of oncoming wave energy is oriented (varies) more spatially than temporally. Rather than mixing the boundary layer fluid when the energy density reaches a critical value, the flow responds by mixing larger regions of fluid (in a more vigorous fashion) over similar time cycles. Aspects of the energetics of the mixing are suggested in the following figures.

Figure 6.2 shows the total dissipation rates (kinetic energy dissipation rate plus potential energy dissipation rates) for six experiments, with wave amplitudes from 0.3 to 0.8. The wave period is 18.4 for these cases. Three curves depict results at $A/A_o = 0.6$ (Cases 21 - 23, with curves labeled 0.6a, 0.6b, and 0.6c). The y-domain for Case 22 (0.6b) is twice as large ($y_l = 2.0$) as the other cases, and the x-domain for

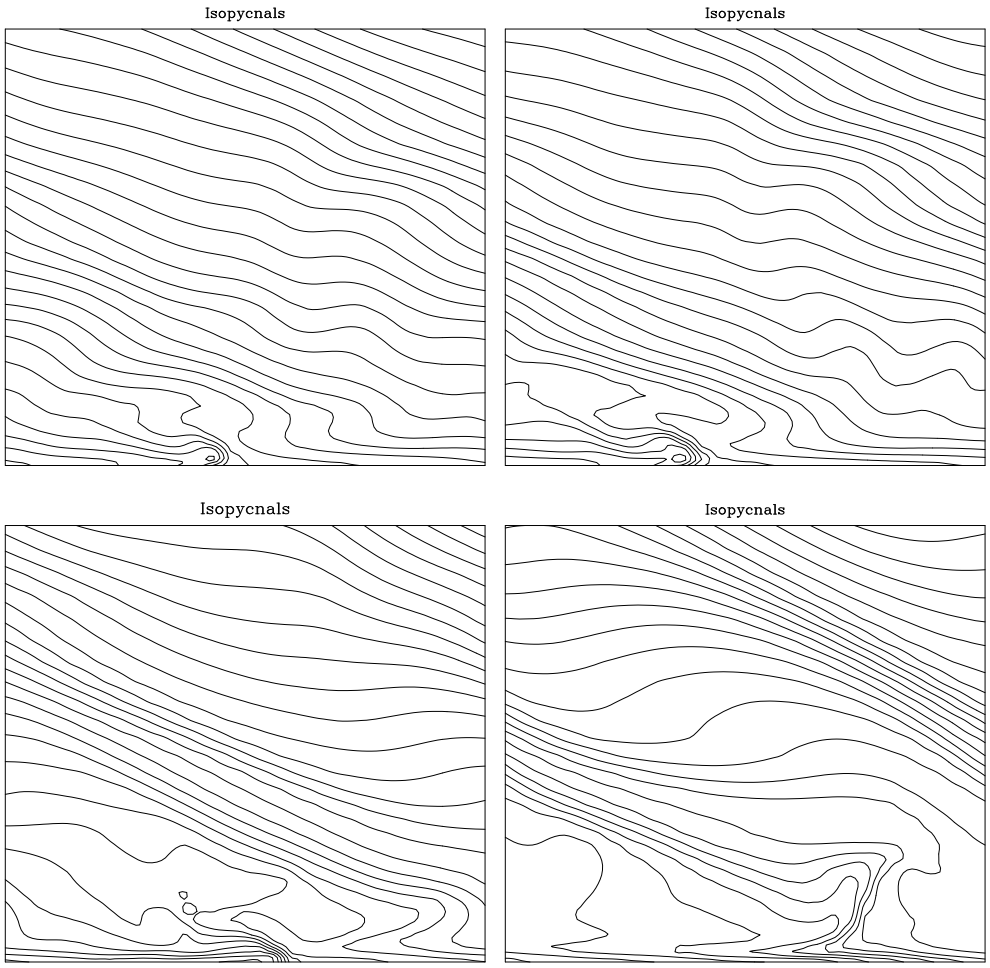

Figure 6.1: Isopycnals for wave amplitudes (A/A_o) of 0.3, 0.45, 0.6, and 0.8 at $t = 85$, in order: upper left, upper right, lower left, lower right.

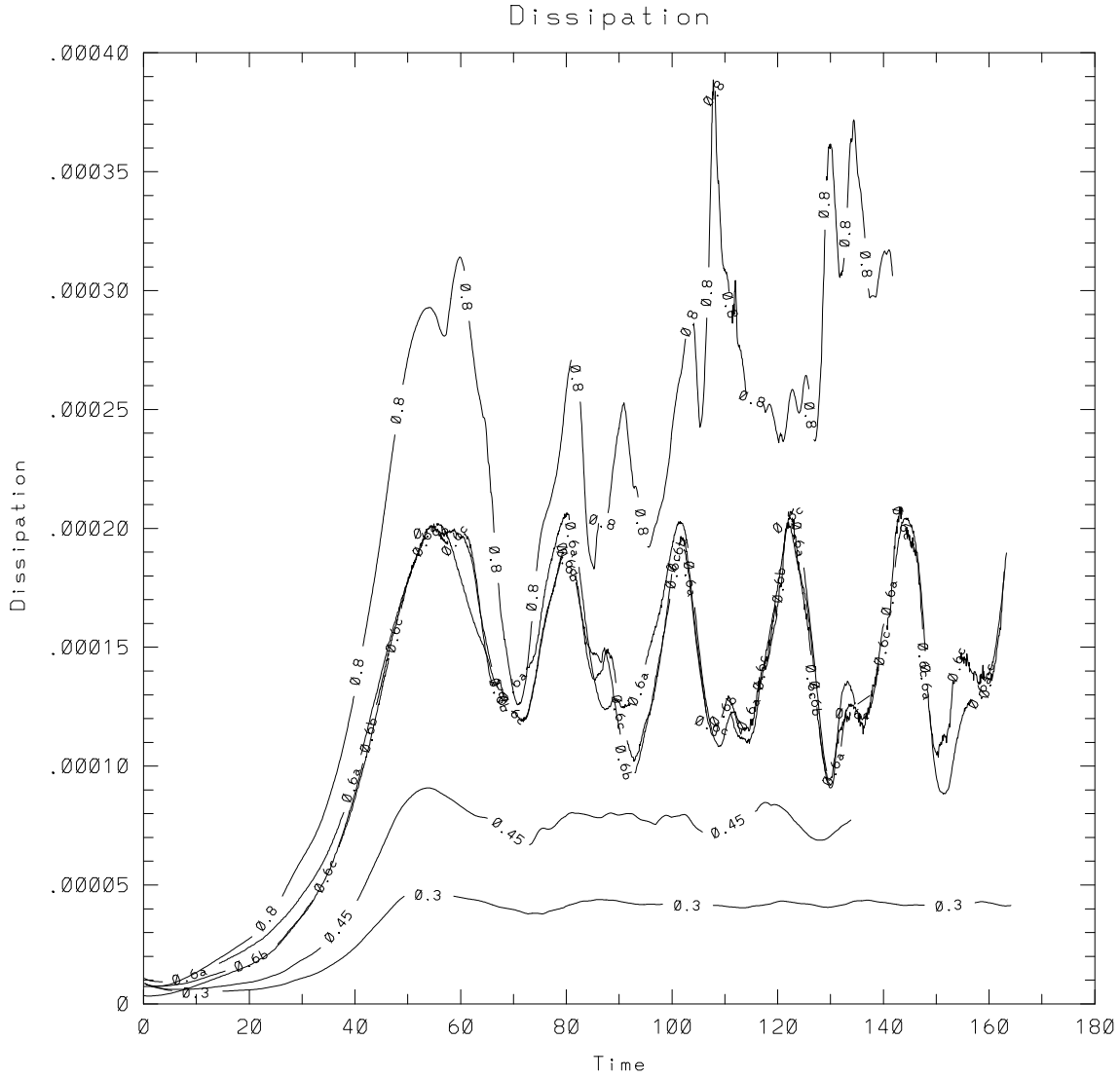

Figure 6.2: The total dissipation rates for six cases with four different wave amplitudes (from 0.3 to 0.8).

Case 23 (0.6c) used two periods of the oncoming wave, while the other simulations used one. The insensitivity of the results for the three similar cases demonstrates that even the smaller y-domain ($y_L = 1.0$) was sufficiently broad to include enough unstable modes for the turbulent boundary layers to develop in similar fashions. In addition, comparison of Case 23 with Cases 21 and 22 indicates that there was no observable interaction between the two separate fronts of the oncoming waves. Case 23 developed similar to the single period waves, with each wave period developing a thermal front that propagated upslope and transitioned to turbulence in similar fashion.

The primary purpose of Figure 6.2 is to examine whether the frequency of the mixing cycle changes with wave amplitude. In this regard the results from Figure 6.2 are not clear. The largest amplitude wave (0.8) appears to follow a different pattern of development from the 0.6 amplitude waves, and the smaller amplitude waves do not appear to have significant periodicity in the dissipation rate. All of the simulations appear to reach the first maximum in dissipation at approximately the same time. This occurs when the waves reach the bottom boundary at $t \approx 40$ and the first mixing cycle develops. The largest wave appears to have approximately two peaks in dissipation for each one observed in the smaller amplitude cycles. This suggests that, as more wave energy is available to be dissipated, the mixing cycle responds by occurring more frequently. Further observations (Figures 6.3 - 6.5), however, dispute this conclusion. Note, too, that there are small amplitude peaks between the large dissipation peaks for the simulations with amplitude of $0.6A_o$ also. Similar intermediate peaks were observed for the 9^o bottom slope (e.g., Figures 4.15, 4.16, 4.26, and 5.1) and appear to distinguish initial wave overturning from subsequent small-scale mixing.

Figure 6.3 shows the volume integrals of mean square shears $\left(\frac{\partial v}{\partial y}\right)^2$ (top) and $\left(\frac{\partial w}{\partial y}\right)^2$ (bottom) for five cases with A/A_o between 0.3 and 0.8 (Case 23 is omitted). The two panels show evidence that both the period and the phase of the mixing cycle are nearly the same for the different amplitudes. The figures demonstrate the

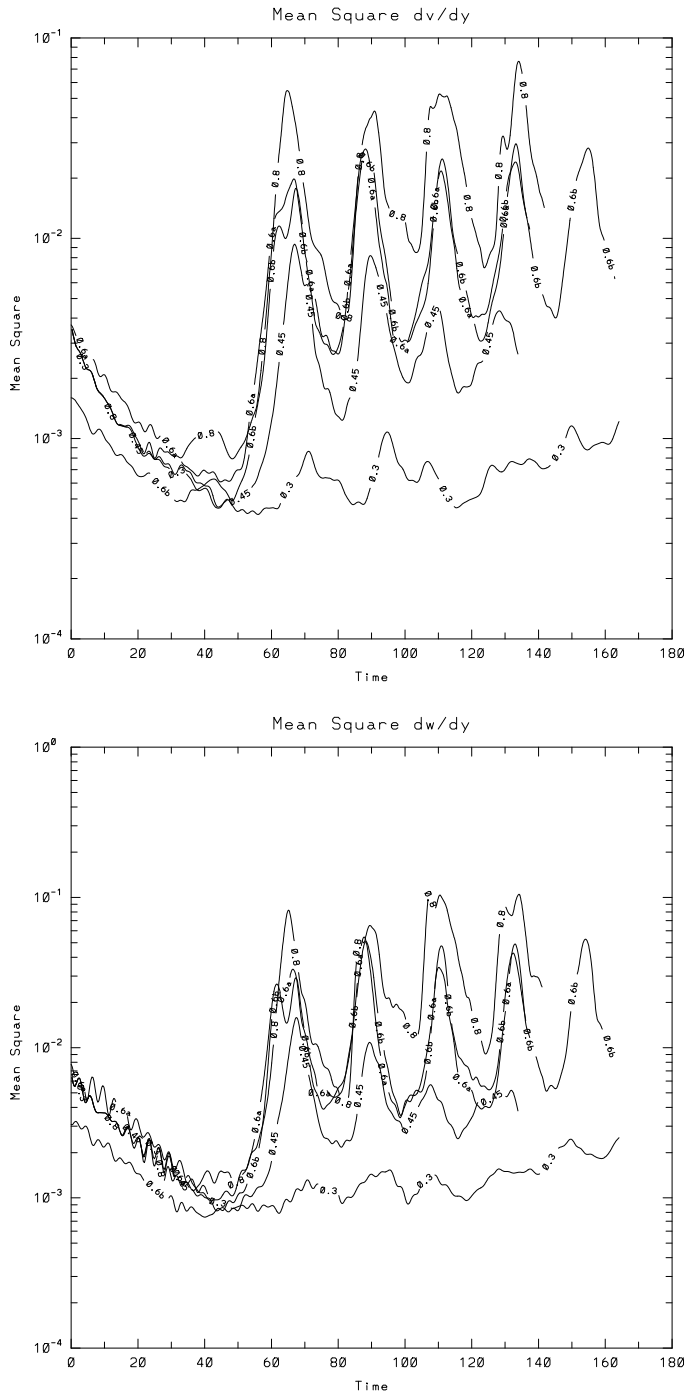

Figure 6.3: The volume integrals of $\left(\frac{\partial v}{\partial y}\right)^2$ (top) and $\left(\frac{\partial w}{\partial y}\right)^2$ (bottom) for five different wave amplitudes over a 20^o bottom slope.

three-dimensional response of wave breakdown and indicate that the times when the flows become the most three-dimensional are similar. The case with $A/A_o = 0.15$ is not included in the figures because it showed constant decay for all three-dimensional components and gave no indications of wave or mixing periodicity.

Through approximately four mixing cycles, each lasting for a time of approximately 21 - 25 (the wave period is 18.1), the turbulence responds at approximately the same times. The slight differences in duration of the mixing cycles (e.g., the 0.45 simulation appears to be slightly shorter) are insufficient to conclude that the mixing period is related to the wave amplitudes or the energy flux into the boundary layer. The energy flux differs by 200% - 400% between these simulations and yet the mixing periods differ by only approximately 10%.

It is not know whether the mixing periods might change at later times in the simulations, but it seems possible, given that greater cumulative changes to the background density profiles and currents are expected for larger amplitude waves. Flow adjustments over longer time scales could alter the angle of propagation of the oncoming waves and influence the mixing cycle.

Figure 6.4 shows volume integrals of v^2 for the same five simulations. Again, the primary evidence is that the different amplitude waves respond at the same mixing periods. Note that the smallest amplitude simulation (0.3) has a very weak response and does not generate significant amounts of v-component of velocity. It does not, however, continue to decay throughout the simulation and is classified as a transitional case in Table 4.1.

The dissipation rates in Figure 6.2 suggest that the mixing cycles varies with wave amplitude while various components of three-dimensionality in Figures 6.3 - 6.4 suggest that the mixing cycle is independent of wave amplitude. It is attempted to clarify and resolve the discrepancy with Figure 6.5. The primary evidence in Figure 6.2 was the existence of two peaks in the dissipation rate for the $0.8A_o$ wave, while the $0.6A_o$ wave showed only one. Figure 6.5 shows volume integrals of $\left(\frac{\partial u}{\partial x}\right)^2$, $\left(\frac{\partial u}{\partial y}\right)^2$, and $\left(\frac{\partial u}{\partial z}\right)^2$ for wave amplitudes of 0.8 (top) and 0.6 (bottom). The $\frac{\partial u}{\partial z}$ shear is

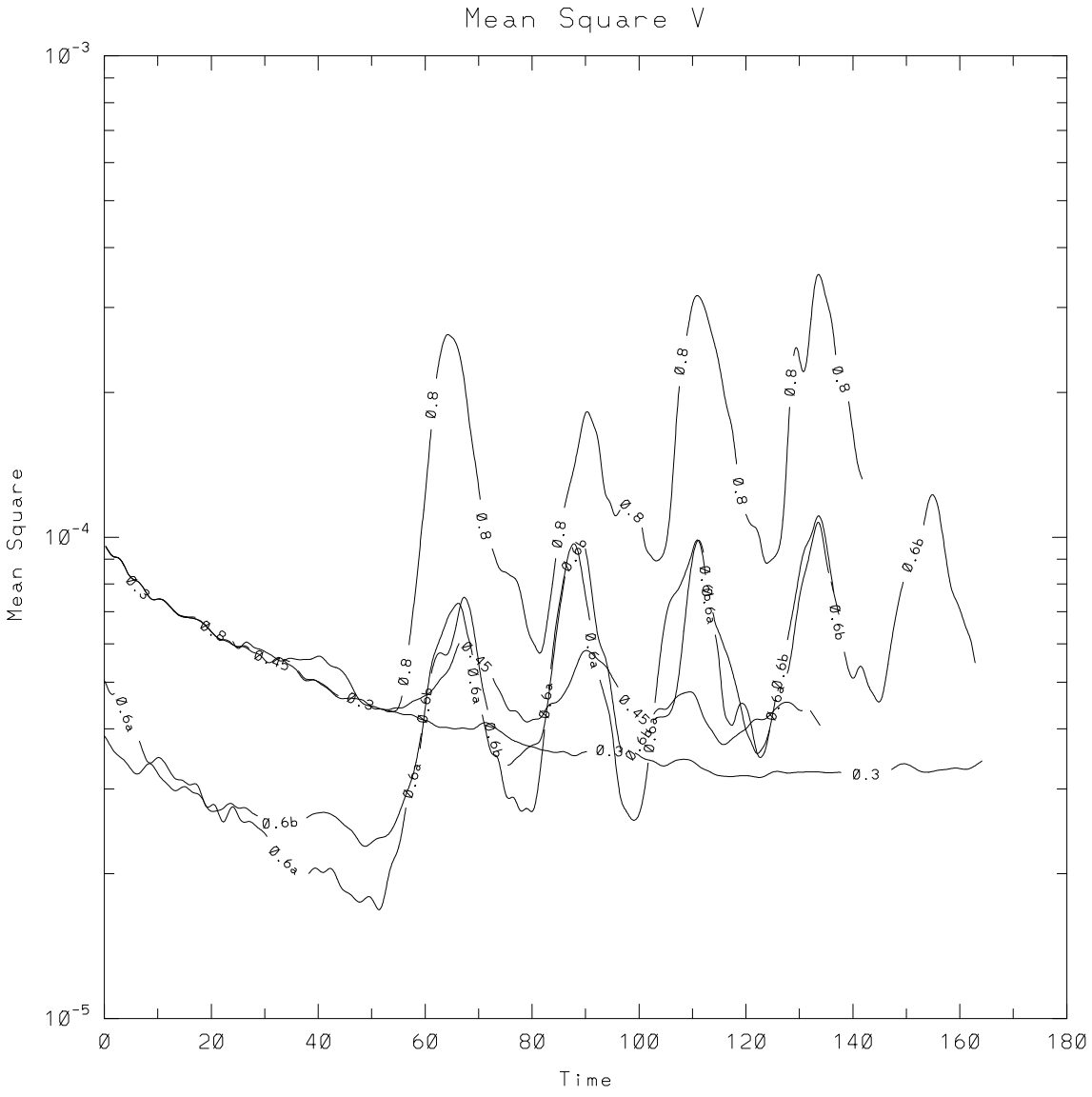

Figure 6.4: The volume integrals of v^2 for five different wave amplitudes over a 20^o bottom slope.

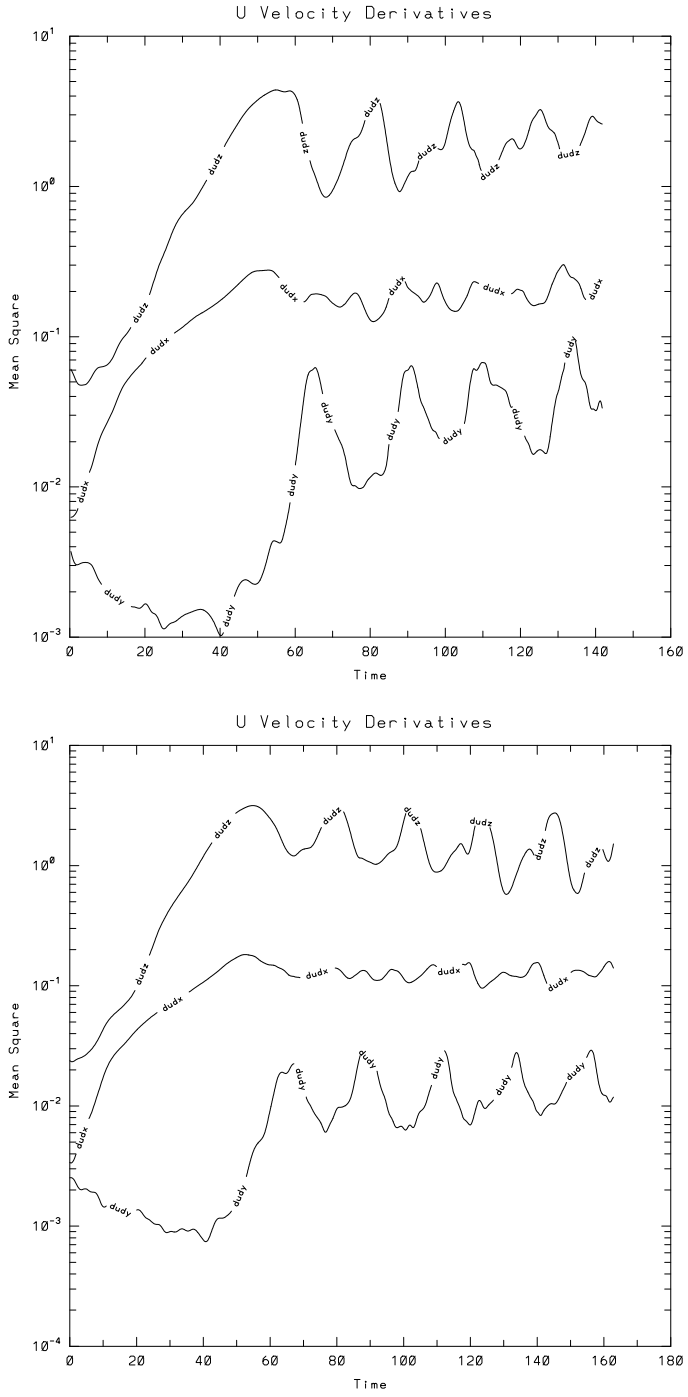

Figure 6.5: Volume integrals of $\left(\frac{\partial u}{\partial x}\right)^2$, $\left(\frac{\partial u}{\partial y}\right)^2$, and $\left(\frac{\partial u}{\partial z}\right)^2$ for the large amplitude waves, $0.8A_o$, from Case 24 (top) and $0.6A_o$, from Case 23 (bottom).

significantly larger than the other two shear rates, $\frac{\partial u}{\partial y}$ and $\frac{\partial u}{\partial x}$. Note, however, that maxima of $\frac{\partial u}{\partial z}$ and $\frac{\partial u}{\partial y}$ are staggered from one another. In the top panel, maxima for $\frac{\partial u}{\partial z}$ occur at $t = 58$, 82, 103, and 125 (Case 24), while maxima for $\frac{\partial u}{\partial y}$ (and all other x and y derivatives; i.e., $\frac{\partial w}{\partial x}$, $\frac{\partial w}{\partial y}$, etc.) occur at $t = 63$, 90, 110, and 135. For Case 24 the two peaks in the dissipation rate occur at both times, e.g., Figure 6.2 shows peaks at 80, 90, 102, 108, 129, and 135.

It appears that for the large amplitude waves ($0.8A_o$) two separate stages of the flow have large dissipation rates of comparable magnitude. Comparison with visualizations of the flow field development (e.g., Figures 6.1, 5.14 - 5.17, and others not pictured shows that the first peak is associated with the stage of initial wave overturning and strong downslope flow near the wall, while the second peak occurs during the later development of small-scale turbulence. While the same staggering of maxima is apparent in the bottom panel of Figure 6.5 for the intermediate amplitude waves, the single peaks in dissipation rate in Figure 6.2 correspond only to the times of the initial wave overturning and strong downslope flow. For the smaller amplitude waves the strongest dissipation rates occur during periods of initial wave overturning and strong downslope flow in the viscous sublayer. Similarly, there is a frequent separation between the times of maximum kinetic and potential energy dissipation rates (not pictured). Maxima of the potential energy dissipation rates frequently occur approximately one fifth of a wave period after corresponding maxima of the kinetic energy dissipation rates. The potential energy dissipation rate maxima appear to be more strongly correlated with the small scale turbulence, while the kinetic energy dissipation rate maxima occur during periods dominated by strong flows in the viscous sublayer and larger scale motions.

In summary, the experiments described in this section support the conclusion that the mixing cycle is associated with the wave period ($T_M \propto 1/\omega$). The strength of the turbulence that develops differs according to the energy density of the oncoming waves, but the mixing period does not change significantly for wave amplitude differing by over a factor of two (energy densities differing by over a factor of four). The

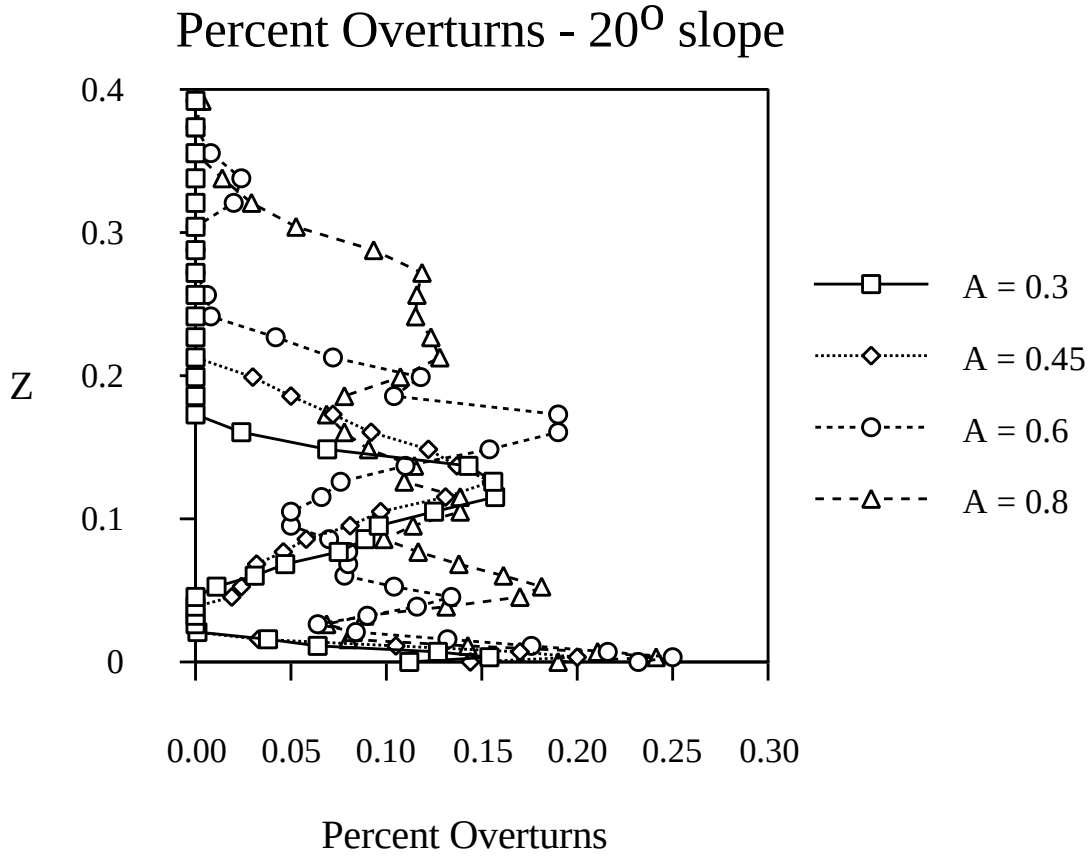

Figure 6.6: The boundary layer thickness measured by the frequency of static instabilities as a function of height for four different oncoming wave amplitudes.

simulations in these comparisons were extended through approximately four mixing cycles; experiments of longer duration could be important to determining if the flow continues to develop with similar mixing cycles.

6.1.2 Boundary Layer Thickness

A second result of varying the wave amplitude is that the depth of the boundary layer changes. For a regime characterized by higher Richardson numbers, Ivey and Nokes (1989) showed that $\delta \approx 5A$, motivating a similar examination for the present study

in which all flow parameters except wave amplitude are held constant. Figure 6.6 shows the boundary layer thickness, measured by the frequency of density inversions by integrating a time series at a fixed location (as described for Figures 4.20 and 5.33) for four wave amplitudes, 0.3, 0.45, 0.6, and 0.8, over a 20^o bottom slope. A fifth simulation with $A/A_o = 0.15$ is also included in the comparisons of boundary layer thickness. The approximate depths for the boundary layers (δ/λ_z), based upon the heights at which overturned fluid is observed, (from smallest to largest wave) are 0.095, 0.17, 0.22, 0.30, and 0.36. The boundary layer thickness of the fourth wave ($A/A_o = 0.6$) is more approximate than the other values. There is a small region $0.3 < z < 0.35$ that experienced overturning approximately 2% of the time, but the interval between $0.25 < z < 0.3$ never experienced overturning. The boundary layer thickness for this case is approximated as 0.3. The results indicate that as the wave amplitude increases the boundary layer thickness also increases. This dependence, however, is only approximately linear. The ratios of $\frac{A\lambda_z}{A_o\delta}$ for the five cases are 1.58, 1.76, 2.05, 2.0, and 2.2 respectively, so that increases in boundary layer thickness do not keep pace with increases in wave amplitude.

6.1.3 Maximum Velocities

Maximum velocities in the boundary layers are shown for the same four simulations in Figure 6.7 (labeled by their Reynolds numbers, 850, 1200, 1800, and 2400). The ratios of the maximum velocities during the simulation to the current speeds of the oncoming waves are (from smallest amplitude to largest amplitude) 3.0, 2.9, 3.1, and 2.9. The additional simulation, with $A/A_o = 0.15$ and $Re = 425$, had a ratio of 3.5. These results are similar to results of Ivey and Nokes (see Section 5.1) who found ratios of approximately 2.5 for a 30^o slope experiment.

Simulations using different amplitude waves have been useful for examining properties of critical angle reflection. Some flow features (boundary layer thickness, current speeds) respond to changes in wave amplitude in a roughly linearly fashion, while other flow features (mixing period, mixing efficiency) are comparatively insensitive to its changes.

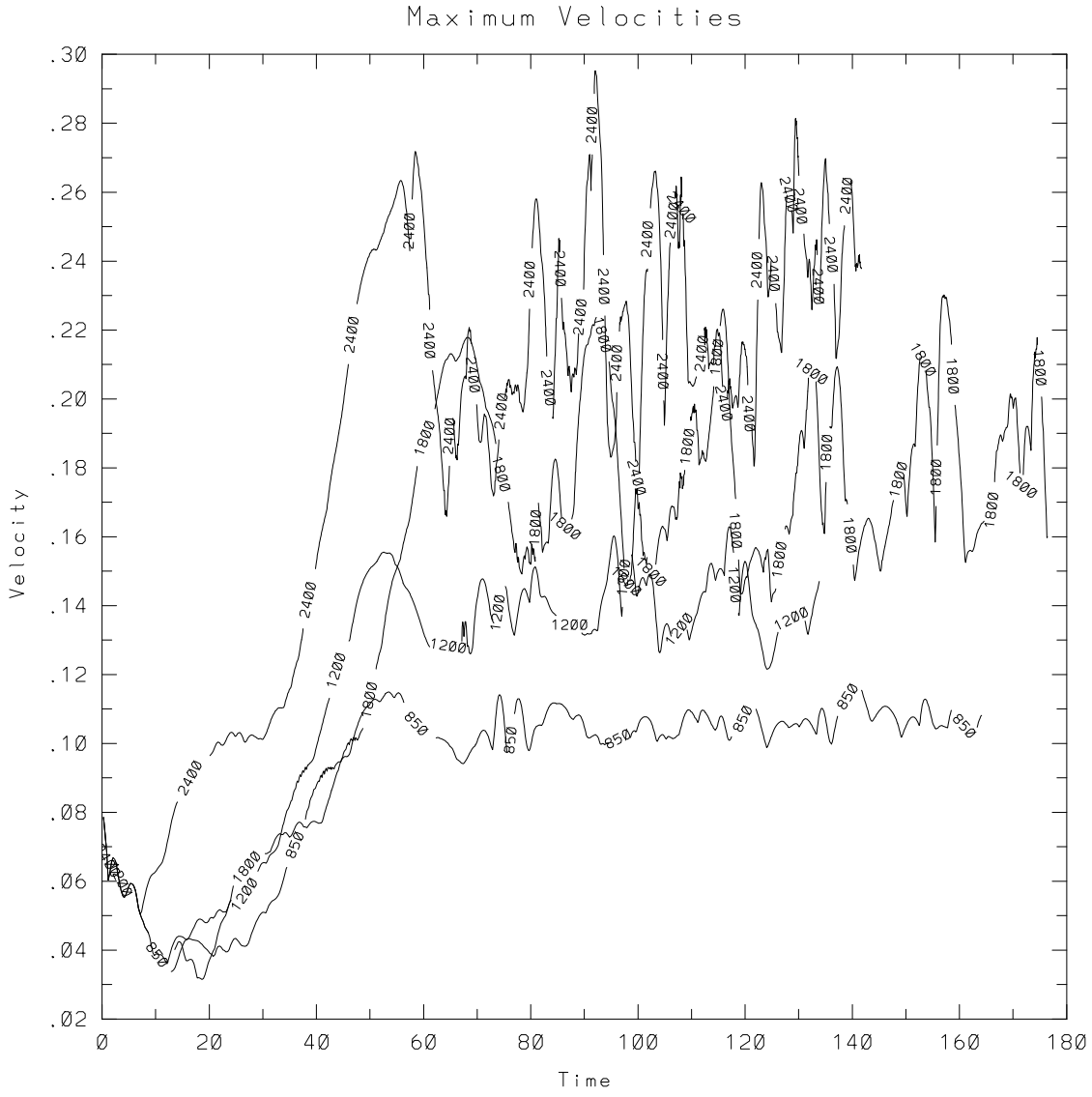

Figure 6.7: The maximum velocities in the boundary layer for four simulations at different Reynolds numbers (850, 1200, 1800, and 2400) and corresponding wave amplitudes (0.3, 0.45, 0.6, and 0.8) over a 20^o bottom slope.

6.2 Dyed Field Results

A key issue related to the wave breakdown process is whether the turbulent boundary layer exchanges fluid with the interior domain or whether it predominantly continues to mix the same fluid (Garrett, 1990). An experiment was designed to examine this issue (see Section 3.5.4 for details) in which the boundary layer fluid is "dyed" with a passive tracer after the flow has reached a quasi-steady state of mixing. Then, as the flow develops for a few wave periods, the flow is examined to determine if the dye is still predominantly located in the boundary layer region or if it has moved off the wall to the interior stratified regions.

For the case presented here, dye is initially released in the turbulent boundary layer for Case 21 ($Re = 1800$, $\alpha = 20^o$) at $t = 74$. The density field (e.g., Figure 6.6) indicates that the turbulent boundary layer has a thickness of $\delta \approx 0.3$. The initial concentration, or magnitude, of the scalar dye field, S_D, is uniform parallel to the boundary, with

$$S_D(x, y, z, 0) = \begin{cases} 1 & 0 \le z \le 0.15 \\ A \sin^2 \left(\pi(z - 0.15)/0.3\right) & 0.15 \le z \le 0.3 \end{cases} . \qquad (6.1)$$

The flow is then calculated for approximately five wave periods ($T_w = 18.1$).

Figures 6.8 and 6.9 illustrate results of the experiment. Figure 6.8 shows the concentration of the dye for the lowest 1.08 vertical wavelengths at three times, where time is measured in wave periods from the initial release of the dye: $t = 0.05T_w$ (top), $t = 2T_w$ (middle), and $t = 4.7T_w$ (bottom). Figure 6.8 is shown in the plane of the slope (x' - z' plane) and should be rotated counter clockwise 20^o to be in the natural reference frame. Viewing the panels in the natural frame emphasizes that the dominant transport of the dyed fluid has been along isopycnals after the first extraction from the boundary layer into the interior stratified regions. The top panel shows the approximate distribution of the dye as it is released. After two wave periods, the dominant feature is a jet or intrusion of dyed fluid reaching upwards to a height of approximately $0.8\lambda_z$. There is also evidence that some fresh (undyed) fluid has penetrated to the boundary and diluted the concentration of the dye in

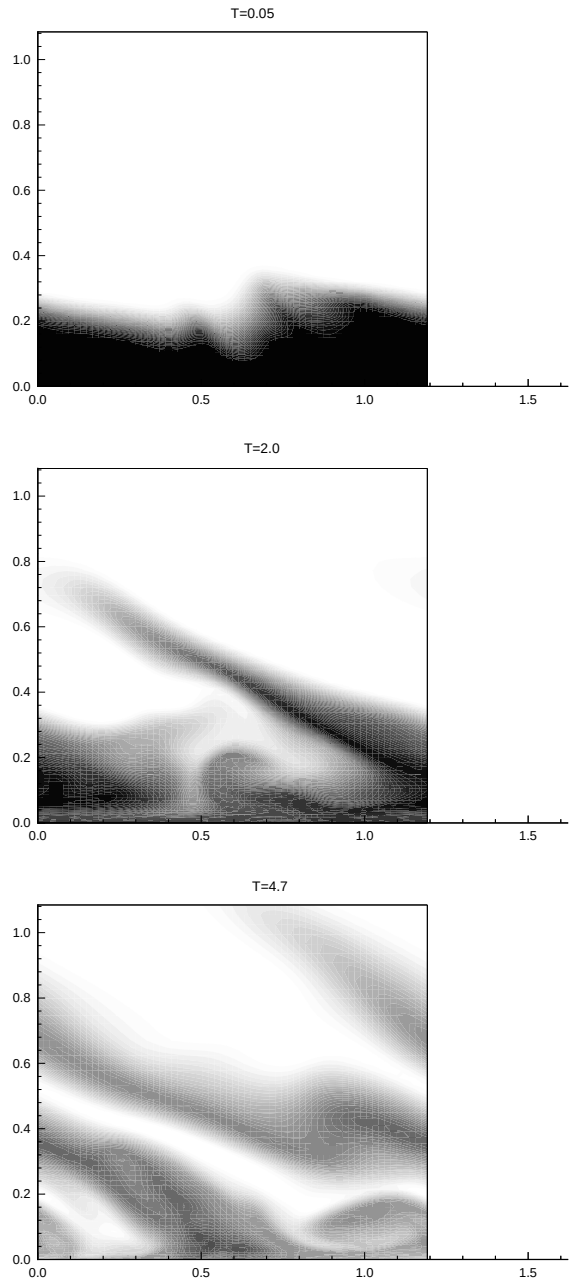

Figure 6.8: The boundary layer fluid, dyed with a passive scalar tracer, shown in the plane of the slope at 0.05, 2.0 and 4.7 wave periods after release.

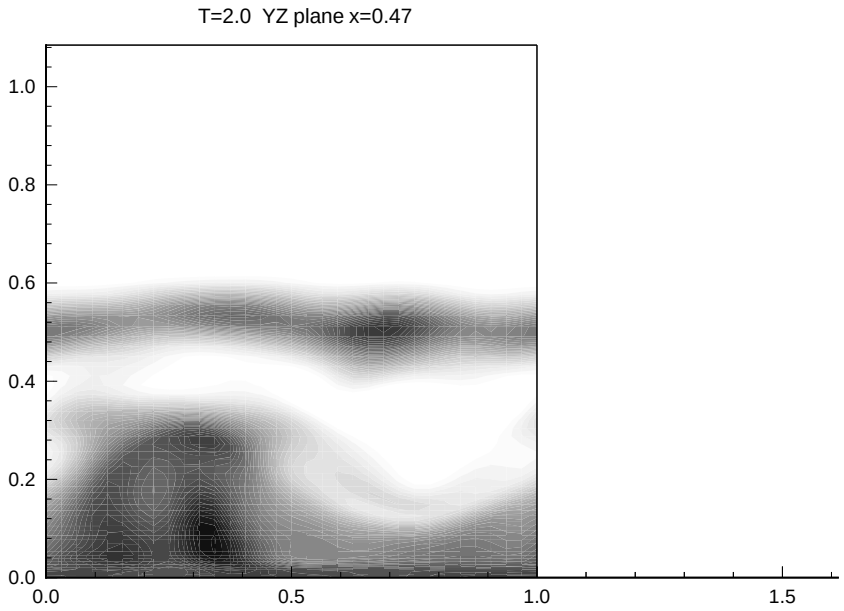

Figure 6.9: The scalar dye tracer shown 2.0 wave periods after being released in the $y-z$ plane located at $x = 0.47$, illustrating the structure of the cross-slope circulation.

the boundary layer. After 4.7 wave periods the dye has been carried to a height of 1.2 λ_z (or over 2 horizontal wavelengths). At this time, the location of the dye is still characterized as an elongated intrusion. The intrusion has spread farther in width, but there is still fresh fluid above and below the dye intrusion. By 4.7 wave periods, the dyed fluid has traveled over 1.0 λ_z in the offwall direction, a distance of approximately three times the nominal boundary layer thickness. Note also that regions of fresh, undyed fluid now appear in the boundary layer.

Figure 6.9 shows a cross slope view (y - z plane) of the dyed fluid at $t = 2T_w$. This figure indicates some of the three-dimensional structure of the flow. The upper layer of dye, centered at about $z = 0.5$, is a cross section of the intrusion, while the lower region shows some of the structure in the boundary layer. The full three-dimensionality of the flow is masked in the dye visualization because of its initial

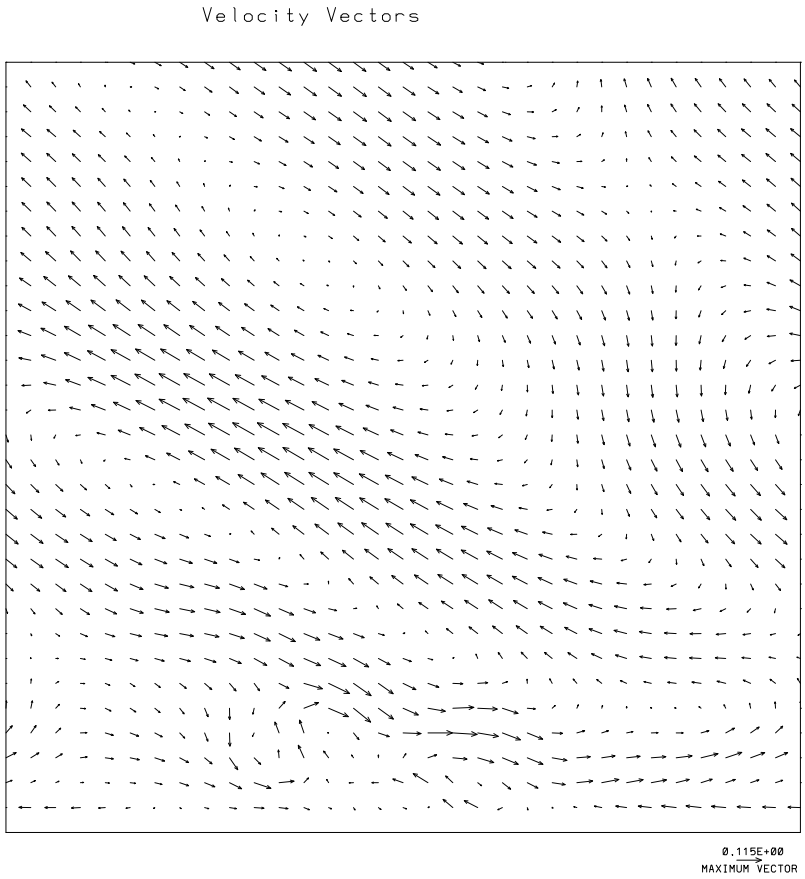

Figure 6.10: The velocity field in the plane of the slope (x - z) at $t = 85$ for Case 21.

uniformity, though some indication of larger scale circulations is beginning to appear (e.g., the mushroom-like structure in the lower left region).

Figure 6.10 illustrates velocity vectors in the same two-dimensional plane as Figure 6.8 at $t = 85$, approximately 1/2 T_w after the dye is released. Here the dominant feature is the shear of the oncoming wave, modified somewhat by recirculation and turbulence in the near wall regions. A significant feature of the boundary mixing process is that the internal wave field outside the boundary layer region plays a very active role. It serves to continuously pump fresh stratified fluid into the mixed layer, while simultaneously extracting the mixed fluid. This process is suggested by the

strong internal wave shear seen in the velocity field in Figure 6.10. This exchange of boundary mixed and stratified fluid is referred to as internal wave pumping.

Further analysis, not pictured here, indicates that cyclical (up and down) transport of dye from the wave shear is approximately eliminated when the results are examined after integral numbers of wave periods (i.e., $2T_w$, $5T_w$), and only the net transport remains. This is because wave motions are periodic, and according to linear theory particles driven by wave motions return to their initial location after a full cycle. In the numerical experiments, nonlinearities or significant deviations (mean currents, recirculations) from the oncoming wave field extend to heights of at least $1.5\lambda_z$ (Section 5.8). By comparing the slope of the scalar transport contours (particularly after integral wave periods) with the slope of the isopycnals (e.g., Figure 6.1) it is evident that the advection process has favored transport along the constant density surfaces, since the scalar contours and isopycnals are predominantly aligned with one another.

These results suggest that the wave field is important in first communicating the boundary mixed fluid into the interior stratified regions and that the mixed fluid is further transported into the interior along constant density surfaces. The process has important implications for oceanic boundary mixing, since sloping boundaries exist at all depths of the ocean (ridges, seamounts, continental slopes). If mixed fluid in the boundary layer can be effectively exchanged with the near boundary pycnocline region, then horizontal mixing processes (occurring at significantly faster rates than vertical mixing processes because they are not inhibited by stratification) can communicate the mixing into the ocean interior and maintain stratification near the boundaries.

Internal wave pumping of fresh fluid into the boundary layer and the simultaneous extraction of mixed fluid is an important immediate link between the two regions. Boundary mixing caused by internal wave reflection is significantly different from boundary mixing in a quiescent fluid such as examined by Hopfinger (1987) (i.e., Figure 1.3). The communication between the mixed layer and the interior stratification can occur much more rapidly when strong local currents (internal wave shear) are

present. These numerical experiments (e.g., Sections 5.3 and 6.1) suggest that the time required to restratify the boundary layer for the 20^o slope and the time required to remix the fresh fluid are approximately equal.

6.3 Particle Diffusion

A second approach was used to examine fluid exchange between the boundary region and the interior stratified fluid. Here, Lagrangian particles were released at various heights to determine if a statistically significant number of particles escape from the boundary mixed layer, or if particles initially outside the boundary layer are entrained into it. (See Section 3.5.3 for details about the method.)

Figure 6.11 shows traces in the x - z (top) and x - y (bottom) planes of the three-dimensional trajectories of a set of 20 fluid particles released at a height of 0.17 λ_z from the wall, well within the mixed layer. A total of 2000 particles were included in this realization, with 200 released on each of ten planes parallel to the boundary. The dimensions of the computational domain for the simulation (Case 21) are $x_l/\lambda_z = 1.2$ and $y_l/\lambda_z = 1.0$. The dimensions in Figure 6.11 are extended to $x = 1.6$ and $y = 1.3$ so that, when a particle crosses a periodic boundary, its path does not appear to jump across the domain.

The Lagrangian particles are released at $t = 74$ and followed for one wave period in the figures. Depending on the phase of the wave and turbulence in the boundary layer at the location of each particle, it initially moves either upward or downward. If the particles had been released in a region of linear wave dynamics then, after one wave period, each would return to its initial locations. This behavior is approximated for particles started at large z'. Since these particles are initially released in a region of turbulence, none of them returns to its initial location at the end of a wave period. Some of the particles are drawn very close to the wall (e.g., those numbered 1 and 2), and one of the particles (17) escapes the boundary layer altogether. After each additional wave period the particle dispersion increases and appears to be more random.

The bottom frame of Figure 6.11 shows the movement of the particles in the y-

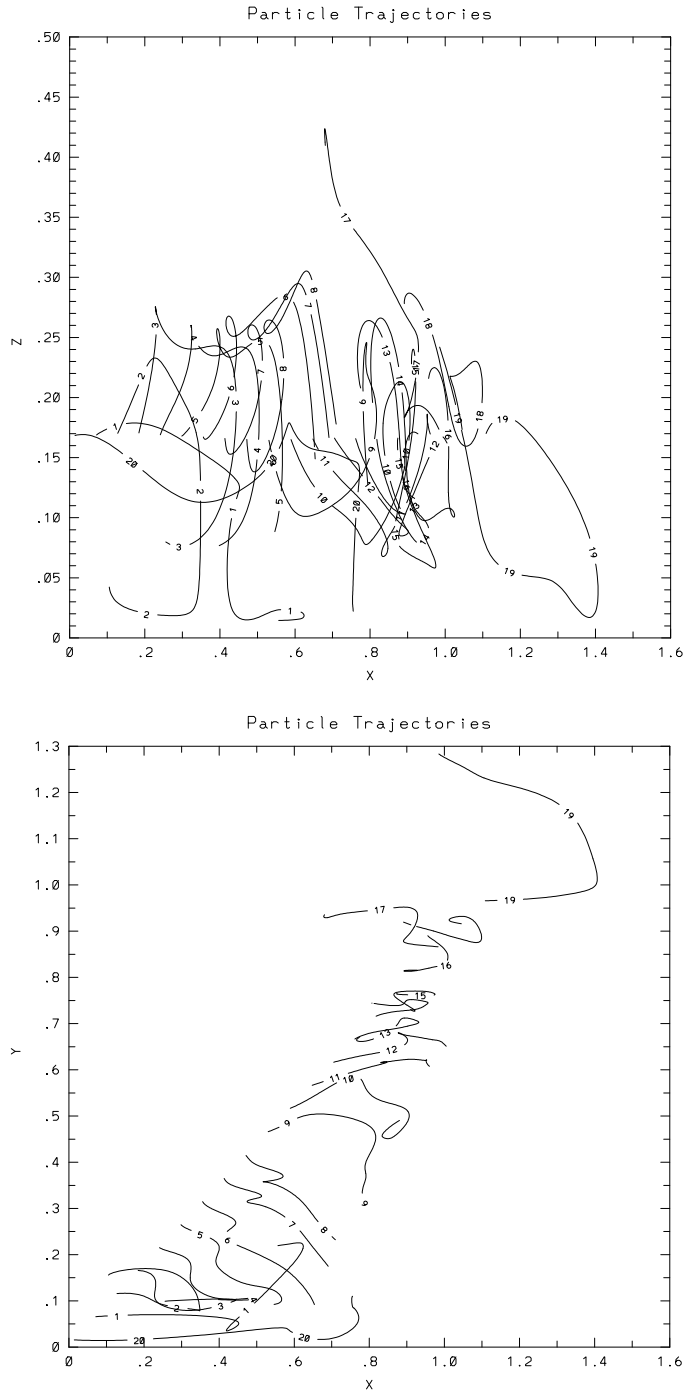

Figure 6.11: Particle trajectories shown in two planes (x - z, top; x - y, bottom) for one wave period. The particles were released at an initial height of $z = 0.17$.

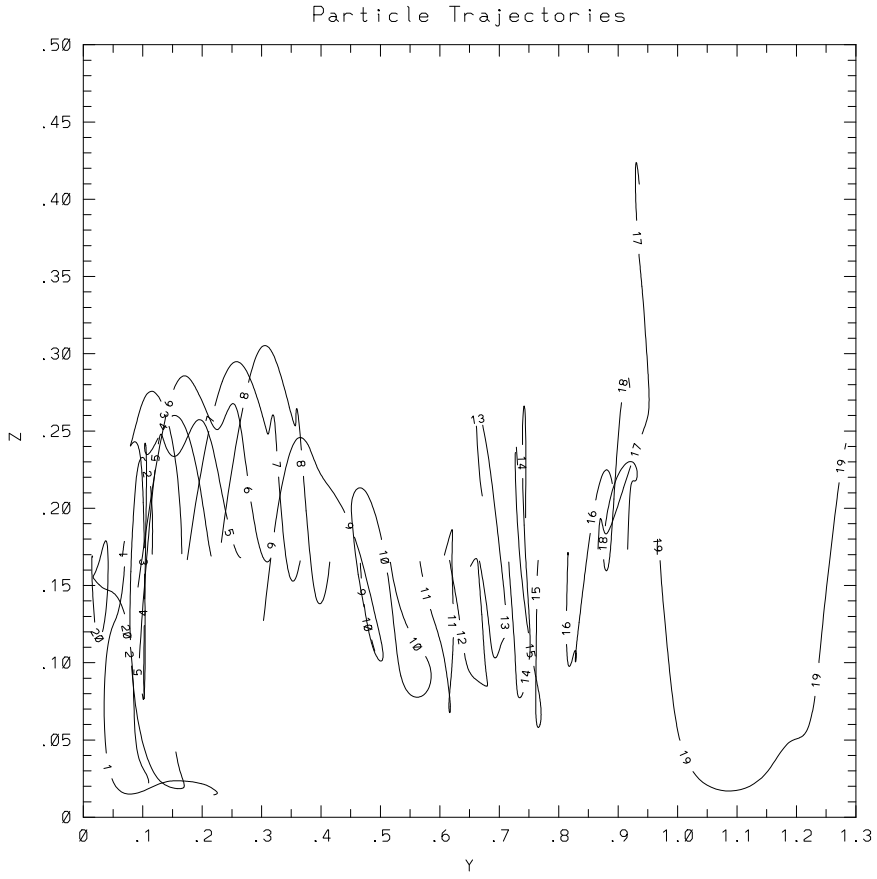

Figure 6.12: Particle trajectories shown in the y - z plane (end view) for the same particles as in Figure 6.12. The paths follow the particles over one wave period for particles released at an initial height of $z = 0.17$.

direction. It appears that, on the average, the particles travel as far in the y-direction as they do in the x-direction, which suggests that the turbulence is somewhat isotropic in this plane.

Figure 6.12 shows traces in the y - z plane of the same particles. Here the view is clear enough to indicate that particles 3 through 8 initially travel upwards in the first portion of the wave period, and particles 10 through 20 initially are carried predominantly downwards. On average, the particles travel farther in the z-direction than in the y-direction.

These, and the following figures, indicate that the vertical distance traveled by a fluid particle over one wave cycle is approximately $0.2\lambda_z$, i.e., a particle moves upwards $0.2\lambda_z$ during the upward phase of wave motion, and returns $0.2\lambda_z$ downwards during the downward phase, in agreement with linear theory. This is relevant to the foregoing analysis of the dyed fluid, showing that the progression of the dye into the interior stratification occurs rapidly and is not simply wave driven. For instance, after 5 wave periods, the dye progressed upwards approximately $1.0\lambda_z$ above its initial location. Thus, the net rate of turbulent diffusion is approximately equal to the sum of all of the upward transport of the gravity waves during upward phases, without any corresponding downward return. This result indicates the strength and importance of mean currents and recirculation set up above the boundary layer.

Figures 6.13 and 6.14 show additional x - z traces of particles released from heights of 0.018 (top), 0.21 (bottom), and 0.37 for Case 21. Note the difference in vertical scales in the axes. (Particle 10 in the top frame of Figure 6.13 jumped across the periodic boundary.) The top frame of Figure 6.13 shows that the dominant particle motion, for particles initially released very close to the boundary, is vertical transport that occurs when the thermal front passes the particles. When the particles encounter this strong upwelling feature (see Figure 5.16, Panels 1 and 2) they are ejected from their location near the wall and lifted to the middle of the boundary layer.

The bottom frame of Figure 6.13 shows what happens to particles initially released in the upper portion of the boundary layer. The nominal boundary layer depth for this simulations is approximately 0.25 - 0.30 (e.g., Figure 6.6). The particles shown in the bottom frame, released at a height of $z = 0.21$, are initially near the interface between the boundary layer and the stratified fluid. Approximately one-third of the particles in this location is initially lifted upwards and escapes the boundary layer after one wave period. Another third of the particles is more deeply entrained into the boundary layer, and the remaining third returns approximately to its initial height after one wave period. Figure 6.14 shows trajectories of particles initially released at a height of 0.37. Here, some of the (fluid) particles are entrained into the boundary layer and some have a net upward motion.

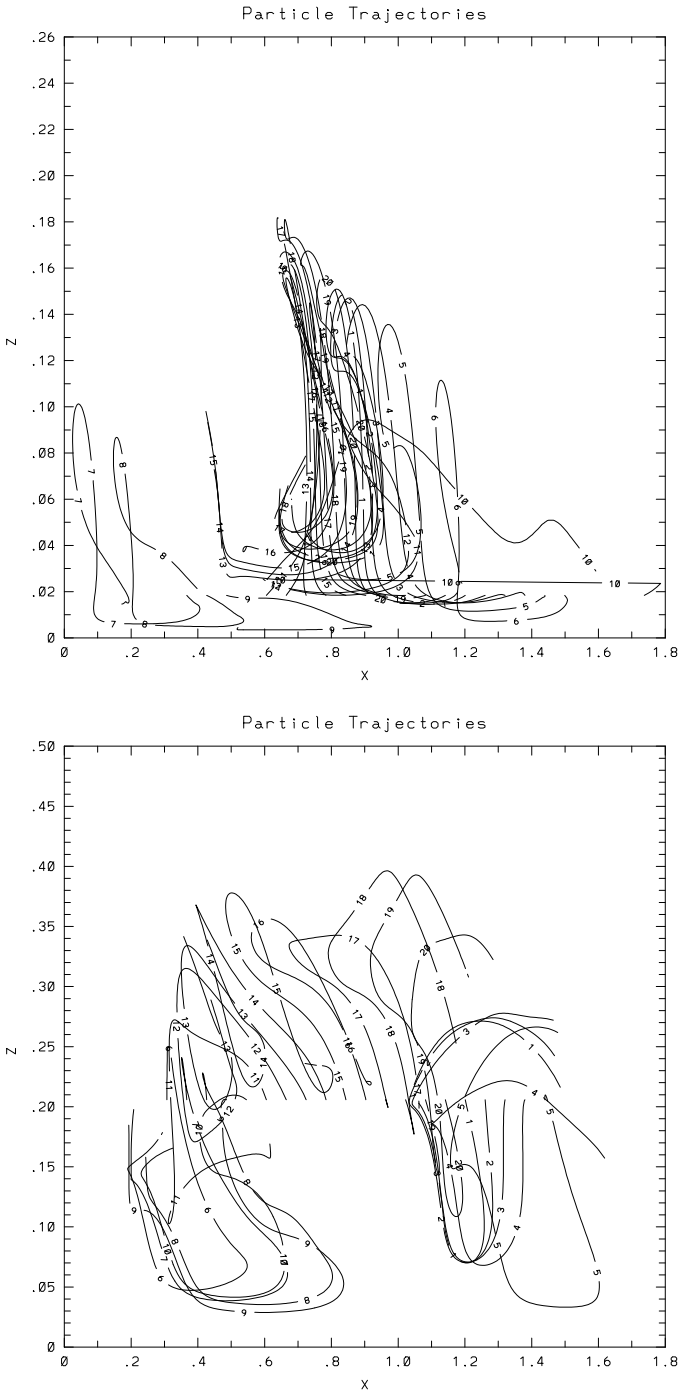

Figure 6.13: Particle trajectories outside the boundary layer shown over one wave period for particles released at an initial heights of $z = 0.018$ and $z = 0.21$.

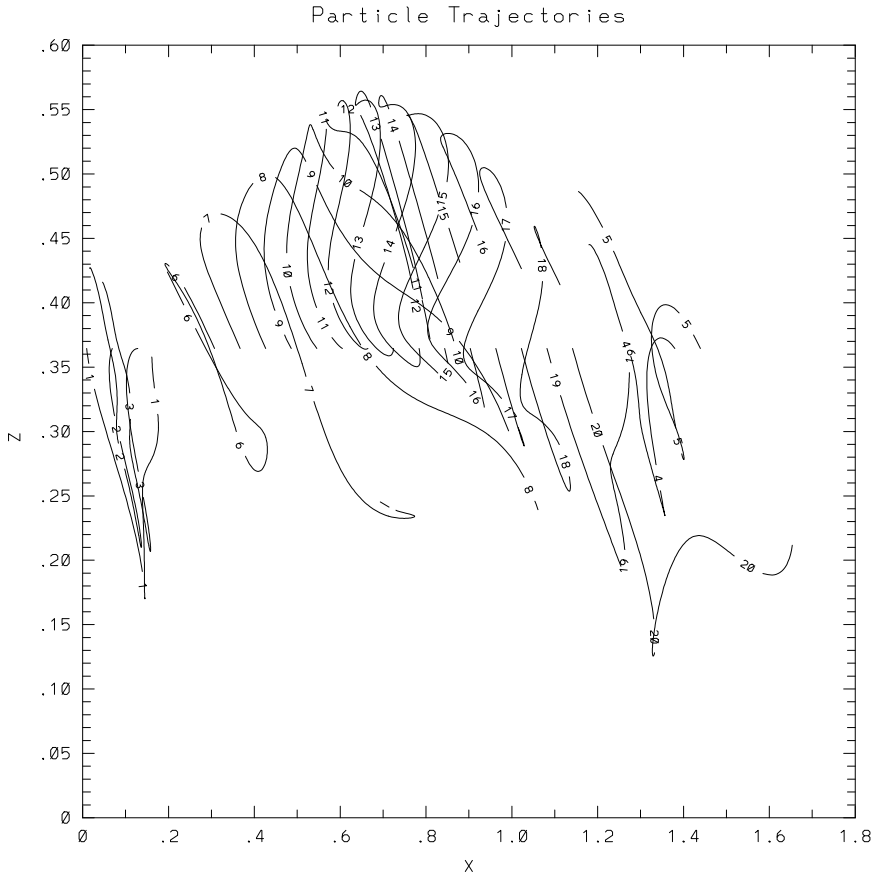

Figure 6.14: Particle trajectories outside the boundary layer shown over one wave period for particles released at an initial height of $z = 0.37$.

At still greater heights (not pictured) the particle motions are more in accord with linear theory. For particles released at a height of approximately 2.0 the motion over a wave period is nearly cyclical. If they are carried by the internal wave currents upwards for the first half of the wave period, then during the second half wave period they are carried back downwards, nearly returning to their initial locations. At intermediate heights ($0.7 < z < 1.5$) the motion is a combination of wave motion and mean current drift. While the particles fail to return to their initial locations, neither do they follow the complicated three-dimensional trajectories seen in the turbulent boundary layer.

The net effects of particle dispersion are quantified in Figure 6.15. Figure 6.15 (top panel) shows the rms displacement in the z'-direction for particles released at heights of (1) 0.018, (2) 0.05, (3) 0.14, (4) 0.37 and (5) 0.68 as a function of time. The calculations were carried out for approximately 3.3 wave periods (from $t = 74$ to $t = 134$). Each curve represents the average of a set of 200 particles released uniformly across a plane parallel to the wall at the specified heights. The net effects of the phases of the wave that are first encountered by the particles (upward or downward motion) are eliminated from the average by distributing sufficient numbers of particles spatially so that all of the wave phases are included. Initially, from $t = 75$ to 80, particles at each height move from their initial locations at similar rates. As time progresses, however, the rates of particle displacement diverge, as some begin to return towards their initial heights. The motions are cyclical (wave component) but with a mean displacement of particles from their initial locations. No attempt was made here to distinguish upward from downward displacements. The largest total displacements occur for particles released at middepth in the boundary layer, with average vertical displacements of approximately $0.32\lambda_z$ after about 3 wave periods. Smaller average displacements occur for particles nearest the wall (curve 1) of approximately 0.17, and for those initially farthest from the wall (curve 5) of approximately 0.19.

The bottom panel of Figure 6.15 translates the mean particle motion into a depth dependent diffusion coefficient defined by $D(z_o) = \frac{1}{2}\frac{\partial\overline{(z - z_o)^2}}{\partial t}$, where $\overline{(z - z_o)^2}$ is the

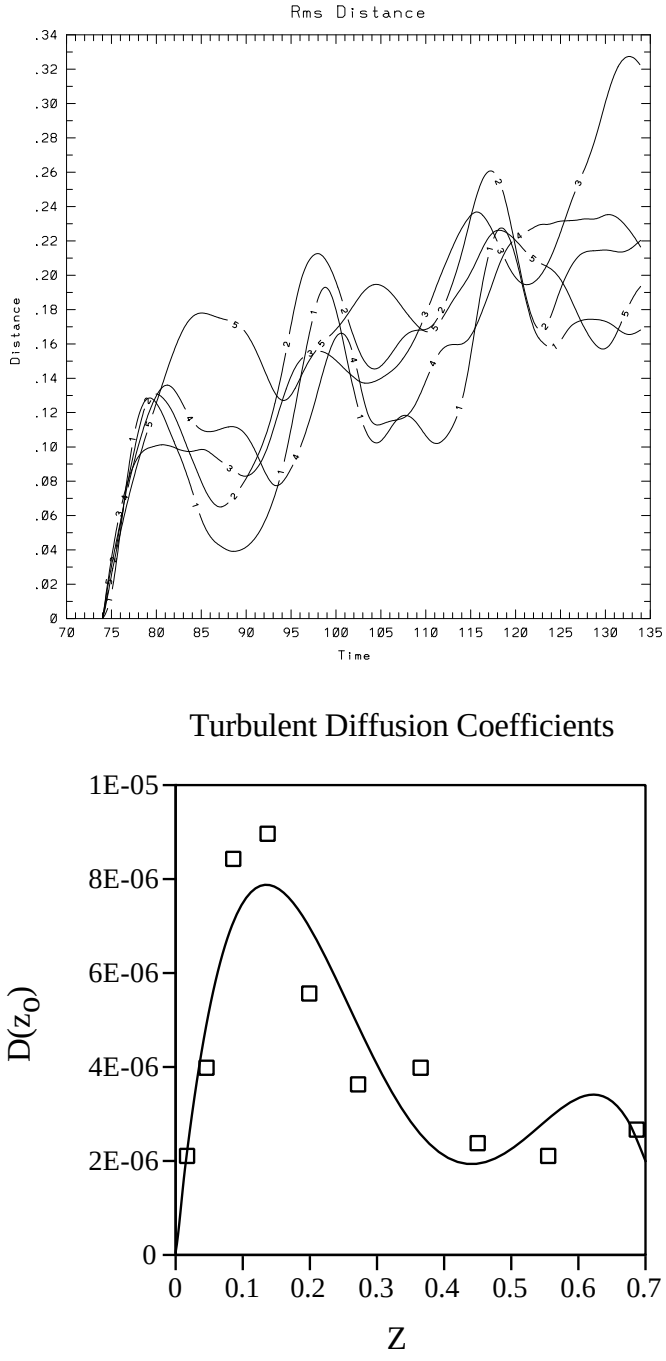

Figure 6.15: Vertical transport of particles (top) released at heights of (1) 0.018, (2) 0.05, (3) 0.14, (4) 0.37 and (5) 0.68 and diffusion coefficients vs. height (bottom).

mean square vertical particle displacement averaged over a set of particles released from an initial height z_o. The time derivatives are estimated using linear regression analysis over three wave periods for data similar to that shown in the top panel of Figure 6.15. The results for $D(z_o)$ are plotted at ten vertical locations between $0 < z < 0.7$. A curve fit to the data is generated with a fourth-order polynomial indicating the general trends. The strongest diffusion occurs for particles initially released between $0.1 < z < 0.2$. Above the turbulent boundary layer at heights $0.4 < z < 0.7$ the rate of turbulent diffusion is approximately constant and about one-third the value in the regions of strongest turbulence. At still greater heights, $z > 1.5$ (not pictured), the diffusion coefficients decrease to less than half the value at $z = 0.7$.

Generally, the results from the particle experiments support the view that there is significant net vertical transport of fluid in the simulations, in agreement with results from the dyed fluid experiments.

6.4 Free-Slip Wall

The fourth of the eight topics to be covered in this chapter is the effect of a free-slip boundary condition on the flow development. Case 21 (Re = 1800, $\alpha = 20^o$) was repeated using a free-slip boundary condition at the sloping boundary. For this simulations the density field used the no-flux boundary condition together with initialization of steady-state buoyancy induced boundary flows (of Phillips's type) derived in Equations (2.66) and (2.67).

Using the free-slip boundary condition is a step towards conducting large eddy simulations, because it eliminates high dissipation rates associated with the viscous sublayer, leaving more wave energy to participate in turbulent mixing. For large-scale (high Reynolds number) flows, a free-slip boundary condition is an approximation, eliminating the complex physics of the near wall region and assuming that the viscous sublayer is negligibly thin (and has small influence on the energetics) compared to other important length scales. For low to moderate Reynolds number flows, as investigated in this study, the free-slip approximation is less valid. It is described

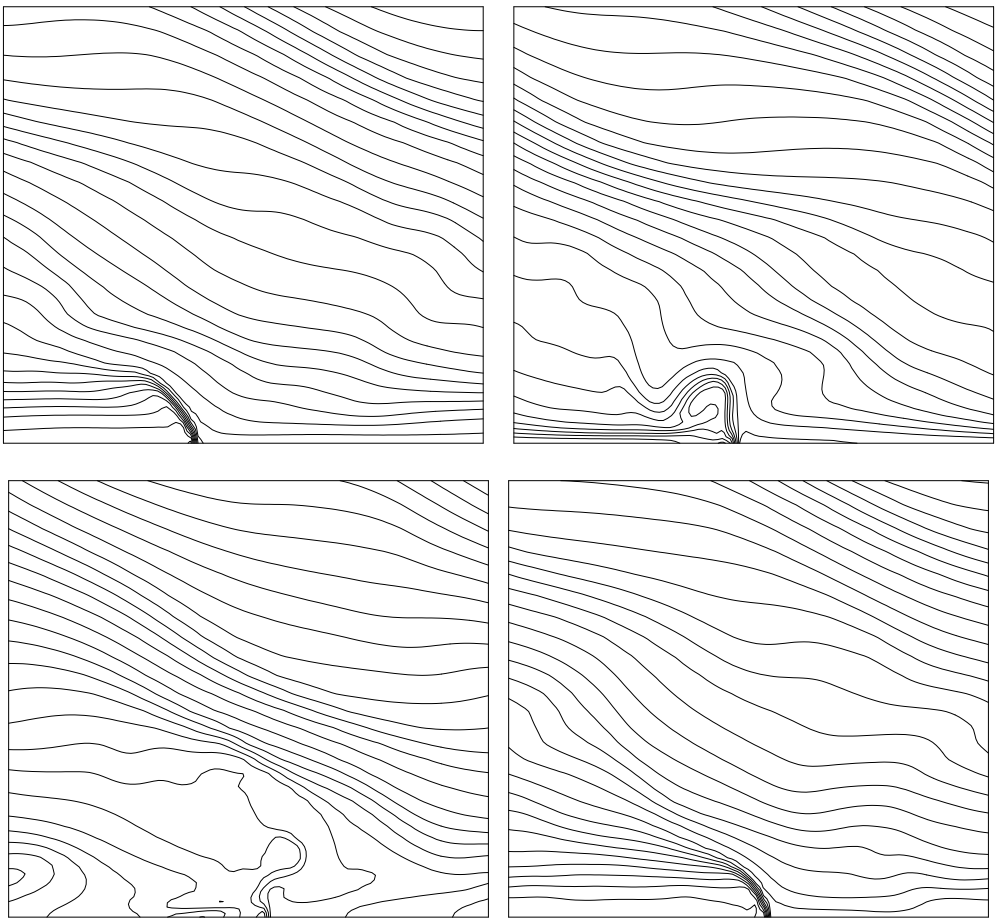

Figure 6.16: Isopycnals for free-slip boundary at $t = 139.5$, 143.4, 148.5 and 159.5, in order: upper left, upper right, lower left, lower right.

here for purposes of comparison with the detailed studies described throughout the thesis and for its potential value in extrapolating results of the simulations to higher Reynolds numbers.

Figure 6.16 shows a sequence of isopycnals throughout a wave period ($T_w = 18.1$) for the free-slip boundary simulation at $t = 139.5$, 143.4, 148.5 and 159.5, in order: upper left, upper right, lower left, lower right. The density field structure shown in the panels may be compared with the similar no-slip simulation illustrated in Figures 5.14 and 5.15. Similar to Case 21, the flow is periodic and characterized by the same

cycle of development: thermal front, wave overturning, wave breakdown, followed by restratification and re-establishment of a thermal front. Key differences appear in the second frame of Figure 6.16: during the development of wave overturning there is stronger recirculation in the region of the thermal front, similar to the turbulent bore identified for the 30^o slope. The similarity with the steeper slope does not continue, however, as the flow with the free-slip 20^o slope passes through the bore-like stage, and the mixing extends across the breadth of the boundary layer before reorganizing for the next mixing cycle. An additional difference apparent in Figure 6.16, compared with the no-slip case, is that the thermal front for the free-slip wall appears to have a stronger density gradient.

Figure 6.17 shows velocity vectors corresponding to the density fields in Figure 6.16; these may be compared with the corresponding plots for the no-slip simulation in Figures 5.16 and 5.17. The maximum vectors in each of the panels in Figure 6.17 are 0.209, 0.256, 0.144, and 0.177, respectively. Note that these velocities are approximately 1.5 times larger than those observed in the no-slip case. The strongest currents in the simulation occur during the phase of the period where the thermal front moves upslope, and are associated with downslope flow swelling over the thermal front. Because the strongest currents occur near the bottom boundary and are not diminished by the proximity of a no-slip boundary condition, the energy density in the near wall region is significantly higher than observed in the no-slip case. (A computational consequence arising from having the largest velocities located in the region of smallest grid spacing is that the time steps for the simulation must be about half the size for the free-slip simulations compared with the no-slip simulations; this simulation was calculated for 30,000 time steps on a 129 x 33 x 130 mesh, requiring approximately 21 days of CPU time on an HP-715/100 workstation.)

Interestingly, the total energy in the simulation, shown in Figure 6.18, does not increase as rapidly as was observed for the corresponding no-slip simulation shown in Figure 4.29. The mixing efficiency for the free-slip case is 0.45, and the integrated rate of dissipation of kinetic energy to heat is 0.49, leaving a radiation/accumulation of energy rate of 0.06 for the free-slip case. This is to be compared with the corresponding

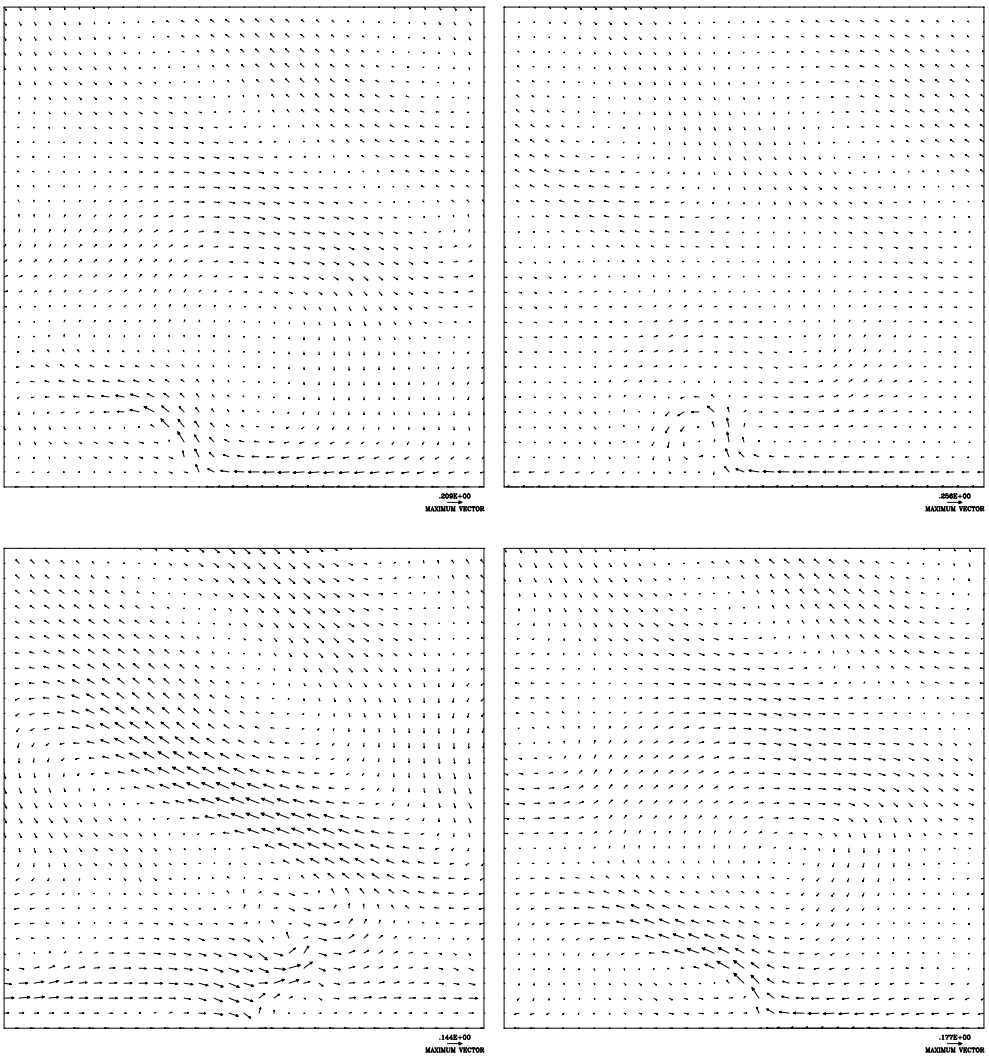

Figure 6.17: Sequence of velocity vectors for frames corresponding to Figure 6.17 for a 20^o bottom slope at $t = 139.5$, 143.4, 148.5 and 159.5, in order: upper left, upper right, lower left, lower right.

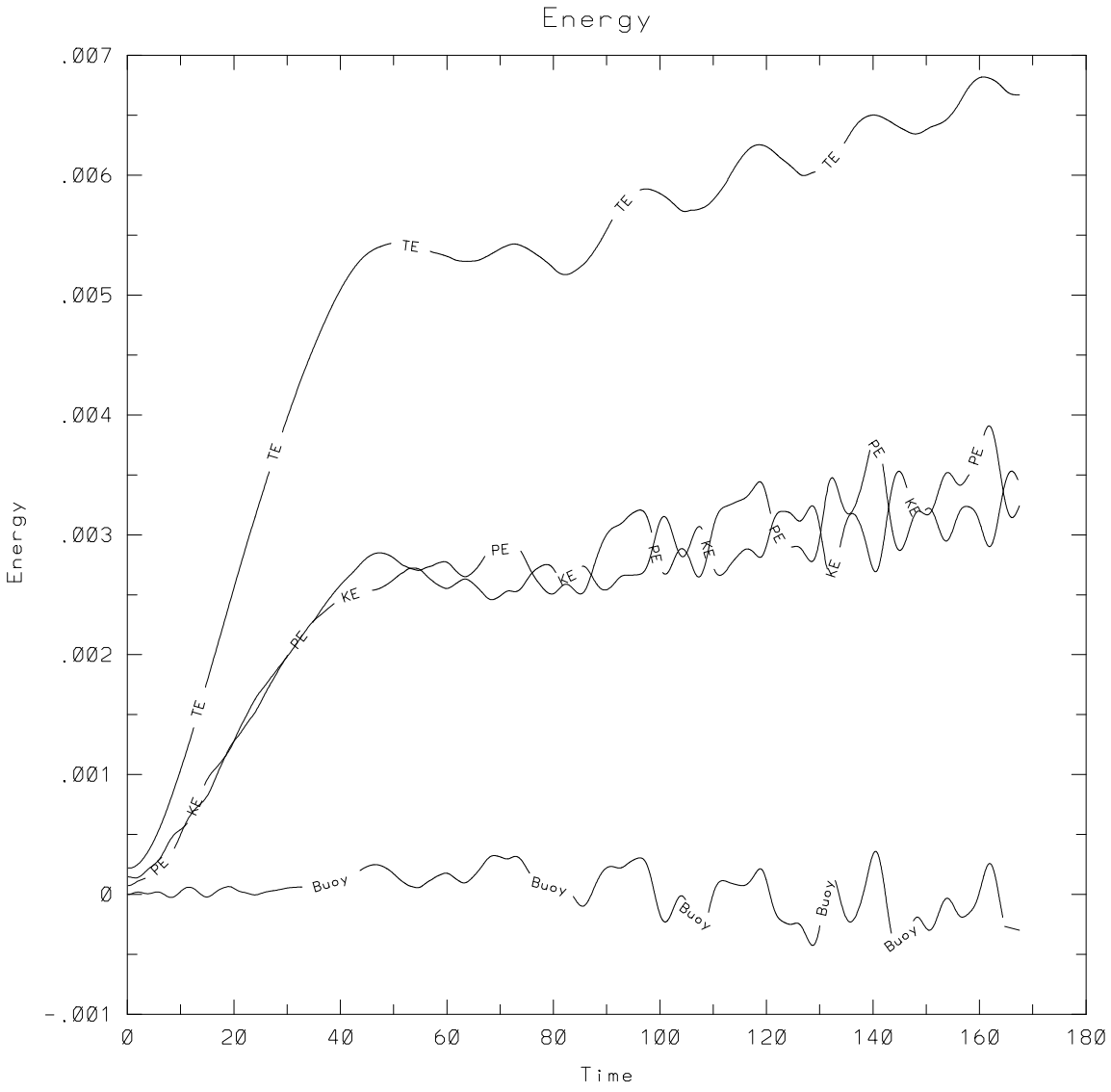

Figure 6.18: The volume integrated kinetic, potential, and total energies and the time integrated buoyancy flux for the free-slip boundary simulation.

values of 0.34, 0.53, and 0.13 for no-slip case.

The energy budget is significant in several ways. First, the mixing efficiency is significantly higher for the free-slip simulation. This agrees with expectations because, as less kinetic energy is dissipated in the viscous sub-layer, there is more wave energy available for mixing. Not only is the mixing-efficiency higher for the free-slip simulation than for the equivalent no-slip simulation, it is higher than all the mixing efficiencies observed in any of the other simulations ($\eta \approx 0.35$). This agrees with the prediction given in Section 5.9 that simulations of free-shear flows would produce mixing efficiencies closer to 0.5 for Prandtl numbers of 1 for non-turbulent flows.

A lower value for the loss of kinetic energy to heat also has a simple explanation. When the viscous sublayer is removed, ϵ decreases significantly in that region. What is unexpected, however, is that the total dissipation rate (sum of χ and ϵ) is higher for the free-slip simulation. A likely explanation is that the higher velocities in the boundary layer and associated strong shears increase the value of ϵ in most regions of the turbulent boundary layer, partially compensating for the decrease in the viscous layer. This result is counter-intuitive based upon previous results which showed that increases in the strength of the turbulence in the boundary layer had corresponding increases in the radiation of energy away from the boundary layer. The previous results, however, arose from different adjustments of flow parameters (such as increasing wave amplitude or Reynolds number) and may represent different responses by nonlinear processes.

The final important point illustrated in Figure 6.18 is that the integrated buoyancy flux for the free-slip simulation is essentially zero. In all of the previous (no-slip) cases the buoyancy flux was significantly negative, indicating the transfer of potential to kinetic energy. For the free-slip simulation, in contrast, the buoyancy flux oscillates about zero. Again, the interpretation is that a significant portion of the net negative buoyancy flux occurs in the viscous sublayer.

Figure 6.19 shows the terms of the kinetic (3.111) and total energy equations (3.113) for the free-slip simulation. They are similar to the terms of the energy

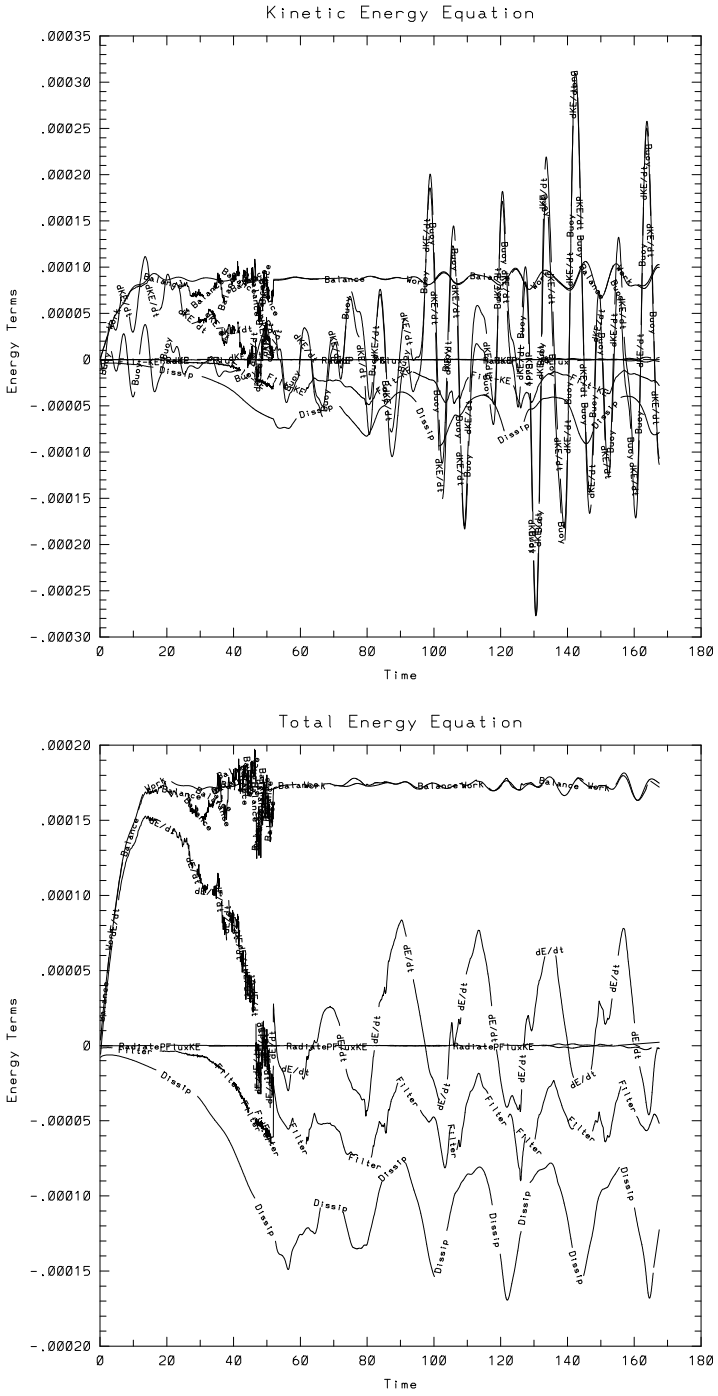

Figure 6.19: Terms of the kinetic and total energy equations for the free-slip simulation.

equations for the no-slip simulations shown in Figure 5.18 (for $Re = 1200$) and the bottom panel of Figure 5.20 (for $Re = 1800$). The noise in the balance and $\frac{\partial E}{\partial t}$ terms before $t = 50$ are due to roundoff errors; these were subsequently eliminated by changing the calculation of the energy terms to double precision after $t = 50$. They do not represent errors in the calculation, and the overall balance of energy is good throughout the simulation. The major differences between this calculation and the no-slip version are that the filter removed significantly more energy (meaning that more energy was transferred to small scales) and that the mean value of $\frac{\partial E}{\partial t}$ is closer to zero, representing a slower accumulation of energy in the system. Otherwise, the energetics of the flows are very similar and appear to be dominated by a rapidly oscillating buoyancy flux, indicative of strong upslope/downslope flows as described previously.

Figures 6.20 and 6.21 compare aspects of the strength of the three-dimensionality of the free-slip and no-slip flows. Figure 6.20 shows the volume integrals of v^2 and Figure 6.21 shows the intensity of the $\left(\frac{\partial w}{\partial y}\right)^2$ component of velocity shear. Unfortunately for the comparison, the strength of the white noise for the free-slip case is approximately two times higher than the strength of the white noise for the no-slip case. This probably makes little difference after the first mixing period, however, because both values grow and decay in a rapid cycle and the difference in initial intensities vanishes from Figure 6.21 after the first mixing cycle.

One important aspect of this comparison to notice is the similarity of the two realizations. The mixing periods occur at approximately the same intervals and have the same characteristic growth and decay rates.

Figure 6.21 shows that the volume integrals of $\left(\frac{\partial w}{\partial y}\right)^2$ have similar intensities. The main difference here is that the peaks for the free-slip case are broader and usually begin slightly sooner, indicating that the three-dimensionality (and hence, turbulence) grows faster (probably because there is more wave-energy present) and lasts longer. The decay rate when the mixing cycle is completed is, however, approximately the same as for the no-slip simulation, indicating that when the mixing is completed the boundary layer relaminarizes in a similar fashion.

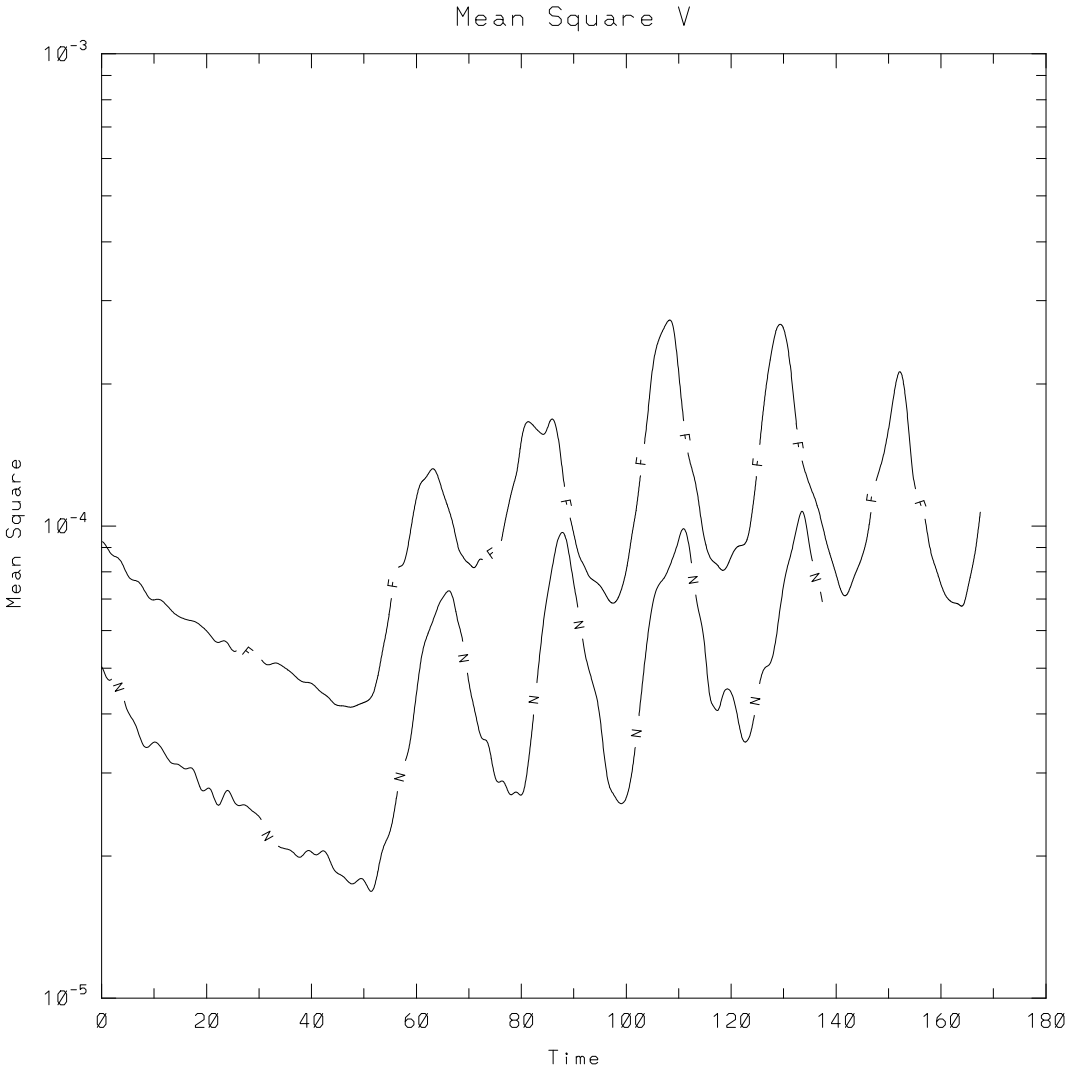

Figure 6.20: Volume integrals of v^2 for simulations using the free-slip boundary condition (F) and a no-slip (N) boundary condition for a 20^o slope and $Re = 1800$.

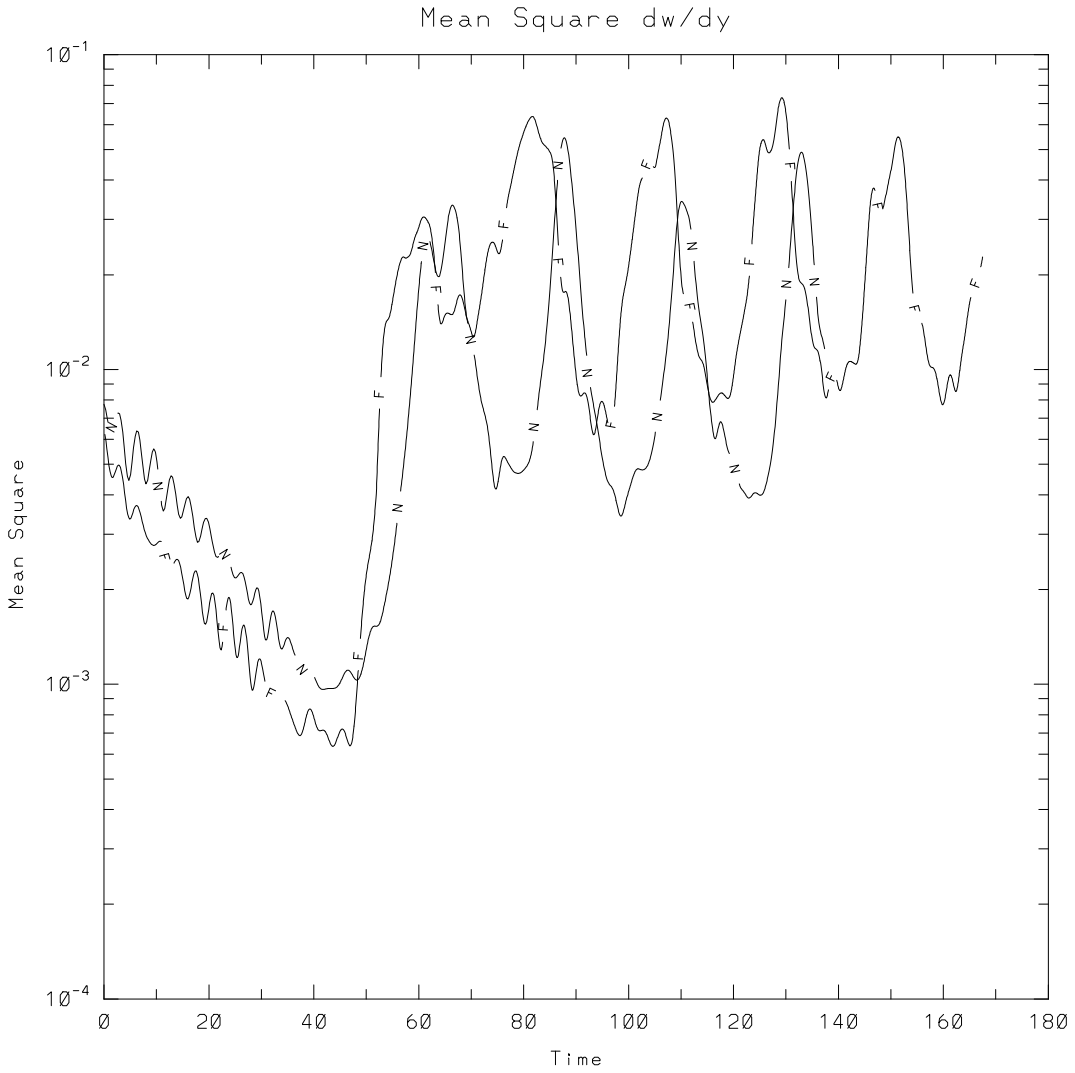

Figure 6.21: Volume integrals of $\left(\frac{\partial w}{\partial y}\right)^2$ for the free-slip simulation and the no-slip boundary condition with the same parameters.

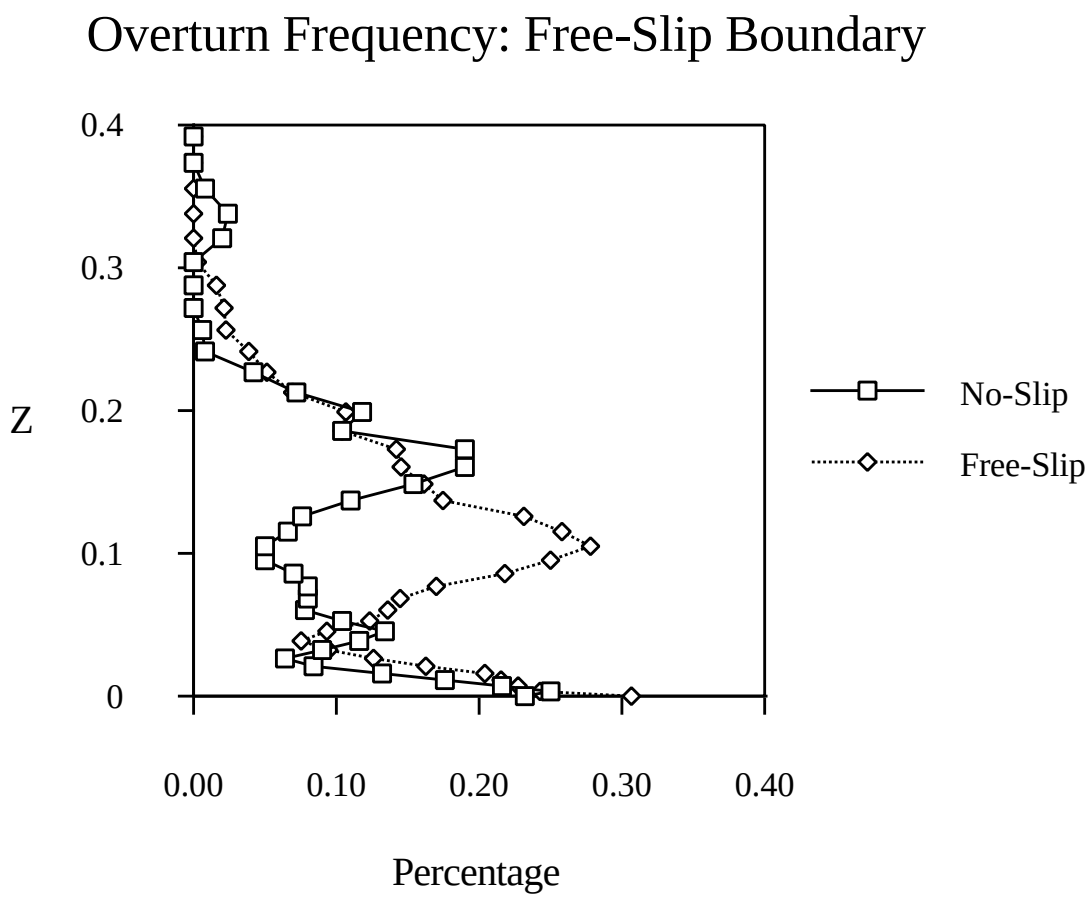

Figure 6.22: The frequency of static instabilities for the free-slip simulation and the no-slip boundary condition with the same parameters.

This presentation of the free-slip simulation is completed by comparing the boundary layer thicknesses of the two cases. Figure 6.22 compares the frequency of statically unstable (overturned) density configurations as a function of distance from the bottom boundary for the free-slip simulation with Case 21. The basic result is that the boundary layers have approximately the same thickness, $\delta \approx 0.3\lambda_z$. The largest difference is that in the free-slip simulation there is a higher percentage of overturned isopycnals in the region from $0.5 < z < 1.5$. This is consistent with the interpretation that the boundary layer contains more energy and has a higher mixing efficiency for the free-slip simulation.

In summary, the results from the simulation with the free-slip boundary condition are quite similar to results for the no-slip boundary condition. The flow development goes through similar phases and develops into a turbulent boundary layer with approximately the same depth and characteristic features (thermal front, upwelling, upslope/downslope periodicity, etc.) as for the no-slip boundary condition. The main differences are that the free-slip flow contains more energy (which is used for mixing in the boundary layer) and, unexpectedly, has a lower rate of radiation of energy from the turbulence than observed for the no-slip boundary condition.

6.5 Wall Shear Rates

Interest in wall shear stresses caused by reflecting internal waves is motivated by two important oceanic considerations. The first is the effect on the sea-bed itself, and especially on the relationship to sediment transport. Depending on the type of sediment on the boundary (sand, clay, corral, etc.) currents generated by internal wave breakdown may be sufficiently strong to suspend and/or deposit sediment from one location to another. When sediment is moved, as for sandy bottoms, the appropriate bottom boundary condition may not be the ideal no-slip boundary, but, in some sense, a combination of both slip and no-slip. Cacchione et al. (1990) have examined in the laboratory (1972) and in field studies (1988) the movement of sediment caused by shoaling internal waves.

A second issue related to strong wall shear is the effect of suspended particles on

the water. Two potentially important effects of particle suspension are changes to the optical properties of the water column (Cacchione and Drake, 1986) and modifications to the turbulence (because the concentration of sediment in the water changes the effective density stratification).

Figures 6.23 - 6.26 show contours of wall shears for three of the critical angle simulations. Figure 6.23 shows contours of the component of the wall shear $\left.\frac{\partial u}{\partial z}\right|_w$ for Case 15 ($Re = 3600$, $\alpha = 9^o$) at $t = 135$ (top), 145 (middle), and 161 (bottom). Downslope flow is indicated by the negative (dashed) contours and upslope flow by positive (solid) contours. At $t = 135$ the spatial variation is primarily two-dimensional. Positive contours in the top two panels occur at the location of the thermal front. At $t = 161$ the flow is in a period of mixing, and the turbulence in the fluid has caused the wall shear to become more three-dimensional. Local highs (H) and lows (L) are indicated on the panels and show that the wall shears range from approximately -28.8 to 17.0. These peak values may be compared with the shear in the oncoming wave as it approaches the turbulent boundary layer. Taking a conservative (high) estimate of the oncoming wave shear, $S_w = \frac{2U_m}{\frac{\lambda_z}{2}}$, for Case 15 gives $S_w \approx 0.6$, where $2U_m$ accounts for the maximum (positive and negative) current speeds of the oncoming wave. Comparison of these values reveals that the shear at the wall is 30 to 50 times higher than the shear in the oncoming wave. This strong amplification of wave shear is caused by amplification of wave currents in the vicinity of the boundary, compression of the vertical length scale of the reflected wave, and the presence of the viscous layer associated with the no-slip boundary condition.

The total wall shear is the vector sum of $\left.\frac{\partial u}{\partial z}\right|_w \hat{i}$ and $\left.\frac{\partial v}{\partial z}\right|_w \hat{j}$. Figure 6.24 shows contours of $\left.\frac{\partial v}{\partial z}\right|_w$ for Case 15 at $t = 135$, 145, and 161. The v components of the shear stresses are much more three-dimensional than for the u fields. The regions of strongest shear generally correspond to the location of the thermal front. The intensities of $\left.\frac{\partial v}{\partial z}\right|_w$ are somewhat smaller than $\left.\frac{\partial u}{\partial z}\right|_w$. The maximum positive and negative values are approximately 10.4 and -13.3, or roughly 1/2 the strength of the

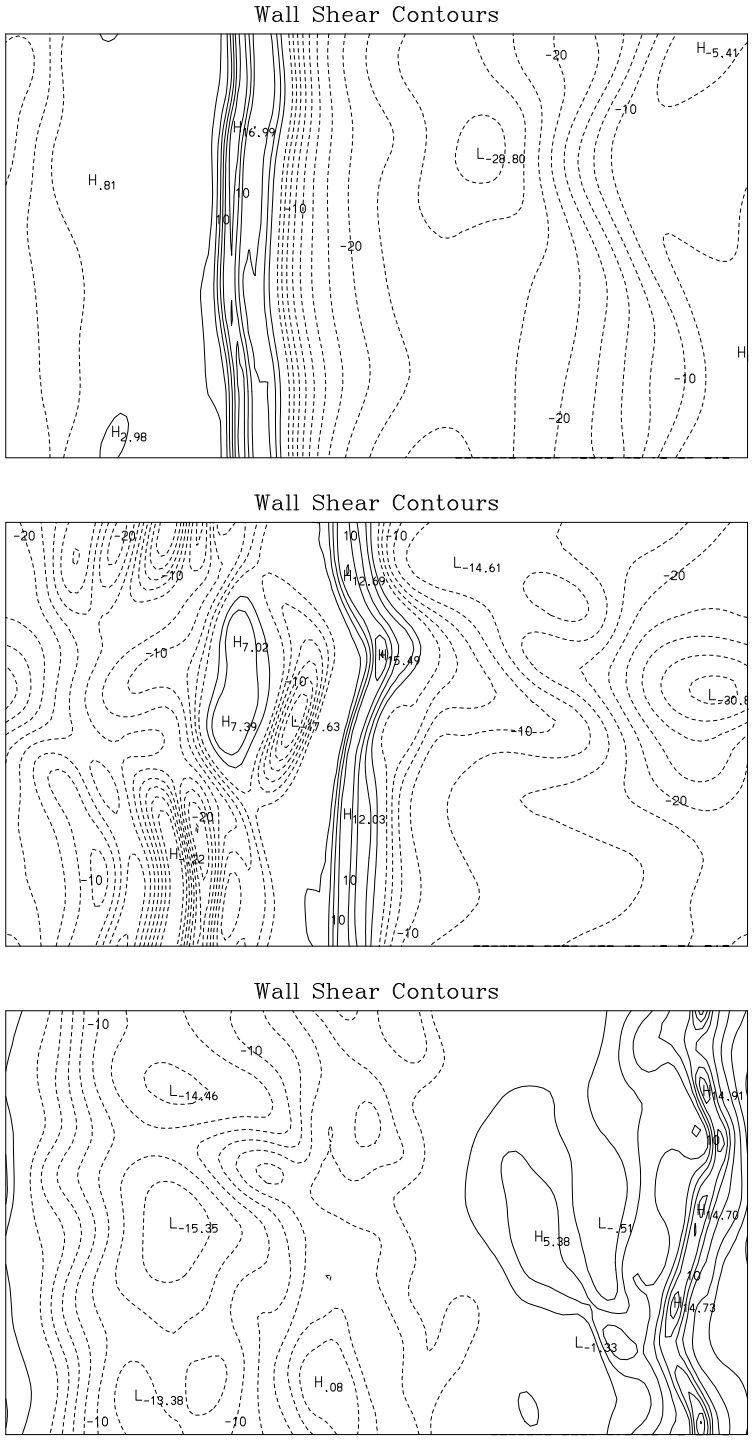

Figure 6.23: Wall shear contours of $\dfrac{\partial u}{\partial z}$ for Case 15 at $t = 135$, 145, and 161.

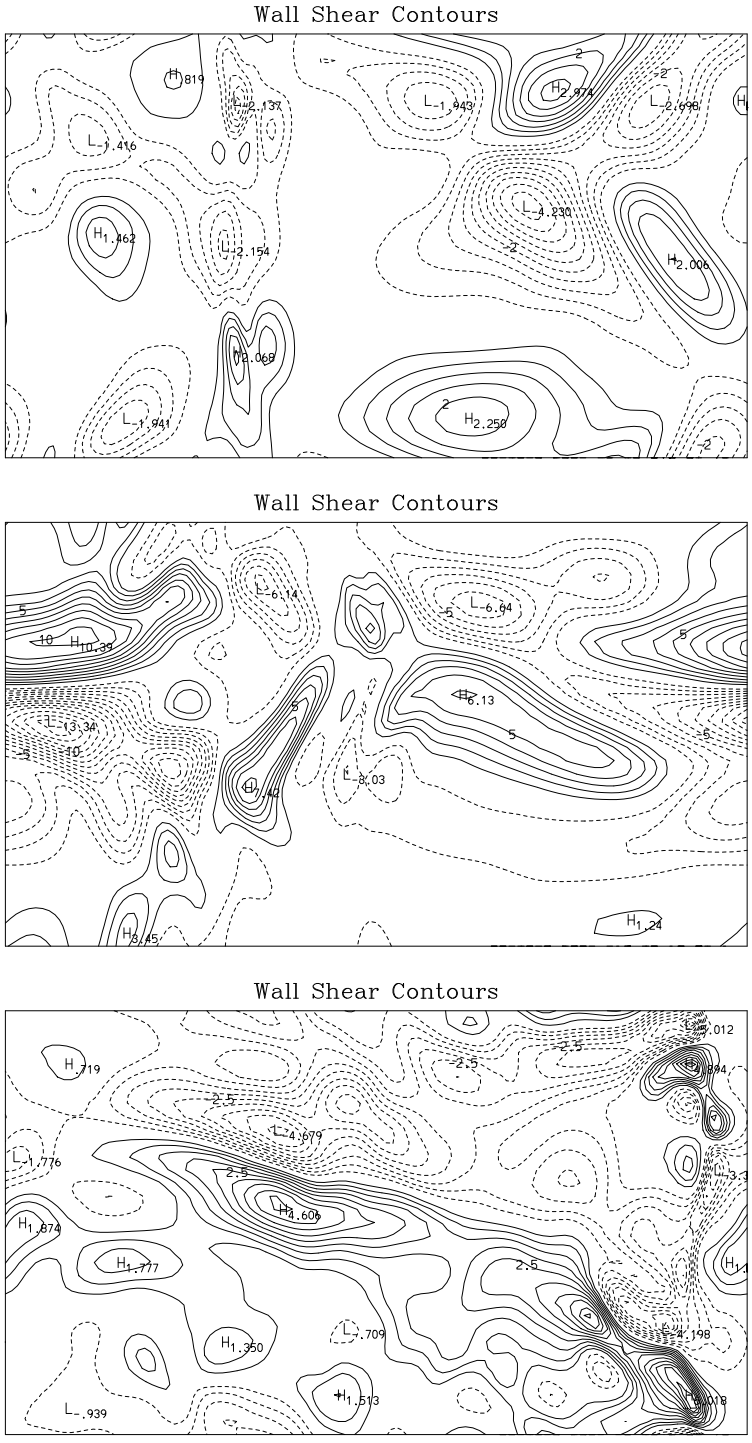

Figure 6.24: Wall shear contours of $\frac{\partial v}{\partial z}$ for Case 15 at $t = 135$, 145, and 161.

$\left.\frac{\partial u}{\partial z}\right|_w$.

The two components of shear are shown at only one time for Case 28 with the 30^o boundary ($Re = 1700$). The quasi-steady flow for this simulation creates wall shears that are similar from one time to another, except that the regions of strongest variability move upslope with the turbulent bore. Figure 6.25 shows wall shear contours of $\frac{\partial u}{\partial z}$ (top) and $\frac{\partial v}{\partial z}$ (bottom) at $t = 144$. The shear rates range from -26 to 26 for the u component and from -6.4 to 7.0 for the v component. These values may be compared with the shear in the oncoming wave $S_w \approx 0.2$. The wave shear is smaller for this case because the velocities in the oncoming wave are lower, but the wall shear values are as high as observed before. For this simulation, the wall shear has local intensities over 100 times stronger than the shear in the oncoming wave.

Finally, Figure 6.26 shows wall shear contours of $\frac{\partial u}{\partial z}$ (left column) and $\frac{\partial v}{\partial z}$ (right column) for Case 19 ($Re = 1100$, $\alpha = 20^o$) at $t = 81$ (top), 85 (middle), and 91 (bottom). Again, the two-dimensional dominance of the thermal front is apparent at early times followed by an increase in the three-dimensionality at $t = 91$ when the wave breaks down. The wave shear for this simulation is $S_w \approx 0.3$, and the wall shears range from approximately -25 to 19.

In summary, wall shears caused by critical internal wave reflection are from one to two orders of magnitude higher than the shear of the oncoming wave. Strong shears, coupled with strong local upwelling features of near boundary fluid (such as flow over the thermal front, e.g., Figure 6.13 and 5.16), make this process an ideal mechanism for resuspension of bottom sediment. While the strongest shear rates are localized, they pass across the boundary each wave period. The simulations support conclusions of other researchers that internal wave reflection may make significant contributions to fluid-sediment boundary interactions.

6.6 Off-Critical Angle Results

A series of simulations was conducted to examine flow behavior for oncoming waves with angles of propagation away from the critical angle. In this set of experiments the

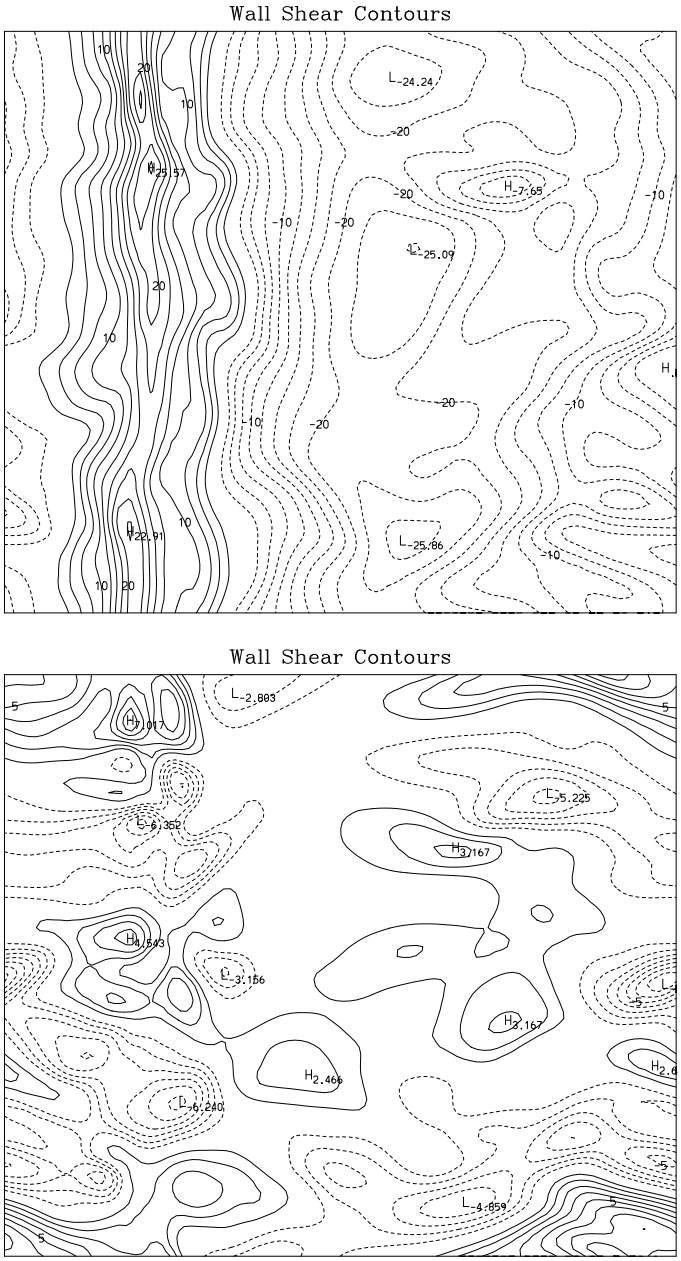

Figure 6.25: Wall shear contours of $\frac{\partial u}{\partial z}$ (top) and $\frac{\partial v}{\partial z}$ (bottom) for Case 28 at $t = 144$.

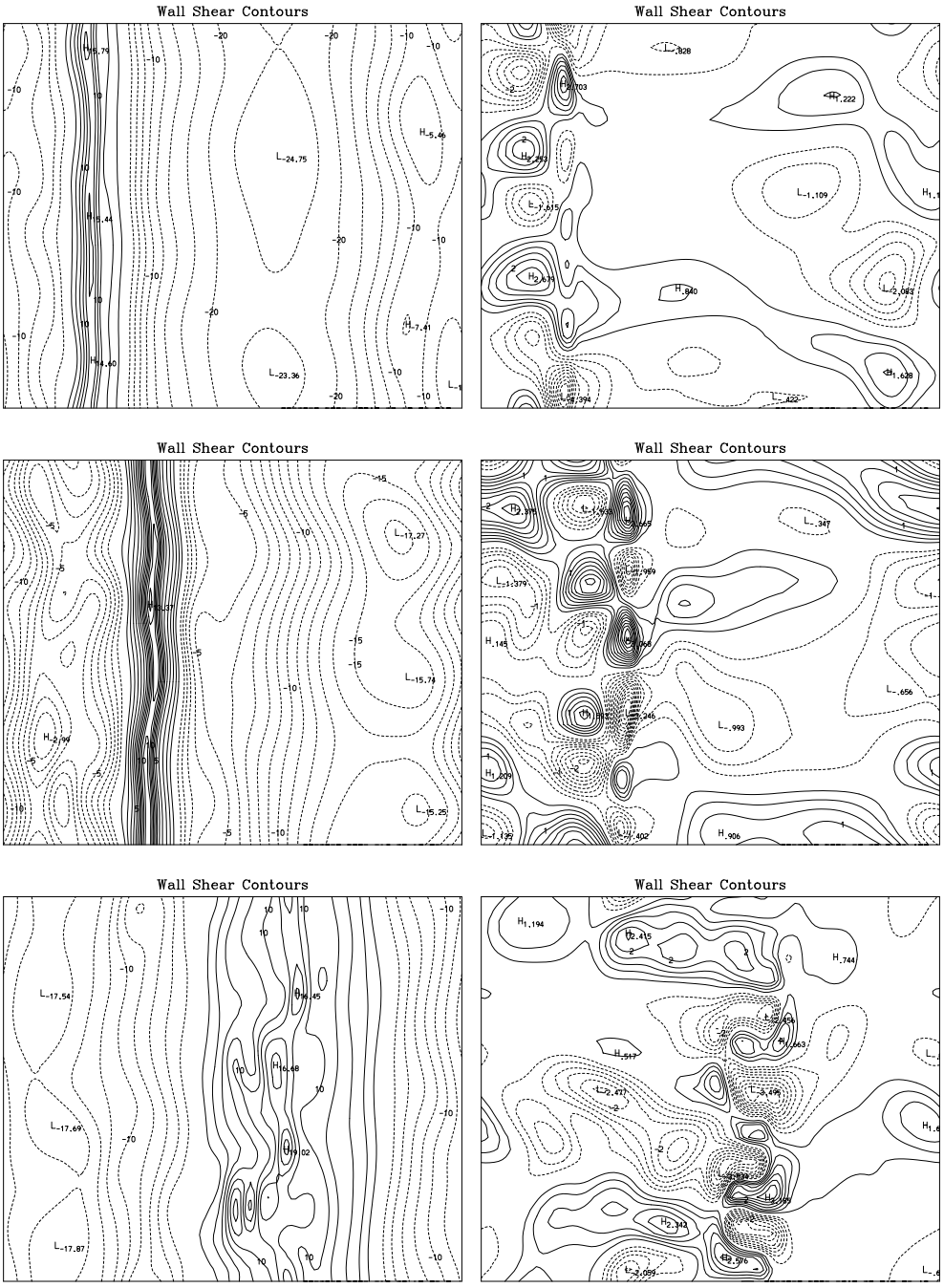

Figure 6.26: Wall shear contours of $\dfrac{\partial u}{\partial z}$ (left column) and $\dfrac{\partial v}{\partial z}$ (right column) for Case 19 at $t = 81$ (top), 85, and 91 (bottom).

Table 6.1: Off Critical Angle Simulations

Case	α	Re	Ri	(A_r/A_i)	Classification
29	0.0	620	235	1.0	laminar
30	0.0	1250	59	1.0	laminar
31	5.0	1100	170	3.3	laminar
32	5.0	1900	94	3.3	transition
33	8.0	1500	37	13.9	turbulent
34	9.2	850	61	∞	laminar
35	9.2	1200	53	∞	transition
36	9.2	2000	40	∞	turbulent
37	9.2	2800	40	∞	turbulent
38	9.2	3600	46	∞	turbulent
39	10.5	950	84	15.1	transition
40	10.5	2470	77	15.1	turbulent
41	10.5	3690	35	15.1	turbulent
42	13.5	970	74	5.2	laminar
43	13.5	2120	62	5.2	turbulent

frequency of all oncoming waves is $\omega = 0.16$, so that the angle of wave propagation with respect to the horizontal is 9.2^o. The bottom slope was varied in the simulations between 0^o and 13.5^o. For the simulations conducted with bottom slopes between 0^o and 9.2^o the waves reflect upslope. This is called supercritical reflection, because the wave frequency is higher than the frequency of a wave propagating at the critical angle associated with the bottom slope. For simulations conducted with bottom slopes of 9.2 and above, the waves reflect downslope (subcritical). The series of off-critical angle simulations presented above in Table 4.2 are duplicated here in Table 6.1. The Table identifies the case number, bottom slope, Reynolds and Richardson numbers, amplification factor (from linear theory, defined in Section 4.1), and the classification of each simulation (e.g., laminar or turbulent).

Simulations conducted over a flat bottom ($\alpha = 0^o$) were used primarily for refer-

ence to other simulations. An additional complication was introduced into the two flat-bottom simulations by using two different types of density boundary conditions. The first one (Case 29) used a no-flux (adiabatic) boundary condition (as did all of the simulations over sloping boundaries). For a sloping boundary the no-flux condition produces a steady secondary flow (Section 2.7.3), maintained by a balance of advection and diffusion, by establishing buoyancy-induced boundary currents. For a flat bottom, however, the no-flux boundary condition does not result in the establishment of boundary currents, and the depth of the boundary layer influenced by diffusion grows steadily, weakening the stratification near the boundary. This effect was removed from the simulation in Case 30 by using a constant density (isothermal) boundary condition. While this condition also influences the flow near the boundary, the effect appears smaller, facilitating comparison with the sloping boundary simulations.

The simulations with 5^o and 13.5^o bottom slopes were chosen to complement one another, because one is approximately 4.25^o above and the other is 4.25^o below the critical angle (9.22^o). Similarly, the simulations at 8^o and 10.5^o are approximately 1.25^o on either side of critical.

In certain aspects, the off-critical angle simulations contain more complexity than the critical angle simulations. The main difference is that the energy of the oncoming wave is not confined, upon reflection, to the boundary layer but reflects away from the slope. The process is illustrated, using linear ray theory, in Figure 1.1. The reflected wave passes through the oncoming wave allowing the possibility of wave-wave interactions to occur remote from the boundary. Thorpe (1989) and Thorpe and Haines (1987) have used weakly nonlinear resonance theory to examine interactions between oncoming and reflected wave trains. The present numerical simulations (e.g., Figure 4.4) have showed evidence of the formation of a third wave caused by near-resonance interactions between oncoming and outgoing waves for reflection from a 5^o bottom slope for a small amplitude simulation.

An issue examined with the present set of simulations is how close to the critical angle an oncoming wave must be to cause similar mixing. Table 6.2 presents results for

Table 6.2: Energy Budgets Off Critical Angle

Case	α	Re	Mixing	Heat	Radiate
29	0.0	620	0.30	0.37	0.33
30	0.0	1250	0.33	0.41	0.25
31	5.0	1100	0.29	0.44	0.27
32	5.0	1900	0.33	0.42	0.25
33	8.0	1500	0.38	0.46	0.16
34	9.2	850	0.36	0.58	0.06
35	9.2	1200	0.38	0.50	0.12
36	9.2	2000	0.36	0.45	0.19
37	9.2	2800	0.37	0.48	0.15
38	9.2	3600	0.32	0.56	0.12
39	10.5	950	0.35	0.46	0.19
40	10.5	2470	0.34	0.56	0.10
41	10.5	3690	0.40	0.45	0.15
42	13.5	970	0.34	0.58	0.08
43	13.5	2120	0.36	0.58	0.06

the energy budgets of the off-critical simulations. This table lists approximate mixing efficiencies, heat loss coefficients, and radiation coefficients (representing wave energy that radiates away from the boundary or causes changes to the background flow).

As described in Section 5.8, the energy values are approximated after the oncoming waves have reached the bottom boundary and a quasi-steady process has commenced. The values are somewhat sensitive to the length of the simulations (most covered only one to two mixing cycles) and to the time when the dissipation integrals are initiated. An approximate estimate of the accuracy of these values is $\pm 10\%$. The error is estimating by examining values from simulations of different duration and by examining the integrals of the dissipation rates from different starting and ending points.

The results from Table 6.2 are plotted in Figures 6.27 and 6.28. Figure 6.27 locates

the values of the radiation coefficient as a function of slope and shows the regression line $y = -0.17x + 0.305$. This approximately linear result emphasizes the trend towards smaller radiation for larger slopes. The trend may not be so pronounced as indicated, however, because the averages at each slope are taken for simulations at different Reynolds and Richardson numbers. In addition, similar to the limit that exists for a flat-bottom slope for which strongest wave reflection occurs, higher slopes (i.e., 20^o - 40^o) also are expected to have high energy reflection coefficients (e.g., reflection from a vertical boundary is the same as from a horizontal boundary). The result is that the average values for the reflection coefficient should again rise for steeper slopes.

These off-critical angle simulations reveal a range of radiation of energy of more than a factor of 3 between the highest and lowest values, depending largely upon the Reynolds number. If additional simulations were conducted at other Reynolds numbers for the 13.5^o slope, it would not be surprising to find a broader distribution for the radiation coefficient.

As seen in Figure 6.27, the radiation coefficient for the flat bottom case is approximately 0.3. For inviscid (linear) waves this value would be approximately 1.0. This difference illustrates the significant viscous losses of energy experienced by waves for the low Reynolds number conditions of these cases ($Re = 620$, 1250).

To examine different regions of wave-energy loss, consider the following three-stages of wave reflection: approach toward the boundary (within a height of approximately $2\lambda_z$), reflection and interaction with the viscous sublayer (thickness of approximately $0.1\lambda_z$), and propagation away from the boundary (to a height of approximately $3.5\lambda_z$). Proportions of wave energy lost in each stage for these Reynolds numbers can be approximated by examining the energetics at different stages of the transient flow development. The results are that approximately 20% of the wave energy is lost while approaching the boundary, 25% is lost in the viscous sublayer, and an additional 25% (for a total of 70%) is lost after reflecting from the boundary. This result depends somewhat on the angle of wave propagation, θ, or, in the model, more precisely, $\theta + \alpha$. For larger values of $\theta + \alpha$ the waves approach the boundary more

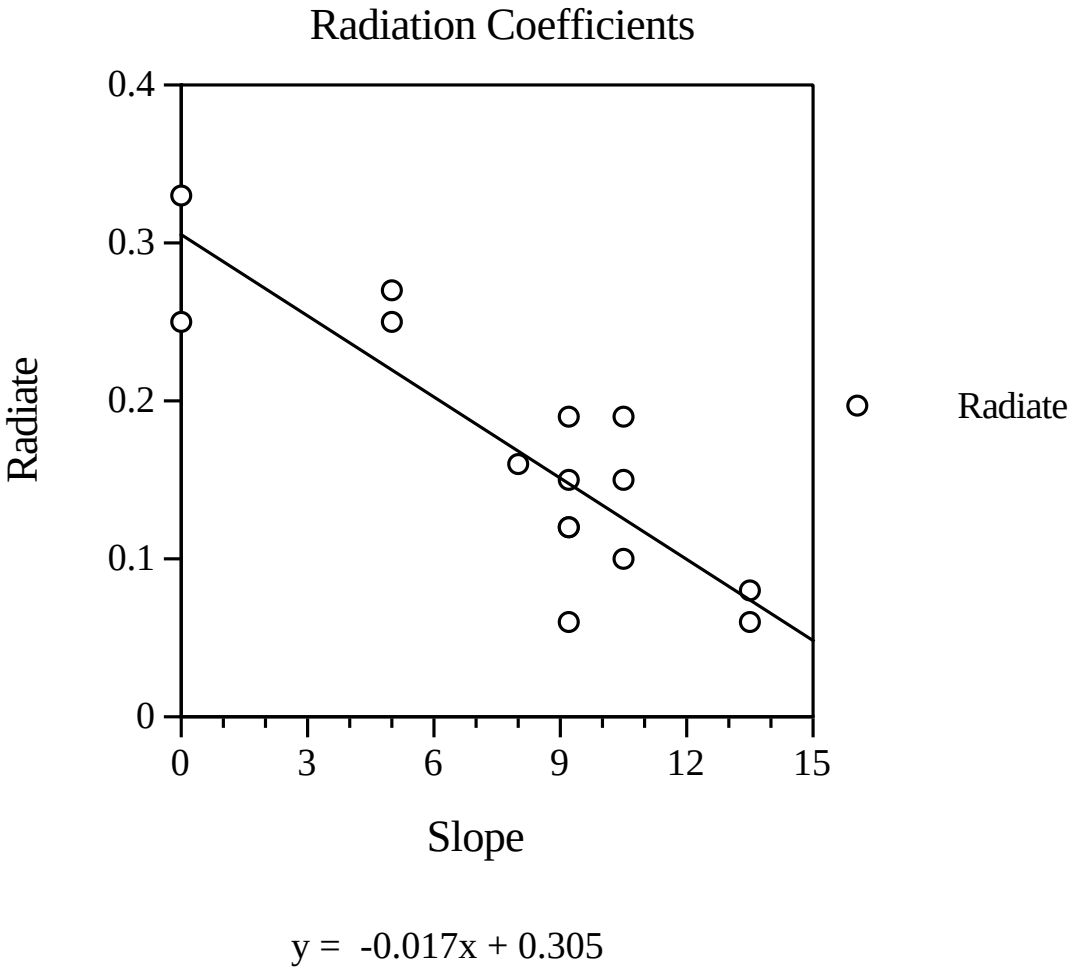

Figure 6.27: Energy radiated from the boundary layer region for simulations with bottom slopes between 0^o and 13.5^o.

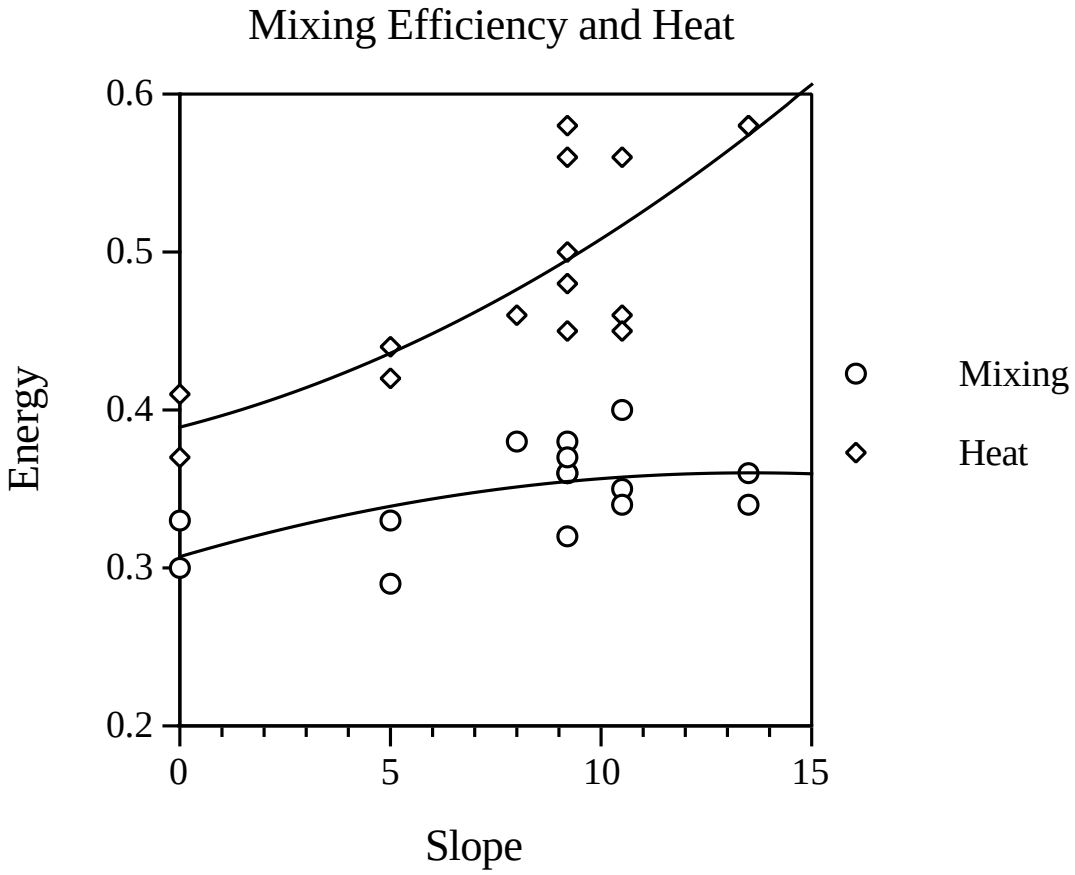

Figure 6.28: Values of mixing efficiency (circles) and heat loss (diamonds) for bottom slopes between 0^o and 13.5^o.

rapidly and less energy is lost to viscous dissipation. Note also that the waves propagate at a shallow (9.2^o) angle to the horizontal, so that they travel approximately six times farther in the horizontal than in the vertical direction.

From Table 6.2, Figure 6.28 locates values of mixing efficiency and losses of kinetic energy to heat as a function of the slope. The curves indicate data trends, fitted with a quadratic function to aid in visualization. Figure 6.28 implies that waves reflected from steeper slopes have lower radiation coefficients because of higher losses to heat rather than higher mixing efficiencies. The mixing efficiencies are generally highest

close to the critical angle, but as seen by the spread in the data at the critical angle, the mixing efficiencies depend on Reynolds number as strongly as they depend on slope.

The simulations indicate that the integrated energetics for the 8^o and 10.5^o slopes are essentially the same as the energetics at the critical angle. The simulations at 5^o and 13.5^o are dissimilar from one another and from the critical angle results. These differences will be discussed in more detail in reference to Figures 6.30 and 6.31.

Figure 6.29 compares total dissipation rates for one simulation at each slope: Case 29, 0^o ($Re = 620$); Case 32, 5^o ($Re = 1900$); Case 33, 8^o ($Re = 1500$); Case 36, 9.2^o ($Re = 2000$); Case 40, 10.5^o ($Re = 2100$); and Case 43, 13.5^o ($Re = 2470$). A principal result of Figure 6.29 is that the duration of the mixing cycles varies with the bottom slope. All the simulations used waves with the same frequency and wave period ($T_w = 39.1$). As noted before, critical angle simulations typically have a mixing cycle approximately 20 - 30% longer than the wave period. Observations of off-critical angle simulations show that the mixing cycle is shortened for slopes above and lengthened for slopes below critical.

Table 6.3 shows the duration of the mixing periods as a function of slope. The values are averages from several simulations at each slope, except for the 5^o slope (which includes estimates based upon similar, longer duration, two-dimensional simulations). Because reflection from a flat bottom slope is observed to become steady and no mixing cycle is observed (except if reflected waves interact nonlinearly with oncoming waves), the mixing period, T_M, for the flat bottom case is listed as infinite. Also included for comparison in Table 6.3 are the wave period for a critical frequency wave, T_{W_c}, for each bottom slope and the ratios of the mixing periods for the off-critical waves to the wave periods of the critical frequency waves, $\frac{T_M}{T_{W_c}}$. Note that the mixing cycles for the off-critical waves (all with wave periods of 39.2) follow a similar trend to the wave periods for critical frequency waves for the other slopes. In addition, as seen in Figure 5.22, mixing cycles for critical frequency waves are typically 20-40% longer than their wave periods for bottom slopes in this range. Therefore, it appears that the off-critical waves have mixing cycles similar to the mixing cycles of

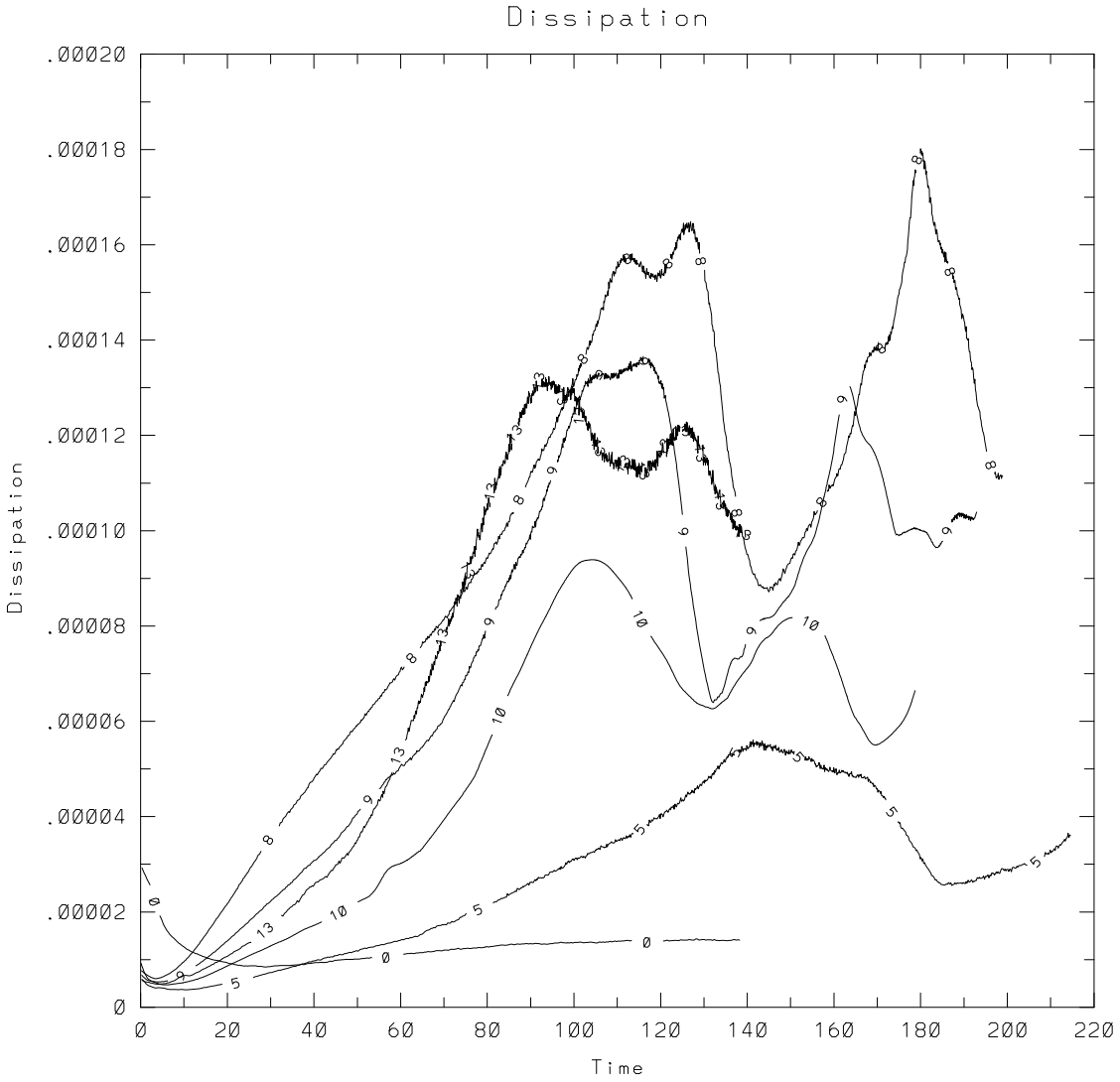

Figure 6.29: Total dissipation rates for off-critical angle simulations with bottom slopes of 0^o, 5^o, 8^o, 9.2^o, 10.5^o, and 13.5^o.

Table 6.3: Mixing Periods for Off Critical Angle Simulations

α	0.0	5.0	8.0	9.2	10.5	13.5
T_M	∞	100	60	48	42	34
T_{W_c}	∞	72	45	39	35	28
$\frac{T_M}{T_{W_c}}$		1.39	1.33	1.23	1.2	1.21

critical frequency waves over the same bottom slopes.

These results show that supercritical reflection has significantly longer mixing cycles than subcritical reflection. This result was described in Section 4.4.3 in relation to the weakening of the background density gradient. For critical angle simulations the angle of propagation of the oncoming wave matches the bottom slope at the beginning of the simulations. But as mixing continues the background density gradient can be weakened, causing the angle of wave propagation to become steeper. The wave can then behave as in supercritical cases and increase the length of the mixing cycle. In the ocean, waves incident to sloping boundaries are not monochromatic. Therefore, if the density stratification adjusts near a boundary so that a certain frequency of waves becomes off-critical, another nearby frequency band of waves will become critical.

The flow fields for the 8^o and 10.5^o slopes are essentially the same as the flow fields that develop for critical angle simulations of similar Reynolds number (Figures 4.10 and 5.3). They are not pictured because the similarity is so strong. Flow fields farther away from the critical angle, however, develop in different manners. Figure 6.30 presents a sequence of isopycnals for Case 32 ($Re = 1900$, $\alpha = 5^o$) at $t = 152$ (top), 178, 190, and 215 (bottom). The density contours show that wave amplification is relatively weak upon reflection. The top and bottom panels show that a periodic thermal front develops in the boundary layer, similar to the critical angle simulations, but the development does not undergo strong wave overturning and breakdown as for near-critical simulations.

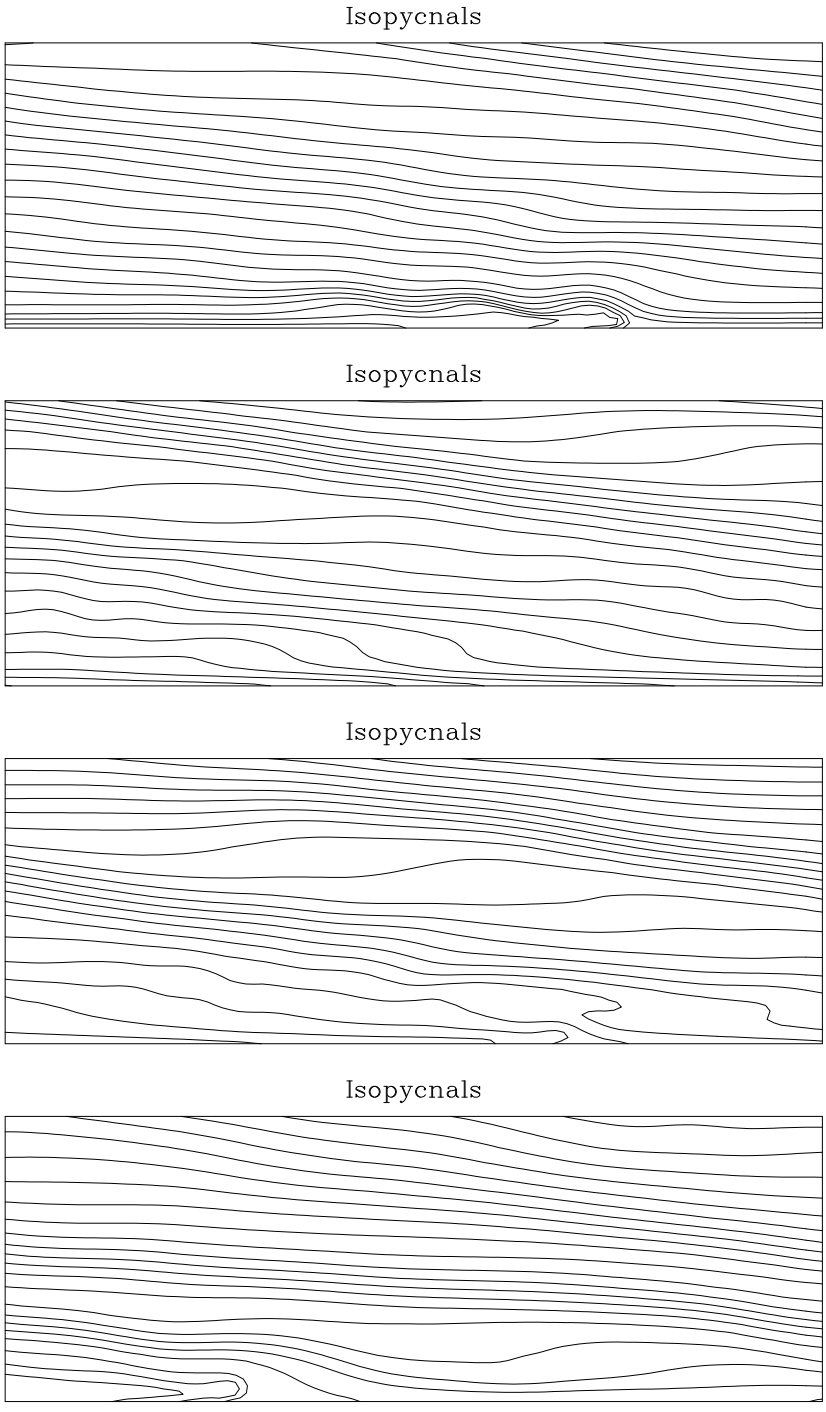

Figure 6.30: Sequence of isopycnals for supercritical reflection over a 5^o slope (Case 32) at $t = 152$ (top), 178, 190, and 215 (bottom).

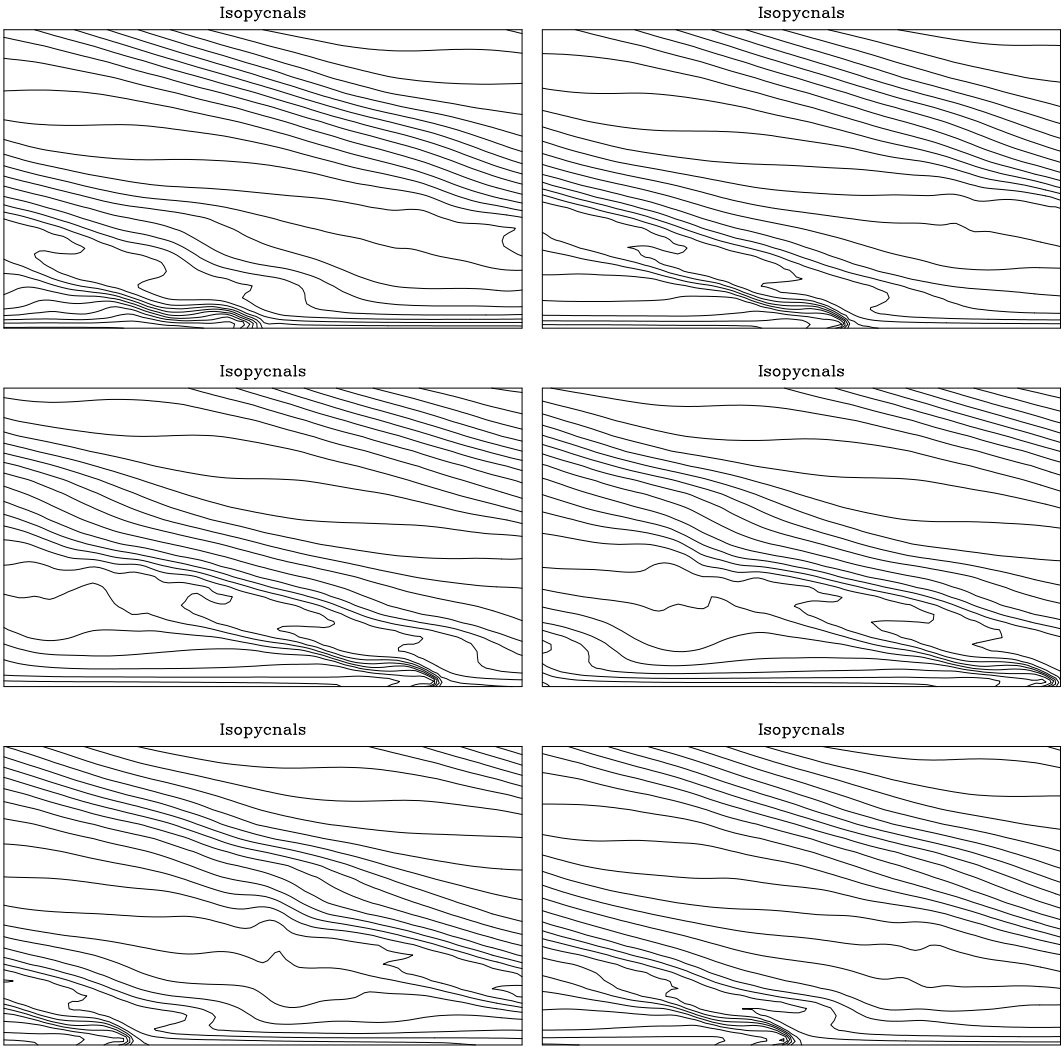

Figure 6.31: Sequence of isopycnals for subcritical reflection over a 13.5^o slope at $t = 98$, 106, 115, 121, 131, and 139, in order: upper left, upper right, middle left, middle right, lower left, lower right.

Figure 6.31 shows the flow development for Case 43 ($Re = 2120$, $\alpha = 13.5^o$) at times 98, 106, 115, 121, 131, and 139, in order: upper left, upper right, middle left, middle right, lower left, lower right. The flow that develops is remarkably different from sequences seen previously. While both the simulations 5^o and 13.5^o are both 4.25^o from the critical angle, the flows that develop (for similar Reynolds and Richardson numbers) are qualitatively different. The flow that develops for the steeper slope is quasi-steady, with a thermal front moving upslope that has a region of wave overturning and breakdown traveling above and behind the thermal front.

Eriksen (1985) theorizes that a difference in character for subcritical and supercritical reflection should exist, suggesting that reflected waves interact with the oncoming waves in different manners, leading to different mixing characteristics. He calls supercritical reflection (e.g., 5^o) transmissive and subcritical reflection (e.g., 13.5^o) reflective. A difference is observed in the numerical simulations and indicates that, in the supercritical case, the reflected waves pass through the oncoming waves in a constructive fashion. In the subcritical case, the reflected waves interfere with the oncoming waves in a more destructive fashion (leading to turbulent mixing). The essential difference is that the oncoming and reflected waves are out of phase with one another, causing wave breakdown to be facilitated. A fuller explanation for the differences is still under investigation.

In summary, it was found that off-critical angle reflection is a complicated process, and this angle is an additional parameter that governs flow development. The angle of the bottom slope influences wave reflection by lengthening the mixing cycle for cases with shallower slopes and shortening the mixing cycle for those with steeper slopes. Wave reflection and breakdown develop in a very similar manner to the critical-angle situation for both subcritical and supercritical waves close to the critical angle. For cases farther from the critical angle, there is an asymmetry to the flow development. Subcritical reflection experiences increased dissipation rates to heat and mixing, while supercritical reflection has a higher component of radiation of energy away from the boundary.

6.7 Comparison with Linear Theory

This study has focused on large amplitude waves with nonlinear behavior. In this section results from linear (inviscid) theory and small amplitude simulations are presented for comparison with the nonlinear simulations. The main point is to determine if some of the major flow features observed in the nonlinear simulations are contained in the results of linear theory.

Figure 6.32 shows isopycnals of three wave fields for a bottom slope of 15^o and an angle of wave propagation of 30^o with respect to the horizontal. The amplification factor, A_r/A_i, for this case is 2.7, and the ratio of the vertical wavelengths, $\lambda_{zi}/\lambda_{zr}$, in the rotated reference frame is 3.7. Figure 6.32 shows the region from the boundary to a height of 0.57 λ_{zi} (or 2.1 λ_{zr}) of a specified oncoming wave (top) with amplitude $A/A_o = 0.1$. The corresponding reflected wave (predicted by linear inviscid theory) is shown in the middle panel of Figure 6.32, and the sum of the oncoming and reflected waves is pictured in the bottom panel. The structure of the summation of the waves is dominated by the reflected wave. The reflected wave has a large amplitude surpassing overturning, which results from the combination of increased amplitude and decreased wavelength. Near the boundary there is a region where the isopycnals are perpendicular to the boundary, similar to the structure of the thermal front observed in the nonlinear simulations. The region of highest density gradient is called the steepening point of the wave, and it is here that the thermal front develops in the simulations. Figure 6.33 shows velocity vectors of the oncoming, reflected, and superposition of waves in corresponding panels. Again, the reflected wave dominates the velocity field shown in the bottom panel.

In the numerical simulations, because of strong viscous losses of wave energy in the boundary layer, reflected wave amplitudes are not so large as predicted by linear theory. Figure 6.34 presents a modification to linear reflection theory to include viscous losses. Here, the oncoming wave is presented as before (with $A/A_o = 0.2$), but the amplitude of the reflected wave is decreased in an *ad hoc* fashion to mimic losses of energy by viscous dissipation. In this example, the reflected wave amplitude

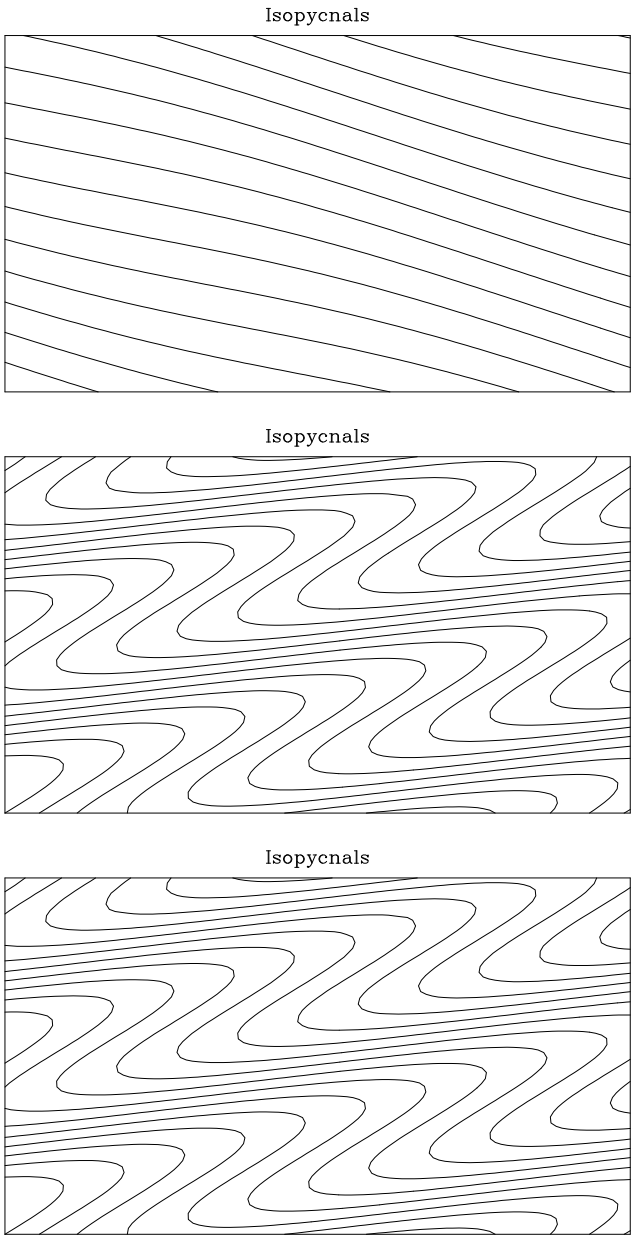

Figure 6.32: Predictions from linear theory for the density fields for oncoming wave (top), reflected wave (middle), and the sum of the two waves (bottom). The bottom slope is 15^o, and the oncoming wave travels at an angle of 30^o to the horizontal.

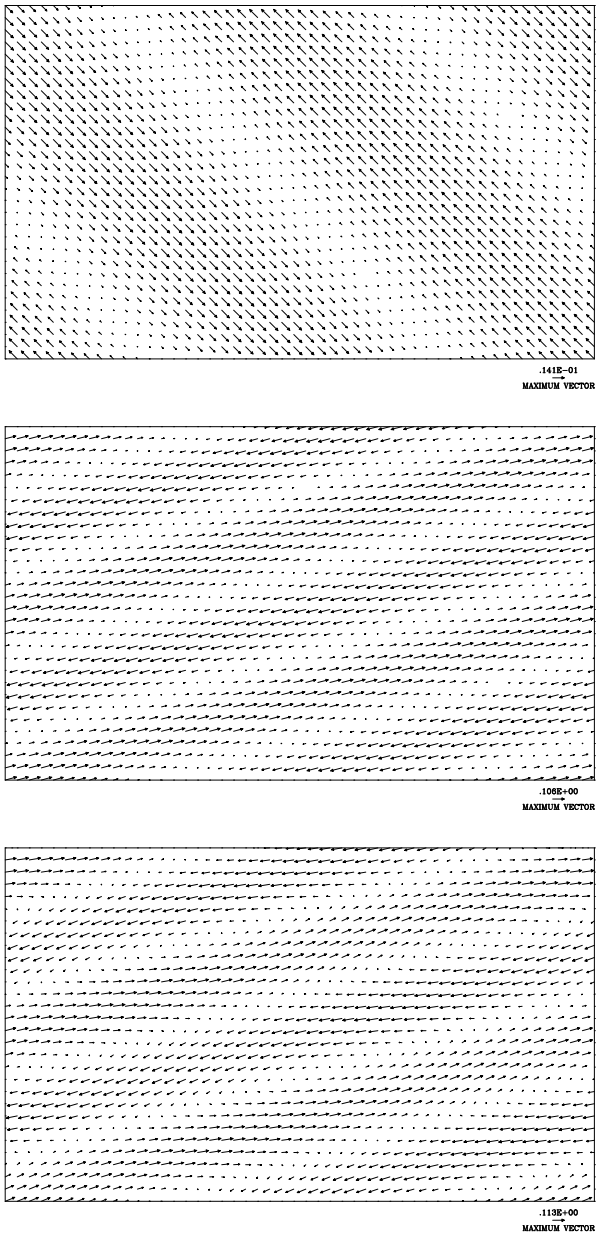

Figure 6.33: Predictions from linear theory for the velocity fields for oncoming wave (top), reflected wave, and the sum of the two waves (bottom). The bottom slope is 15^o and the oncoming wave travels at an angle of 30^o to the horizontal.

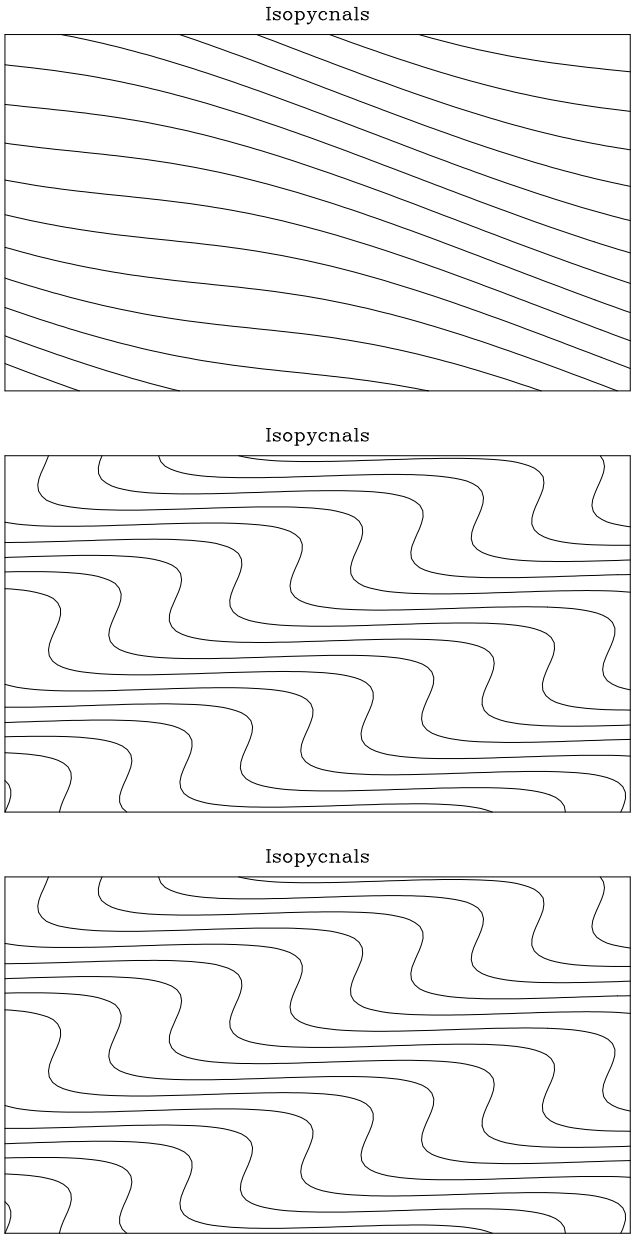

Figure 6.34: Predictions from linear theory with viscous losses for the density fields for oncoming wave (top), modified reflected wave, and the sum of the two waves (bottom). The bottom slope is 15^o, and the oncoming wave travels at an angle of 30^o to the horizontal.

is scaled down by a factor of four (reflected wavelengths are not changed). As a result, the oncoming and reflected waves have comparable amplitude. Again, the most notable near-wall feature is the steepening point, which resembles the thermal front.

Figure 6.35 shows the corresponding velocity vectors (from linear theory with dissipation) for the oncoming (top), modified reflected, and sum of the two waves (bottom). Here, the interesting result is the circulation zones that occur from the superposition of the oncoming and reflected waves. In the near wall regions the flow resembles regions of convergence and divergence observed in the nonlinear simulations. Farther away from the wall, the regions of circulation are similar to those seen in some of the off-critical angle simulations (for cases when significant energy reflects from the boundary).

Another topic related to linear wave reflection was explored with a series of two-dimensional simulations using wave packets with amplitude of $A_o/40,000$. These waves, though linear in behavior, are still affected by viscous dissipation in the simulations. It was found that, even for very small amplitude waves, reflection from sloping terrain can be a strong sink of internal wave energy. For cases near critical, small amplitude waves lost approximately the same proportions of their energy as large amplitude waves, indicating that diffusion in the viscous sub-layer is effective in dissipating wave energy (for the Reynolds numbers of the simulations and the resulting long residence time in the viscous boundary layer of near critical waves).

6.8 Comparisons with Two-Dimensional Simulations

Two-dimensional simulations were used extensively during the initial stages of this study to gain familiarity with wave reflection and to test and develop the numerical model. The results from two-dimensional simulations contain many similarities to the three-dimensional flows but also differ in significant aspects. Two-dimensional simulations were especially useful in determining appropriate parameters for which interesting flows might develop. A principle advantage is that two-dimensional simulations utilize less computer resources and can be conducted in significantly less time than

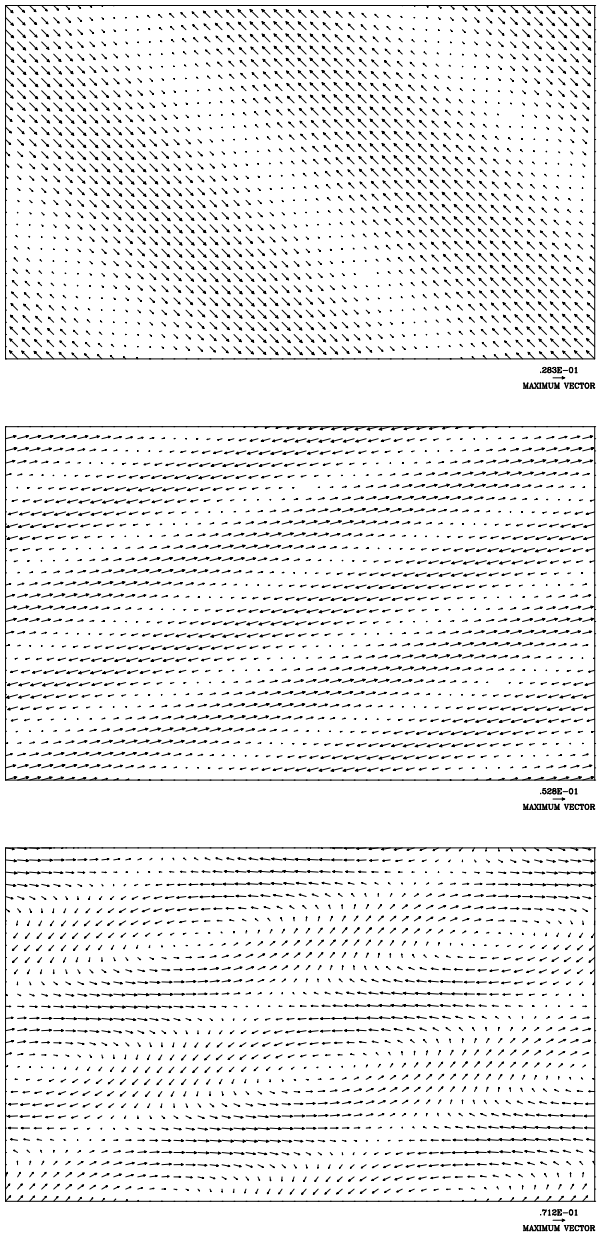

Figure 6.35: Predictions from linear theory for the velocity fields for oncoming wave (top), modified reflected wave, and the sum of the two waves (bottom). The bottom slope is 15^o, and the oncoming wave travels at an angle of 30^o to the horizontal.

three-dimensional simulations. Parallel two-dimensional simulations were conducted for the majority of the cases listed in Table 4.1. For the laminar and transitional simulations, little difference exists between the two- and three-dimensional experiments. For the turbulent simulations, however, important differences develop. Near transition, three-dimensional simulations are required to determine if the flow will develop into turbulence. Two-dimensional simulations, while giving some indication, are not very helpful in predicting transition Reynolds numbers. The two-dimensional simulations tend to overpredict wave amplification and may indicate wave overturning in cases where three-dimensional simulations do not.

In this section results from a pair of two-dimensional critical angle simulations will be compared with parallel three-dimensional simulations (Cases 15 and 28) presented in Chapters 4 and 5. The two-dimensional simulations used grid resolution of 201 x 210 points with the same parameters (Reynolds number, Richardson number, amplitude, etc.) as their three-dimensional counterparts. The presentation begins with a comparison with Case 15, a turbulent simulation with a 9^o bottom slope and Reynolds number of 3600.

Figure 6.36 shows a sequence of isopycnals of the flow at $t = 89.6$ (top), 94, 101, and 108 (bottom). These figures may be compared with Figures 4.19 and 4.10. The flow field at $t = 89.6$ is very similar to that for the three-dimensional simulations, and remains so throughout the period of initial wave overturning until approximately $t = 94$. By the third panel ($t = 101$), however, significant differences have emerged. Regions of overturned density exhibit more complicated interleaving and occupy a greater depth than for the three-dimensional boundary layer case. Observations indicate that the two-dimensional model takes significantly longer to mix the overturned fluid. Statically unstable density arrangements, caused by wave amplification, break down significantly faster in three-dimensions than in two. A similar result has been reported by Winters and Riley (1992) for internal waves that overturn and break down when approaching a critical layer. The periodicity between mixing cycles was found to be approximately equal for the two- and three-dimensional simulations. A difference occurs, however, in the length of time spent performing mixing during the cycle. For

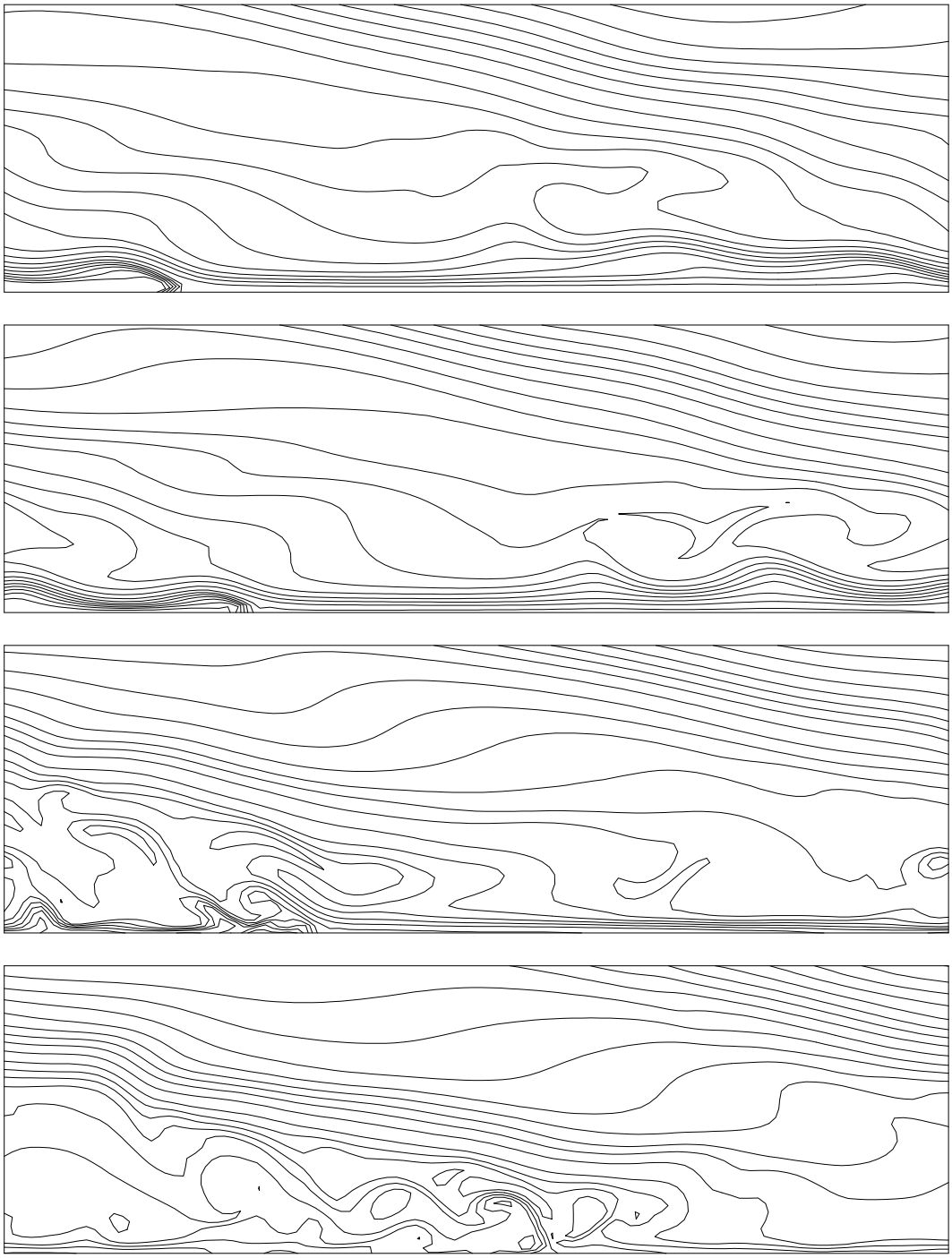

Figure 6.36: Sequence of isopycnals for a two-dimensional simulations of critical reflection over a 9^o slope at $t = 89.6$ (top), 94, 101, and 108 (bottom).

the three-dimensional simulation mixing occurs for approximately one-third of the mixing cycle, while for the two-dimensional simulation mixing takes approximately one-half of the mixing cycle.

Figure 6.37 continues the sequence of isopycnals for the two-dimensional simulation at $t = 117$ (top), 126, 133, and 156 (bottom). The flow continues to resemble the three-dimensional flow pictured in Figure 4.10, with the same two major dissimilarities: increased complexity in the two-dimensional density structure, and an increase in the depth of the boundary layer.

Figure 6.38 shows the velocity vectors corresponding to the density fields pictured in Figure 6.36 at $t = 89.6$ (top), 94, 101, and 108 (bottom). The primary differences between these velocity fields and those pictured in Figures 4.11 and 4.12 occur during the bottom two frames, when mixing is strongest. The velocity vectors in the two-dimensional simulation indicate greater intensities and more complexity in the small scale eddies, because all oncoming wave energy must be dissipated in a two-dimensional plane. The additional degree of freedom available for wave breakdown in three-dimensional simulations permits a more efficient way to dissipate the wave energy, as is characteristic of turbulence.

The mixing efficiency and loss of kinetic energy to heat for the two-dimensional simulation are somewhat different from the three-dimensional results. For the two-dimensional simulation the mixing efficiency is 0.34, compared with 0.32 for the three-dimensional simulation (where all coefficients have accuracy limits of ± 0.02). The losses to heat are 0.50 (2-D) and 0.56 (3-D). The radiation coefficients, representing the buildup of energy in the domain, are 0.16 (2-D) and 0.12 (3-D). These values indicate that the largest net change in the energetics, going from three-dimensions to two, is a decrease in the kinetic energy dissipation rate. This is consistent with the loss of the additional degree of freedom for the fluid motions.

Figure 6.39 shows the volume integrals of kinetic, potential, and total energies, and the time integrated buoyancy flux for the two-dimensional simulation. Its three-dimensional counterpart is Figure 4.27 (page 153). In general, the consistency between the two realizations is quite strong. Differences include that the total energy

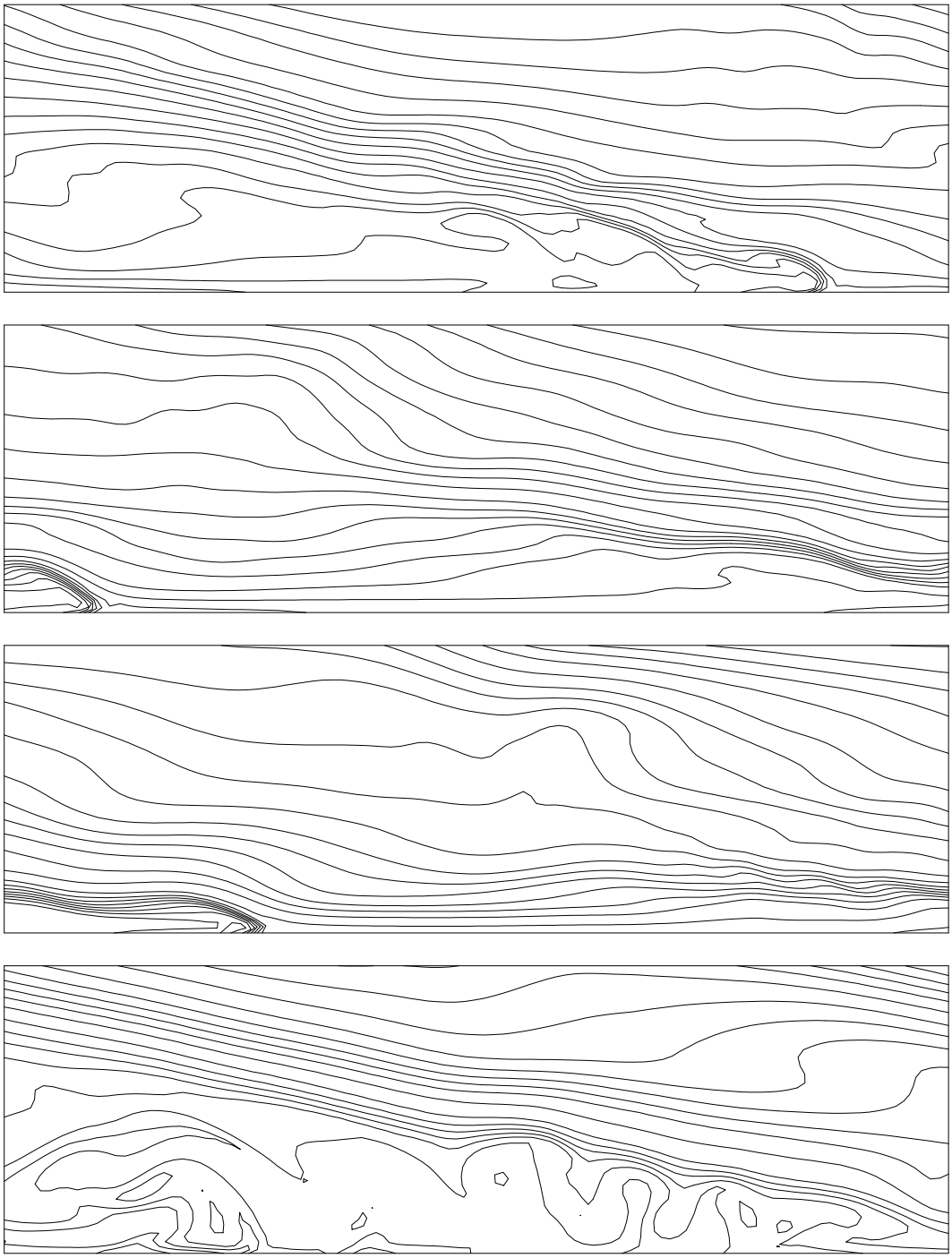

Figure 6.37: Sequence of isopycnals for a two-dimensional simulations of critical reflection over a 9^o slope at $t = 117$ (top), 126, 133, and 156 (bottom).

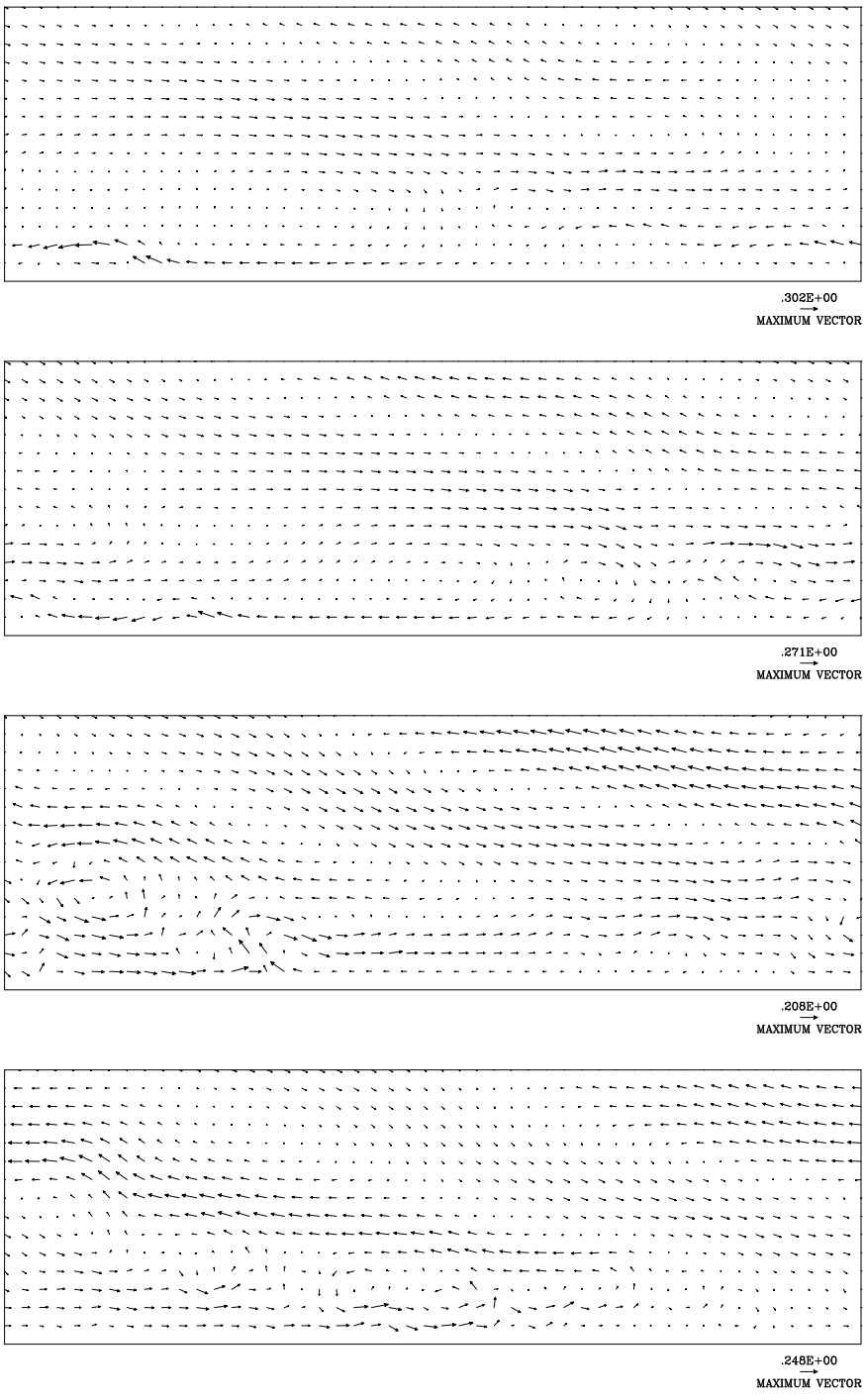

Figure 6.38: Sequence of velocity vectors for a two-dimensional simulations of critical reflection over a 9^o slope at $t = 89.6$ (top), 94, 101, and 108 (bottom).

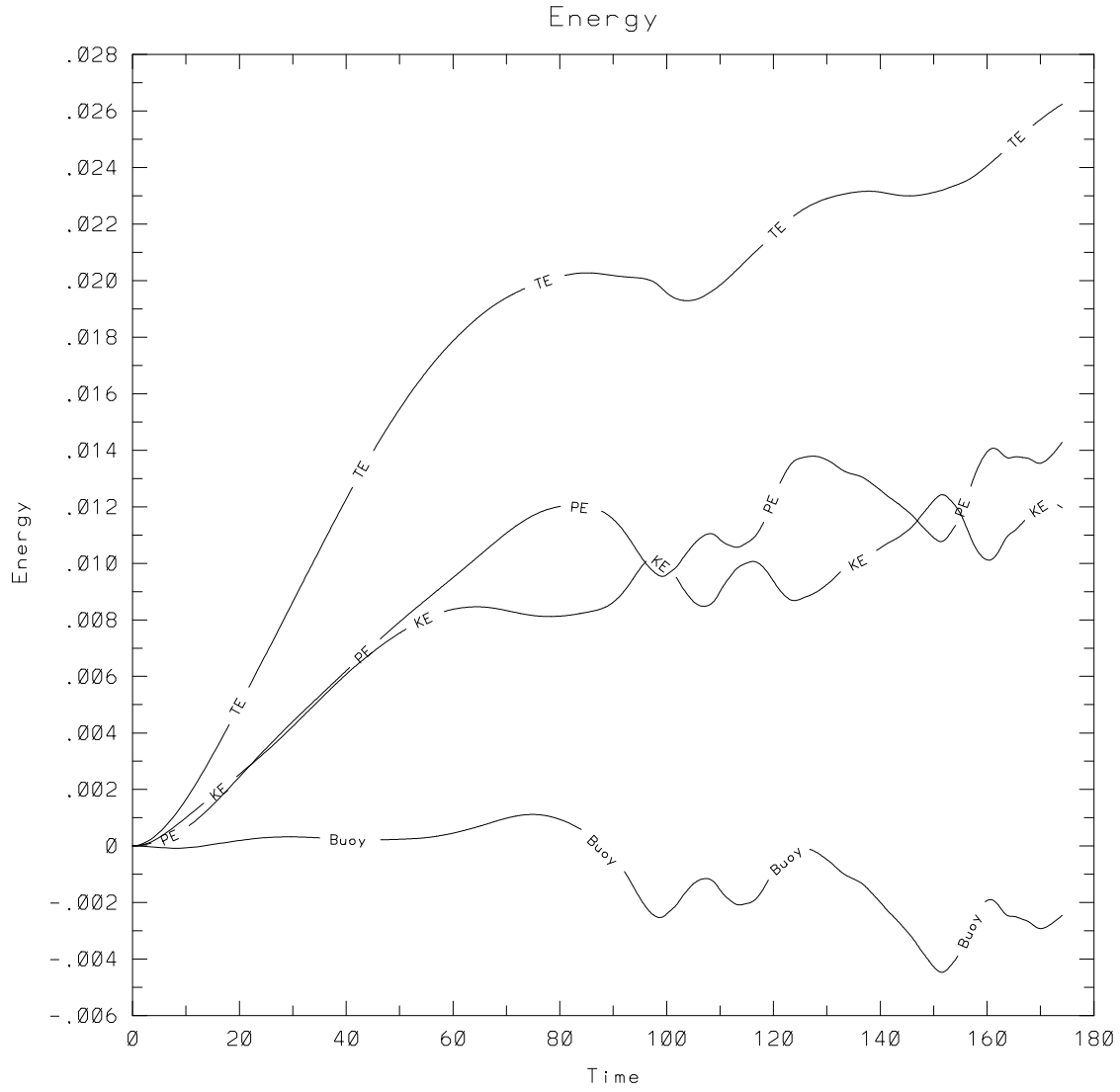

Figure 6.39: The volume integrals of kinetic, potential, and total energies as a function of time for the two-dimensional repetition of Case 15. Also shown is the time integrated buoyancy flux.

in the system grows faster (consistent with the higher radiation coefficient), and that the time-integrated buoyancy flux shows a weaker net accumulation (consistent with the lower heat loss) in the two-dimensional system.

Figure 6.40 shows the terms of the kinetic energy equation for the two-dimensional simulation (compare Figure 4.30, page 158). While the energetics follow similar patterns, the amplitudes of the buoyancy fluxes, the rate of change of kinetic energy, and the dissipation rates are significantly different. The largest difference appears to be in the amplitude of the oscillations of the buoyancy fluxes. Note, for example, that for $125 < t < 155$ (a period of strong mixing) the buoyancy flux in the two-dimensional simulation is continuously positive, while the three-dimensional simulation shows a shorter period of positive buoyancy flux. This is indicative that mixing takes longer to complete in the two-dimensional simulation.

Figure 6.41 shows the terms of the total energy equation for the two-dimensional simulation (compare Figure 4.32, page 162). The results are similar, with the major difference being that the time rate of change of total energy is more positive in the two-dimensional case. Comparing the cases, the total dissipation rates are very similar, going through parallel mixing cycles. In many ways, therefore, the two-dimensional model appropriately represents bulk characteristics of the flow.

For the two cases, Figure 6.42 compares boundary layer thickness, δ, with δ defined using the criteria of the depth and frequency of overturned density profiles. The three-dimensional simulation has a boundary layer thickness of $\delta = 0.32\lambda_z$. The two-dimensional simulation differs in two significant aspects. First, it shows overturns occurring up to a height of $\delta = 0.7\lambda_z$, or about twice the height of the three-dimensional boundary layer. Second, the region $0.1 < z < 0.2$ shows significantly more frequent overturned fluid. This is representative of the longer portion of the mixing cycle spent doing mixing and the increased amount of time that it takes in two-dimensions for unstable density profiles to begin to breakdown.

Figure 6.43 shows a sequence of isopycnals for a two-dimensional simulation of critical angle reflection over a 30^o slope at $t = 86$ (top), 99, 109, and 126 (bottom). Comparable figures for the three-dimensional simulation (Case 28) are shown

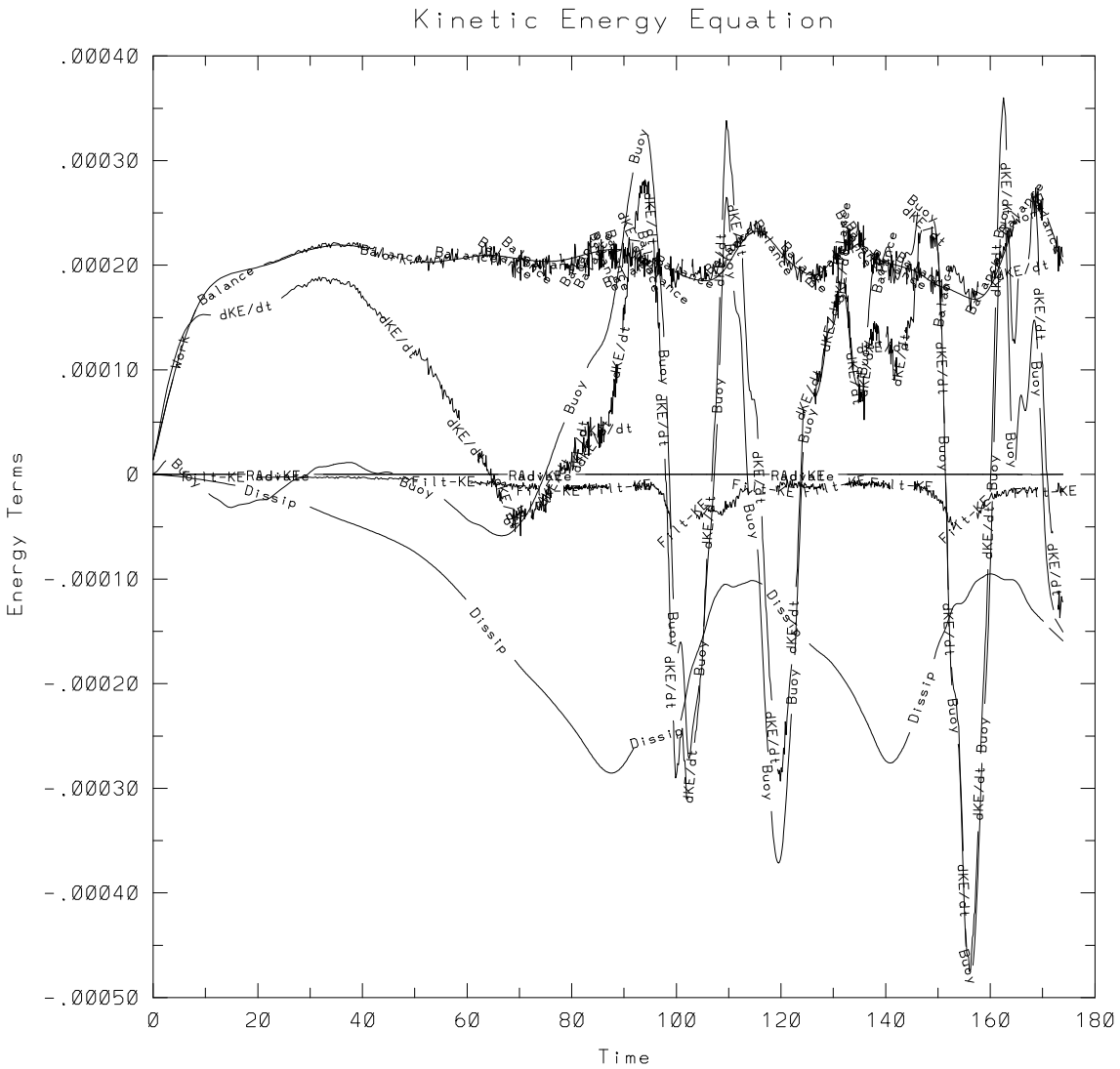

Figure 6.40: Terms of the kinetic energy equation as a function of time for the two-dimensional repetition of Case 15.

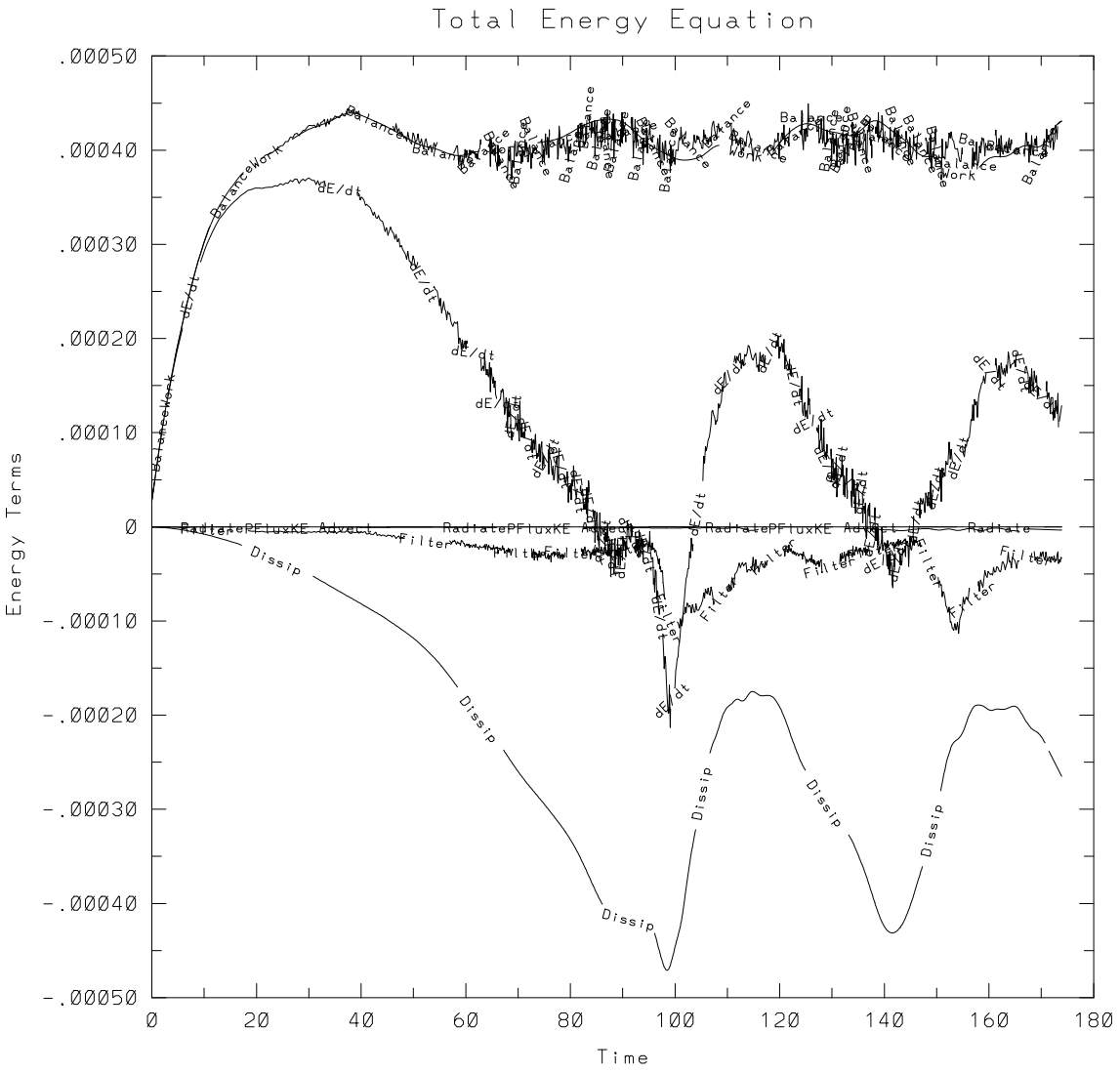

Figure 6.41: Terms of the total energy equation as a function of time for the two-dimensional repetition of Case 15.

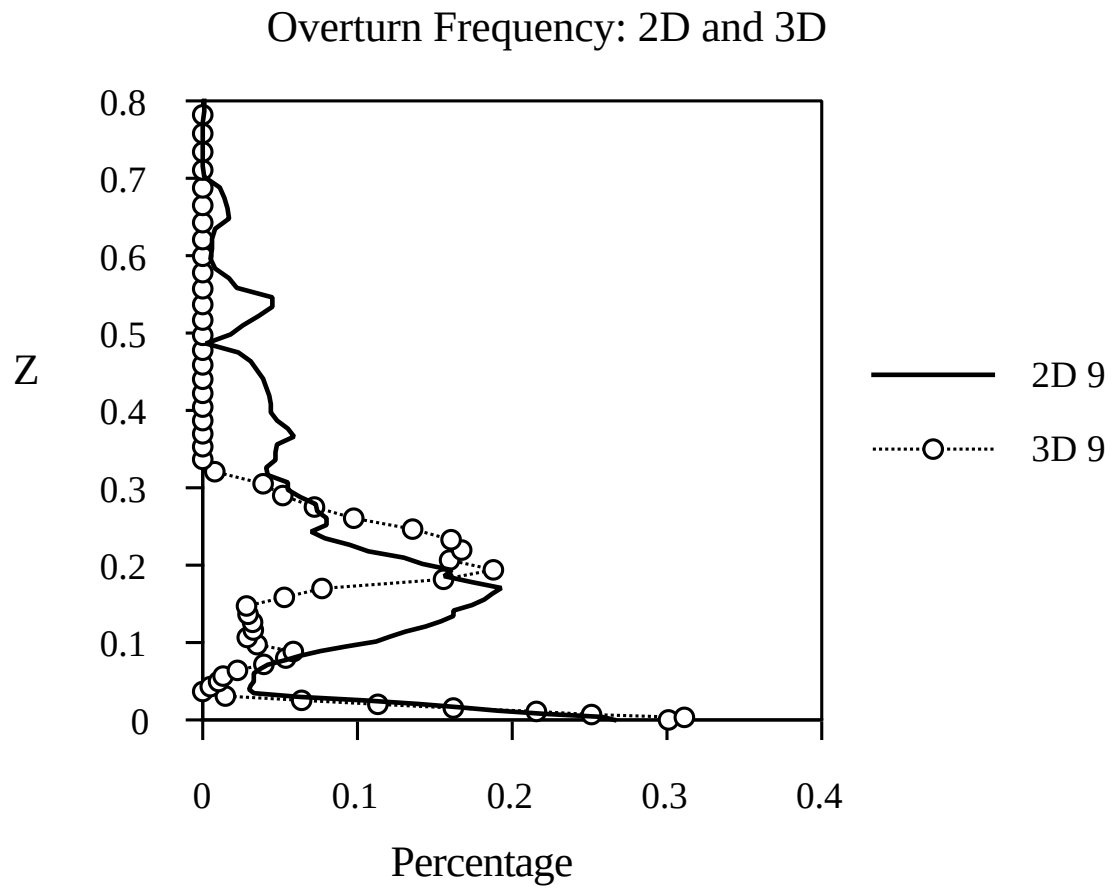

Figure 6.42: Comparison of the boundary layer thickness δ, as determined by the depth and frequency of overturned regions of fluid, for two- and three-dimensional critical angle simulations with $Re = 3600$ and $\alpha = 9.2^o$.

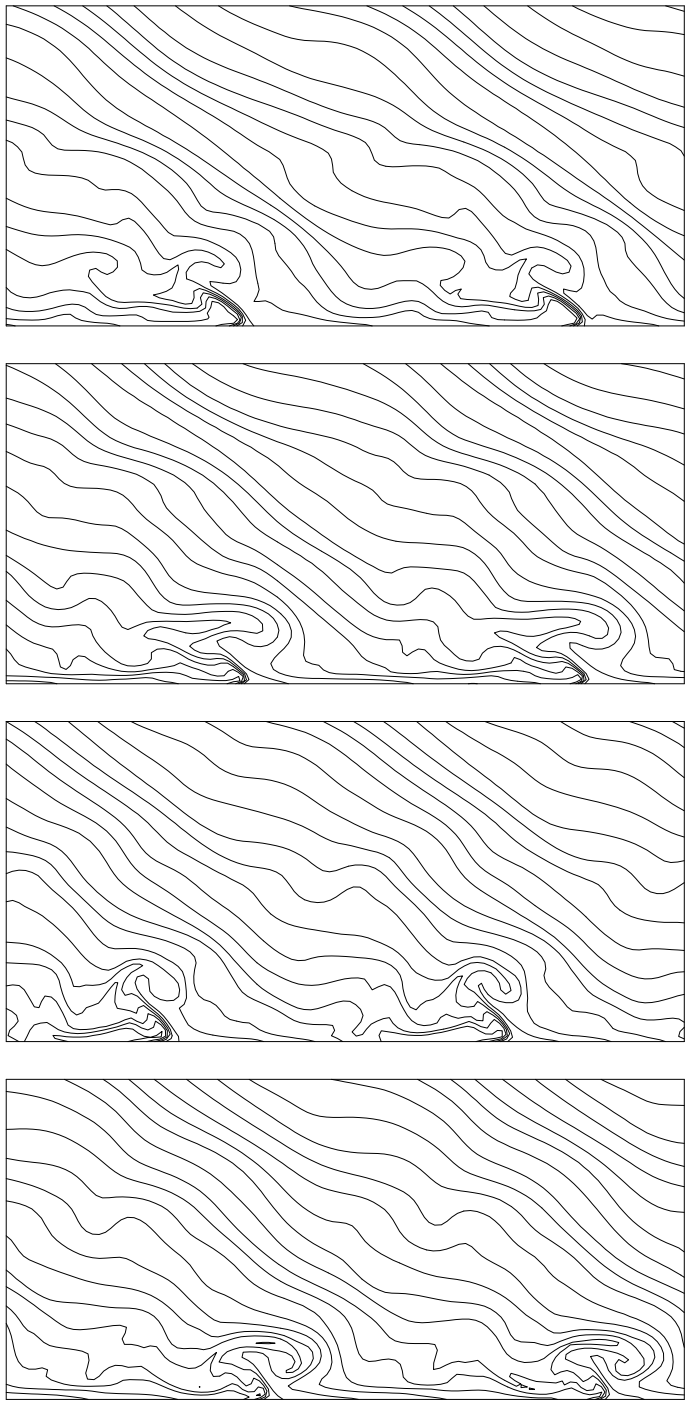

Figure 6.43: Sequence of isopycnals for a two-dimensional simulations of critical angle reflection over a 30^o slope at $t = 86$ (top), 99, 109, and 126 (bottom).

in Figures 5.4 and 5.5 (pages 186 and 187). The overall appearances of the flow development is quite similar, showing the quasi-steady nature of the bore that develops. Figure 6.44 shows corresponding velocity vectors (compare Figure 5.6). The mixing region near the wall has stronger currents in the two-dimensional realization. In addition, the variations from the structure of the oncoming gravity waves are greater and extend farther from the boundary.

Figure 6.45 shows the volume-integrated kinetic, potential, and total energies, and may be compared with Figure 4.28 (page 155). Both the two-dimensional and three-dimensional simulations for a 30^o slope show a comparative leveling off of the total energy compared with the 9^o slope. The mixing efficiency for the two-dimensional simulation is 0.42 compared with 0.37 for the three-dimensional simulation. The losses of wave energy to heat are 0.55 (2-D) and 0.61 (3-D). Each of these realizations leaves little energy to accumulate in the flows. The radiation coefficients are 0.03 (2-D) and 0.02 (3-D). The largest differences between the two- and three-dimensional realizations are the magnitudes of the fluctuations in kinetic and potential energy. In addition, the decrease in the heat coefficient manifests itself as a smaller net buoyancy flux for the two-dimensional case.

The terms in the kinetic and total energy equations are plotted in Figures 6.46 and 6.47 (compare Figures 5.10 and 5.11, pages 196 and 197). As seen for the 9^o case, the amplitude of the buoyancy flux oscillations are significantly larger in the two-dimensional simulation. This simulation was initialized without white noise in the boundary layer, causing the initial period to develop somewhat differently. After the first mixing cycle, however, the simulations continue with parallel development. The total energy equations are similar, with the variations attributed to differences in the specific structures that develop in the "turbulent" bore.

Figure 6.48 shows density contours in the near-wall region $z < \lambda_z$ at a fixed (x, y) location from $0 < t < 127$ for the two-dimensional simulation (compare Figure 5.7, page 191). The flat contours at the left-hand side of Figure 6.48 indicate the density field before appearance of the oncoming waves at the location of measurement. The bore passes through the location of the measurements nine times during the simula-

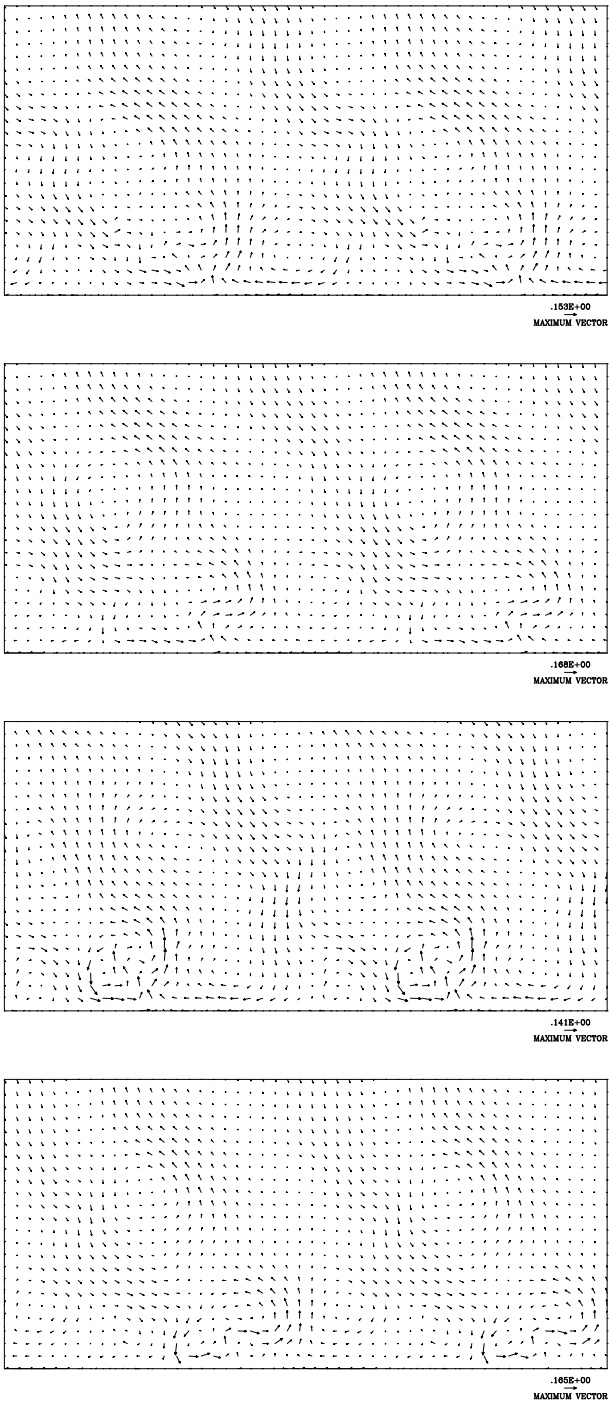

Figure 6.44: Velocity vectors for a two-dimensional simulations of critical angle reflection over a 30^o slope at $t = 86$ (top), 99, 109, and 126 (bottom).

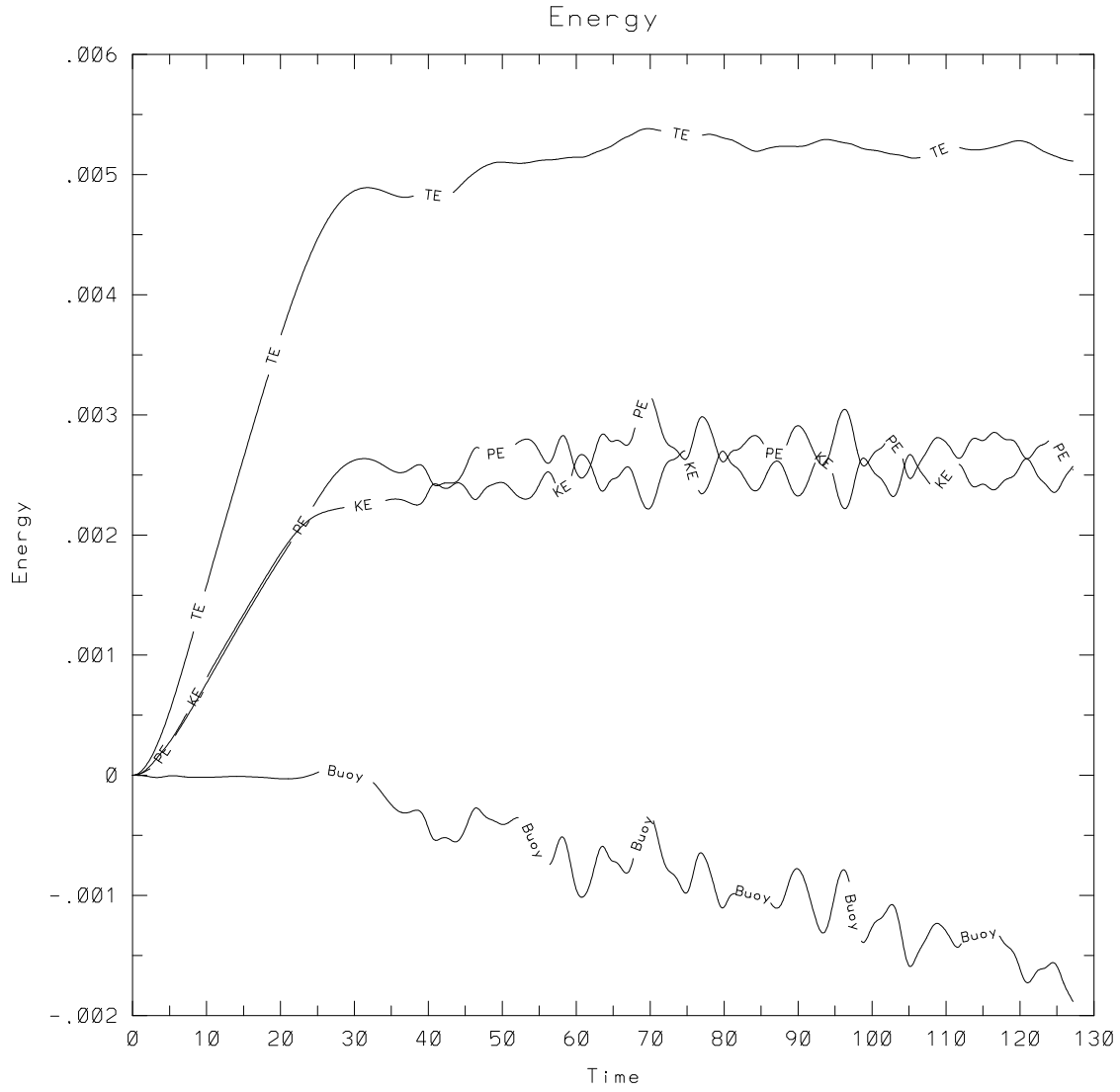

Figure 6.45: The volume integrals of kinetic, potential, and total energies as a function of time for the two-dimensional repetition of Case 28. Also shown is the time integrated buoyancy flux.

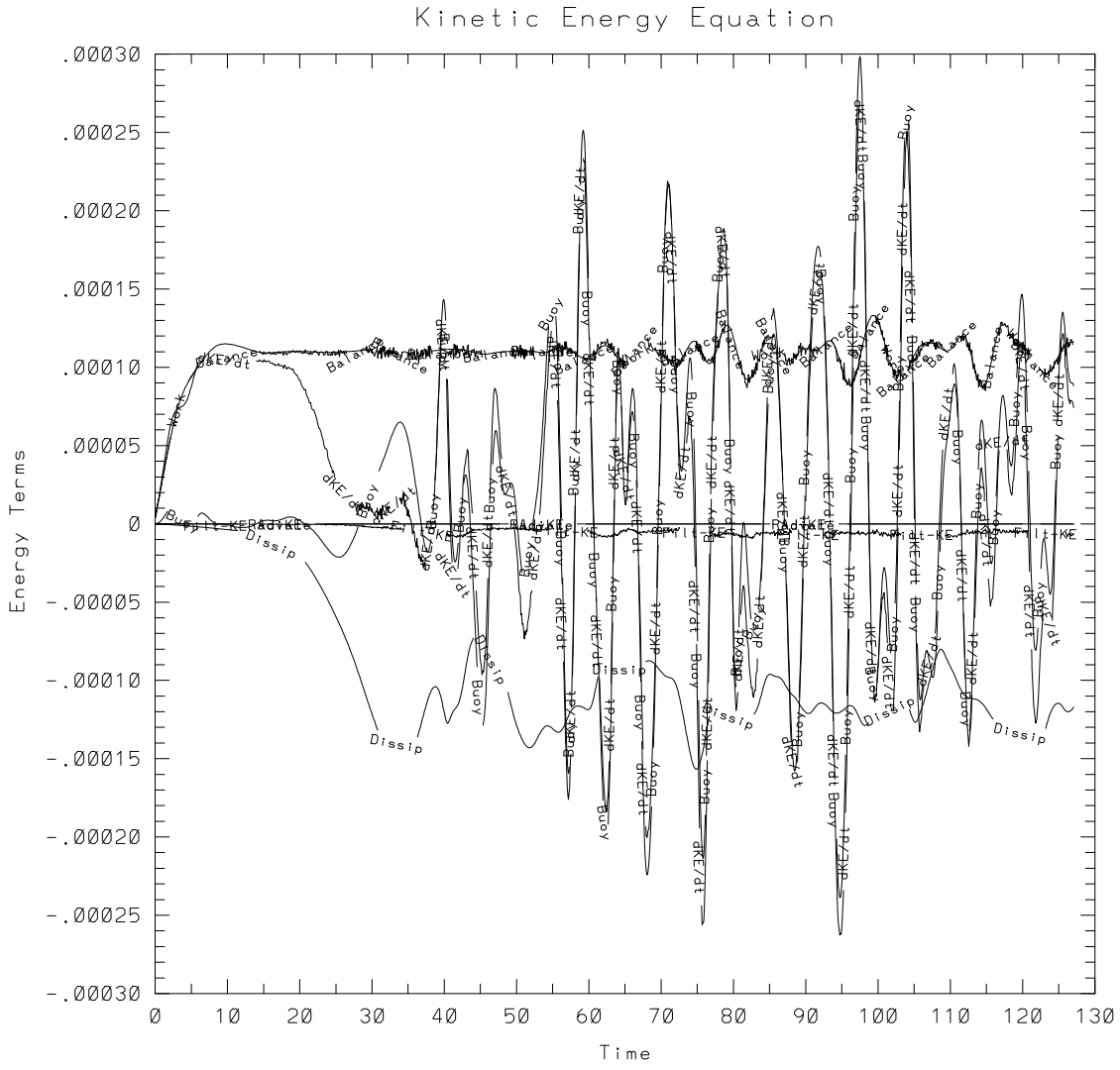

Figure 6.46: Terms of the kinetic energy equation as a function of time for the two-dimensional repetition of Case 28.

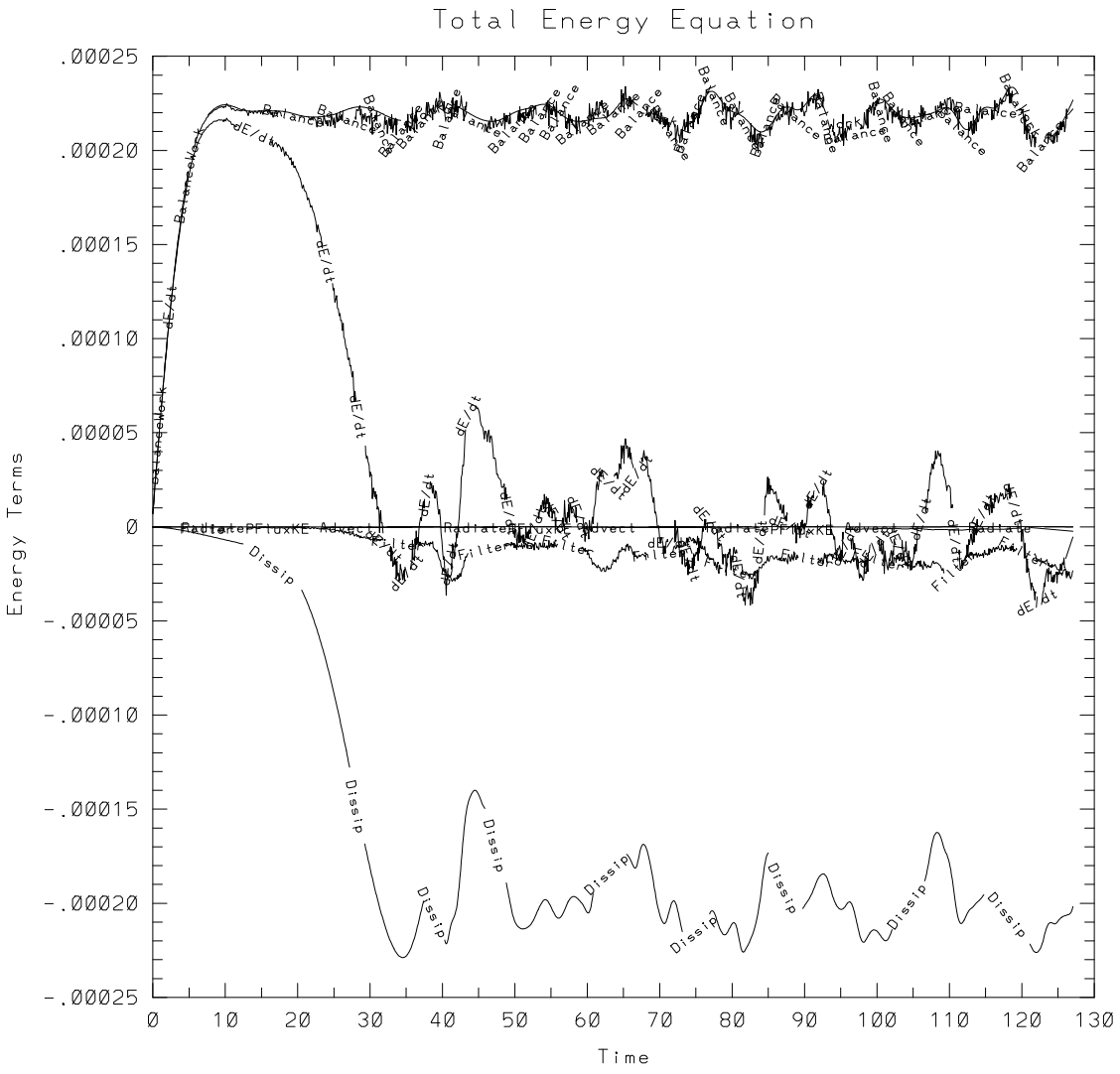

Figure 6.47: Terms of the total energy equation as a function of time for the two-dimensional repetition of Case 28.

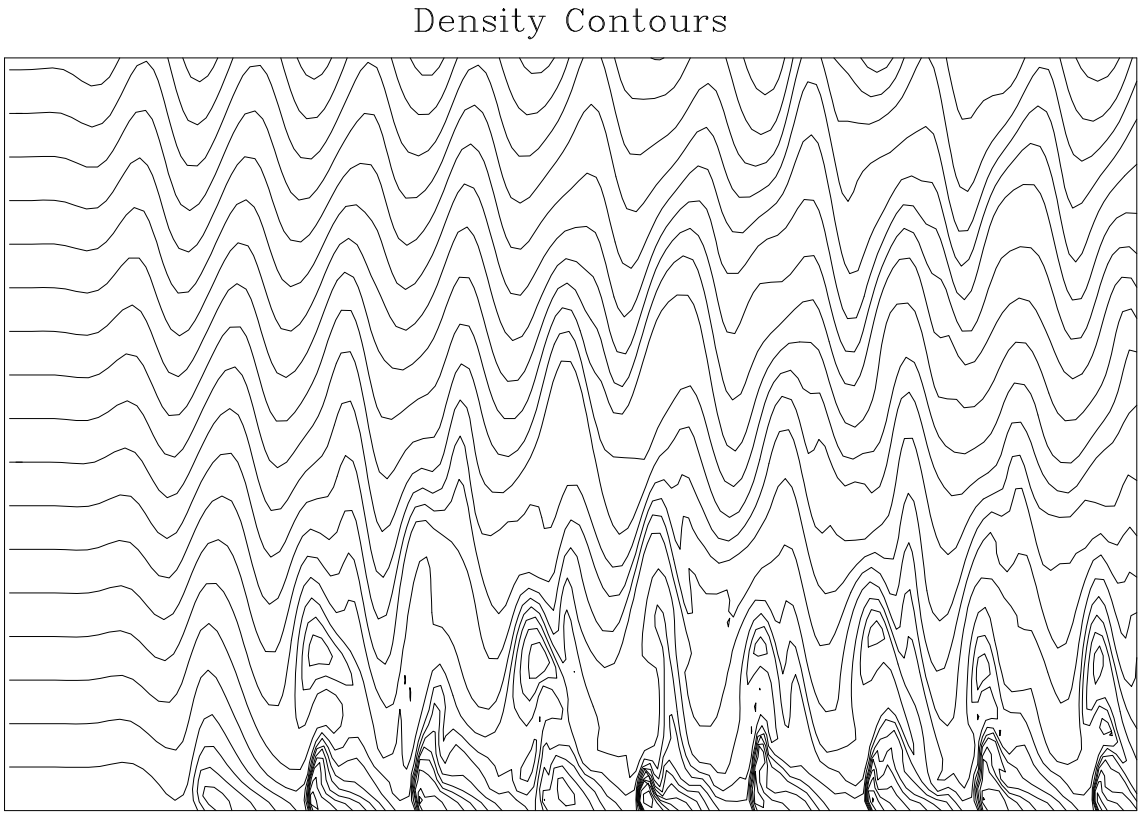

Figure 6.48: Density contours in the near wall region $z < \lambda_z$ at a fixed location as a function of time for the two-dimensional simulation with a 30^o slope and $Re = 1700$.

tion. Generally the structures are very similar to the three-dimensional observations, but the overturned regions in the two-dimensional case appear to occupy a larger portion of time.

Figure 6.49 confirms this observation by comparing the frequency of overturned regions between the cases. For the 30^o slope simulations the boundary layer thicknesses are approximately equal. The frequency of density inversions within the boundary, however, differ significantly. At a depth of $0.1 < z < 0.2$ the two-dimensional simulation has overturned fluid in the boundary layer approximately 25% of the time, while the three-dimensional simulation has similar density inversions only 10-15% of the time.

In summary, two-dimensional simulations are similar to three-dimensional simulations in predicting the times and general features of wave breakdown. They differ significantly, however, in the details of wave breakdown and mixing. Important features such as boundary layer thickness, loss of energy to heat, radiation of energy from the boundary, time required for waves to break down, and strengths of the currents in the boundary layer require three-dimensional modeling to make accurate predictions for turbulent flows. The two-dimensional models were used primarily in this study to aid in model development and in finding appropriate parameter ranges for the three-dimensional simulations.

A potentially valuable use for two-dimensional models is for testing various mixing models and turbulence closure schemes against three-dimensional direct numerical simulations. Two-dimensional simulations including mixing models could be validated based upon their abilities to produce results similar to three-dimensional simulations for features such as boundary layer thickness and current speeds. Comparisons of simple and complex closure models for stratified turbulence for this problem have not yet been attempted, but authors such as Kunze et al. (1990) and Wijesekera et al. (1993) have begun to examine theoretical models that could be tested for moderate Reynolds number. Validation of the mixing models could aid in their becoming more frequently included in large scale ocean models that require parameterization of small-scale mixing.

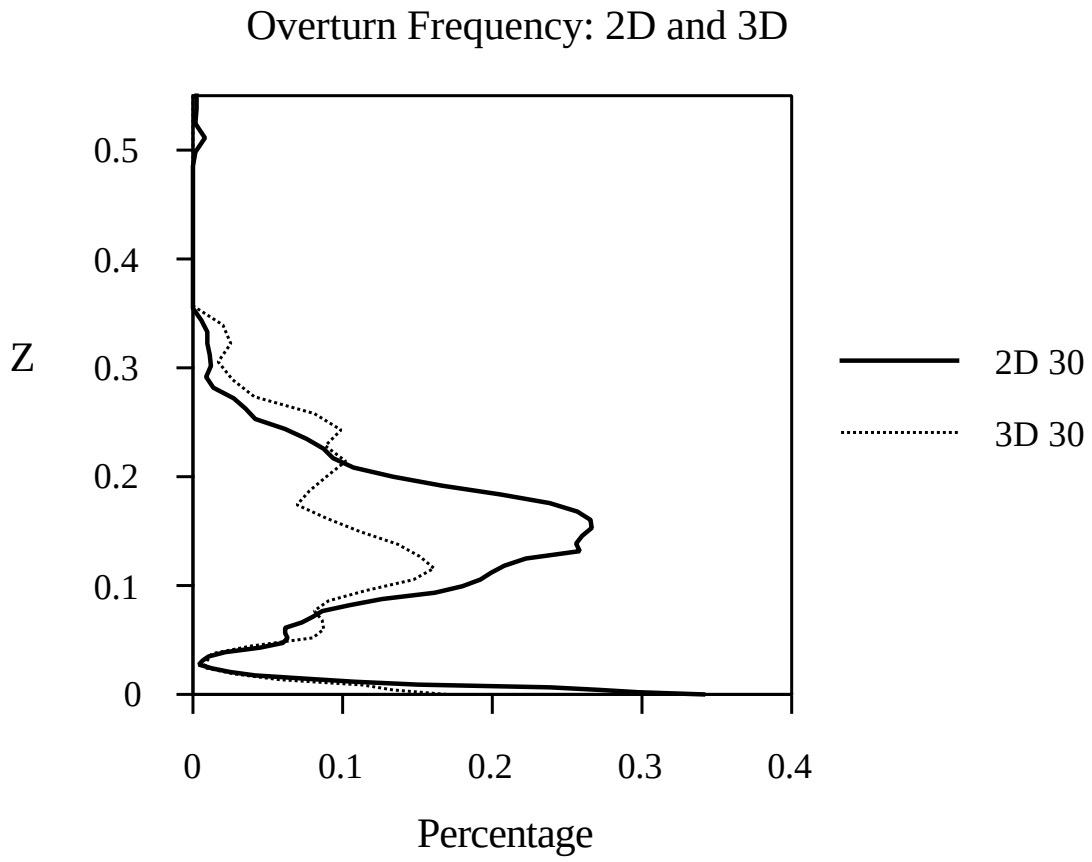

Figure 6.49: Comparison of the boundary layer thickness δ as determined by the depth and frequency of overturned regions of fluid for two- and three-dimensional critical angle simulations with $Re = 1700$ and $\alpha = 30^o$.

6.9 Summary

This chapter has covered eight specialized topics: (1) effects of varying wave amplitude, (2) exchange of fluid between the mixed layer and the stratified fluid, (3) transport of fluid particles, (4) flow development for a free-slip wall, (5) wall shear stresses, (6) off-critical angle simulations, (7) comparison of simulations to linear theory, and (8) two-dimensional simulation results. The primary conclusions from the examinations in this chapter are summarized here.

It was found that varying the wave amplitude changes the boundary layer thickness and the intensity of the turbulence but has less influence on the mixing period or overall mixing efficiency. Also, it was found that the mixing process extends into the interior stratified fluid and is not restricted to a well-mixed boundary region. A key process in this interior communication is the participation of the internal wave field. The oncoming internal wave acts to pump boundary-mixed fluid into the interior and stratified fluid into the boundary layer. After the mixed fluid is communicated into the stratified regions, the fluid is transported further into the interior, along constant density surfaces. Particle and dye studies aided in visualization and tracking of net fluid motions and indicated that there is significant vertical transport of fluid.

Experiments with a free-slip boundary provided increased understanding of Reynolds number effects in the simulations. Viscous damping of internal wave energy in the near-wall region acts to decrease the mixing efficiency of wave breakdown. Examinations of wall shear stress, caused by internal wave reflection, have indicated shear rates approximately two orders of magnitude higher than contained in the oncoming waves. The related strong shear stresses may be instrumental, e.g., in the resuspension of bottom sediment.

Wave reflection away from the critical angle was also examined. It was found that, close to critical conditions, the flow behaves similar to its behavior at the critical angle, with similar mixing efficiencies and boundary layer thicknesses. It was also determined that off-critical reflection lengthens the mixing cycle for shallower slopes and shortens it for steeper slopes. Reflection away from the critical angle develops

in different manners. Waves reflecting from slopes steeper than their critical angle exhibit increased dissipation rates to heat and mixing, while waves reflecting from shallower slopes experience higher radiation of energy.

Comparisons of three-dimensional simulations to predictions from linear (inviscid) theory have aided in determining that the thermal front observed in the simulations is characteristic of linear wave reflection. The thermal front occurs at the steepening point of the wave and travels upslope at the wave's phase speed.

Finally, two-dimensional simulations were presented to illustrate that wave breakdown has important three-dimensional features. The two-dimensional simulations predict many features of the three-dimensional flow. The oncoming wave is the driving force for the flow and is two-dimensional, as is the thermal front that develops in the boundary layer. Similarities are especially strong for the lower Reynolds number simulations. The two-dimensional model, however, does not predict important flow features such as the boundary layer thickness and the length of time required for overturned waves to break for the more turbulent flows.

Chapter 7

CONCLUSIONS AND RECOMMENDATIONS

7.1 Conclusions

We have examined strong fluid-boundary interactions that occur when internal waves reflect from a slope. The turbulent boundary layer that develops from wave breakdown has been suggested as a major contributor to vertical mixing in the ocean. The process has been investigated using numerical simulations and linear theory. The model problem has led to insights into the physics of the related oceanographic flow.

Several aspects of the internal wave reflection problem have been addressed. Of fundamental interest has been the transition of the incident waves to turbulence and, in particular, the types of instabilities present and how the waves break down. The resulting turbulence has also been examined, especially in terms of its mixing efficiency and resulting changes to the environment. The effect of a number of important parameters have been investigated, including the bottom slope, wave amplitude, Reynolds number, Richardson number, and Prandtl number. The behavior of oncoming waves when the angle of incidence is near to the critical angle has been the main emphasis. Linear theory is not valid in this range, and recent laboratory studies have focused on different types of internal waves and reflection from relatively steep slopes. The primary results of the thesis are reviewed below.

In this study numerical simulations have been successfully developed that accurately capture the fundamental physics of internal wave reflection from sloping boundaries. The development of an accurate and efficient numerical model, using state-of-the-art numerics not commonly used in geophysical simulations, has been one of the key accomplishments of the project. The model is based upon the Navier-Stokes equations for a stratified incompressible flow using the Boussinesq approximation. The model incorporates variable time stepping, using a third-order Adams-Bashforth

scheme, together with compact spatial differencing, a new method developed in the aerospace engineering community and which, to date, has been used primarily in compressible flow models.

A new wave-forcing mechanism has been developed, which sends a continuous, monochromatic internal wave of specified wavelength and frequency in a desired direction of propagation. Its usefulness should prove much broader than to just the current problem. Additional numerical features, such as a clustered grid to resolve the boundary layer adequately and the use of the pressure projection method, make this a robust and attractive boundary layer model. Over 40 high-resolution three-dimensional numerical experiments have been conducted to explore several aspects of the wave reflection problem.

Internal wave reflection from critically sloping topography is a strong sink of internal wave energy. For a broad range of experiments (covering many wave amplitudes, bottom slopes, and Reynolds numbers) 80-100% of the oncoming wave energy is dissipated to heat and in mixing of the background density profile. Oncoming waves transition into locally turbulent regions for Reynolds numbers of about 500 for slopes of 30^o, and about 1500 for slopes of about 5^o.

The results are in qualitative and approximate quantitative agreement with related laboratory studies, and show similar development for features such as boundary layer current velocities, flow dynamics, and transition Reynolds numbers. Boundary layer profiles for these simulations have shown that δ, the boundary layer thickness, has a maximum value of approximately $\lambda_z/2$ for large amplitude oncoming waves. The boundary layer thickness was shown to be nearly a linear function of wave amplitude.

The simulations have shown that the flow behavior and the nature of the turbulence that develop over shallow slopes differ from those for steep slopes. For the steep slope case (30^o) the flow may be characterized as a turbulent bore, which moves upslope at the phase speed of the oncoming wave. It produces almost continuous, localized mixing that restratifies behind the bore because the turbulence generated during one wave period does not have time to decay before the next mixing cycle begins. For the shallower slopes (3^o - 20^o) the turbulence is intermittent and occurs

across the breadth of the boundary layer.

The boundary layer goes through a mixing cycle approximately once in 1.0 - 1.5 wave periods, where the duration of the cycle is also a function of the bottom slope, increasing as the slope decreases. Between mixing cycles, the boundary layer relaminarizes, restratifies, and sets up a flow field whose most defining feature is a thermal front, which moves upslope at the x-component of the phase speed of the oncoming wave. The observed restratification of the boundary layer by buoyancy forces is key to the participation of boundary mixing in contributing to continuous diapycnal mixing in the ocean.

It was found that varying the wave amplitude changes the intensity of the turbulence but does not change the mixing period or overall mixing efficiency. Wave amplification in the turbulent boundary layer causes strong wall-shear stresses to develop, with approximately two orders of magnitude higher shear rates than contained in the oncoming waves. These strong shear stresses, combined with strong local upwelling flow features near the boundary, may be important in the resuspension of bottom sediment.

The energetics of the flow have shown that there is a net negative buoyancy flux for most of the simulations, transferring wave potential energy to kinetic energy, possibly to be dissipated as heat, especially in the viscous dominated region near the wall. Another prominent feature of the energetics is a strongly temporally oscillating buoyancy flux, indicative of strong upslope/downslope flow that occurs twice per wave period. It appears that the upslope flow, generated by a phase of the oncoming wave interacting with the presence of the boundary, is responsible for setting up wave overturning in the boundary layer, which leads to subsequent wave breakdown into turbulence.

Mixing efficiencies for the simulations have been examined and compared to a new, exact solution for a plane wave. The mixing efficiencies for critical angle reflection are approximately 0.35. The numerical experiments have also been successful in showing the behavior of internal wave reflection away from the critical angle. It was found that, close to critical conditions, the flow behaves in a fashion similar to the critical angle

flows, with similar mixing efficiencies and boundary layer thicknesses. It was also determined that off-critical reflection lengthens the mixing cycle for shallower slopes and shortens it for steeper slopes. Waves reflecting from slopes steeper than their critical angle exhibit increased dissipation rates and mixing, while waves reflecting from shallower slopes experience greater reflection from the boundary.

The wave breakdown process is essentially three-dimensional in nature. Two-dimensional simulations predict reasonable estimates of the times and general features of wave breakdown. They fail, however, to accurately predict important features such as boundary-layer thickness, mixing efficiency, and the length of time required for overturned waves to break.

The turbulence in the boundary layer radiates energy back upwards across the path of the oncoming internal waves. Changes to the background density profile and the generation of mean currents occur in regions significantly farther from the wall than the depth of the turbulent boundary layer. Mixing extends into the interior stratified fluid on relatively short time scales and is not restricted to a well-mixed boundary region. A key process in this interior communication is internal wave pumping of mixed fluid into the interior and stratified fluid into the boundary layer. A net result is a steady weakening of the interior stratification. After the mixed fluid is advected into the stratified regions, it is further transported into the interior along constant density surfaces. This process has important implications regarding for the capability of internal wave breakdown near sloping boundaries to make a large contribution to the overall vertical mixing in the ocean.

7.2 Recommendations

This thesis has focused on an important model problem that contains essential physics of internal wave interaction with sloping boundaries. The motivating problem from physical oceanography contains complexity not included in the present study. Important extensions may be pursued by increasing the complexity of the physical, mathematical, or numerical model. It is recommended that future work on this problem should represent more realistic oceanic conditions. As computational capabilities

continue to improve, complicated aspects of the problem will become more accessible to investigation. A number of extensions are suggested here.

- Consideration of internal waves that approach the boundary at oblique angles, out of the plane of the slope, should yield new information not obtained in this study. The problem includes increased across-shelf three-dimensionality, which could change the character of the mixing process. An especially attractive reason to study this case is that the current numerical model is capable of performing the simulations in its present form. Indeed, a number of preliminary low resolution oblique angle simulations were conducted to aid in code development.

- The current model is also capable of including rotational effects (Coriolis forces) in the flow. The oceanic internal wave field contains significant energy in low (inertial) frequencies that are influenced by rotational effects. As with oblique angle simulations, rotational effects increase the three-dimensionality of the problem. It is likely that each of these types of simulations would have lower transitional Reynolds numbers than the numerical experiments reported here, because of the enhanced three-dimensionality of the oncoming waves. In addition, it is expected that numerical studies should prove more useful than laboratory experiments for examining shallow bottom slopes (most common on the ocean floor) and low frequency internal waves (containing most of the oceanic internal wave energy). Laboratory experiments are especially difficult for low frequency waves because of their large horizontal wavelengths and long dimensions required for the bottom slope. For example, the experiment conducted in a four meter long wave tank by Ivey and Nokes (1989) for a 30^o slope would require a 47 meter long wave tank for a 3^o bottom slope experiment.

- Exploring higher Reynolds number regimes should be a primary focus future work. Large eddy simulations should be successful at reducing the influence of the high rates of kinetic energy dissipation that occurred in the viscous sublayer

in this study. Simulations at higher Reynolds (and Prandtl) numbers should be capable of providing useful information regarding mixing efficiencies and flow development for conditions similar to field experiments.

- The model could be modified in a straightforward manner to include broad-banded forcing of the wave field, typical of oceanic conditions. It would be interesting to see how the enhancement of waves close to the critical angle manifests itself in the presence of a typical oceanic internal wave field. Numerical experiments of this nature should provide more direct comparisons with field measurements.

- The issue of resuspension and deposition of particulates deserves closer study. Simple models for particle deposition and suspension from the boundary could be coupled with the current fluid dynamical model to examine sediment transport and optical properties of the water. In addition, the effects of particle loading on stratified turbulence and/or turbulence near a boundary could be explored more fully with this model. With simple changes to the initial conditions the numerical model developed for the wave reflection problem may be used as a general purpose boundary layer model.

- The fundamental question concerning the magnitude of the contribution of internal wave breakdown near sloping boundaries should be explored using theoretical methods. The energy in the internal wave field may be estimated as a function of wavelength and frequency as a probability density function using the Garrett and Munk spectrum at different latitudes. Probability density functions for the ocean bottom slopes may also be obtained. Together these should provide sufficient basis to estimate the global contribution of this process to diapycnal mixing in the ocean (using estimates based upon field, laboratory, and numerical experiments of mixing rates near the critical angle.) Eriksen (1985) has estimated that if just 8% of the internal wave energy is converted to mixing at the boundaries, then the process of internal wave reflection from

sloping boundaries would be a sufficient source to account for all of the vertical mixing in the ocean.

- Additional realism may be added to the mathematical model by including a variable background density gradient and/or background mean currents such as a bottom Ekman layer. This increasing level of complexity should provide new insights concerning the relative strength of wave breakdown to other boundary layer phenomena.

- Further analysis of the simulations already conducted may also prove valuable. For example, energy budgets might be examined on a zonal rather than global basis or alternative definitions of potential energy might be employed (Winters et al., 1995) to examine changes related to irreversible mixing. In addition, longer time integrations with the current model would be desirable, in order to examine the slow-time-scale evolution of the background flow and quasi-steady processes.

- One of the most interesting avenues of continuing research would be to compare two-dimensional models that employ turbulence closure and mixing models for stratified turbulence against three-dimensional direct numerical simulations. The potential exists to determine which of the simplified closure schemes is most accurate and appropriate, in some sense, for use in larger scale models that require parameterization of stratified turbulence.

- One of the most idealized assumptions in the current model is the smooth slope. Further model development would be required to permit the introduction of variable topography, but such an ability would be valuable for determining the behavior of internal wave reflection from concave and convex surfaces, or more generally, from topographic features of comparable length scales to the internal waves.

- Finally, a related problem involving amplification and reflection of internal gravity waves should be considered for examination. When internal wave packets or solitons progress towards shallower water, as in the coastal zone, their energy density increases. In this case, wave reflection occurs from both the ocean floor and the free surface. The associated wave amplification has been observed (e.g., Liu, 1988) to lead to turbulence and mixing.

BIBLIOGRAPHY

[1] Adam, Y. 1977: "Highly accurate compact implicit methods and boundary conditions", *J. Comp. Phys.,* **24,** 10-22.

[2] Anderson, D. A., Tannehill, J. C., Pletcher, R. H. 1984: *Computational Fluid Mechanics and Heat Transfer,* (Hemisphere Publishing, New York, 599 pp.)

[3] Armi, L. 1978: "Some evidence for boundary mixing in the deep ocean," *J. Geophys. Res.,* **83,** 1971-1979.

[4] Bell, J. B., Colella, P., Glaz, H. M. 1989: "A second-order projection method for the incompressible Navier-Stokes equations," *J. Comp. Physics,* **85,** 257-283.

[5] Bender, C. M., Orszag, S. A. 1978: *Advanced Mathematical Methods for Scientists and Engineers,* (McGraw-Hill, New York, 593 pp.)

[6] Bickley, W. G. 1948: *Quat. J. Mech. 1*, **260,** 35-42.

[7] Cacchione, D. A., Drake, D. E. 1986: "Nepheloid layers and internal waves over continental shelves and slopes," *Geo-Marine Letters,* **6,** 147-152.

[8] Cacchione, D. A., Southard, J. B. 1974: "Incipient sediment movement by shoaling internal gravity waves," *J. Geophys. Res.,* **79,** 2237-2242.

[9] Cacchione, D., Wunsch, C. 1974: "Experimental study of internal waves over a slope," *J. Fluid Mech.,* **66,** 223-239.

[10] Canuto, C., Hussaini, M. Y., Quarteroni, A., Zang, T. A. 1988: *Spectral Methods in Fluid Dynamics,* (Springer-Verlag, New York, 557 pp.).

[11] Chorin, A. J. 1984: "Book Review, Computational Methods for Fluid Flow," *Bull. Amer. Math. Soc.,* **5,** 87-89.

[12] Chorin, A. J. 1968: "Numerical solution of the Navier-Stokes equations," *Math. Comput.,* **22,** 745-762.

[13] Davies, H. C. 1983: "Limitations of some common lateral boundary schemes used in regional NWP models," *Monthly Weather Review,* **111,** 1002-1012.

[14] Davies, H. C. 1976: "A lateral boundary formulation for multi-level prediction models," *Quart. J. Royal Meteorol. Soc.,* **102,** 405-418.

[15] Delisi, D. P., Orlanski, I. 1975: "On the role of density jumps in the reflexion and breaking of internal gravity waves, *J. Fluid Mech.,* **69,** 445-464.

[16] Drazin, P. G. 1977: "On the instability of an internal gravity wave," *Proc. Roy. Soc. A,* **356,** 411-432.

[17] Durran, D. R., Klemp, J. P. 1983: "A compressible model for the simulation of moist mountain waves," *Mon. Weather Rev.,* **111,** 2341-2361.

[18] Durran, D. R. 1992: *Computational Fluid Dynamics for Atmospheric Modeling.* (Class Notes for Atmospheic Sciences 544 and 591, University of Washington, Unpublished Manuscript, "Numerical methods for the simulation of wavelike flow," 250 pp.)

[19] Durran, D. R. 1991: "The third-order Adams-Bashforth method: An attractive alternative to leapfrog time differencing," *Mon. Weather Rev.,* **119,** 3, 702-720.

[20] Durran, D. R., Brown, R., Slinn, D. N., Yang, M. J. 1993: "Towards more accurate wave-permeable boundary conditions," *Mon. Weather Rev.,* **121,** 604-620.

[21] Eriksen, C. C. 1995: "Internal wave reflection and mixing at Fieberling Guyot," to appear in *J. Geophys. Res., Oceans*

[22] Eriksen, C. C. 1985: "Implications of ocean bottom reflection for internal wave spectra and mixing," *J. Phys. Ocean.,* **15,** 9, 1145-1156.

[23] Eriksen, C. C. 1982: "Observations of internal wave reflection off sloping bottoms," *J. Geophys. Res.,* **87,** C1, 525- 538.

[24] Eriksen, C. C. 1978: "Measurements and models of fine structure, internal gravity waves, and wave breaking in the deep ocean," *J. Geophys. Res.,* **83,** C6, 2989-3009.

[25] Fletcher, C. A. J. 1991: *Computational Techniques for Fluid Dynamics, Volume II, Specific Techniques for Different Flow Categories,* (Springer-Verlag, New York, 493 pp.)

[26] Fortin, M., Peyret, R., Temam, R., 1971: "Calcul des ecoulements d'un fluide visqueux incompressible," in *Lecture Notes in Physics,* **8,** (Springer-Verlag, New York), 337-342.

[27] Fovell, R., Durran, D., Holton, J. R. 1992: "Numerical simulations of convectively generated gravity waves in the stratosphere," submitted to *J. Atmos. Sciences*

[28] Garrett, C. 1991a: "Marginal Mixing Theories," *Atmosphere-Ocean,* **29,** 313-339.

[29] Garrett, C. 1991b: "Paradigm Lost?", in *Dynamics of Oceanic Internal Gravity Waves,* proceedings Hawaiian Winter Workshop, Univerisity of Hawaii, 433-449.

[30] Garrett, C. 1990: "The role of secondary circulation in boundary mixing," *J. Geophys. Res.,* **95,** C3, 3181-3188.

[31] Garrett, C., Gilbert, D. 1988: "Estimates of vertical mixing by internal waves reflected off a sloping bottom," in *Small-scale Turbulence and Mixing in the Ocean,* J. C. J. Nihoul and B. M. Jamart, eds., (Elsevier, Amsterdam, 405-423.)

[32] Garret, C. 1979: "Comment on 'Some evidence for boundary mixing in the deep ocean' by Laurence Armi", *J. Geophys. Res.,* **84,** C8, 5095.

[33] Garrett, C., Munk, W. 1979: "Internal waves in the ocean," *Ann. Rev. Fluid Mech.,* **11,** 339-369.

[34] Garrett, C., Munk, W. 1972: "Oceanic mixing by breaking internal waves," *Deep-Sea Res.,* **19,** 823-832.

[35] Gargett, A. E. 1984: "Vertical eddy diffusivity in the ocean interior," *J. Marine Res.,* **42,** 359-393.

[36] Gear, C. W., Watanabe, D. S. 1974: "Stability and convergence of variable order multistep methods," *SIAM J. Numer. Anal.,* **11,** 5, 1044-1058.

[37] Gilbert, D., Garrett, C. 1989: "Implications for ocean mixing of internal wave scattering off irregular topography," *J. Phys. Ocean.,* **19,** 1716-1729.

[38] Gill, A. E. 1982: *Atmosphere-Ocean Dynamics,* (Academic Press, Orlando, 662 pp.)

[39] Gordon, R. L. 1980: "Boundary layer under near-inertial internal waves over a critically sloping bottom," *J. Phys. Ocean.,* **10,** 1032-1038.

[40] Gregg, M. C. 1987: "Diapycnal mixing in the thermocline: a review," *J. Geophys. Res.,* **92,** 5249-5286.

[41] Gresho, P. M. 1990: "On the theory of semi-implicit projection methods for viscous incompressible flow and its implementation via a finite element method

that also introduces a nearly consistent mass matrix. Part 1: Theory," *Intern. J. Numerical Methods in Fluids,* **11,** 587-620.

[42] Gresho, P. M., Sani, R. L. 1987: "On pressure boundary conditions for the incompressible Navier-Stokes equations," *Intern. J. Numer. Methods in Fluids,* **7,** 1111-1145.

[43] Hirsh, R. S. 1975: "Higher order accurate difference solutions of fluid mechanics problems by a compact differencing technique," *J. Comp. Phys.* **19,** 90-109.

[44] Hirst, E. 1991: "Internal wave-wave resonance theory: fundamentals and limitations," in *'Aha Huliko'a, Dynamics of Oceanic Internal Gravity Waves,* 211-226.

[45] Holmboe, J. 1962: "On the behavior of symmetric waves in stratified shear layers," *Geofys. Publ.,* **24,** 67-113.

[46] Holloway, G. 1980: "Oceanic internal waves are not weak waves," *J. Phys. Ocean.,* **10,** 906-914.

[47] Hopfinger, E. J. 1987: "Turbulence in stratified fluids: A review," *J. Geophys. Res.,* **92,** C5, 5287-5303.

[48] Itsweire, E. C., Helland, K. N., Van Atta, C. W. 1986: "The evolution of grid-generated turbulence in a stably stratified fluid," *J. Fluid Mech.,* **162,** 299-338.

[49] Ivey, G. N., Nokes, R. I. 1989: "Vertical mixing due to the breaking of critical internal waves on sloping boundaries," *J. Fluid Mech.*, **204,** 479-500.

[50] Ivey, G. N. 1987a: "The role of boundary mixing in the deep ocean," *J. Geophys. Res.,* **92,** C11, 11,873-11,878.

[51] Ivey, G. N. 1987b: "Boundary mixing in a rotating, stratified fluid," *J. Fluid Mech.,* **183,** 25-44.

[52] Ivey, G. N., Corcos, G. M. 1982: "Boundary mixing in a stratified fluid," *J. Fluid Mech.,* **121,** 1-26.

[53] Karniadakis, G. E., Israeli, M., Orszag, S. A. 1991: "High-order splitting methods for the incompressible Navier-Stokes equation," *J. Comp. Physics,* **97,** 414-443.

[54] Kim, J., Moin, P. 1985: "Application of a fractional-step method to incompressible Navier-Stokes equations," *J. Comp. Physics,* **59,** 308-323.

[55] Klemp, J. B., Lilly, D. K. 1978: "Numerical simulation of hydrostatic mountain waves," *J. Atmos. Sciences,* **35,** 78-107.

[56] Kreiss, H. O. 1972: *O. Math. Comput.,* **26,** 605-624.

[57] Kunze, E., Kennelly, M. A., Sanford, T. B. 1992: "The depth dependence of shear finestructure off point arena and near pioneer seamount," *J. Phys. Ocean.,* **22,** 1, 29-41.

[58] Kunze, E. 1990: "Observations of shear and vertical stability from a neutrally buoyant float," *J. Geophys. Res.,* **95,** 18,127-18,142.

[59] Ledwell, J. R., Watson, A. J., Law, C. S. 1993: "Evidence for slow mixing across the pycnocline from an open-ocean tracer-release experiment," *Nature,* **364,** 701-703.

[60] Lele, S. K. 1992: "Compact finite difference schemes with spectral-like resolution," *J. Comp. Physics,* **103,** 16-42.

[61] Lesieur, M. 1987: *Turbulence in fluids: Stochastic and numerical modelling,* (Martinus Nijhoff Publishers, Dordrecht, 286 pp.)

[62] Liu, A. K. 1988: "Analysis of nonlinear internal waves in the New York Bight," *J. Geophys. Res.,* **93,** 12317-12329.

[63] Lombard, P. N. 1994: *The stability of finite amplitude gravity waves,* (Ph.D. Thesis, University of Washington, 161 pp.)

[64] Lombard, P. N., Riley, J. J. 1995: "On the breakdown into turbulence of propagating internal waves," to appear in *Dynamics Atmos. Oceans.*

[65] MacCready, P., Rhines, P. B. 1991: "Buoyant inhibition of Ekman transport on a slope and its effect on stratified spin-up," *J. Fluid Mech.,* **223,** 631-661.

[66] MacCready, P., Rhines, P. B. 1991: "Slippery bottom boundary layers on a slope," *J. Phys. Ocean.* **23,** 5-22.

[67] Meid, R. R. 1976: "The occurrence of parametric instabilities in finite-amplitude internal gravity waves," *J. Fluid Mech.,* **78,** 763-784.

[68] Motz, H. 1946: *Quart. Appl. Math.,* **4,** 371-377.

[69] Müller, P., Holloway, G., Henyey, F., Pomphrey, N. 1986: "Nonlinear interactions among internal gravity waves," *Rev. of Geophys.,* **24,** 3, 493-536.

[70] Munk, W. H. 1966: "Abyssal recipes," *Deep-Sea Res.,* **13,** 707-730.

[71] Oakey, N. S. 1982: "Determination of the rate of dissipation of turbulent energy from simultaneous temperature and velocity shear microstructure measurements," *J. Phys. Oceanography,* **12,** 256-271.

[72] Olbers, D. J. 1983: "Models of the oceanic internal wave field," *Rev. of Geophys. Space Phys.,* **21,** 1567-1606.

[73] Orlanski, I. 1972: "On the breaking of standing internal gravity waves," *J. Fluid Mech.,* **54,** 577-598.

[74] Orlanski, I. Cerasoli, C. P. 1980: "Resonant and non-resonant wave-wave interactions for internal gravity waves," in *Marine Turbulenc,* J. C. J. Nihoul editor, (Elsevier Scientific Publishing Co.) 65-100.

[75] Pedlosky, J. 1987: *Geophysical Fluid Dynamics,* (Springer-Verlag, New York, 710 pp.)

[76] Peyret, R., Taylor, T. D. 1983: *Computational Methods for Fluid Flow,* (Springer-Verlag, New York, 358 pp.)

[77] Phillips, O. M., Shyu, J.-H., Salmun, H. 1986: "An experiment on boundary mixing: mean circulation and transport rates," *J. Fluid Mech.,* **173,** 473-499.

[78] Phillips, O. M., 1977: *The Dynamics of the Upper Ocean,* 2nd ed., (Cambridge University Press, New York, 336 pp.)

[79] Phillips, O. M., 1970: "On flows induced by diffusion in a stably stratified fluid," *Deep-Sea Res.,* **17,** 435-443.

[80] Pond, S., Pickard, G. L. 1983: *Introductory Dynamical Oceanography,* (Permagon Press, Oxford, 329 pp.)

[81] Rai, M. M., Moin, P. 1991: "Direct simulations of turbulent flow using finite-difference schemes," *J. Comp. Physics,* **96,** 15-53.

[82] Rehmann, C. R., Koseff, J. R. 1994: "Mixing efficiency of decaying grid turbulence in a stratified fluid," Fourth International Symposium on Stratified Flow, Institute de Mecanique, Grenoble, France.

[83] Rhines, P., MacCready, P. 1989: "Boundary control over the large-scale circulation," Proceedings of the 'Aha Huliko'a workshop, University of Hawaii.

[84] Riley, J. J., Lelong, M.-P., Slinn, D. N. 1990: "Organized structures in strongly stratitied flows", in *Turbulence and Coherent Structures,* M. Lesieur and O. Metais editors, (Kluwer Academic Publishers,) 413-428.

[85] Riley, J. J., Lelong, M.-P. J., Slinn, D. N., 1991: "Weak wave and vortex interactions," in *Dynamics of Oceanic Internal Gravity Waves,* proceedings Hawaiian Winter Workshop, Univerisity of Hawaii, 193-209.

[86] Roberts, J. 1975: *Internal gravity waves in the ocean,* (Marcel Dekker, Inc., New York, 274 pp.)

[87] Rohr, J., Van Atta, C. 1987: "Mixing efficiency in stabley stratified growing turbulence," *J. Geopys. Res.,* **92,** 5481-5488.

[88] Salmun, H., Phillips, O. M. 1992: "An experiment on boundary mixing, Part 2. The slope dependence at small angles," *J. Fluid Mech.*, **92,** 355-377.

[89] Sanford, L. P., Grant, W. D. 1987: "Dissipation of internal wave energy in the bottom boundary layer on the continental shelf," *J. Geophys. Res.,* **92,** C2, 1828-1844.

[90] Sorenson, R. M. 1993: *Basic wave mechanics: for coastal and ocean engineers,* (Wiley, New York, 284 pp.)

[91] Southard, J. B., Cacchione, D. A. 1972: "Experiments on bottom sediment movement by breaking internal waves," in *Shelf Sediment Transport,* (Edited by Swift, Duane, and Pilkey; Dowden, Hutchinson, and Ross, Inc. Stroudsburg, Pa.) 83-97.

[92] Squires, K. D., Eaton, J. K. 1990: "Particle response and turbulence modification in isotropic turbulence," *Physics of Fluids A*, **2,** 1191-1203.

[93] Stillinger, D. C., Helland, K. N., Van Atta, C. W. 1983: "Experiments on the transition of homogenoeus turbulence to internal waves in a stratified fluid, *J. Fluid Mech.,* **131,** 91-122.

[94] Taylor, J. R. 1993: "Turbulence and mixing in the boundary layer generated by shoaling internal waves," *Dynamics of Atmos. and Oceans,* **19,** 233-258.

[95] Temam, R. 1969: *Archiv. Ration. Mech. Anal.,* **32,** 377-385.

[96] Thomas, L. H. 1949: Elliptic problems in linear difference equations over a network, *Watson Sci. Comput. Lab. Rept.*, Columbia Univeristy, New York.

[97] Thorpe, S. A. 1992: "Thermal fronts caused by internal gravity waves reflecting from a slope," *J. Phys. Ocean.,* 22, 105-108.

[98] Thorpe, S. A. 1989: "The distortion of short internal waves produced by a long wave, with application to ocean boundary mixing," *J. Fluid Mech.*, **208,** 395-415.

[99] Thorpe, S. A. 1988: "Benthic boundary layers on slopes," in *Small-Scale Turbulence and Mixing in the Ocean,* J. C. J. Nihoul and B. M. Jamart editors, (Elsevier, Amsterdam) 425-433.

[100] Thorpe, S. A. 1987a: "Current and temperature variability on the continental slope," *Phil. Trans. R. Soc. London.,* A, **323,** 471-517.

[101] Thorpe, S. A. 1987b: "Transitional phenomena and the development of turbulence in stratified fluids: a review," *J. Geophys. Res.,* **92,** C5, 5231-5248.

[102] Thorpe, S. A., Haines, A. P. 1987: "On the reflection of a train of finite-amplitude internal waves from a uniform slope," *J. Fluid Mech.,* **178,** 279-302.

[103] Thorpe, S. A. 1982: "On the layers produced by rapidly oscillating a vertical grid in a uniformly stratified fluid," *J. Fluid Mech.,* **124,** 391-409.

[104] Turner, J. S. 1973: *Buoyancy Effects in Fluids*, (Cambridge University Press, 368 pp.)

[105] Weatherly, G. L., Martin, P. J. 1978: "On the structure and dynamics of the oceanic boundary layer," *J. Phys. Ocean.,* **8,** 557-570.

[106] Wijesekera, H., Padman, L., Dillon, T., Levine, M., Paulson, C., Pinkel, R. 1993: "The application on internal-wave dissipation models to a region of strong mixing," *J. Phys. Ocean.,* **23,** 269-286.

[107] Winters, K. B. 1989: *Intensification and instability of internal gravity waves at caustics and critical levels,* Ph.D. Thesis, University of Washington, 194 pp.

[108] Winters, K. B., Lombard, P. N., Riley, J. J., D'Asaro, E. A. 1995: "Available potential energy and mixing in density stratified fluids," *J. Fluid Mechanics,* **289,** 115-128.

[109] Winters, K. B., Riley, J. J., 1992: "Instability of internal waves near a critical level," *Dynamics of Atmos. and Oceans,* **16,** 249-278.

[110] Wunsch, C. 1970: "On oceanic boundary mixing," *Deep-Sea Res.,* **17,** 293-301.

[111] Wunsch, C. 1968: "On the propagation of internal waves up a slope," *Deep-Sea Res.,* **15,** 251-258.

Appendix A

SECOND DERIVATIVE VON NEUMANN BOUNDARY CONDITION

Taylor series expansions

$$f_2 = f + hf' + \frac{h^2}{2}f'' + \frac{h^3}{6}f''' + \frac{h^4}{24}f^{(4)} + \frac{h^5}{120}f^{(5)} + \cdots \ , \tag{A1}$$

$$f_3 = f + 2hf' + 2h^2f'' + \frac{4h^3}{3}f''' + \frac{2h^4}{3}f^{(4)} + \frac{4h^5}{15}f^{(5)} + \cdots \ , \tag{A2}$$

$$f_4 = f + 3hf' + \frac{9h^2}{2}f'' + \frac{9h^3}{2}f''' + \frac{27h^4}{8}f^{(4)} + \frac{81h^5}{40}f^{(5)} + \cdots \ , \tag{A3}$$

$$f_2'' = f'' + hf''' + \frac{h^2}{2}f^{(4)} + \frac{h^3}{6}f^{(5)} + \cdots \ , \tag{A4}$$

may be used to construct boundary conditions of various orders of accuracy for f'' using the compact scheme. Following the method suggested by Lele (1992), a 3rd-order accurate solution is sought to the equation

$$f_1'' + \alpha f_2'' = \frac{1}{h}af_1' + \frac{1}{h^2}\left[bf_2 + cf_3 + df_4\right] \ . \tag{A5}$$

Replacing (A1) - (A4) in (A5) yields

$$f'' + \alpha f'' + \alpha h f''' + \frac{\alpha h^2}{2}f^{(4)} + \frac{\alpha h^3}{6}f^{(5)} = \frac{a}{h}f' + \frac{b}{h^2}f +$$

$$\frac{b}{h}f' + \frac{b}{2}f'' + \frac{bh}{6}f''' + \frac{bh^2}{24}f^{(4)} + \frac{bh^3}{120}f^{(5)} + \frac{c}{h^2}f + \frac{2c}{h}f'$$

$$+2cf'' + \frac{4ch}{3}f''' + \frac{2ch^2}{3}f^{(4)} + \frac{4ch^3}{15}f^{(5)} + \frac{d}{h^2}f + \frac{3d}{h}f' +$$

$$\frac{9d}{2}f'' + \frac{9dh}{2}f''' + \frac{27dh^2}{8}f^{(4)} + \frac{81dh^3}{40}f^{(5)} + \cdots \ . \tag{A6}$$

The constraints on the coefficients are determined by setting equal powers of h to zero. The five constraints on the five undetermined coefficients, which yield 3rd-order accuracy, are

$$b + c + d = 0 \,, \tag{A7}$$

$$a + b + 2c + 3d = 0 \,, \tag{A8}$$

$$1 + \alpha = \frac{b}{2} + 2c + \frac{9d}{2} \,, \tag{A9}$$

$$\alpha = \frac{b}{6} + \frac{4c}{3} + \frac{9d}{2} \,, \tag{A10}$$

$$\frac{\alpha}{2} = \frac{b}{24} + \frac{2c}{3} + \frac{27d}{8} \,. \tag{A11}$$

The leading order error term is

$$\left(-\frac{\alpha}{6} + \frac{b}{120} + \frac{4c}{15} + \frac{81d}{40} \right) h^3 f^{(5)} \,. \tag{A12}$$

The solution of (A7) - (A11) is

$$\alpha = \frac{85}{29}, \quad a = -\frac{78}{29}, \quad b = -\frac{81}{29} \quad c = \frac{84}{29}, \quad d = -\frac{3}{29} \,. \tag{A13}$$

Hence, with (A13), equation (A5) yields the desired 3rd-order accurate boundary condition

$$f_1'' + \frac{85}{29} f_2'' = -\frac{78}{29h} f_1' + \frac{1}{h^2} \left[-\frac{81}{29} f_2 + \frac{84}{29} f_3 - \frac{3}{29} f_4 \right] \,, \tag{A14}$$

or alternatively

$$29 f_1'' + 85 f_2'' = -\frac{78}{h} f_1' + \frac{1}{h^2} \left[-81 f_2 + 84 f_3 - 3 f_4 \right] \,. \tag{A15}$$

The truncation error on the right hand side of (A15) is

$$\frac{89}{1740} h^3 f^{(5)} \approx \frac{1}{19.5} h^3 f^{(5)} \,. \tag{A16}$$

Appendix B

COMPACT FILTERING ON VARIABLE GRID

It was shown in Section 3.1.3 that the filtered field can be obtained on the uniform grid by (3.27)

$$0.4\check{u}_{i-1} + \check{u}_i + 0.4\check{u}_{i+1} = 0.4u_{i-1} + u_i + 0.4u_{i+1} - \frac{1}{80}\left(u_{i+2} - 4u_{i+1} + 6u_i - 4u_{i-1} + u_{i-2}\right) , \quad (B1)$$

which is equivalent to writing

$$0.4\check{u}_{i-1} + \check{u}_i + 0.4\check{u}_{i+1} = 0.4u_{i-1} + u_i + 0.4u_{i+1} - \frac{1}{5}(\Delta x)^4 \left.\frac{\partial^4 u}{\partial x^4}\right|_i . \quad (B2)$$

In the discussion on grid metrics in Section 3.4.4 the equivalent expression for the fourth derivative is given by (3.90)

$$\frac{\partial^4 u}{\partial z^4} = \Gamma_1^4(\zeta)\frac{\partial^4 u}{\partial \zeta^4} + 6\Gamma_1^2(\zeta)\Gamma_2(\zeta)\frac{\partial^3 u}{\partial \zeta^3} + \left[4\Gamma_1(\zeta)\,\Gamma_3(\zeta) + 3\Gamma_2^2(\zeta)\right]\frac{\partial^2 u}{\partial \zeta^2} + \Gamma_4(\zeta)\frac{\partial u}{\partial \zeta} , \quad (B3)$$

where Γ_1 – Γ_4 are given above in section 3.4.4. Combining equations (B2) and (B3) yields the fourth-order compact filter on the clustered grid

$$\begin{aligned} 0.4\check{u}_{i-1} + \check{u}_i + 0.4\check{u}_{i+1} = {} & 0.4u_{i-1} + u_i + 0.4u_{i+1} \\ & - \frac{1}{80}\left(u_{i+2} - 4u_{i+1} + 6u_i - 4u_{i-1} + u_{i-2}\right) \\ & - \frac{\Delta\zeta}{80}\left(\frac{6\Gamma_2}{\Gamma_1^2}\right)_i \left(\frac{u_{i+2} - 2u_{i+1} + 2u_{i-1} - u_{i-2}}{2}\right) \\ & - \frac{\Delta\zeta^2}{80}\left(\frac{4\Gamma_3}{\Gamma_1^3} + \frac{3\Gamma_2^2}{\Gamma_1^4}\right)_i \left(u_{i+1} - 2u_i + u_{i-1}\right) \\ & - \frac{\Delta\zeta^3}{80}\left(\frac{\Gamma_4}{\Gamma_1^4}\right)_i \left(\frac{u_{i+1} - u_{i-1}}{2}\right) . \end{aligned} \quad (B4)$$

Appendix C

LIST OF SYMBOLS

English Alphabet

a_n	N'th coefficient in Taylor series expansion
a_1	Coefficient for compact filter
a_ζ	A constant relating ζ and z
A	Amplitude in wave initialization and forcing
A_i	Amplitude of incident wave
$A_l(x)$	Variable coefficient in elliptic equation
A_n	N'th coefficient in numerator of Padé series expansion
A_f	Amplification factor from linear theory
$A_f(z)$	Shape funcion of emitted wave (cosine part)
A'_f	First derivative of $A_f(z)$
$A'''_f(z)$	Third derivative of $A_f(z)$
A_o	Amplitude of overturning wave
A_r	Amplitude of reflected wave
A_t	Coefficient for variable time step
$A_x(x, y, z)$	Variable coefficient in elliptic equation
$A_{xx}(x, y, z)$	Variable coefficient in elliptic equation
A_w	Wave amplitude
b_1	Coefficient for compact filter
b_ζ	A constant relating ζ and z
b	Coefficient determining width of $F(z)$

English Alphabet

$B_f(z)$	Shape funcion of emitted wave (sine part)
B'_f	First derivative of $B_f(z)$
$B'''_f(z)$	Third derivative of $B_f(z)$
B_f	Buoyancy flux
$\overline{B_f}$	Integrated buoyancy flux
B_i	Finite difference value at grid point i
$B_l(x)$	Variable coefficient in elliptic equation
B_m	M'th coefficient in denominator of Padé expansion
B_t	Coefficient for variable time step
$B_y(x,y,z)$	Variable coefficient in elliptic equation
$B_{yy}(x,y,z)$	Variable coefficient in elliptic equation
BF_t	Volume integral of buoyancy flux
c_1	Coefficient for compact filter
$C_M(x,y,z)$	Variable coefficient in elliptic equation
$C_l(x)$	Variable coefficient in elliptic equation
C_{fl}	Courant number
$\vec{C}_g$	Wave group velocity
C_{gx}	x-component of group velocity
C_{gz}	z-component of group velocity
$\vec{C}_{ph}$	Phase velocity
C_t	Coefficient for variable time step
$C_z(x,y,z)$	Variable coefficient in elliptic equation
$C_{zz}(x,y,z)$	Variable coefficient in elliptic equation
C_1	Constant in wave forcing analytic solution
C_2	Constant in wave forcing analytic solution

English Alphabet

C_3	Constant in wave forcing analytic solution
dx	Differential element in x direction
dz	Differential element in z direction
d_1	Coefficient for compact filter
D	Estimate of viscous dissipation
$D(z_o)$	Diffusion coefficient at height z_o
$D_{f_{ke}}$	Dissipation of kinetic energy by filter
$D_{f_{pe}}$	Dissipation of potential energy by filter
D_{ke}	Volume integral of dissipation of kinetic energy
D_{pe}	Volume integral of dissipation of potential energy
D_x	Coefficient in stability analysis
D_z	Coefficient in stability analysis
e	2.718281828
E_r	Energy density of reflected waves
E_i	Energy density of incident waves
f	An arbitrary example function
f'	First derivative of f
f_1	Value of a function f at grid point 1
f_1''	Second derivative of f at grid point 1
$f^{(5)}$	Fifth derivative of arbitrary function f
$F(z)$	Wave packet localization function
$F'(z)$	Localization function derivative
$F'''(z)$	Third derivative of localization function
F_{max}	Maximum height of $F(z)$
Fr	Froude number

English Alphabet

F_ρ	Wave forcing function for density equation
$\mathcal{F}^n$	Flux of U at time level n
g	Gravitational acceleration
$\mathbf{g}$	Gravity vector
$G(z)$	Grid metrics inverse transform function
$G_1(z)$	Grid metrics inverse transform function
$G_2(z)$	Grid metrics inverse transform function
h	Grid spacing in arbitrary direction
H	Heat loss coefficient
i	$\sqrt{-1}$
$\hat{i}$	Unit vector in x-direction
$\imath_{\mathbf{3}}$	Unit vector in z direction
$\hat{j}$	Unit vector in y-direction
j	An integer counter (depending on context)
k	Wavenumber in x direction
k'	Wavenumber in x' direction
k'_r	Reflected wavenumber in the x'-direction
k'_i	Incident wavenumber in the x'-direction
$\hat{k}$	Unit vector in z-direction
$\vec{k}$	Wavenumber
K	Cutoff wavenumber in truncated Fourier series
KE_t	Volume integral of total kinetic energy
$\overline{KE}$	Integrated kinetic energy
l	Wavenumber in y direction
l'	Wavenumber in y' direction

English Alphabet

L	Characteristic length scale
L_F	Characteristic width of $F(z)$
L_x	Maximum boundary $0 \leq x \leq L_x$
L_y	Maximum boundary $0 \leq y \leq L_y$
L_z	Maximum boundary $0 \leq z \leq L_z$
m	Wavenumber in z direction
m'	Wavenumber in z' direction
m'_r	Reflected wavenumber in the z'-direction
m'_i	Incident wavenumber in the z'-direction
m_f	Vertical wavenumber of resonantly forced wave
ME_t	Volume integral of mixing efficiency
m_i	Vertical wavenumbers of incident wave
m_r	Vertical wavenumbers of reflected wave
MSV_t	Volume integral of mean square vorticity
n	An integer counter (depending on context)
N_m	Number of terms in Fourier series
N	Buoyancy frequency
$\mathbf{N}$	Normal vector to boundary surface
N_L	Local buoyancy frequency
$\tilde{p}$	Dimensional perturbation pressure field
$p(x, y, z)$	Perturbation pressure field
$\overline{p}^{n+1}$	Pressure average between time n and $n+1$
p_o	Reference pressure in hydrostatic balance
$\tilde{p}_t$	Total pressure field
P	Gain in potential energy per wave period

English Alphabet

$\overline{PE}$	Integrated potential energy
Pr	Prandtl number
$P_M^N(x)$	Padé series, N terms in numerator M terms in denominator
PE_t	Volume integral of total potential energy
P_x	Periodicity for Fourier decomposition is $2P_x$
$R(x,z)$	Right hand side of second order elliptic equation
R	Radiation coefficient
Re	Reynolds number
Re_d	Dissipation Reynolds number
Re_δ	Boundary layer Reynolds number
Re_w	Wave Reynolds number
Ri	Richardson number
Ri_{λ_z}	Richardson number based upon vertical wavelength
Ri_L	Local Richardson number
S_D	Scalar dye field added to flow
S	Salinity
Sc	Schmidt number
Sp_{ke}	Kinetic energy absorbed by sponge layer
S_w	Shear in the oncoming wave
t	Time
$\tilde{t}$	Dimensional time
t_f	Final time for mixing integration
t_i	Initial time for mixing integration
T	Temperature
$T_N(x)$	N terms of a Taylor series expansion

English Alphabet

TE_t	Volume integral of total energy
$\overline{TE}$	Integrated total energy
$T_c(\omega_c)$	Transfer function for compact filter
T_B	Buoyancy period
T_M	Period of mixing cycle
T_w	Wave period
T_{W_c}	Wave period at critical frequency
$\mathbf{u}(\mathbf{x}, \mathbf{y}, \mathbf{z})$	Velocity field
$\tilde{\mathbf{u}}$	Dimensional velocity field
$\tilde{u}$	Dimensional u velocity
$u(x, y, z)$	Velocity component in x direction
$u_{i,k}$	Discrete function value at 2-D grid point (i, k)
$\hat{u}$	Fourier transform of u
$\breve{u}_i$	One dimensional filtered value of u_i
$\breve{u}_{i,k}$	Two dimensional filterd value of $u_{i,k}$
$\mathbf{u}^*$	Auxiliary velocity field in fractional time step
$\mathbf{u^n}$	Velocity field at time level n
u_{xi}	First derivative at grid point i
$u_{xx(i+1)}$	Second derivative at grid point i
$\tilde{u}_3$	Dimensional velocity in z direction
$\vec{u}_p(x, y, z, t)$	Fluid velocities at particle locations
U	Characteristic velocity scale
$\bar{U}(x)$	Mean velocity for linearization
U_m	Maximum current speed in oncoming wave
U_p	Peak velocity in the boundary layer

English Alphabet

U_w	Current speed of the oncoming wave
U_{max}	Maximum velocity in flow field
U_∞	Maximum velocity in the boundary layer
$\tilde{v}$	Dimensional v velocity
$v(x, y, z)$	Velocity component in y direction
$\overline{v}_{rms}(z)$	Rms average v component of velocity
$w(x, y, z)$	Velocity component in z direction
$\tilde{w}$	Dimensional w velocity
$w'_m(k\Delta x)$	Modified wavenumber of first derivative
$w''_m(k\Delta x)$	Modified wavenumber of second derivative
W_{KE}	Work input to the kinetic energy equation
W_{PE}	Work input to the potential energy equation
w'	Velocity component in the z'-direction
W	Work input to generate the internal wave
$\tilde{x}_3$	Dimensional coordinate in z direction
$\mathbf{x}$	Coordinate system
(x, y, z)	Cartesian (or rotated) coordinate system
(x', y, z')	Rotated coordinate system
x'	Alongslope direction
x_l	Domain length scale x-direction
$\vec{X}_p(x, y, z, t)$	Particle locations
y'	Across-slope direction
y_l	Domain length scale y-direction
z'	Off-slope direction
z_o	Initial height of particle release

Greek Alphabet

α	Angle of bottom slope
α_1	Coefficient for compact filter
β	Diffusion stability parameter
β_1	Coefficient for compact filter
β_ρ	Diffusion stability limit for density equation
γ	Constant used in Phillips solution
γ_4	Filter strength coefficient
$\Gamma_1(\zeta)$	Grid metrics transform function
$\Gamma_2(\zeta)$	Grid metrics transform function
$\Gamma_3(\zeta)$	Grid metrics transform function
$\Gamma_4(\zeta)$	Grid metrics transform function
δ	Boundary layer thickness
δ_{mixed}	Boundary mixed layer thickness
Δt	Discrete time step interval
Δt_1	Time step between time level $n+1$ and n
Δt_2	Time step between time level n and $n-1$
Δt_3	Time step between time level $n-1$ and $n-2$
Δx	Distance between grid points in x direction
Δy	Distance between grid points in y direction
Δz	Distance between grid points in z direction
Δz_{min}	Smallest grid spacing on variable grid
$\Delta\zeta$	Grid spacing on uniform computational grid
$\frac{\partial}{\partial x}$	Partial derivative operator
$\frac{\partial u}{\partial x}_i$	Difference derivitive at point i
$\overline{\frac{\partial u}{\partial x}}(z)$	Average shear as a function of height

Greek Alphabet

$\frac{\partial u}{\partial z}\Big\vert_w$	Wall shear component
ϵ	Dissipation rate
ϵ_f	Kinetic energy removed by filter
κ_v	Vertical eddy diffusivity
κ	Coefficient of diffusion of density
κ_s	Coefficient of diffusivity of scalar dye
λ	Wavelength
λ_P	Characteristic wavelength of the wave packet
λ_x	Horizontal wavelength in x direction
λ_y	Horizontal wavelength in y direction
λ_z	Vertical wavelength
$\lambda_{x'i}$	Wavelength of incident wave in x' direction
$\lambda_{x'r}$	Wavelength of reflected wave in x' direction
λ_{zi}	Vertical wavelength of incident wave
λ_{zr}	Vertical wavelength of reflected wave
μ	Arbitrary function in Rayleigh damping discussion
μ_{io}	Target for ϕ in sponge layer
$\overline{\mu}n$	Relaxed value in sponge layer at time level n
ν	Kinematic viscosity
ν_τ	Turbulent eddy viscosity
η	Mixing efficiency
η_o	Overall mixing efficiency
η_1	Actual mixing efficiency
η_2	Field based definition for mixing efficiency

Greek Alphabet

η_3	Laboratory based definition for mixing efficiency
η_4	Alternate definition for mixing efficiency
π	3.141592654...
ϕ	$(kx + mz - \omega t)$
Φ	Viscous dissipation function
Φ_ρ	Potential energy dissipation function
ψ	Solution function for steady forcing
Ψ	Forcing stream function
Ψ_v	Stream function for visualization
$\tilde{\rho}$	Dimensional fluctuating density field
$\tilde{\rho}_t$	Total density field
$\rho(x, y, z)$	Perturbation density field
ρ_o	Background density
$\frac{\partial \overline{\rho}}{\partial z}$	Background density gradient
σ_i	Damping coefficient at grid point i
θ	Angle of wave propagation
θ_{Cg_i}	Angle of group velocity from horizontal
χ	Potential energy dissipation rate
χ_f	Potential energy removed by filter
ζ	Offslope coordinate used in variable grid

Greek Alphabet

ω	Internal wave frequency
ω_c	Frequency of Fourier wavenumber
ω_I	Imaginary part of wave frequency
ω_R	Real part of wave frequency
ω_f	Frequency of resonantly forced wave
ω_r	Frequency of reflected wave
ω_i	Frequency of incident wave
$\vec{\omega}$	Vorticity vector
ω_x	Vorticity component in x-direction
ω_y	Vorticity component in y-direction
ω_z	Vorticity component in z-direction
$\lvert\vec{\omega}\rvert$	Vorticity magnitude
$\mathbf{\Omega}$	Rotation vector of the reference frame

Other Symbols

∞	Infinity
$(\tilde{})$	A dimensional quantity
$(\_)$	Spatially integrated value
$\tilde{\nabla}$	Dimensional gradient operator
$\tilde{\nabla}^2$	Dimensional Laplacian operator
∇	Gradient operator
∇^2	Laplacian operator
$O(\Delta x)$	Big O, "of the order of"

VITA

Donald N. Slinn

Education

- Ph.D. in Mechanical Engineering, University of Washington, 1995.
- M.S. in Mechanical Engineering, University of Washington, 1989.
- B.S. in Mechanical Engineering, Brigham Young University, 1988.

Publications

- J. J. Riley, M.-P. Lelong, D. N. Slinn, 1990. "Organized structures in strongly stratified flows," in *Turbulence and Coherent Structures,* 413-428, (M. Lesieur and O. Metais, eds.), Kluwer Academic Publishers, Boston.
- J. J. Riley, M.-P. Lelong, D. N. Slinn, 1991. "Weak wave and vortex interactions," in *Dynamics of Oceanic Internal Gravity Waves,* 193-209, (P. Muller and C. Miles eds.), Hawaii Institute of Geophysics, Honolulu.
- D. N. Slinn, J. J. Riley, 1992. "Vertical mixing due to internal wave reflection off a sloping boundary," Proceedings, AMS Tenth Symposium on Turbulence and Diffusion, J5, 113-116, American Meteorological Society, Boston.
- D. R. Durran, M. Z. Yang, D. N. Slinn, R. Brown, 1993. "Toward more accurate wave-permeable boundary conditions," *Monthly Weather Review,* **121**, 604-620.

- D. N. Slinn, J. J. Riley, 1995. "Turbulent mixing in the oceanic boundary layer due to internal wave reflection from sloping terrain," accepted for publication in *Dynamics of Atmospheres and Oceans*.

- D. N. Slinn, 1995. "Numerical simulation of turbulent mixing caused by internal wave reflection from sloping boundaries," Ph.D. Dissertation, University of Washington.

Professional Affiliations

- American Society of Mechanical Engineers (ASME)

- American Meteorological Society (AMS)

- American Geophysical Union (AGU)

Address

Donald Slinn
2215 Benton Ave.
Richland, Wa. 99352
(509) 375-4150 hm
email: slinn@reynolds.me.washington.edu